Functionalization of aeronautical thermal barrier systems elaborated by slurry (FONBAT)

Benjamin Grégoire

ÉCOLE DOCTORALE

Sciences et Ingénierie en Matériaux, Mécanique, Energétique et Aéronautique (SIMMEA)

Université de la Rochelle

Laboratoire des Sciences de l'Ingénieur pour l'Environnement - LaSIE (UMR–CNRS 7356)

THÈSE DE DOCTORAT

Présentée et soutenue le 24 Novembre 2017 par :

Benjamin GRÉGOIRE

pour l'obtention du grade de Docteur de l'Université de La Rochelle

Discipline : Chimie des Matériaux

Fonctionnalisation des barrières thermiques aéronautiques élaborées par barbotines (FONBAT)

Composition du jury :

Rapporteurs :	
Pr. Michel VILASI	Professeur à l'Université de Lorraine
Dr. HDR Vladislav KOLARIK	Directeur de recherche à l'Institut Fraunhofer ICT (Allemagne)
Examinateurs :	
Dr. Bruno MORTAIGNE	Directeur scientifique à la DGA-Ministère de la Défense
Dr. HDR Xabier MONTERO	Chargé de recherche HDR à la DECHEMA-Forschungsinstitut (Allemagne)
Dr. Maël MOLLARD	Ingénieur de recherche, Air France Industries
Dr. Luc BIANCHI	Ingénieur de recherche, SAFRAN TECH
Directeurs de thèse :	
Pr. Fernando PEDRAZA	Professeur à l'Université de La Rochelle
Pr. Gilles BONNET	Professeur à l'Université de La Rochelle

ÉCOLE DOCTORALE

Sciences et Ingénierie en Matériaux, Mécanique, Energétique et Aéronautique (SIMMEA)

Université de la Rochelle

Laboratoire des Sciences de l'Ingénieur pour l'Environnement - LaSIE (UMR–CNRS 7356)

THÈSE DE DOCTORAT

Présentée et soutenue le 24 Novembre 2017 par :

Benjamin GRÉGOIRE

pour l'obtention du grade de Docteur de l'Université de La Rochelle

Discipline : Chimie des Matériaux

Functionalization of aeronautical thermal barrier systems elaborated by slurry (FONBAT)

Composition du jury :

Rapporteurs :	
Pr. Michel VILASI	Professeur à l'Université de Lorraine
Dr. HDR Vladislav KOLARIK	Directeur de recherche à l'Institut Fraunhofer ICT (Allemagne)
Examinateurs :	
Dr. Bruno MORTAIGNE	Directeur scientifique à la DGA-Ministère de la Défense
Dr. HDR Xabier MONTERO	Chargé de recherche HDR à la DECHEMA-Forschungsinstitut (Allemagne)
Dr. Maël MOLLARD	Ingénieur de recherche, CRMA - Air France Industries
Dr. Luc BIANCHI	Directeur de recherche, SAFRAN TECH
Directeurs de thèse :	
Pr. Fernando PEDRAZA	Professeur à l'Université de La Rochelle
Pr. Gilles BONNET	Professeur à l'Université de La Rochelle

Remerciements

Ces travaux de thèse se sont déroulés dans l'axe B2 « Protection des matériaux et revêtements » du laboratoire LaSIE (UMR-CNRS 7356). Je tiens en premier lieu à remercier le Professeur Karim Aït-Mokhtar, directeur du laboratoire, pour son accueil au sein du LaSIE.

Je remercie vivement la Direction Générale de l'Armement (DGA – Ministère de la Défense et Ministère des Armées) pour le soutien financier apporté au long de ces trois années de thèse (bourse n° 2014.60.0059). Je remercie particulièrement les personnes qui ont assuré le suivi administratif de la thèse. Mes sincères remerciements à Monsieur Bruno Mortaigne, membre de l'état-major des armées et directeur scientifique au sein de la DGA, pour son accompagnement au cours de la thèse et pour l'honneur qu'il me fait de participer à mon jury de thèse.

J'adresse mes sincères remerciements au Professeur Michel Vilasi (Institut Jean Lamour, Université de Lorraine) et au directeur de recherche Vladislav Kolarik (Fraunhofer ICT, Allemagne) pour avoir accepté de rapporter la thèse. Je leur souhaite une très bonne lecture et me réjouit de bénéficier de leur expérience pour la discussion des résultats.

Je tiens à remercier le Docteur Luc Bianchi (Directeur de recherche à SAFRAN TECH, Châtellerault) et le Docteur Maël Mollard (Ingénieur de recherche à CRMA - Air France Industries, Elancourt) pour leur participation au jury et pour leur évaluation de ces travaux de recherche avec leur expérience du secteur aéronautique. Je remercie chaleureusement le Docteur Xabier Montero (Chargé de recherche HDR à la DECHEMA-Forschungsinstitut, Allemagne) de participer à mon jury de thèse et pour son précieux soutien lors de mon séjour à la DECHEMA.

Je souhaite exprimer ma profonde reconnaissance à mes directeurs de thèse, les Professeurs Fernando Pedraza et Gilles Bonnet. Merci de m'avoir transmis le virus de la « haute température » depuis mes années d'études en Licence jusqu'à ce jour. Votre soutien, vos conseils avisés et votre sympathie permanente ont grandement facilité la bonne conduite de la thèse et sa réussite. Je vous remercie de votre disponibilité et de votre patience tout au long de la thèse aussi bien pour l'encadrement scientifique que pour les relations humaines. Je garderai un très bon souvenir de la thèse pour laquelle vous avez été des piliers essentiels. Les échecs que l'on doit parfois surmonter sont finalement nos plus grandes réussites dans une formation telle que le doctorat.

Remerciements

Je tenais à remercier très chaleureusement le Docteur Mathias Galetz et une nouvelle fois le Docteur Xabier Montero de m'avoir accueilli au sein de la DECHEMA à Francfort. Merci de m'avoir consacré de votre temps pour la bonne conduite de mon séjour et pour la transmission de votre savoir. J'ai beaucoup appris au cours de ces trois mois et j'espère que nous pourrons travailler de nouveau en collaboration dans le futur. Merci à toute l'équipe « HTW » de la DECHEMA pour son accueil très chaleureux et pour les échanges très constructifs auxquels j'ai pu participer. Je remercie en particulier Monsieur Gerald Schmidt et Madame Mélanie Braun pour les analyses EPMA. Sincères remerciements à Monsieur Mathias Röhrig pour son aide hors-pair lors du montage des essais de corrosion à chaud.

Je remercie également Madame Josseline Balmain, maître de conférences au LaSIE, pour ses précieux conseils lors de la préparation des essais de traitement thermique. Je remercie tout spécialement Monsieur Baptiste Bouchaud, ex-Ingénieur de recherche au LaSIE et travaillant maintenant chez GE, pour m'avoir donné goût aux sciences expérimentales lors de mon stage de Master 1. Je voudrais faire un clien d'œil à Monsieur John Twomey, mon tuteur de stage de fin d'études chez SR Technics à Cork (Irlande). Merci John de votre bienveillance lors de mon séjour sur l'île d'Emeraude et de m'avoir convaincu de réaliser une thèse.

Je voudrais remercier l'ensemble des personnels techniques pour leur disponibilité et leur aide précieuse pour toutes les questions « pratiques » du laboratoire, merci à vous Christelle, Cyril, Stéphane, Mathieu et (la star du labo) Bruno. Un grand merci au personnel administratif de l'Université, merci à Martine, Nadine, Camille, Isabelle Gaubert, Jennifer, Isabelle Hirsch et Roselyne. Je remercie également Egle et Guillaume pour la préparation des séances de microscopie et les nombreux échanges que j'ai eus avec vous au cours de ces trois années.

J'en viens à mes partenaires de la « HT team ». Merci à toi ma biche (Claire) et à toi boy (Germain) pour tous ces bons moments passés ensemble. Nos routes vont peut-être se séparer à l'avenir mais nous resterons à jamais liés par cette aventure commune. J'ai du mal à réaliser que l'après-thèse peut signifier sans Claire ou sans Germain, enfin du moins sans vous comme voisins de paillasse…

Je remercie tous les doctorants, post-docs, stagiaires et ingénieurs d'étude que j'ai côtoyés au sein du laboratoire tout au long de ma thèse pour leur bonne humeur, leurs conseils et leur soutien. La liste serait bien trop longue entre les « anciens » et les « jeunes » du labo mais le cœur y est ! Bonne continuation à mes partenaires de promo : Charlotte, Claiiiiire, Rymiaou, Shaq, Mr. Li et à toi l'Auvergnat. Et bonne chance à tous ceux qui se sont lancés ou se lancent dans l'aventure !

Je voudrais terminer mes remerciements par ma famille. Merci à mes parents, ma soeusoeur, mes frérots et leurs pièces rapportées, pour leur soutien infaillible et leurs encouragements. Merci de leur patience et de toutes les valeurs qu'ils ont pu me transmettre. Et enfin, merci à vous mes poussins et mes poulettes d'avoir toujours cru en tonton Benj.

Introduction

The selection of structural materials for a given application is generally firstly based on their mechanical properties (mechanical engineering) and then on their environmental resistance (surface engineering). By optimizing these two factors, it is therefore possible to increase the durability of the structural materials since their degradation is unavoidable with time.

Metallic materials are used in a wide field of structural applications including aero and land-based gas turbine engines. For such applications, metallic materials are carefully designed by adjusting their chemical composition and microstructure to meet the highly-demanding mechanical resistance. In the hottest sections of gas turbine engines, the high-temperature resistance of the metallic materials is of utmost importance for safety, economic and environmental considerations. For aeronautical applications, antagonist properties are generally required since the materials must exhibit superior mechanical properties, high surface stability (corrosion and oxidation resistance), lightweight and also be cost effective.

Gas turbine components (blades, vanes and disks) are submitted to highly corrosive environments (O_2, SO_2, H_2O) with pressurized hot gases, combustion impurities and different types of erosive particles (sand, salts, volcanic ashes, etc.). To withstand these extreme conditions, nickel-based superalloys are employed because their improved microstructure based on coherent γ-γ' precipitation and optimized chemistry provide high creep and fatigue resistance at elevated temperatures (mechanical engineering).

In contrast, the surface stability of nickel-based superalloys is not sufficiently adequate over extended exposures at high temperatures under corrosive conditions. Therefore, the application of protective coatings on the surface allows to limit the corrosion and oxidation of the substrates (surface engineering). The application of protective coatings significantly increases the high-temperature surface stability of nickel-based superalloys and are essential for the integrity of gas turbine components in such aggressive environments. Depending on the temperature regime, different modes of degradation can be observed including hot corrosion, oxidation and CMAS (Calcium Magnesium Alumino-Silicates)-induced degradation phenomena.

Based on the Brayton thermodynamic cycle, the efficiency of gas turbine engines is a direct consequence of the turbine inlet temperature (TIT). The higher this temperature, the greater the thermodynamic efficiency of the engine. Increasing the TIT by 50°C enhances the specific thrust by 10% and reduces the fuel consumption by 5%. Consequently, this temperature has been continuously risen since the beginning of modern aviation and the materials employed had to be more and more resistant. The increasing TIT also affected the usually non-attacked components (low stages of the turbine) to become sensitive to high-temperature corrosion. This will in future broaden the application of protective coatings to these stages.

For high-temperature oxidation resistance, industrial protective coatings are usually based on CVD-related techniques to enrich the surface of nickel-based superalloys with Al (i.e. nickel aluminide coatings). The nickel aluminide coatings, based on the β-NiAl phase, decrease the oxidation kinetics of the underlying substrate by forming a dense and continuous α-Al_2O_3 scale on the surface. When spallation of the α-Al_2O_3 scale occurs upon thermal cycling conditions (in particular because of thermal stresses induced by the fast cooling from elevated temperatures), the β-NiAl phase promotes the outward diffusion of Al for its selective oxidation into α-Al_2O_3. For the hottest sections (i.e. high-pressure turbine or HPT), thermal barrier coatings (TBC) combined with internal cooling schemes are employed to decrease the surface temperature of the turbine components. The thermal barrier coatings, with low thermal conductivity, are usually based on YSZ (Yttria-Stabilized Zirconia). The combination of the metallic bond coat (usually a Pt-modified aluminide coating) and the ceramic top coat constitutes a so-called complete thermal barrier system. When hot corrosion resistance is required, Si and Cr enrichments offer the best protection forming respectively SiO_2 and Cr_2O_3 at intermediate temperatures (between 600 and 1000°C). The corrosion resistance is usually conferred with thermal spray coatings (MCrAlY and MCoCrAlY coatings) or Si-modified aluminide coatings.

The increasing TIT implies that the turbine components of the low stages will need to be coated to fight against hot corrosion and that the thermal barrier systems will be extrapolated to the first stages of the low-pressure turbine (LPT). It is worth to notice that the conventional industrial processes handle hazardous chemicals (halide activators, chromic acid, etc.) and can produce lots of waste in the particular case of pack-cementation. Moreover, these coating processes are time-consuming as they involve many different steps. Therefore, to comply with environmental and safety regulations (e.g. REACh, Registration Evaluation Authorization and Restriction of Chemicals), new approaches have been developed in the last decades for the high-temperature protection of metallic materials.

As a promising alternative approach, different studies have been carried out in the LaSIE laboratory under the European FP7 project "PARTICOAT". This approach was based on the formation of a complete thermal barrier system (metallic bond coat + oxide scale + ceramic barrier coating) from water-based Al microparticles-containing slurries. The complete thermal barrier system was formed in a single-step process with a nickel aluminide bond coat and a ceramic top coat composed of hollow Al_2O_3 spheres. The thermal insulation performances of these ceramic top coats appear greater than that of industrial YSZ thermal spray coatings, which lets expect their potential applications as thermal barrier systems. However, these thermal barrier systems present a low resistance to erosion and meet some limits because of the formation of inward grown coatings with high-activity microstructures.

Therefore, the main objectives of the present study were to control the activity of Al upon the slurry aluminizing process of nickel-based materials by introducing tailored amounts of Cr microparticles in the composition of the slurry or by changing the periodicity of the Cr and Al deposited layers. We focused our studies on the influence of the coating process parameters on the formation of the metallic bond coats and the complete thermal barrier systems. The present study focused on the addition of Cr microparticles in the Al slurry compositions as a potential candidate to overcome the above-mentioned limitations.

This manuscript has been structured in 6 main chapters:

Chapter I presents the state of the art and the industrial context for the high-temperature corrosion and protection of metallic materials in gas turbine engines. A general overview of the technological outcomes is given. The different modes of degradation encountered in gas turbine engines and their solution in the form of protective coatings are also introduced.

Chapter II describes the experimental methods of the present study including the materials of study, the elaboration of the slurry coatings and the environmental degradation tests performed. The characterization techniques carried out in this work are also presented.

In Chapter III, the influence of Cr additions on the exothermic reactions occurring between Al microparticles and nickel substrates is investigated. Different coating architectures were tested on pure nickel for a better comprehension of the mechanisms of formation before extrapolation to a Ni-Cr alloy and a nickel-based superalloy in Chapter IV.

The influence of the atmosphere (Ar, air) on the formation of complete thermal barrier systems is studied in Chapter V as well as the role of Cr on the involved aluminothermic reactions.

Finally, Chapter VI presents the environmental resistance of the slurry coatings designed in this work. Hot corrosion and oxidation tests were performed to evaluate the protective behaviour of the slurry coatings.

Table of contents

Introduction 1

Chapter I – State of the art: context and motivations of the study 10

I. Degradation and durability of metallic materials 11

II. Gas turbine engines: selection of the materials for high-temperature applications. 13

III. Nickel-based superalloys for gas turbine components 15

III.1. Generalities 15

III.2. Microstructural and compositional evolution 17

IV. Degradation of metallic materials at high-temperature 19

IV.1. Oxidation 19

IV.2. Hot corrosion 20

IV.3. Need for high-temperature protection of nickel-based superalloys 23

V. High-temperature protection of nickel-based superalloys 24

V.1. High-temperature protection: an overview 24

V.2. Aluminium diffusion coatings 25

V.3. Thermal Barrier Coatings (TBC) 28

V.4. Degradation of protective coatings in operation 29

VI. Motivations of the present study: from "PARTICOAT" to "FONBAT" 31

VI.1. Presentation of the "PARTICOAT" concept 31

VI.2. Functionalization of aeronautical thermal barrier systems elaborated by slurry (FONBAT) .. 33

References 35

Chapter II - Experimental methods 40

I. Materials of study 41

II. Elaboration of the slurry coatings on metallic substrates 44

II.1. Characterization of the metallic powders 44

II.2. Composition and preparation of the slurries 46

II.3. Deposition of the slurries by air brush on metallic substrates 47

II.4. Thermal treatments 49

III. Environmental degradation of the slurry coatings 50

III.1. Isothermal and cyclic oxidation 51

III.2. Hot corrosion tests 53

IV. Characterization methods 55

IV.1. Calorimetry and thermal analyses 55

a) Differential Scanning Calorimetry (DSC) 55

b) Laser Flash Analysis (LFA) 56

IV.2. Crystallographic and structural analyses 58

a) X-Ray Diffraction (XRD) 58

b) Raman-microspectrometry and Cr^{3+} fluorescence 58

IV.3. Microscopic and elemental analyses 60

a) Optical microscopy 60

b) Scanning Electron Microscopy (SEM) and Energy Dispersie X-ray Spectroscopy (EDS) . 60

c) Electron Probe Micro-Analysis (EPMA) 61

References 62

Chapter III – Reactivity of Al and Cr powders for aluminizing purposes and mechanisms of formation of the slurry coatings on pure nickel 65

I. Reactivity of Al and Cr powders with no substrate 67

I.1. Preparation of Al-Cr mixtures 67

I.2. Reactivity of Al and Cr powders measured by DSC 69

II. Synthesis of Al-Cr intermetallic compounds 73

III. Reactivity of Al, of Cr and of Al-Cr mixtures with pure nickel substrate 77

III.1. Reactivity of the metallic powders with pure nickel substrate 77

III.2. Reactivity of Al-Cr mixtures with pure nickel substrate 80

III.3. Synthesis of Al-Cr intermetallic compounds from Al-Cr mixed slurries for aluminizing 82

IV. Mechanisms of formation of the diffusion layers on pure nickel 86

IV.1. Aluminizing of pure nickel with different Al-Cr mixed slurries: influence of Cr addition on the Al activity 86

IV.2. Outward diffusion of nickel at high temperature (i.e. 1000°C and 1080°C) 88

V. Mechanisms of formation of the diffusion layers from Al-Cr and Cr-Al double-layer systems 91

V.1. Elaboration of Al-Cr and Cr-Al double-layer systems 91

V.2. Mechanims of formation for the Al-Cr double-layer system 91

V.3. Mechanims of formation for the Cr-Al double-layer system 97

VI. Summary and outlook 106

References 108

Chapter IV – Slurry aluminizing of nickel-based alloys from Al and Cr microparticles 110

I. Slurry aluminizing of polycrystalline Ni20Cr 111

I.1. From Al microparticles 111

I.2. From Al-Cr mixed slurries 115

I.3. Functional design: Cr-Al double-layer system 119

II. Slurry aluminizing of a nickel-based superalloy: CM-247 LC 123

II.1. Aluminizing from Al-Cr mixed slurries 123

II.2. Low-activity high-temperature (LAHT) coatings from the Cr-Al double-layer system 131

a) Low-activity conventional heat treatment (400°C-3h + 1080°C-6h) 131

b) Complete heat teeatment (400°C-1h + 700°C-2h + 1100°C-2h) 135

c) Discussion 138

II.3. High-activity high-temperature (HAHT) coatings from the Cr-Al double-layer system 142

a) Low-activity conventional heat treatment (400°C-3h + 1080°C-6h) 142

b) Complete heat teeatment (400°C-1h + 700°C-2h + 1100°C-2h) 145

c) Discussion 148

III. Summary and outlook 154

References 155

Chapter V – Influence of the atmosphere (Ar, air) on the formation of thermal barrier coatings (TBC) from simple Al and Cr-Al double-layer systems 158

I. General background on the oxidation of Al particles and the formation of hollow alumina spheres 159

II. Influence of the atmosphere (Ar, air) on the aluminizing of pure nickel from Al microparticles 163

II.1. Diffusion heat treatment (400°C-1h + 700°C-2h) 163

II.2. Complete heat treatment (400°C-1h + 700°C-2h + 1100°C-2h) 167

II.3. Complete heat treatment with introduction of synthetic air upon annealing 173

II.4. Discussion 177

III. Influence of the atmosphere (Ar, air) for the Cr-Al double-layer system 181

III.1. Characterization of the top coat structure after heat treatment in Ar 181

III.2. Influence of the atmosphere (Ar, air) on the formation of the Cr-Al double-layer system on pure nickel 182

III.3. Reactivity between Al microparticles and oxide powders (NiO, Cr_2O_3 and Al_2O_3) 191

III.4. Discussion 196

IV. Summary and outlook 200

References 202

Chapter VI – Environmental resistance of diffusion coatings elaborated by slurry 206

I. State of the art 207

I.1. Simulation of Type-II hot corrosion conditions at laboratory scale 207

I.2. Oxidation resistance of simple and modified aluminide coatings 210

II. Oxidation resistance of uncoated and slurry coated nickel at 700°C 211

II.1. Characterization of the diffusion coatings elaborated on pure nickel 211

II.2. Influence of pSO_3 on the oxidation-sulfidation of pure nickel 213

a) Oxidation of pure nickel in synthetic air 213

b) Oxidation-sulfidation of pure nickel in synthetic air + 0.5% SO_2 215

c) Discussion 219

II.3. Influence of pSO_3 on the oxidation resistance of simple and Cr-modified slurry coatings 222

a) Oxidation in synthetic air 222

b) Oxidation in synthetic air + 0.5% SO_2 225

c) Discussion 229

III. Type-II hot corrosion resistance of uncoated and slurry coated nickel at 700°C ... 233

III.1. Hot corrosion of pure nickel at 700°C 233

III.2. Hot corrosion of simple and Cr-modified surry aluminide coatings on pure nickel 238

III.3. Discussion 245

IV. Oxidation resistance of Cr-Al double-layer system developed on CM-247 LC 250

IV.1. Characterization of the low-activity high-temperature (LAHT) coating 250

IV.2. Cyclic oxidation at 1000°C 251

IV.3. Isothermal oxidation at 1000°C 258

IV.4. Discussion 262

V. Summary and outlook 263

References 265

Conclusions and perspectives 269

Annexes 275

Chapter I- State of the art: context and motivations of the study

I. Degradation and durability of metallic materials 11

II. Gas turbine engines: selection of the materials for high-temperature applications. 13

III. Nickel-based superalloys for gas turbine components 15

III.1. Generalities 15

III.2. Microstructural and compositional evolution 17

IV. Degradation of metallic materials at high-temperature 19

IV.1. Oxidation 19

IV.2. Hot corrosion 20

IV.3. Need for the high-temperature protection of nickel-based superalloys 23

V. High-temperature protection of nickel-based superalloys 24

V.1. High-temperature protection: an overview 24

V.2. Nickel aluminide coatings 25

V.3. Thermal Barrier Coatings (TBCs) 28

V.4. Degradation of protective coatings in operation 29

VI. Motivations of the present study: from "PARTICOAT" to "FONBAT" 31

VI.1. Presentation of the "PARTICOAT" concept 31

VI.2. Functionalization of aeronautical thermal barrier systems elaborated by slurry (FONBAT) .. 33

References 35

I. Degradation and durability of metallic materials

Metallic materials are widely used for structural applications thanks to their unique properties compared to ceramics, polymers and composite materials. However, metals are generally not found in the nature in their native state (except gold, copper…) but under the form of more complex compounds (sulfides, sulfates, oxides, etc.). These compounds are formed over a long period of time due to the aggressive substances present in the atmosphere (oxygen, moisture, sulfur, etc.). Therefore, the production of metals generally requires a step of reduction of corresponding oxides and a step of purification. Two types of degradation can consequently be observed for metallic materials: electrochemical corrosion (Fig. I-1a) and oxidation (Fig. I-1b), which bring metals back to their thermodynamically stable oxidised state. Electrochemical corrosion and oxidation processes are governed by ionic and electronic exchanges at the surface of the metal.

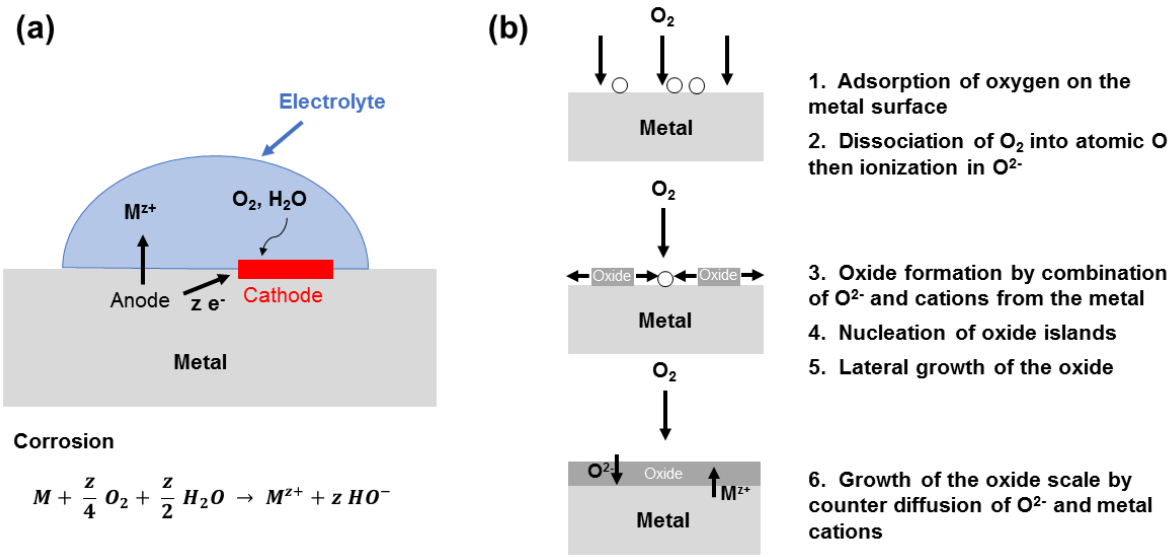

Fig. I-1. Schematic representation of (a) the electrochemical corrosion and (b) oxidation mechanisms.

Although some metals can be used in their pure state, metallic materials generally contain different other elements to increase the metal properties (constituting an alloy). Metallurgy is the science dealing with the elaboration of metallic materials by adjusting the chemical composition and carefully processing the material to get the desired microstructure. The main objective is to confer to the material the optimal properties for a given application (materials by design). In advanced applications, the durability of metallic materials may be shortened. Considering high-temperature structural applications, for energy and aeronautical industries for instance, the degradation of metallic materials usually results from several factors, often with a synergistic effect (Fig. I-2).

For high-temperature structural applications, the durability of metallic materials is a matter of safety, economic and environmental considerations. In the particular case of gas turbine engines, the performance of metallic materials is of utmost importance to ensure the security of the whole aircraft. The selection of materials is particularly difficult for these applications requiring antagonist properties: lightweight materials, superior mechanical properties, good resistance to corrosion and oxidation and cost effective.

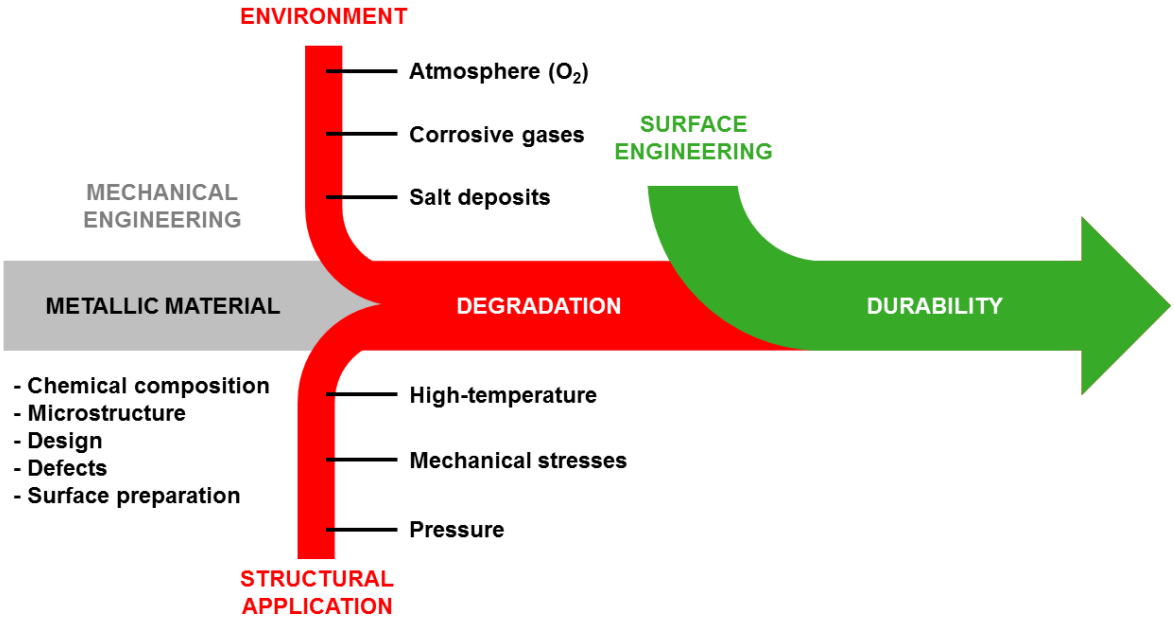

Fig. I-2. Schematic representation of the synergy between the environment and the structural conditions leading to the degradation of the metallic material in the high-temperature field.

Concerning the degradation of metallic materials, both thermodynamic and kinetic approaches must be considered. Thermodynamics can predict whether the constitution of a material is impaired or not for a given application whereas kinetics is useful to estimate how quickly the potential degradation of the material is detrimental. In high-temperature aeronautical applications, metallic materials are exposed to harsh environments, at an elevated range of temperature and pressure and must withstand incredibly high mechanical loads [1-3]. These factors lead to the unavoidable degradation of the parent material. These structural materials must then be carefully designed to resist at the very best to these extreme conditions (Mechanical engineering). For high-temperature protection of metallic materials, the key point is to limit ionic and electronic exchanges at the surface. Therefore, surface engineering is a critical issue to sustain the durability of metallic materials in aeronautical structural applications for elevated temperatures (Fig. I-2).

II. Gas turbine engines: selection of the materials for high-temperature applications

Today, most civil and military aircrafts are provided with gas turbine engines (or turbofans) following the Brayton thermodynamic cycle [4,5]. The aim of a turbofan is to generate a propulsive thrust from the combustion of ingested air over the atmosphere. According to Newton's Third Law "Action and reaction forces pairs", the thrust leads to the propulsion of the aircraft [5,6]. Unlike military engines, only a portion of the air (about 20%) goes through a civil jet engine (primary flow). The remaining 80% (secondary flow) is used to cool turbine components and to reduce noise pollution. These engines, called "high-bypass" [1,6], are particularly fuel efficient and provide the majority of civil aircrafts. Indeed, a large portion of the thrust is given by the secondary flow. For maximum propulsion (higher velocity), the whole ingested air is usually burned in military aircrafts.

Based on the Brayton thermodynamic cycle [4,5], turbofans are split in several units (Fig. I-3a). First, air is ingested by aspiration through a large fan. The air flow is progressively compressed in the low-pressure compressor then in the high-pressure compressor. As a result, a pressure greater than 30 bars [4] can be achieved increasing the temperature of the air flow (Fig. I-3b). Pressurized air is then injected in the combustion chamber and mixed with kerosene droplets. This mixture is ignited producing exothermic reactions which increases the temperature up to 1700°C [1,6]. Then, pressurized and hot gases are ejected from the combustion chamber (or combustor) to the next unit; the turbine (highlighted by the red rectangle in Fig. I-3a).

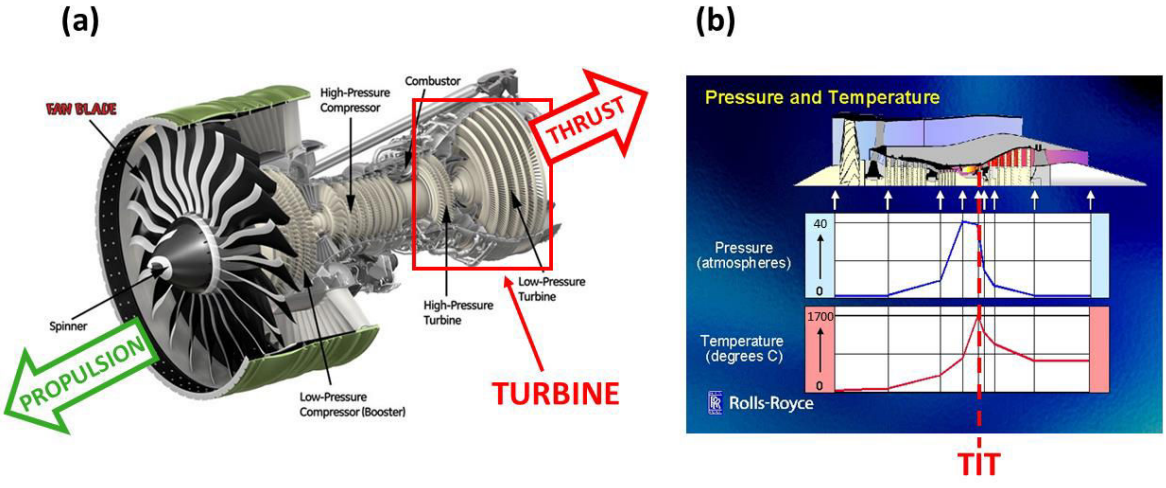

Fig. I-3. (a) Schematic view in cross section of a high-bypass turbofan [7] and (b) evolution of the temperature and the pressure through the engine [8].

A turbine is divided into two sections, the high-pressure and low-pressure turbines (HPT and LPT respectively). The hot gases expand through the turbine and let the cylindrical shafts to rotate by friction on turbine blades (mobile stages). HPT and LPT rotate at two different speeds and they are in charge of driving the fan and the compressor (the high-pressure shaft spins at a higher velocity than the low-pressure one). The greater the velocity of the turbines the greater the air ingestion by the fan. A turbofan operates therefore as an air flow cycle engine. For a better yield, turbofans are usually formed with alternatively fixed (stator) and mobile (rotor) stages [6]. Finally, the heated and pressurized gases are expelled through the exhaust nozzle and generate the thrust of the aircraft over the ambient air for propulsion (Fig. I-3a).

According to aviation requirements in terms of energy, time and cost savings, jet engines are expected to be more and more efficient and so require- mechanical, aerodynamic and material improvements. The thermodynamic efficiency of a gas turbine engine is ensured by the Turbine Inlet Temperature (TIT in Fig. I-3b) referring to the Brayton cycle [4,5]. For instance, increasing the TIT by 50°C enhances the specific thrust by 10% and reduces the fuel consumption by 5%. Thus, this temperature has been continuously rising (more than 300°C in 30 years [1,6]) and the materials used to fabricate turbine components need to be carefully selected according to their metallurgy and mechanical properties (chemical composition, solidification process, creep and strain resistance). Obviously, in order to save energy and reduce environmental damages, the use of lightweight materials is a priority for aeronautical applications. However, the conditions are so aggressive in the turbine (high temperatures, strong mechanical stresses and corrosive atmosphere) that, only nickel and cobalt superalloys were found to withstand such extreme conditions [1]. These superalloys also present a relatively good oxidation resistance at intermediate temperatures (between 500°C and 800°C). Nickel-based superalloys are mainly used in the turbine where the temperature and the conditions are the most harmful. For instance, most LPT and HPT blades and vanes are made of nickel-based superalloys.

III. Nickel-based superalloys for gas turbine components

III.1. Generalities

Nickel-based superalloys are the preferred materials for the production of gas turbine components of military and civil aircrafts. A superalloy can be defined as a refractory metallic material designed to maintain superior mechanical properties even at temperatures close to its melting point [1,9]. Nickel-based superalloys rely on the austenitic γ-Ni matrix which is a face-centered cubic crystal structure (FCC) [9,10]. The stability of the γ-Ni phase from room temperature to its melting point allows the addition of other elements [2,11]. Therefore, nickel-based superalloys are complex materials containing usually five to ten alloying elements (Fig. I-4) [9-11]. Each alloying element has a potential effect on the mechanical properties, the corrosion/oxidation resistance and the density of the superalloy. Therefore, the alloying elements and their concentration must be carefully selected to produce a component with specific properties.

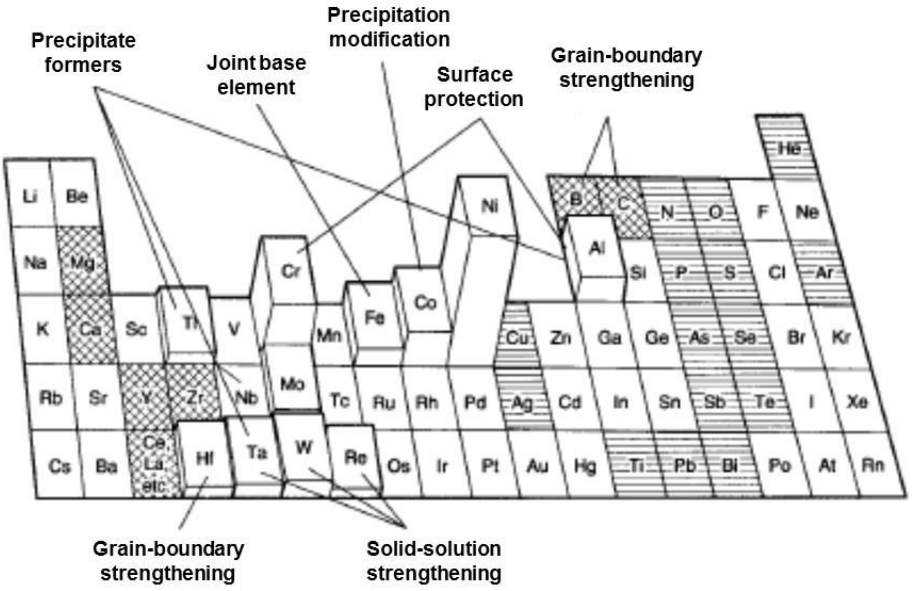

Fig. I-4. Elements commonly selected for the constitution of nickel-based superalloys and their respective contribution to the microstructure [1].

Solid solution elements like Co, Cr or Fe, with atomic radius close to that of nickel and refractory elements like Mo and W can reinforce and stabilise the FCC γ-Ni phase [1]. Hardening elements allow the formation of coherent precipitates in the matrix with a FCC γ'-Ni_3X structure (where X refers to Al, Ti or Ta) [1,9,12]. Thus, nickel-based superalloys display a duplex γ-γ' microstructure (Fig. I-5) which can be cuboidal or spherical according to the superalloy and the post heat treatment [9-13]. With their typical γ-γ' microstructure, nickel-based superalloys present high creep, strain and fatigue resistance by impeding the motions of dislocations in the metallic structure [3].

The mechanical behaviour of the superalloy is a direct consequence of the proportion of the γ' phase. Today, this phase represents about 70% by volume of a nickel-based superalloy [9,11]. By little addition of carbon in the chemical composition, the precipitation of carbides occurs during the solidification process [1,9,14]. These carbides mainly located at the grain boundaries increase the creep behaviour of nickel-based superalloys and reduce the impact of grain boundaries defects (formed during the solidification process) [2,14]. However, these carbides may serve as cracks initiation sites during fatigue for long term exposure [9,14,15].

Nickel-based superalloys display a good compromise between mechanical behaviour at high temperature and weight reduction in spite of a density between 7.7 to 9 $g.cm^{-3}$ [2,9]. Even though new classes of lighter metallic materials have recently appeared, i.e. TiAl alloys [16,17], nickel-based superalloys are still the materials of choice for the production of gas turbine components of military and civil aircrafts.

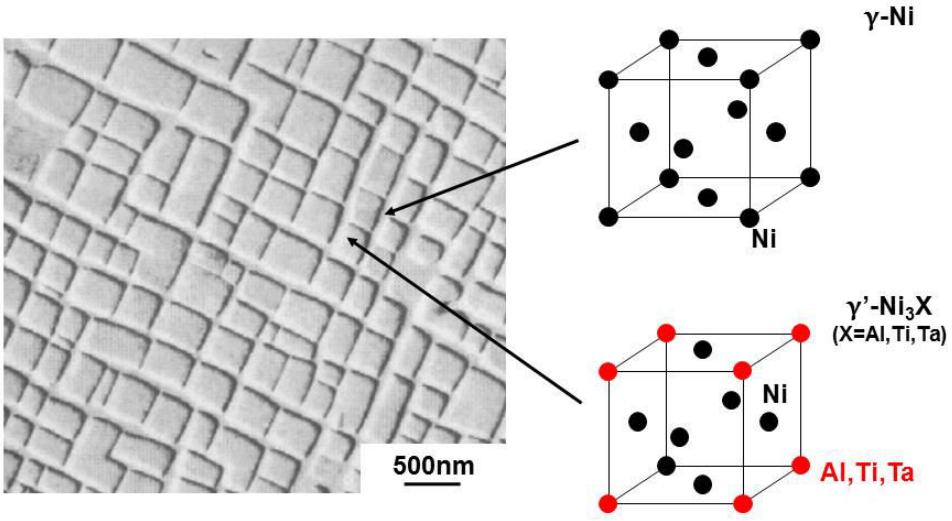

Fig. I-5. Duplex γ-γ' microstructure of a nickel-based superalloy [3] and corresponding crystal structures.

III.2. Microstructural and compositional evolution

With the recent advances in aviation engine technology, the materials have to be more and more mechanically resistant with good strain and creep resistance because of high thermomechanical loads [10,18] and to better withstand the increase of the TIT over the last years. Nickel-based superalloys have been extensively developed through their chemical composition and microstructure to continuously improve their mechanical behaviour at elevated temperatures [1,9]. In the 1970's, turbine blades were made from wrought metallurgy (cast billets were deformed and reheated in a several steps process to give the component its final shape). Then, nickel superalloys containing more and more refractory elements (Mo and W mainly), the components had to be elaborated by powder metallurgy because of lack of ductility [2]. For these two technologies, the solidification process limited the exclusive production of equiaxed microstructures (Fig. I-6a). However, grain boundaries considerably decrease the high temperature creep resistance and thermo-mechanical fatigue (TMF) behaviour of the turbine components [2,19].

Since early 1980's, gas turbine components are mainly produced by investment casting [2,9,20]. With a better control of the solidification process, turbine components manufactured by investment casting present superior mechanical properties. In this process, the alloy is solidified in a preferential crystallographic orientation parallel to the applied-stress direction. This prevents the initiation of cracks through the grain boundaries in operation [9,21]. Turbine components manufactured by directional solidification can present a columnar crystal structure (Fig. I-6b) with oriented grain boundaries or a single crystal (Fig. I-6c).

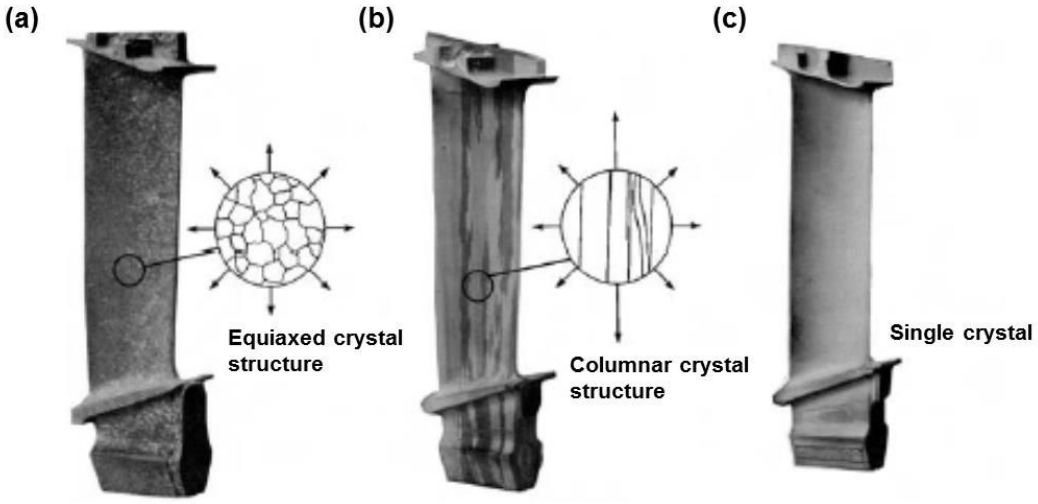

Fig. I-6. Cast turbine blades with (a) a polycrystalline structure (EQ), (b) a directionally solidified structure (DS) and (c) a single crystal (SX) [1].

With the investment casting process, the elaboration of cooling channels within the turbine components was made possible [1,2]. Cooling channels are useful to decrease the surface temperature of the alloy and to lighten the turbine components. Turbine blades are mainly produced by investment casting whereas vanes and disks can be produced by powder metallurgy. HPT blades are usually cast as a single crystal with cooling channels whereas LPT blades are usually produced with DS or polycrystalline superalloys (Fig. I-6). Indeed, single crystal superalloys are particularly expensive to produce and are located in the most critical region of the engine. The selection of the microstructure of the superalloy is a direct consequence of the temperature range (i.e. thermomechanical stresses level) [2].

In the second generation, the addition of Re, at the expense of Mo and W, considerably improved the creep resistance of nickel-based superalloys [12,14,22]. The Re concentration was then increased up to 6 wt.% in the third generation [22]. In the fourth generation, other elements such as Ru were added for the stabilization of the γ-γ' microstructure [23]. However, these strengthening elements increase both the price and the density of the alloys. Therefore, their concentration must be carefully selected to limit the weight of turbine components, which is of utmost importance for aeronautical applications.

IV. Degradation of metallic materials at high-temperature

Depending on the temperature on the alloy surface, three modes of degradation are usually considered (Fig. I-7). Unlike oxidation, hot corrosion phenomena are hardly predictable and lead to the fast degradation of the material at temperatures where the oxidation of the material is, usually, not detrimental.

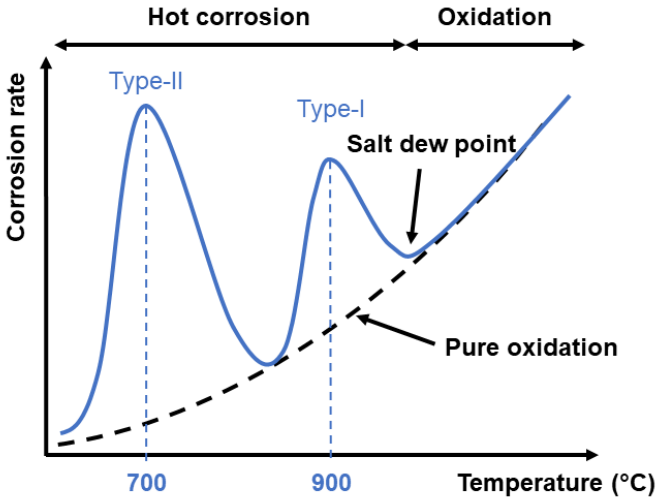

Fig. I-7. Schematic illustration of the temperature dependence on the corrosion rate.

IV.1. Oxidation

Oxidation is unavoidable in gas turbine engines due to the excess of oxygen in the atmosphere (the p_{O_2} is greater than the partial pressure required for the metal to be thermodynamically stable). The overall reaction of oxidation *(Eq. I-1)* can be written:

$$\mathrm{n}\, M + \frac{y}{2}\, O_2 \rightarrow M_n O_y \qquad \textbf{(Eq. I-1)}$$

With:

M: metal

M_nO_y*:* corresponding oxide

n: number of metallic atoms in the stoichiometry of the oxide

With a negative standard Gibbs free energy change for the reaction *(Eq. I-1)* ($\Delta_r G^0 < 0$) [3], the oxide is more thermodynamically stable. However, oxidation is not necessarily detrimental for the metallic material and the kinetics of oxidation have to be considered to evaluate the progress of the degradation. Several steps are usually considered in the mechanisms of oxidation (Fig. I-1b). The composition and the morphology of the oxide formed is detrimental for the surface stability of the

metallic material. Therefore, an oxide growing according to a parabolic law is usually preferred since this evolution is characteristic of a slow growing oxide. In the temperature range encountered in the turbines (Fig. I-3b), only a few oxides are able to bring a protection against oxidation to metallic surfaces: chromia (Cr_2O_3), silica (SiO_2) and alumina (Al_2O_3) [2,3,24]. These oxides present a slow growth rate and a good adherence to the underlying material. On the contrary, fast growing oxides such as nickel oxide (NiO), spinels ($NiAl_2O_4$ or $NiCr_2O_4$) or cobalt oxide (CoO) are very porous and present a lot of defects. The porosity and the density of point defects is detrimental in oxide scales since they are paths for the diffusion of ionic and molecular species.

Another important parameter to evaluate the protective behaviour of an oxide scale is the Pilling and Bedworth ratio (PBR) [3]. The PBR is defined by the relation *(Eq. I-2)*:

$$PBR = \frac{V(oxide\ formed)}{V(metal\ consumed)} = \frac{1}{n} * \frac{M(oxide)/\rho(oxide)}{M(metal)/\rho(metal)} \qquad \textbf{(Eq. I-2)}$$

With:

M(oxide): molar mass of the oxide ($g.mol^{-1}$)

M(metal): molar mass of the metal ($g.mol^{-1}$)

n: number of metal atoms in the stoichiometry of the oxide

ρ(oxide): density of the oxide ($g.cm^{-3}$)

ρ(metal): density of the metal ($g.cm^{-3}$)

If the PBR is less than 1, the oxide scale is exposed to tensile stresses whereas with a PBR superior to 1 the oxide scale undergoes compressive stresses. These stresses may induce cracks within the oxide scale and cause spallation. Therefore, an oxide scale with a PBR close to unity will be more protective in most cases. This parameter is of utmost importance under thermal cycling conditions since the CTE (Coefficient of Thermal Expansion) mismatch between the oxide and the underlying metal is large. With a PBR of 1.28, alumina has the closest value to unity which explains why alumina forming alloys are particularly resistant to spallation in thermal cycling conditions encountered in gas turbine engines for aircraft power generation.

IV.2. Hot corrosion

Hot corrosion of high-temperature materials is an accelerated degradation induced by the condensation of a salt or a solid deposit on the surface of the metallic material. For aircraft gas turbines, the most common salt deposit is Na_2SO_4 (sodium sulfate) [25], resulting from the combustion of ingested NaCl with the gas flow comprising O_2 and SO_2 [26,27]. The suggested overall reaction of Na_2SO_4 deposition *(Eq. I-3)* is:

$$2\,NaCl\,(g) + SO_2\,(g) + O_2\,(g) \rightarrow Na_2SO_4\,(s) + Cl_2\,(g) \qquad \textit{(Eq. I-3)}$$

In the presence of water vapour, the overall reaction *(Eq. I-4)* of Na_2SO_4 deposition is:

$$4\,NaCl\,(g) + 2\,SO_2\,(g) + 2\,H_2O\,(g) + O_2\,(g) \rightarrow 2\,Na_2SO_4\,(s) + 4\,HCl\,(g) \qquad \textit{(Eq. I-4)}$$

Two types of hot corrosion are usually considered depending on the range of temperature and of the salt composition (Fig. I-7). Assuming pure Na_2SO_4, Type-I hot corrosion occurs within the temperature range 850-950°C [18,28-30] (HTHC: High Temperature Hot Corrosion) and Type-II within the range 650-800°C [18,29,31] (LTHC: Low Temperature Hot Corrosion). With a melting point of 884°C [30,31], Na_2SO_4 is then solid in Type-II conditions and liquid in Type-I conditions, which differentiates the two corrosion processes. However, the presence of other contaminants such as V_2O_5 (vanadium pentoxide) can lead to the formation of eutectic compounds with Na_2SO_4 (eutectic point lower than 600°C [26,30]), hence accelerating the corrosion rate [32]. When the temperature is higher than the salt dew point, dry corrosion referred to pure oxidation occurs (Fig. I-7). The different aspects of hot corrosion have been extensively studied for more than 50 years on metallic alloys and coatings for marine and aeronautical applications [33]. It is now well accepted than the mechanisms of hot corrosion consist in an incubation stage and a propagation stage [25]. During the incubation stage, an oxide scale is formed on the substrate and withstands the presence of the deposit at first. In the propagation stage, breakdown of the oxide scale occurs and internal oxidation occurs together with sulfidation, depending on the metallic coating and the temperature range.

- **<u>Type-I:</u> High Temperature Hot Corrosion**

For Type-I hot corrosion, the salt fluxing model is the most widely accepted one. In liquid phase, Na_2SO_4 decomposes on the metallic surface through the reaction *(Eq. I-5)*:

$$Na_2SO_4\,(l) \rightarrow SO_3\,(g) + Na_2O\,(l) \qquad \textit{(Eq. I-5)}$$

Oxides can be dissolved in fused Na_2SO_4 as anionic species (basic fluxing) or cationic species (acidic fluxing) depending on the activities of SO_3 (acidic) and Na_2O (basic) [33]. As a consequence, a porous oxide scale is formed with an irregular metal-scale interface and an internal attack occurs within the material through the formation of sulfides. The solubility of an oxide can be estimated as a function of Na_2O activity and SO_3 partial pressure and is commonly represented in a solubility diagram [33] (Fig. I-8a). Rapp and Goto proposed that a "negative solubility" gradient in the fused salt film must exist to sustain the hot corrosion attack (Fig. I-8b). Chromia, alumina and silica are the most promising oxides

for hot corrosion resistance. Silica is virtually insoluble in fused Na_2SO_4 but is usually less protective than chromia for Type-I hot corrosion [34].

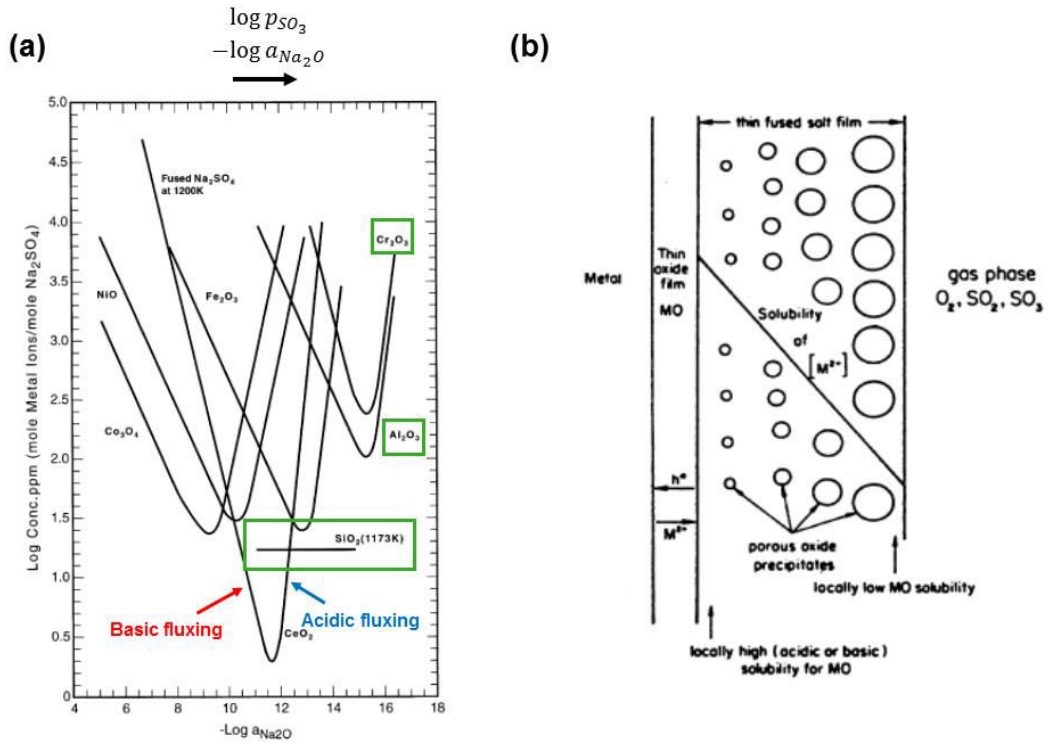

Fig. I-8. (a) Solubilities of most common oxides in fused Na_2SO_4 at 927°C [35] and (b) representation of the negative solubility gradient [35].

- **<u>Type-II:</u> Low Temperature Hot Corrosion**

Low temperature hot corrosion was first observed in marine environment [34]. Since Na_2SO_4 is a solid in Type-II conditions, a sufficient amount of SO_3 is necessary to observe hot corrosion [25,31]. The presence of SO_3 converts NiO or CoO into sulfates hence inducing the formation of eutectic phases with the Na_2SO_4 deposit (T_e (Na_2SO_4-$NiSO_4$) = 671°C and T_e (Na_2SO_4-$CoSO_4$) = 565°C [36]). Type-II hot corrosion is usually characterized by a non-uniform attack of the metallic material in the form of pitting with minimal or no sulfidation.

From an engineering point of view, the key point to get protection against hot corrosion is to extend the incubation stage duration since no degradation of the material is observed at this stage. Alumina and chromia are expected to be stable in the normal conditions (considering the p_{SO_3}). However, the presence of Ni or Co within the oxide scale may change the mechanisms by forming eutectic phases with Na_2SO_4. Therefore, the purer the alumina or chromia scale the greater the hot corrosion resistance of the underlying material.

IV.3. Need for the high-temperature protection of nickel-based superalloys

Gas turbine blades and vanes located just after the combustion chamber are particularly exposed to hot corrosive gases and impurities coming from the kerosene, leading to the chemical degradation of the material. Because of the high concentration of oxygen in the combustion gases, surfaces oxidize in operation and the composition/morphology of the developed oxide scales are critical for the surface stability and the durability of the whole component [3]. Designed for superior mechanical resistance, nickel-based superalloys are vulnerable to aggressive environments forming non-protective oxide scales on the surface [18]. The concentration of beneficial elements (i.e. Al and Cr) is indeed proven to be not high enough to confer them good corrosion and oxidation resistance in the long term. Fig. I-9 represents the evolution of the Cr and strengthening elements (Mo, Re, Ru) contents along the different generations of nickel-based superalloys. From mechanical considerations, Cr has been progressively replaced by these strengthening elements. Consequently, the new generations of nickel-based superalloys became particularly sensitive to hot corrosion since Cr is known as a beneficial element for hot corrosion resistance [33,37]. However, at temperatures above 900°C, chromia may form volatile species (e.g. CrO_3) [18,24] and alumina is consequently the preferred oxide for higher temperatures.

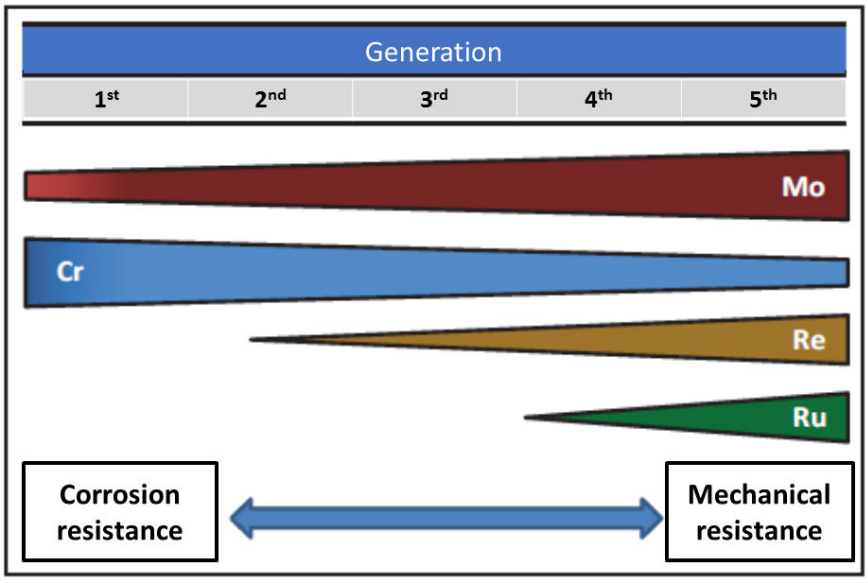

Fig. I-9. Evolution of the Cr and strengthening elements content over the different generations of monocrystalline nickel-based superalloys, from Wu et al. [38].

Therefore, in the hottest regions of the engine, nickel-based superalloys need to be coated to confer the required corrosion and oxidation resistance. The high-temperature protection increases the durability of the gas turbine components by slowing down the degradation rate on their surface (surface engineering).

V. High-temperature protection of nickel-based superalloys

V.1. High-temperature protection: an overview

Since the oxidation phenomenon is thermodynamically unavoidable, the key point is to reduce at its lowest extent the kinetics of degradation. The driving force is to slow down ionic and electronic exchanges through the oxides on the metallic surface. Surface engineering has become an important research area for aeronautical applications. For the oxidation and corrosion resistance, metallic coatings are generally employed to promote the formation of a thin, continuous and dense oxide scale on the surface [3,18]. When the temperature range is higher, e.g. in the high-pressure turbine, thermal barrier coatings (TBCs) must be added on the underlying metallic coatings for thermal insulation [3]. Due to their low thermal conductivity, thermal barrier coatings can decrease the temperature on the surface of the alloy by up to 170°C [39-41].

Metallic coatings must present a mechanical and a chemical compatibility with the underlying substrate [3]. For aeronautical applications, metallic coatings are generally divided in two categories: overlay and diffusion coatings [6,12,18,39]. Overlay coatings, usually referred as MCrAlY, are particularly resistant to both Type-I and Type-II hot corrosion depending on the concentration of Cr [12,18]. These coatings are produced from metallic powders with a selected chemical composition and deposited on the surfaces of the alloy by plasma spray or by high velocity oxy-fuel (HVOF) [3]. Due to the elaboration process, the chemistry and the microstructure of the alloy do not play an important role on the final properties of an overlay coating.

Diffusion coatings are formed by the surface enrichment of the alloy whether with Al, Cr or Si and involve interdiffusion between the donor and the substrate [6,12,18]. Diffusion coatings are generally produced by chemical vapour deposition (CVD) [18], like pack cementation [28,42-44] and different type of gas phase processes [28,44-46]. Slurry coating processes are also classified as diffusion coatings [42,47]. Slurry processes present a high flexibility and they are easily applicable on metallic surfaces. Historically, these coatings were mainly used for repair purposes [47]. Recently, the European project "PARTICOAT" demonstrated the possibility to elaborate a complete thermal barrier system (aluminide coating + ceramic thermal barrier coating) from environmentally-friendly slurries [48].

The enrichment of the substrate surface with a protective element (i.e. Al, Cr or Si) allows the formation of a thin and adherent oxide scale, sharply decreasing the kinetics of oxidation. The formation of alumina is particularly interesting since this oxide maintains a good stability at elevated temperatures and there is barely any point defects in the scale [3]. Therefore, diffusion coatings developed on nickel-based superalloys for oxidation resistance are generally based on Al (aluminizing). Depending on the service conditions, these coatings can be modified with one or several elements to confer them specific properties and increase their performance.

V.2. Nickel aluminide coatings

Aluminium diffusion coatings are based on the β-NiAl intermetallic phase (Fig. I-10) generally formed in the range 1000-1100°C during the aluminizing process [18]. The β-NiAl phase is highly resistant to corrosion and oxidation through the formation of a thin, continuous and adherent alumina scale on the surface [49-51]. The stable form of alumina (α-Al_2O_3) is characterized by a slow growth rate and a good resistance to spallation. Under cyclic oxidation occurring in gas turbine engines, thermal cycles induce alternatively compressive and tensile stresses within the oxide scale and can lead to a local failure of the alumina scale upon cooling. However, due to the significant Al reservoir, outward diffusion of Al occurs to heal the oxide scale [50,51].

The β-NiAl phase is particularly interesting for high-temperature applications with a high melting point (Fig. I-10) and a relatively low density (5.9 $g.cm^{-3}$ [52-54]). The β-NiAl phase also presents a coefficient of thermal expansion (CTE) close to that of nickel-based superalloys [52,53] which is of utmost importance under thermal cycling conditions.

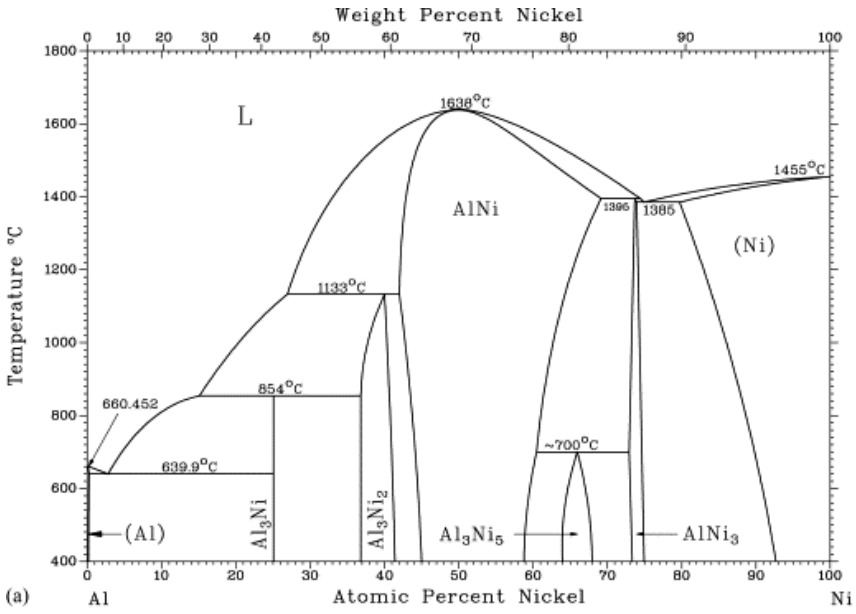

Fig. I-10. Binary Al-Ni phase diagram [43].

a) High-activity and low-activity diffusion coatings

During the aluminizing process, the thermodynamic activity of Al has a tremendous effect on the final microstructure of the diffusion coating [17]. Two types of aluminium diffusion coatings are usually considered on nickel-based superalloys: high-activity and low-activity (Fig. I-11) [12,18,42,55]. The differences in the microstructure for the two types of coating is a direct consequence of the mechanisms of formation (i.e. the coating growth direction). These differences rely on the different

interdiffusion coefficient between Al and Ni in the phases of the Al-Ni system [56], which is dependent on the temperature and the Al donor source.

- **HALT: High-Activity Low-Temperature**

When the donor is rich in Al (i.e. with a high thermodynamic activity of Al), the inward diffusion of Al into the substrate occurs at relatively low temperature because the mobility of Al is higher than that of Ni at such temperatures [56]. The fast diffusion of Al drives the formation of Al-rich Ni_xAl_y phases (i.e. $NiAl_3$ and Ni_2Al_3) in the substrate. In these phases, the diffusion of Ni is not significant at low temperatures [56] and Al continues to diffuse inward [42]. Consequently, the slowly diffusing refractory elements (e.g. W, Mo, Ta) precipitate in the outer region of the coating. The inert substrate carbides are also entrapped in the inwardly growing layer (Fig. I-11). The initial surface of the substrate therefore remains at the outer surface of the coating upon aluminizing [57]. After the aluminizing step, the diffusion layer is based on Ni_2Al_3 [42]. Since Ni_2Al_3 is brittle and not stable at high temperature, a further annealing is required to obtain the desired β-NiAl phase [42,57]. The annealing is usually carried out between 1000°C and 1100°C [18]. Because of the nickel withdrawal from the substrate during the annealing treatment, an interdiffusion zone rich in precipitates formed above the unmodified substrate. This microstructure is commonly observed for high-activity pack cementation process when Al powder is directly poured in the pack mixture [42,55,58,59] and simple aluminide slurry coatings [42,60].

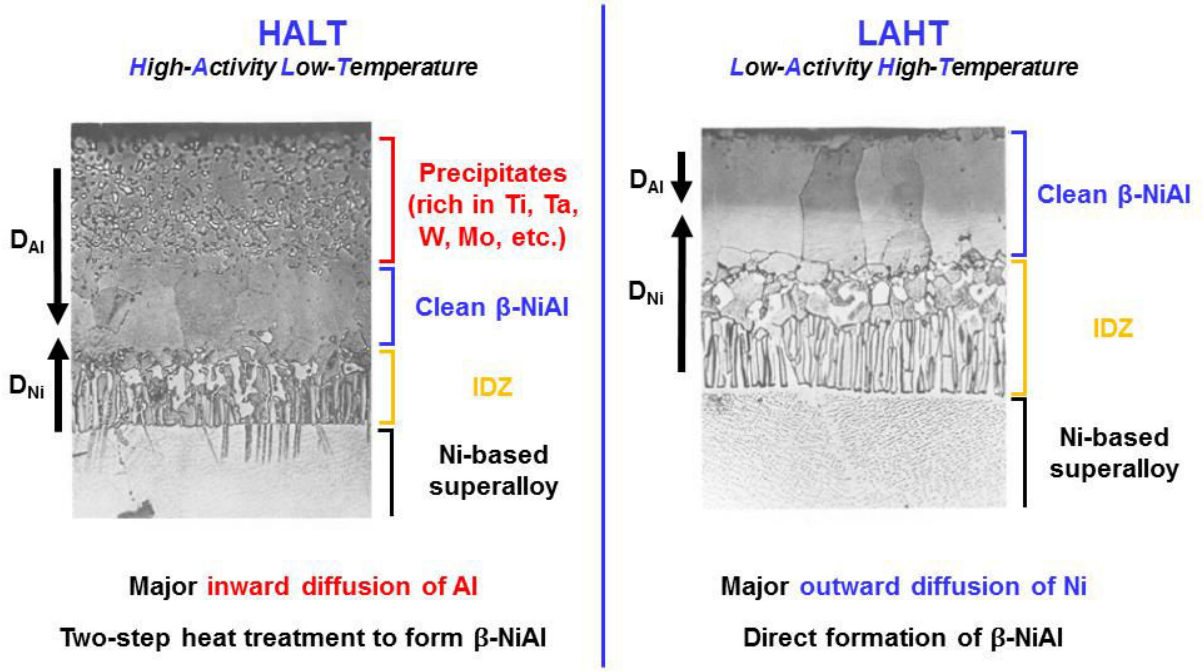

Fig. I-11. Comparison between high-activity low-temperature (HALT) and low-activity high-temperature (LAHT) nickel aluminide coatings [42].

- **LAHT: Low-Activity High-Temperature**

The microstructure of low-activity diffusion coatings is different from high-activity one with an interdiffusion zone and an additive layer (pure β-NiAl layer) with approximately the same thickness (Fig. I-11). By alloying Al with Ni [42] or Cr [17,45] (i.e. masteralloys), the thermodynamic activity of Al is decreased. Thus, Al is not able to diffuse inward at low temperature. At the aluminizing temperature (between 1000°C and 1100°C generally), Ni is able to diffuse outwardly and directly forms the Ni-rich β-NiAl phase by interdiffusion with the Al supply at the surface [42,61]. Since the diffusion coefficient of Ni is higher than that of Al in the stoichiometric and Ni-rich β-NiAl phase [56,62], the coating mainly grows by outward diffusion of Ni. As a consequence, the β-NiAl additive layer is free of precipitates from the slowly diffusing elements, present in the substrate, whose remain entrapped in the interdiffusion zone with the carbides [42]. Therefore, low-activity diffusion coatings are preferred for high-temperature protection as the external β-NiAl layer is cleaner (Fig. I-11) and show better oxidation resistance than high-activity coatings [63]. This microstructure is commonly observed with out-of-pack processes [45,55,59,64] and pack cementation using masteralloys as Al donors [42]. Recently, Montero et al. achieved low-activity slurry coatings on nickel-based superalloys using pre-alloyed Al and Cr microparticles [61,65].

b) Simple and modified aluminide coatings

Nickel aluminide coatings are particularly resistant to oxidation at temperatures up to 1100°C [28]. When additional resistance is required to ensure the durability of the coating, nickel aluminide coatings are modified with beneficial elements. By decreasing the critical amount of Al to form an exclusive alumina scale [66,67], the addition of Cr is interesting for high-temperature protection. Thus, with the addition of 5 at.% Cr in the Al-Ni system, the critical level is reduced from 35 at.% Al to about 12 at.% Al [57]. This is commonly referred as the "third element effect" and was first proposed by Wagner [68]. The presence of Cr is also beneficial to accelerate the transformation of θ-Al_2O_3 to the stable α-Al_2O_3 [50]. For the hot corrosion protection, nickel aluminide coatings are generally modified with Cr and Si. Numerous studies investigated the beneficial effect of Cr and Si on the Type-I and Type-II hot corrosion behaviour of aluminide coatings [37,47,59,69-71].

Reactive elements (RE) like Ce, Hf or Y were found to promote the adherence of alumina, especially in cyclic oxidation conditions [72,73]. Their addition was found to decrease the growth rate of alumina preventing the formation of voids underneath the oxide scale by forming mechanical bonding through oxide pegs at the surface of the diffusion coating [74]. RE were also assumed to limit the detrimental influence of S segregation at the coating-oxide interface [64].

In the hottest region of the engine, nickel aluminide coatings are modified with Pt to enhance the oxidation and hot corrosion resistance and can be used as environmental coatings or as bond coats for thermal barrier coatings [45,46,51]. The role of Pt on the oxidation resistance has been intensively studied over the last years [51,58,72,75]. However, there is no widely accepted effect on the beneficial role of Pt and different mechanisms were proposed. One beneficial effect commonly reported is the selective oxidation of Al with the addition of Pt, preventing the transient formation of Ni-rich oxides within the oxide scales [51,72]. Pt also improves the adherence of the alumina scale and prevents spallation in cyclic conditions [58,76].

For Pt-modified aluminide coatings, Pt is first electroplated (about 5-10µm thick) and is subsequently annealed to promote interdiffusion between Pt and the substrate. After the aluminizing process, the coating usually exhibits a single β-(Ni,Pt)Al phase [12,45,46,51]. However, a dual $PtAl_2$ + β-(Ni,Pt)Al layer can be formed in the outer part of the coating depending on the initial Pt concentration and the Al activity during aluminizing [12,45,46,51,77-79]. When Pt-modified aluminide coatings are used as bond coats for TBCs, the developed alumina scale acts as a TGO (Thermally Grown Oxide) ensuring a chemical and mechanical bonding between the metallic bond coat and the ceramic top coat in operation [51,80-82]. The stability of the TGO is detrimental for the adherence of the ceramic top coat and is usually the critical life-limiting factor for TBC systems [80,83-85].

V.3. Thermal Barrier Coatings (TBCs)

Thermal barrier coatings have been applied on gas turbine components for thermal insulation due to the continuously increasing TIT. These advanced coatings enhance the temperature capability of the underlying material by decreasing the temperature at the surface. In the HPT section of current gas turbine engines, these coatings are applied together with the elaboration of cooling channels within the material [3].

The conventional TBC systems are applied on gas turbine components located in the hottest region of the turbine (i.e. for HPT blades and vanes). They are composed of two distinct layers (Fig. I-12):

- A metallic bond coat generally developing an alumina scale at elevated temperatures acting as a TGO (Thermally Grown Oxide) to ensure a chemical and mechanical bond with the ceramic top coat.
- A ceramic top coat with a low thermal conductivity to decrease the temperature at the surface of the metallic material.

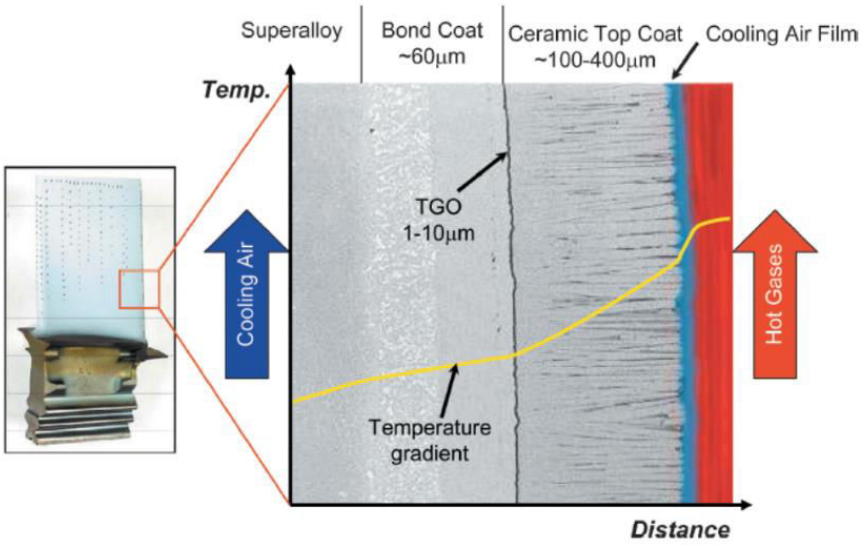

Fig. I-12. SEM cross section image of a conventional TBC system (Pt-modified aluminide bond coat + YSZ EB-PVD top coat) showing the thermal insulation effect for a HPT blade [41].

In current gas turbine engines, the top coat is usually deposited by air plasma spray (APS) or electron-beam physical vapour deposition (EB-PVD) [28]. TBCs are usually made of yttria-stabilized zirconia (YSZ). With a low thermal conductivity, the ceramic top coat can decrease the temperature at the surface of the metallic material by up to 170°C [39-41]. These coatings present a lot of porosity and pathways allowing the diffusion of O_2 toward the bond coat to grow and maintain the TGO at the interface bond coat-top coat. TBCs are also strain compliant and are able to accommodate thermal stresses in cyclic conditions due to porosity. The bond coats are generally made of Pt-modified aluminide coatings with the β-(Ni,Pt)Al phase (low-activity coatings) or MCrAlY coatings by plasma spray. The aim of these bond coats is to promote the formation of a pure α-Al_2O_3 scale (TGO) at the interface with the ceramic top coat. Since there is no chemical and mechanical continuity between the bond coat and the top coat, the TGO is a critical point for the durability of the whole TBC system [41,86].

V.4. Degradation of protective coatings in operation

In addition to the general mechanisms of degradation occurring in high-temperature structural applications (cf. IV.), more peculiar degradation can be observed on protective coatings in operation. These modes of degradation are a direct consequence of the microstructure and the morphology of the coatings (intrinsic) or due to the environment (extrinsic).

- **Al depletion of nickel aluminide coatings:**

Diffusion mechanisms are thermally activated and are very important at the elevated temperatures encountered in gas turbine engines. Under thermal cyclic conditions, the protective oxide scale developed on aluminide coatings is subjected to spallation. As a result, Al diffuses outwardly to maintain a protective alumina scale and Al is thus progressively consumed from the coating. In addition, Al diffuses into the substrate in operation due to the positive Al gradient between the coating and the substrate. Consequently, the progressive Al depletion of the coating causes the β-NiAl to γ'-Ni_3Al transformation, which is usually observed in the grain boundaries of the coating at first [19,75,87]. As long as the activity of Al is sufficient in the coating, a protective alumina scale will be maintained on the surface. However, when the Al content reaches a critical value, non-protective oxides start to form and increase the oxidation kinetics. According to Giggins and Pettit, the critical amount of Al to maintain an exclusive alumina scale can be lowered with the addition of Cr [66]. The inward diffusion of Al into the substrate in operation is also responsible for the formation of a secondary reaction zone (SRZ) below the coating [88]. The progressive enrichment in Al of the substrate underneath the coating decreases the solubility of solid solution strengthening elements like W, Re or Mo [88]. Thus, the formation of needle-like brittle phases or topologically-closed packed phases (TCPs) is observed in the SRZ hence decreasing the mechanical properties of the alloy.

- **TBCs failure:**

TBCs failure is critical in operation since TBCs do not provide self-rejuvenating protection. In other words, when the TBCs spall off, the thermal insulation is lost [41]. The failure of TBC systems can result from different intrinsic or extrinsic features:

- Rumpling of the metallic bond coat and the TGO due to extensive thermal cycling (formation of periodic undulations at the interface with the ceramic top coat) [51]
- Formation of non-protective oxides rather than pure α-Al_2O_3 in the TGO due to the progressive Al depletion of the bond coat
- Delamination across the interface bond coat-TGO or in the ceramic top coat due to erosion or FOD (Foreign Object Damage)
- Environmental attack of the TBCs through the deposition and penetration of CMAS (Calcium-Magnesium-Alumino-Silicates)

Therefore, TBCs are exposed to a combination of chemical and mechanical degradations in operation usually with a synergistic effect. The particular case of CMAS attack has been extensively studied over the last decades as it appeared as a critical failure mode for TBC systems [89-91]. CMAS results from the ingestion of siliceous mineral debris in the engine. When the temperature is high enough (usually

over 1200°C), the CMAS melt and infiltrate the TBCs down to the TGO. As a result, the strain compliance of the ceramic top coat decreases and becomes brittle upon cooling [89,90]. The sintering of the ceramic top coat by the CMAS induces extensive delamination in cyclic conditions. Erosion of TBCs is also an important mode of degradation especially when large solid particles hit the surface of the component (FOD) [92].

The degradation of protective coatings in operation is therefore a combination of several features with, most of time, a synergistic effect. In order to propose the adequate or the most appropriate protection, the comprehension of the degradation mechanisms is of utmost importance. At laboratory scale, surface engineering tends to identify the influence of each mode of degradation on the durability of materials. Surface engineering also proposes to investigate the potential improvements (microstructural, compositional or architectural) to enhance the performance of metallic materials.

VI. Motivations of the present study: from "PARTICOAT" to "FONBAT"

With the overall increase of the temperature in gas turbine engines, for performance and socio-economic considerations, the use of thermal barrier coatings need to be extended from the HPT to the LPT section (Fig. I-3). From an economic point of view, the extrapolation of current thermal barrier systems (cf. paragraph V.3) is not possible at an industrial scale. CVD-related techniques are particularly expensive, involve hazardous chemicals (halides) and produce lots of wastes in the case of pack cementation processes. EB-PVD and plasma spray coatings are also very expensive to produce and require high electrical supply. Moreover, some turbine components which used to be unaffected by high-temperature corrosion are now susceptible to low temperature hot corrosion (Type-II) in the low-pressure turbine. Therefore, many studies and projects came up recently to propose viable and cost effective alternative solutions. Among them, the slurry coatings appeared as a convincing choice to answer these energy issues, especially for the aircraft industry. In this way, the University of La Rochelle was involved in the European FP7 project "PARTICOAT" (2008-2012) [48].

VI.1. Presentation of the "PARTICOAT" concept

The main objective of the European project "PARTICOAT" was to propose a complete thermal barrier system (diffusion coating + ceramic top coat) in a single step process from Al microparticles in water-based slurries (Fig. I-13). The mechanisms of formation of the coating were studied in argon on pure Ni [93], in air on nickel-based superalloys [94,95] and iron-based alloys [96].

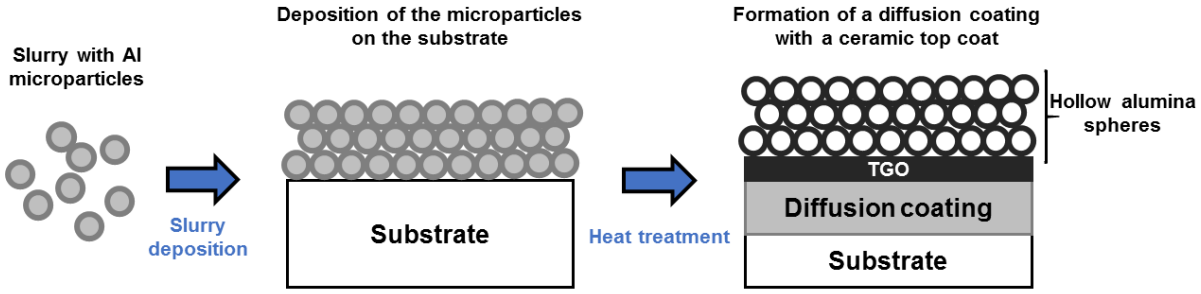

Fig. I-13. Schematic representation of the complete thermal barrier system developed under the PARTICOAT project [97].

The formation of the coatings on different nickel-based substrates was found to involve self-propagating high-temperature synthesis (SHS) or combustion synthesis [95]. A schematic representation of the different steps for the mechanisms of formation is given in Fig. I-14. The diffusion layer grows very quickly due to the high exothermic reactions occurring between the nickel substrate and the Al microparticles. The reaction synthesis is mainly controlled by molten Al progressively dissolving Ni and forming Al-rich Ni_xAl_y intermetallic phases at the surface. When the whole Al from the slurry deposit microparticles has reacted, solid state diffusion occurs between the Al-rich coating and the Ni substrate forming a continuous Ni_2Al_3 layer. As observed for other high-activity diffusion processes (cf. paragraph V.2), an annealing treatment at high temperature (i.e. 1000-1100°C) is necessary to obtain the β-NiAl phase. Simultaneously, the shells of the initial Al microparticles oxidize on the surface of the diffusion layer and sinter together. The resulting ceramic top foam [93] was found to present a thermal conductivity close to conventional APS thermal barrier coatings [98].

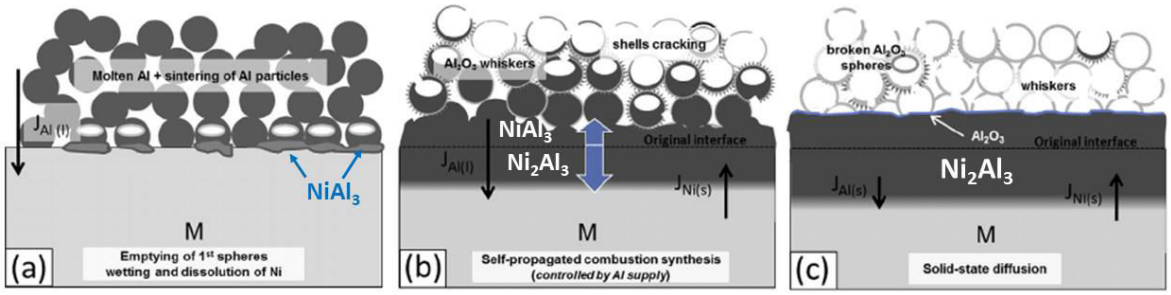

Fig. I-14. Mechanisms of formation of the thermal barrier system on a metal substrate proposed by Bouchaud et al. [60].

The oxidation resistance of these coatings was investigated under isothermal [99,100] and cyclic conditions [63] in air and in water vapour [101], in comparison with conventional diffusion coatings produced by pack cementation or by out-of-pack. The slurry coatings elaborated on pure nickel and nickel-based superalloys have shown faster oxidation kinetics than the conventional coatings [97,99,100]. However, the ceramic top coat containing alumina hollow spheres was found to contribute the most to the oxidation kinetics. The presence of the ceramic top coat was found to limit rumpling of the oxide scale [99]. In cyclic conditions, the presence of substrate elements in the outer region of the coating due to the high Al-activity upon aluminizing was found to decrease the oxidation resistance [63]. The thickness of the alumina shells was particularly thin and the ceramic top coat presented poor erosion resistance. Therefore, the functionalization of the coatings developed under the PARTICOAT project was required for both military and civilian applications in aircraft industry.

VI.2. Functionalization of aeronautical thermal barrier systems elaborated by slurry (FONBAT)

The present study (Functionalization of aeronautical thermal barrier systems elaborated by slurry: FONBAT) is funded by the DGA (Direction Générale de l'Armement – French Defense Ministery) and has potential applications in both military and civilian fields. Based on the works of Benoit Rannou [102] and Maël Mollard [97] done at the LaSIE laboratory, the targeted improvements of the coating systems were to:

- Control the Al activity upon aluminizing.
- Increase the oxidation and hot corrosion resistance of the bond coat.
- Increase the erosion resistance of the thermal barrier system.
- Improve the thermal insulating effect of the ceramic top coat.

Since the previous works were focused on the elaboration of the coatings with simple aluminide coatings, the present study aims at elucidate the influence of doping agents into the slurry composition. Different doping agents were susceptible to increase the performance of the coating systems:

- Addition of Cr to control the Al activity upon aluminizing.
- Addition of Cr to improve the hot corrosion resistance.
- Mixtures of Al + Al_2O_3 to synthesize composite materials to enhance the erosion resistance.

The present study focused on the influence of Cr since this element has a potential beneficial effect on several features. First, the addition of Cr was expected to decrease the activity of Al upon aluminizing hence to promote the formation of a diffusion coating with a low-activity microstructure [61,65] (Fig. I-11). The Cr also has a potential beneficial influence on the hot corrosion and oxidation resistance of slurry aluminide coatings promoting the selective oxidation of Al.

In order to clearly identify the role of Cr addition in the slurry compositions, the reactivity of the microparticles was first investigated without metallic substrate (Fig. I-15). Considering the exothermic reactions usually involved for the formation of the slurry coatings, the reactivity of the microparticles with a metallic substrate was also studied. The influence of the atmosphere (Ar and air) was investigated on the formation of the coatings. The composition of the atmosphere exerts a particular effect on the mechanisms of oxidation of the microparticles and on their sintering in the ceramic top coat [103]. Thanks to the versatility of the slurry process, different architectures were elaborated to tailor the coating with chemical and mechanical gradients. The combination of several doping agents was also investigated to design the coating with the applicative expectation in mind. After the selection of the most promising systems, the different potential improvements were evaluated.

If the oxidation resistance of water-based Al slurry coatings has already been studied, little is known on the hot corrosion resistance. Therefore, hot corrosion tests were performed with the collaboration of Dr. Ing. Mathias Galetz and Dr. Xabier Montero in DECHEMA-Forschungsinstitut at Frankfurt-am-Main (Germany). The addition of three elements (Cr, Si and Co) to the simple Al slurry aluminide coatings and their potential effect on the hot corrosion resistance was investigated. For the sake of clarity, only the results obtained with the simple aluminide and the Cr-modified aluminide coatings will be discussed in this manuscript.

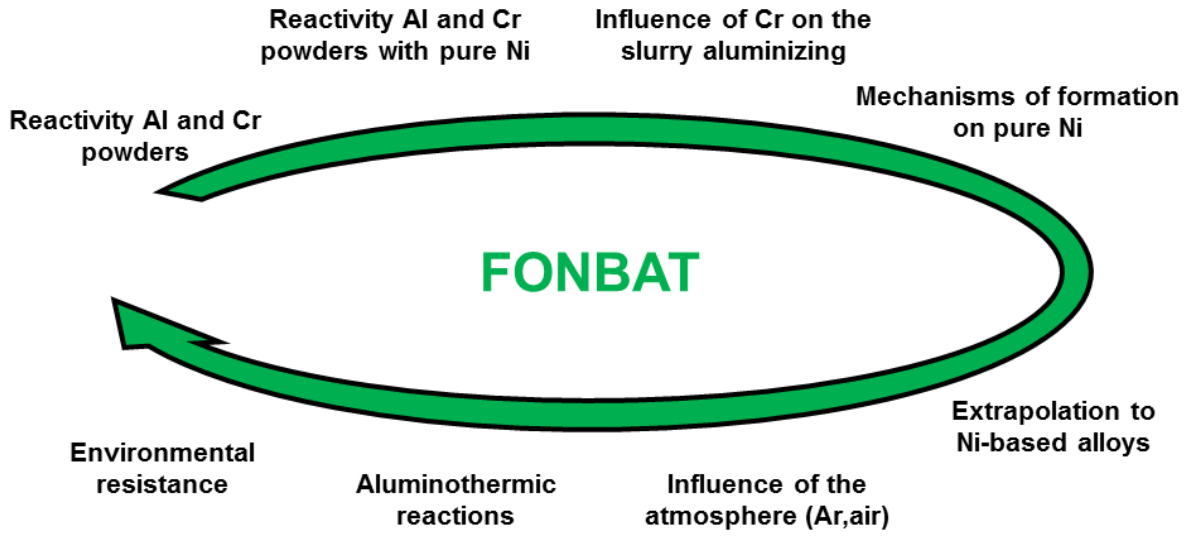

Fig. I-15. Graphical abstract of the study.

References

[1] R.C. Reed, *The Superalloys Fundamentals and Applications,* Cambridge University Press (2006).

[2] M. Donachie, S. Donachie, *Superalloys: A Technical Guide 2nd edition,* ASM International (2002).

[3] S. Bose, *High Temperature Coatings,* Elsevier Science & Technology Books (2007).

[4] D.R. Greatrix, *Powered Flight: The Engineering of Aerospace Propulsion,* Springer-Verlag London Limited (2012).

[5] P. Jansohn, Modern gas turbine system: High efficiency, low emission, fuel flexible power generation, Woodhead Publishing (2013).

[6] N. Eliaz, G. Shemesh, R.M. Latanision, *Engineering Failure Analysis* ***9*** (2002), pp. 31-43.

[7] https://www.pinterest.com, Photo courtesy of GE.

[8] H. Bhadeshia, http://www.msm.cam.ac.uk/, Photo courtesy of Rolls Royce.

[9] T.M. Pollock, S. Tin, *Journal of Propulsion and Power* ***22*** (2006), pp. 361-374.

[10] T.J. Carter, *Engineering Failure Analysis* ***12*** (2005), pp.237-247.

[11] F. Pyczak, B. Devrient, F.C. Neuner, H. Mughrabi, *Acta Materialia* ***53*** (2005), pp. 3879-3891.

[12] M.J. Pomeroy, *Materials and Design* ***26*** (2005), pp. 223-231.

[13] J.S. Van Sluytman, T.M. Pollock, *Acta Materialia* ***60*** (2012), pp. 1771-1783.

[14] R.A. MacKay, T.P. Gabb, A. Garg, R.B. Rogers, M.V. Nathal, *Materials Characterization* ***70*** (2012), pp. 83-100.

[15] L.R Liu, J. Jin, N.R. Zhao, X.F. Sun, H.R. Guan, Z.Q. Hu, *Materials Science and Engineering A* ***361*** (2003), pp. 191-197.

[16] B.P. Bewlay, S. Nag, A. Suzuki, M.J. Weimer, *Materials at High Temperatures* ***33*** (2016), pp. 549-559.

[17] J. Grüters, M.C. Galetz, *Intermetallics* ***60*** (2015), pp. 19-27.

[18] R. Rajendran, *Engineering Failure Analysis* ***26*** (2012), pp. 355-369.

[19] J.A. Haynes, B.A. Pint, Y. Zhang, I.G. Wright, *Surface and Coatings Technology* ***204*** (2009), pp.816-819.

[20] P.N. Quested, M. McLean, *Materials Science and Engineering* ***65*** (1984), 171-180.

[21] F.L. Versnyder, M.E. Shank, *Materials Science and Engineering* ***6*** (1970), pp. 213-247.

[22] P. Caron, T. Khan, *Aerospace Science Technology* ***3*** (1999), pp. 513-523.

[23] A.C. Chou, A. Sato, T. Kobayashi, H. Harada, *Materials Science and Engineering A* ***490*** (2008), pp. 445-451.

[24] F.H. Stott, G.C. Wood, J. Stringer, *Oxidation of Metals* ***44*** (1995), pp. 113-145.

[25] F.S. Pettit, *Oxidation of Metals* ***76*** (2011), pp. 1-21.

[26] P. Hancock, *Corrosion Science* ***22*** (1982), pp. 51-65.

[27] V. Lemoine, P. Steinmetz, B. Roques, *Corrosion Science* ***25*** (1985), pp. 431-447.

[28] J.R. Nicholls, *Journal of Minerals, Metals and Materials Society* ***52*** (2000), pp. 28-35.

[29] J. Stringer, *Materials Science and Technology* ***3*** (1987), pp. 482-493.

[30] P. Hancock, *Materials Science and Technology* ***3*** (1987), pp. 536-544.

[31] G.H. Meier, *Materials Science and Engineering A* ***120*** (1989), pp. 1-11.

[32] X. Montero, M.C. Galetz, *Surface and Coatings Technology* ***304*** (2016), pp. 211-221.

[33] R.A. Rapp, *Corrosion Science* ***44*** (2002), pp. 209-221.

[34] R.A. Rapp, *Pure and Applied Chemistry* ***62*** (1990), pp. 113-122.

[35] R.A. Rapp, K.S. Goto, *Hot Corrosion of Metals by Molten Salts, Molten Salts 1,* Electrochemical Society Pennington (1981), p. 159.

[36] T. Gheno, M. Zahiri Azar, A.H. Heuer, B. Gleeson, *Corrosion Science* ***101*** (2015), pp. 32-46.

[37] K. Godlewski, E. Godlewska, *Materials Science and Engineering* ***88*** (1987), pp. 103-109.

[38] R.T. Wu, K. Kawagishi, H. Harada, Presentation for the Second German-Japanese workshop on thermal barrier coatings for gas turbines, Kyoto, May 2009.

[39] G.W. Goward, *Surface and Coatings Technology* ***108-109*** (1998), pp. 73-79.

[40] Y. Wang, H. Liu, X. Ling, Y. Weng, *Applied Thermal Engineering* ***102*** (2016), pp. 234-242.

[41] B. Gleeson, *Journal of Propulsion and Power* ***22*** (2006), pp. 375-383.

[42] G.W. Goward, D.H. Boone, *Oxidation of Metals* ***3*** (1971), pp.475-495.

[43] C. Houngninou, S. Chevalier, J.P. Larpin, *Applied Surface Science* ***236*** (2004), pp. 256-269.

[44] B.M. Warnes, D.C. Punola, *Surface and Coatings Technology* ***94-95*** (1997), pp. 1-6.

[45] J. Benoist, K.F. Badawi, A. Malié, C. Ramade, *Surface and Coatings Technology* ***194*** (2005), pp. 48-57.

[46] Y.Q. Wang, G. Sayre, *Surface and Coatings Technology* ***203*** (2009), 1264-1272.

[47] T.A. Kircher, B.G. McMordie, A. McCarter, *Surface and Coatings Technology* ***68-69*** (1994), pp. 32-37.

[48] www.particoat.eu.

[49] R. Prescott, M.J. Graham, *Oxidation of Metals* ***38*** (1992), pp. 233-254.

[50] H.J. Grabke, *Intermetallics* ***7*** (1999), pp. 1153-1158.

[51] D.K. Das, *Progress in Materials Science* ***58*** (2013), pp. 151-182.

[52] R. Darolia, W.S. Walston, M.V. Nathal, *Superalloys: NiAl alloys for turbine airfoils* (1996), pp. 561-570.

[53] G. Frommeyer, R. Rablbauer, *Steel Research International* ***79*** (2008), pp. 507-513.

[54] G.K. Dey, *Sadhana* ***28*** (2003), pp. 247-262.

[55] J. Angenete, K. Stiller, *Surface and Coatings Tehnology* ***150*** (2002), pp. 107-118.

[56] J.M. Brossard, B. Panicaud, J. Balmain, G. Bonnet, *Acta Materialia* ***55*** (2007), pp. 6586-6595.

[57] J. Angenete, *Aluminide diffusion coatings for Ni-based superalloys*, PhD Thesis, Chalmers University of Technology, Göteborg University (2002).

[58] K. Shivarni, S. Firouzi, A. Rashidghamat, *Corrosion Science* ***55*** (2012), pp. 378-384.

[59] R.E. Malush, P. Deb, D.H. Boone, *Surface and Coatings Technology* ***36*** (1988), pp. 13-26.

[60] B. Bouchaud, B. Rannou, F. Pedraza, *Materials Chemistry and Physics* ***143*** (2013), pp. 416-424.

[61] X. Montero, M.C. Galetz, M. Schütze, *Surface and Coatings Technology* ***222*** (2013), pp. 9-14.

[62] S. Shankar, L.L. Seigle, *Metallurgical Transactions A* ***9*** (1978), pp. 1467-1476.

[63] F. Pedraza, M. Mollard, B. Rannou, B. Bouchaud, J. Balmain, G. Bonnet, *Oxidation of Metals* ***85*** (2016), pp. 231-244.

[64] J.A. Haynes, B.A. Pint, K.L. More, Y. Zhang, I.G. Wright, *Oxidation of Metals* ***58*** (2002), pp. 513-544.

[65] X. Montero, M.C. Galetz, M. Schütze, *Journal of Minerals, Metals and Materials Society* ***67*** (2014), pp. 79-86.

[66] C.S. Giggins, F.S. Pettit, *Journal of The Electrochemical Society* ***118*** (1971), pp. 1782-1790.

[67] G.R. Wallwork, A.Z. Hed, *Oxidation of Metals* ***3*** (1971), pp. 171-184.

[68] C. Wagner, *Corrosion Science* ***5*** (1965), pp. 751-764.

[69] B. Gleeson, W.H. Cheung, W. Da Costa, D.J. Young, *Oxidation of Metals* ***38*** (1992), pp. 407-424.

[70] M.N. Task, B. Gleeson, F.S. Pettit, G.H. Meier, *Surface and Coatings Technology* ***206*** (2011), pp. 1552-1557.

[71] E. Godlewska, K. Godlewski, *Oxidation of Metals* ***22*** (1984), pp. 117-131.

[72] B.A. Pint, *Surface and Coatings Technology* ***188-189*** (2004), pp. 71-78.

[73] B.A. Pint, I.G. Wright, W.Y. Lee, Y. Zhang, K. Prüssner, K.B. Alexander, *Materials Science and Engineering A* ***245*** (1998), pp. 201-211.

[74] B.A. Pint, *Oxidation of Metals* ***48*** (1997), pp. 303-328.

[75] J. Angenete, K. Stiller, E. Backchinova, *Surface and Coatings Technology* ***176*** (2004), pp. 272-283.

[76] V.K. Tolpygo, *Surface and Coatings Technology* ***202*** (2007), pp. 617-622.

[77] F. Pedraza, A.D. Kennedy, J. Kopecek, P. Moretto, *Surface and Coatings Technology* ***200*** (2006), pp. 4032-4039.

[78] G.R. Krishna, D.K. Das, V. Singh, S.V. Joshi, *Materials Science and Engineering A* ***251*** (1998), pp. 40-47.

[79] J. Benoist, K.F. Badawi, A. Malié, C. Ramade, *Surface and Coatings Technology* ***182*** (2004), pp. 14-23.

[80] J.A. Haynes, M.J. Lance, B.A. Pint, I.G. Wright, *Surface and Coatings Technology* ***146-147*** (2001), pp. 140-146.

[81] K.M. Carling, E.A. Carter, *Acta Materialia* ***55*** (2007), pp. 2791-2803.

[82] S. Kitaoka, T. Kuroyama, M. Matsumoto, R. Kitazawa, Y. Kagawa, *Corrosion Science* ***52*** (2010), pp. 429-434.

[83] L. Qiu, F. Yang, W. Zhang, X. Zhao, P. Xiao, *Corrosion Science* ***89*** (2014), pp. 13-20.

[84] A. Rabiei, A.G. Evans, *Acta Materialia* ***48*** (2000), pp. 3963-3976.

[85] P.K. Wright, A.G. Evans, *Current Opinion in Solid State and Materials Science* ***4*** (1999), pp. 255-265.

[86] R.W. Jackson, D.M. Lipkin, T.M. Pollock, *Acta Materialia* ***80*** (2014), pp. 39-47.

[87] H.J. Kim, M.E. Walter, *Materials Science and Engineering A* ***360*** (2003), pp. 7-17.

[88] M. Reid, M.J. Pomeroy, J.S. Robinson, *Journal of Materials Processing Technology* ***153-154*** (2004), pp. 660-665.

[89] M.H. Vidal-Setif, N. Chellah, C. Rio, C. Sanchez, O. Lavigne, *Surface and Coatings Technology* ***208*** (2012), pp. 39-45.

[90] R. Wellman, G. Whitman, J.R. Nicholls, *Int. Journal of Refractory Metals and Hard Materials* ***28*** (2010), pp. 124-132.

[91] X. Chen, *Surface and Coatings Technology* ***200*** (2006), pp. 3418-3427.

[92] X. Chen, R. Wang, N. Yao, A.G. Evans, J.W. Hutchinson, R.W. Bruce, *Materials Science and Engineering A* ***352*** (2003), pp. 221-231.

[93] F. Pedraza, M. Mollard, B. Rannou, J. Balmain, B. Bouchaud, G. Bonnet, *Materials Chemistry and Physics* ***134*** (2012), pp. 700-705.

[94] X. Montero, M.C. Galetz, M. Schütze, *Surface and Coatings Technology* ***206*** (2011), pp. 1586-1594.

[95] M.C. Galetz, X. Montero, M. Mollard, M. Günthner, F. Pedraza, M. Schütze, *Intermetallics* ***44*** (2014), pp. 8-17.

[96] V. Kolarik, R. Roussel, M. Juez Lorenzo, H. Fietzek, *Materials at High Temperatures* ***29*** (2008), pp. 89-94.

[97] M. Mollard, Elaboration de systèmes barrière thermique par barbotine. Comportement du nickel et de ses superalliages revêtus en oxydation cyclique à haute température, PhD Thesis, Université de La Rochelle (2012).

[98] F. Pedraza, G. Boissonnet, B. Fernandez, B. Bouchaud, R. Podor, *Synthesis and related properties of low conductivity TBCs with hollow alumina microspheres*, 43rd ICMCTF (25-29 April 2016), San Diego (USA).

[99] B. Rannou, B. Bouchaud, J. Balmain, G. Bonnet, F. Pedraza, *Oxidation of Metals* ***81*** (2014), pp. 139-149.

[100] M. Mollard, B. Rannou, B. Bouchaud, J. Balmain, G. Bonnet, F. Pedraza, *Corrosion Science* ***66*** (2013), pp. 118-124.

[101] M. Brossard, *Influence de l'eau (vapeur, liquide) et du régime d'oxydation sur la dégradation de revêtements alumino-formeurs sur superalliage à base nickel*, PhD Thesis, Université de La Rochelle (2014).

[102] B. Rannou, Slurry coatings from aluminium microparticles on Ni-based superalloys for high-temperature oxidation protection, PhD Thesis, Université de La Rochelle (2012).

[103] F. Pedraza, R. Podor, *Materials Characterization* ***113*** (2016), pp. 198-206.

Chapter II– Experimental methods

I. Materials of study 41

II. Elaboration of the slurry coatings on metallic substrates 44

II.1. Characterization of the metallic powders 44

II.2. Composition and preparation of the slurries 46

II.3. Deposition of the slurries by air brush on metallic substrates 47

II.4. Thermal treatments 49

III. Environmental degradation of the slurry coatings 51

III.1. Isothermal and cyclic oxidation 51

III.2. Hot corrosion tests 53

IV. Characterization methods 55

IV.1. Calorimetry and thermal analyses 55

a) Differential Scanning Calorimetry (DSC) 55

b) Laser Flash Analysis (LFA) 56

IV.2. Crystallographic and structural analyses 58

a) X-Ray Diffraction (XRD) 58

b) Raman micro-spectrometry and Cr^{3+} fluorescence 58

IV.3. Microscopic and elemental analyses 60

a) Optical microscopy 60

b) Scanning Electron Microscopy (SEM) and Energy Dispersive X-ray Spectroscopy (EDS) .. 60

c) Electron Probe Micro-Analysis (EPMA) 61

References 62

I. Materials of study

Several nickel-based materials were used in the study for the formation of diffusion and thermal barrier coatings by slurry process (Table II-1). Pure Ni and Ni20Cr were used as model materials to study the mechanisms of formation of the coatings before extrapolation to Ni-based superalloys presenting more complex chemical composition. The influence of the microstructure of the alloys was investigated after optimization of the slurry compositions. Directionally solidified superalloys such as CM-247 LC (low carbon) and DS200 are used to produce turbine components of the first LPT stages [1] whereas equiaxed superalloys, such as IN100, are employed for further LPT stages [1].

Table II-1. Chemical composition (wt.%) of the investigated nickel-based materials.

Material	Ni	Cr	Si	Al	Co	W	Mo	Ti	Ta	Hf
Pure Ni (EQ)	Bal.									
Ni20Cr (EQ)	Bal.	20.0	1.5							
CM-247 LC (DS)	Bal.	8.0	-	5.6	9.3	9.5	0.5	0.7	3.2	1.4
DS200 (DS)	Bal.	8.4	-	5.0	10.0	12.5	-	1.8	-	2.2
IN100 (EQ)	Bal.	10.0	-	5.5	15.0	-	3.0	4.7	-	-

For pure Ni, Ni20Cr and CM-247 LC materials, the samples were prepared from cylindrical rods with a Struers Secotom-50 cutting blade in the form of coupons of approximately 2.0±0.2 mm thickness. Different Ni substrates were used depending on the application. The details are given in Table II-2. To investigate the reactivity between pure Ni and the metallic powders by DSC, a 4.0±0.1 mm diameter substrate was used allowing the introduction of the samples in the alumina crucibles. Due to the availability of the material, the development of the coatings and the hot corrosion tests were done using the Ni substrate with a diameter of 12.7±0.1 mm. The DS200 and IN100 materials were used to extrapolate the slurry coatings developed during the study on aircraft nickel-based superalloys (*results not presented in the manuscript*). For these two materials, the samples were prepared from non-repairable gas turbine blades kindly provided by SR Technics Airfoils Services (Cork, Ireland). The use of engine run components as parent materials was considered as a first step to transfer the research of the present study to an industrial scale.

Table II-2. Summary of the substrates used for the different applications in the study.

Application	Material	Diameter (mm)	Supplier
Reactivity between Ni and powders **(Chapter III)**	**Pure Ni**	**4.0±0.1**	Goodfellow
Development of the coatings **(Chapters III, IV and V)**	**Pure Ni**	**12.7±0.1**	Goodfellow
	Ni20Cr	12.0±0.1	Goodfellow
	CM-247 LC	20.0±0.1	Siemens
Hot corrosion tests **(Chapter VI)**	**Pure Ni**	**12.7±0.1**	Goodfellow
Oxidation tests **(Chapter VI)**	**Pure Ni**	**12.7±0.1**	Goodfellow
	CM-247 LC	20.0±0.1	Siemens
Extrapolation to gas turbine blades	DS200	Airfoil	SR Technics
	IN100	Airfoil	SR Technics

Pure Ni and Ni20Cr materials present a γ-(Ni) matrix whereas the CM-247 LC superalloy display a γ-γ' microstructure. The XRD patterns of the different materials are presented in Fig. II-1. The FCC structure of γ-(Ni) was identified for both pure Ni and Ni20Cr materials. Note the preferential orientation of pure nickel through the (111) crystallographic direction. For the CM-247 LC superalloy, only the (200) crystallographic direction was observed as expected for this directionally-solidified material.

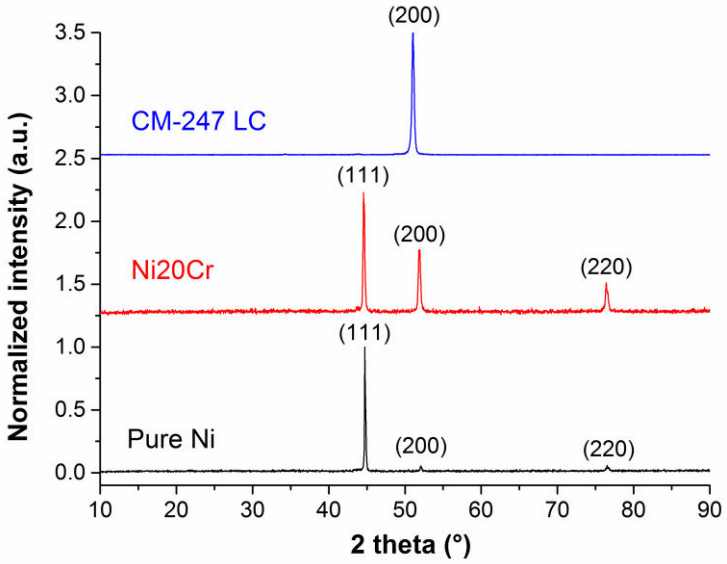

Fig. II-1. XRD patterns of the nickel-based materials investigated in the study.

The microstructure of an "as-cast" CM-247 LC superalloy was investigated after electrolytic etch with 10% oxalic acid (Fig. II-2). If the superalloy was mainly composed of a regular γ-γ' duplex microstructure (Fig. II-2b) [2-7], undissolved carbides were observed in the interdendritic regions (Fig. II-2a). These (Hf,Ta,W)-rich carbides (according to EDS spot measurements and literature [5]) resulted from the dissociation of MC into M_6C with a surrounding γ' envelope [8-10]. In the dendritic regions, the coarsening of γ' was observed with a rafted microstructure [6,9,11].

The carbides originally present in the substrate were used as natural markers to identify the initial surface of the substrate after aluminizing and thus to determine the coating growth direction [12,13].

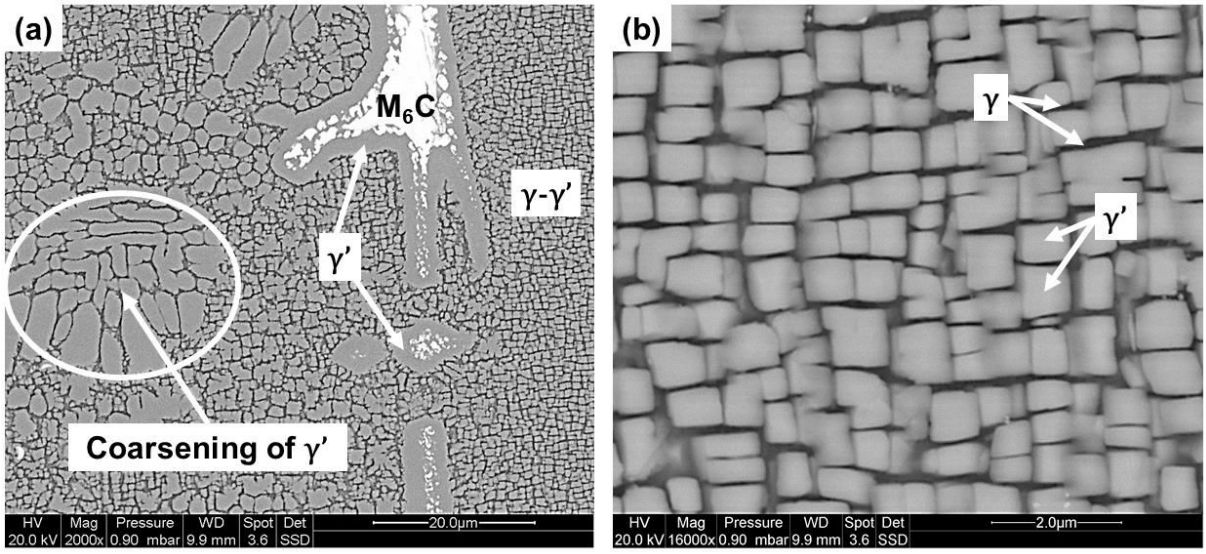

Fig. II-2. (a) Microstructure of the CM-247 LC superalloy in an interdendritic region and (b) zoom in the γ-γ' duplex microstructure (electrolytically etched with 10% $H_2C_2O_4$).

II. Elaboration of the slurry coatings on metallic substrates

The slurry coatings developed in the present study were based on the environmentally-friendly composition developed during the European project "PARTICOAT" [14,15]. The elaboration of a slurry coating follows the sequence:

1. Surface preparation of the metallic substrate to be coated.
2. Preparation of the slurry (organic binder + deionized water + metallic powders).
3. Deposition of the slurry by air brush then drying of the slurry deposit.
4. Heat treatment in Ar or in air to form the diffusion coating or the complete thermal barrier system.

The next paragraphs will present the experimental procedure for the elaboration of the slurry coatings once the metallic powders used in the present study characterized.

II.1. Characterization of the metallic powders

Different metallic powders were selected to investigate their reactivity before the preparation of the slurries (Table II-3). The Al powder supplied by Sibthermochim (Russia) was composed of spherical microparticles with a mean diameter of 8±2µm (Fig. II-3). These microparticles were elaborated by wire electrical explosion (WEE) [16,17] and were passivated to limit their reactivity prior to shipping [18]. Two different Cr powders supplied by Goodfellow were selected in the study. The fine Cr powder was composed of microparticles with a complex geometry and a mean diameter of 5±1µm (Fig. II-3). The microparticles of the coarse Cr powder were approximately ten times larger than that of the fine Cr powder (Fig. II-3). The influence of the size of the Cr microparticles on their reactivity with the Al ones was investigated according to their respective specific surface area (Chapter III). The use of the coarse Cr powder was found to be detrimental upon aluminizing in order to obtain homogeneous diffusion layers and the ceramic top coat. Therefore, the fine Cr powder was selected for the development and the production of the coatings on metallic substrates afterwards.

Table II-3. Characteristics of the metallic powders investigated in the study.

Powders	Supplier	Theoretical size (µm)	Experimental size (µm)	Geometry
Al	Sibthermochim	<20	2-17	Spherical
Cr (fine)	Goodfellow	<10	2-10	Complex
Cr (coarse)	Goodfellow	38-45	20-70	Complex

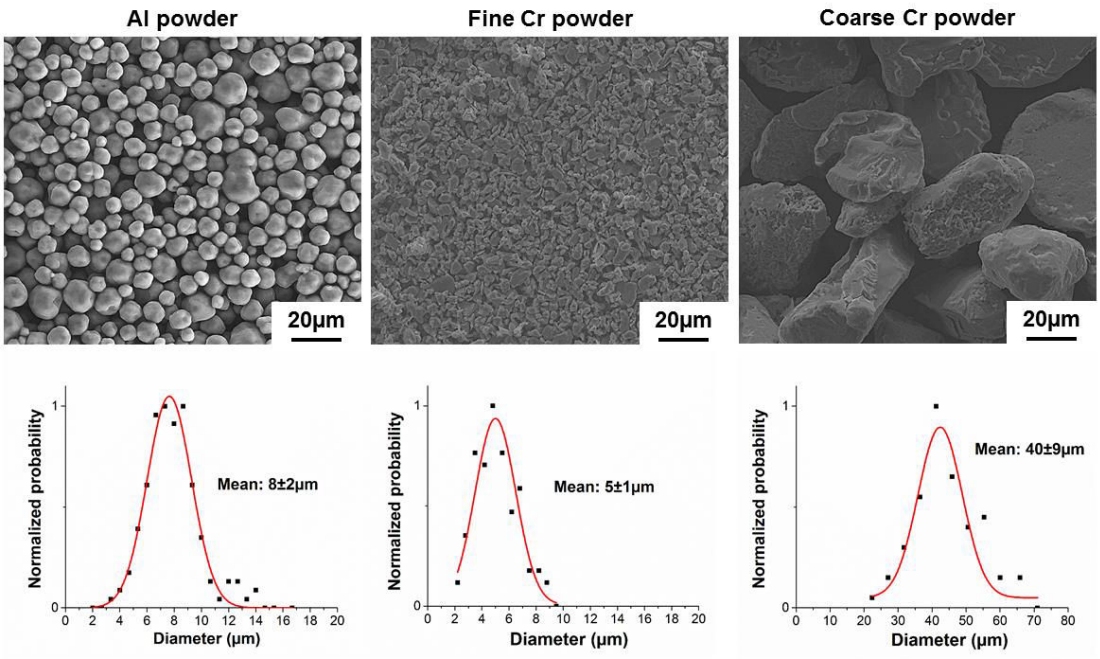

Fig. II-3. SEM images and size dispersion of the microparticles for the three powders investigated in the study.

The metallic powders were analysed by Energy-Dispersive X-ray Spectroscopy (EDS) to detect the potential presence of impurities and determine their oxidation level. The results are summarized in Table II-4. The presence of impurities was not reported with the resolution of the EDS measurements. However, the O content was significantly higher for the Cr powders than for the Al ones. This probably resulted from the peripheral passivation/oxidation of the Cr microparticles (observation of a cellular microstructure on the coarse Cr microparticles in Fig. II-3). The three metallic powders were characterized by X-ray diffraction (XRD) to identify their crystal structures. The XRD patterns given in Fig. II-4 were used as references to study the reactivity between Al and Cr microparticles (Chapter III).

Table II-4. EDS window analyses of the different metallic powders investigated in the study.

	Al		Cr		O	
Powders	**wt.%**	**at.%**	**wt.%**	**at.%**	**wt.%**	**at.%**
Al	96 ± 1	94 ± 2	-	-	4 ± 1	6 ± 2
Cr (fine)	-	-	91 ± 2	75 ± 2	9 ± 2	25 ± 2
Cr (coarse)	-	-	92 ± 2	77 ± 2	8 ± 2	23 ± 2

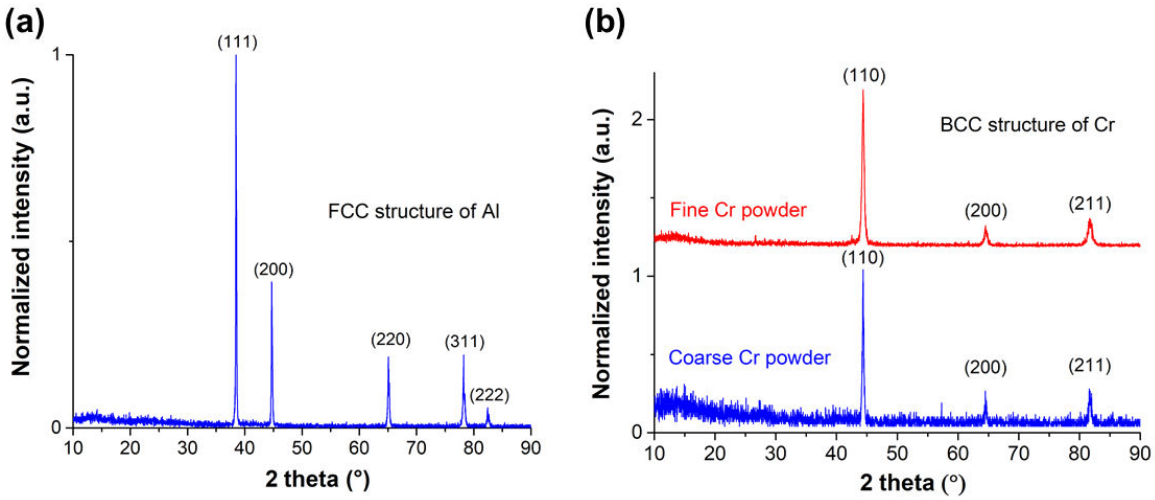

Fig. II-4. XRD patterns of (a) the Al powder and (b) the two Cr powders investigated in the study.

II.2. Composition and preparation of the slurries

The different slurries used in the present study were composed of:

- Metallic powders (pure Al, pure Cr or Al-Cr mixtures)
- Polyvinyl alcohol (PVA) furnished by Sigma Aldrich as an organic binder soluble in water [19]
- Milli-Q water as a solvent

The PVA was dissolved in milli-Q water at approximately 80°C under magnetic stirring. For all the slurry compositions, the PVA/water ratio was fixed at 1/10 in weight. Rannou et al. have shown that there was no influence of the ageing time for this composition up to at least 9 days [14]. For a good reproducibility, the slurry coatings elaborated for testing the reactivity with the substrate and for the development of the coatings (Chapters III, IV and V) were done with as-prepared solutions. To produce a larger number of samples (for oxidation and hot corrosion tests, Chapter VI), a more important amount of solution was prepared and used up to one week afterwards to save time and products. The ageing of the solution with time was found to have no influence neither upon aluminizing nor on the final microstructure of the coatings.

Thereafter, the metallic powders were added to the organic solution in a pill box with the proportions given in Table II-5. The proportions of the metallic powders for each composition were selected empirically after deposition tests to obtain an appropriate "visual" viscosity (not measured in this study) and a good coverage of the metallic substrate by air brush.

Table II-5. Compositions of the different slurries investigated in the study using the Al powder delivered by Sibthermochim and the fine Cr powder delivered by Goodfellow.

Slurry	Composition of the metallic part	Amounts in the pill box	Metallic part in the slurry composition (wt.%)
Al	100 wt.% Al	2g Al	45
Cr	100 wt.% Cr	4g Cr	61
67Al33Cr	67 wt.% Al + 33 wt.% Cr	1.6g Al + 0.8g Cr	48
44Al56Cr	44 wt.% Al + 56 wt.% Cr	1.5g Al + 1.9g Cr	57
20Al80Cr	20 wt.% Al + 80 wt.% Cr	0.9g Al + 3.6g Cr	63

II.3. Deposition of the slurries by air brush on metallic substrates

Before applying the slurries, the samples were ground using a SiC #180 paper grade then rinsed with de-ionized water and finally ultrasonically cleaned in ethanol. This surface preparation improved the adherence of the microparticles-containing slurries onto the metallic substrates as well as their good coverage over the whole surface. The deposition of the slurries was realized using an air brush (AZTEK A4709T model) with a nozzle of 0.7 mm in diameter (Fig. II-5a). During the slurry deposition, the sample holder (Fig. II-5b) rotated with a constant speed of 5.25×10^{-3} m.s^{-1} (1 rpm) [20]. The distance between the nozzle and the metallic substrates was fixed at 10 cm for better reproducibility. One can see the progressive drying of the slurry deposit upon the rotation of the sample holder in Fig. II-5b. For reproducibility and to control the amount of slurry deposited on the metallic surfaces, the samples were weighed before and after spray with a 10^{-4} g precision balance.

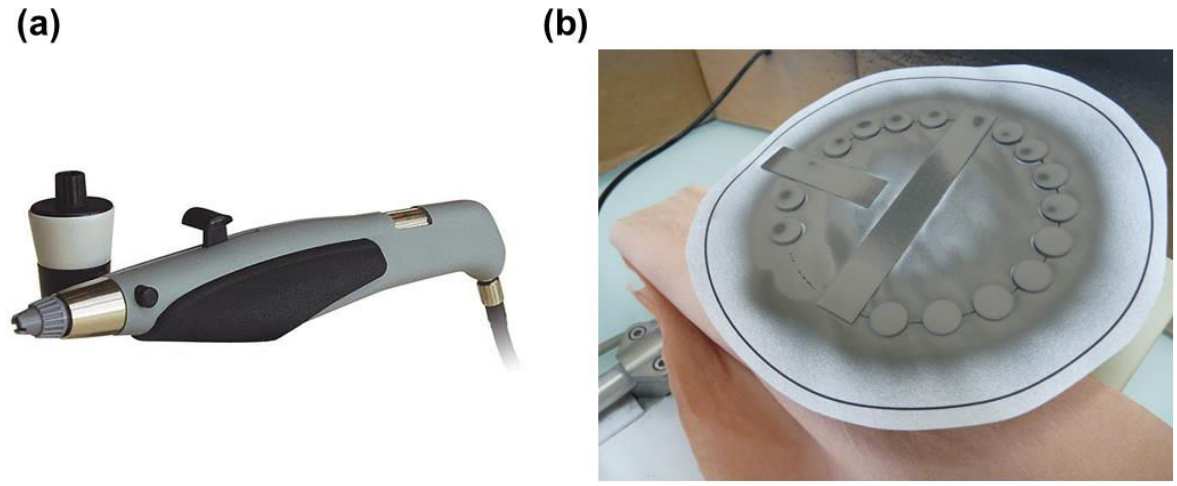

Fig. II-5. (a) Picture of the air brush and (b) view of the samples after deposition of the slurry by air brush.

As discussed in the paragraph VI.2 of Chapter I, the addition of Cr in the slurry compositions was expected to play a beneficial role on different parameters. For simple Al slurry coatings, the aluminizing of the substrates was found to be fast with the formation of liquid phases because of highly exothermic reactions [21]. This resulted in the formation of high-activity coatings with a significant amount of substrate elements in the outer layer of the coating [22]. In order to decrease the Al activity upon aluminizing [23,24], three different Al-Cr architectures were envisaged (Fig. II-6). The mechanisms of formation of the coatings for these different architectures were investigated using pure Ni as a model material (Chapter III). Depending on the initial architecture, different coatings were successfully obtained with different chemical and mechanical gradients. The elaboration of the coatings was performed keeping in mind the required final application ("materials by design"). Therefore, the optimization of the compositions was carefully processed before extrapolation to industrial alloys. The main objective was to increase the performances of the coatings for high-temperature applications.

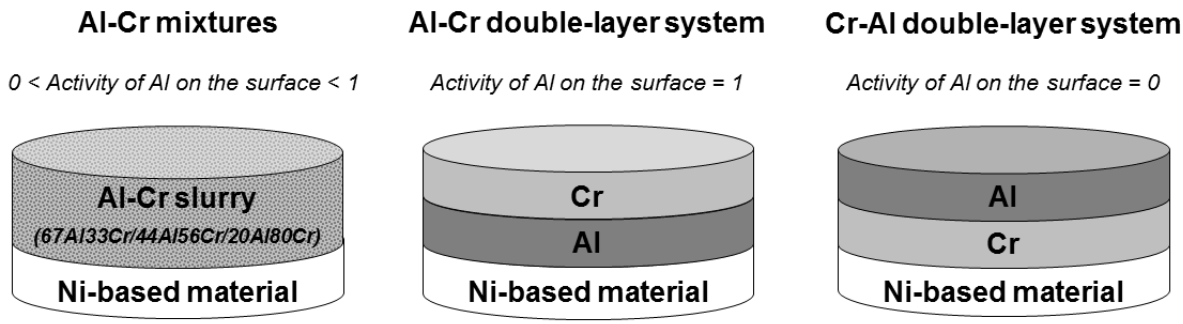

Fig. II-6. Architectures of the three different Al-Cr systems investigated in the study.

SEM and EDS techniques were carried out to investigate the morphology and the composition of the slurry deposits to prove the reliability of the air brush deposition. The macrographs and the SEM surface images of the different slurry deposits are given in Fig. II-7. According to the surface macrographs, the deposition of the slurries was homogeneous with a good coverage of the surface (barely no edge effects). For the three Al-Cr slurry mixtures, a random distribution of Al and Cr microparticles can be observed in Fig. II-7. EDS window analyses on different areas of the samples demonstrated that the experimental Al/Cr ratio of the deposits was very close to that of the initial mixture for the three compositions. For the 67Al33Cr, 44Al56Cr and 20Al80Cr slurry mixtures, the EDS measurements (in wt.%) gave respectively, 69±2 Al:31±2 Cr, 47±2 Al:53±2 Cr and 22±2 Al:78±2 Cr.

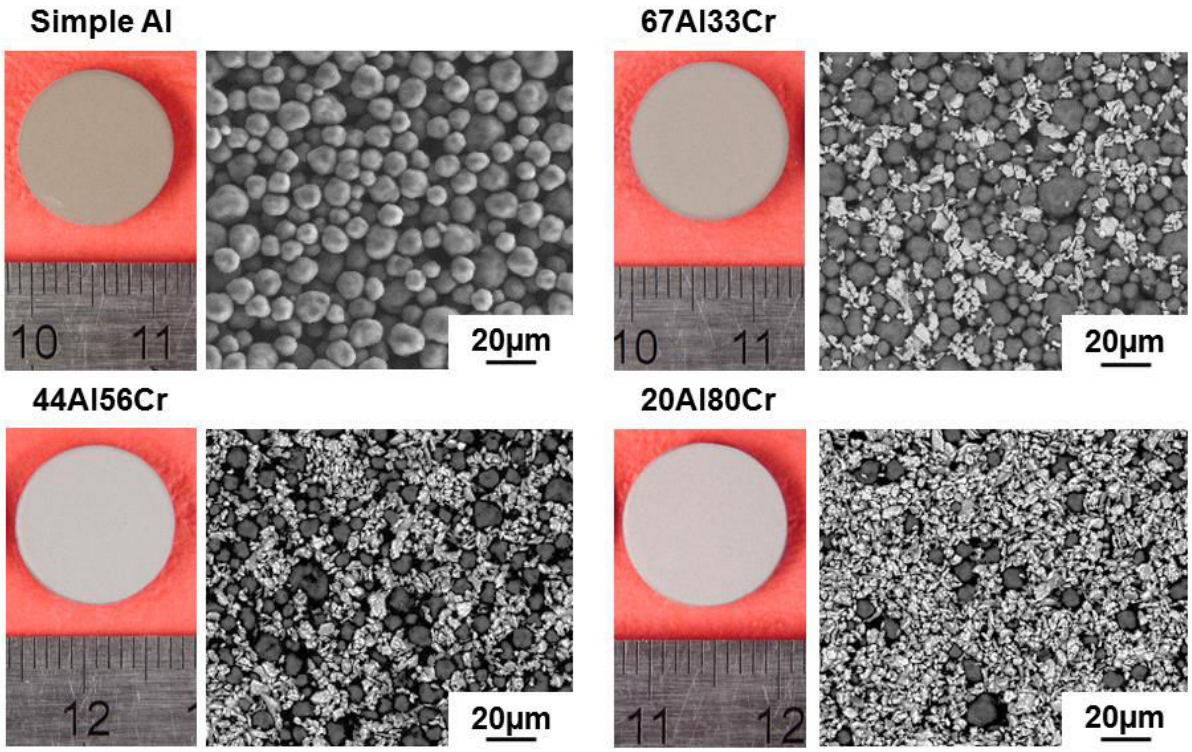

Fig. II-7. Macrographs and SEM surface images (BSE mode) of pure Ni after deposition of the different slurry compositions.

After deposition of the slurry, the samples were left at least one hour for drying in laboratory air before any other step [14]. The further formation of the coatings was realized by heat treatment in an inert atmosphere (Ar) or in air depending on the design of the coating (environmental coating or complete thermal barrier system).

II.4. Thermal treatments

Two different experimental set-ups were employed to perform the heat treatments.

- **Thermogravimetric analysis (TGA):**

A SETARAM TGA 92 thermobalance with a 10^{-6} g accuracy was employed to study the evolution with time of the different slurry coatings on pure nickel (Chapter III). The evolution of the mass variation during the heat treatment was indeed helpful to detect the different events occurring on the sample (water evaporation, binder decomposition and oxidation of the microparticles). Before the heat treatment, the gas pressure in the reaction chamber was first decreased with a vacuum pump (down to $5x10^{-2}$ mbar) and then argon was progressively introduced. Upon annealing, the reaction chamber was ventilated with an Ar flow (20 mL/min). The heating rate was fixed at 5°C/min and the cooling rate at 50°C/min to keep the microstructure developed at the annealing temperature to room temperature

for a better comprehension of the mechanisms of formation. All samples were systematically cured for 3 hours at 400°C in order to expel the organic binder. The different heat treatments performed in the TGA are summarized in Table II-6.

Table II-6. Details of the heat treatments performed in the TGA to investigate the mechanisms of formation on pure Ni.

Slurry systems	Decomposition of the organic binder	Diffusion step	Homogenization step
Pure Al Al-Cr mixtures Al-Cr double-layer Cr-Al double-layer	400°C-3h	650°C-5h	-
Pure Al Al-Cr mixtures Al-Cr double-layer Cr-Al double-layer	400°C-3h	650°C-5h	1000°C-3h
Al-Cr mixtures Cr-Al double-layer	400°C-3h	1080°C-6h	-
Pure Al [20,25,26]	400°C-1h	700°C-2h	1100°C-2h

According to the supplier, small amount of impurities are present in the gas bottle (5 vpm H_2O and 2 vpm O_2). Referring to the Ellingham diagram (thermodynamic considerations), the content of these oxidizing species is sufficient to provoke the oxidation of Al and Cr at temperatures above 600°C. To investigate the oxidation and the sintering of the microparticles upon annealing (Chapter V), some heat treatments were also performed partially or completely in synthetic air (80 vol.% N_2 + 20 vol.% O_2). Note that the heat treatment selected in previous studies in the group of F. Pedraza [20,25,26] was also performed to investigate the influence of the atmosphere (Ar and synthetic air) on the aluminization of pure nickel from Al microparticles (Chapter V).

- **Horizontal furnace:**

For the simultaneous production of several samples and the aluminizing of larger samples, a Carbolite horizontal furnace with a quartz tube was employed. In order to remove moisture, the reaction chamber was first purged with a vacuum pump down to approximately 1.0 mbar. Then, the argon flow was alternatively turned on and off for 30 minutes (three cycles in total) while keeping the vacuum pump on to clean thoroughly the furnace. After the procedure, the internal pressure in the furnace decreased down to less than 0.2 mbar. Then, the furnace was filled with argon at a pressure slightly over the atmospheric pressure. During the annealing, the furnace was ventilated with a flow of argon. The same heat treatments than the TGA experiments were performed depending on the slurry coatings deposited on the samples. However, the cooling rate was slower than in the TGA because of the inertia of the furnace.

III. Environmental degradation of the slurry coatings

III.1. Isothermal and cyclic oxidation

The oxidation behaviour of the coated and uncoated samples was investigated under isothermal and cyclic conditions under atmospheric pressure. The samples were oxidized for short (3 to 100 hours) and long term exposures (up to 1000 hours). The different thermogravimetric experiments (continuous or discontinuous isothermal testing and cyclic oxidation testing) were expected to give an overview of the high-temperature resistance of the coatings elaborated during the study [27,28].

- **Isothermal oxidation:**

For short term exposure (up to 100 hours), isothermal oxidation tests were done in a SETARAM TGA 92 thermobalance in synthetic air (80 vol.% N_2 + 20 vol.% O_2) to continuously monitor the mass variation of the samples (10^{-6} g accuracy). As previously described, the reaction chamber was first purged with a vacuum pump down to 5.10^{-2} mbar then filled with Ar. The heating ramp was fixed at 50°C/min under flowing Ar (20 mL/min). Once the dwell temperature was reached, the reaction chamber was purged for about 8 seconds before the introduction of synthetic air (16 mL/min). At the end of the oxidation test, the samples were cooled down to ambient temperature at 50°C/min.

The continuous isothermal long term oxidation tests were realized up to 500 hours and 1000 hours using a Pyrox furnace in laboratory air. The mass variation of the samples was recorded with a Sartorius Quintix Secura 10^{-5} g precision balance to extrapolate the short term measurements done in TGA.

- **Cyclic oxidation:**

To simulate thermal cycling conditions observed in aircraft gas turbines [27], cyclic oxidation tests were performed using a Delta Thermique cyclic rig (Fig. II-8a). This rig displays two independent furnaces able to work separately and to execute two different thermal cycling procedures (temperature, dwell time and frequency of the cycles). The cycles are performed automatically thanks to pneumatic cylinders moving up and down the ceramic block holding the samples (Fig. II-8b). A cycle is decomposed as follows:

- introduction of the samples in the furnace at the oxidation temperature,
- hot dwell time at the oxidation temperature,
- removal of the samples from the furnace and fast cooling with compressed air.

The cooling of the samples is ensured with four cooling nozzles flushing compressed air during the cold dwell time (Fig. II-8b). With a diameter of 200 mm, the ceramic block allows to place several alumina boats at the same time (Fig. II-8c). The right furnace (Fig. II-8a) working up to 1300°C was used in this study for the cyclic oxidation tests at 1000°C. Standard cycles of 1 hour were performed (45 minutes at 1000°C and 15 minutes of cooling). After 15 minutes of cooling, the temperature of the samples decreases below 80°C. The temperature inside the furnace was continuously measured with a type-S thermocouple (Pt-Rh10/Pt) protected in an alumina sheath (Fig. II-8c). A computer was connected to the furnace to follow the thermal cycles. The mass variation of the samples was regularly measured with a Sartorius Quintix Secura 10^{-5} g precision balance to follow the oxidation kinetics.

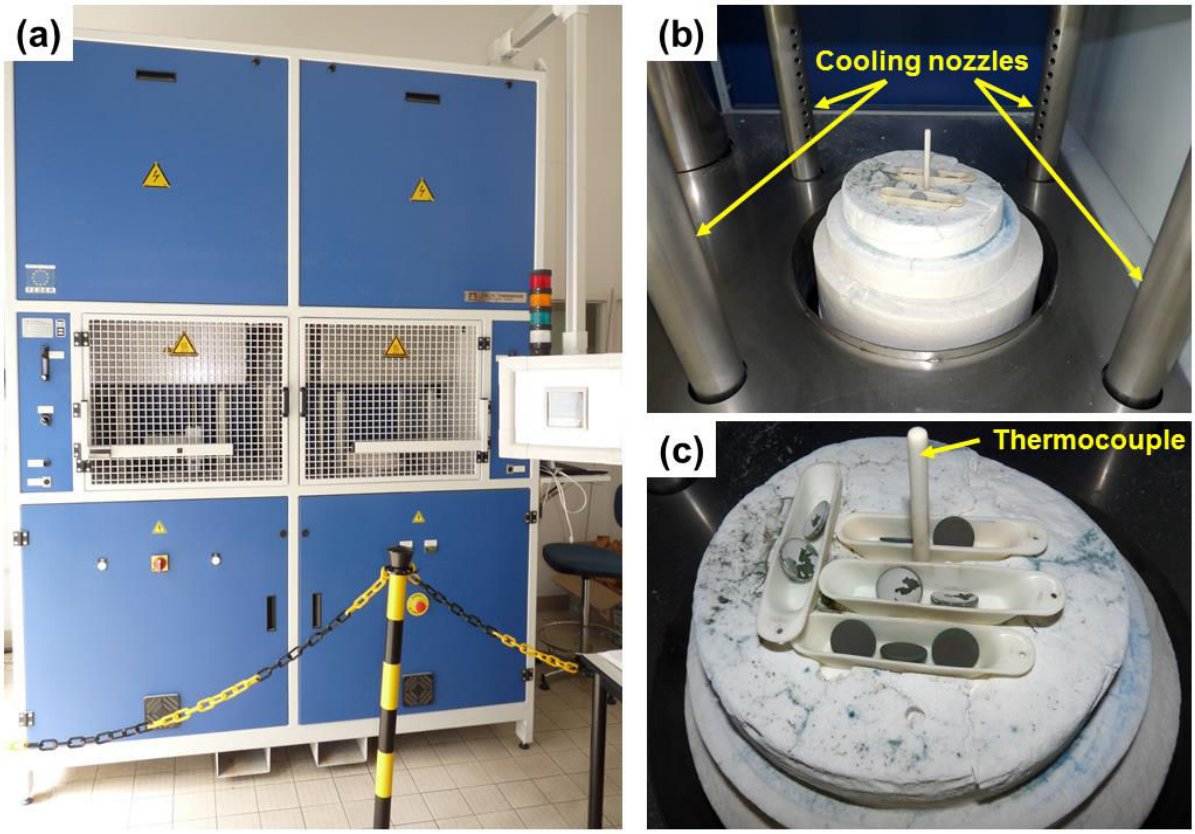

Fig. II-8. Images of the Delta Thermique rig with (a) view of the two furnaces with the panel program on the right side, (b) view of the cooling nozzles and the ceramic block and (c) alumina boats containing the samples and placed around the thermocouple.

III.2. Hot corrosion tests

The hot corrosion tests were carried out during a three months stay in DECHEMA-Forschungsinstitut with the collaboration of Dr. Hab. Mathias C. Galetz and Dr. HDR Xabier Montero. A schematic representation of the experimental set up is given in Fig. II-9a. The hot corrosion tests were performed in a horizontal furnace (Fig. II-9b) at 700°C in a synthetic air-0.5% SO_2 atmosphere corresponding to Type-II hot corrosion conditions [29]. Since Na_2SO_4 is the most common salt deposit in aircraft gas turbines [30], this salt was selected in this study. In Type-II hot corrosion conditions, a sufficient partial pressure of SO_3 is required in the gas flow to stabilize liquid sulfates [31,32]. Therefore, four iron zeolite catalysts were placed in the gas flow upstream of the samples to oxidize SO_2 following reaction *(Eq. II-1)*:

$$SO_2(g) + \frac{1}{2}O_2(g) \rightarrow SO_3(g) \qquad \textbf{(Eq. II-1)}$$

Each iron zeolite catalyst was in the form of a 15 cm long tube with a diameter of approximately 3 cm. To increase the specific surface area in contact with the gas flow and optimize the conversion rate of reaction *(Eq. II-1)*, the catalysts had a honeycomb shape. The calculated equilibrium p_{SO_3} was 7.5x10^{-3} atm. at 700°C from data in Ref. [30]. The gas flow rate was adjusted at 100 mL/min (6 L/h) with an overall pressure in the furnace slightly over 1 atm. This value is higher than the minimum p_{SO_3} required for the formation of liquid phases at 700°C (3x10^{-4} atm. according to Ref. [33]). Even though Na_2SO_4 is solid at 700°C, liquid phases can be observed in the presence of nickel and cobalt sulfates

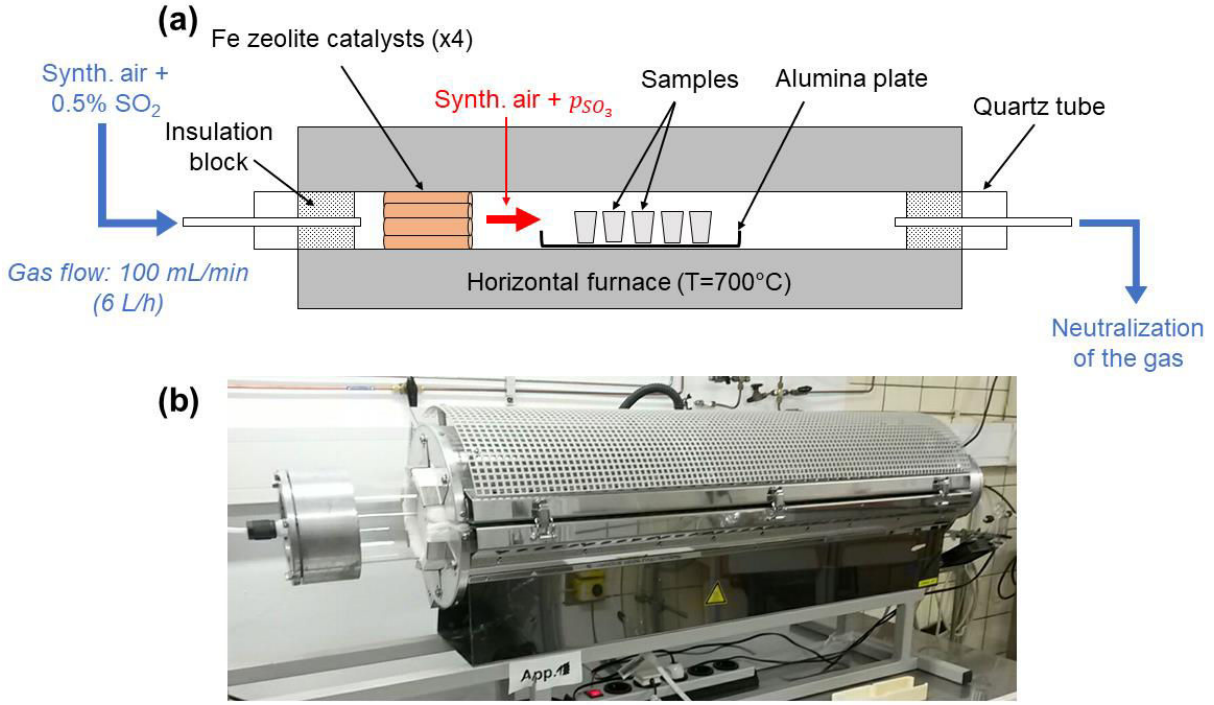

Fig. II-9. (a) Experimental set up and (b) picture of the horizontal furnace used for the hot corrosion tests in DECHEMA-Forschungsinstitut.

($T_e(Na_2SO_4\text{-}NiSO_4)$=671°C and $T_e(Na_2SO_4\text{-}CoSO_4)$=565°C [34]). According to the thermodynamic stability diagrams calculated by Gheno et al., the p_{SO_3} of the present study was too low to form aluminium and chromium sulfates [34]. The temperature of the furnace was calibrated with a type-K thermocouple (Ni-Cr/Ni-Alumel). The "hot zone" of the furnace was approximately 14 cm long allowing the simultaneous treatment of up to 24 samples for each batch.

To simulate hot corrosion tests, two different experimental procedures are usually considered in the literature: salt spraying or salt recoating methods [29,34-39] and half or full embedding in the corrosive salt [40-43]. These experiments progressively replaced the burner rig tests [44,45] at laboratory scale for practical and economic reasons. The half-embedding method (or crucible test method) was selected in this study since this method is highly useful for preliminary screening of materials and coatings [46]. With only half of the sample embedded in the salt, it is possible to characterize three distinct zones for one sample (atmosphere only, salt + atmosphere and the interface between the two zones) [43]. Depending on the initial material or coating, the size of the samples (12.7 mm diameter for pure Ni) appeared to be a limitation to clearly differentiate these areas after long term exposure (> 100h). With the crucible test method, the analysis of the salt was also possible after the experiments. For reproducibility, the same amount of Na_2SO_4 was poured in the alumina crucibles (approximately 2.5 g of salt).

The hot corrosion tests were performed for 20h, 100h and 300h of exposure to describe an evolution and investigate the corrosion mechanisms. To emphasize the influence of the atmosphere and the presence of Na_2SO_4 on the corrosion rate, complementary tests were done and are summarized in Table II-7. Therefore, by comparison of experiments 1a and 2a, the influence of Na_2SO_4 in a SO_3-containing atmosphere was investigated whereas the comparison of experiments 1a and 1b was useful to study the influence of p_{SO_3} on the oxidation behaviour of the materials and the coatings. The experiment 1b was done in a box furnace in DECHEMA-Forschungsinstitut calibrated with a type-K thermocouple (Ni-Cr/Ni-Alumel).

For the hot corrosion tests, the slurry diffusion coatings were elaborated on pure Ni to clearly investigate the role of each alloying element on the hot corrosion resistance. Indeed, the complex composition of nickel-based superalloys (Table II-1) may disturb the corrosion mechanisms with the inclusions of substrate elements in the oxide scales developed on the surface. Since the experimental set up was build up for this study, pure nickel samples were submitted to each batch as reference samples. By comparison with literature [29,47,48], it was then possible to evaluate the corrosiveness of the atmosphere and validate the experimental set up.

Table II-7. Synthetic table for the different corrosion tests done in DECHEMA-Forschungsinstitut. The thermogravimetric measurements were done in La Rochelle.

Test	Principle	Atmosphere	Temperature (°C)	Furnace
1a	Half-embedding	Synth. air + SO_2/SO_3	700	Horizontal furnace (Fig. II-9b)
1b	Half-embedding	Lab air		Box furnace
2a	Without salt	Synth. air + SO_2/SO_3		Horizontal furnace (Fig. II-9b)
2b	Without salt	Synth. air		TGA
		Lab air		Box furnace

IV. Characterization methods

IV.1. Calorimetry and thermal analyses

a) Differential Scanning Calorimetry (DSC)

The DSC technique is able to detect thermal events occurring in the investigated system by comparison with a reference sample. The DSC analyses were carried out using a SETARAM Labsys Evo 1600 thermal analysis. The measurements were performed in flowing Ar (20 mL/min) to limit oxidation phenomena and prevent secondary reactions in the system. For the different systems investigated, energy changes and temperatures of reaction or transformation were measured with the Calisto software coupled to the DSC instrument. Different heat treatments were performed, using alumina crucibles (90 µL), depending on the system (Table II-8). The alumina crucibles were systematically cured at 1350°C before DSC tests to avoid any contribution from the crucible on the measurements. The DSC was particularly helpful to analyse the reactivity between Al and Cr powders without and with substrate.

Table II-8. Parameters for the different heat treatments performed with the DSC.

System	Heating rate	Maximum temperature	Cooling rate
Elemental powders	10°C/min	1300°C	10°C/min
Mixture of powders	10°C/min	1300°C	10°C/min
	5°C/min	650°C	50°C/min (quench)
Substrate + powders	10°C/min	1300°C	10°C/min
Substrate + slurry deposit	5°C/min	1200°C	5°C/min

b) Laser Flash Analysis (LFA)

Since the thermal barrier coatings are applied to metallic components to decrease the metal temperature, the determination of their thermophysical properties is of utmost importance to ensure the integrity of the underlying metal substrate. Indeed, the thermal conductivity of TBC coatings together with the coating thickness control the temperature drop between the atmosphere and the metal-coating interface [49,50]. The porosity of the coatings has a particularly great influence on the thermal conductivity values of the full thermal barrier system [51-53]. Increasing the porosity lowers the thermal conductivity values which attests the attractive design of the thermal barrier system elaborated by slurry coatings [15,20,25,54].

The fundamental relationship to determine the thermal conductivity is given in equation *(Eq. II-2)*:

$$\lambda = \alpha \cdot c_p \cdot \rho \qquad \textbf{(Eq. II-2)}$$

With λ: the thermal conductivity, α: the thermal diffusivity, c_p: the specific heat capacity and ρ: the density.

The determination of the thermal diffusivity of the slurry coatings was carried out using a laser flash technique [49]. The laser flash technique is an ASTM standard method (E1461) [55]. A schematic of this technique is given in Fig. II-10a. The test involves:

- subjecting the entire front surface of a sample to a short duration radiant energy pulse from a laser (less than 2 ms usually),
- recording the rear face temperature rise after absorption of the pulse by the front surface.

The thermal diffusivity is calculated from the sample thickness and the time required to the heat from the front surface to reach a certain percentage of the maximum temperature at the rear surface of the sample [49]. The determination of the thermal diffusivity is given by equation *(Eq. II-3)*:

$$\alpha = K_x \cdot \frac{L^2}{t_x} \qquad \textbf{(Eq. II-3)}$$

With α: the thermal diffusivity, K_x: a constant corresponding to the x percentage of the maximum temperature rise, L: the sample thickness and t_x: the time required for the rear surface temperature to reach the x percentage.

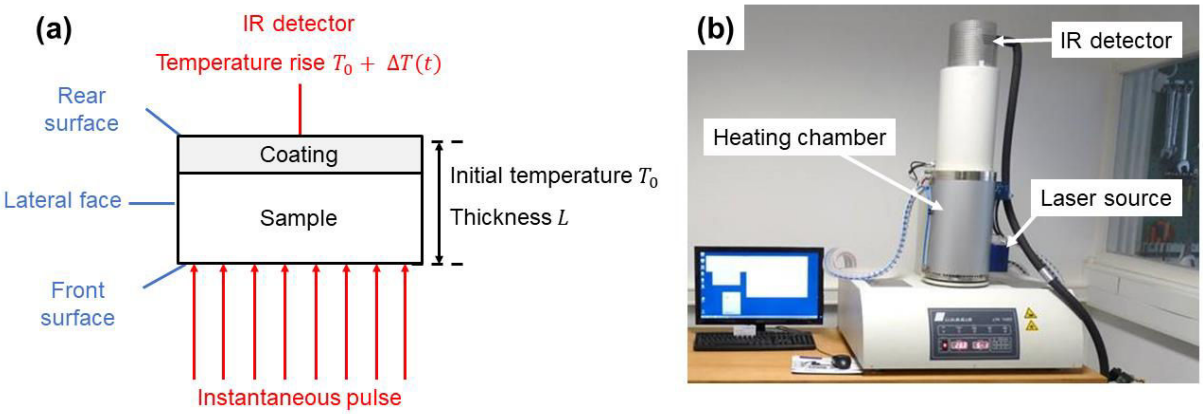

Fig. II-10. (a) Schematic of the laser flash technique from Ref. [55] and (b) image of the LFA used in the study.

The laser flash measurements were performed with a LINSEIS LFA 1000 (Fig. II-10b). The thickness of the samples was measured with a 10^{-3} mm caliper. The samples with a metallic substrate were generally about 1 mm thick whereas the self-standing coatings measured less than 1 mm thick. To avoid heat losses, both surfaces of the samples were sprayed with graphite (Graphit 33, Kontakt Chemie). For self-standing coatings, a gold layer was deposited by sputtering before graphite spray for a better absorption of the laser pulse [55]. With the experimental set up, up to six samples can be simultaneously analysed. A vacuum of approximately 5.10^{-2} mbar was maintained in the reaction chamber during the measurements.

The measurements were done at different temperatures to describe the evolution of the thermal diffusivity of the coating with the working temperature. For repeatability, five laser pulses were done at each temperature for each sample. Between each measuring temperature, the heating ramp was fixed at 10°C/min and a 10 minutes dwell was done before the first laser pulse to stabilize the temperature of the samples (given with a type-S thermocouple placed at the centre of the sample holder). The frequency of the laser pulses was fixed at 1 minute. Each thermogram was saved after the laser pulse and the thermal diffusivity was directly calculated by the software. For validation, the fitting curve must be accurate to at least 95%.

IV.2. Crystallographic and structural analyses

a) X-Ray Diffraction (XRD)

The X-ray diffraction (XRD) allows to determine the crystallographic structure of mineral and metallic compounds. Combined with the SEM or the Raman micro-spectrometry, XRD is particularly helpful to differentiate products with the same chemical composition but different crystal structures. The surfaces of as-deposited, as-coated and degraded samples were analysed by X-ray diffraction (XRD) using a Bruker AXS D8 Advance with Cu $K_{\alpha 1}$ radiation (λ=0.15406 nm). The XRD patterns were acquired for a 2θ range between 10° and 90° with a step size of 0.02° (DIFFRAC^{plus} XRD Commander software). The accumulation time was fixed at 5s for the 5° grazing incidence procedure and 2s in Bragg-Brentano configuration (θ-2θ mode). The first one allows to collect information from the uppermost surface (e.g. thermally grown oxides) whereas the symmetrical mode makes X-rays penetrate deeper into the bulk [25]. The identification of the crystal structures for the different metallic or intermetallic phases and the oxides was realized using the DIFFRAC^{plus} EVA software by comparison with the JCPDS database (Joint Committee Powder Diffraction files System). Some crystal structures were identified by comparison with data from the literature.

b) Raman micro-spectrometry and Cr^{3+} fluorescence

Raman micro-spectrometry is a non-destructive method for local structural analyses (lateral resolution of approximately 1µm [56]). This technique allows the characterization of the molecular composition and of the crystalline structure of non-metallic compounds from their vibrational transitions (oxides, sulfates and sulfides for instance). For this, a monochromatic radiation (usually from a laser) is directed to the sample with a known frequency corresponding to the emission of the photons. By interaction with the probed area, these photons are either reflected, absorbed or diffused. Some of the photons are diffused non-elastically and present therefore a different frequency (Raman scattering). The non-elastic diffusion is characteristic of an energy change between the incident photon and the compound, corresponding to a transition between two vibrational energy levels [57]. Depending on the frequency (or energy) of the diffused photons compared to incident ones, the scattering can be qualified as Stokes or as anti-Stokes [57]. The frequency is usually converted in wave number $\bar{\nu}$ (cm^{-1}) for the acquisition and the presentation of the results considering the equation *(Eq. II-4)*:

$$\bar{\nu} = \frac{\nu}{c} = \frac{1}{\lambda} \qquad \textbf{(Eq. II-4)}$$

With ν: the frequency, c: the speed of light and λ: the wavelength of the emission source

In this work, a high-resolution micro-spectrometer Jobin Yvon Horiba (LabRam HR8000 model) with a He-Ne monochromatic laser (λ=632.817 nm) was employed. An Olympus confocal microscope is coupled to the micro-spectrometer to visualize the sample and focus the laser (10x, 50x and 100x magnifications). The data are collected with a CCD detector, cooled by Peltier effect, with a spectral resolution of approximately 0.5 cm^{-1}. Different filters can be used to adjust the intensity of the laser depending on the products investigated. The depth of the analyses is comprised between 1 and 5µm according to the setup parameters and the sample.

The analyses were performed using the 50x magnification or 100x magnification to characterize thin oxide scales. Since the Raman micro-spectrometry is a local technique, several measurements were realized on different locations of the surface for each sample for repeatability. Depending on the wave number range, different signals can be obtained by Raman spectrometry. The Raman measurements were usually done between 100 and 2000 cm^{-1}. The intensity of the laser source and the exposure time were adapted for each system investigated to optimize the measurements. In the range 1000-2000 cm^{-1}, fluorescence signals can be obtained. The fluorescence spectrometry is due to the excitation of a fluorophore compound. This method of detection is particularly helpful to characterize the nature of thermally grown oxide (TGO) scales and their stress rate [58-60]. Indeed, the presence of small amounts of Cr^{3+} in the Al_2O_3 matrix favours the appearance of the different polymorphs of alumina by fluorescence [61,62]. For instance, it is possible to differentiate the θ phase from the α phase of alumina by fluorescence (Fig. II-11a). However, since the wavelength of the laser and the experimental set up could result in different Raman shifts for the same compound, there is no reference database in the literature. Therefore, it is necessary to get the reference signals of each compound for a given wavelength for a precise identification. In Fig. II-11b, the Raman signal of a powder of α-Al_2O_3 is given. The α-Al_2O_3 doublet is accompanied with satellite vibrations.

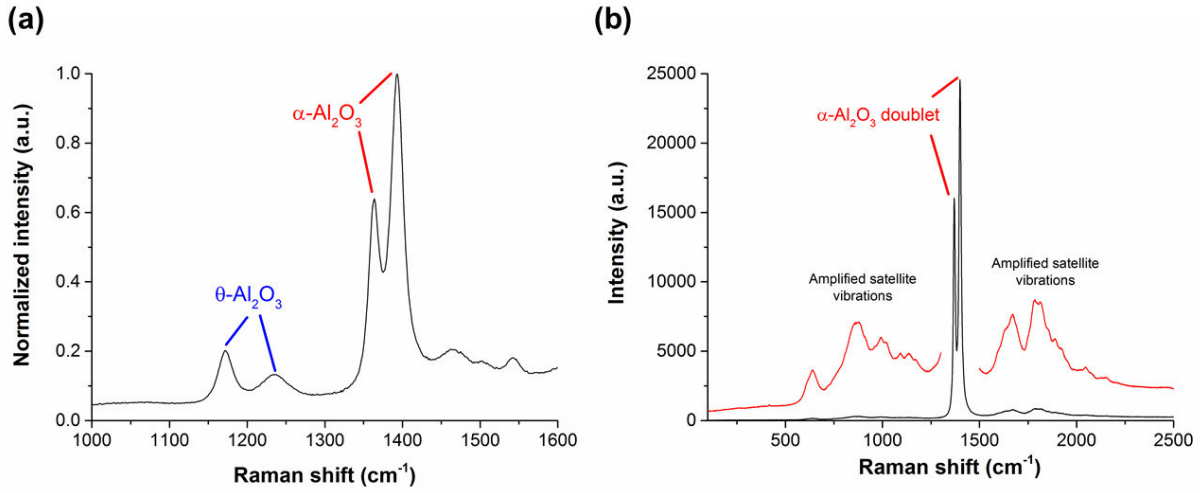

Fig. II-11. (a) Fluorescence signals of Cr^{3+} in θ-Al_2O_3 and α-Al_2O_3 and (b) analysis of an α-Al_2O_3 powder showing the α-Al_2O_3 doublet and the corresponding satellite vibrations.

IV.3. Microscopic and elemental analyses

a) Optical microscopy

Optical microscopy generally comes after the visual inspection to investigate the surface of a sample. This simple method is particularly interesting to get a first idea of the surface morphology before advanced characterization methods like XRD, Raman micro-spectrometry and SEM. A LEICA DMRM microscope coupled to a LEICA MC170 HD camera was used to characterize the samples in La Rochelle. The measurements were done with the LAS (Leica Application Suite) software equipped with the microscope. Thicknesses of the coatings were measured in cross section at 200x magnification in different areas of the sample for reproducibility. When a finer resolution and elemental analyses were required, the samples were characterized by SEM/EDS.

In DECHEMA-Forschungsinstitut, the samples were characterized with a LEICA DMRM microscope coupled to a LEICA DFC450 camera. This microscope was used for the metal loss measurements after the hot corrosion tests. Up to twelve micrographs were taken at x100 magnification on different areas of the samples to do the measurements. This probabilistic approach was particularly interesting to estimate the degradation of the coatings in hot corrosion conditions.

b) Scanning Electron Microscopy (SEM) and Energy Dispersive X-ray Spectroscopy (EDS)

With the SEM, a sample is scanned with a focused beam of electrons and the incident energy is transferred to the atoms of the material increasing their potential energy. After being excited, the atoms return to their fundamental state by de-excitation in the form of a secondary radiation. Depending on the activation energy, different radiations are likely to be observed. The formation of images is due to a contrast difference coming from the topography or a difference of chemical composition. Two imaging modes are usually considered in a SEM:

- **Secondary electrons imaging (SEI):** secondary electrons are produced by the repulsion of the electrons of an atom by the incident electrons (inelastic interaction). With a low energy (< 50eV), only the secondary electrons extracted from the surface can be detected. Therefore, the SE mode gives a good topography resolution.
- **Back-scattered electrons imaging (BSEI):** back-scattered electrons result from the elastic interaction of the incident electrons with the nuclei of atoms. The energy released by this interaction is a function of the atomic number. Therefore, this mode mainly produces a contrast of chemical composition. Heavier elements appear brighter whereas lighter elements appear darker in BSE mode.

Surface and cross-section analyses were carried out with an environmental microscope FEI Quanta 200F equipped with a Schottky field emission gun (FEG). For cross-section observations, the samples were first mounted in a polymeric resin and progressively grinded with finer SiC papers up to #4000 grade then polished with a 1µm water based diamond suspension (Struers). The samples were finally polished with a colloidal silica suspension (Struers OP-S 0.04µm) for a better revelation of the microstructures. The energy of the electron beam was fixed at 20 kV with a working distance of 10 mm and a spot size between 3.4 and 3.7. With conductive samples, the analyses were performed in high vacuum ($P < 10^{-5}$ bar). To limit the charge effects of low-conductive samples (the ceramic top coat for instance) and avoid further surface preparation, the analyses were performed in low vacuum (0.9 mbar). For elemental analyses, the SEM is coupled to an EDAX detector. Energy dispersive X-ray spectroscopy was carried out to analyse the chemical composition of the products by X-rays micro-diffraction. Depending on the energy of the emitted photons X, this technique is able to differentiate an element from another. In this study, spot analyses, window analyses and map analyses were performed depending on the investigated sample. EDS map analyses give the distribution of the elements in the scanned area by counting the probability to find a distinct element for a given position. This is particularly helpful in the case of diffusion coatings and heterogeneous compounds with concentration gradients of the different elements.

In DECHEMA-Forschungsinstitut, a Philips XL40 microscope combined with an EDAX detector was carried out for SEM and EDS characterization. To perform the analyses in high vacuum, the samples were sputtered with graphite and the edges were coated with a silver paste to ensure a good conductivity.

c) Electron Probe Micro-Analysis (EPMA)

The EPMA characterization was done in DECHEMA-Forschungsinstitut by Dr. Gerald Schmidt and Dr. Melanie Braun during my three months stay in their premises. The EPMA is coupled to a scanning electron microscope JEOL JXA-8100 and gives high resolution (about 1 µm) elemental maps. The energy of the electron beam was fixed at 15 kV and the analyses were performed in high vacuum. To avoid charge effects, the samples were sputtered with graphite and the edges were coated with a silver paste.

References

[1] M. Donachie, S. Donachie, *Superalloys: A Technical Guide 2nd edition*, ASM International (2002).

[2] T.M. Pollock, S. Tin, *Journal of Propulsion and Power* ***22*** (2006), pp. 361-374.

[3] J.S. Van Sluytman, T.M. Pollock, *Acta Materialia* ***60*** (2012), pp. 1771-1783.

[4] M.S. Chiou, S.R. Jian, A.C. Yeh, C.M. Kuo, *The Minerals, Metals and Materials Society*, In: Marquis F. (eds) Proceedings of the 8th Pacific Rim International Congress on Advanced Materials and Processing (2013), pp. 521-527.

[5] M.Z. Alam, D. Chatterjee, B. Venkataraman, V.K. Varma, D.K. Das, *Materials Science and Engineering A* ***527*** (2010), pp. 6211-6218.

[6] M.Z. Alam, D.V.V. Satyanarayana, D. Chatterjee, R. Sarkar, D.K. Das, *Materials Science and Engineering A* ***536*** (2012), pp. 14-23.

[7] I.S. Kim, B.G. Choi, S.M. Seo, D.H. Kim, C.Y. Jo, *Materials Letters* ***62*** (2008), pp. 1110-1113.

[8] R.A. MacKay, T.P. Gabb, A. Garg, R.B. Rogers, M.V. Nathal, *Materials Characterization* ***70*** (2012), pp. 83-100.

[9] L.R. Liu, T. Jin, N.R. Zhao, X.F. Sun, H.R. Guan, Z.Q. Hu, *Materials and Science Engineering A* ***361*** (2003), pp. 191-197.

[10] L.Z. He, Q. Zheng, X.F. Sun, H.R. Guan, Z.Q. Hu, A.K. Tieu, C. Lu, H.T. Zhu, *Materials and Science Engineering A* ***397*** (2005), pp. 297-304.

[11] S. Draper, D. Hull, R. Dreshfield, *Metallurgical Transactions A* ***20*** (1989), pp. 683-688.

[12] G.W. Goward, D.H. Boone, *Oxidation of Metals* ***3*** (1971), pp.475-495.

[13] D.K. Das, V. Singh, S.V. Joshi, *Metallurgical and Materials Transactions A* ***29*** (1998), pp. 2173-2188.

[14] B. Rannou, F. Velasco, S. Guzman, V. Kolarik, F. Pedraza, *Materials Chemistry and Physics* ***134*** (2012), pp. 360-365.

[15] X. Montero, M.C. Galetz, M. Schütze, *Surface and Coatings Technology* ***206*** (2011), pp. 1586-1594.

[16] R. Sarathi, T.K. Sindhu, S.R. Chakravarthy, *Materials Characterization* ***58*** (2007), pp. 148-155.

[17] A. Gromov, A. Ilyin, U. Förter-Barth, U. Teipel, *Propellants Explosives Pyrotechnics* ***31*** (2006), pp. 401-409.

[18] A. Gromov, Y. Strokova, U. Teipel, *Chemical Engineering and Technology* ***32*** (2009), pp. 1049-1060.

[19] J.M. LeBeau, Y. Boonyongmaneerat, *Materials Science and Engineering A* ***458*** (2007), pp. 17-24.

[20] M. Mollard, *Elaboration de systèmes barrière thermique par barbotine. Comportement du nickel et de ses superalliages revêtus en oxydation cyclique à haute température*, PhD Thesis, Université de La Rochelle (2012).

[21] M.C. Galetz, X. Montero, M. Mollard, M. Gunthner, F. Pedraza, M. Schütze, *Intermetallics* ***44*** (2014), pp. 8-17.

[22] B. Rannou, B. Bouchaud, J. Balmain, G. Bonnet, F. Pedraza, *Oxidation of Metals* ***81*** (2014), pp. 139-149.

[23] X. Montero, M.C. Galetz, M. Schütze, *Surface and Coatings Technology* ***222*** (2013), pp. 9-14.

[24] X. Montero, M.C. Galetz, M. Schütze, *Journal of Minerals, Metals and Materials Society* ***67*** (2014), pp. 79-86.

[25] B. Rannou, *Slurry coatings from aluminium microparticles on Ni-based superalloys for high-temperature oxidation protection*, PhD Thesis, Université de La Rochelle (2012).

[26] M. Brossard, *Influence de l'eau (vapeur, liquide) et du régime d'oxydation sur la dégradation de revêtements alumino-formeurs sur superalliage à base nickel*, PhD Thesis, Université de La Rochelle (2014).

[27] M. Schütze, M. Malessa, *Reliable assessment of high temperature oxidation resistance by the development of a comprehensive code of practice for thermocycling oxidation testing (COTEST)*, EFC Publications Number 47, pp. 279-296, Woodhead Publishing in Materials (2008).

[28] M. Schütze, M. Malessa, *Influence of cycling parameter variation on thermal cycling oxidation testing of high temperature materials (COTEST)*, EFC Publications Number 47, pp. 334-362, Woodhead Publishing in Materials (2008).

[29] T. Gheno, B. Gleeson, *Oxidation of Metals* ***84*** (2015), pp. 567-584.

[30] F.S. Pettit, *Oxidation of Metals* ***76*** (2011), pp. 1-21.

[31] K.H. Luthra, D.A. Shores, *Journal of the Electrochemical Society* ***127*** (1980), pp. 2202-2210.

[32] J.E. García-Herrera, J.M. Alvarado-Orozco, J. Muñoz-Saldaña, L. Garcia-Fresnillo, G.H. Meier, *Oxidation of Metals* ***84*** (2015), pp. 233-240.

[33] A.K. Misra et al., *Journal of the Electrochemical Society* ***129*** (1982), pp. 1840-1845.

[34] T. Gheno, M. Zahiri Azar, A.H. Heuer, B. Gleeson, *Corrosion Science* ***101*** (2015), pp. 32-46.

[35] M.N. Task, B. Gleeson, F.S. Pettit, G.H. Meier, *Oxidation of Metals* ***80*** (2013), pp. 125-146.

[36] M.N. Task, B. Gleeson, F.S. Pettit, G.H. Meier, *Oxidation of Metals* ***80*** (2013), pp. 541-552.

[37] N.J. Simms, A. Encinas-Oropesa, J.R. Nicholls, *Materials Science Forum* ***461-464*** (2004), pp. 941-948.

[38] P. Lortrakul, R.W. Trice, K.P. Trumble, M.A. Dayananda, *Corrosion Science* ***80*** (2014), pp. 408-415.

[39] ISO 17224:2015, Corrosion of metals and alloys – Test method for high temperature corrosion testing of metallic materials by application of a deposit of salt, ash, or other solids (04.2015).

[40] I. Gurrappa, *Oxidation of Metals* ***59*** (2003), pp. 321-332.

[41] I. Gurrappa, *Surface and Coatings Technology* ***139*** (2001), pp. 272-283.

[42] P. Steinmetz, C. Duret, R. Morbioli, *Materials Science and Technology* ***2*** (1986), pp. 262-271.

[43] ISO 17248:2015, Corrosion of metals and alloys – Test method for high temperature corrosion testing of metallic materials by embedding in salt, ash, or other solids (04.2015).

[44] S.R.J Saunders, J.R. Nicholls, *Materials at High Temperatures* ***13*** (1995), pp. 115-120.

[45] J. Sumner, A. Encinas-Oropesa, N.J. Simms, J.E. Oakey, *Materials at High Temperatures* ***28*** (2011), pp. 369-376.

[46] I. Gurrappa, I.V.S. Yashwanth, I. Mounika, H. Murakami, S. Kuroda, The Importance of Hot Corrosion and Its Effective Prevention for Enhanced Efficiency in Gas turbines, Intech, DOI: 10.5772/59124 (2015), pp. 55-102.

[47] M.C. Pope, N. Birks, *Oxidation of Metals* ***12*** (1978), pp. 173-181.

[48] K.P. Lillerud, P. Kofstad, *Oxidation of Metals* ***21*** (1984), pp. 233-270.

[49] R.E. Taylor, X. Wang, X. Xu, *Surface and Coatings Technology* ***120-121*** (1999), pp. 89-95.

[50] B. Gleeson, *Journal of Propulsion and Power* ***22*** (2006), pp. 375-383.

[51] Y. Wang, H. Liu, X. Ling, Y. Weng, *Applied Thermal Engineering* ***102*** (2016), pp. 234-242.

[52] L. Wang, Y. Wang, X.G. Sun, J.Q. He, Z.Y. Pan, Y. Zhou, P.L. Wu, *Materials and Design* ***32*** (2011), pp. 36-47.

[53] S. Wei, W. Fu-chi, F. Qun-Bo, M. Zhuang, *Applied Mathematical Modelling* ***36*** (2012), pp. 1995-2002.

[54] F. Pedraza, M. Mollard, B. Rannou, J. Balmain, B. Bouchaud, G. Bonnet, *Materials Chemistry and Physics* ***134*** (2012), pp. 700-705.

[55] ASTM E1461-11, Standard Test Method for Thermal Diffusivity by the Flash Method, ASTM International, (2011).

[56] www.horiba.com.

[57] I.R. Lewis, H.G.M. Edwards, L.A. Nafie, Handbook of Raman Spectroscopy: From the Research Laboratory to the Process Line, Marcel Dekker Inc., (2001).

[58] V.K. Tolpygo, D.R. Clarke, *Materials at High Temperatures* ***17*** (2000), pp. 59-70.

[59] D. Renusch, M. Grimsditch, I. Koshelev, B.W. Veal, P.Y. Hou, *Oxidation of Metals* ***48*** (1997), pp. 471-495.

[60] B. Bouchaud, J. Balmain, D. Barrere, T. Delannoye, F. Pedraza, *Corrosion Science* ***68*** (2013), pp. 176-185.

[61] J.K. Wright, R.L. Williamson, D. Renusch, B. Veal, M. Grimsditch, P.Y. Hou, R.M. Cannon, *Materials Science and Engineering A* ***262*** (1999), pp. 246-255.

[62] Q. Wen, D.M. Lipkin, D.R. Clarke, *Journal of the American Ceramic Society* ***81*** (1998), pp. 3345-3348.

Chapter III - Reactivity of Al and Cr powders for aluminizing purposes and mechanisms of formation of the slurry coatings on pure nickel

Slurry aluminide coatings have been widely used for several years to protect metallic substrates from oxidation and corrosion. Their microstructure is comparable to high aluminium activity coatings because of the high Al content in the donor [1-3]. Such microstructure results from the high exothermal reactions occurring by self-propagating high-temperature synthesis (SHS) [1,4,5]. Montero et al. added pre-alloyed Al-Cr microparticles to the slurry composition and achieved coatings with a microstructure comparable to that of low-activity coatings produced by CVD related techniques [6,7]. Cr addition was found to control the Al activity, hence to promote the outward diffusion of nickel to form the coating at elevated temperature (i.e. 1100°C). However, this requires a previous mechanical attrition of the Al and Cr powders, hence an additional manufacturing step. In addition, and despite their expensive use in current aluminizing processes, either by CVD or by slurry, little is known about the reactivity between Al and Cr that controls the aluminizing of metallic substrates.

Therefore, the role of introducing Cr in the slurry for aluminizing purposes was studied in this chapter. First, the reactivity between Al and Cr microparticles was investigated by DSC with no substrate and with pure nickel as a model material for nickel-based superalloys. Then the mechanisms of formation of the coatings from mixtures of Al and Cr powders was studied on pure nickel. Finally, double-layer architectures (Al-Cr and Cr-Al systems) were elaborated to control the mechanisms of formation of the coatings.

The main objective of Chapter III was to elucidate the effect of Cr addition in the slurry deposit on the mechanisms of formation of the diffusion coatings. This Chapter focused on pure nickel as a model material to highlight the reactions involved and simplify the interpretation of the results before extrapolation to a Ni-Cr alloy and an industrial nickel-based superalloy in Chapter IV.

Chapter III – Reactivity of Al and Cr powders for aluminizing purposes and mechanisms of formation of the slurry coatings on pure nickel

I. Reactivity of Al and Cr powders with no substrate 67

I.1. Preparation of Al-Cr mixtures 67

I.2. Reactivity of Al and Cr powders measured by DSC 69

II. Synthesis of Al-Cr intermetallic compounds 73

III. Reactivity of Al, of Cr and of Al-Cr mixtures with pure nickel substrate 77

III.1. Reactivity of the metallic powders with pure nickel substrate 77

III.2. Reactivity of Al-Cr mixtures with pure nickel substrate 80

III.3. Synthesis of Al-Cr intermetallic compounds from Al-Cr mixed slurries for aluminizing 82

IV. Mechanisms of formation of the diffusion layers on pure nickel 86

IV.1. Aluminizing of pure nickel with different Al-Cr mixed slurries: influence of Cr addition on the Al activity 86

IV.2. Outward diffusion of nickel at high temperature (i.e. 1000°C and 1080°C) 88

V. Mechanisms of formation of the diffusion layers from Al-Cr and Cr-Al double-layer systems 91

V.1. Elaboration of Al-Cr and Cr-Al double-layer systems 91

V.2. Mechanisms of formation for the Al-Cr double-layer system 91

V.3. Mechanisms of formation for the Cr-Al double-layer system 97

VI. Summary and outlook 106

References 108

I. Reactivity of Al and Cr powders with no substrate

I.1. Preparation of Al-Cr mixtures

Different Al-Cr compositions were selected from the Al-Cr phase diagram (Fig. III-1) and literature (Table III-1) to investigate the potential exothermic and endothermic reactions. The role of Cr as a moderator of the aluminizing reactions will be thus derived on model materials (Ni, Ni20Cr) and nickel-based superalloys from selected Al-Cr mixtures. Part of this work has been published in Ref. [8].

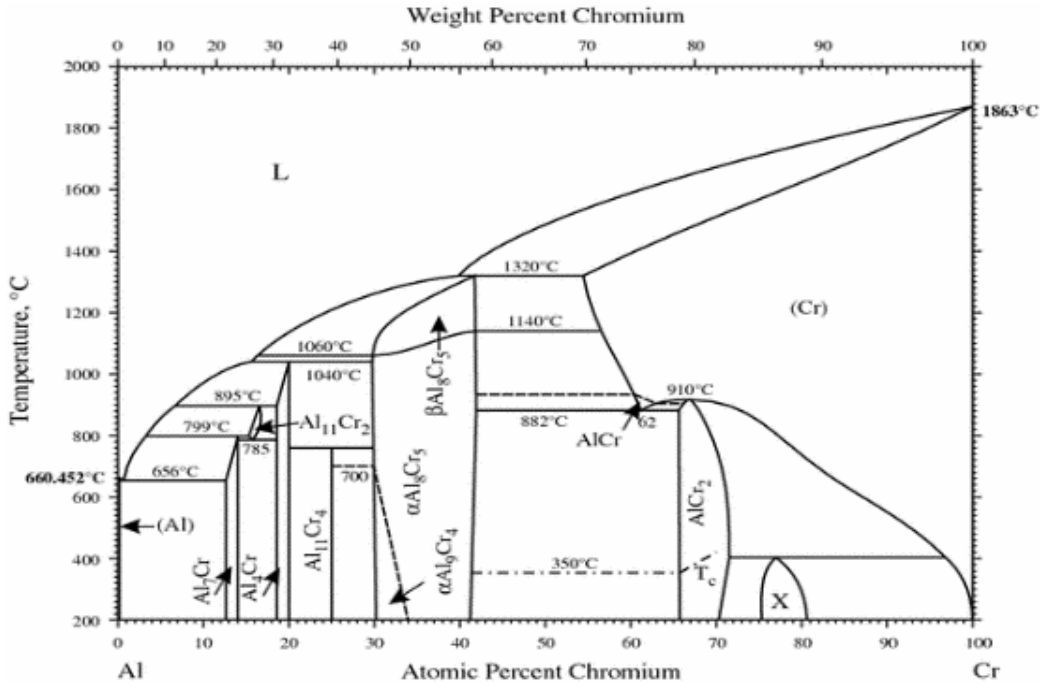

Fig. III-1. Binary Al-Cr phase diagram [9].

The Al-Cr phase diagram (Fig. III-1) is relatively complex, with six intermetallic compounds (Al_7Cr, $Al_{11}Cr_2$, Al_4Cr, $Al_{11}Cr_4$, Al_8Cr_5 and $AlCr_2$) [9-14]. In the range 30 to 42 at.% Cr, Grushko et al. demonstrated the existence of only one high-temperature and one low-temperature phase [15]. The intermetallic compounds Al_9Cr_4 and Al_8Cr_5 therefore present a compositional continuity in this range with a high-temperature and a low-temperature sub-region [16]. Grushko et al. also reported a new phase ($Al_{11}Cr_4$) at about 75 at.% Al [12]. The latter would decompose into Al_4Cr and Al_8Cr_5 at 829°C [17]. These Al-Cr phases were often investigated through differential thermal analysis (DTA) and the mechanisms of formation proposed after homogenisation in liquid phase and subsequent cooling for different Al-Cr compositions [10,11]. Other studies by Chen et al. focused on the sintering of Al-Cr alloy targets by different powder metallurgy methods using micro-sized Al and Cr particles [18]. Depending on the method and the temperature reached, different intermetallic compounds were synthesized ($Al_{11}Cr_2$, Al_8Cr_5 and $AlCr_2$). Therefore, despite the good knowledge of the Al-Cr system,

no study has been carried out so far to investigate the reactivity between Al and Cr microparticles, which is of utmost importance to control the self-propagating high-temperature synthesis (SHS) reactions upon slurry aluminizing. The formation of intermetallic phases by SHS can be predicted by the amount of energy released during the exothermic reaction and the maximum temperature reached [13,19,20].

Table III-1. Selected compositions for DSC tests in weight % and atomic % and corresponding Al activity in the powder mixtures. For consistency, all compositions will be presented in weight% in the study.

Weight %	Atomic %	Al activity in the powder mixtures
100 wt.% Al	100 at.% Al	1
82 wt.% Al, 18 wt.% Cr	90 at.% Al, 10 at.% Cr	0.9
67 wt.% Al, 33 wt.% Cr	80 at.% Al, 20 at.% Cr	0.8
55 wt.% Al, 45 wt.% Cr	70 at.% Al, 30 at.% Cr	0.7
44 wt.% Al, 56 wt.% Cr	60 at.% Al, 40 at.% Cr	0.6 [21]
30 wt.% Al, 70 wt.% Cr	45 at.% Al, 55 at.% Cr	0.45 [21]
20 wt.% Al, 80 wt.% Cr	33 at.% Al, 67 at.% Cr	0.33 [6,21]
12 wt.% Al, 88 wt.% Cr	20 at.% Al, 80 at.% Cr	0.2
100 wt.% Cr	100 at.% Cr	0

For the DSC tests, the experimental trials were made by weighing (with a 10^{-4} g accurate balance) and mixing the selected compositions of Al and Cr powders (Table III-1) in an alumina crucible. The heating and cooling rates were fixed at 10°C/min with a maximum temperature of 1300°C. Upon annealing, the reaction chamber was ventilated with a flow of Ar (20 mL/min) to limit oxidation phenomena and prevent secondary reactions in the system. For each composition, energy changes and temperatures of transformation were measured with the Calisto software coupled to the DSC technique.

The DSC thermograms for the pure Al and Cr powders are given as references in Fig. III-2. For the pure Al powder (Fig. III-2a), an endothermic reaction was observed at 654 ± 1°C and can be associated with the melting point of Al. This temperature was lower than the theoretical melting point of Al (660.5°C [9]), probably due to impurities in the powder (not detected by EDS) [1,22]. The experimental enthalpy of fusion for the Al powder was 10.5 ± 0.2 $kJ.mol^{-1}$, which was close to the value given in the literature (10.7 $kJ.mol^{-1}$ [23]). Upon cooling, the recrystallization of Al was observed in the range 630-650°C. For the two Cr powders (Fig. III-2b), no energy change was observed up to 1300°C, which is far below the melting point of Cr (1863°C [9]).

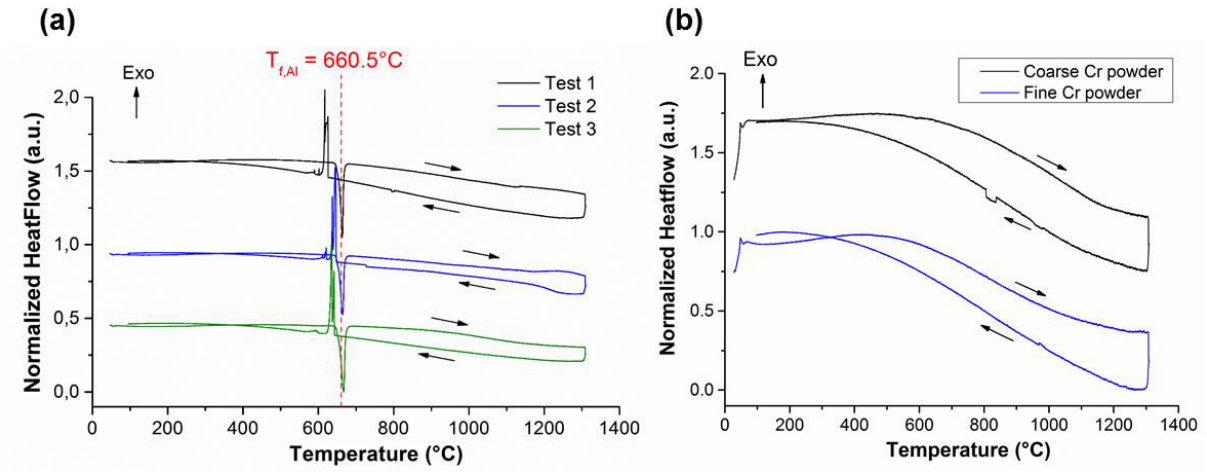

Fig. III-2. DSC thermograms of (a) the pure Al powder and (b) the fine and coarse Cr powders (heating and cooling ramps of 10°C/min) under flowing Ar (20 mL/min).

I.2. Reactivity of Al and Cr powders measured by DSC

The DSC thermograms obtained for the heating ramp from 40°C to 1300°C at 10°C/min for the selected Al-Cr compositions are given in Fig. III-3. For the two systems, an exothermic reaction was identified at a temperature lower than the experimental melting point of Al for all Al-Cr compositions. This suggests that the transformation should be of the eutectic type as proposed by Mahdouk and Gachon [24]. Therefore, this transformation would occur at a definite chemical composition (as soon as a small percentage of Cr reacts with Al due to its limited solubility in (Al) [24,25]). The onset temperature of this reaction was determined at 637 ± 2°C by mixing Al powder with the fine Cr powder (Fig. III-4a). Using the coarse Cr powder, the onset temperature was shifted to 650 ± 2°C (Fig. III-4b). This difference was ascribed to the greater contact surface, hence the reactivity, of the Al microparticles with the fine Cr powder compared to the coarse Cr powder [13]. Nevertheless, the amount of heat released during the exothermic reaction appeared to be dependent on the initial Al-Cr composition both systems (Fig. III-4a and Fig. III-4b). The greatest release of heat arose from the 67Al33Cr composition with an exchanged heat of approximately -370 J/g with the fine Cr powder and -308 J/g with the coarse one. For greater Cr contents (≥ 45 wt.% Cr), the heat quantity progressively decreased as the Cr content increased.

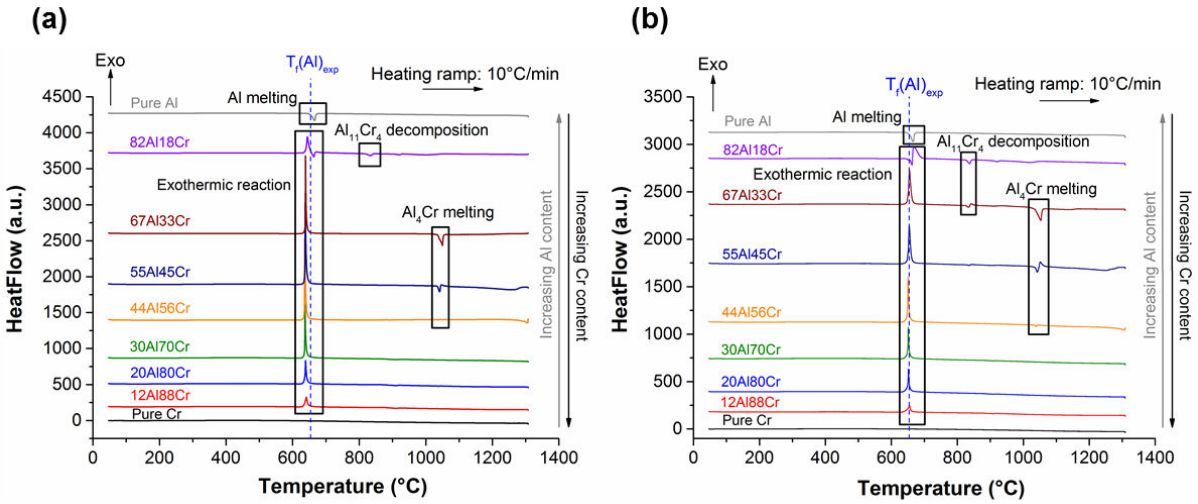

Fig. III-3. DSC thermograms (heating branches, 10°C/min) for the different Al-Cr compositions mixing the Al powder with (a) the fine and (b) the coarse Cr powder (20 mL/min Ar flow).

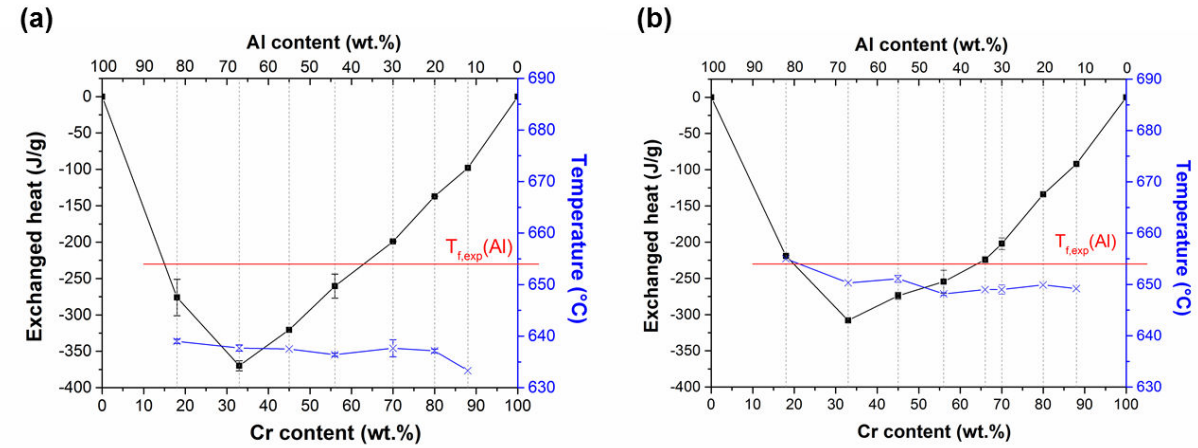

Fig. III-4. Evolution of the heat released for the different Al-Cr compositions measured for the exothermic reaction (20 mL/min Ar flow) for mixtures of Al powder with (a) fine and (b) coarse Cr powder.

For the 82Al18Cr composition, the endothermic signal of Al melting overlaps the exothermal peak for the two systems (Fig. III-3). This means that Cr was the limiting reagent for this composition [13]. The endothermic signal of Al melting was not observed for the other Al-Cr compositions and this indicates that Al was the limiting reagent this time. After the exothermic reaction, the whole Al reacted with Cr for compositions with 33 wt.% Cr and more. Depending on the initial Al-Cr composition, different intermetallic compounds likely formed. The experimental data collected from the DSC experiments upon heating are given in Table III-2. For each transformation, three temperatures were determined experimentally (T_{onset}, T_{peak}, T_{offset}).

Table III-2. Experimental data extracted from the DSC tests (heating branches) for the different Al-Cr compositions. The values given refer to the mixtures of Al with the fine ("F") and coarse ("C") Cr powders.

Study				Literature	
Composition (wt.%)	**T_{onset} (°C)**	**T_{peak} (°C)**	**T_{offset} (°C)**	**Transformation**	**T (°C)**
Al (F)	637 ± 2	643 ± 2	647 ± 2	Al-Cr eutectic	656 [9,24]
Al (C)	650 ± 2	655 ± 2	659 ± 3		
82Al18Cr (F)	654	664	666	Al melting	660.5 [9,24]
82Al18Cr (C)	655	662	664		
82Al18Cr (F)	819	833	841	$Al_{11}Cr_4$ decomposition	829 [17]
82Al18Cr (C) 67Al33Cr (C) 55Al45Cr (C)	829 ± 1	835 ± 1	839 ± 1		
82Al18Cr (F)	908	920	927	L + Al_4Cr ↔ $Al_{11}Cr_2$	895 [24]
82Al18Cr (C)	909	920	929		902 [25]
67Al33Cr (F) 55Al45Cr (F) 44Al56Cr (F)	1037 ± 1	1041 ± 1	1043 ± 1	L + Al_8Cr_5 ↔ Al_4Cr	1040 [9] 1037 [24]
67Al33Cr (C) 55Al45Cr (C) 44Al56Cr (C) 30Al70Cr (C)	1035 ± 1	1041 ± 3	1044 ± 5		1035 [25]
30Al70Cr (F) 20Al80Cr (F) 12Al88Cr (F)	882 ± 1	910 ± 1	917 ± 2	Convolution (Cr) ↔ Al_8Cr_5 + $AlCr_2$ (Cr) ↔ $AlCr_2$	882-910 [9] 874-906 [25] 870-910 [24]
30Al70Cr (C) 20Al80Cr (C) 12Al88Cr (C)	891 ± 6	908 ± 2	914 ± 2		

For the 82Al18Cr composition, an endothermic peak was observed between 820-840°C (Fig. III-3a and Fig. III-5a). This endothermic transformation was also identified for the 67Al33Cr and 55Al45Cr compositions by mixing Al with the coarse Cr powder (Fig. III-3b and Fig. III-5a). This probably refers to the decomposition of $Al_{11}Cr_4$ phase which was recently found to occur at 829°C [17]. The second (endothermic) transformation in the range 908-929°C should correspond to the peritectic transformation L + Al_4Cr ↔ $Al_{11}Cr_2$ [25]. For intermediate Al-Cr compositions (67Al33Cr, 55Al45Cr, 44Al56Cr and also 30Al70Cr by mixing Al with the coarse Cr powder), an endothermic reaction was identified at a temperature of 1035-1037°C. Considering the Al-Cr phase diagram in Fig. III-1 and literature [12,17,25], this endothermic reaction probably refers to the Al_4Cr melting (peritectic transformation at 33 wt.% Cr). In agreement with the Al-Cr phase diagram, the highest amount of energy released for this reaction was for the 67Al33Cr composition (Fig. III-5c). For the Al-Cr compositions with high Cr contents (30Al70Cr, 20Al80Cr and 12Al88Cr), the convolution of two endothermic reaction was observed in the temperature range 882-917°C (Fig. III-5b). This could be related to the peritectoid reaction (Cr) ↔ Al_8Cr_5 + $AlCr_2$ and the congruent reaction (Cr) ↔ $AlCr_2$ occurring in a very narrow range of temperature [9,25].

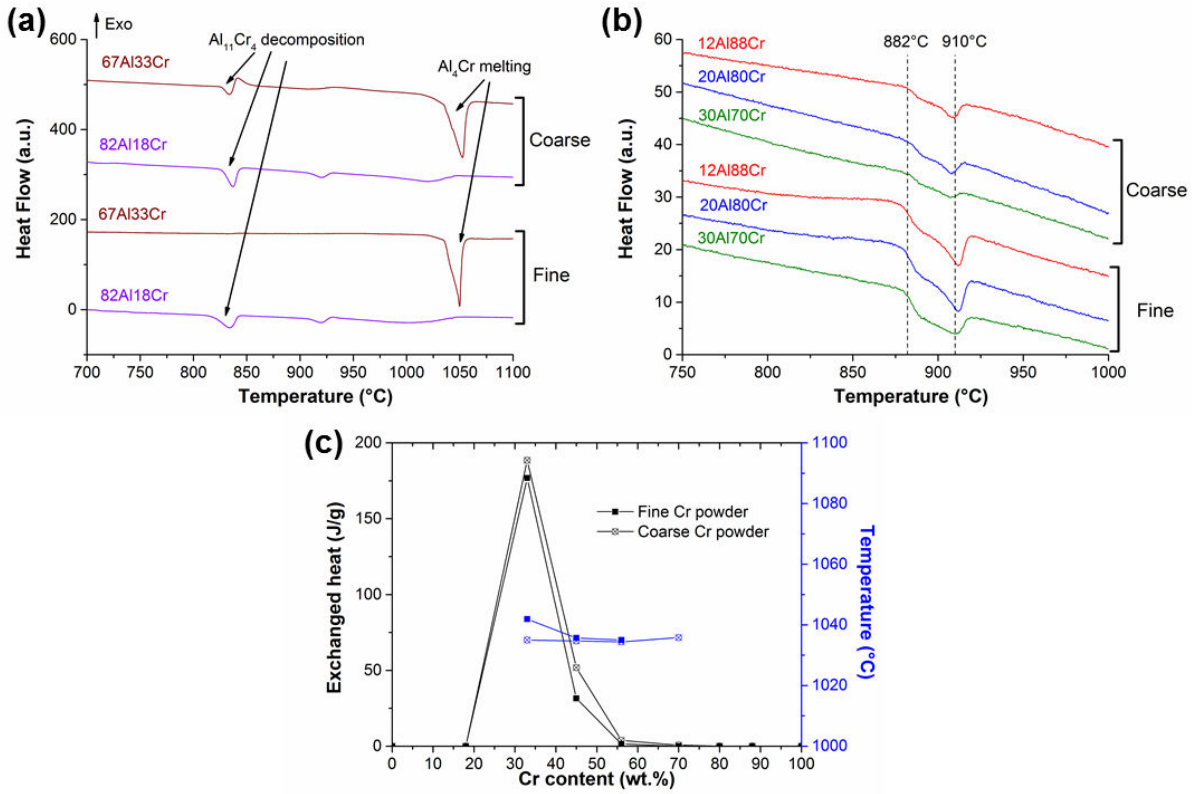

Fig. III-5. (a), (b) DSC heating branches (10°C/min) and (c) evolution of the exchanged heat and the T_{onset} for the peritectic transformation of the Al_4Cr phase for the different Al-Cr compositions.

From these experiments, three Al-Cr compositions were selected for the characterization of the microstructures after the exothermic reaction:

- The 67Al33Cr composition with the highest energy change during the exothermic reaction.
- The 44Al56Cr composition with an intermediate exchanged heat.
- The 20Al80Cr composition with a low exchanged heat.

The main objective was to characterize the intermetallic phases formed during the exothermic reaction and the potential transformation of these phases upon annealing at different temperatures. For the rest of the study, only the fine Cr powder was considered since the coarse Cr powder was not suited to obtain the desired coating design.

II. Synthesis of Al-Cr intermetallic compounds

The three selected compositions (67Al33Cr, 44Al56Cr and 20Al80Cr in wt.%) were heated to 650°C at 5°C/min, held at this temperature for 10 minutes and then quenched at 50°C/min to freeze the microstructure and the crystal phase of the compounds synthesized during the exothermic reaction. The SEM images of the three Al-Cr mixtures before and after heat treatment in DSC are given on Fig. III-6. Before annealing, the Al and Cr microparticles were clearly distinguished in the back-scattered electron (BSE) mode. The Al microparticles were dark and spherical whereas the Cr ones were bright with a complex geometry (Fig. III-6).

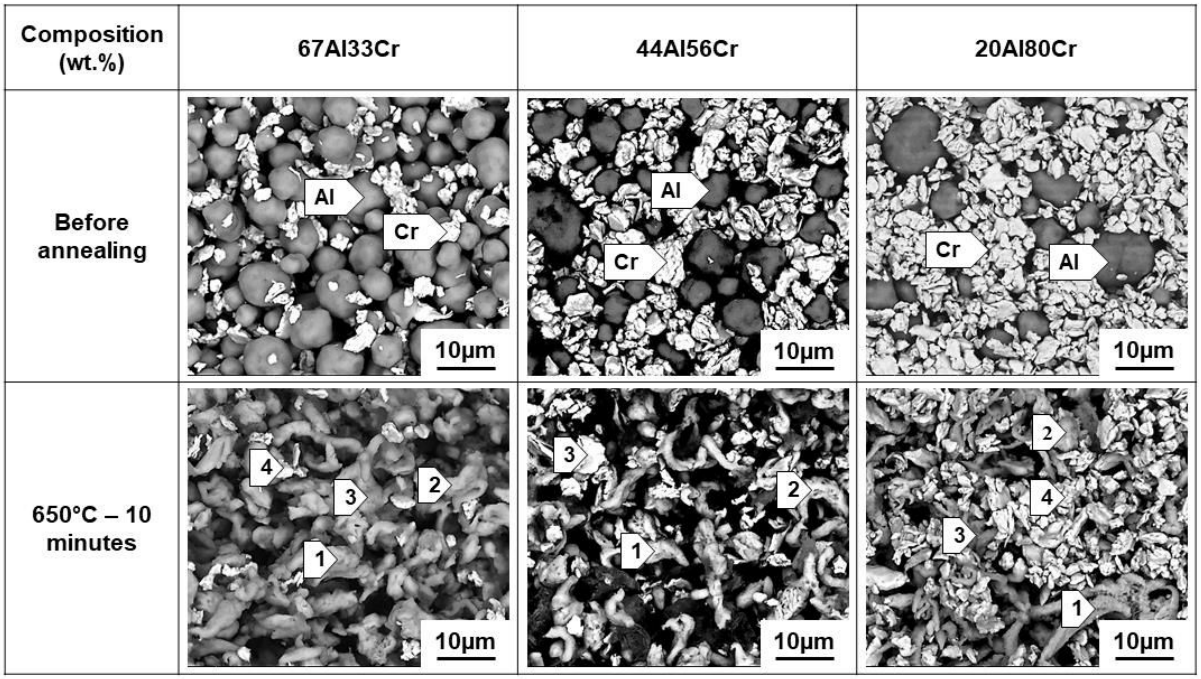

Fig. III-6. SEM images (BSE mode) of the three different Al-Cr mixtures before and after annealing at 650°C for 10 minutes (20 mL/min Ar flow).

The X-ray patterns of the three Al-Cr mixtures before annealing are given as references in Fig. III-7a. The face-centered cubic structure of Al and the body-centered cubic structure of Cr were distinctly identified. After annealing of the Al-Cr mixtures (Fig. III-7b), different Al_xCr_y intermetallic compounds appeared while the peaks of Al disappeared. This is in good agreement with the DSC measurements (Fig. III-3) and with the absence of Al microparticles in the SEM images after 10 minutes annealing at 650°C (Fig. III-6). These observations suggested that the whole Al reacted with Cr to form intermetallic phases at a temperature lower than the experimental melting point of Al (Fig. III-4). Such intermetallic phases presented an intermediate contrast in BSE mode (Fig. III-6). Their elongated morphology suggested the appearance of liquid phases during the exothermic reaction. Also, it was observed that a greater fraction of Cr remained unreacted with increasing the Cr content in the mixtures. The EDS spot analyses on different locations (Fig. III-6) also revealed different Al and Cr contents on the

synthesized phases (Table III-3). In conjunction with the XRD analyses and the literature, the main intermetallic phases were $Al_{11}Cr_2$ for the 67Al33Cr and 44Al56Cr compositions and $Al_{11}Cr_4$ for the 20Al80Cr one.

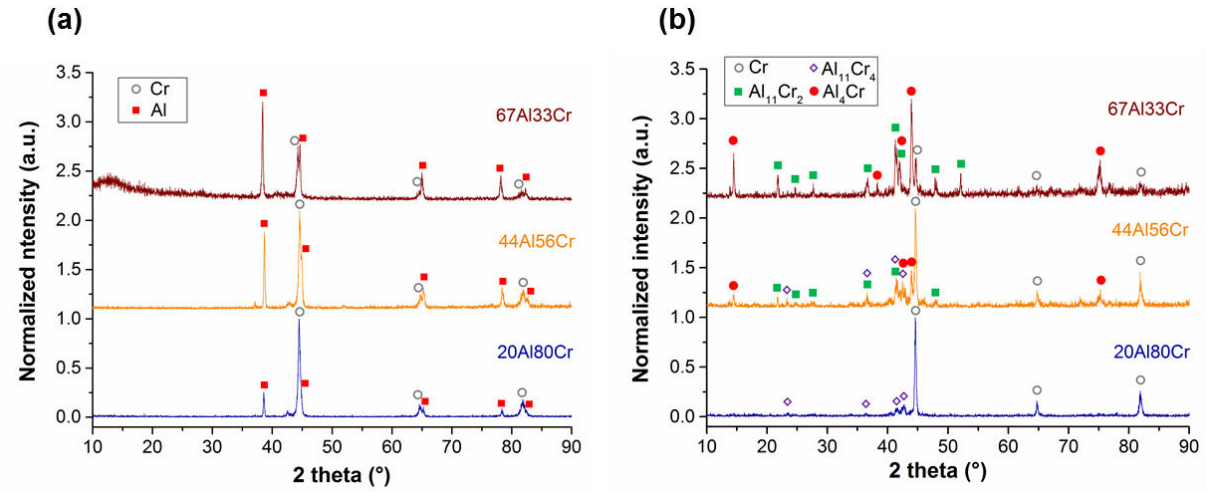

Fig. III-7. XRD patterns for the three Al-Cr mixtures (a) before annealing and (b) after annealing at 650°C for 10 minutes (20 mL/min Ar flow).

Table III-3. Summary of the EDS spot measurements (Fig. III-6) and XRD analyses (Fig. III-7b) for the different Al-Cr mixtures after annealing (650°C for 10 minutes) and the suggested phase compositions of synthesized products.

Al-Cr mixture (wt.%)	EDS spot location	EDS spot measurements		Possible phase	Crystal structures observed by XRD	Phase composition of synthesized products	
		Al (at.%)	Cr (at.%)			Dominant aluminide	Secondary aluminide(s)
67Al33Cr	1	81.7	18.3	$Al_{11}Cr_2$ [11]	$Al_{11}Cr_2$, Al_4Cr [26], (Cr)	$Al_{11}Cr_2$	Al_4Cr
	2	83.3	16.7				
	3	80.4	19.6	Al_4Cr [9]			
	4	17.5	82.5	(Cr) [9]			
44Al56Cr	1	82.1	17.9	$Al_{11}Cr_2$ [11]	$Al_{11}Cr_2$, Al_4Cr [26], $Al_{11}Cr_4$ [17], (Cr)	$Al_{11}Cr_2$	Al_4Cr, $Al_{11}Cr_4$
	2	82.1	17.9				
	3	12.2	87.8	(Cr) [9]			
20Al80Cr	1	75.2	24.7	$Al_{11}Cr_4$ [11]	$Al_{11}Cr_4$ [17], (Cr)	$Al_{11}Cr_4$	Al_8Cr_5
	2	76.2	23.8				
	3	70.9	29.1	Al_8Cr_5 [11]			
	4	2.5	97.5	(Cr) [9]			

The exothermic reaction identified at 637 ± 2°C by mixing Al and fine Cr powders (Fig. III-3a) was associated with the formation of Al_xCr_y intermetallic compounds with different stoichiometry depending on the maximum temperature reached during the synthesis. Chen et al. reported that the $Al_{11}Cr_2$ phase could form at temperatures (500°C) lower than ours but this required the 55Al45Cr powders to be hot isostatically pressed [18]. In such 55Al45Cr mixture of powders, nearly all the Al had reacted with Cr to form the $Al_{11}Cr_2$ phase at 600°C. The formation of such Al-rich intermetallic

compounds at temperatures lower than the Al melting point was related to the high exothermic reactions between Al and Cr [14] and Al and Cr_2O_3 [27]. The local increase in temperature due to the formation of intermetallic phases makes the residual Al to melt and the obtained liquid Al progressively dissolves Cr. Since the adiabatic temperature of the mixtures is not reached, the reaction is self-sustained as far as none of the reagents is exhausted. This is commonly known as self-propagating high temperature synthesis [14] or combustion synthesis if oxygen is present in the reacting media [27]. In this study, the heat released by the exothermic reaction was then indicative of the advancement of the reaction between Al and Cr microparticles. Clearly, the heat released increased from 0 till 33 wt.% Cr and then decreased till 100 wt.% Cr (Fig. III-4). Therefore, Al became the limiting reagent of the reaction for compositions greater than 67Al33Cr as confirmed by the results of SEM (Fig. III-6), EDS (Table III-3) and XRD (Fig. III-7).

The DSC measurements (heating rate of 5°C/min and cooling rate of 50°C/min) of the three Al-Cr compositions selected and the 82Al18Cr one are given in Fig. III-8. The thermograms present the same evolution than the ones presented in Fig. III-3a with an exothermic reaction occurring at 637 ± 2°C. The heat released by the exothermic reaction was very close to the values presented in Fig. III-4a for the four Al-Cr compositions. Therefore, the heating rate (5 or 10°C/min) was not found to play a significant role on the exothermic reaction and the synthesis of the Al-Cr intermetallic phases. For the 82Al18Cr composition, a convolution of the exothermic reaction with the endothermic signal of Al melting was observed. The recrystallization of Al upon cooling was only observed for this composition, which is in agreement with the SEM images of the different compositions after annealing (Fig. III-6 and Fig. III-9). For the 82Al18Cr composition, the EDS spot measurements of the synthesized intermetallic phases were in the composition range of the Al_7Cr phase (86-87.5 at.% Al [9,16]).

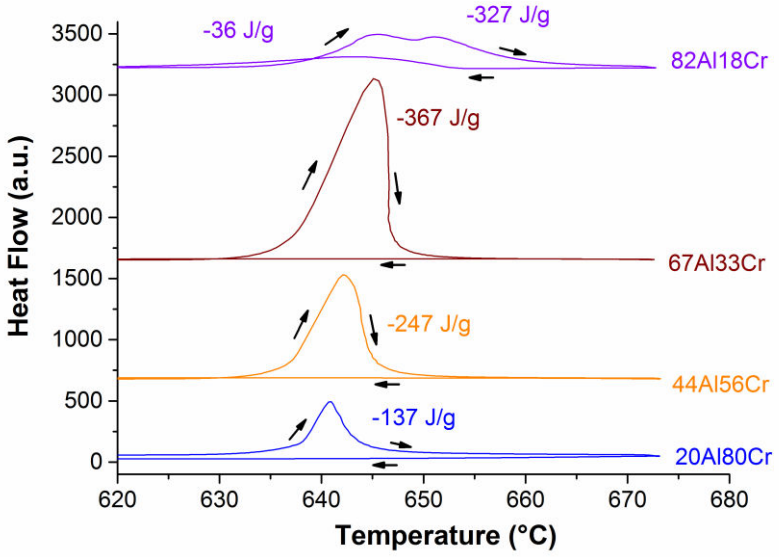

Fig. III-8. Evolution of the heat flow around the exothermic reaction for different Al-Cr compositions (650°C-10 min + quench). The recrystallization of liquid Al was only observed for the 82Al18Cr composition.

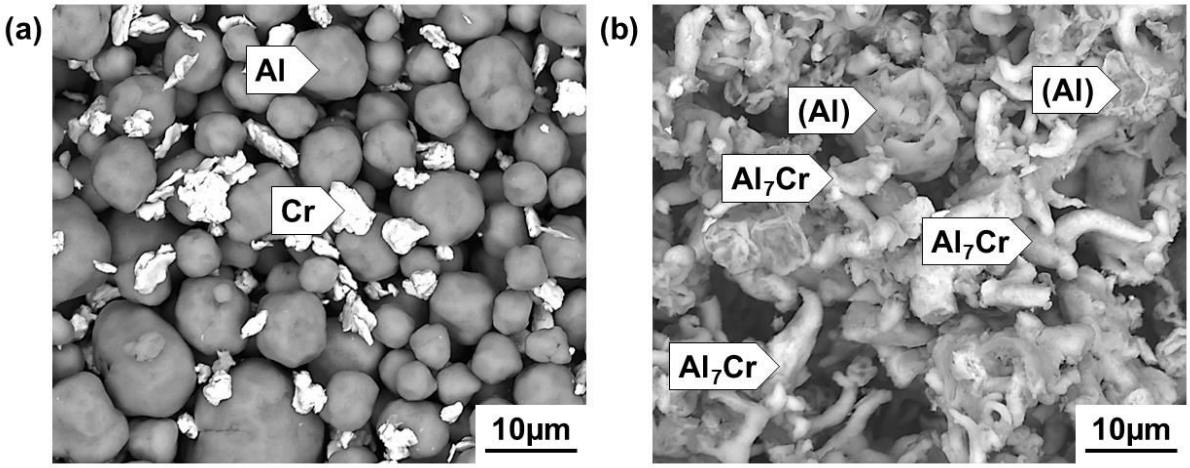

Fig. III-9. SEM images (BSE mode) of the 82Al18Cr composition (a) before and (b) after annealing at 650°C for 10 minutes (20 mL/min Ar flow).

Naplocha et al. demonstrated that the synthesis of mixed Al and Cr powders proceeds through the peritectic transformations L + Al_7Cr → L + $Al_{11}Cr_2$ → L + Al_4Cr and that the synthesis began with the formation of Al_7Cr [13]. They performed DTA measurements (heating branches) for three different Al-Cr ratios (78Al22Cr, 67Al33Cr and 54Al46Cr in wt.%) and observed that the initial ratio changed the maximum temperature reached during the exothermic reaction. The maximum temperature recorded for each composition was about 777, 877 and 1000°C for respectively, 78Al22Cr, 67Al33Cr and 54Al46Cr. Therefore, the greater the Cr content in the mixture, the higher the local increase in temperature. This suggests that the Cr-rich compositions of the present study were more susceptible to form Cr-rich intermetallic compounds with a high melting point, for instance the Al_8Cr_5 compound. Considering these results and the Al-Cr binary phase diagram (Fig. III-1), it was then possible to predict the synthesized compounds during the exothermic reaction. For the 67Al33Cr composition, with a maximum temperature estimated at 877°C above the Al_7Cr peritectic transformation, the $Al_{11}Cr_2$ phase should be formed. Because of the narrow concentration range between $Al_{11}Cr_2$ and Al_4Cr phases, the Al_4Cr compound was also expected to form. For the intermediate composition (44Al56Cr), the maximum temperature should be at least 1000°C according to Naplocha et al. [13]. However, the presence of both $Al_{11}Cr_2$ and Al_4Cr in the microstructure suggested that the increase in temperature was local and did not lead to a full transformation of these phases. The mechanism of formation for the $Al_{11}Cr_4$ phase was not fully understood in the present study and the formation of this phase is still under debate in literature [12]. Finally, for the 20Al80Cr composition, Al_4Cr was not observed in the microstructure probably because the local increase in temperature was higher than the peritectic transformation of Al_4Cr in the 1035-1040°C range. This would explain the detection of the Al_8Cr_5 phase in the microstructure after the quench. The sequence L + Al_7Cr → L + $Al_{11}Cr_2$ → L + Al_4Cr for the SHS reaction between Al and Cr microparticles proposed by Naplocha et al. [13], seems to describe very well the mechanisms of formation in the present study.

III. Reactivity of Al, of Cr and of Al-Cr mixtures with pure nickel substrate

III.1. Reactivity of the metallic powders with pure nickel substrate

To investigate the mechanisms of formation of the slurry diffusion coatings on metal substrates, it is necessary to identify the reactions occurring between the metallic powders and the underlying substrate. Therefore, pure nickel substrate was employed as a model material for nickel-based superalloys. The reactivity of the metallic powders with pure nickel substrate was studied by DSC. Different compositions were tested to separate out the contribution of each reactive. For the tests, planar nickel samples (approximately 1 mm thick) were prepared from a 4.0 mm diameter nickel rod (99.9% purity). For consistency with TGA experiments (cf. Chapter II), the nickel samples were ground with #180 SiC paper then rinsed in distilled water and cleaned with ethanol under ultrasonic agitation before any further step.

Three different systems were then considered for the DSC tests (Fig. III-10). The pure nickel substrate was first measured as a reference to identify the intrinsic transformations (Fig. III-11). One can see the reversible Curie point of nickel at 357 ± 2°C [28] corresponding to a change of the magnetic properties of nickel. No other transformation was identified for the nickel sample.

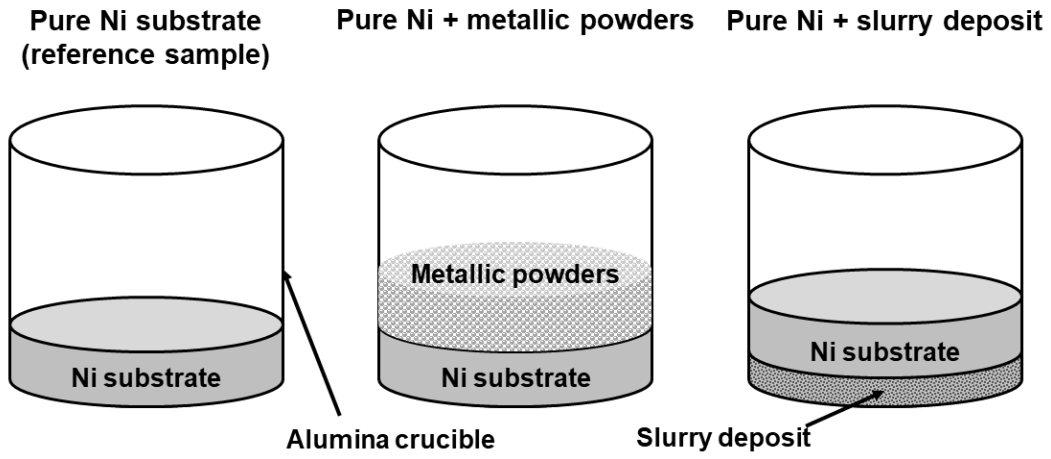

Fig. III-10. Principle of the DSC tests to study the reactivity between (a) pure nickel substrate with (b) the metallic powders (without organic binder) or (c) slurry deposits.

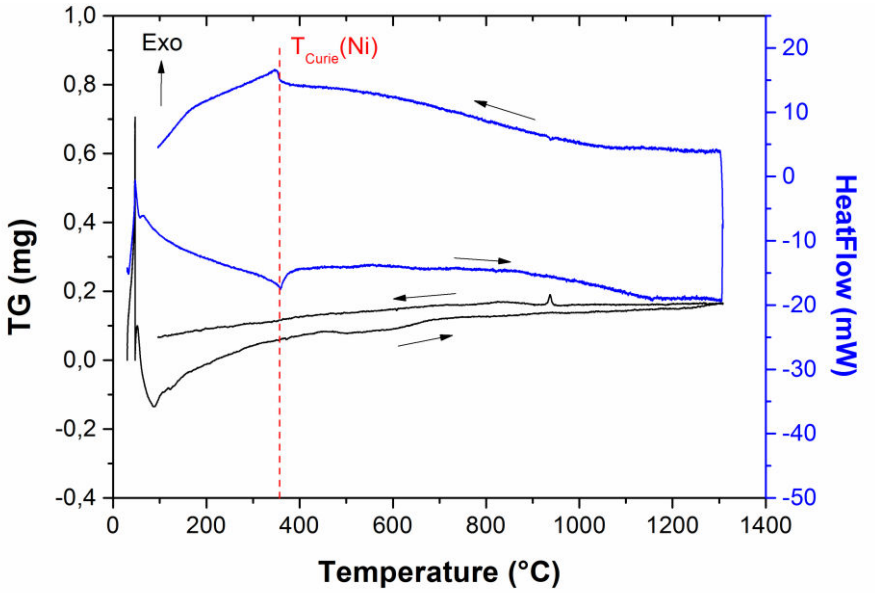

Fig. III-11. DSC thermograms of a pure nickel sample (heating and cooling ramps of 10°C/min, 20 mL/min Ar flow).

As a reference test for high-activity coatings [1], the reactivity between pure nickel and Al powder was first investigated. Since the mechanisms of formation of the slurry diffusion coatings were studied from slurries deposited on metallic substrates (cf. IV), the same conditions were followed for this study (Fig. III-10c). The reactivity between pure nickel with the Al metallic powder (without binder) was also investigated for comparison (Fig. III-10b). The DSC thermograms for these two systems are given in Fig. III-12. Considering the test with Al powder (without binder, Fig. III-12a), a strong endothermic peak referring to the Al melting was observed at T_{onset} = 655°C. The exchanged heat of the reaction (5.7 kJ.mol^{-1} calculated from the initial amount of Al) was lower than the one for the pure Al powder (cf. I.1). This difference suggests that a fraction of the Al powder reacted with the nickel substrate. Nevertheless, the exothermic signal characteristic of the reaction between nickel and Al [1] was not clearly identified. Two other endothermic transformations were observed for this system (Fig. III-12a) at 861 ± 2°C ($NiAl_3$ melting [5,20]) and 1134 ± 2°C (Ni_2Al_3 melting [5,20]). There was no recrystallization upon cooling suggesting that the whole Al reacted with the nickel substrate. This system (Fig. III-10b) was expected to be less representative of what exactly occurred during slurry aluminizing than the experiment presented in Fig. III-10c.

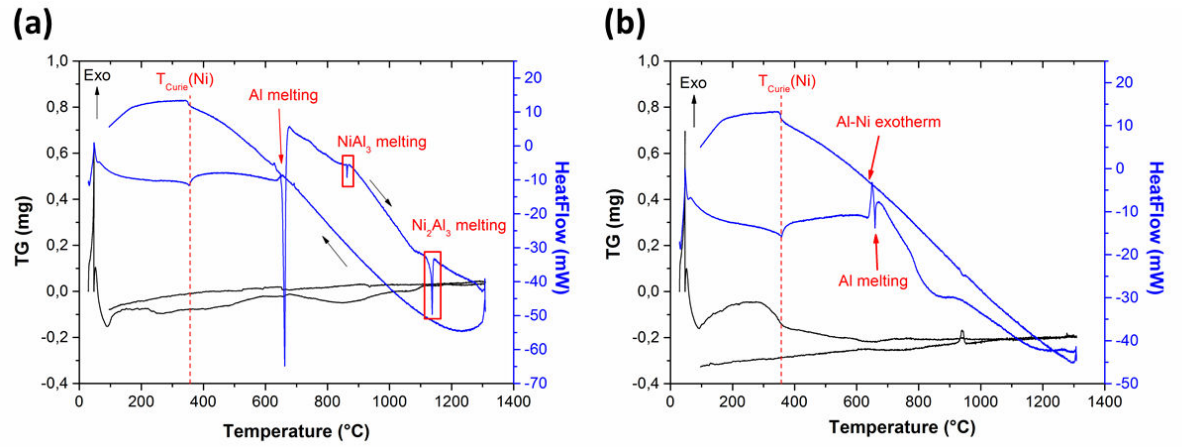

Fig. III-12. DSC thermograms for the pure nickel substrate in contact with (a) the Al metallic powder (without organic binder) and (b) the Al slurry deposit.

Considering the reactivity between pure nickel and the Al slurry deposit (Fig. III-10c), an exothermic reaction was identified at 643 ± 2°C convoluted with the endothermic signal of Al melting (Fig. III-12b). This exothermic reaction probably refers to the formation of Al-rich Ni_xAl_y intermetallic phases preceded by the melting of $NiAl_3$-Ni(Al) eutectic at 640°C [19,20]. This reaction is characteristic of the high-activity slurry aluminizing of nickel and has been demonstrated to proceed by self-propagation [1]. By comparison with the pure nickel substrate (Fig. III-11), a variation of the heat flow was observed in the range 750-900°C. Unlike for the nickel sample in contact with the Al powder (Fig. III-12a), no melting of $NiAl_3$ nor Ni_2Al_3 was observed on the DSC curve of Fig. III-12b. This suggested therefore that solid-state diffusion between Ni and Al occurred after the initial exothermic reaction [1].

The samples were analysed in cross-section to observe the diffusion layers after the annealing treatment in the DSC (Fig. III-13). EDS spot measurements were performed to identify the phases formed after the heat treatment [29]. With the Al powder (Fig. III-10b), a thick diffusion zone of 210 ± 10µm thickness was formed on the nickel substrate (Fig. III-13a). This diffusion zone was composed of three different layers as depicted by the contrast difference in the BSE mode of the SEM (Al-rich β-NiAl, Ni-rich β-NiAl and γ'-Ni_3Al). With the Al slurry deposit (Fig. III-13b), the diffusion zone was thinner and presented two distinct layers. A mixed outer layer of 60 ± 5µm thickness composed of both Ni-rich β and γ' phases and a continuous inner layer with the γ'-Ni_3Al phase (16 ± 3µm). Such differences in the coating microstructures were attributed to different Al reservoirs initially in contact with the nickel substrate.

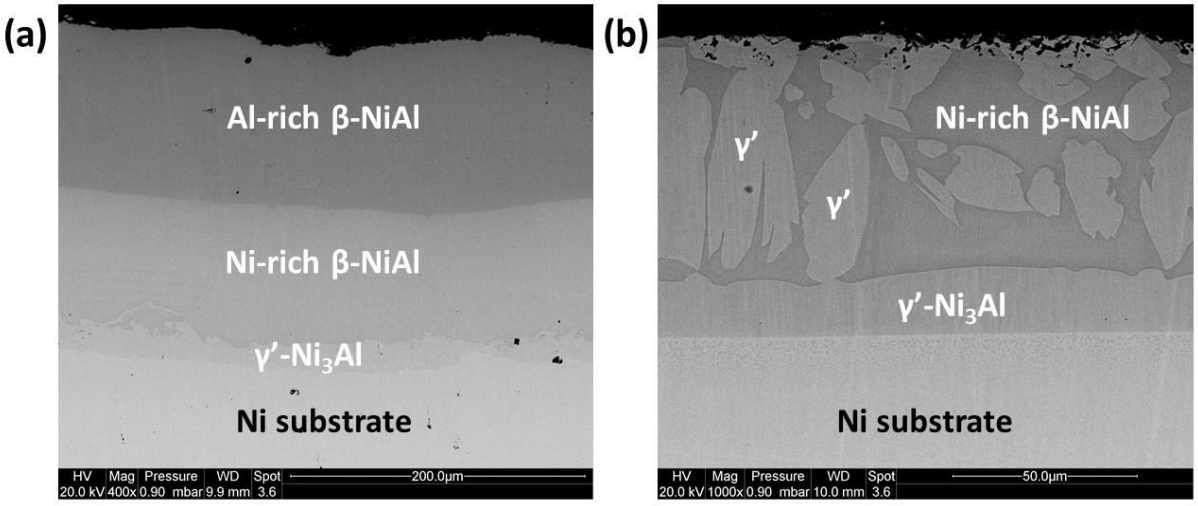

Fig. III-13. SEM cross-section images (BSE mode) of the pure nickel samples after DSC experiment in contact with (a) the Al metallic powder and (b) the Al slurry deposit.

III.2. Reactivity of Al-Cr mixtures with pure nickel substrate

The reactivity of Al-Cr mixtures with pure nickel substrate was investigated and compared with the DSC measurements realized for the Al-Cr mixtures with no substrate. The main objective was to determine if the addition of Cr to the slurry limits or supresses the exothermic reaction between Ni and Al. The three Al-Cr slurry compositions (Table III-4) were deposited on pure nickel as depicted in Fig. III-10c. The deposited mass was greater for the Al-Cr slurries than for the pure Al in order to have a sufficient Al content in the donor for diffusion. The DSC thermograms are given in Fig. III-14.

Table III-4. Composition for the different slurries prepared in this work and corresponding Al activity in the powder mixtures.

Slurry	Al:Cr (wt.%)	Al:Cr (at.%)	Al activity	Deposited mass ($mg.cm^{-2}$)
Al	100:0	100:0	1	10
67Al33Cr	67:33	80:20	0.8 (High)	10-12
44Al56Cr	44:56	60:40	0.6 (Intermediate)	15-18
20Al80Cr	20:80	33:67	0.33 (Low)	25-30

For the two Al-Cr mixtures (20Al80Cr and 44Al56Cr), a single exothermic peak was observed at T_{onset} = 638 ± 2°C. One can see that the intensity of the exothermic reaction was greater for the 44Al56Cr composition as observed in Fig. III-8 with no substrate. Unlike the Al slurry deposit (Fig. III-12b), the endothermic signal of Al melting was not observed for the Al-Cr mixtures. This suggested that the whole Al reacted with Cr in the slurry deposits as shown in Fig. III-6. Therefore, this reaction was mainly associated with the exothermic reaction identified by mixing Al and Cr microparticles in I.2. The addition of Cr in the slurry compositions limited the SHS reactions between Al and the nickel substrate usually observed for high-activity slurry coatings [1].

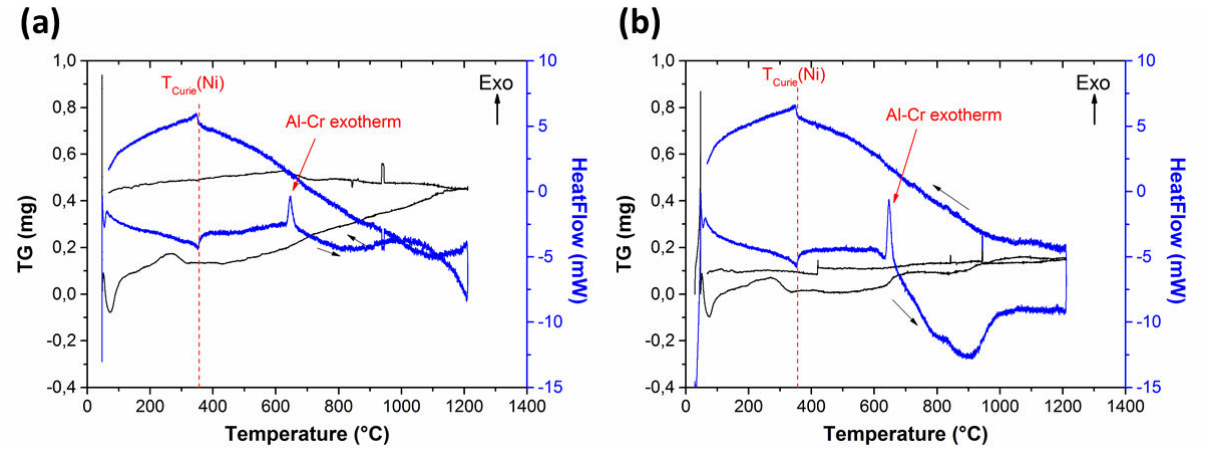

Fig. III-14. DSC thermograms for the pure nickel substrate in contact with (a) the 20Al80Cr and (b) the 44Al56Cr slurry deposits.

After the exothermic reaction, a variation of the heat flow was observed with a broad endothermic signal between 650°C and approximately 1000°C (Fig. III-14). This variation was not observed for the nickel reference sample and the different Al-Cr mixtures (with no substrate). Therefore, this variation was characteristic of an interaction between the nickel substrate and the slurry deposit. This broad endothermic signal was more energetic for the 44Al56Cr composition and may be attributed to the interdiffusion between Al-Cr intermetallic compounds present in the slurry deposit and the nickel substrate.

III.3. Synthesis of Al-Cr intermetallic compounds from Al-Cr mixed slurries for aluminizing

The reactivity of Al-Cr microparticles in the deposited slurries was investigated for the three selected compositions (Table III-4) in order to investigate the role of Cr addition in slurry compositions upon aluminizing. The slurries were deposited on pure nickel substrate (12.7 mm diameter) by air brush. The deposited slurry quantity was greater for the Al-Cr slurries than for the pure Al (Table III-4) in order to have a sufficient Al content in the donor for diffusion. The samples were systematically cured for 3 hours at 400°C to remove water and expel the organic binder before any further step [30]. The heat treatments were performed in TGA under flowing Ar and were as follows:

- **650°C-10 min**: repeats the heat treatment performed in DSC for reproducibility.
- **650°C-5h**: diffusion step for the homogenization of intermetallic phases and comparison with pure Al slurry (high-activity).
- **650°C-5h + 1000°C-3h**: complete heat treatment to promote the outward diffusion of Ni at 1000°C and stabilize the β-NiAl phase.
- **1080°C-6h**: conventional "low-activity" heat treatment for the repair of aluminide coatings on LPT blades and vanes made of nickel-based superalloys.

The SEM cross-section images (Fig. III-15) of the samples for the three Al-Cr compositions and corresponding surface XRD patterns (Fig. III-16a) demonstrate that the Al_xCr_y intermetallic compounds already formed just after 10 minutes of annealing at 650°C, as also observed by DSC (Fig.

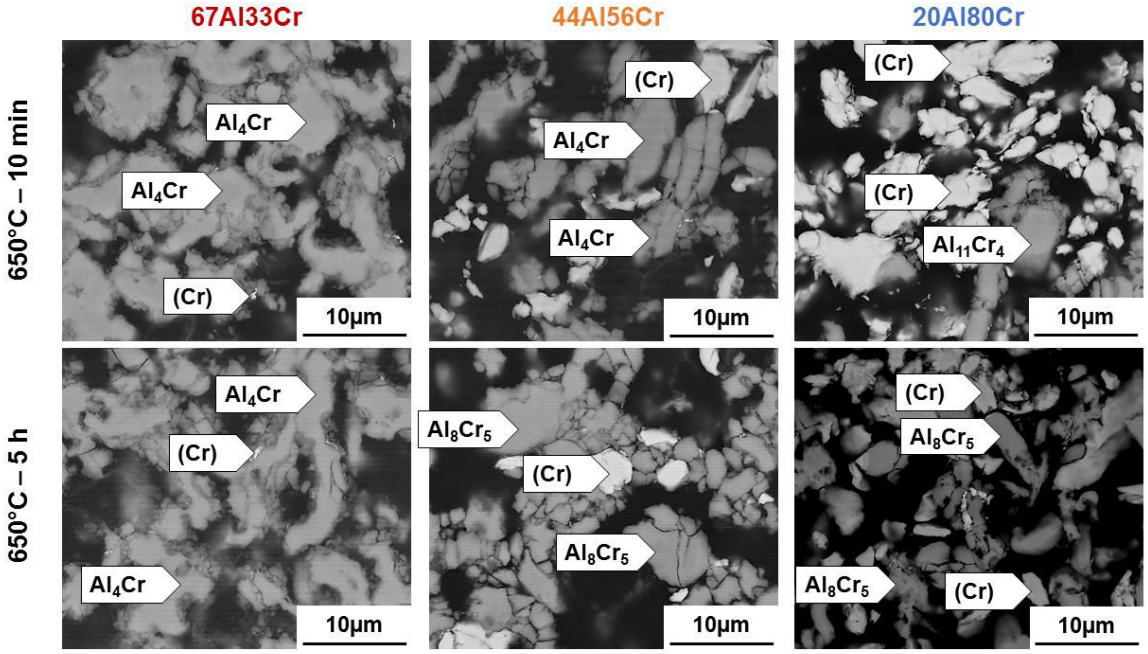

Fig. III-15. BSE cross-section images for the 67Al33Cr, 44Al56Cr and 20Al80Cr slurry compositions deposited on pure Ni after annealing at 650°C for 10 minutes and 5 hours in TGA (20 mL/min Ar flow).

III-6). In the 67Al33Cr mixture, coarse intermetallic phases formed (Fig. III-15) with a chemical composition close to Al_4Cr according to the EDS measurements (81 ± 1 at.% Al) [9,16]. Only small remnants of Cr were revealed in the microstructure whereas an additional phase (i.e. $Al_{11}Cr_2$) was identified by XRD. With this 67Al33Cr mixture, the microstructure and the composition of the intermetallic phases did not substantially change with increasing the annealing time to 5 hours (Fig. III-15).

For the 44Al56Cr and 20Al80Cr compositions, the fraction of unreacted Cr increased with the increasing content of Cr in the mixtures. XRD and EDS analyses revealed the formation of different intermetallic phases in the slurry deposits (Fig. III-16). The XRD patterns indicated additional species like $Al_{11}Cr_2$ for the 67Al33Cr and $Al_{11}Cr_4$ for both the 44Al56Cr and 20Al80Cr compositions. Such differences can be explained by the different probed depths. Indeed, the XRD analyses were performed in θ-2θ mode (Bragg-Brentano) and the depth of the analyses was about 10-20µm. In contrast, the SEM images were taken in the slurry deposit close to the Ni substrate, i.e. about 50µm deep. It was also noticed that Cr_2O_3 formed in 44Al56Cr and 20Al80Cr mixtures after 5 hours of annealing. This probably results from the oxidation of Cr by the oxygen (2 vpm) and water (5 vpm) impurities in the Ar flow (cf. Chapter II).

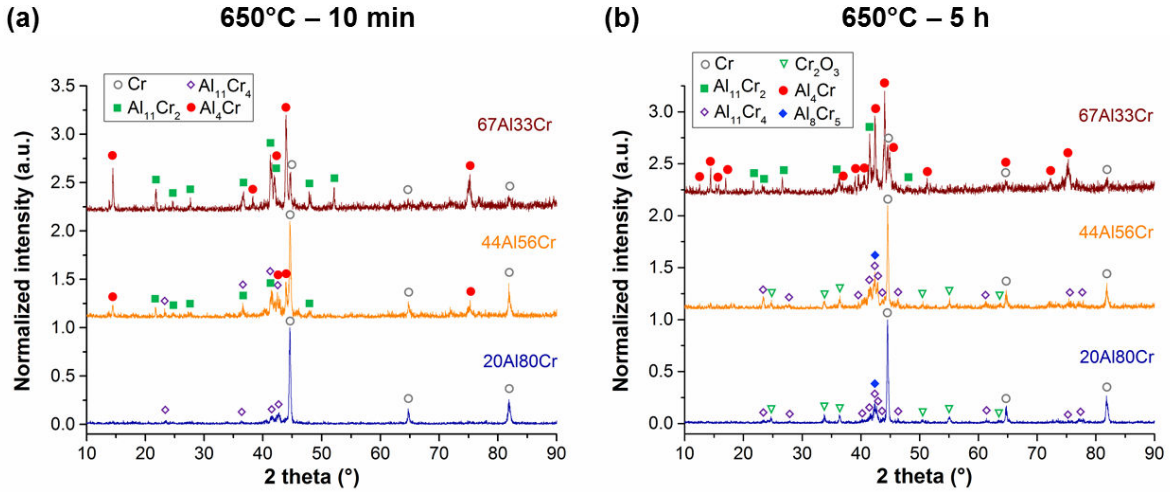

Fig. III-16. XRD patterns of the surfaces for the 67Al33Cr, 44Al56Cr and 20Al80Cr slurry compositions deposited on pure Ni after annealing at 650°C for (a) 10 minutes and (b) 5 hours (20 mL/min Ar flow).

After the further annealing at 1000°C for 3 hours, a change in composition occurred in the three Al-Cr slurry deposits. Indeed, the intermetallic phases displayed a more homogeneous contrast in the BSE mode of the SEM of Fig. III-17. Since no transformation was identified by DSC for the 67Al33Cr composition between 650°C and 1000°C (Fig. III-5a), it is assumed that these phases were formed by a solid-state diffusion process. The Al_8Cr_5 phase was the predominant aluminide phase for the 67Al33Cr and 44Al56Cr compositions (Fig. III-17a and Fig. III-17b). In the 44Al56Cr slurry deposit, the

$AlCr_2$ phase was also identified by XRD (Fig. III-17d). However, the EDS measurements suggested that the composition of some of the phases was in the Al_8Cr_5 + $AlCr_2$ field (42-65 at.% Al according to the binary phase diagram). For the 20Al80Cr composition, only the $AlCr_2$ intermetallic phase was detected by XRD (Fig. III-17d). In Fig. III-17c, the progressive transformation of unreacted Cr particles into $AlCr_2$ compound was observed with a difference of contrast between the two phases in BSE mode (confirmed with EDS analyses). Since $AlCr_2$ is not stable at 1000°C, this phase was probably formed upon cooling following the (Cr) ↔ $AlCr_2$ congruent reaction [9,24,25]. For the three Al-Cr compositions, α-Al_2O_3 was also detected by XRD (Fig. III-17d). The alumina may have several different origins but probably referred to the oxidation of Al-Cr intermetallic compounds by the low partial pressure of O_2 and H_2O in the reaction chamber (2 vpm O_2 and 5 vpm H_2O in the Ar bottle). For the two Cr-rich compositions, the three peaks corresponding to the body-centered cubic structure of Cr were still identified. Thus, the homogenization of the composition between Al and Cr was not complete for these two compositions after 3 hours at 1000°C.

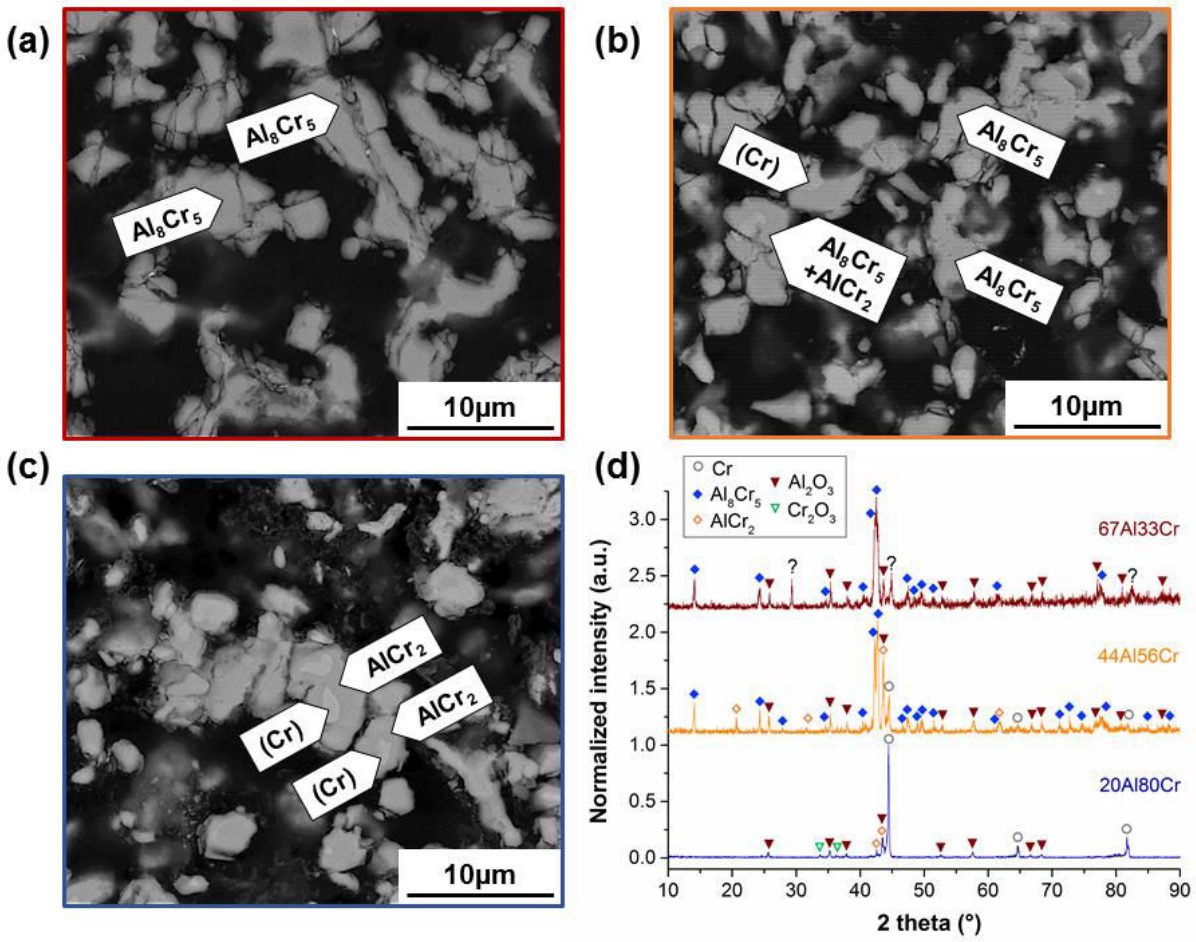

Fig. III-17. BSE cross-sections images for (a) the 67Al33Cr, (b) 44Al56Cr and (c) 20Al80Cr slurry compositions deposited on pure nickel and (d) corresponding XRD patterns of the surfaces after the complete heat treatment (650°C-5h + 1000°C-3h) under Ar.

- ***Intermediate summary:***

After annealing of the powders at different temperatures (650°C and 1000°C), the intermetallic compounds became progressively richer in Cr. For instance, after 5 hours of annealing at 650°C, the Al_xCr_y intermetallics were Al_4Cr and $Al_{11}Cr_2$ for the 67Al33Cr mixture, and Al_8Cr_5 and $Al_{11}Cr_4$ for both the 44Al56Cr and 20Al80Cr mixtures. Such Cr enrichment was fostered after the final step at 1000°C (i.e. Al_8Cr_5 and $AlCr_2$) and is believed to result from solid state diffusion (homogenization of the chemical composition between Al and Cr). Depending on the stoichiometry of the Al-Cr intermetallic phases synthesized, the thermodynamic activities of Al and Cr on the substrate surface may be different [21]. The intermetallic compounds synthesized in the slurry deposits can be assimilated to masteralloys in the aluminizing process. The main difference when using the slurries is that the masteralloys are in direct contact with the metallic substrate and not decomposed in a gas phase from halides activators by comparison with CVD-related techniques [21,31,32].

Based on these results, the formation of the identified Al-Cr intermetallic phases in the slurry deposits was therefore expected to decrease the Al activity on the surface of the substrate prior aluminizing. The objective was to limit the inward diffusion of Al in the substrate at low temperature while promoting the outward diffusion of nickel at high temperature to produce a coating with a "low-activity" microstructure. The next part presents the mechanisms of formation of Al-Cr slurry coatings on pure nickel (as a model material) before extrapolation to a Ni-Cr alloy and a nickel-based superalloy (Chapter IV). The role of Cr addition in slurry compositions upon aluminizing was first investigated using Al-Cr mixed slurries. Then, different architectures of coatings were tested by adjusting the composition and the periodicity of the layers to control the mechanisms of formation of the coatings.

IV. Mechanisms of formation of the diffusion layers on pure nickel

IV.1. Aluminizing of pure nickel with different Al-Cr mixed slurries: influence of Cr addition on the Al activity

In order to study the role of Cr addition upon aluminizing, three Al-Cr slurry coatings (67Al33Cr, 44Al56Cr and 20Al80Cr) were deposited on pure Ni and then submitted to a diffusion heat treatment (650°C-5h). The simple Al slurry coating (with an Al activity equal to 1) is given as a reference. The SEM cross-section images and the concentration profiles of Al and Cr for the four coating systems after the diffusion heat treatment are given in Fig. III-18. For the simple Al coating (Fig. III-18a), three different layers were observed. The outer phase, with a thickness of approximately 35µm, consisted in the Ni_2Al_3 phase with a high Al content (approximately 60 at.%). The two other layers were thinner and contained less Al with respectively β-NiAl (intermediate contrast) and γ'-Ni_3Al phases (bright layer). Both β-NiAl and γ'-Ni_3Al layers had a thickness of approximately 3-5µm. This microstructure was typical of a high activity slurry coating [4,22]. According to the EDS analyses, Al diffused in the Ni substrate with up to 6 at.% at 10µm below the γ'-Ni_3Al-substrate interface.

For the three Al-Cr compositions, the diffusion of Al into the Ni substrate was considerably hampered by the addition of Cr. None of the diffusion layers that formed on the surface exceeded 10 microns in thickness (Fig. III-18). According to the EDS analyses, β-NiAl and γ'-Ni_3Al phases were identified. However, the diffusion layers were not continuous for the three compositions and this might be explained because either Al or Cr were in direct contact with the Ni substrate after deposition of the slurry. Kirkendall porosities were observed between the Ni substrate and the γ'-Ni_3Al phase suggesting that the outward diffusion of Ni from the substrate to react with Al and Al-rich intermetallics was not compensated by Al inward diffusion. As such, approximately 3 at.% Ni incorporated to the Al-Cr intermetallic compounds above the substrate. Conversely, an increasing amount of Cr was dissolved in the coating and diffused into the Ni substrate with the greater Cr content in the mixtures (Fig. III-18f).

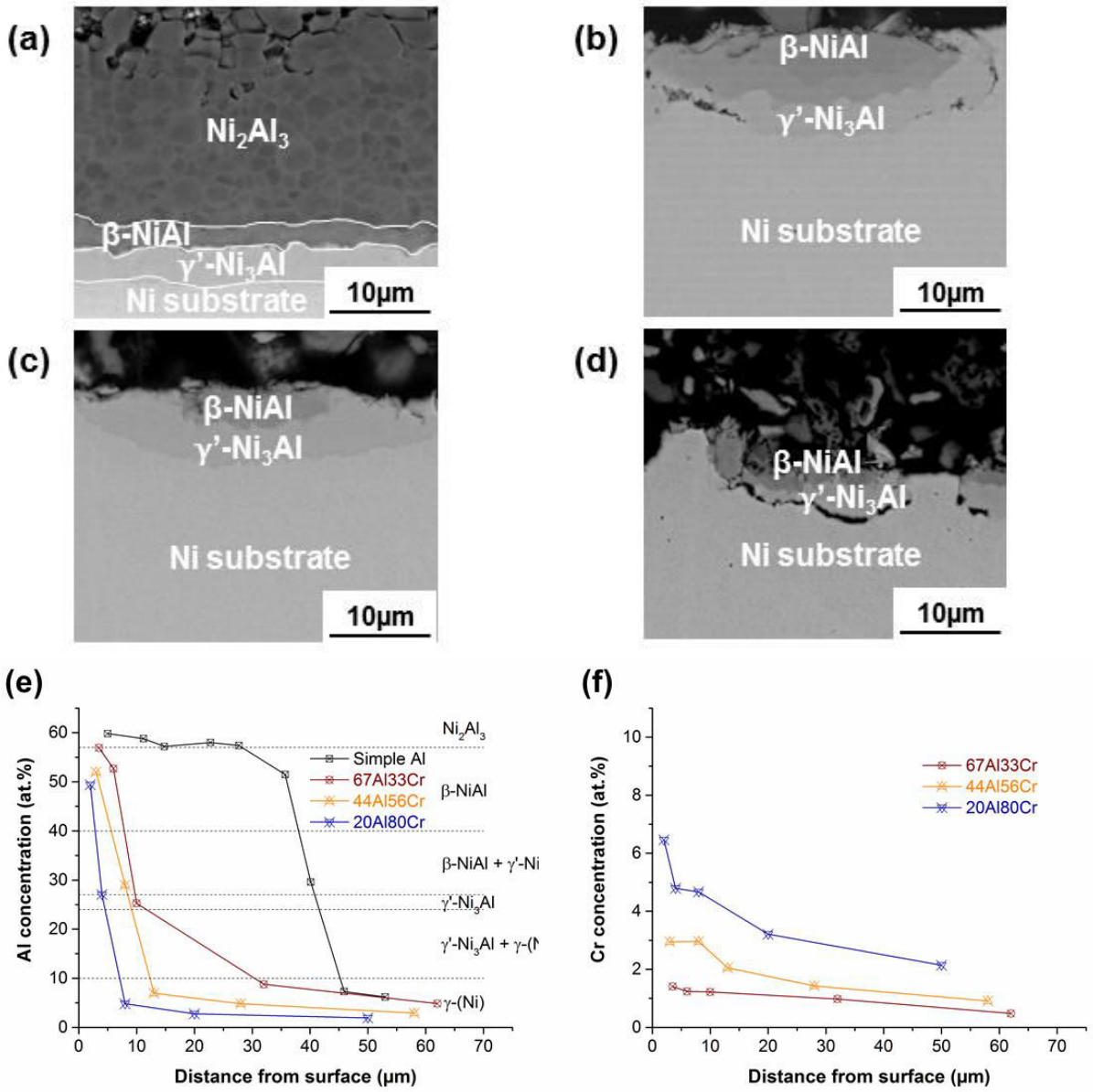

Fig. III-18. BSE cross-sections images for (a) simple Al, (b) 67Al33Cr, (c) 44Al56Cr and (d) 20Al80Cr slurry coatings on pure nickel after the diffusion heat treatment under Ar atmosphere and corresponding (e) Al and (f) Cr EDS concentration profiles.

Upon aluminizing at 650°C, concurrent reactions occurred at the surface of the nickel substrate between Al, Cr and Ni. Al preferentially reacted with Cr within the slurry deposit to result in the formation of Al_xCr_y intermetallics above the Ni substrate. These intermetallic compounds hampered the inward diffusion of Al into the Ni substrate. Therefore, the SHS reactions between Ni and Al usually reported for high-activity slurry coatings seemed to be limited [1,4,5]. This would explain why the diffusion layers were thin and discontinuous for all three Al-Cr compositions after 5 hours at 650°C (Fig. III-18).

IV.2. Outward diffusion of nickel at high temperature (i.e. 1000°C and 1080°C)

- ***Complete heat treatment (400°C-3h + 650°C-5h + 1000°C-3h):***

After the complete heat treatment, the simple Al slurry coating grew a β-NiAl phase by interdiffusion of Ni and Al (Fig. III-19a). The external β-NiAl phase was relatively thick (about 40µm) with an Al-rich β-NiAl layer in the outer region (β-NiAl with more than 50 at.% Al [33,34]). The intermediate γ'-Ni_3Al layer was about 5µm thick. For the 67Al33Cr composition (Fig. III-19b), three different layers were identified and corresponded to Al-rich β-NiAl, β-NiAl and γ'-Ni_3Al phases. The overall thickness of the diffusion layers was close to that of simple Al slurry coating. Therefore, interdiffusion between the Ni substrate and the Al_xCr_y intermetallic compounds was promoted at 1000°C. However, the coating was found to be less homogeneous than with the simple Al. For the 44Al56Cr and 20Al80Cr slurries

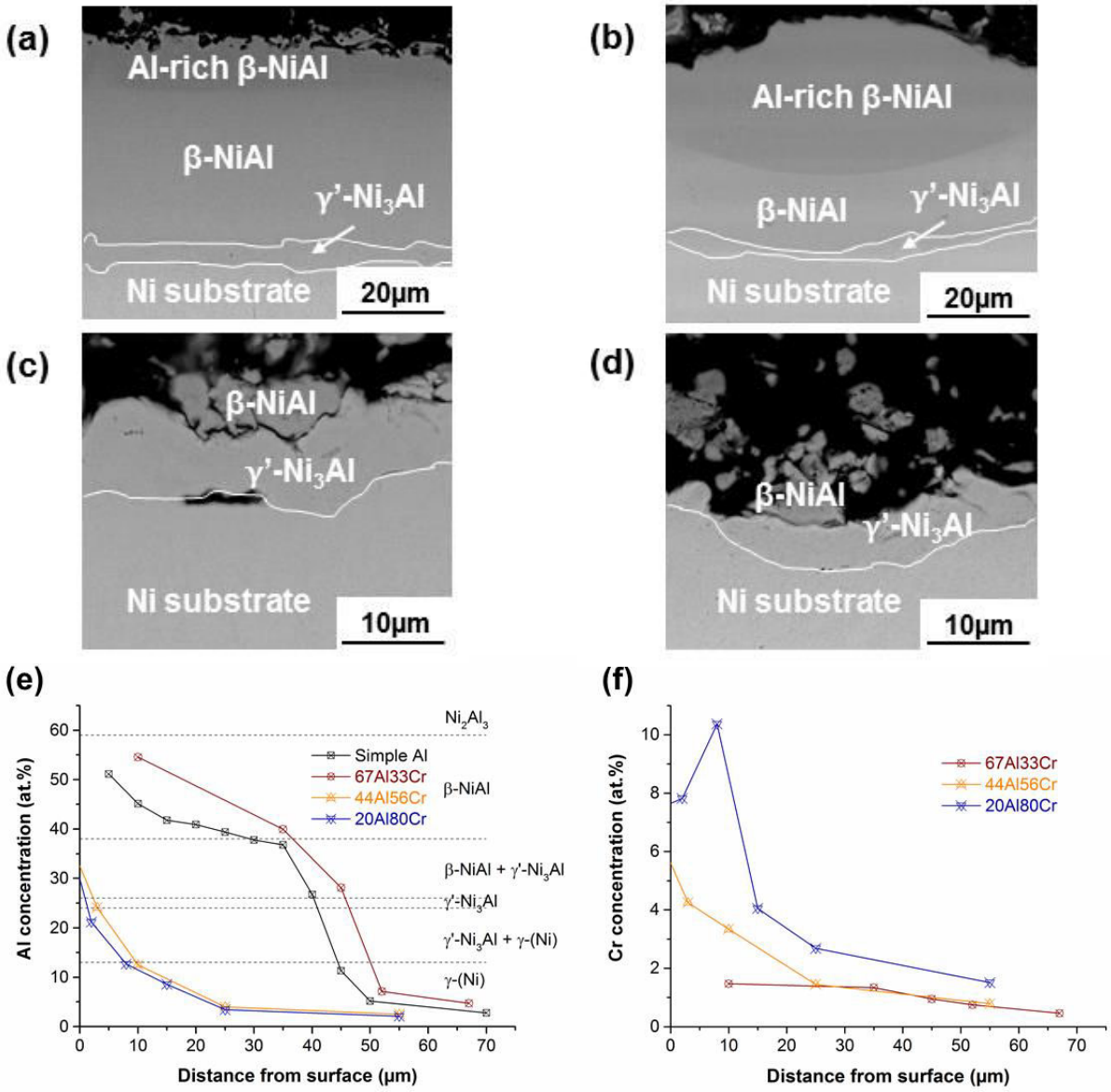

Fig. III-19. BSE cross-sections images for (a) simple Al, (b) 67Al33Cr, (c) 44Al56Cr and (d) 20Al80Cr slurry coatings on pure nickel after the complete heat treatment under Ar atmosphere and corresponding (e) Al and (f) Cr EDS concentration profiles.

(Fig. III-19c and Fig. III-19d), the Al enrichment of the substrate was considerably reduced by the high Cr content of these mixtures (Fig. III-19e). The diffusion layer was neither continuous nor homogeneous in composition. Kirkendall porosities were observed at the diffused layer/substrate interface and might be attributed to an enhanced outward diffusion of Ni at 1000°C [35]. For these two compositions, the Al reservoir on the surface was very small compared to the simple Al and 67Al33Cr coatings. Nevertheless, the Cr concentration of the diffusion layers was much higher for the 44Al56Cr and 20Al80Cr compositions (Fig. III-19f).

Interdiffusion between the Ni substrate and the Al_xCr_y intermetallic phases synthesized in the slurry deposit was promoted with the additional annealing at 1000°C for 3 hours. Depending on the Al and Cr activities of the intermetallic phases, the Al and Cr contents of the coatings were found to be different for the three Al-Cr compositions. For the 67Al33Cr (Al_4Cr phase formed at 650°C), the Al activity was high enough at 1000°C to grow a β-NiAl layer almost as thick as with the simple Al slurry (Fig. III-19b). At this temperature, Ni was expected to diffuse outwardly and dissolve the Al_xCr_y phases resulting in the formation of β-NiAl phase with dissolved Cr [36,37] (less than 2 at.% Cr according to the EDS measurements presented in Fig. III-19b). The significant amount of Al_8Cr_5 formed on the surface at 1000°C (Fig. III-15) had a dramatic effect on the formation of the β-NiAl coating as Al was retained in this stable structure at 1000°C and could not incorporate further into the Ni substrate. Therefore, β-NiAl can only form in the very external layer of the coatings (Fig. III-19c and Fig. III-19d) and the diffusion layers remained thin and discontinuous.

- ***Conventional low-activity heat treatment (400°C-3h + 1080°C-6h):***

Three nickel samples were coated with the 67Al33Cr, 44Al56Cr and 20Al80Cr slurry compositions and heat treated in TGA following the conventional low-activity heat treatment employed in the repair industry. The SEM cross-section images of the samples and corresponding X-ray maps are given in Fig. III-20. A 50µm thick coating formed from the 67Al33Cr composition. The outer layer was composed of the β-NiAl phase and the inner layer presented a composition close to the γ'-Ni_3Al phase. The Cr content of the diffusion zone remained low (less than 2 at.%) because of the limited solubility of Cr in the β-NiAl phase [36-38]. Some Cr-rich precipitates were indeed observed in the external region of the coating (Fig. III-20a). For the 44Al56Cr composition, the outward diffusion of nickel was clearly observed with the coalescence of Kirkendall porosities at the initial surface of the substrate (Fig. III-20b). Above the nickel substrate, a heterogeneous diffusion zone was formed with a composition close to the β-NiAl phase. The precipitation of α-Cr occurred within the β-NiAl phase and suggested that this diffusion zone was formed by the dissolution of Al_xCr_y intermetallic phases due to the outward diffusion of nickel. The Al reservoir of the slurry deposit was too low for this composition to grow a continuous β-NiAl layer.

For the 20Al80Cr composition (Fig. III-20c), some islands with the β-NiAl composition were observed above the nickel substrate. The Al content of the slurry deposit was too low in this composition to grow a continuous β-NiAl layer. In the slurry deposit, the initial Al-Cr phases were enriched in nickel. According to the X-ray maps, the nickel substrate was enriched with Cr for the 44Al56Cr and 20Al80Cr slurry compositions. Oxygen was found to be mainly associated with Cr and Al. This would be explained by the greater affinity for oxygen of Cr and Al than that of Ni.

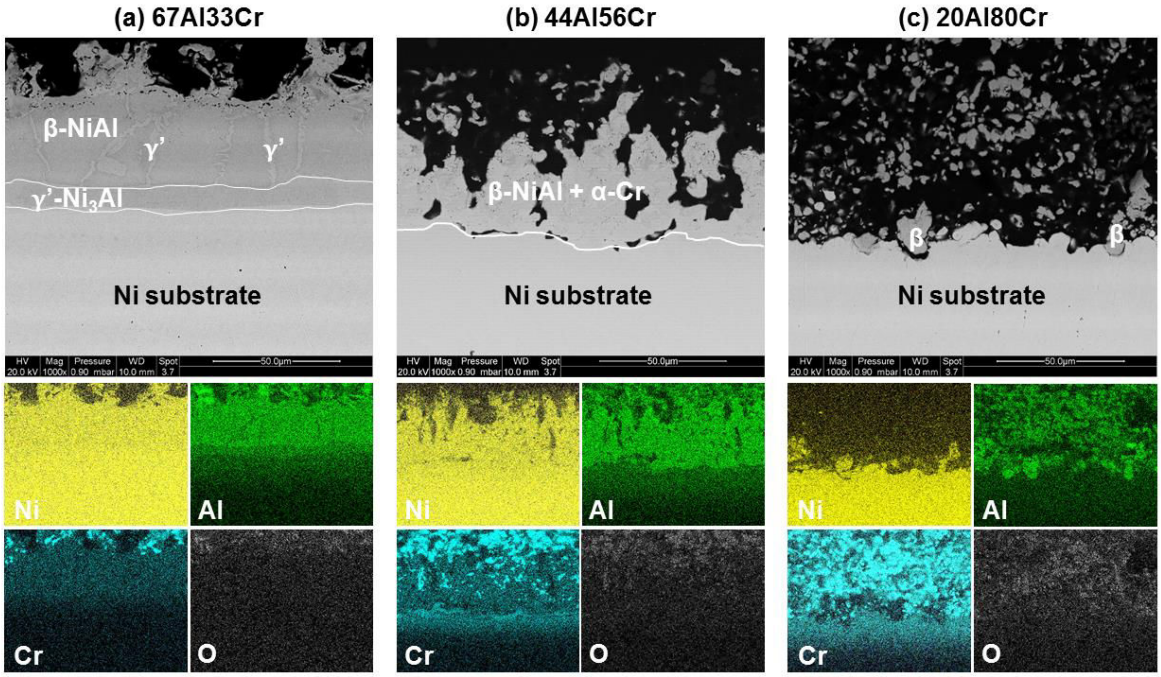

Fig. III-20. BSE cross-section images and X-ray maps for the (a) 67Al33Cr, (b) 44Al56Cr and (c) 20Al80Cr slurries elaborated on pure nickel after heat treatment in TGA (400°C-3h + 1080°C-6h).

V. Mechanisms of formation of the diffusion layers from Al-Cr and Cr-Al double-layer systems

V.1. Elaboration of Al-Cr and Cr-Al double-layer systems

Double-layer systems have been studied as an alternative to Al-Cr mixed slurries developed in paragraph IV. Thanks to the flexibility of the slurry coatings, it is possible to adjust the architecture of the coatings to optimize their properties ("coatings by design"). Two double-layer systems have been elaborated (Fig. III-21) to investigate the mechanisms of formation of the coatings on pure nickel substrate. After the application of the first layer, the samples were let to dry in a fume cupboard for one hour before the application of the second layer [22]. The deposited mass of Cr was fixed at 10 mg.cm^{-2} for the two systems to study the influence of the Al/Cr ratio by varying the Al content (5 or 10 mg.cm^{-2}), see Fig. III-21. For the sake of clarity, the Al/Cr ratio of the slurry deposits (in wt.%) was considered to differentiate the different architectures tested in this work. For the Al-Cr double-layer system, the 33Al-67Cr and 50Al-50Cr compositions refer respectively, to the system with 5 and 10 g.cm^{-2} of Al. For the Cr-Al double-layer system, the 67Cr-33Al and 50Cr-50Al compositions refer respectively to the system with 5 and 10 g.cm^{-2} of Al.

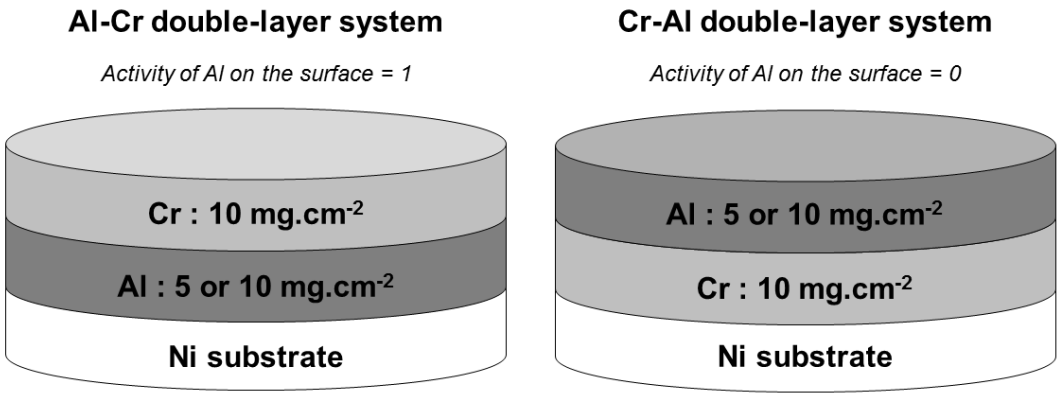

Fig. III-21. Architecture of the Al-Cr and Cr-Al double-layer systems elaborated on pure nickel.

V.2. Mechanisms of formation for the Al-Cr double-layer system

- ***Diffusion heat treatment (400°C-3h + 650°C-5h):***

To determine the mechanisms of formation for the Al-Cr double-layer system, a first sample coated with the 50Al-50Cr composition was treated in DSC. The SEM cross-section image and corresponding X-ray maps of Cr, Ni and Al of the sample are given in Fig. III-22. Four distinct layers can be observed after heat treatment. The top layer with a bright contrast in BSE mode was composed of unreacted Cr microparticles. The second layer with a thickness of approximately 100µm and an intermediate contrast was composed of Al-Cr intermetallic phases resulting from the exothermic reaction between Al and Cr microparticles. The EDS spot measurements suggested the Al_8Cr_5 composition as previously observed for the 44Al56Cr and 20Al80Cr powder mixtures in Fig. III-15 after annealing at 650°C for

5 hours. The presence of alumina shells between these intermetallic compounds and the underlying substrate suggested that this reaction occurred at the interface between the initial Al and Cr layers (Fig. III-21). Therefore, the Cr top layer progressively consumed the Al reservoir upon annealing as depicted by the X-ray maps. Consequently, only a fraction of the Al reservoir reacted with the nickel substrate to grow a diffusion zone of approximately 15µm of thickness (Fig. III-23).

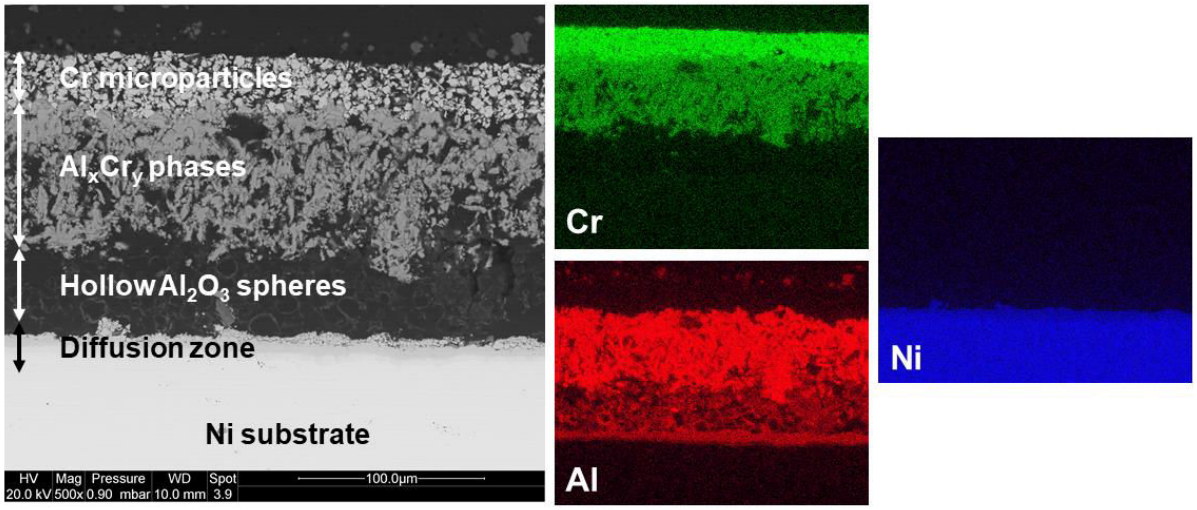

Fig. III-22. BSE cross-section image and X-ray maps of Cr, Al and Ni for the 50Al-50Cr double-layer system elaborated on pure nickel in DSC (20 mL/min Ar flow).

The diffusion zone was composed of three different layers. The outer layer was brittle with a composition close to the Ni_2Al_3 phase. The intermediate layer was free of cracks with a thickness of approximately 5-6µm and was identified as the β-NiAl phase. The third layer with a contrast close to the nickel substrate in BSE mode corresponded to the γ'-Ni_3Al phase. By comparison with the Al slurry coating (Fig. III-18a) and in spite of the greater mass of slurry deposited, one can observe that the overall thickness of the diffusion zone was considerably reduced due to the Cr top layer. If the β-NiAl

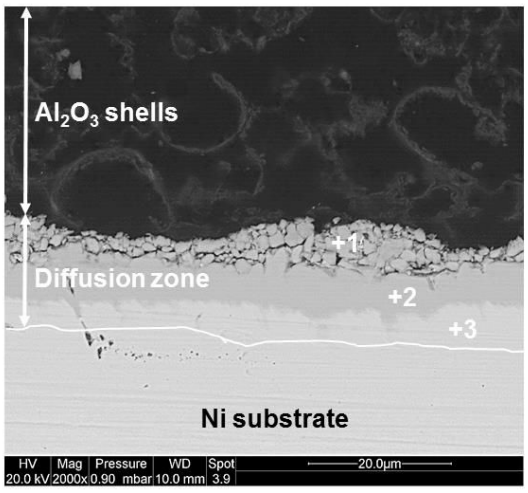

EDS spot	Al (at.%)	Ni (at.%)	Cr (at.%)	Possible phase
1	58.0	40.9	1.1	Ni_2Al_3
2	52.9	46.1	1.0	β-NiAl
3	26.4	72.7	1.0	γ'-Ni_3Al

Fig. III-23. BSE cross-section image and EDS spot measurements of the diffusion zone identified in Fig. III-22.

and γ'-Ni_3Al layers presented a thickness close to that of the Al slurry coating, the formation of the brittle Ni_2Al_3 phase was considerably limited for the Al-Cr double-layer system at 650°C. These observations suggested that the Cr top layer was able to limit the diffusion of Al toward the substrate by forming Al_xCr_y intermetallic phases in the slurry deposit. However, the presence of the Ni_2Al_3 phase suggested that the SHS reactions between Al and Ni were not suppressed.

- ***Influence of the annealing time at the diffusion temperature (i.e. 650°C):***

Complementary experiments were done in TGA in the same conditions. The annealing treatment at 650°C was also prolonged up to 20 hours to emphasize the influence of the dwell time on the composition and the thickness of the diffusion layers (Fig. III-24). With the low Al reservoir (33Al-67Cr system), only two distinct layers were observed with a composition close to β-NiAl and γ'-Ni_3Al according to the EDS spot measurements. The overall thickness of the diffusion zone was not substantially changed after 20 hours. For the high Al reservoir (50Al-50Cr system), the diffusion zone presented an outer heterogeneous layer after 5 hours with γ-(Ni), β-NiAl and Ni_2Al_3 phases identified. The presence of γ-(Ni) in the outer region of the diffusion zone might come from the dissolution of nickel by molten Al during the SHS reactions [39]. After 20 hours of annealing, the diffusion zone was more homogeneous in composition probably due to solid state diffusion between Al and Ni. Some remnants of the Ni_2Al_3 phase were observed at the extreme surface of the diffusion zone whereas some grains with the γ'-Ni_3Al composition were identified through the β-NiAl layer. The overall thickness of the diffusion zone was close for both Al reservoirs.

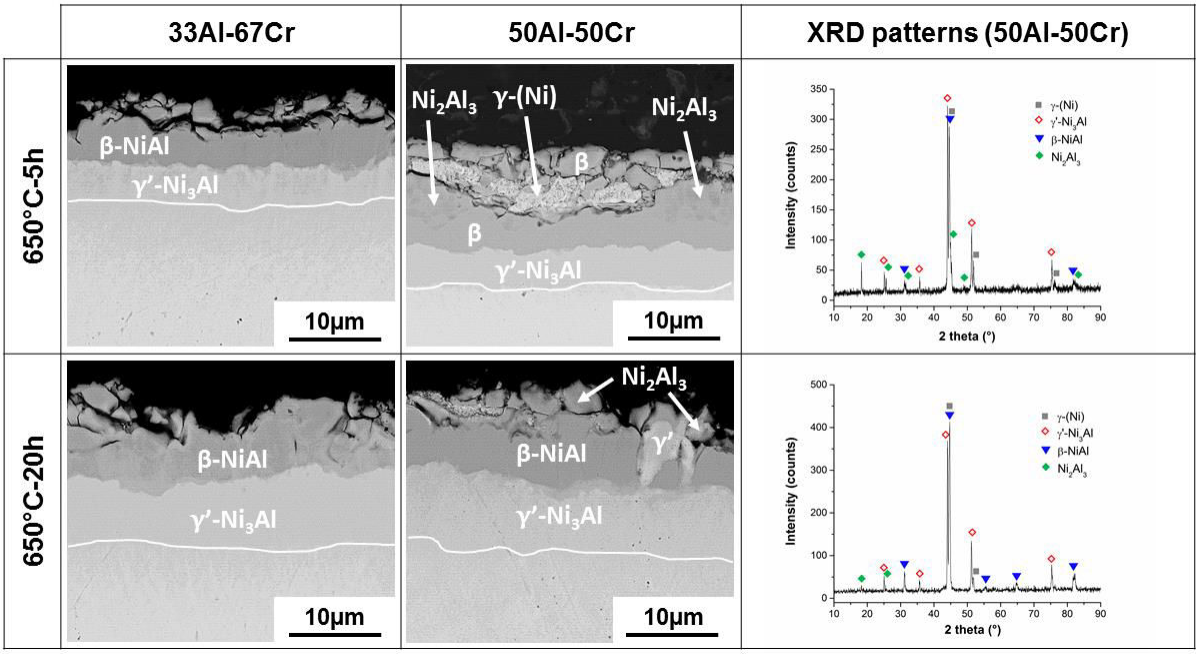

Fig. III-24. BSE cross-sections images of the diffusion layers formed after annealing at 650°C for the Al-Cr double-layer systems on pure nickel (TGA, 20 mL/min Ar flow) and corresponding XRD surface patterns (without top coat).

The addition of Cr above the Al slurry layer was able to limit the thickness of the diffusion zone and the formation of the Ni_2Al_3 phase on nickel substrate. However, the SHS reactions between Ni and Al [20,39] were not suppressed for the Al-Cr double-layer system because of the initial contact between Al microparticles and pure nickel substrate (Fig. III-21). Therefore, the diffusion zones were found to be heterogeneous in thicknesses and composition and an additional step at a higher temperature (i.e. 1000°C) was required to promote nickel outward diffusion [22].

Above the diffusion zone in the top coat (Fig. III-22), the unreacted Cr microparticles were oxidized after annealing. The peripheral oxidation of the Cr microparticles (Fig. III-25) probably resulted from the low partial pressure of O_2 and H_2O in the reaction chamber (2 vpm O_2 and 5 vpm H_2O). The formation of chromia was confirmed with the Raman surface analyses of the top coats showing the five characteristic peaks of chromia [40-42]. Note the progressive oxidation of the Cr microparticles on the SEM cross-section images (Fig. III-25a and Fig. III-25b).

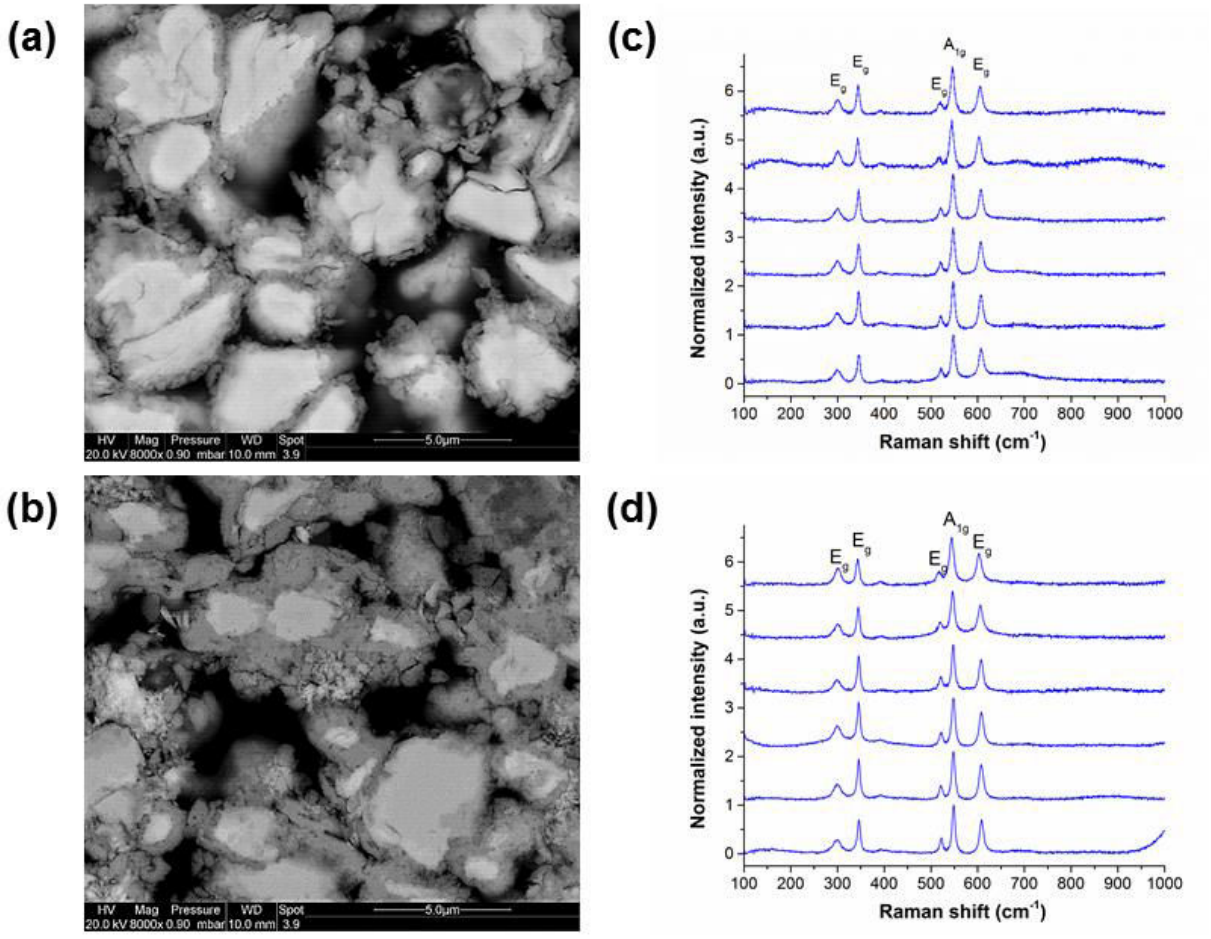

Fig. III-25. BSE cross-section images showing the peripheral oxidation of Cr microparticles after (a) 650°C-5h and (b) 650°C-20h in Ar and (c), (d) corresponding surface Raman analyses.

- ***Complete heat treatment (400°C-3h + 650°C-5h + 1000°C-3h):***

After an additional step at high temperature (1000°C-3h), a 10-15µm thickness γ'-Ni_3Al phase was formed on the nickel substrate (Fig. III-26). The initial Al reservoir did not play any significant role on the thickness and the composition of the diffusion layers. The β-NiAl phase was no longer identified after annealing at 1000°C and was probably transformed into γ'-Ni_3Al by depletion of Al due to the great diffusion gradient between the initial β-NiAl layer and the nickel substrate. The step at 1000°C did not permit further Al ingress in the diffusion layer from the Al-Cr intermetallic phases formed in the slurry deposit (Fig. III-22). Therefore, the layer of hollow alumina spheres between these phases and the underlying substrate (Fig. III-23) seemed to act as a barrier to diffusion. This layer of alumina shells was found to be brittle [43] and caused the spallation of the top coat composed of Al_xCr_y phases and Cr microparticles (Fig. III-22).

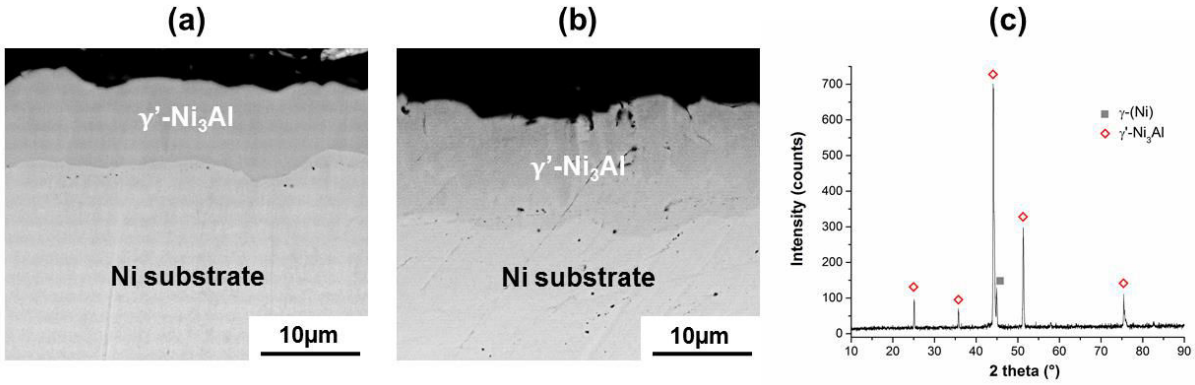

Fig. III-26. BSE cross-section images of the diffusion layers formed on pure nickel for the (a) 33Al-67Cr and (b) 50Al-50Cr double-layer systems and (c) corresponding XRD pattern of the surface.

- ***Mechanisms of formation for the Al-Cr double-layer system:***

The mechanisms of formation for the Al-Cr double-layer system elaborated on pure nickel are proposed in Fig. III-27 based on the experimental observations. For this architecture, the Al presents two concurrent gradients of diffusion. Therefore, the Al was rapidly depleted in the slurry deposit by reaction with the nickel substrate on one side and with the Cr microparticles on the other side (Fig. III-22). The initial contact between Al and the nickel substrate fostered the SHS reactions with the formation of Al-rich Ni_xAl_y phases on nickel [5,20,39]. The exothermic reaction between Al and Cr microparticles leads to the formation of Al-rich Al_xCr_y intermetallic compounds in the slurry deposit. Therefore, a significant fraction of the Al reservoir was depleted by the Cr microparticles. The diffusion zone formed on the nickel substrate was then limited in thickness and significantly limited the Al uptake of the nickel substrate. When the whole Al reacted, an intermediate layer of hollow alumina spheres remained between the diffusion zone and the Al_xCr_y phases formed. This layer of thin alumina shells

was found to cause spallation of the top coat [43]. An excess of oxidized Cr microparticles was present in the top layer after annealing.

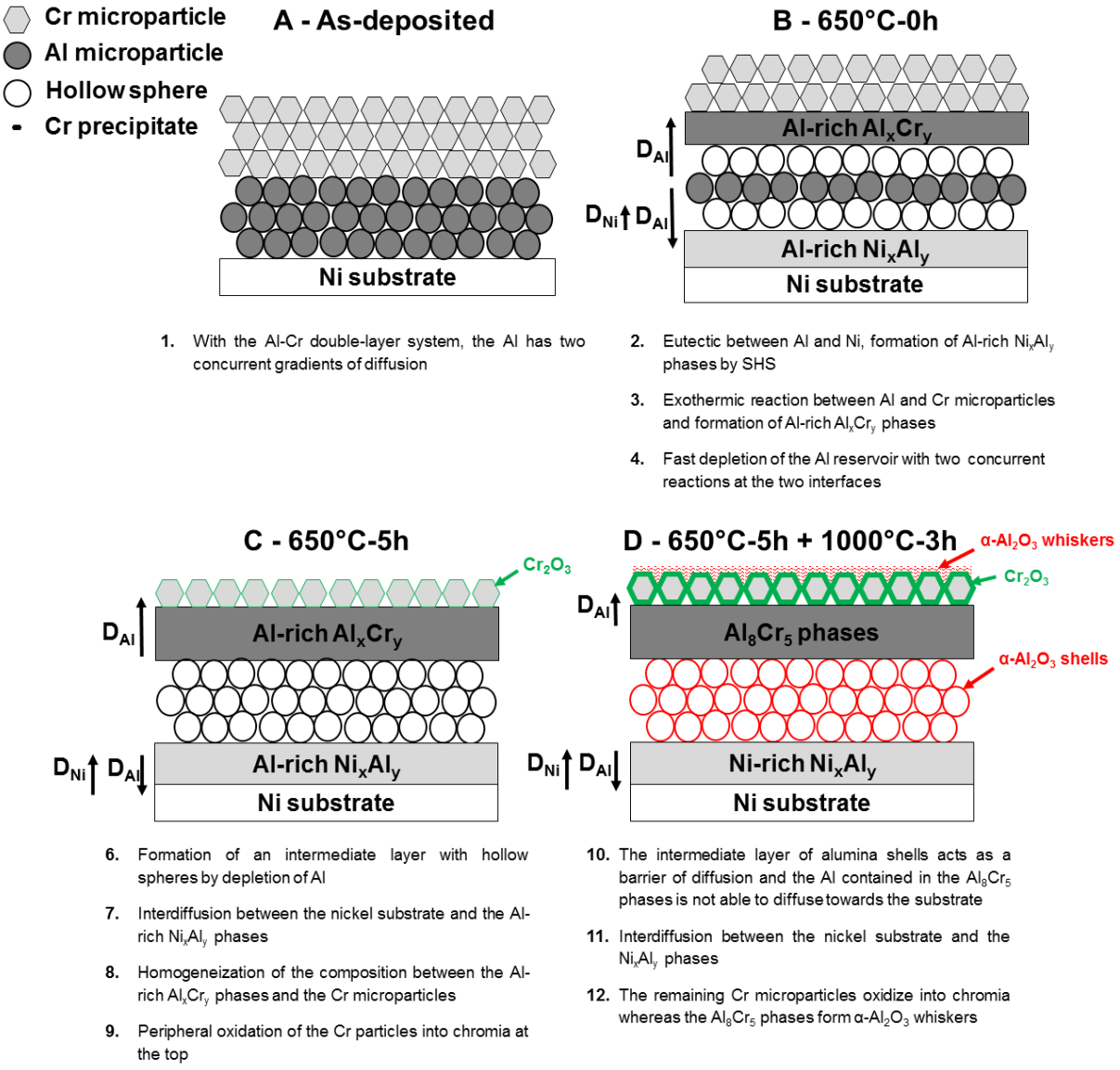

Fig. III-27. Sequence proposed for the mechanisms of formation of the Al-Cr double-layer system elaborated on pure nickel.

V.3. Mechanisms of formation for the Cr-Al double-layer system

- ***Reactivity of the slurry deposit with pure nickel:***

Unlike for the Al-Cr double-layer system, the Cr-Al one permitted to avoid the Al microparticles to be in direct contact with the nickel substrate (Fig. III-21). The DSC thermogram for a 56Cr-44Al double-layer system elaborated on pure nickel substrate is given in Fig. III-28. For this system, the evolution of the heat flow was close to the one observed for the 44Al56Cr slurry composition (Fig. III-14b). The onset temperature of the exothermic reaction was determined experimentally at 638°C. Considering the architecture of the Cr-Al double-layer system, the SHS reactions between the nickel substrate and the Al microparticles should be avoided. Therefore, this exothermic reaction could correspond to the reaction between Al and Cr microparticles identified in Fig. III-3.

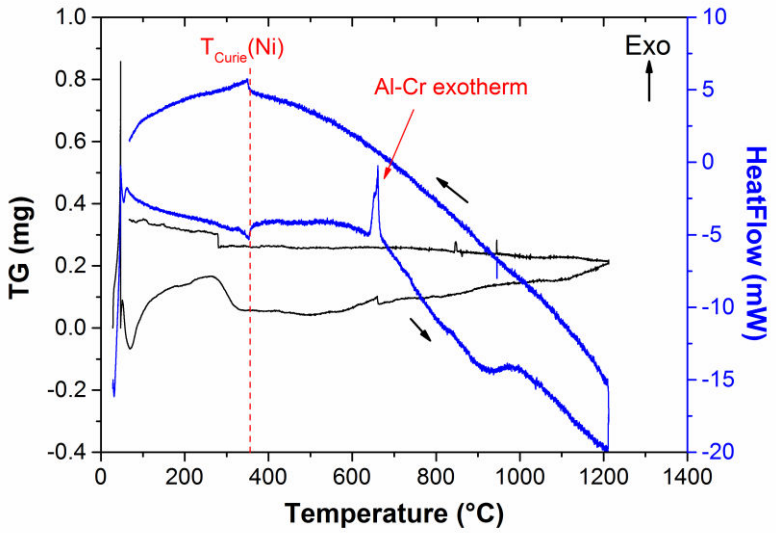

Fig. III-28. DSC thermogram for the Cr-Al double-layer system elaborated on pure nickel substrate.

- ***Diffusion heat treatment (400°C-3h + 650°C-5h):***

To investigate the mechanisms of formation for the Cr-Al double-layer system on pure nickel, a first sample was submitted to the diffusion heat treatment in TGA. The SEM cross-section image and X-ray maps of the sample are given on Fig. III-29. All the Al microparticles reacted with the Cr ones after the diffusion heat treatment resulting in a top layer with hollow alumina spheres [22] and an intermediate layer with Al-rich Al_xCr_y intermetallic phases. A layer of Cr microparticles was still identified above the nickel substrate suggesting that Al was the limiting reagent for this composition (50Cr-50Al system). This result was relevant with the conclusions drawn from Fig. III-6. An oxygen enrichment was observed in the Cr-rich layer and probably refers to the peripheral oxidation of the Cr microparticles (Fig. III-25).

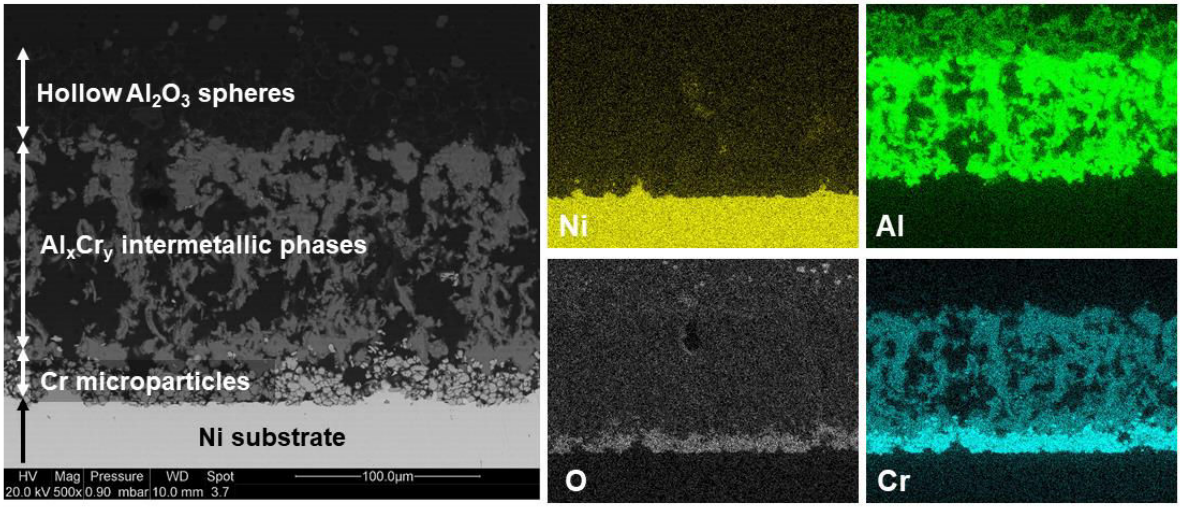

Fig. III-29. BSE cross-section image and corresponding X-ray maps for the 50Cr-50Al double-layer system elaborated on pure nickel after the diffusion heat treatment in Ar.

EDS spot measurements obtained for the two Al reservoirs in the region close to the surface of the nickel substrate are given in Fig. III-30. The layer of Cr microparticles acted as a diffusion barrier for Al avoiding the SHS reactions between Al microparticles and the nickel substrate [1]. Interdiffusion occurred between Ni, Al and Cr. However, the Al and Cr contents at the extreme surface of the nickel substrate remained low with less than 10 at.%. The composition of the Al_xCr_y intermetallic compounds synthesized above the nickel substrate ranged from 78 at.% to 85 at.% of Al. By comparison with the Ni-Al-Cr ternary diagram at 700°C [44], this would correspond to the $Al_{11}Cr_2$, Al_4Cr and $Al_{11}Cr_4$ phases (single-phase or two phases). To identify the crystal structures and compare with the EDS measurements, the sample with the 50Cr-50Al system was also characterized by XRD (Fig. III-31a). The three Al-rich Al-Cr phases were identified by XRD. The characteristic diffraction peaks of γ-Al_2O_3 were also detected on the XRD pattern [45,46]. Kolarik et al. emphasized the formation of γ-Al_2O_3 on 2-5µm Al particles from approximately 550°C using HT-XRD measurements in air [45]. γ-Al_2O_3 transformed progressively into the stable α-Al_2O_3 phase at temperatures greater than 800°C. Therefore, the detection of γ-Al_2O_3 was probably coming from the top coat structure based on hollow Al_2O_3 spheres (Fig. III-29) [46,47].

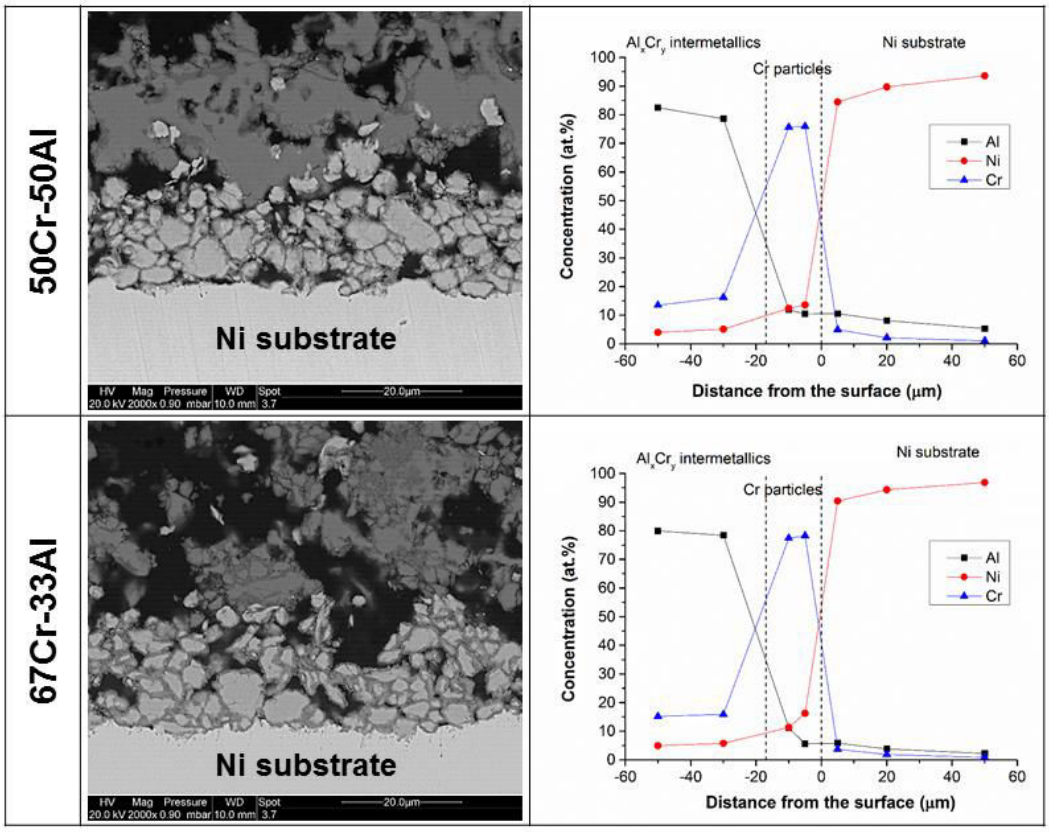

Fig. III-30. BSE cross-sections images and EDS concentration profiles for the Cr-Al double-layer systems elaborated on pure nickel after the diffusion heat treatment in Ar.

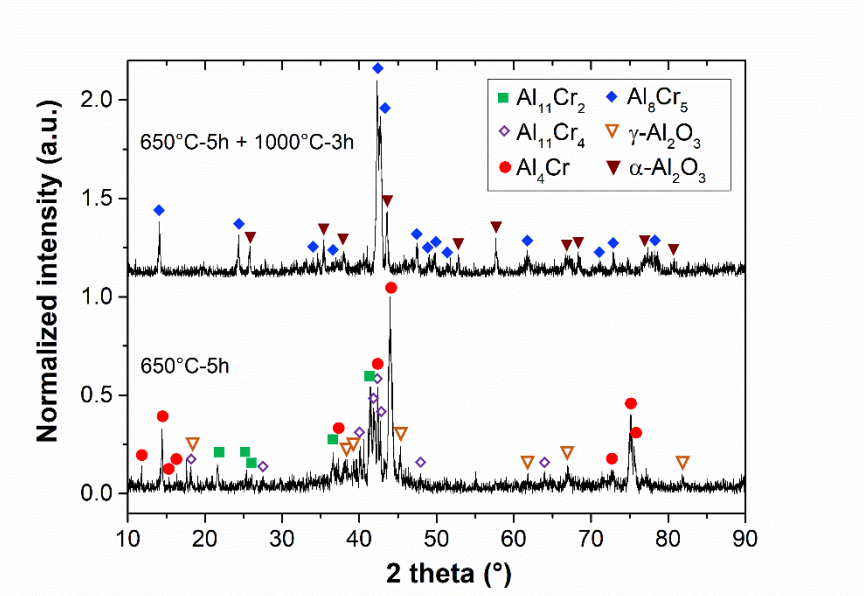

Fig. III-31. XRD patterns of the surfaces for the 50Cr-50Al double-layer system elaborated on pure nickel after (a) the diffusion and (b) the complete heat treatment in TGA.

- ***Complete heat treatment (400°C-3h + 650°C-5h + 1000°C-3h):***

After the complete heat treatment, a diffusion zone was formed in the outer region of the nickel substrate (Fig. III-32). This diffusion zone was rich in Ni and Al suggesting the formation of Ni_xAl_y intermetallics. Cr-rich precipitates within the diffusion layer were also emphasized on the X-ray maps. This indicates the low solubility of Cr in the phases formed in the diffusion zone. According to the EDS spot measurements (Fig. III-33) and the XRD patterns (Fig. III-31), the Al-rich Al_xCr_y intermetallics formed at 650°C transformed into the stable Al_8Cr_5 phase with the additional annealing period at 1000°C for 3 hours. It thus seems that Al_8Cr_5 released Al to grow a diffusion zone by interdiffusion with nickel. The alumina hollow spheres were still observed on the surface and converted into the stable α-Al_2O_3 after 3 hours of annealing at 1000°C [22] (Fig. III-31).

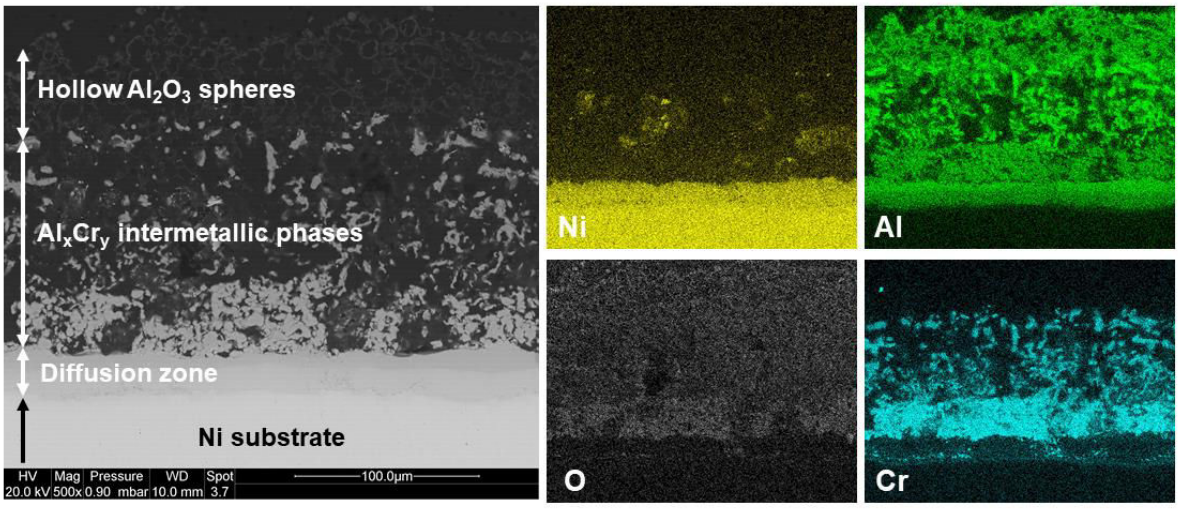

Fig. III-32. BSE cross-section image and corresponding X-ray maps for a 50Cr-50Al double-layer system elaborated on pure nickel after the complete heat treatment in TGA.

At higher magnification (Fig. III-33), three distinct layers were observed in the diffusion zone for the 50Cr-50Al composition. The outer dark layer in BSE mode was identified as the Al-rich β-NiAl phase. The intermediate layer was composed of the Ni-rich β-NiAl phase with dissolved Cr (approximately 5 at.%). The third layer was very thin and located just above the nickel substrate with a composition close to the γ'-Ni_3Al phase. The transformation of Al_xCr_y into Ni_xAl_y phases by reaction with Ni results from the greater thermodynamic stability of the latter, whose enthalpies of formation are much greater than the Ni_xCr_y ones [44]. Subsequently, a large fraction of Cr remained undissolved in the newly formed Ni_xAl_y phases because of its low solubility [36-38]. The exact composition of the Cr-rich phases was not determined from the SEM-EDS analyses but suggested the presence of α-(Cr).

In contrast, the Al content of the Al-Cr intermetallic phases formed above the substrate with the 67Cr-33Al system was too low to grow a diffusion zone (Fig. III-33). In other words, the Al activity of the slurry deposit was too low to grow a continuous β-NiAl layer. The phases observed at the interface between the nickel substrate and the deposit were indeed rich in Cr (Fig. III-33) suggesting the α-(Cr) solid solution.

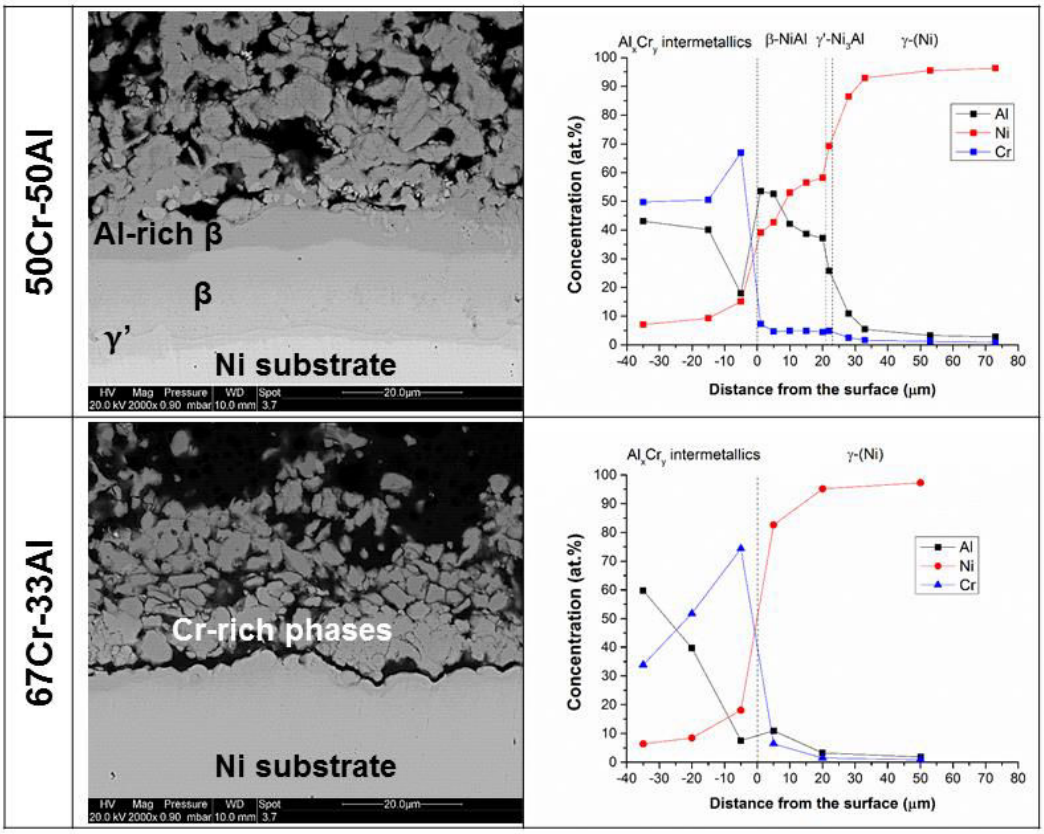

Fig. III-33. BSE cross-sections images and EDS concentration profiles for the Cr-Al double-layer systems elaborated on pure nickel after the complete heat treatment in Ar.

By comparing 50Cr-50Al and 67Cr-33Al double-layer systems, the sequence of reaction can be described following equations *(Eq. III-1)* and *(Eq. III-2)*:

$$xAl + yCr \rightarrow Al_xCr_y \qquad \textbf{(Eq. III-1)}$$

$$Ni + Al_xCr_y \rightarrow \beta\text{-NiAl} + \alpha\text{-(Cr)} \qquad \textbf{(Eq. III-2)}$$

The stoichiometry of the Al_xCr_y phases synthesized in the slurry deposit is dependent on the initial contents of Al and of Cr in the reaction *(Eq. III-1)*. The driving force of the reaction *(Eq. III-2)* is therefore the initial Al content of the slurry deposit. The transformation *(Eq. III-2)* implies that β-NiAl is readily formed and that the outward diffusion of nickel prevails upon the aluminizing process. This is characteristic of low-activity coatings [48,49]. Based on these observations, it appeared therefore that the simplified transformation *(Eq. III-2)* was controlling the growth of the coating for the 50Cr-50Al system.

On the opposite, the large excess of α-(Cr) after the exothermic reaction for the 67Cr-33Al compositions considerably decreased the driving force for diffusion and transformation *(Eq. III-2)*. The growth of the coating was therefore considerably hampered. This would require longer time or higher temperatures to foster the interdiffusion between the nickel substrate and the Cr-rich phases (denoted α-(Cr) in the reaction). These observations confirmed that the control of the Al-Cr ratio is of utmost importance to obtain the desired coating design. Considering the Cr-Al double-layer system, it is therefore possible to adjust the deposited mass of Cr and Al to optimize the final microstructure of the coating.

- ***Mechanisms of formation for the Cr-Al double-layer system:***

The sequence for the mechanisms of formation of the Cr-Al double-layer system elaborated on pure nickel is proposed in Fig. III-34. When the temperature reached approximately 640°C (Fig. III-28), the exothermic reaction between Al and Cr microparticles started in the slurry deposit. During this exothermic reaction, different Al-rich Al-Cr intermetallic compounds were formed at the interface between Cr and Al layers. After annealing for 5 hours at 650°C (Fig. III-29), the whole Al had reacted with the Cr microparticles to form these intermetallic phases (Fig. III-31). However, a layer of unreacted Cr microparticles was still observed above the nickel substrate. The p_{O_2} of the reaction chamber was sufficient to oxidize the surface of the Cr microparticles and the hollow alumina spheres.

In the presence of a Cr interlayer, the SHS reactions usually observed between the substrate and Al microparticles were thus completely supressed with this architecture. Increasing the temperature to 1000°C resulted in the formation of a diffusion zone of approximately 25µm of thickness (Fig. III-32) with the 50Cr-50Al system. The presence of undissolved Cr particles within the growing diffusion zone confirmed that the outward diffusion of nickel was governing the formation of the diffusion zone. The Al-Cr intermetallic phases were progressively dissolved and became richer in Cr with time (Fig. III-31 and Fig. III-32). In the ceramic top coat, the oxidation of the alumina shells was fostered at 1000°C and converted the transition aluminas into the stable α-Al_2O_3 phase [22,45].

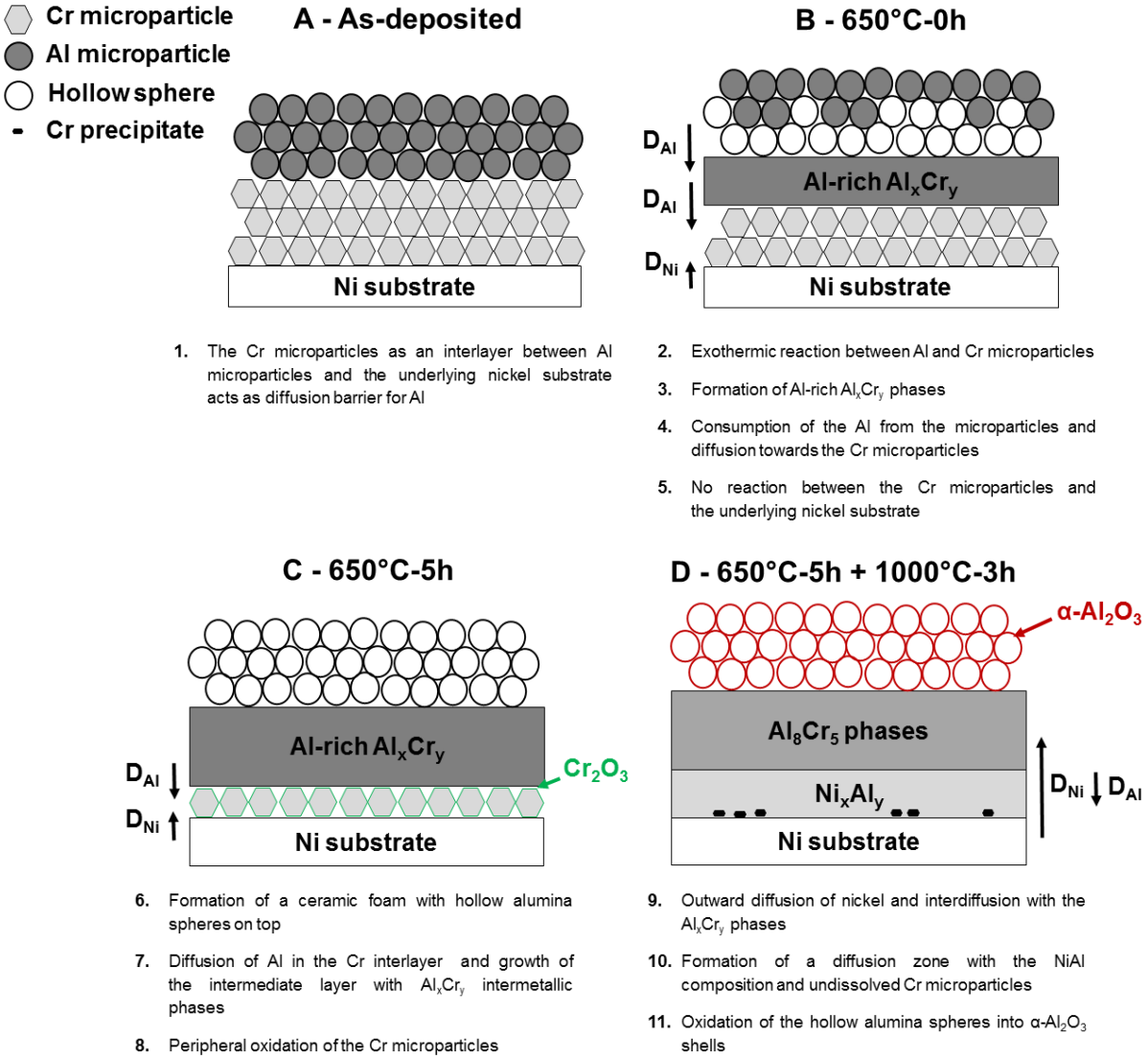

Fig. III-34. Sequence proposed for the mechanisms of formation of the Cr-Al double-layer system elaborated on pure nickel.

The Cr-Al double-layer system was found to successfully decrease the activity of Al on the surface of the substrate upon aluminizing. The diffusion of Al at low temperature (650°C) into the nickel substrate was hampered by the layer of Cr microparticles through the formation of Al-Cr intermetallic compounds in the slurry deposit. This architecture avoided the SHS reactions usually observed for high-activity slurry aluminizing of nickel substrates [1,4,5]. With the additional annealing at 1000°C for 3 hours, interdiffusion between the nickel substrate and the Al_xCr_y intermetallic phases synthesized in the slurry deposit was promoted. Therefore, a diffusion zone composed of the β-NiAl phase grew by outward diffusion of nickel.

- ***Conventional low-activity heat treatment (400°C-3h + 1080°C-6h):***

Pure nickel samples slurry coated with the Cr-Al double-layer system were also submitted to the conventional "low-activity" heat treatment employed in the repair industry before extrapolation to nickel-based superalloys. Two compositions were tested (50Cr-50Al and 67Cr-33Al) to characterize the microstructure and confirm the hypotheses of the outward growth of the coating.

For the 67Cr-33Al composition, a continuous β-NiAl layer was formed above the nickel substrate with a thickness of approximately 15-20µm (Fig. III-35a). The delamination between the nickel substrate and the β-NiAl layer suggested that the outward diffusion of nickel was more active than the inward diffusion of Al and of Cr. Indeed, nickel from the substrate diffused in the slurry deposit and reached 60 at.% Ni at the extreme surface of the diffusion zone (Fig. III-35c). Some α-Cr precipitates were highlighted by X-ray map in the β-NiAl phase because of the low solubility of Cr in the β-NiAl phase [36,37]. Above the β-NiAl layer, a Cr-rich layer was observed (more than 20 at.% Cr) and confirmed that the formation of Ni_xAl_y phases was thermodynamically more stable than the formation of Ni_xCr_y ones. For the 50Cr-50Al composition, the β-NiAl layer was thicker with a thickness of approximately 45-50µm (Fig. III-35b). The precipitation of α-Cr occurred in the outer region of the coating whereas Cr-rich phases remained above the diffusion zone (Fig. III-35d). In both microstructures, a γ'-Ni_3Al network was observed within the β-NiAl phase (Fig. III-35a and Fig. III-35b). This probably referred to the grain boundaries of the coatings. Formation of γ'-Ni_3Al within the grain boundaries would also confirm the hypothesis of predominant outward diffusion of nickel upon aluminizing.

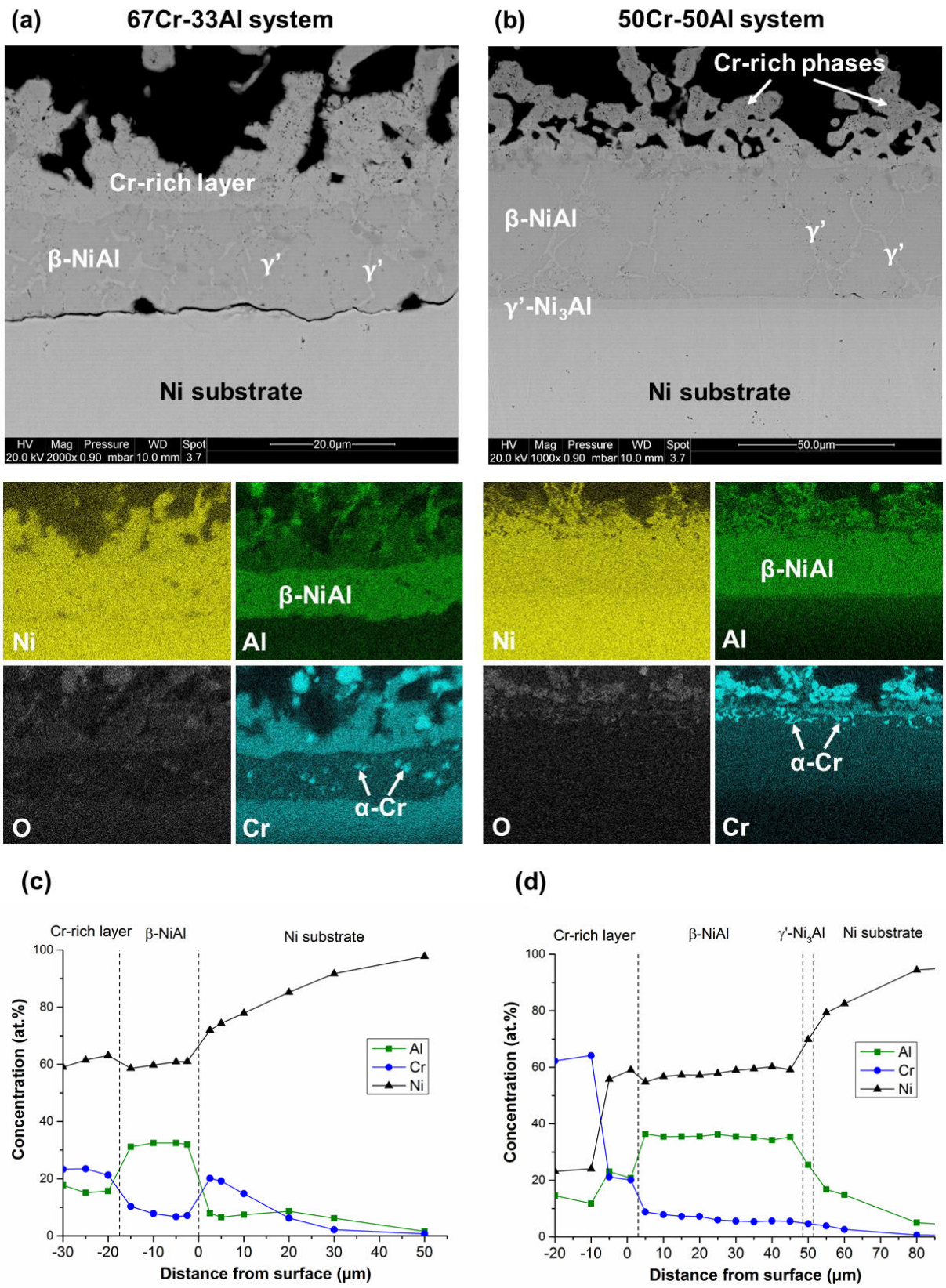

Fig. III-35. (a), (b) BSE cross-section images and X-ray maps for the Cr-Al double-layer systems elaborated on pure nickel and (c), (d) corresponding EDS concentration profiles after the conventional low-activity heat treatment in Ar.

VI. Summary and outlook

- ***Reactivity of Al and Cr powders:***

Different invariant reactions from the Al-Cr phase diagram were identified by investigating the reactivity between Al and Cr microparticles through DSC analyses. A strong exothermic reaction between Al and Cr was observed at a temperature lower than the Al melting point, and was attributed to the formation of Al_xCr_y intermetallic compounds. The formation of these Al_xCr_y phases was found to be fast, involving liquid phases and following self-propagating high-temperature synthesis (SHS) mechanisms. Depending on the initial Al-Cr ratio and the maximum temperature reached during the exothermic reaction, different Al_xCr_y intermetallic compounds were then synthesized. By mixing Al microparticles with Cr ones, it appeared thus possible to decrease the Al activity by forming these Al-Cr phases. In a second part, the reactivity of the metallic powders with a model substrate (pure nickel) was investigated. The addition of Cr in the slurry compositions was found to limit the SHS reactions usually observed between Al and the nickel substrate for high-activity slurry coatings.

- ***Influence of Cr addition upon aluminizing:***

Upon aluminizing, Al preferentially reacted with Cr in the slurry rather than with the pure nickel substrate, thereby limiting the SHS reactions between Al and Ni at low temperature (i.e. 650°C). Therefore, unlike simple Al slurry coatings, Al-rich nickel aluminides were barely formed on the nickel substrate at 650°C when using Al-Cr mixed slurries. Depending on the initial Al-Cr ratio of the slurry, the Al_xCr_y phases synthesized in the slurry deposit released the Al to grow a diffusion zone in the substrate after annealing at high temperature (i.e. 1000°C and 1080°C). At these temperatures, nickel could diffuse outwardly and react with the Al-Cr intermetallic phases formed above the substrate. The dissolution of Al-Cr phases by nickel resulted in the formation of the β-NiAl phase. A fraction of Cr was found to be in solid solution in β-NiAl whereas α-Cr precipitates were also observed in the microstructures. With pure nickel substrate, only the 67Al33Cr composition allowed to grow a continuous β-NiAl layer with the conventional repair "low-activity" heat treatment (400°C-3h + 1080°C-6h). Richer Cr contents in the Al-Cr mixtures impeded a homogeneous supply of Al to the nickel substrate.

- ***Mechanisms of formation of the functional coating designs:***

The addition of Cr in the slurry compositions was found to successfully decrease the activity of Al through the formation of Al_xCr_y phases above the substrate. Thanks to the flexibility of the slurry technique, different architectures of coatings were elaborated to elucidate the mechanisms of formation of the coatings on pure nickel. Two double-layer systems (Al-Cr and Cr-Al double-layer systems) were thus investigated by alternative deposition of Al and Cr microparticles. For the Al-Cr double-layer system, the Cr top layer was found to deplete the Al reservoir by forming Al_xCr_y intermetallics. As a result, the diffusion of Al towards the substrate was limited at 650°C and the formation of Al-rich Ni_xAl_y intermetallic phases (namely $NiAl_3$ and Ni_2Al_3) was considerably hampered on the substrate surface. The additional annealing at high temperature (i.e. 1000°C-3h) did not lead to further Al ingress in the diffusion zone since the layer of hollow alumina spheres acted as a barrier to diffusion. This layer, composed of thin alumina shells, was found to be brittle and not adherent to the underlying substrate.

For the Cr-Al double-layer system, the Cr interlayer acted as a diffusion barrier for Al. For the two Cr-Al ratios investigated (approximately 50Cr-50Al and 67Cr-33Al in wt.%), unreacted Cr microparticles were observed above the nickel substrate after 5 hours of annealing at 650°C. With this architecture, the SHS reactions between Al microparticles and the nickel substrate were thus completely suppressed. Heat treatment at high temperature (i.e. 1000°C or 1080°C) resulted in the formation of a continuous diffusion zone with mainly the β-NiAl composition. These results suggested that the coatings were formed by major outward diffusion of nickel from the substrate. The outward motion of nickel progressively dissolved the Al_xCr_y phases synthesized in the slurry deposit and foster the direct formation of Ni-rich β-NiAl. Since Cr has a low solubility in the β-NiAl phase, undissolved Cr was observed in the form of Cr-rich phases in the diffusion zone. The sequence of reaction can be described following equations *(Eq. III-3)* and *(Eq. III-4)*:

$$xAl + yCr \rightarrow Al_xCr_y \qquad \textbf{(Eq. III-3)}$$

$$Ni + Al_xCr_y \rightarrow \beta\text{-}NiAl + \alpha\text{-}(Cr) \qquad \textbf{(Eq. III-4)}$$

The initial Cr-Al ratio of the slurry deposit therefore played an important role on the composition and the homogeneity of the diffusion layers formed on nickel substrate. The conventional "low-activity" heat treatment (400°C-3h + 1080°C-6h) was particularly effective to form homogeneous diffusion layers with the desired microstructure. Therefore, this heat treatment was selected for the elaboration of Cr-Al slurry coatings on a Ni-Cr alloy and CM-247 LC superalloy (Chapter IV).

References

[1] M.C. Galetz, X. Montero, M. Mollard, M. Günthner, F. Pedraza, M. Schütze, *Intermetallics* ***44*** (2014), pp. 8-17.

[2] A.J. Rasmussen, A. Agüero, M. Gutierrez, M.J.L. Østergård, *Surface and Coatings Technology* ***202*** (2008), pp. 1479-1485.

[3] B. Rannou, B. Bouchaud, J. Balmain, G. Bonnet, F. Pedraza, *Oxidation of Metals* ***81*** (2014), pp. 139-149.

[4] B. Bouchaud, B. Rannou, F. Pedraza, *Materials Chemistry and Physics* ***143*** (2013), pp. 416-424.

[5] P. Zhu, J.C.M. Li, C.T. Liu, *Materials Science and Engineering A* ***329-331*** (2002), pp. 57-68.

[6] X. Montero, M.C. Galetz, M. Schütze, *Surface and Coatings Technology* ***222*** (2013), pp. 9-14.

[7] X. Montero, M.C. Galetz, M. Schütze, *Journal of Minerals, Metals and Materials Society* ***67*** (2014), pp. 79-86.

[8] B. Grégoire, G. Bonnet, F. Pedraza, *Intermetallics* ***81*** (2017), pp. 80-89.

[9] H. Okamoto, *Journal of Phase Equilibria and Diffusion* ***29*** (2008), pp. 112-113.

[10] J.G. Costa Neto, S. Gama, C.A. Ribeiro, *Journal of Alloys and Compounds* ***182*** (1992), pp. 271-280.

[11] M. Audier, M. Durand-Charre, E. Laclau, H. Klein, *Journal of Alloys and Compounds* ***220*** (1995), pp. 225-230.

[12] B. Grushko, B. Przepiórzyński, E. Kowalska-Strzeciwilk, M. Surowiec, *Journal of Alloys and Compounds* ***420*** (2006), pp. 51-54.

[13] K. Naplocha, K. Granat, *Journal of Alloys and Compounds* ***480*** (2009), pp. 369-375.

[14] C.L. Yeh, J.Z. Lin, *Intermetallics* ***33*** (2013), pp. 126-133.

[15] B. Grushko, E. Kowalska-Strzeciwilk, B. Przepiórzyński, M. Surowiec, *Journal of Alloys and Compounds* ***402*** (2005), pp. 98-104.

[16] Y. Liang, C. Guo, C. Li, Z. Du, *Journal of Alloys and Compounds* ***460*** (2008), pp. 314-319.

[17] H. Wu, M. Zhang, B. Xu, G. Ling, *Journal of Alloys and Compounds* ***610*** (2014), pp. 492-497.

[18] K.M. Chen, D.A. Tsai, H.C. Liao, I.G. Chen, *Journal of Alloys and Compounds* ***663*** (2016), pp. 52-59.

[19] A. Biswas, S.K. Roy, K.R. Gurumurthy, N. Prabhu, S. Banerjee, *Acta Materialia* ***50*** (2002), pp. 757-773.

[20] A. Biswas, S.K. Roy, *Acta Materialia* ***52*** (2004), pp. 257-270.

[21] J. Grüters, M.C. Galetz, *Intermetallics* ***60*** (2015), pp. 19-27.

[22] F. Pedraza, M. Mollard, B. Rannou, J. Balmain, B. Bouchaud, G. Bonnet, *Materials Chemistry and Physics* ***134*** (2012), pp. 700-705.

[23] D.R. Lide, CRC Handbook of Chemistry and Physics, 1995.Boca Raton, Section 12:159.

[24] K. Mahdouk, J.-C.Gachon, *Journal of Phase Equilibria* ***21*** (2000), pp. 157-166.

[25] B. Hu, W. Zhang, Y. Peng, Y. Du, S. Liu, Y. Zhang, *Thermochimica Acta* ***561*** (2013), pp. 77-90.

[26] Pang, Y. Zhan, Y. Du, *Journal of Solid State Chemistry* ***198*** (2013), pp. 344-356.

[27] D. Osso, O. Tillement, A. Mocellin, G. Le Caer, O. Babushkin, T. Lindbäck, *Journal of European Ceramic Society* ***15*** (1995), pp. 1207-1212.

[28] A.S. Bolokang, M.J. Phasha, *Advanced Powder Technology* ***22*** (2011), pp. 518-521.

[29] A. Urrutia, S. Tumminello, S.F. Aricó, S. Sommadossi, *Calphad* ***44*** (2014), pp. 108-113.

[30] B. Rannou, F. Velasco, S. Guzman, V. Kolarik, F. Pedraza, *Materials Chemistry and Physics* ***134*** (2012), pp. 360-365.

[31] R. Rajendran, *Engineering Failure Analysis* ***26*** (2012), pp. 355-369.

[32] M.J. Pomeroy, *Materials and Design* ***26*** (2005), pp. 223-231.

[33] J.M. Brossard, B. Panicaud, J. Balmain, G. Bonnet, *Acta Materialia* ***55*** (2007), pp. 6586-6595.

[34] S. Shankar, L.L. Seigle, *Metallurgical Transactions A* ***9*** (1978), pp. 1467-1476.

[35] J. Angenete, "Aluminide diffusion coatings for Ni based superalloys", PhD Thesis, Chalmers University of Technology, Göteborg University (2002).

[36] W.H. Tian, C.S. Han, M. Nemoto, *Intermetallics* ***7*** (1999), pp. 59-67.

[37] B. Grushko, W. Kowalski, D. Pavlyuchkov, B. Przepiórzyński, M. Surowiec, *Journal of Alloys and Compounds* ***460*** (2008), pp. 299-304.

[38] J.D. Cotton, R.D. Noebe, M.J. Kaufman, *Journal of Phase Equilibria* ***14*** (1993), pp.579-582.

[39] Q. Fan, H. Chai, Z. Jin, *Intermetallics* ***9*** (2001), pp. 609-619.

[40] B. Bouchaud, L. Douminge, F. Pedraza, *Defect and Diffusion Forum* ***289-292*** (2009), pp. 493-500.

[41] M. Kemdehoundja, J.F. Dinhut, J.L. Grosseau-Poussard, M. Jeannin, *Materials Science and Engineering A* ***435-436*** (2006), pp. 666-671.

[42] A.J. Lopez, M. Proy, V. Utrilla, E. Otero, J. Rams, *Materials and Design* ***59*** (2004), pp. 94-102.

[43] V. Kolarik, R. Roussel, M. Juez Lorenzo, H. Fietzek, *Materials at High Temperatures* ***29*** (2012), pp. 89-94.

[44] Y. Wang, G. Cacciamani, *Journal of Alloys and Compounds* ***688*** (2016), pp. 422-435.

[45] V. Kolarik, M. Juez-Lorenzo, H. Fietzek, *Materials Science Forum* ***696*** (2011), pp. 290-295.

[46] R. Roussel, *Investigación de recubrimientos multifuncionales en base de micropartículas esféricas de aluminio para aplicación a altas temperaturas,* PhD Thesis, Universidad Complutense de Madrid (2013).

[47] R. Roussel, V. Kolarik, M. Juez Lorenzo, H. Fietzek, *Oxidation of Metals* ***81*** (2014), pp. 179-189.

[48] G.W. Goward, *Current Research on the Surface Protection of Superalloys for Gas Turbine Engines*, *Journal of Metals* ***22*** (1970), pp. 31-39.

[49] G.W. Goward, D.H. Boone, *Oxidation of Metals* ***3*** (1971), pp.475-495.

Chapter IV – Slurry aluminizing of nickel-based alloys from Al and Cr microparticles

I. Slurry aluminizing of polycrystalline Ni20Cr 111

I.1. From Al microparticles 111

I.2. From Al-Cr mixed slurries 115

I.3. Functional design: Cr-Al double-layer system 119

II. Slurry aluminizing of the CM-247 LC nickel-based superalloy 123

II.1. Aluminizing from Al-Cr mixed slurries 123

II.2. Low-activity high-temperature (LAHT) coatings from the Cr-Al double-layer system 131

a) Low-activity conventional heat treatment (400°C-3h + 1080°C-6h) 131

b) Complete heat treatment (400°C-1h + 700°C-2h + 1100°C-2h) 135

c) Discussion 138

II.3. High-activity high-temperature (HAHT) coatings from the Cr-Al double-layer system 142

a) Low-activity conventional heat treatment (400°C-3h + 1080°C-6h) 142

b) Complete heat treatment (400°C-1h + 700°C-2h + 1100°C-2h) 145

c) Discussion 148

III. Summary and outlook 154

References 155

I. Slurry aluminizing of polycrystalline Ni20Cr

Nichrome (nickel with 20 wt.% Cr) was one of the first nickel-based alloys used for high-temperature applications and served as a basis for the development of more complex alloys [1-5]. The addition of Cr considerably increased the high-temperature corrosion resistance of nickel by forming through oxidation a protective chromia scale on the surface [2,4,6,7]. Although Ni-Cr alloys are not present in gas turbine engines anymore, they are still used for structural applications in the industry. Polycrystalline Ni20Cr (with 1.5 wt.% Si) was employed in this study as a model alloy to investigate the influence of Cr in the parent material upon aluminizing [8-10]. This study aimed at elucidating the coating formation and the beneficial influence of Cr addition in slurry compositions upon aluminizing of a Ni-Cr alloy before extrapolation to nickel-based superalloys.

I.1. From Al microparticles

As previously described, aluminizing of Cr-free and Cr-poor substrates from slurries containing Al microparticles occurs very quickly by wetting, dissolution of the parent material (e.g. Ni or Fe) and the resulting self-propagating synthesis and final state diffusion [11]. In contrast, the presence of Cr into the Ni20Cr (1.5 wt.% Si) substrate was found to considerably affect the mechanisms of formation of the diffusion zone from slurries containing Al microparticles [12]. After a complete heat treatment in flowing Ar (400°C-1h + 700°C-2h + 1100°C-2h), B. Rannou observed the partial detachment of the top coat and the formation of random diffusion islands from both dissolution of the substrate into the molten Al and solid-state diffusion of Al [12]. However, other random areas were completely free from diffusion. The island-like diffusion morphology was associated with the segregation of chromium at the interface between the aluminized layer and the substrate [12]. Cr has indeed a limited solubility in Al-rich Ni_xAl_y phases [13-16] and is also known to block Al diffusion [17]. In the case of Ni20Cr, the chromium aluminides formed upon aluminizing process even at low temperature (625°C) were responsible for such blockage [10]. Such Al-Cr intermetallic phases are a consequence of the fast inward diffusion of Al into the substrate promoting the formation of $NiAl_3$ and Ni_2Al_3 phases [11,18]. Since the solubility of Cr is low in these phases (i.e. about 2 at.% in Ni_2Al_3) [16,19], Cr is expelled out from the Ni_2Al_3 matrix and combines with further Al ingress to form Al_8Cr_5 grains [8,9,10,15]. The formation of α-(Cr) and Al_8Cr_5 grains at the interface between the aluminized layer and the substrate acted as a diffusion barrier for Al ingress. An additional consequence of the blockage is the appearance of Kirkendall porosity at the interface between the additive and the interdiffusion layers that arises from the major outward diffusion of Ni that is not compensated by the Al ingress as it is trapped by Cr.

In this study, Ni20Cr samples were aluminized from Al microparticles in flowing Ar with the same conditions than those of B. Rannou [12]. The optical surface micrographs and SEM cross-section images of the samples after diffusion heat treatment and complete heat treatment are given in Fig. IV-1. In Fig. IV-1a, the raw substrate was clearly identified (bright areas) together with the random distribution of diffusion spots (dark areas). In the cross-section (Fig. IV-1c), the island-like diffusion morphology reported by B. Rannou [12] was observed. After the complete heat treatment (Fig. IV-1d), the aluminized layer appeared heterogeneous and exhibited diffusion islands. In addition, the top coat was not adherent regardless of the annealing treatment.

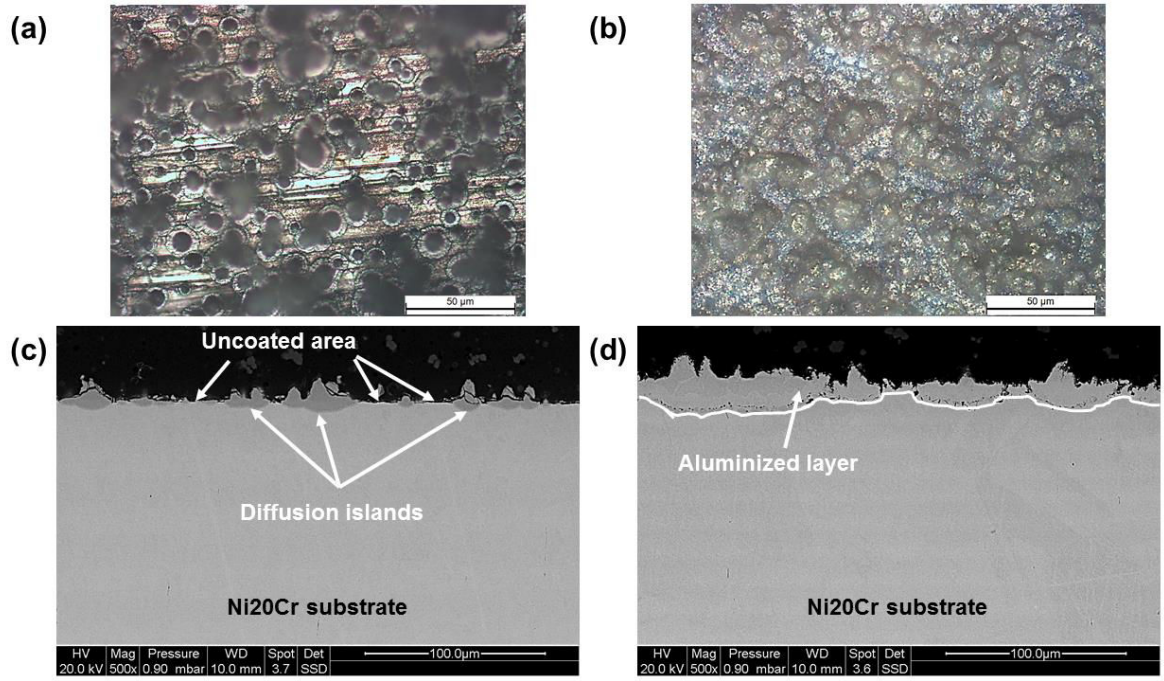

Fig. IV-1. Optical surface micrographs and SEM cross-section images (BSE mode) for Ni20Cr aluminized with Al microparticles after (a), (c) the diffusion heat treatment (400°C-1h + 700°C-2h) and (b), (d) the complete heat treatment (400°C-1h + 700°C-2h + 1100°C-2h) in flowing Ar.

At higher magnification, the elongated morphology of the diffusion islands (Fig. IV-2a) suggests that Cr acted as a barrier of diffusion preventing further Al ingress into the substrate. However, after the complete heat treatment, the aluminized layer was discontinuous and Cr-rich phases precipitated at the interface of the coating with the substrate (Fig. IV-2b). The composition of these phases was in the α-(Cr) domain [19] according to EDS spot measurements (approximately 3 at.% Al, 76 at.% Cr and 21 at.% Ni). The Cr concentration of β-NiAl and γ'-Ni_3Al phases of the aluminized layer did not exceed 5 at.%.

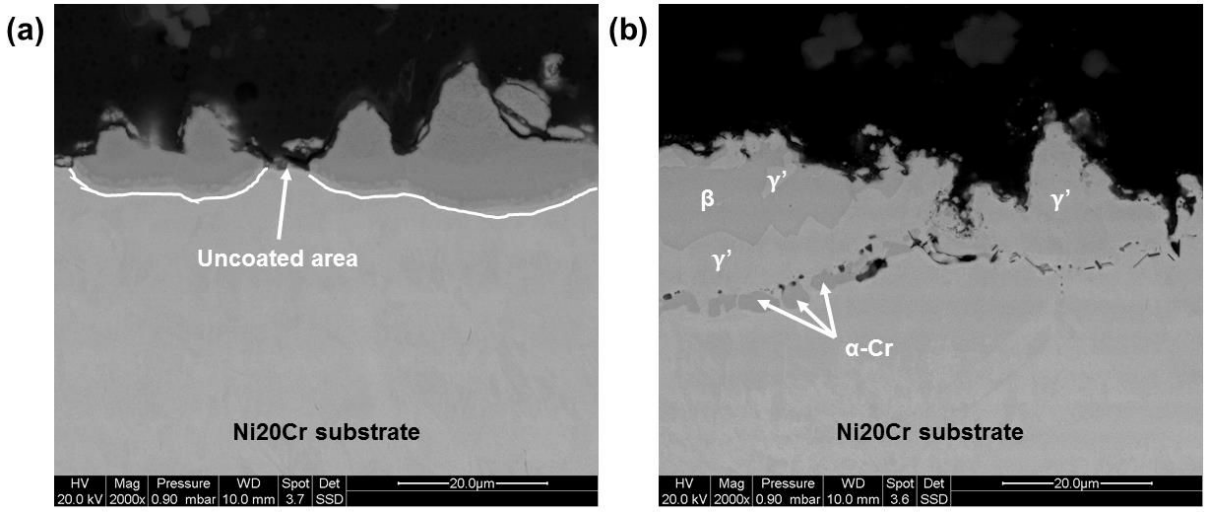

Fig. IV-2. BSE cross-section images of Ni20Cr substrate slurry coated with Al after (a) the diffusion heat treatment (400°C-1h + 700°C-2h) and (b) the complete heat treatment (400°C-1h + 700°C-2h + 1100°C-2h).

In the work of Le Guevel et al., polycrystalline Ni20Cr (1.5 wt.% Si) was aluminized by out-of-pack process (APVS, Snecma process) at 1080°C for 6 hours [20]. This low-activity high-temperature (LAHT) process fostered the formation of an outward grown coating based on the β-NiAl phase [21,22]. The coating thickness was even with an outer β-NiAl matrix free of Cr-containing precipitates [20,23]. Chromium was mainly located at the inner interdiffusion zone in the form of elongated precipitates [10]. Brossard et al. elaborated thin aluminide coatings on Ni20Cr (1.5 wt.% Si) by first depositing an Al film by using DC cathodic magnetron sputtering technique [7]. The initial deposition of approximately 3 µm Al films resulted in the formation of a Ni_2Al_3 matrix after annealing at 600°C for 1 hour. Further annealing at 900°C brought about the stabilization of β-NiAl whereas both β-NiAl and γ'-Ni_3Al phases were observed after annealing at 1100°C [7]. Tu et al. successfully aluminized several arc-melted Ni-Cr alloys by pack cementation process [8]. The Ni-Cr alloys containing between 5 at.% Cr and 35 at.% Cr were aluminized between 800 and 1150°C using AlF_3 activator. The pack composition was adjusted to modify the Al activity upon aluminizing using pure Al microparticles or pre-alloyed Al and Ni powders [8]. Depending on the pack composition and the aluminizing treatment (dwell time and temperature), different microstructures were obtained for the coatings. For these processes, the coatings were homogeneous in thickness and did not exhibit island-like diffusion morphology as observed by Rannou [12] and in the present study (Fig. IV-2).

Out-of-pack and pack cementation processes involved the deposition of Al on the substrate from a gaseous phase [24]. Even though a solid Al film was deposited on Ni20Cr in the work of Brossard et al. [7], the diffusion heat treatment was realized at a temperature lower (600°C) than the melting temperature of Al (i.e. 660°C [25]). Therefore, the coating formation involved only solid-state diffusion. Unlike these processes, the coating formation on a nickel-based material slurry coated with Al microparticles involved self-propagating high-temperature synthesis reactions [11,18]. These high exothermal reactions typical of high Al activity slurry aluminizing, were attributed to provoke the island-like diffusion morphology observed by B. Rannou [12] and in this study. The formation of liquid phases upon high Al activity aluminizing led to the dissolution of the Ni20Cr substrate and fostered the precipitation of Cr at the reaction front between the aluminized layer and the substrate that impeded homogeneous diffusion. This brought us about the idea of limiting the exothermal reactions occurring between the Al microparticles and the Ni20Cr substrate by adding Cr to the slurry composition [26].

I.2. From Al-Cr mixed slurries

The aluminizing of pure nickel substrate with Al-Cr mixed slurries using a typical low-activity heat treatment employed in the repair industry (annealing at 1080°C for 6 hours [20,27]) fostered the formation of the β-NiAl phase by interdiffusion between nickel and Al_xCr_y intermetallic compounds (cf. paragraph IV.2. in Chapter III). Therefore, the same heat treatment was carried out to elaborate the Al-Cr mixed slurry coatings on Ni20Cr substrate. The cross-section micrographs of the aluminized layers for the three Al-Cr mixtures (67Al33Cr, 44Al56Cr and 20Al80Cr in wt.%) are shown in Fig. IV-3. For the three compositions, the reaction front between the aluminized layers and the underlying substrate was quite even. These observations suggest that the addition of Cr to the Al microparticles was highly beneficial for the slurry aluminizing of Ni20Cr substrate. As observed with pure nickel, the higher the Al concentration in the initial mixture, the thicker the diffusion layer after annealing. For the three compositions, the top coat was composed of intermetallic phases and oxides and remained adherent on the surface (Fig. IV-3).

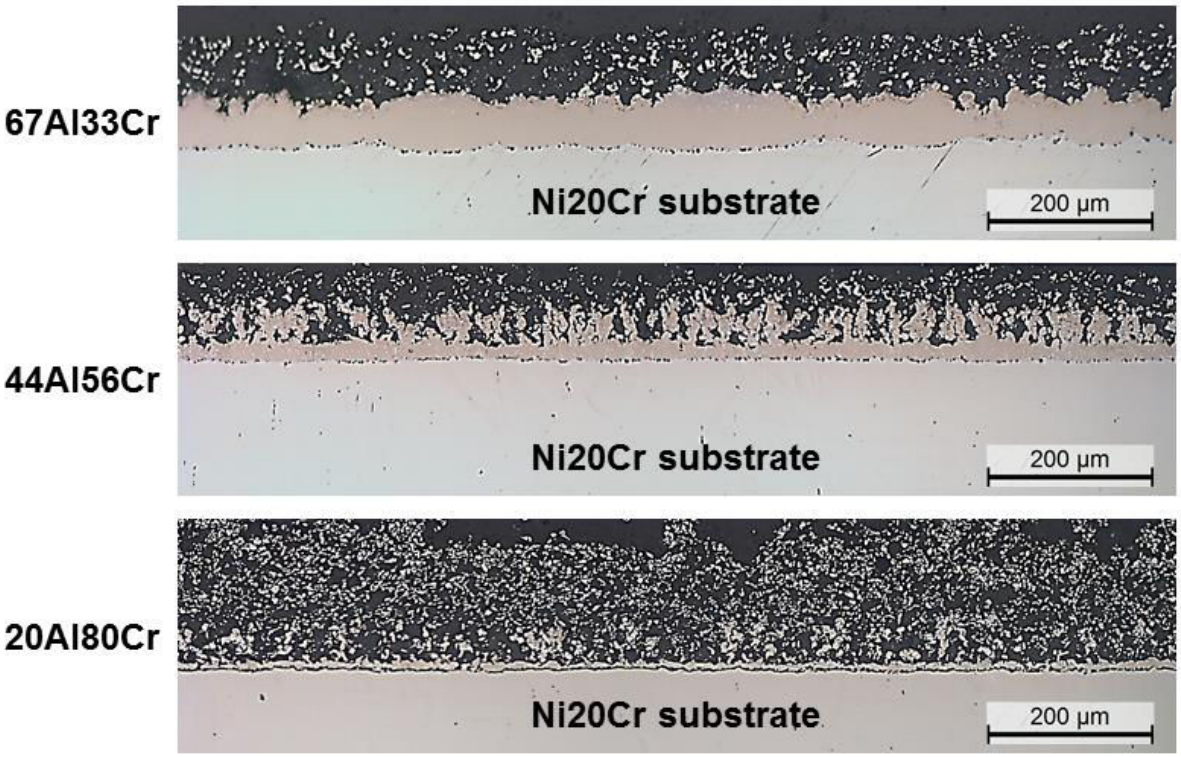

Fig. IV-3. Optical cross-section micrographs (low magnification) of Ni20Cr substrate slurry coated with Al-Cr mixtures after annealing in flowing Ar (400°C-3h + 1080°C-6h).

The diffusion layers were based on the β-NiAl phase for the three compositions (Fig. IV-4) and the thickness of the continuous aluminized layer reached about 50µm, 20µm and 10µm for respectively; the 67Al33Cr, 44Al56Cr and 20Al80Cr slurry mixtures. Some voids were present at the interface between the aluminized layer and the underlying substrate (Fig. IV-4a and b). These voids resulted from counter-current vacancy flow to the motion of Ni, Cr and Al [28] and strongly suggested that the

outward diffusion of Ni was faster than the inward diffusion of Al upon aluminizing. A lateral decohesion of the coating layers seemed to occur by coalescence of these voids when using the richest Cr composition (20Al80Cr) (Fig. IV-4c). Some Cr-rich precipitates (identified as α-Cr) were found in the β-NiAl matrix because of the low solubility of Cr in β-NiAl [9,13].

For a better comprehension of the mechanisms of formation of the coatings, X-ray maps were performed on representative areas to get the elemental distribution after annealing (Fig. IV-5). For both 44Al56Cr (Fig. IV-5a) and 20Al80Cr (Fig. IV-5b) slurry mixtures, a nickel-depleted area was clearly identified at the interface between the aluminized layer and the substrate, where the voids are observed. A Cr enrichment was also observed in the nickel-depleted area and suggested that the outward diffusion of Ni was faster than that of Cr at 1080°C [28]. As a result, the outward diffusion of nickel was clearly observed above the continuous aluminized layer.

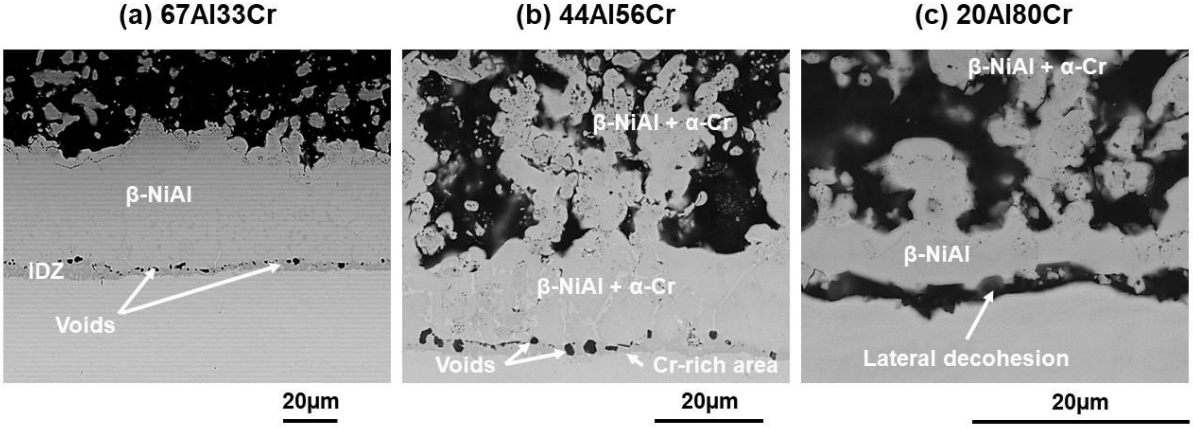

Fig. IV-4. SEM cross-section images of Ni20Cr substrate slurry coated with different Al-Cr mixtures after annealing in flowing Ar (400°C-3h + 1080°C-6h).

The EDS concentration profiles of the cross-section of Ni20Cr substrate slurry coated with the 44Al56Cr and the 20Al80Cr compositions are given in Fig. IV-6a and Fig. IV-6b. Note that the interface between the substrate and the coating was taken as the origin to perform the EDS spot analyses. As observed with the pure nickel substrate, nickel dissolved the Al-Cr intermetallic phases resulting in the direct formation of the β-NiAl phase (Fig. IV-6). Nickel indeed presents a low solubility in Al_4Cr and Al_8Cr_5 (respectively about 1 at.% and 3 at.% [16]). In addition, since the solubility of Cr in the β-NiAl is lower than 8 at.% at 1080°C [2,13], undissolved Cr was trapped in the β-NiAl matrix. According to the X-ray maps (Fig. IV-5), nickel diffused up to 55µm and 45µm from the substrate surface, in the 44Al56Cr and in the 20Al80Cr deposits, respectively. For both systems, the outermost region of the slurry deposit did not react with nickel and was still composed of Al_xCr_y phases together with α-(Cr) solid solution (Fig. IV-6). Oxygen was found to be mainly associated with Cr and Al, in relation with the higher affinity of these two elements for oxygen than that of nickel.

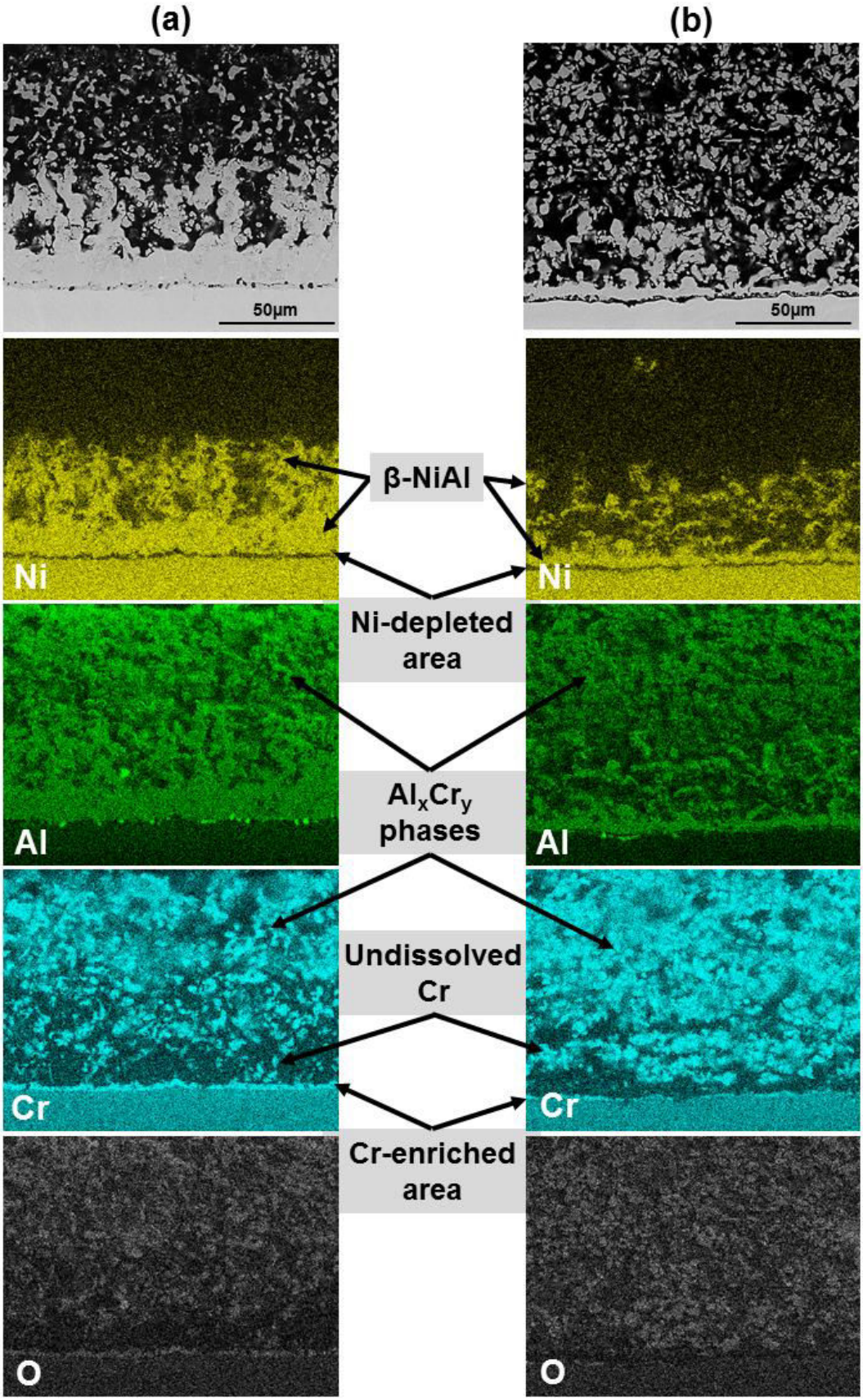

Fig. IV-5. SEM cross-section images and corresponding elemental distribution by X-ray mapping of Ni20Cr slurry coated with (a) 44Al56Cr and (b) 20Al80Cr composition.

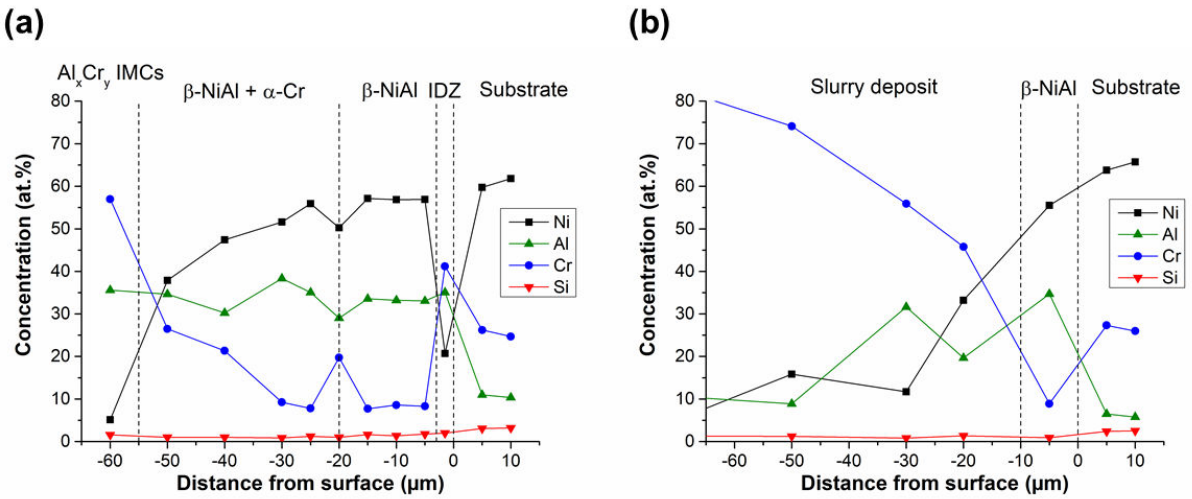

Fig. IV-6. EDS concentration profiles for Ni20Cr substrate slurry coated with (a) 44Al56Cr and (b) 20Al80Cr mixtures after annealing (400°C-3h + 1080°C-6h).

Therefore, the addition of Cr in the slurry composition was found to successfully decrease the Al activity on the substrate surface upon aluminizing and to promote the growth of the coating by predominant outward diffusion of nickel [8]. The highly exothermic reactions occurring between the Al microparticles and the nickel-based substrate were limited by the formation of Al_xCr_y in the slurry deposit at low temperature (around 640°C) [26]. However, the subsequent increase of temperature at 1080°C for 6 hours fostered the direct formation of the β-NiAl phase and resulted in homogeneous diffusion layers. For the 44Al56Cr and 20Al80Cr mixtures, the Al content of the slurry deposit was too low to grow a diffusion layer as obtained by conventional low-activity CVD process [20,23]. The threshold to obtain suitable low-activity coatings on Ni20Cr substrate was therefore ranging from 67Al33Cr to 44Al56Cr composition (mixtures between 80 at.% Al and 60 at.% Al). These Al concentrations were higher than the threshold considered with pack cementation process where the outward diffusion of nickel predominates for packs with less than 50 at.% Al [8]. This difference might be explained by the absence of gas phases in the study with respect of the CVD reactions ruling pack cementation, out-of-pack and CVD itself [29].

I.3. Functional design: Cr-Al double-layer system

Since the Cr-Al double-layer architecture was found to form functional coatings on pure nickel (cf. paragraph V.3. in Chapter III), this system was also conducted on Ni20Cr substrate. The initial Al/Cr ratio of the slurry deposit was adjusted between 67Al33Cr and 44Al56Cr composition to obtain outwardly grown coatings. A SEM cross-section image of a Cr-Al double-layer system elaborated on Ni20Cr substrate is given on Fig. IV-7a. Before heat treatment, two successive layers of approximately 9.0 mg.cm^{-2} of Cr and 11.0 mg.cm^{-2} of Al were deposited on the substrate (cf. Fig. II-6 in Chapter II). The initial Al/Cr ratio was therefore about 55/45 in wt.%.

After annealing (Fig. IV-7a), the microstructure of the coating was very close to the one obtained by conventional low-activity CVD process on the same substrate [20,23]. Three distinct layers were identified in the BSE mode of the SEM and by EDS spot measurements (Fig. IV-7b). An outer Al-rich β-NiAl layer of approximately 8-10µm thickness, an intermediate β-NiAl layer with a thickness of 35±2µm and an interdiffusion zone (IDZ) formed within the substrate with a thickness of 6-8µm. The Cr-rich phases above the coating resulted from interdiffusion between nickel from the substrate and the Al_xCr_y intermetallic phases initially synthesized on the substrate surface. Although the XRD surface analyses of the sample were not carried out to identify the crystal structure(s) of these phases, the EDS spot measurements in the cross-section revealed a composition (27Al-1Si-64Cr-7Ni in at.%) alike to a three-phase range (Cr)-β-γ_2 when considering a temperature of 1080°C [16]. The γ_2 phase is the low-temperature phase of the Al_8Cr_5 compound [16,30]. Since a slow cooling ramp was used for the heat treatment (5°C/min), the congruent transformation (Cr) → $AlCr_2$ occurred at about 910°C upon cooling [31]. Indeed, Huang et al. found that $AlCr_2$ can precipitate in both α-(Cr) and β-NiAl phases upon cooling [10,15].

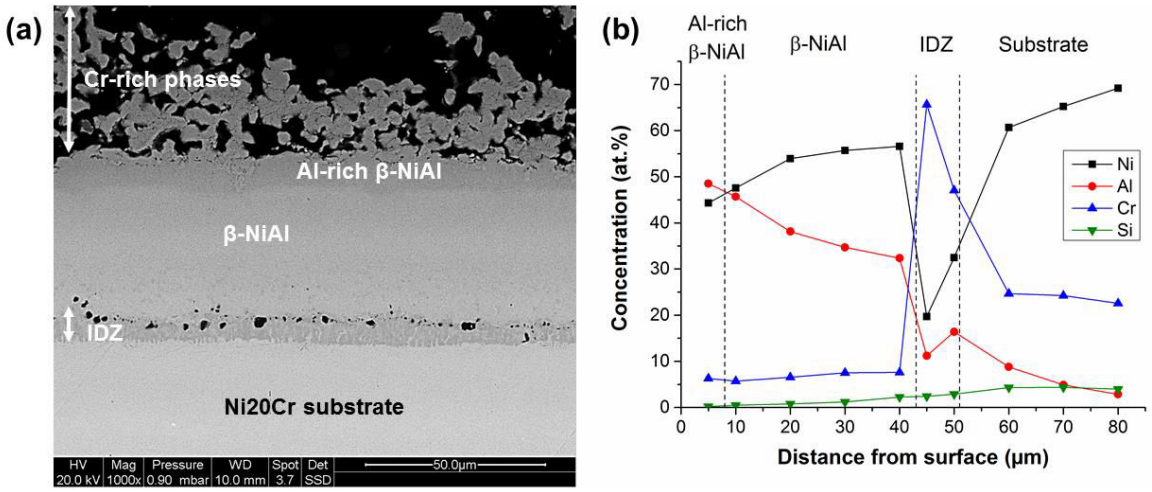

Fig. IV-7. (a) SEM cross-section image and (b) EDS concentration profile for the 45Cr-55Al double-layer system elaborated on Ni20Cr after annealing in Ar (400°C-3h + 1080°C-6h).

Elemental X-ray maps of the cross-section were performed to depict the elemental distribution of nickel, chromium, aluminium and oxygen (Fig. IV-8). The interdiffusion zone (IDZ) was easily identified by both the depletion of nickel and the enrichment in chromium. Some Al-rich spots were observed just above the IDZ (Fig. IV-8b). These areas did not coincide with oxygen nor silicon distribution and therefore could not be attributed to the formation of alumina or Al_xSi_y phases. Probably, such Al-rich precipitates can be associated with carbides but the whole surface is contaminated with C and we cannot confirm this hypothesis. Alternatively, they can correspond to oxidized Al microparticles but the resolution of the X-ray map of O does not allow to depict the periphery. Unlike the X-ray maps obtained for Al-Cr mixed slurries in Fig. IV-5, the ones of Ni and Al in Fig. IV-8 with the Cr-Al double-layer attested the formation of an even β-NiAl layer of about 45µm thickness.

If a small quantity of Cr was found to be dissolved in the β-NiAl coating matrix, fine Cr-rich precipitates were detected right above the IDZ (Fig. IV-8c). Similar precipitates were also observed with a conventional low-activity process on Ni20Cr [23]. Some Cr was found to be trapped in the outer Al-rich β-NiAl phase. The large particles observed suggested that these Cr enrichments were not caused by precipitation [10,13,15] but because of the entrapment of Cr-rich phases from the slurry deposit upon aluminizing. Gleeson et al. and Streiff and collab. also observed this phenomenon in outwardly grown coatings, where alumina pack inclusions were trapped in the additive layer [32,33]. The distribution of Cr in the coating was different from the one observed by Huang et al. on Ni15Cr alloy aluminized by high Al activity pack [10]. This suggested that the coating presented in Fig. IV-8 was formed by predominant outward diffusion of nickel at high temperature (i.e. 1080°C). The oxygen enrichment in the IDZ (Fig. IV-8d) may result from the interferences between the emitted photons $O^{K\alpha}$ and $Cr^{L\alpha}$.

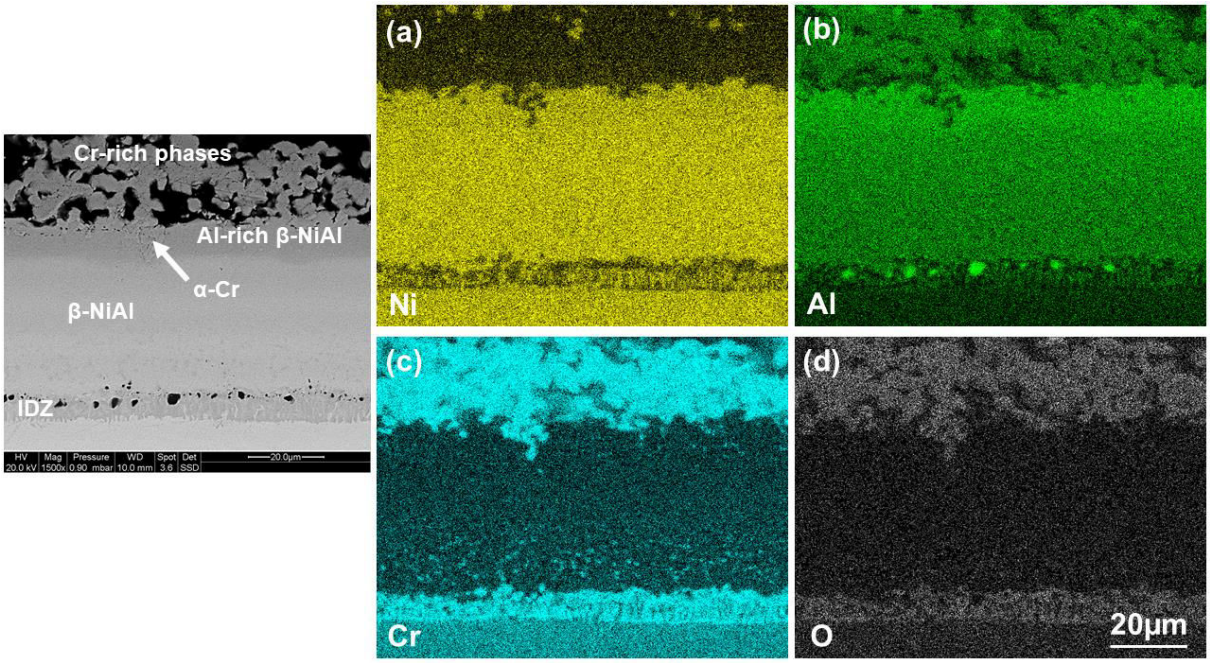

Fig. IV-8. BSE cross-section image and corresponding EDS maps of (a) Ni, (b) Al, (c) Cr and (d) O. The map of Si is not presented since this element did not segregate in the coating.

Fig. IV-9a shows a low magnification BSE image of a corner after elaboration of the Cr-Al double-layer system. The frontline between the aluminized layer and the underlying substrate was quite even on all areas. This indicates that the slurry covers very well the whole sample surface and demonstrates the beneficial effect of the Cr interlayer on the slurry aluminizing of Ni20Cr substrate. Further investigation of the IDZ developed upon aluminizing was done after electrolytic etching of the sample cross-section with oxalic acid (Fig. IV-9b). The microstructure of the Ni20Cr substrate revealed a duplex γ-γ' microstructure with the precipitation of cube-like γ'-Ni_3Al in the γ-(Ni) matrix [10]. Precipitation of γ'-Ni_3Al within the γ-(Ni) matrix was confined below the IDZ and presumably resulted from the Al enrichment of the substrate surface (Fig. IV-7b). In this study, the microstructure of the IDZ was close to the one obtained by Huang et al. after pack aluminizing of a Ni15Cr alloy [10]. The IDZ was composed of alternating β-NiAl and α-(Cr) grains elongated in the Al diffusion direction [10,28]. These authors also observed the precipitation of fine $AlCr_2$ in β-NiAl and α-(Cr) phases by TEM [10,15]. In order to confirm Huang's observations, EDS spot measurements were realized on several areas to identify the phases (cf. Table IV-1). Coarse α-(Cr) precipitates were identified at the interface between β-NiAl coating matrix and the IDZ (EDS spots in zone 1 and zone 2 with a darker contrast).

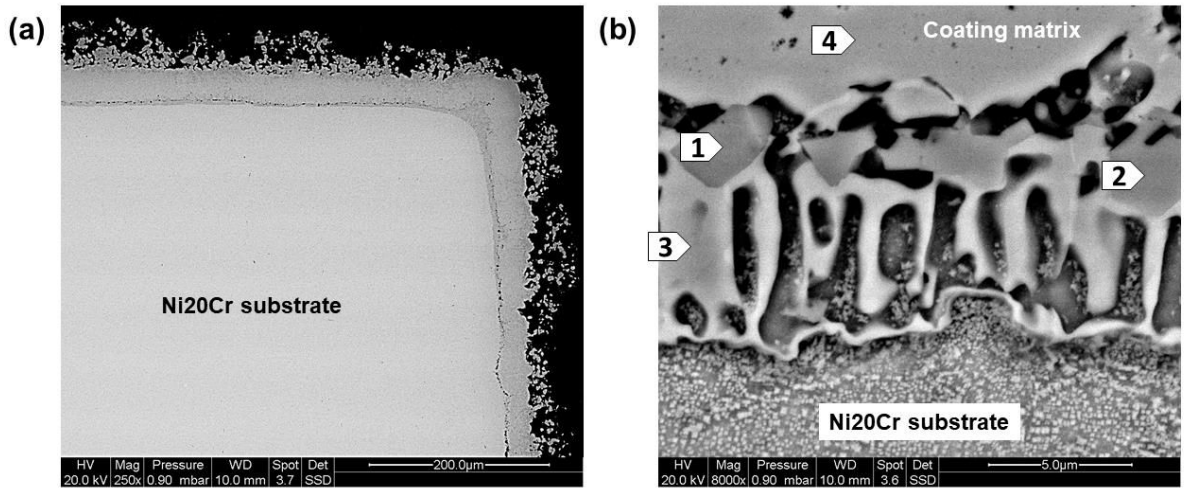

Fig. IV-9. (a) Low magnification BSE image of a corner and (b) details of the interdiffusion zone (electrolytically etched with 10 vol.% $H_2C_2O_4$) after elaboration of the 45Cr-55Al double-layer system on Ni20Cr substrate.

Table IV-1. Summary of the EDS spot measurements (Fig. IV-9b) and suggested phases.

EDS spot location	EDS spot measurements				Possible phase(s)
	Al (at.%)	Si (at.%)	Cr (at.%)	Ni (at.%)	
1	9.0	0.9	70.0	20.1	α-(Cr)
2	6.0	1.1	71.6	21.3	α-(Cr)
3	17.3	2.2	49.7	30.8	β-NiAl + α-(Cr)
4	32.6	1.9	7.2	58.3	β-NiAl

The Ni20Cr substrate with the Cr-Al double-layer system was also submitted to the complete heat treatment (400°C-1h + 700°C-2h + 1100°C-2h) for comparison with the simple aluminide coating (Fig. IV-1 and Fig. IV-2). The initial thicknesses of the Cr and Al layers were adjusted to obtain two different Cr/Al ratios (50Cr-50Al and 40Cr-60Al in wt.%). The surface and cross-section micrographs of the annealed samples are presented on Fig. IV-10. For both samples, the top coat structure made of hollow alumina spheres remained adherent after annealing (Fig. IV-10a and Fig. IV-10b). The aluminized layers were homogeneous in thickness (Fig. IV-10c and Fig. IV-10d) and the island-like diffusion morphology (Fig. IV-1d) was not observed this time. Both aluminized layers were divided in three distinct layers: an outer Al-rich β-NiAl layer, an intermediate β-NiAl layer and an IDZ rich in precipitates. After aluminizing, the Cr-rich phases remained at the surface of the coating. Some of them were trapped in the outer Al-rich β-NiAl layer because of the limited solubility of Cr in it [13]. The overall microstructure of the diffusion coatings was similar between the 50Cr-50Al (Fig. IV-10c) and 40Cr-60Al (Fig. IV-10d) double-layer systems. However, the Al-rich β-NiAl layer was thicker for the 40Cr-60Al composition than the 50Cr-50Al one. These observations confirmed that the initial composition of the slurry deposit exerts a direct impact on the final microstructure of the coating. It is therefore of the utmost importance to control the Cr-Al ratio to obtain the desired coating design.

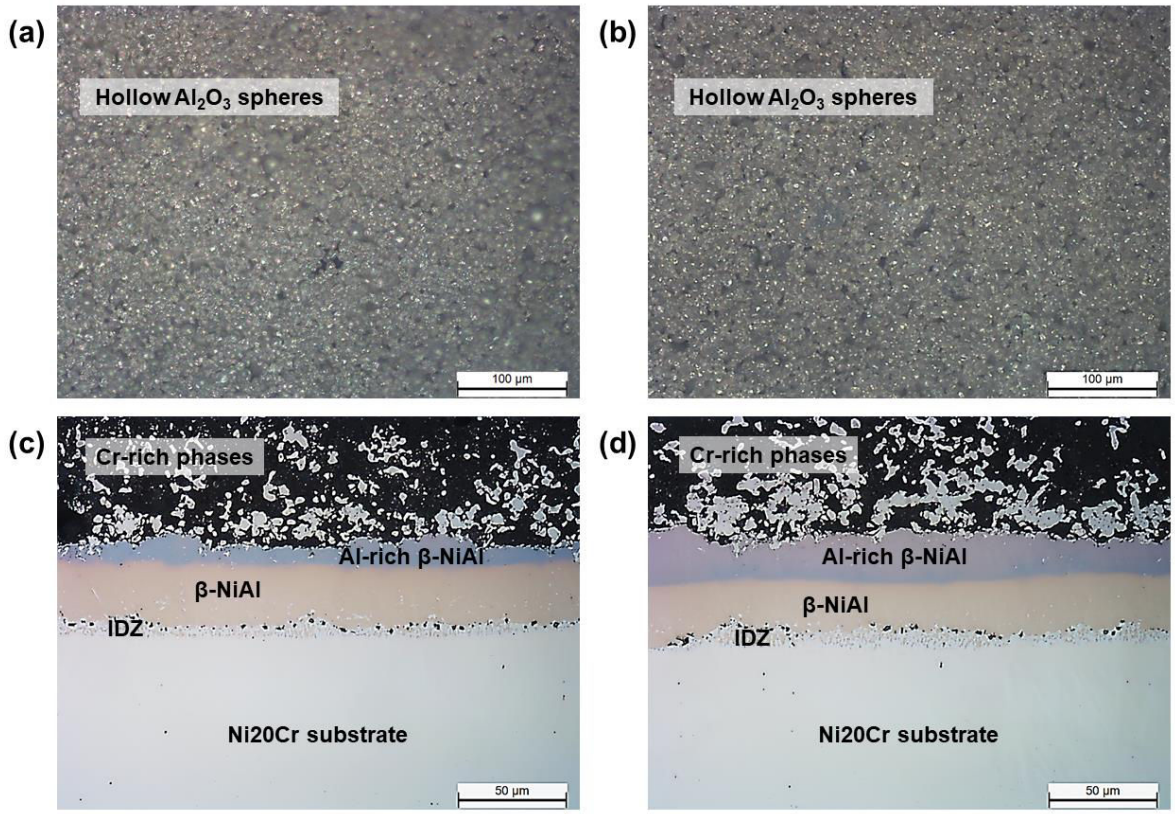

Fig. IV-10. Micrographs of the Cr-Al double-layer system elaborated on Ni20Cr substrate after complete heat treatment (400°C-1h + 700°C-2h + 1100°C-2h) with (a), (c) 50Cr-50Al (wt.%) and (b), (d) 40Cr-60Al (wt.%) initial compositions.

II. Slurry aluminizing of the CM-247 LC nickel-based superalloy

II.1. Aluminizing from Al-Cr mixed slurries

Based on the aluminizing of model materials (pure nickel and Ni20Cr alloy), the CM-247 LC was used to investigate the influence of Cr upon aluminizing of an industrial alloy. As discussed in paragraph I of Chapter II, the directionally solidified CM-247 LC superalloy displays a duplex γ-γ' microstructure [34-36]. Aluminizing of CM-247 LC was realized on as-received samples without either solutionizing or ageing treatments, which are required for mechanical testing like creep [36] or tensile tests [34,35] but not for coating manufacture [37-39]. Some carbides were originally present in the interdendritic regions of the superalloy (cf. Fig. II-2a). These inert carbides were particularly helpful to investigate the mechanisms of formation of the diffusion coatings as they acted as natural markers to determine the initial substrate surface location before aluminizing [40,41]. The aluminizing of CM-247 LC from high Al activity slurries has already been reported in Refs. [12,11,39,42].

The three Al-Cr mixed slurries selected in this study (67Al33Cr, 44Al56Cr and 20Al80Cr in wt.%) were deposited on the CM-247 LC superalloy. The resulting coatings produced after aluminizing treatment in flowing Ar (400°C-3h + 1080°C-6h) are presented in Fig. IV-11.

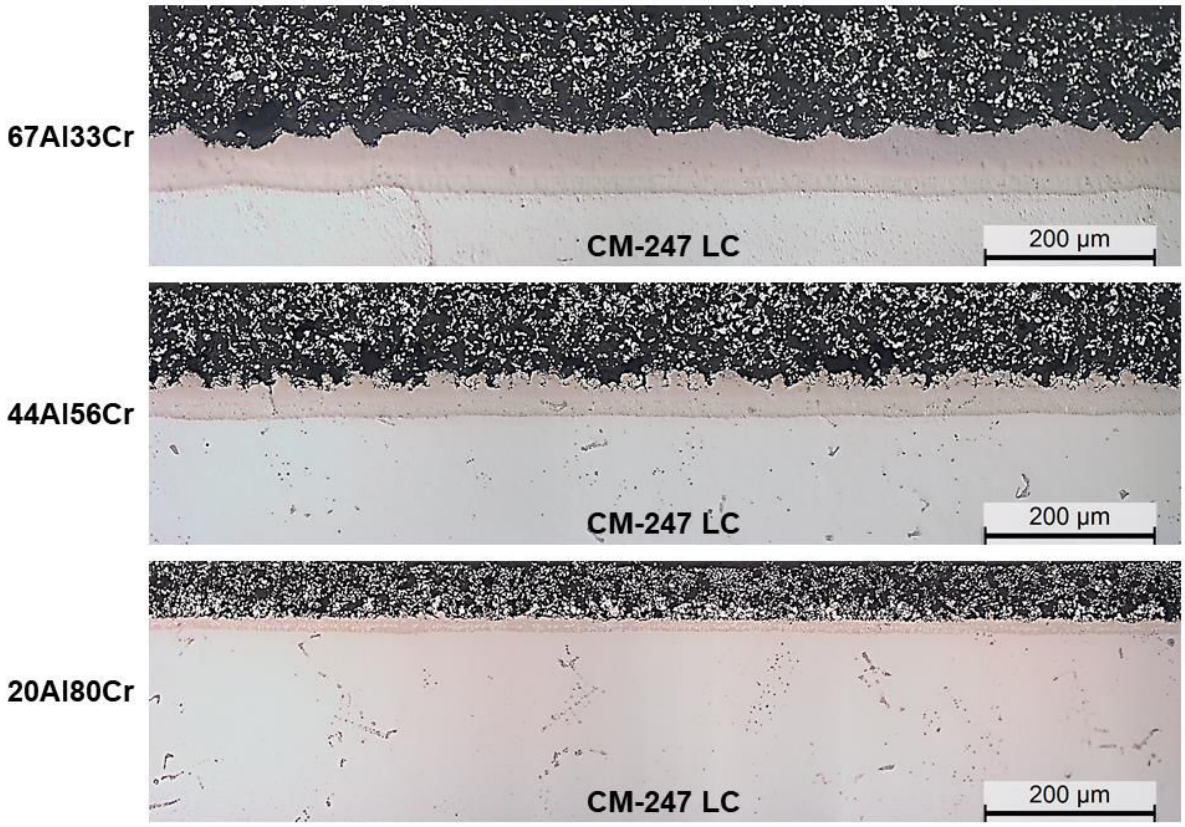

Fig. IV-11. Optical cross-section micrographs (low magnification) of CM-247 LC superalloy slurry coated with Al-Cr mixtures after annealing in flowing Ar (400°C-3h + 1080°C-6h).

For the three Al-Cr slurry mixtures, the entire samples were successfully coated attesting the very good coverage of the surface after slurry deposition. The top coat structure, composed of Al_xCr_y intermetallic phases and other Cr-rich phases resulting from the aluminizing process, was adherent to the diffusion zone after annealing (Fig. IV-11). In addition, the thickness of the coatings appeared quite homogeneous all around the contour of the samples according to the cumulative probability plots of Fig. IV-12. As observed with the Ni20Cr substrate (Fig. IV-3), the thickness of the diffusion zone after annealing increased with increasing the Al content of the slurry mixture.

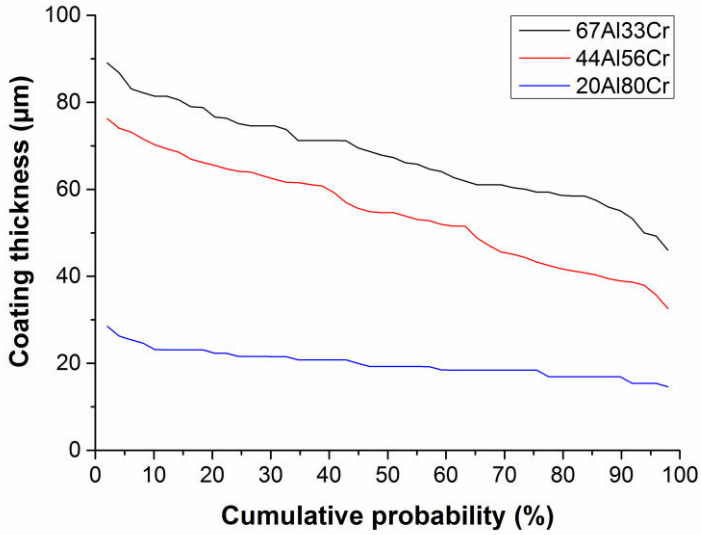

Fig. IV-12. Coating thickness measurements (diffusion zone) after annealing of the three Al-Cr mixed slurries on CM-247 LC superalloy.

The surfaces of the three CM-247 LC samples were analysed by XRD to identify the formed crystal structures (Fig. IV-13). They were compared with EDS spot measurements to propose the possible corresponding phases. Note that only the Al, Cr, Ni and O contents were quantified by EDS in the top coat structure since the concentrations of the remaining elements (Ti, Co, Ta and W) fell below the uncertainty limit of the EDS analyses.

For the 44Al56Cr slurry mixture, the tetragonal $AlCr_2$ phase [15,31] was clearly identified together with low reflections of α-Al_2O_3 structure. This phase was probably formed during the slow cooling ramp (5°C/min) following the (Cr) → $AlCr_2$ invariant reaction around 910°C [31]. For the 20Al80Cr one, three broad peaks were observed at 2θ positions typical of a cubic structure and the EDS analyses revealed average compositions of 24Al-75Cr-1Ni in at.%. This suggests that the cubic structure probably refers to (Cr) containing dissolved Al and Ni, which is consistent with different reports whereby Cr dissolves about 25 at.% of Al between 0 and 1000°C [31,43] and even up to 43 at.% at 1000°C [16,43]. The incorporation of Al and Ni in the Cr lattice modified its parameters which could

thus explain the broad diffraction peaks (Fig. IV-13). An additional structure was identified and probably referred to the $AlCr_2$ phase by correlation with EDS spot measurements (32Al-67Cr-1Ni in at.%). For the 67Al33Cr slurry composition, α-(Cr) and $AlCr_2$ crystal structures were also identified. The characteristic diffraction peaks of α-Al_2O_3 clearly appeared and this oxide probably resulted from the peripheral oxidation of the Al-containing phases or from the Al microspheres oxide shells of the top coat structure [12,44]. Additional peaks were also revealed by XRD for the 67Al33Cr composition and were attributed to the β-NiAl phase.

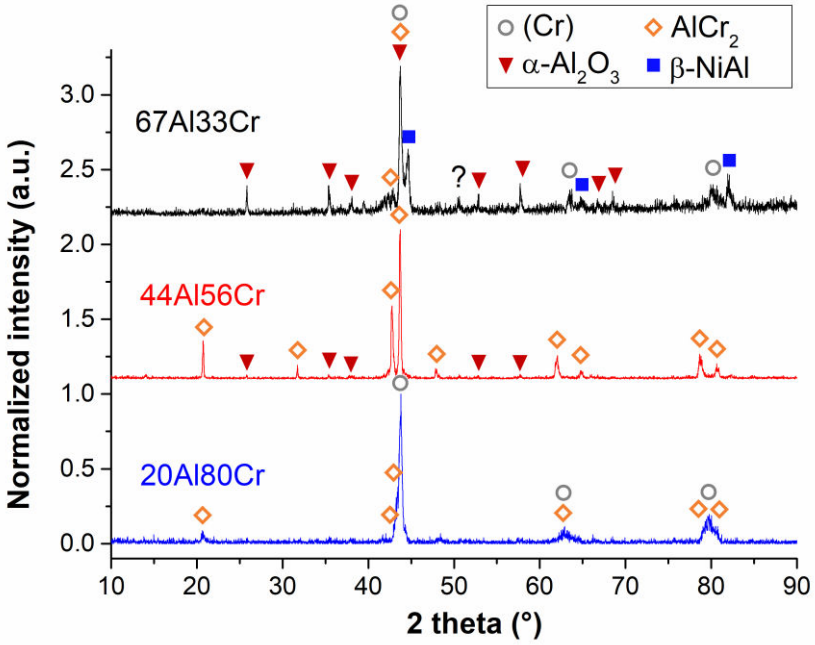

Fig. IV-13. XRD patterns of the surfaces for the 67Al33Cr, 44Al56Cr and 20Al80Cr slurry compositions elaborated on CM-247 LC superalloy after annealing in flowing Ar (400°C-3h + 1080°C-6h).

After characterization of the top coat structure, the diffusion coatings formed after annealing of the different Al-Cr mixed slurries on CM-247 LC superalloy were investigated by SEM and EDS. The cross-section images and the corresponding EDS spot measurements made on representative areas of the samples are given in Fig. IV-14. Both the thickness and the microstructure of the coatings were different for each of the three compositions. For the 67Al33Cr composition (Fig. IV-14a), the final microstructure of the coating was close to the one obtained from Al microparticles [12,44]. Two distinct layers were formed with an outer β-NiAl layer of approximately 40µm and an inner interdiffusion zone (IDZ) of about 20µm (Fig. IV-14b). The IDZ resulted from the precipitation of substrate elements having low solubility in the β-NiAl phase (Cr, Ta and W) [40,41]. Some Ta and W-rich precipitates were also found in the outer region of the coating as observed in high Al activity slurry aluminizing [39]. This suggests that the formation of the diffusion zone with the 67Al33Cr slurry

mixture involved both inward diffusion of Al at low temperature and outward diffusion of Ni at high temperature. It therefore appeared that the Al content of the 67Al33Cr slurry mixture was too high to produce a coating with a low-activity microstructure.

For the samples aluminized with the 44Al56Cr slurry mixture (Fig. IV-14c), two layers were identified: an outer additive layer with a rough surface and an inner IDZ with a thickness of approximately 20µm. The additive layer was composed of the Ni-rich β-NiAl phase with an Al concentration ranging from 36 to 40 at.% (Fig. IV-14d). This phase was found to dissolve more Cr than the one obtained with the 67Al33Cr slurry mixture (Fig. IV-14b). The outer region of the additive layer was free of precipitates and carbides from the substrate suggesting that outward diffusion of nickel predominantly occurred upon aluminizing [1,40,42]. However, some fine Ta and W-rich precipitates were randomly distributed across the additive layer. These precipitates probably resulted from the initial reaction between Al microparticles and the underlying substrate at low temperature (at about 640°C [11]). This reaction was presumably concomitant with the exothermic reaction occurring at 637±2°C between Al and Cr microparticles in the slurry deposit [26]. Because of the random distribution of the Al microparticles on the substrate surface after slurry deposition (Fig. II.7. of Chapter II), this reaction was only possible on local spots where Al was in direct contact with the substrate. The initial phases formed upon aluminizing where thus different from one area to another, which modified the motion of Al and Ni. The initial formation of Ni_2Al_3 would facilitate Al motion whereas the direct formation of Ni-rich β-NiAl phase would promote the nickel outward diffusion upon aluminizing [45,46]. This would explain the rough surface of the coating after annealing.

For the 20Al80Cr composition, the overall thickness of the aluminized layer did not exceed 20µm and was mainly composed by the interdiffusion zone (Fig. IV-14e). As depicted with the EDS concentration profile on Fig. IV-14f, coarse precipitates with different compositions were formed in a β-NiAl matrix. The nickel enrichment of the phases formed above the aluminized layer suggested that nickel outward diffusion occurred upon aluminizing. However, the Al content of the 20Al80Cr slurry was too low to grow a thicker diffusion zone. These results are in good agreement with the observations done on pure nickel substrate (paragraph IV.2. of Chapter II) and on Ni20Cr substrate (paragraph I.2. of Chapter III).

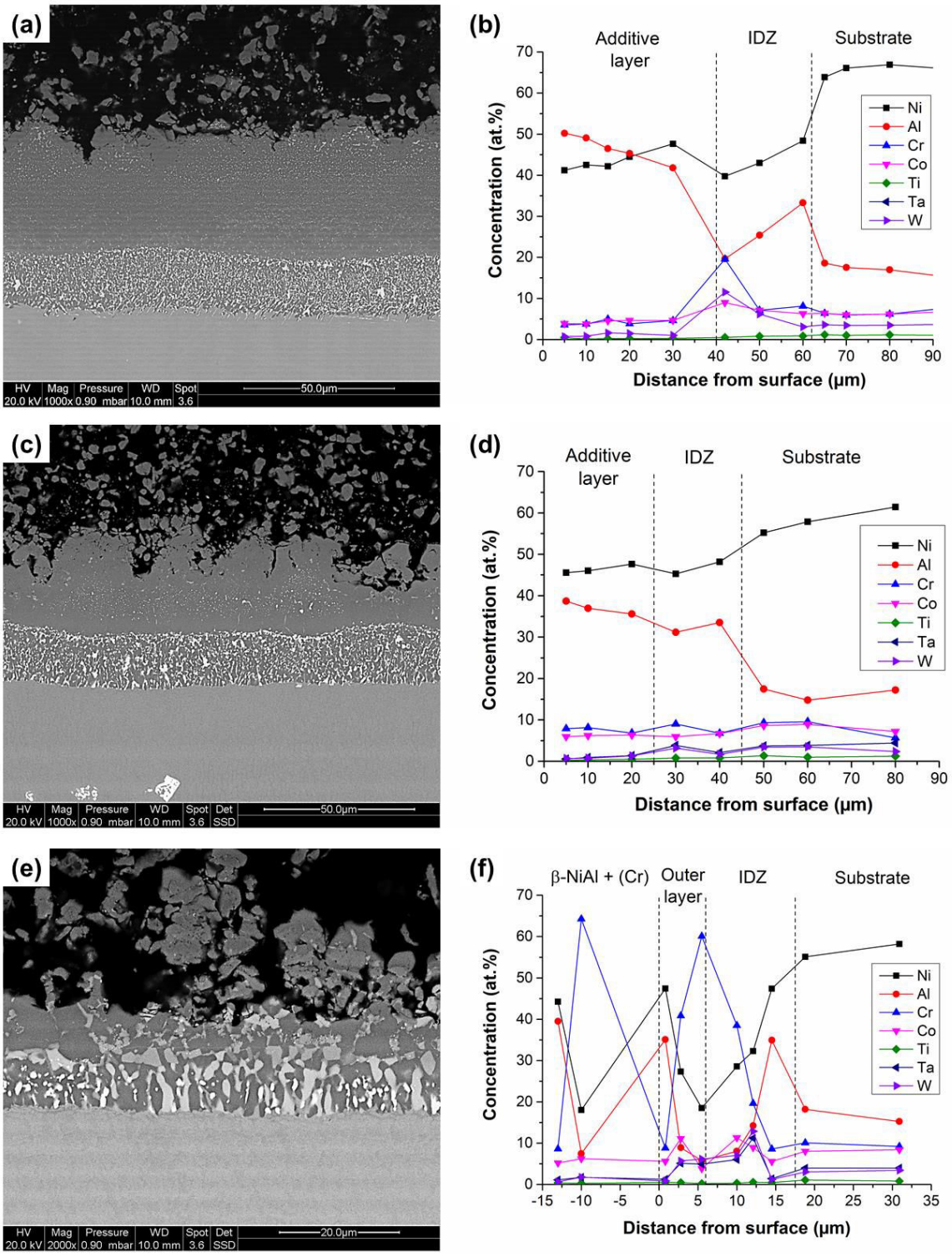

Fig. IV-14. BSE cross-section images and EDS concentration profiles for CM-247 LC superalloy slurry coated with (a), (b) 67Al33Cr, (c), (d) 44Al56Cr and (e), (f) 20Al80Cr mixtures after annealing in flowing Ar (400°C-3h + 1080°C-6h).

The elemental distributions of Ni, Al, Cr and Ta for the three Al-Cr mixed slurries were also determined after annealing (Fig. IV-15). Note that the X-ray maps of W were generally very close to the one of Ta and, for the sake of clarity, only X-ray maps of Ta are presented in the manuscript. Ta and W were found to preferentially precipitate in the IDZ for the three slurry mixtures. For the 44Al56Cr composition, fine Ta and W precipitates were aligned at the interface between the additive layer and the IDZ, which is typical of outwardly grown coatings [40]. For the three compositions, Cr-rich phases present in the top coat were easily identified and contained great amounts of Al. For the 20Al80Cr slurry mixture (Fig. IV-15c), Cr and Ta (W) coarse precipitates were identified through the β-NiAl coating matrix. Above the aluminized layer, both β-NiAl and α-(Cr) phases (Fig. IV-14f) were distinctively observed. This confirmed the preferential formation of Ni_xAl_y phases over Ni_xCr_y phases upon nickel outward diffusion from the substrate into the Al_xCr_y phases present above the diffusion zone (cf. Fig. III-20 in Chapter III).

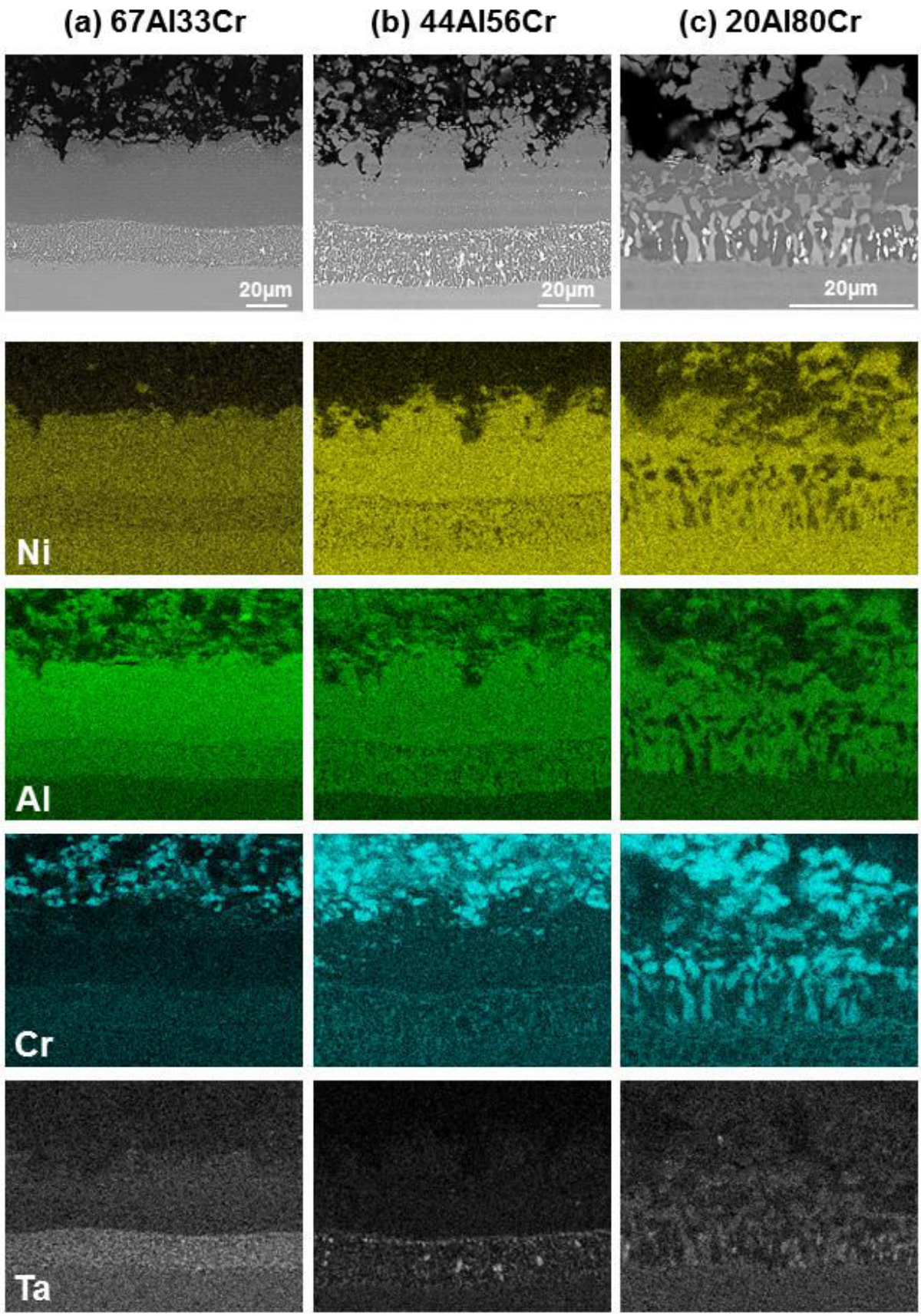

Fig. IV-15. BSE cross-section images and X-ray maps of Ni, Al, Cr and Ta for the (a) 67Al33Cr, (b) 44Al56Cr and (c) 20Al80Cr mixed slurries elaborated on CM-247 LC superalloy after annealing in Ar (400°C-3h + 1080°C-6h).

Since the aluminizing treatment must not modify the microstructure of the parent material to maintain the original mechanical properties, an aluminized sample was electrolytically etched with oxalic acid (Fig. IV-16). This metallographic attack preferentially etches the γ-(Ni) phase, which allowed to reveal the γ-γ' microstructure of the superalloy underneath the diffusion zone (Fig. IV-16a). Note also that the microstructure of the coating was similar to the one obtained with high Al activity slurry aluminizing [12,39,40,44,47]. This observation confirmed that the Al content of the 67Al33Cr composition was too high to foster the direct formation of β-NiAl. The greater magnification image of the interface between the IDZ and the substrate (Fig. IV-16b) demonstrated that the γ-γ' microstructure of the substrate was maintained after annealing at 1080°C for 6 hours.

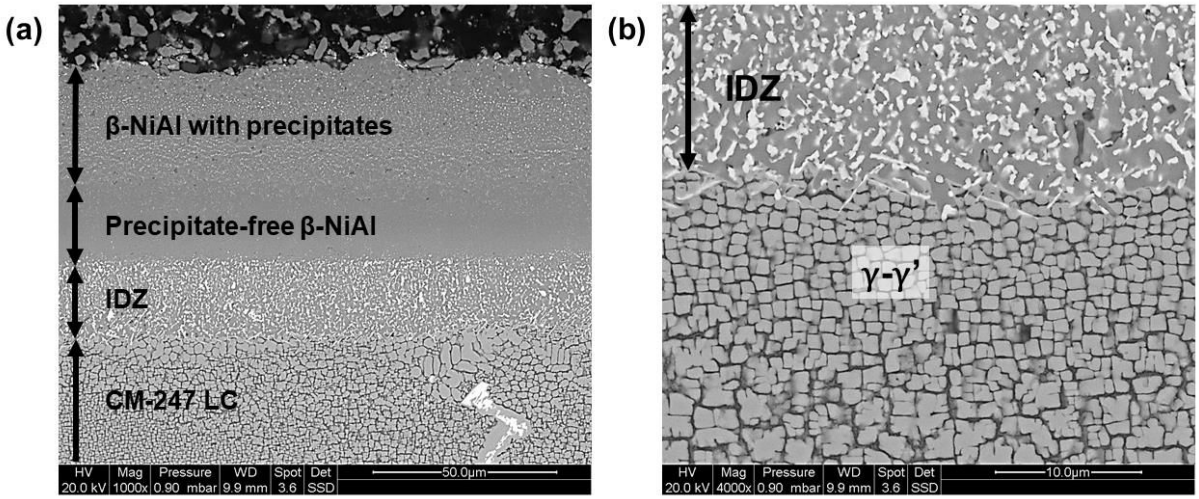

Fig. IV-16. (a) BSE cross-section image of the 67Al33Cr slurry mixture elaborated on CM-247 LC superalloy after annealing in flowing Ar (400°C-3h + 1080°C-6h) and (b) details of the interface between the IDZ and the underlying substrate (10 vol.% $H_2C_2O_4$ electrolytically etch).

As observed with the model materials (pure nickel and Ni20Cr substrate), Al and Cr microparticles reacted in the slurry deposits and formed Al_xCr_y intermetallic compounds. The initial Al content of the Al-Cr slurry mixture was of utmost importance to control the Al activity upon aluminizing [42]. Unlike pack cementation [37,41,48] or out-of-pack processes [21,22], the synthesized Al-Cr masteralloys were in direct contact with the substrate to aluminize with no need of halide activators [42,26]. The stoichiometry of the synthesized Al_xCr_y phases was found to considerably modify the mechanisms of formation of the diffusion coatings. This particularly modified the motion of Ni and of Al upon aluminizing and hence the preferential growth of the coating by inward diffusion of aluminium at low temperature or outward diffusion of nickel at high temperature.

II.2. Low-activity high-temperature (LAHT) coatings from the Cr-Al double-layer system

a) Low-activity conventional heat treatment (400°C-3h + 1080°C-6h)

The aluminizing tests on CM-247 LC from Al-Cr mixed slurries demonstrated that the 44Al56Cr composition was suitable to limit the inward diffusion of Al at low temperature and to foster the outward diffusion of nickel at high temperature. The Al activity of this composition seemed to be the threshold to obtain low Al activity coatings from elemental powders at 1080°C. Therefore, the 44Al56Cr composition was selected to elaborate a low Al activity coating on CM-247 LC superalloy based on the Cr-Al double-layer system (cf. Fig. II-6. In Chapter II). For this, a first layer of approximately 10 mg.cm^{-2} of Cr and a second layer of approximately 8 mg.cm^{-2} of Al were deposited on the superalloy by air brush (close to the 56Cr-44Al ratio in wt.%). The sample was subsequently heat treated in flowing Ar at 400°C for 3 hours and 1080°C for 6 hours. A macrograph of the sample after annealing is given on Fig. IV-17a. The alumina top coat structure was not adherent and the surface micrograph suggested the presence of intermetallic phases formed in the slurry deposit upon annealing (Fig. IV-17b). A cross-section micrograph of the coating after annealing is given on Fig. IV-18a.

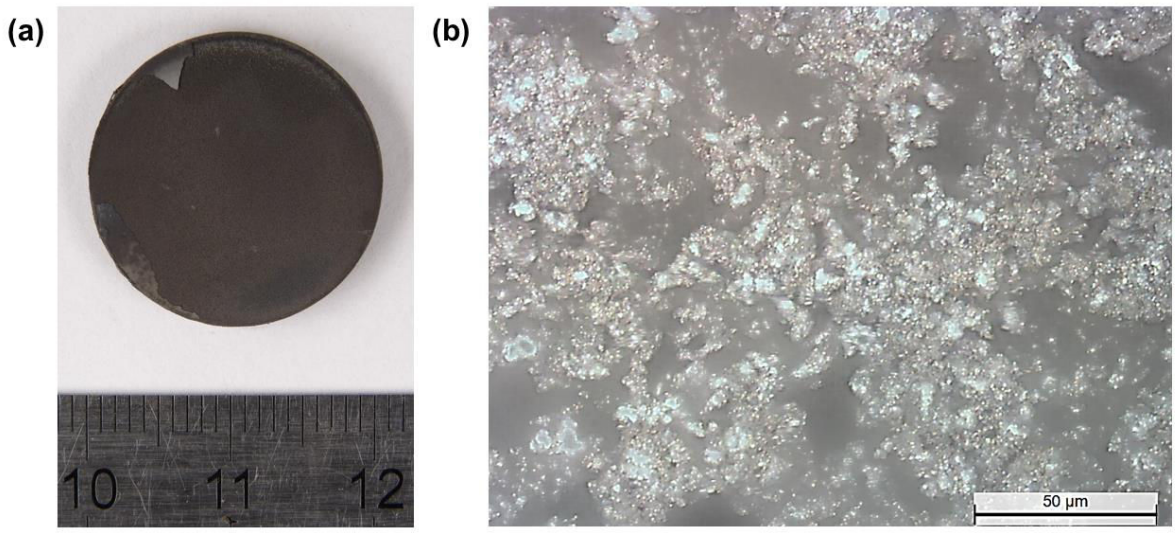

Fig. IV-17. (a) Macrograph and (b) surface micrograph of the CM-247 LC sample slurry coated with the 56Cr-44Al double-layer system after annealing in flowing Ar (400°C-3h + 1080°C-6h).

The microstructure of the coating was completely different than the one obtained from high Al activity aluminizing [12,39,41,44,47]. The coating structure consisted of three main layers: an interdiffusion zone (IDZ), an intermediate layer with fine dispersion of Cr and an outer layer with Cr-rich phases in the coating matrix (Fig. IV-18a). The thicknesses of both additive layer (A.L.) and IDZ were very close over the whole sample with an IDZ/A.L. ratio close to one [37]. The final microstructure of the coating was very close to the Cr-modified aluminide coating obtained by Gleeson et al. from pack co-deposition process (Fig. IV-18b) [32]. The Cr enrichment of the additive layer was confined to approximately 20% of the total coating thickness, which is also in good agreement with the results obtained by Gleeson et al. [32]. The substrate carbides highlighted on Fig. IV-18a were entrapped in the interdiffusion zone after annealing. This suggested the predominant outward diffusion of nickel upon aluminizing [40,41].

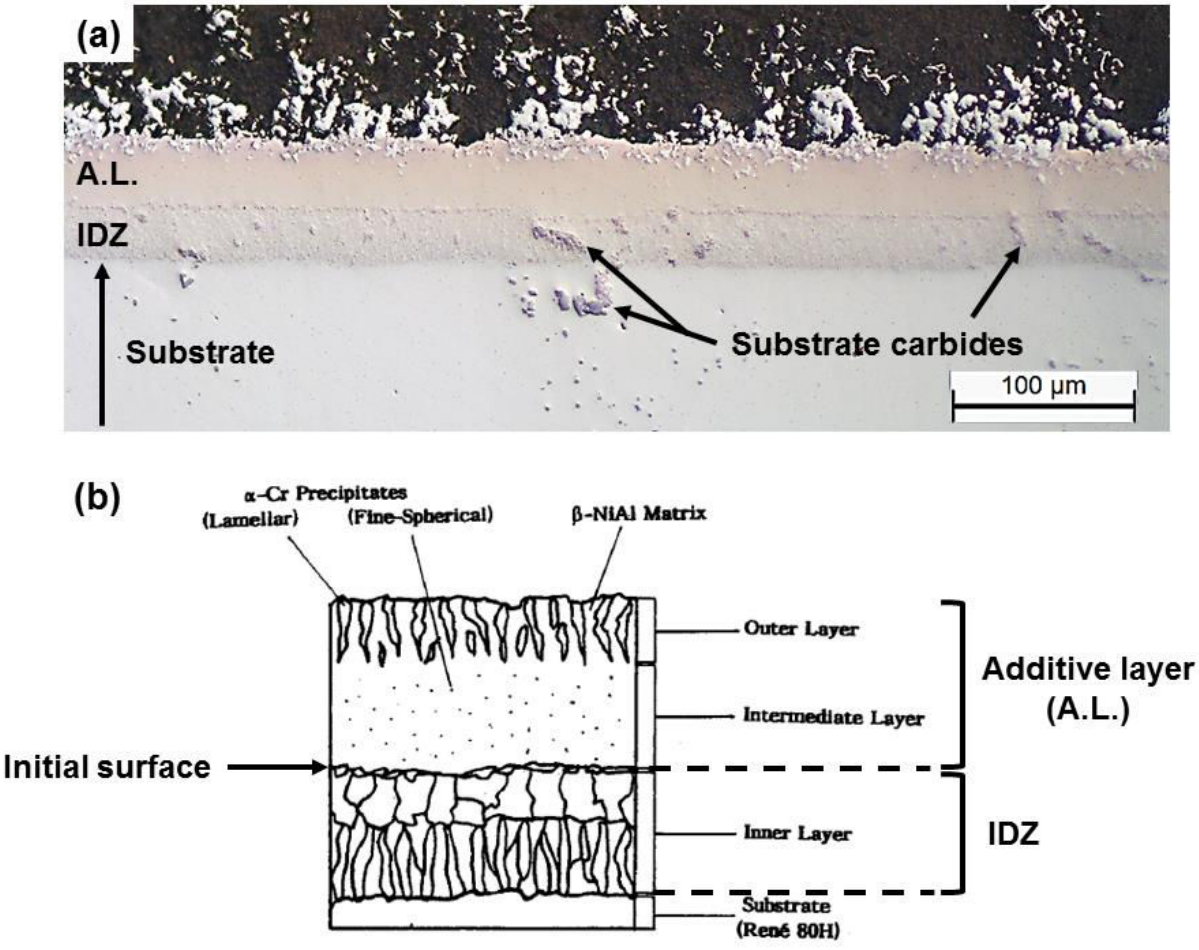

Fig. IV-18. Cross-section optical micrograph of the 56Cr-44Al double-layer system elaborated on CM-247 LC superalloy after annealing in flowing Ar (400°C-3h + 1080°C-6h) and (b) microstructure of the Cr-modified aluminide coating produced by Gleeson et al. [32].

The SEM technique was carried out to image in BSE mode the cross-section of a representative area and get the elemental distribution (Fig. IV-19). Although both β-NiAl and Cr-rich phases presented a close contrast in BSE mode, the precipitation of α-Cr in the outer region of the coating matrix could be easily observed on Fig. IV-19c. The composition of the Cr-rich phases resulting from the aluminizing process was approximately 26Al-66Cr-1Co-7Ni (at.%). Even though XRD was not carried out on this sample, this composition suggested the formation of the $AlCr_2$ phase by correlation with the results obtained for the 44Al56Cr slurry mixture (Fig. IV-13). Ta and the other elements with low solubility in the β-NiAl phase (i.e. W and Hf) were found to precipitate exclusively in the IDZ. Therefore, the β-NiAl additive layer was free of substrate elements precipitates, which is typical of outwardly grown coatings [1,40-42].

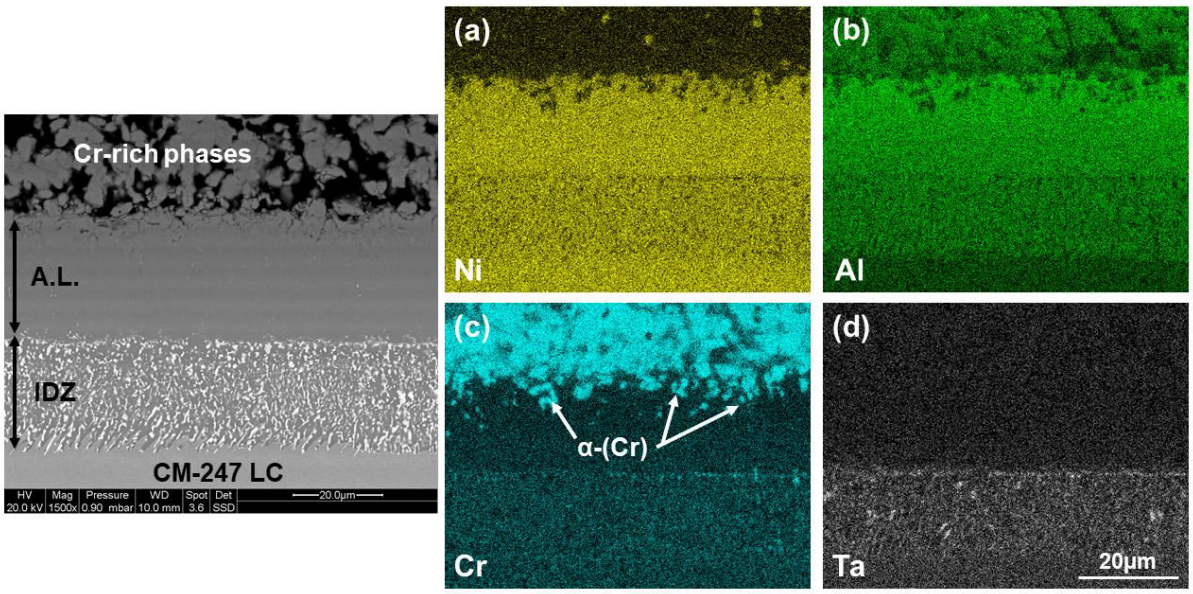

Fig. IV-19. BSE cross-section image and corresponding X-ray maps of (a) Ni, (b) Al, (c) Cr and (d) Ta for the 56Cr-44Al double-layer system elaborated on CM-247 LC after annealing in flowing Ar (400°C-3h + 1080°C-6h).

The concentration profile of the coating is given in Fig. IV-20. Note that the EDS spot measurements in the outer region of the coating were realized in the β-NiAl coating matrix between the α-Cr precipitates. The determination of the exact composition of the α-Cr precipitates was not possible by EDS because of the relatively large spot resolution. Ta and W enrichments were confined in the IDZ (Fig. IV-20). The larger atomic sizes of Ta and W and their very low solubility limits into β-NiAl can probably explain their low concentrations in the additive layer [49,50,51]. This observation is in favour of outward grown coating where Cr and Co are the faster diffusing elements with Ni and Al [40,41,49]. The low Ti content of CM-247 LC (0.7 at.%) led to a very low concentration gradient with the outward growing β-NiAl phase and could explain its low concentration within the additive layer after only 6 hours diffusion at 1080°C [49]. However, one can expect that for longer annealing time (e.g. upon oxidation), the substrate elements with high diffusivity in the β-NiAl phase (mainly Ti, Ta and Hf) will diffuse towards the surface [50,52,53].

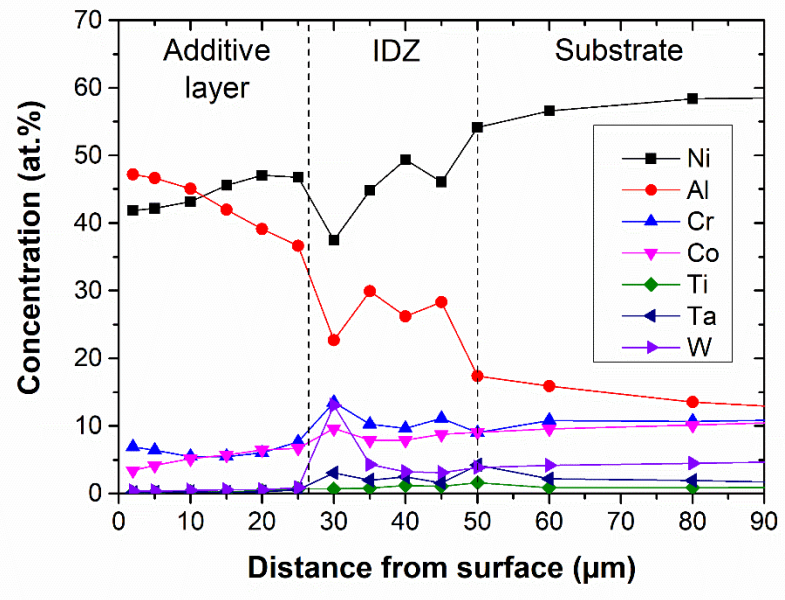

Fig. IV-20. EDS concentration profile of the 56Cr-44Al double-layer system elaborated on CM-247 LC superalloy after annealing in flowing Ar (400°C-3h + 1080°C-6h).

b) Complete heat treatment (400°C-1h + 700°C-2h + 1100°C-2h)

For comparison with high Al activity coatings elaborated by slurry [12,27,39,44,47], the same heat treatment (400°C-1h + 700°C-2h + 1100°C-2h) was performed on a Cr-Al double-layer system elaborated on CM-247 LC superalloy. The initial amount of Cr and Al deposited on the surface was close to the 56Cr-44Al (wt.%) composition for comparison with the coating presented on Fig. IV-18a. The surface macrograph of the sample shows that the top foam was relatively adherent after annealing though presenting some cracks (Fig. IV-21a). The optical micrograph of the surface (Fig. IV-21b) suggested the presence of a ceramic top foam based on hollow alumina microspheres [12,18,27,44,47,54]. The mechanisms of formation of the hollow alumina microspheres will be discussed in Chapter V.

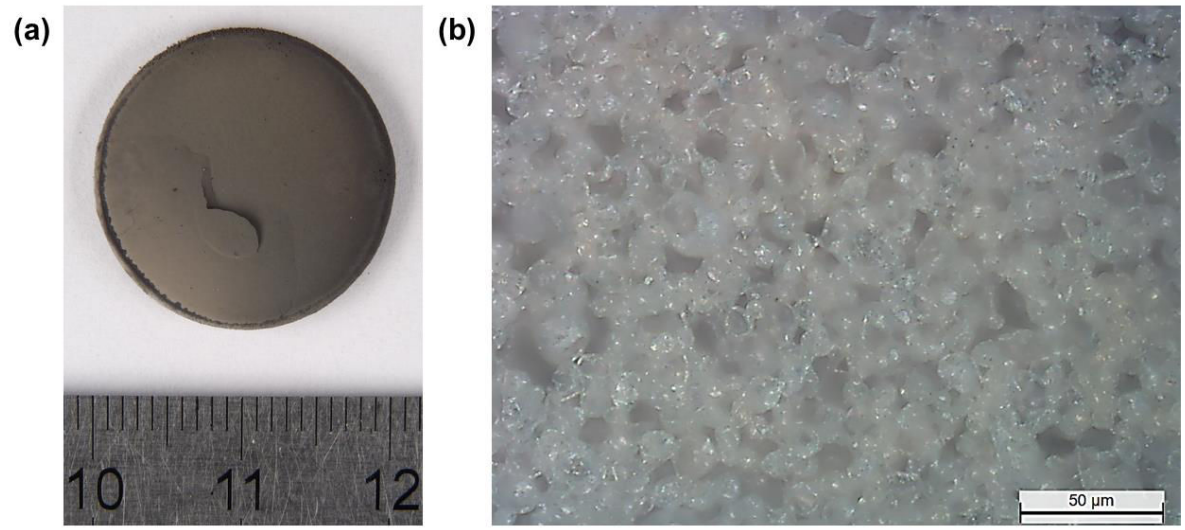

Fig. IV-21. (a) Macrograph and (b) surface micrograph of the top coat structure observed for the CM-247 LC sample slurry coated with the 56Cr-44Al double-layer system after annealing in flowing Ar (400°C-1h + 700°C-2h + 1100°C-2h).

The coating microstructure was formed of an inner interdiffusion zone and an outer additive layer (Fig. IV-22) as observed with the conventional low-activity heat treatment. Both layers were approximately 20µm thick with an IDZ/A.L. ratio close to one over the whole surface of the sample. As observed on Fig. IV-18a, the substrate carbides were confined in the IDZ after annealing suggesting that the growth of the coating predominantly occurred by outward diffusion of nickel at high temperature. By comparison with the sample heat treated with the conventional low-activity heat treatment (Fig. IV-18a), the additive layer on Fig. IV-22 presented a darker contrast under light optical microscopy. This darker contrast suggested the formation of the Al-rich β-NiAl phase as observed on the Ni20Cr substrate (Fig. IV-10c and d). The distribution of bright phases under light microscopy within the additive layer (Fig. IV-22) suggested that the Cr enrichment was greater than the one observed after the conventional low-activity heat treatment (Fig. IV-18a). These bright phases were observed over the whole thickness of the additive layer, which means up to approximately 50% of the total coating

thickness. Consequently, the coating microstructure obtained by performing the two-step heat treatment (Fig. IV-22) was slightly different than the one obtained by Gleeson et al. (Fig. IV-18b) and closer to the one obtained by Streiff and Boone with a two-step chromizing-vapour phase aluminizing process [55].

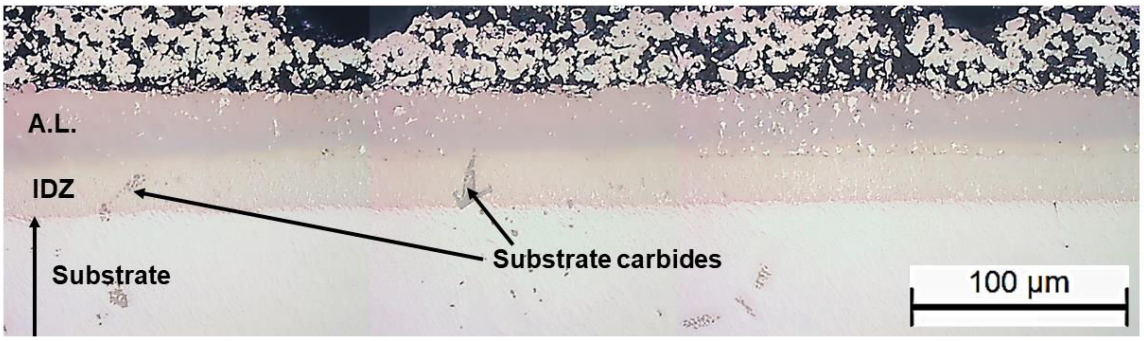

Fig. IV-22. Cross-section optical micrograph of the 56Cr-44Al double layer system elaborated on CM-247 LC superalloy after annealing in flowing Ar (400°C-1h + 700°C-2h + 1100°C-2h).

X-ray maps were performed on the cross-section of a representative area to get the elemental distribution (Fig. IV-23). These analyses clearly showed the Cr enrichments of the β-NiAl additive layer in the form of α-(Cr) precipitates (Fig. IV-23c). As suggested with the optical micrographs, these Cr enrichments were dispersed in the whole thickness of the diffusion layer. Therefore, it is most likely to consider that these Cr-rich phases resulted from the aluminizing process and attested the preferential formation of Ni_xAl_y compounds rather than Ni_xCr_y ones during the outward diffusion of nickel. The direct formation of the β-NiAl phase upon aluminizing implied the segregation of Cr as α-(Cr) phases within the coating layer [32]. The X-ray map of Ta (Fig. IV-23d) confirmed that its

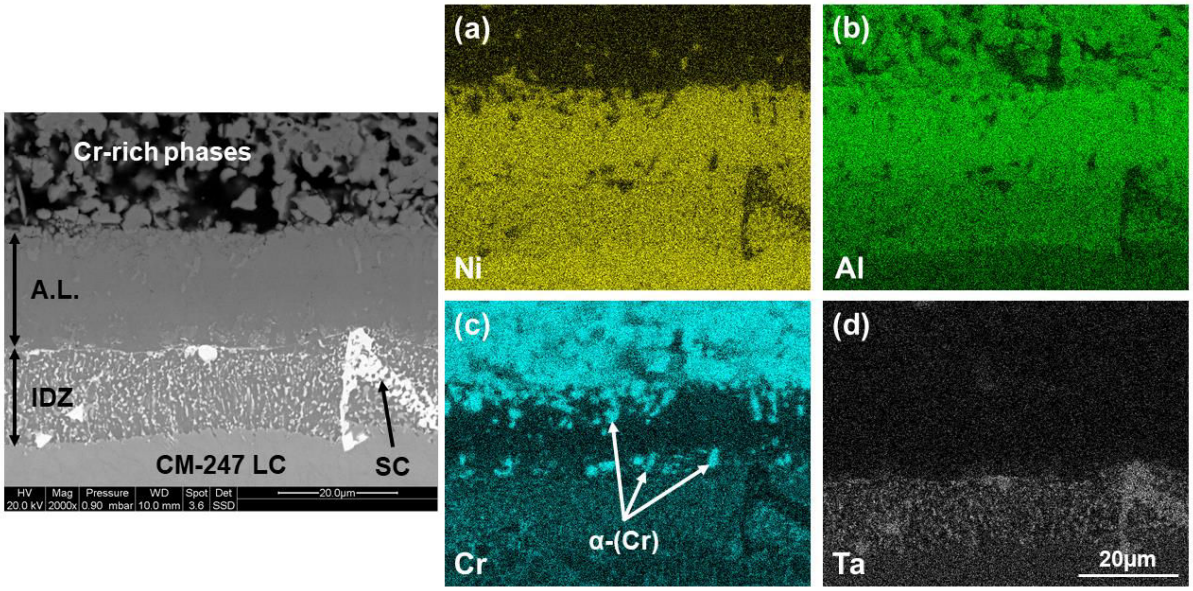

Fig. IV-23. BSE cross-section image and corresponding EDS maps of (a) Ni, (b) Al, (c) Cr and (d) Ta for the 56Cr-44Al double-layer system elaborated on CM-247 LC after annealing in flowing Ar (400°C-2h + 700°C-2h + 1100°C-2h).

precipitation was confined in the IDZ (same observations for W). The substrate carbides (identified as the bright coarse phases in the BSE image of Fig. IV-23) were enriched in Hf, Ta and W.

The mean composition of the Cr-rich phases present above the additive layer was approximately 37Al-56Cr-1Co-6Ni in at.%. By comparison with the results obtained with the low-activity heat treatment (i.e. 26Al-66Cr-1Co-7Ni in at.%), it appeared that the Al concentration of these phases was higher after the two-step heat treatment. This could be explained by the longer dwell time at high temperature for the low-activity heat treatment (i.e. 1080°C-6h) than for the two-step heat treatment (i.e. 1100°C-2h). So, the longer the diffusion time, the greater the outward diffusion of nickel to react with the Al-Cr phases of the slurry deposit. Consequently, the amount of Al dissolved from the Al-Cr phases to foster the formation of β-NiAl was greater after 6 hours at 1080°C than after only 2 hours at 1100°C. The longer dwell time at high temperature was also observed to promote the dissolution of the Cr-rich phases enclosed within the β-NiAl coating matrix. This also implied their segregation in the outer region of the coating. All the different observations confirmed that the outward diffusion of nickel was controlling the growth of the coating.

EDS spot measurements in the cross-section of the coating were performed to plot the concentration profile (Fig. IV-24). The analyses confirmed that the additive layer was mainly composed of the Al-rich β-NiAl phase with local Cr enrichments. This phase extended up to the interface IDZ-additive layer where the concentration of Al sharply decreased. The IDZ was mainly composed of the Ni-rich β-NiAl phase where the substrate elements having low solubility in this phase (Cr, Ta and W) precipitated during the aluminizing process [40,41].

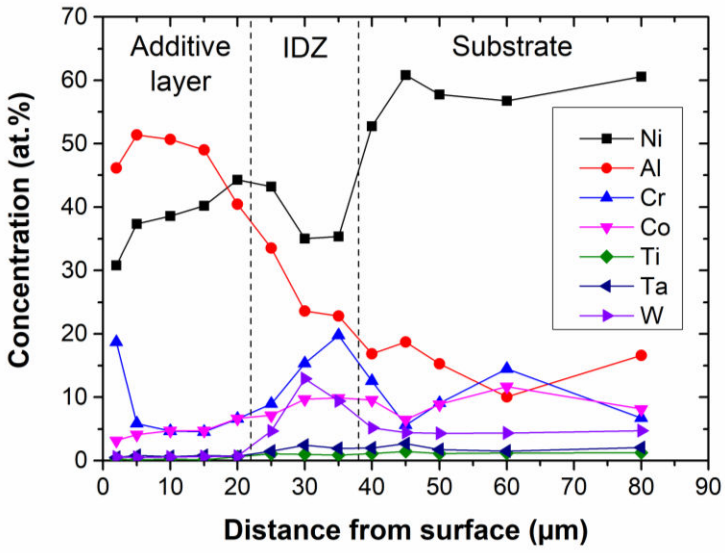

Fig. IV-24. EDS concentration profile of the 56Cr-44Al double-layer system elaborated on CM-247 LC superalloy after annealing in flowing Ar (400°C-1h + 700°C-2h + 1100°C-2h).

c) Discussion

- ***Growth of the coating:***

The coating microstructure observed on Fig. IV-18a and Fig. IV-22 suggested that the growth predominantly occurred by outward diffusion of nickel at high temperature [40]. As previously described by Goward et al., outwardly grown coatings foster the direct formation of the Ni-rich β-NiAl compound on the substrate surface [1,40]. Since Ni diffusivity is more significant than that of Al in Ni-rich β-NiAl phase at high temperature [45,46], Ni outward diffusion from the substrate is promoted and an additive layer based on the Ni-rich β-NiAl phase is formed above the initial surface of the substrate by reaction with Al [1,40]. Because of nickel withdrawal from the underlying substrate, an interdiffusion zone is formed where substrate elements having low solubility in β-NiAl precipitate (Ta and W typically). The inert carbides originally present in the substrate could also be observed in the coating microstructure but remained in the interdiffusion zone [40,41]. The β-NiAl additive layer was therefore "cleaner" than inward-grown coatings. This therefore suggests that the composition of the additive layer should be in the Ni-rich β-NiAl domain after annealing as observed on the concentration profile of Fig. IV-20.

- ***Mechanisms of formation:***

The significant Cr enrichments in the additive layers of the slurry coatings suggested that these enrichments were associated with undissolved Cr-rich phases rather than with precipitation in the β-NiAl phase, as also observed by Gleeson et al. [32]. Considering the original system of the present study, Al_xCr_y intermetallic compounds were synthesized in the slurry deposit at low temperature (at about 640°C). The Al activity was thus greatly reduced on the substrate surface, considerably limiting the Al inward diffusion at low temperature (i.e. 650°C) [26,42]. At high temperature (i.e. 1080°C or 1100°C), nickel outwardly diffused and reacted with the Al_xCr_y intermetallic phases synthesized in the slurry deposit (cf. Fig. III-34 in Chapter III). Since nickel has low solubility in these Al-Cr phases (about 1 at.% in Al_4Cr and 3 at.% in Al_8Cr_5) [16], and because the enthalpy of formation of Ni_xAl_y phases is more exothermic than the one of Ni_xCr_y phases, nickel dissolved the Al-Cr phases and preferentially combined with Al. Consequently, the outward diffusion of nickel fostered the direct formation of Ni-rich β-NiAl with a small fraction of dissolved Cr. With a low solubility in the β-NiAl phase (less than 8 at.% [2,13,55]), a large fraction of Cr remained undissolved in the additive layer. Therefore, the growth of the coating with the 56Cr-44Al double-layer system seemed to be governed by the simplified reaction *(Eq. IV-1)*:

$$Ni + Al_xCr_y \rightarrow \beta\text{-}NiAl + \alpha\text{-}(Cr) \qquad \textbf{(Eq. IV-1)}$$

The continuous outward diffusion of nickel upon aluminizing progressively consumed the Al_xCr_y phases (i.e. by combination with Al). Therefore, reaction *(Eq. IV-1)* occurred until the Al_xCr_y donors were completely dissolved. The SEM characterization of the samples after annealing also showed that a fraction of Al was still present in the slurry deposit and did not incorporate in the diffusion coating (Fig. IV-19). This external Al content was mainly coming from $AlCr_2$ and α-(Cr) phases after the aluminizing process (Fig. IV-13). Since the $AlCr_2$ phase is not stable at temperatures higher than 910°C (Fig. III-5b in Chapter III), this phase was not present in the microstructure at the aluminizing temperature (1080°C or 1100°C) and was formed upon cooling [56-58]. Considering the Ni-Al-Cr ternary equilibrium [19] and the observations of Huang et al. [10], only β-NiAl and α-(Cr) phases were stable at the aluminizing temperature. Therefore, the growth of the coating should occur until the Al_xCr_y donor of reaction *(Eq. IV-1)* is converted into α-(Cr). As soon as α-(Cr) constitutes the main fraction of the slurry deposit (i.e. the Al donor), the kinetics of aluminizing should decrease because of the very low driving force of the new simplified reaction *(Eq. IV-2)*:

$$\mathrm{Ni} + \alpha\text{-}\mathrm{Cr(Al)} \rightarrow \beta\text{-}\mathrm{NiAl} + \alpha\text{-}(\mathrm{Cr}) \qquad \textbf{(Eq. IV-2)}$$

After annealing, undissolved α-(Cr) phases remained in the additive layer suggesting that the outward diffusion of nickel was significantly higher than the inward diffusion of Al at all time during the aluminizing process [32,33,55].

- ***Influence of the cooling ramp on the formation of Al-rich β-NiAl phase:***

For the sample annealed at 1100°C for 2 hours (Fig. IV-22), the formation of the Al-rich β-NiAl layer should not possible at the diffusion temperature (1100°C) because of the major outward diffusion of nickel. The appearance of this Al-rich β-NiAl zone in the additive layer can be explained by the effect of the cooling ramp on the final microstructure of the coating. For example, a layer of Al-rich β-NiAl was highlighted by EPMA on low-activity coatings produced by out-of-pack CVD process on different nickel-based superalloys [44]. For this process, halide activators are used to attack Cr-Al masteralloys and form a gaseous phase to allow aluminium transport towards the sample surface [22]. During the vapour phase process, the coating box is heated to the aluminizing temperature (typically in the range 1050°C-1150°C) [22,59]. After adsorption of the gaseous molecules on the substrate, solid diffusion of deposited Al in the substrate occurs. At the end of the diffusion dwell time, the coating box is cooled down to room temperature. Because of the inertia of the retort, the temperature profile of the cooling ramp is usually divided in two sections: a first section with a continuous decrease of the temperature down to an intermediate temperature (in the range 800°C-900°C) and a second section with a slow cooling ramp down to room temperature [59]. At temperatures below 900°C, the diffusivity of Al is

more significant than that of Ni in β-NiAl phase [46]. Because gaseous aluminium phases are still present in the coating box upon cooling, deposition of Al on the sample surface is maintained. Therefore, Al diffuses into the β-NiAl additive layer, which converts into Al-rich β-NiAl phase thanks to the continuous supply of Al. In Al-rich β-NiAl, aluminium diffuses ten times faster than nickel and this can explain that this layer could reach 10 to 15µm in the outer region of the coating after the aluminizing process [44].

The cooling profile of the horizontal furnace used for the aluminizing tests (cf. paragraph II.4. in Chapter II) was experimentally determined and found to be close to the one given by Wang et al. for a conventional low-activity CVD process [59]. Therefore, it is believed that the Al-rich β-NiAl layer observed in the coating microstructure (Fig. IV-22) also formed upon cooling in this work. Unlike CVD techniques, the Al donors were in direct contact with the underlying substrate here [26] thus giving a continuous Al supply upon cooling until its diffusion becomes negligible at low temperature.

- ***Influence of the heat treatment parameters on the formation of Al-rich β-NiAl phase:***

Since the Al-rich β-NiAl phase was not formed after the conventional low-activity heat treatment (Fig. IV-18), the heat treatment parameters were also found to influence its formation. The initial reaction between Al and Cr microparticles to form the intermetallic compounds, occurring at approximately 640°C, was found to be very fast [26]. After further annealing for 5 hours at 650°C, little transformation occurred within the slurry deposits of Al-Cr mixed slurries (cf. Fig. III-15) and Cr-Al double-layer systems (cf. Fig. III-31). It can therefore be estimated that the 2 hours annealing at 700°C in the two-step heat treatment had barely any effect on the diffusion mechanisms between the slurry deposit and the CM-247 LC superalloy. However, at higher temperatures (i.e. 1080°C-1100°C), the predominant outward diffusion of nickel dissolved the Al_xCr_y intermetallic phases and progressively formed the β-NiAl coating layer following reaction *(Eq. IV-1)*. The main difference between the two heat treatments was therefore the annealing time (6 hours at 1080°C or 2 hours at 1100°C).

Increasing the annealing time should lead to a greater Al consumption from the Al_xCr_y phases because of the continuous nickel outward diffusion at such high temperatures. Assuming an initial slurry deposit with the same Cr-Al ratio before heat treatment (56Cr-44Al in wt.% in this case), the remaining Al content in the slurry deposit would be higher after two hours of annealing than after six hours (progressive supply of Al to form the β-NiAl phase). Consequently, this implies that the driving force of reaction *(Eq. IV-1)* (or even *(Eq. IV-2)*) is much higher after the 1100°C-2h annealing than the 1080°C-6h one. Upon cooling, the driving force (i.e. the Al activity of the Al donors) was high enough after the

two-step heat treatment to foster the inward diffusion of Al into the Ni-rich β-NiAl layer. This progressively saturated the Ni-rich β-NiAl layer and led to the formation of Al-rich β-NiAl instead. After the complete heat treatment, a homogeneous Al-rich β-NiAl layer can therefore be observed in the additive layer of the coating (Fig. IV-22) as previously reported in out-of-pack low-activity coatings [44].

- ***Comparison with the Al-Cr mixed slurries:***

The 44Al56Cr and 20Al80Cr mixed slurries were found to greatly reduce the Al activity on substrate surface and to foster the outward diffusion of nickel at high temperature [26]. It is likely to consider that the reactions *(Eq. IV-1)* and *(Eq. IV-2)* were controlling the coating growth as proposed with the 56Cr-44Al double-layer system. After 5 hours annealing at 650°C in Ar (Fig. III-15), both slurry mixtures were found to mainly form the Al_8Cr_5 phase with an excess of Cr (most probably α-(Cr) solid solution). After further annealing at 1000°C for 3 hours (Fig. III-17), Al_8Cr_5 was still identified for the 44Al56Cr mixture whereas the 20Al80Cr one was mainly composed of α-(Cr) at temperature. This therefore implies that the driving forces of reactions *(Eq. IV-1)* and *(Eq. IV-2)* were significantly different between the two compositions. For the 20Al80Cr mixed slurry, the major presence of α-(Cr) phases as Al donors at the initial stage of aluminizing considerably limited the growth of the coating. This was well illustrated in Fig. IV-12 and Fig. IV-15c with the very thin aluminized layers formed on the CM-247-LC superalloy. For the 44Al56Cr mixed slurry, the initial Al content was low enough to ensure the major outward diffusion of nickel and high enough to grow an aluminized layer of significant thickness (Fig. IV-12 and Fig. IV-15c).

On the other hand, the fine precipitation of refractory metals (i.e. Ta and W) in the outer region of the coating for the 67Al33Cr mixed slurry (Fig. IV-16a) confirmed that the mechanisms of formation were different. This implies that the reactions *(Eq. IV-1)* and *(Eq. IV-2)* were not controlling the coating growth when performing the slurry aluminizing with the 67Al33Cr. For a better comprehension of such discrepancies, CM-247 LC samples were slurry coated with a 33Cr-67Al double-layer system and annealed in the same conditions than the 56Cr-44Al double-layer system.

II.3. High-activity high-temperature (HAHT) coatings from the Cr-Al double-layer system

The results of paragraph II.1 demonstrated the importance of the Al/Cr ratio of the slurry deposit on the microstructure of the diffusion coating. The initial Al/Cr ratio has a significant influence on the stoichiometry of the Al_xCr_y phases synthesized upon annealing on the substrate surface, hence, on the Al activity [26,48]. The sample slurry coated with the 67Al33Cr composition (in wt.%) was found to present a final microstructure close to that of high Al activity coatings. Therefore, this composition was selected to produce a Cr-Al double-layer system on CM-247 LC superalloy in order to compare the results to the ones obtained with the low-activity high-temperature coatings (LAHT) of paragraph II.2. The different samples presented in paragraph II.3 were slurry coated with 6±1 mg.cm^{-2} Cr and 12±1 mg.cm^{-2} Al to maintain a Cr/Al ratio close to 33Cr/67Al (in wt.%).

a) Low-activity conventional heat treatment (400°C-3h + 1080°C-6h)

The CM-247 LC superalloy slurry coated with the 33Cr-67Al double-layer system was first subjected to the low-activity conventional heat treatment. A macrograph of the annealed sample is given on Fig. IV-25a. Some cracks highlighted by white circles, were observed in the top foam structure composed of hollow alumina microspheres (Fig. IV-25b) [12,18,27,44,47,54] while the diffusion area looked quite homogeneous in the optical cross-section (Fig. IV-26a).

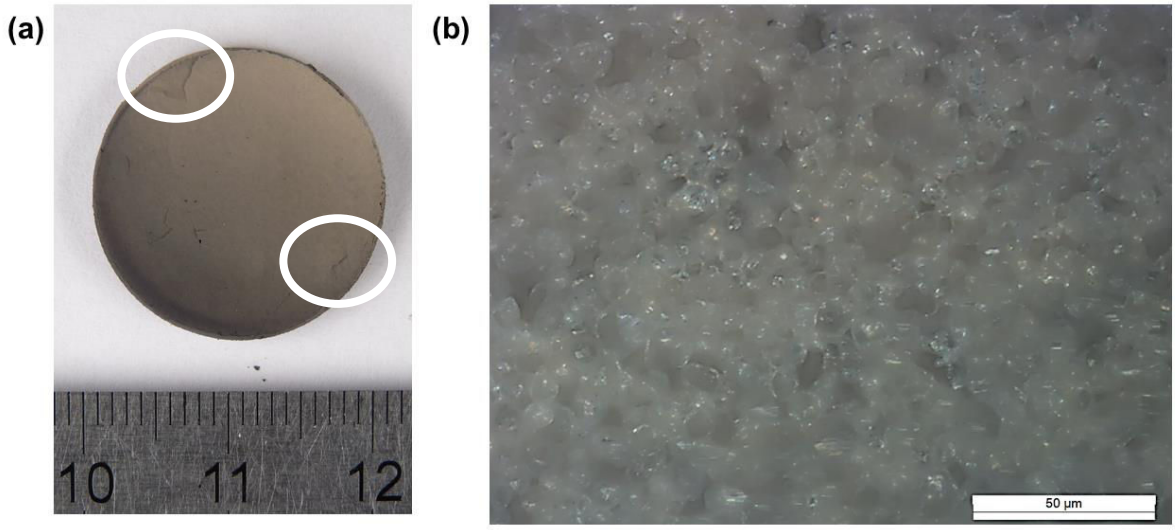

Fig. IV-25. (a) Macrograph and (b) surface micrograph of the top coat structure observed for the CM-247 LC sample slurry coated with the 33Cr-67Al double-layer system after annealing in flowing Ar (400°C-3h + 1080°C-6h).

The coating microstructure was however significantly different than the one obtained in Fig. IV-18a with the 56Cr-44Al double-layer system. The aluminized layer was approximately 80µm thick, which is almost 30µm thicker than the outwardly grown coatings presented in paragraph II.2. In addition, the substrate carbides were now observed at the extreme surface of the diffusion zone, which indicated that the initial surface of the substrate before aluminizing remained at the interface between the diffusion zone and the slurry deposit [41]. The microstructure of the coating was very close to the one obtained by Das et al. after a single-step high Al activity pack aluminizing of CM-247 LC superalloy [41]. A schematic representation of the coating formation is given on Fig. IV-26b [41]. The different layers identified by Das et al. after such coating formation are reported on Fig. IV-26a. The coating can be divided in three distinct layers: an outer layer rich in precipitates predominantly formed by inward diffusion of Al (INL + ONLS), an intermediate layer free of precipitates formed by outward diffusion of nickel (ONLO) and an interdiffusion layer (IDZ).

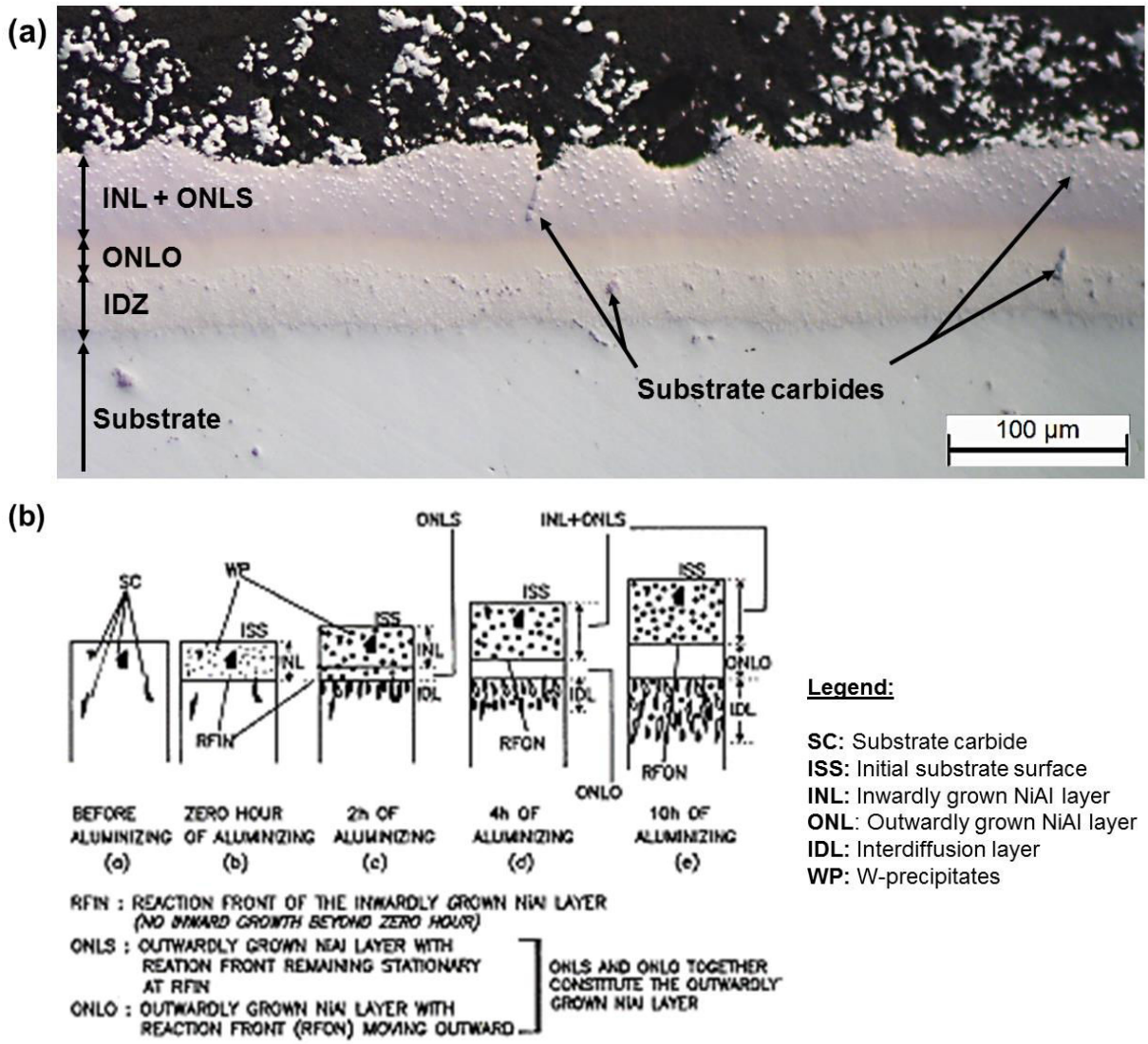

Fig. IV-26. (a) Cross-section optical micrograph of the 33Cr-67Al double-layer system elaborated on CM-247 LC superalloy after the conventional heat treatment in flowing Ar and (b) schematic representation of the coating formation proposed by Das et al. [41].

The IDZ/D.L. ratio of the diffusion coating was approximately 0.35, which is 3 times lower than the one obtained on outwardly grown coatings (cf. paragraph II.2). The SEM was carried out to image in BSE mode the cross-section of the 33Cr-67Al double-layer coating and get the X-ray maps (Fig. IV-27). The bright phases observed in the outer region of the diffusion layer (D.L.) were enriched in Ta (Fig. IV-27d) and Hf (cf. Annex 1) and confirmed the presence of the substrate carbides (SC). This attested that the initial surface of the substrate remained at the extreme surface of the coating upon aluminizing (cf. Annex 1 and Ref. [41]). The X-ray map of Cr emphasized the fine precipitation of α-(Cr) in the outer region of the diffusion layer (Fig. IV-27c).

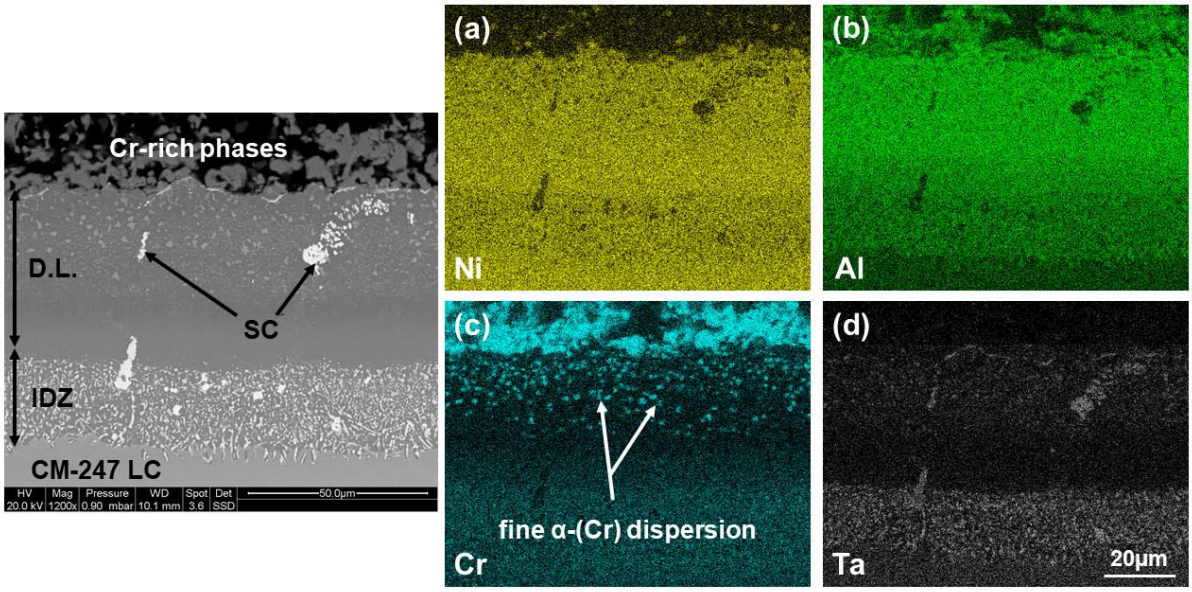

Fig. IV-27. BSE cross-section image and corresponding EDS maps of (a) Ni, (b) Al, (c) Cr and (d) Ta for the 33Cr-67Al double-layer system elaborated on CM-247 LC after annealing in flowing Ar (400°C-3h + 1080°C-6h).

EDS spot measurements were also performed in cross-section to get the concentration profile of the coating layer (Fig. IV-28a). The outer region of the diffusion layer was mainly composed of Al-rich β-NiAl phase with local Cr enrichments, as suggested from the optical micrograph. Note that the concentrations of W and Ta in the diffusion layer were not negligible here in comparison with the outward grown coatings of paragraph II.2. The detailed view of the outer region of the coating in BSE mode (Fig. IV-28b) emphasized the fine distribution of Cr-rich phases with an intermediate contrast. Note that a finer dispersion of bright spots was also observed in the coating matrix, attributed to Ta and W-rich precipitates. These observations confirmed that the initial growth of the coating occurred by inward diffusion of Al into the CM-247 LC superalloy.

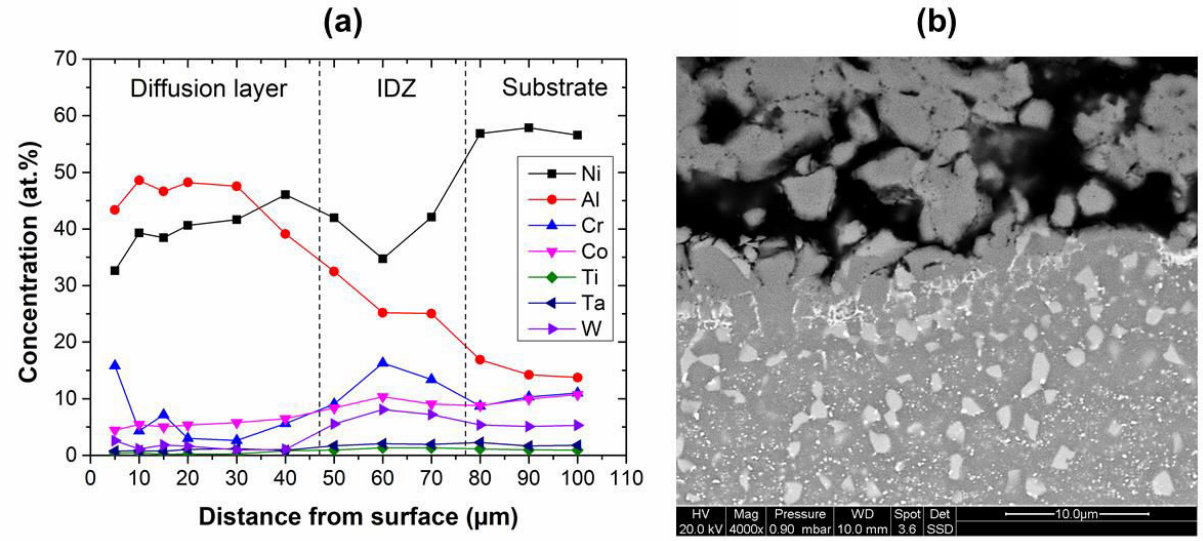

Fig. IV-28. (a) EDS concentration profile of the 33Cr-67Al double-layer system elaborated on CM-247 LC after annealing in flowing Ar (400°C-3h + 1080°C-6h) and (b) detailed view of the outer region of the diffusion layer.

b) Complete heat treatment (400°C-1h + 700°C-2h + 1100°C-2h)

A sample slurry coated with the 33Cr-67Al double-layer system was submitted to the complete heat treatment (400°C-1h + 700°C-2h + 1100°C-2h) tailored for the formation of the full thermal barrier system on nickel-based superalloys [12,27,44,47]. The surface macrograph attested the great homogeneity of the sample and the adherence of the top coat structure (Fig. IV-29a). The characteristic top coat structure composed of hollow alumina microspheres was observed on the sample surface by optical microscopy (Fig. IV-29b) [12,27,44,47].

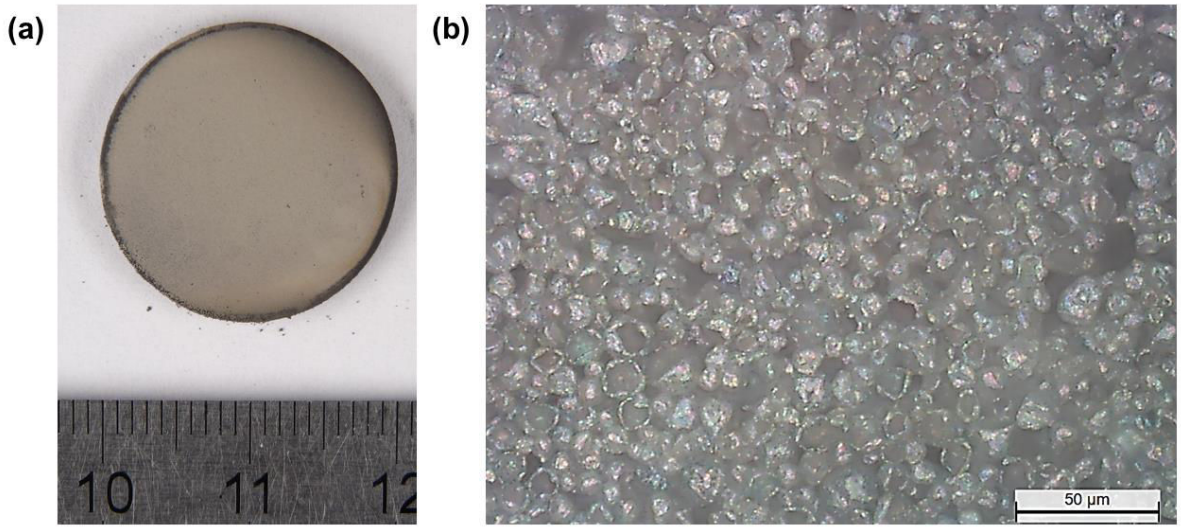

Fig. IV-29. (a) Macrograph and (b) surface micrograph of the top coat structure observed for the CM-247 LC sample slurry coated with the 33Cr-67Al double-layer system after annealing in flowing Ar (400°C-1h + 700°C-2h + 1100°C-2h).

A low magnification micrograph of the cross-section is given on Fig. IV-30. The overall thickness of the aluminized layer was of approximately 80µm, which is twice thicker than the outward grown coatings of Fig. IV-22. The diffusion layer, highlighted here with a dark contrast, mostly composed the coating whereas the IDZ at the interface additive layer-substrate was only 18±2µm thick. These observations were in good agreement with the microstructures obtained by Das et al. from single-step high Al activity packs after 2 hours of aluminizing at 1034°C (cf. Fig. IV-26b). Unlike the 56Cr-44Al double-layer system (Fig. IV-22a), substrate carbides were observed in the outer region of the coating. This confirmed the predominant inward diffusion of Al at the early stages of the aluminizing process [41]. The reaction front between the IDZ and the underlying substrate was not even for the 33Cr-67Al double-layer system compared to the 44Cr-56Al one. This could also be related to the initial inward growth of the coating and the delayed outward diffusion of nickel. The schematic representation of the coating formation proposed by Das et al. seems to very well fit with the present study (Fig. IV-26b).

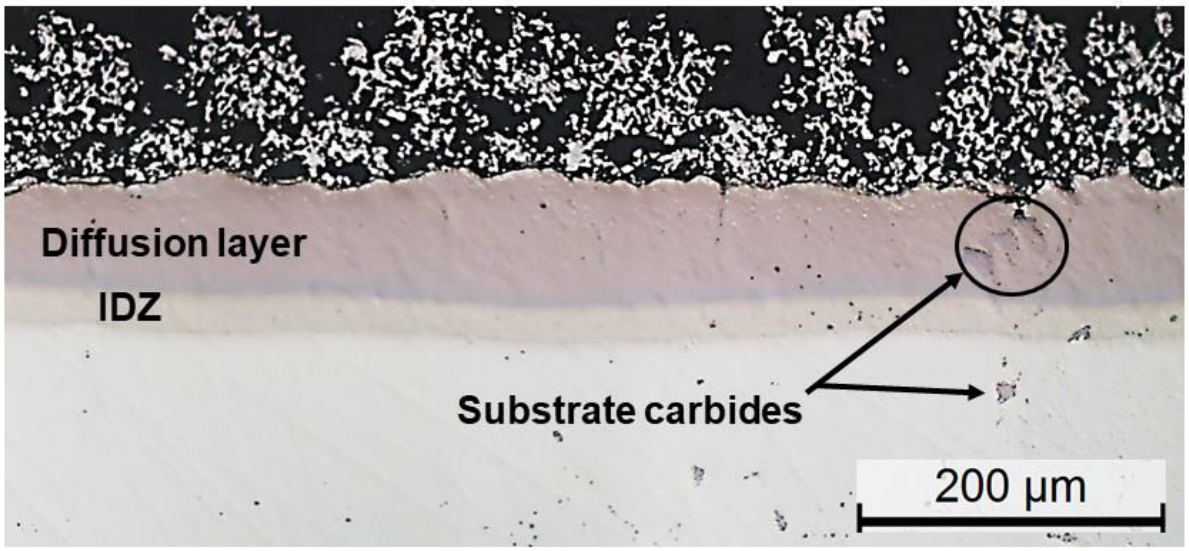

Fig. IV-30. Cross-section optical micrograph of the 33Cr-67Al double-layer system elaborated on CM-247 LC superalloy after the complete heat treatment in flowing Ar.

The EDS concentration profile of the coating layer is given in Fig. IV-31a. The high Al concentration of the diffusion layer confirmed that the Ni-rich β-NiAl phase was not directly formed during the aluminizing process and that Al-rich β-NiAl was formed instead. Since the Ni_2Al_3 phase has a very small domain of stability at temperatures greater than 1000°C [16], the formation of Al-rich β-NiAl was considered instead [41]. The W concentration in the diffusion layer was much higher than the one measured for the 56Cr-44Al composition after the complete heat treatment (Fig. IV-24). This was a consequence of the fast inward diffusion of Al in the superalloy causing the slow-diffusing elements to stay in the outer region of the diffusion layer. The BSE cross-section image highlighted the substrate carbides trapped within the inwardly grown coating (Fig. IV-31b). The formation of a thin IDZ suggested that nickel outward diffusion also occurred during the aluminizing process but to a lesser extent than the inward diffusion of Al. The mean composition of the Al_xCr_y phases was determined by EDS (44Al-49Cr-1Co-6Ni in at.%) and suggested the major formation of the Al_8Cr_5 phase [14,19].

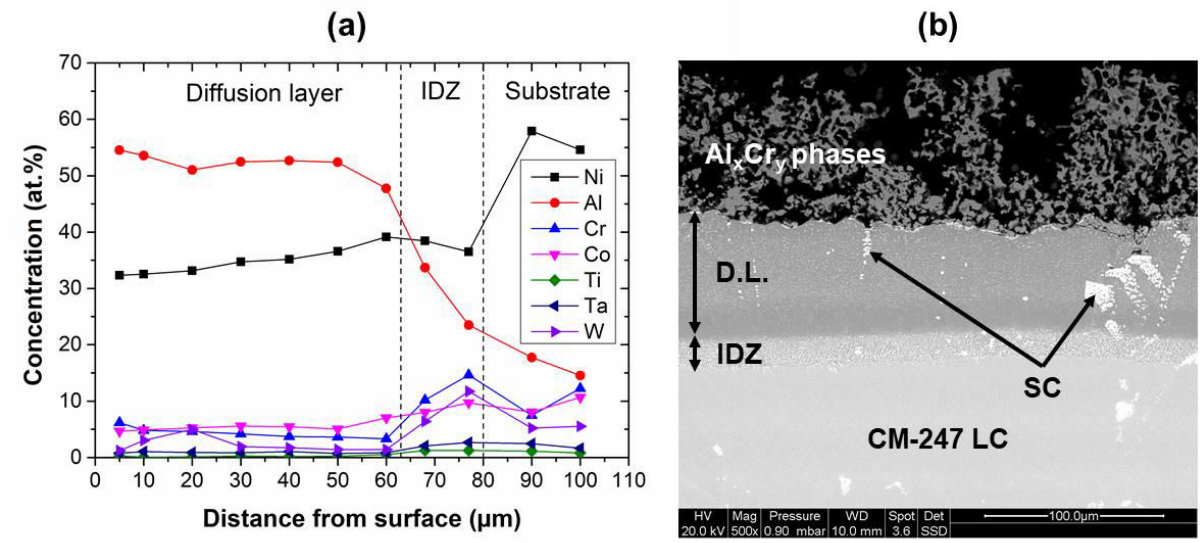

Fig. IV-31. EDS concentration profile of the 33Cr-67Al double-layer system elaborated on CM-247 LC after annealing in flowing Ar (400°C-1h + 700°C-2h + 1100°C-2h).

c) Discussion

The Cr/Al ratio of the Cr-Al double-layer system was found to significantly influence the microstructure of the coatings (Fig. IV-32) as observed in Chapter III for pure nickel substrate. Such differences resulted from the different mechanisms of formation of the coatings and especially from the predominant outward diffusion of Ni or inward diffusion of Al upon aluminizing [1,32,40,41,55]. Such differences were highlighted with the position of the substrate carbides in the coating allowing to determine the initial surface of the substrate before aluminizing (cf. Annex 1).

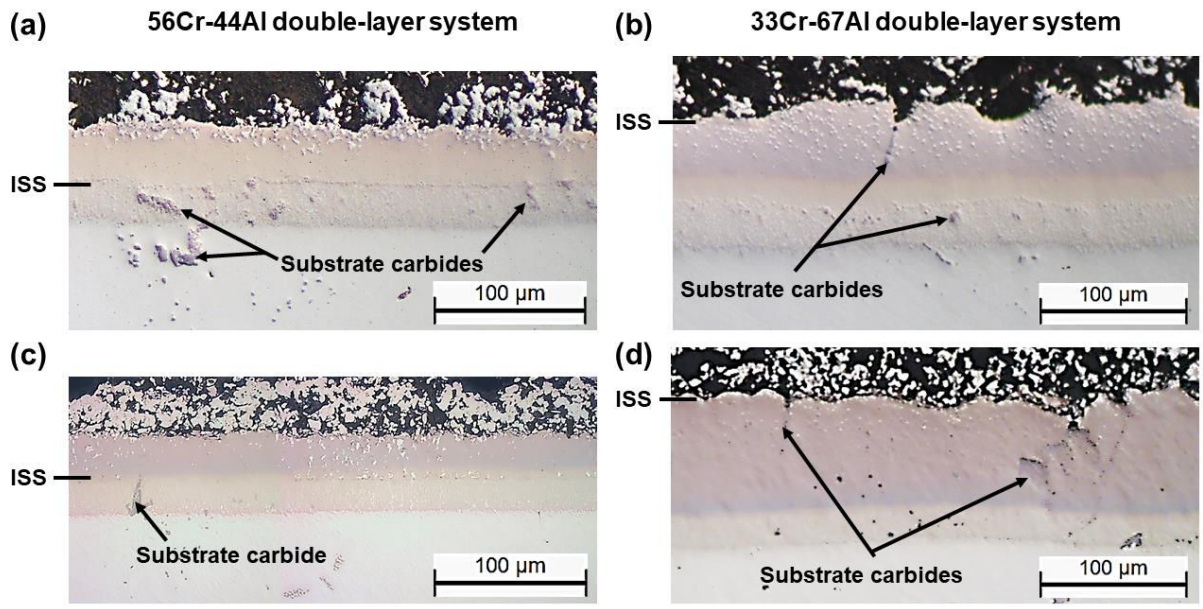

Fig. IV-32. Cross-section micrographs of the two Cr-Al double-layer system elaborated on CM-247 LC superalloy after (a), (b) conventional low-activity (400°C-3h + 1080°C-6h) and (c), (d) two-step heat treatment (400°C-1h + 700°C-2h + 1100°C-2h).

- ***Formation of "low-activity" coatings from the Cr-Al double-layer system:***

For the 56Cr-44Al composition (Fig. IV-32a and Fig. IV-32c), the coating was formed by predominant outward diffusion of nickel at high temperature. The Ni-rich β-NiAl phase was readily formed on the substrate surface with an outer additive layer free of precipitates above the initial substrate surface (ISS), cf. Annex 1. Because of the design of the present system, undissolved α-(Cr) phases were entrapped in the additive layer. The growth of the coating with the 56Cr-44Al double-layer system can therefore be simplified by the reaction *(Eq. IV-3)*:

$$Ni + Al_xCr_y \rightarrow \beta\text{-}NiAl + \alpha\text{-}(Cr) \qquad \textbf{(Eq. IV-3)}$$

The predominant outward diffusion of nickel dissolved the Al_xCr_y phases synthesized in the slurry deposit because of its limited solubility in Al-Cr phases (about 1 at.% in Al_4Cr and 3 at.% in Al_8Cr_5) [16]. Since the aluminizing treatment was done between 1080°C and 1100°C, the formation of Ni_2Al_3 phase was avoided and direct formation of β-NiAl occurred [40,41]. Since Cr has a low solubility in the β-NiAl phase, a large fraction of Cr remained undissolved as α–(Cr) phases through the β-NiAl coating matrix even after 6 hours at 1080°C (Fig. IV-32a).

The continuous outward diffusion of nickel upon aluminizing progressively consumed the Al_xCr_y phases in Al resulting in the formation of Cr-rich phases within the slurry deposit. Since the Cr solid solution dissolves up to 43 at.% of Al [16,43], the transformation of the Al_xCr_y phases into Cr(Al) considerably decrease the driving force of reaction *(Eq. IV-3)* and the new simplified reaction can be written:

$$\mathrm{Ni} + \alpha\text{-}\mathrm{Cr(Al)} \rightarrow \beta\text{-}\mathrm{NiAl} + \alpha\text{-}(\mathrm{Cr}) \qquad \textbf{(Eq. IV-4)}$$

Considering the Ni-Al-Cr ternary equilibrium [19] and the observations of Huang et al. [10], only β-NiAl and α-(Cr) phases are stable at the aluminizing temperature. Therefore, as soon as α-Cr(Al) constitutes the main fraction of the slurry deposit (i.e. the Al donor), the kinetics of aluminizing decreased because of the very low driving force of reaction *(Eq. IV-4)*. This would explain why the aluminized layer of the sample heat treated with the 20Al80Cr mixed composition was so thin (Fig. IV-14e).

As discussed in paragraph II.2, the formation of the Al-rich β-NiAl phase for the sample presented in Fig. IV-32c is most likely to form upon cooling [41,45,46]. This layer was not observed for the sample heat treated with the conventional heat treatment. After 6 hours of aluminizing at 1080°C, the slurry deposit should be composed of α-(Cr) phases thus considerably limiting the Al activity. Upon cooling, the Al activity was then not high enough to foster the formation of an Al-rich β-NiAl layer by inward diffusion of Al. Even though the aluminizing temperature was higher for the complete heat treatment (1100°C), the shorter time of diffusion (2 hours) did not allow the full decomposition of the Al_xCr_y phases (confirmed with EDS measurements). The Al activity of the slurry deposit was therefore high enough upon cooling to cause inward diffusion of Al into the β-NiAl coating matrix. This Al enrichment fostered the formation of Al-rich β-NiAl phase, composing nearly the whole additive layer after annealing (Fig. IV-32c) because of the greater diffusivity of Al than of Ni in such Al-rich β–NiAl phase [45,46].

- ***Formation of "high-activity" coatings from the Cr-Al double-layer system:***

The mechanisms of formation of the coatings for the 33Cr-67Al double-layer system were different than the ones observed for the 56Cr-44Al explaining the different microstructures observed (Fig. IV-32b and Fig. IV-32d). One key aspect here is that inert substrate carbides were found in the outer region of the aluminized layer, which indicated that the initial substrate surface remained at the aluminized layer-slurry deposit interface (cf. Annex 1). Based on the work of Das et al. [41], the coating formation involved inward diffusion of Al upon heating through the formation of Al-rich β-NiAl phase. Once the high temperatures reached (1034°C in the work of Das et al.), outward diffusion of nickel from the substrate was promoted. This differs from the state-of-the art "two-step" high activity processes where Al inward diffusion occurs in a first step at low temperature (700°C-900°C) and nickel outward diffusion is promoted in a second step at high temperature (1000°C-1150°C) to stabilize the β-NiAl phase [33,40,55]. Das et al. observed that the single-step process resulted in a non-stationary reaction front moving outwardly during the aluminizing process. The mechanisms of coating formation are summarized on Fig. IV-26b.

Since the coating formation of the 33Cr-67Al double-layer system started by inward diffusion of aluminium, the reaction *(Eq. IV-3)* was not governing the aluminizing process. In this system, the Cr interlayer acted as a barrier for Al ingress into the substrate (cf. Fig. III-29 in Chapter III). Upon heating, Al progressively reacted with the Cr interlayer forming Al-rich Al_xCr_y phases in the slurry deposit (cf. Fig. III-16 in Chapter III). Considering the 67Al33Cr composition, the main synthesized compound at 650°C was the Al_4Cr phase. Upon heating in DSC, the decomposition of this phase following the invariant reaction $Al_4Cr \rightarrow L + Al_8Cr_5$ was found to occur at approximately 1040°C (cf. Fig. III-5a in Chapter III). One could therefore expect that this reaction is likely to happen in the slurry deposit. However, this reaction was presumably not the only driving force to explain the coating formation through the appearance of a liquid phase. To confirm that, a CM-247 LC slurry coated sample with the 33Cr-67Al double-layer system was annealed at a temperature lower than 1040°C. A SEM cross-section image of the sample after annealing (400°C-3h + 1000°C-6h) is given on Fig. IV-33. The microstructure of the aluminized layer was very close to the one obtained by Das et al. with single-step high activity pack in the early stage of aluminizing [41]. A thin IDZ was formed under the main coating diffusion layer. The substrate carbides were found in the whole thickness of the aluminized layer attesting that its formation predominantly involved inward diffusion of Al. The Al_xCr_y intermetallic compounds were still present above the aluminized layer after annealing.

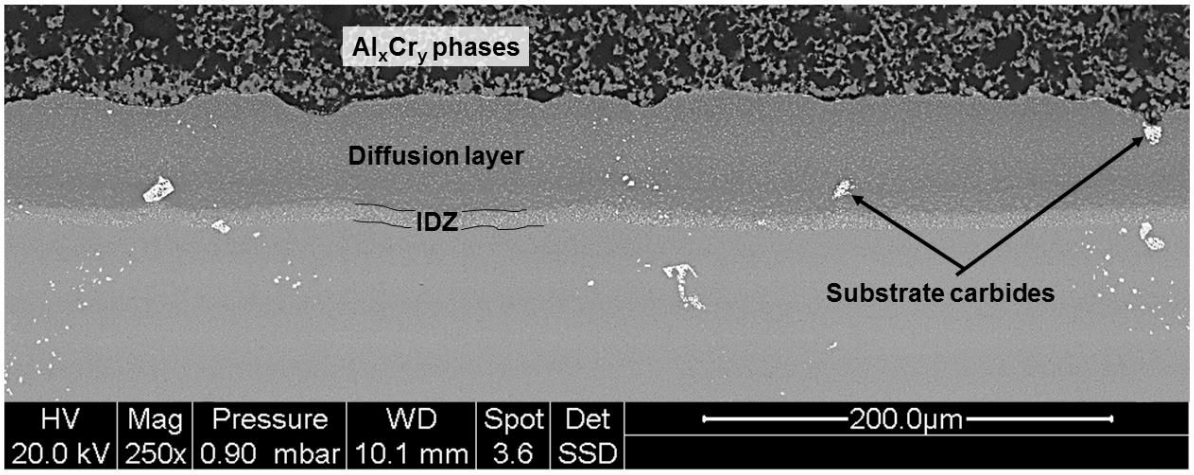

Fig. IV-33. BSE cross-section image of CM-247 LC slurry coated with the 33Cr-67Al double-layer system after annealing in flowing Ar (400°C-3h + 1000°C-6h).

To confirm the hypothesis that the coating formation followed the mechanisms proposed by Das et al., the composition of the diffusion layer must be found in the Al-rich β-NiAl domain [41]. The EDS concentration profiles (Fig. IV-34b) were realized on a representative area of the sample (Fig. IV-34a). Note that the coating formed on the CM-247 LC superalloy was composed of an additional layer made of hollow alumina spheres [39]. The overall Al concentration of the diffusion layer remained below 55 at.%. and was not constant in the diffusion layer. The Cr concentration of the outer region of the diffusion layer was higher than that of high activity slurry aluminized CM-247 LC [11,12,44], which indicates that some Cr diffused in the diffusion layer. A deeper characterization of the outer region of the coating highlighted the major composition of both Cr-rich phases and Ni-rich phases (Fig. IV-35a). The distribution of fine bright precipitates corresponded to substrate elements with low solubility in the β-NiAl phase (mainly Ta and W). On the BSE image of Fig. IV-35a, the coating matrix with a dark contrast refers to the Ni-enriched phase whereas the phases with an intermediate contrast were Cr-enriched. The exact composition of the phases could not be determined because of the large spot resolution of the EDS but, according to literature, were presumably Al-rich β-NiAl and Al_8Cr_5 phases [8,10]. This two-phase stability is in good agreement with Ni-Al-Cr ternary diagram at 1000°C [14,16]. These observations confirmed that the Al inward diffusion was significantly faster than the nickel outward diffusion for the 33Cr-67Al double-layer system.

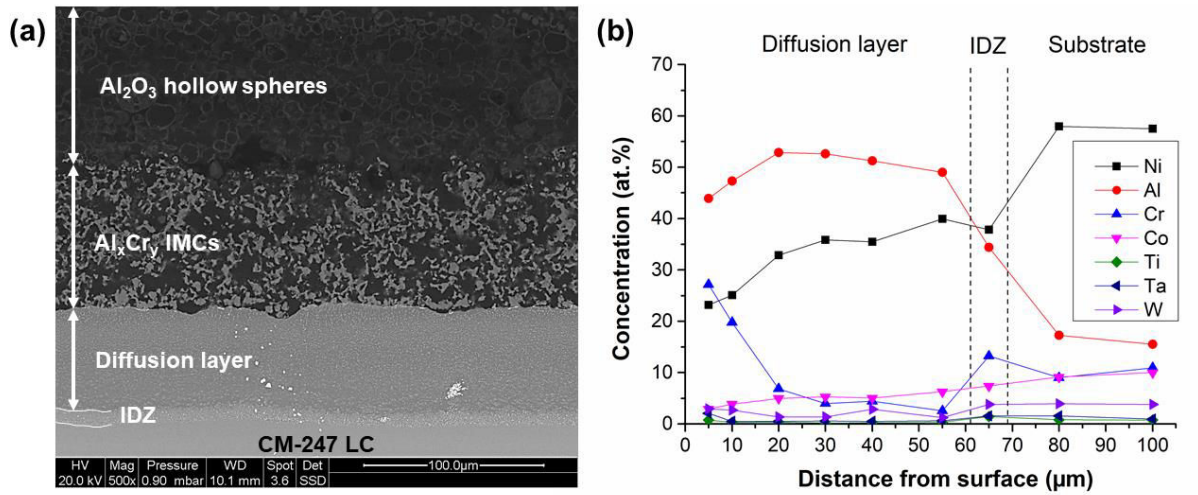

Fig. IV-34. (a) BSE cross-section image and (b) EDS concentration profile of CM-247 LC slurry coated with the 33Cr-67Al double-layer system after annealing in flowing Ar (400°C-3h + 1000°C-6h).

EDS spot measurements were performed in the Al_xCr_y phases present above the diffusion layer (Fig. IV-35a). Two different phases were observed in the BSE images at higher magnification (not shown) and gave average composition of 61Al-34Cr-1Co-3Ni (at.%) and 45Al-50Cr-1Co-4Ni (at.%). By correlation with the surface XRD pattern (Fig. IV-35b) and the Ni-Al-Cr ternary diagram at 1000°C [14,16], the presence of both Al_8Cr_5 and $AlCr_2$ phases was suggested ($AlCr_2$ was formed upon cooling from α-(Cr) phases). Note that α-Al_2O_3 was not detected neither by XRD nor Raman surface analyses whereas some reflections were identified as the γ-Al_2O_3 [60,61]. The detection of γ-Al_2O_3 was probably coming from the top coat structure based on hollow Al_2O_3 spheres emphasized on Fig. IV-34a [61,62]. These analyses therefore suggested that the transformation of γ-Al_2O_3 into α-Al_2O_3 did not occur on the oxide shells after the 6 hours annealing at 1000°C in Ar. This result is not in agreement with the observations of Kolarik et al. upon oxidation in air of 2-5µm Al particles [60]. This discrepancy

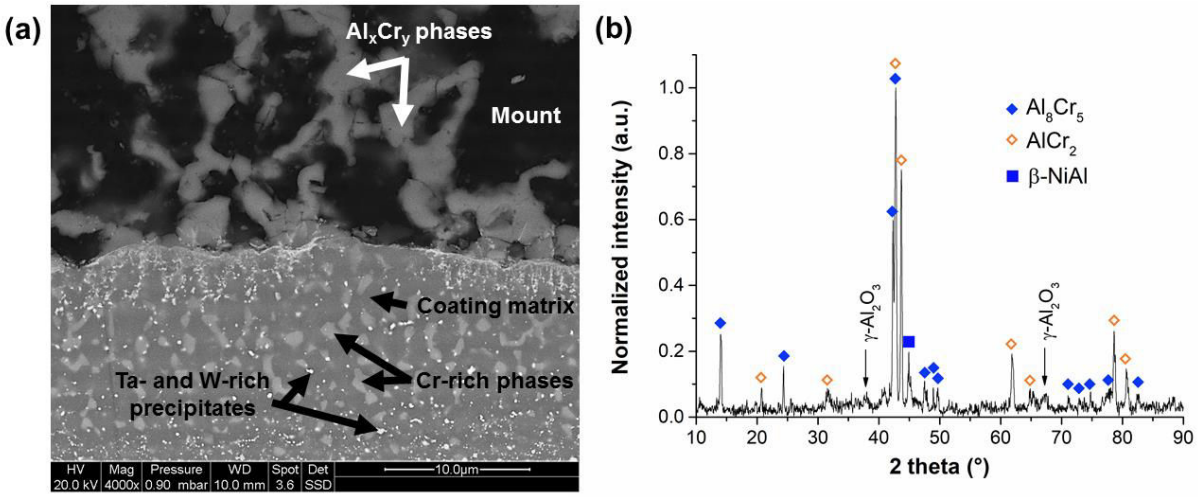

Fig. IV-35. (a) Details of the outer region of the diffusion layer in BSE mode and (b) surface XRD pattern (full system presented on Fig. IV-34b).

will be discussed in Chapter V by investigating the influence of the atmosphere on the peripheral oxidation of Al microparticles.

Considering the 33Cr-67Al composition, Al_4Cr was the main synthesized compound before reaching the dwell temperature of 1000°C (cf. Fig. III-15 in Chapter III). The high Al activity of this phase seemed to be high enough to foster the inward diffusion of Al into the substrate. The evidence of inward diffusion of Al after annealing at 1000°C confirmed that the reaction $Al_4Cr \rightarrow L + Al_8Cr_5$ was not responsible of the coating formation. The Al-Cr phases synthesized in the slurry deposit therefore released the Al diffusing inwardly into the underlying substrate. Consequently, the composition of the intermetallic phases changed from Al_4Cr to Al_8Cr_5 and $AlCr_2$ after 6 hours annealing at 1000°C. This change in composition attested the progressive Al depletion of the Al-Cr donors to diffuse in the substrate. Since the Ni_2Al_3 phase has a very low domain of stability at 1000°C [16], Al-rich β-NiAl formed that expelled Cr out. Further Al ingress combined with the segregated Cr and led to a fine precipitation of Cr-rich phases (presumably Al_8Cr_5 [10]) in the coating matrix (Fig. IV-35a).

- ***Influence of the aluminizing temperature on the outward diffusion of nickel:***

The BSE cross-section images of 33Cr-67Al system presented on Fig. IV-36a and Fig. IV-36b suggested that the aluminizing temperature had a significant influence on the resulting microstructure of the coating. The interdiffusion zone (IDZ) was much thicker for the sample annealed at 1080°C (Fig. IV-36a) suggesting that the outward diffusion of nickel was more important than that for the sample annealed at 1000°C (Fig. IV-36b). This also confirms that the formation of such coatings first involved inward diffusion of Al and then the delayed outward diffusion of nickel [41].

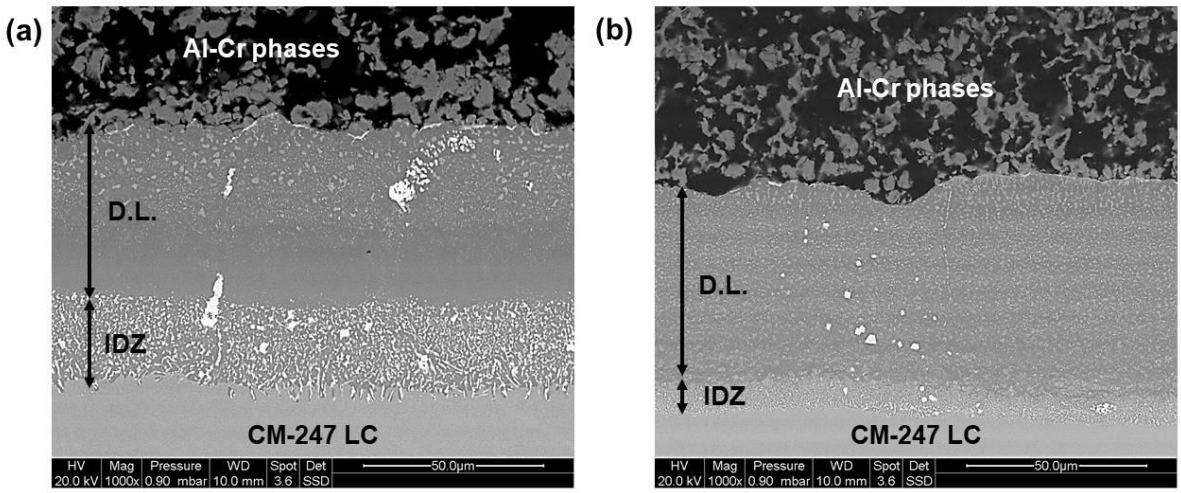

Fig. IV-36. BSE cross-section images of the 33Cr-67Al double-layer system elaborated on CM-247 LC after (a) 400°C-3h + 1080°C-6h and (b) 400°C-3h + 1000°C-6h in Ar.

III. Summary and outlook

Table IV-2 summarizes the different slurry coating systems elaborated on CM-247 LC superalloy. The details of the coating microstructures obtained after annealing treatments in flowing Ar are also given. Their potential abilities to confer hot corrosion and oxidation resistance are also indicated whereas only two systems were found to confer a potential thermal insulation with an adherent top coat composed of hollow alumina microspheres.

Table IV-2. Summary of the different slurry coating systems elaborated on CM-247 LC superalloy in flowing Ar. HT-1: 400°C-3h +1080°C-6h, HT-2: 400°C-1h + 700°C-2h + 1100°C-2h, HT-3: 400°C-3h + 1000°C-6h. HA for high-activity and LA for low-activity.

	Al-Cr mixed slurry			Cr-Al double-layer system				
	67Al33Cr	44Al56Cr	20Al80Cr	56Cr-44Al		33Cr-67Al		
Heat treatment	HT-1			HT-1	HT-2	HT-1	HT-2	HT-3
Top coat	Adherent	Adherent	Adherent	Detached	Partially detached	Partially detached	Adherent	Adherent
Coating microstructure	HA type	LA type	Complex	LA type	LA type	HA type	HA type	HA type
Major phases	β-NiAl	β-NiAl	β-NiAl + precipitates	β-NiAl	β-NiAl	β-NiAl	β-NiAl	β-NiAl + Al_8Cr_5
IDZ/Diffusion layer ratio	~0.4	0.4 to 1	~2	~1	~1	~0.4	~0.2	~0.1
Capability of the coating	Bond coat + top coat	Not suitable	Not suitable	Bond coat	Bond coat	Bond coat	Bond coat + top coat	Bond coat + top coat
Potential resistance	Oxidation	-	-	Hot corrosion + oxidation	Hot corrosion + oxidation	Hot corrosion + oxidation	Hot corrosion + oxidation	Hot corrosion + oxidation
Potential thermal insulation	-	-	-	-	-	-	Yes	Yes

From these experiments, two systems were selected for the oxidation tests (Chapter VI): the low-activity Cr-Al double-layer system (with HT-1) as a bond coat and the 33Cr-67Al double-layer system (with HT-3) as a complete thermal barrier system. The 2 hours dwell at 700°C of HT-2 presumably conferred a better adherence of the top coat on the underlying diffusion coating for both 56Cr-44Al and 33Cr-67Al systems. However, the oxide shells of the alumina hollow microspheres remained thin after annealing in flowing Ar (Fig. IV-34a) and the top coat is expected to be unable to provide the required erosion resistance. In this way, Chapter V will present the functionalization of the complete thermal barrier system. The influence of the atmosphere (Ar, air) on the aluminizing and the formation of the complete thermal barrier system will be investigated. Special attention will be given on the thickening and the sintering of the alumina shells forming the ceramic top coat.

References

[1] G.W. Goward, *Current Research on the Surface Protection of Superalloys for Gas Turbine Engines*, *Journal of Metals* **22** (1970), pp. 31-39.

[2] J. Stringer, *Design of coatings for high temperature corrosion protection*, In: R. Kossowly, S.C. Singhal. NATO ASI Series vol. **85** (1984), pp. 561-587. Springer, Dordrecht.

[3] M. Donachie, S. Donachie, *Superalloys: A Technical Guide 2nd edition,* ASM International (2002).

[4] B. Ahmad, P. Fox, *Oxidation of Metals* ***52*** (1999), pp. 113-138.

[5] A. Ul-Hamid, *Materials Chemistry and Physics* ***80*** (2003), pp. 135-142.

[6] D.P. Whittle, J. Stringer, *Philosophical Transactions of the Royal Society London A* ***295*** (1980), pp. 309-329.

[7] J.-M. Brossard, J. Balmain, F. Sanchette, G. Bonnet, *Oxidation of Metals* ***64*** (2005), pp. 43-61.

[8] D.C. Tu, L.L. Seigle, *Thin Solid Films* ***95*** (1982), pp. 47-56.

[9] H.L. Huang, Y.Z. Chen, D. Gan, *Materials Science and Engineering A* ***328*** (2002), pp. 238-244.

[10] H.L. Huang, D. Gan, *Materials Science and Engineering A* ***485*** (2008), pp. 550-557.

[11] M.C. Galetz, X. Montero, M. Mollard, M. Gunthner, F. Pedraza, M. Schütze, *Intermetallics* ***44*** (2014), pp. 8-17.

[12] B. Rannou, *Slurry coatings from aluminium microparticles on Ni-based superalloys for high-temperature oxidation protection*, PhD Thesis, Université de La Rochelle (2012).

[13] W.H. Tian, C.S. Han, M. Nemoto, *Intermetallics* ***7*** (1999), pp. 59-67.

[14] W. Huang, Y.A. Chang, *Intermetallics* ***7*** (1999), pp. 863-874.

[15] A. Chien, D. Gan, P. Shen, *Materials Science and Engineering A* ***206*** (1996), pp. 215-224.

[16] B. Grushko, W. Kowalski, D. Pavlyuchkov, B. Przepiórzyński, M. Surowiec, *Journal of Alloys and Compounds* ***460*** (2008), pp. 299-304.

[17] W.J. Cheng, C.J. Wang, *Applied Surface Science* ***277*** (2013), pp. 139-145.

[18] F. Pedraza, M. Mollard, B. Rannou, J. Balmain, B. Bouchaud, G. Bonnet, *Materials Chemistry and Physics* ***134*** (2012), pp. 700-705.

[19] Y. Wang, G. Cacciamani, *Journal of Alloys and Compounds* ***688*** (2016), pp. 422-435.

[20] Y. Le Guevel, B. Grégoire, B. Bouchaud, P. Bilhé, A. Pasquet, M. Thiercelin, F. Pedraza, *Surface and Coatings Technology* ***292*** (2016), pp. 1-10.

[21] J. Benoist, K.F. Badawi, A. Malié, C. Ramade, *Surface and Coatings Technology* ***182*** (2004), pp. 14-23.

[22] J. Benoist, K.F. Badawi, A. Malié, C. Ramade, *Surface and Coatings Technology* ***194*** (2005), pp. 48-57.

[23] Y. Le Guevel, *Dissolution sélective de produits de corrosion et revêtements sur matériaux de turbine aéronautique par méthodes électrochimiques*, PhD Thesis, Université de La Rochelle (2016).

[24] B.M. Warnes, D.C. Punola, *Surface and Coatings Technology* ***94-95*** (1997), pp. 1-6.

[25] D.R. Lide, CRC Handbook of Chemistry and Physics, 1995.Boca Raton, Section 12:159.

[26] B. Grégoire, G. Bonnet, F. Pedraza, *Intermetallics* ***81*** (2017), pp. 80-89.

[27] M. Brossard, *Influence de l'eau (vapeur, liquide) et du régime d'oxydation sur la dégradation de revêtements alumino-formeurs sur superalliage à base nickel*, PhD Thesis, Université de La Rochelle (2014).

[28] S.M. Merchant, M.R. Notis, J.I. Goldstein, *Metallurgical Transactions A* ***21*** (1990), pp. 1901-1909.

[29] F. Pedraza, C. Tuohy, L. Whelan, A.D. Kennedy, *Materials Science Forum* ***461-464*** (2004), pp. 305-312.

[30] B. Grushko, E. Kowalska-Strzęciwilk, B. Przepiórzyński, M. Surowiec, *Journal of Alloys and Compounds* ***402*** (2005), pp. 98-104.

[31] Pang, Y. Zhan, Y. Du, *Journal of Solid State Chemistry* ***198*** (2013), pp. 344-356.

[32] B. Gleeson, W.H. Cheung, W. Da Costa, D.J. Young, *Oxidation of Metals* ***38*** (1992), pp. 407-424.

[33] R. Streiff, J.M. N'Gandu Muamba, D.H. Boone, *Thin Solid Films* ***119*** (1984), pp. 291-300.

[34] I.S. Kim, B.G. Choi, S.M. Seo, D.H. Kim, C.Y. Jo, *Materials Letters* ***62*** (2008), pp. 1110-1113.

[35] M.Z. Alam, D. Chatterjee, B. Venkataraman, V.K. Varma, D.K. Das, *Materials Science and Engineering A* ***527*** (2010), pp. 6211-6218.

[36] M.Z. Alam, D.V.V. Satyanarayana, D. Chatterjee, R. Sarkar, D.K. Das, *Materials Science and Engineering A* ***536*** (2012), pp. 14-23.

[37] Z.D. Xiang, J.S. Burnell-Gray, P.K. Datta, *Journal of Materials Science* ***36*** (2001), pp. 5673-5682.

[38] X. Montero, M.C. Galetz, M. Schütze, *Surface and Coatings Technology* ***206*** (2011), pp. 1586-1594.

[39] F. Pedraza, M. Mollard, B. Rannou, B. Bouchaud, J. Balmain, G. Bonnet, *Oxidation of Metals* ***85*** (2016), pp. 231-244.

[40] G.W. Goward, D.H. Boone, *Oxidation of Metals* ***3*** (1971), pp.475-495.

[41] D.K. Das, V. Singh, S.V. Joshi, *Metallurgical and Materials Transactions A* ***29*** (1998), pp. 2173-2188.

[42] X. Montero, M.C. Galetz, M. Schütze, *Surface and Coatings Technology* ***222*** (2013), pp. 9-14.

[43] J.G. Costa Neto, S. Gama, C.A. Ribeiro, *Journal of Alloys and Compounds* ***182*** (1992), pp. 271-280.

[44] M. Mollard, *Elaboration de systèmes barrière thermique par barbotine. Comportement du nickel et de ses superalliages revêtus en oxydation cyclique à haute température*, PhD Thesis, Université de La Rochelle (2012).

[45] S. Shankar, L.L. Seigle, *Metallurgical Transactions A* ***9*** (1978), pp. 1467-1476.

[46] J.M. Brossard, B. Panicaud, J. Balmain, G. Bonnet, *Acta Materialia* ***55*** (2007), pp. 6586-6595.

[47] B. Rannou, B. Bouchaud, J. Balmain, G. Bonnet, F. Pedraza, *Oxidation of Metals* ***81*** (2014), pp. 139-149.

[48] J. Grüters, M.C. Galetz, *Intermetallics* ***60*** (2015), pp. 19-27.

[49] H. Wei, H.Y. Zhang, G.C. Hou, X.F. Sun, M.S. Dargusch, X. Yao, Z.Q. Hu, *Journal of Alloys and Compounds* ***481*** (2009), pp. 326-335.

[50] B. Han, Y. Ma, H. Peng, L. Zheng, H. Guo, *Corrosion Science* ***102*** (2016), pp. 222-232.

[51] R.J. Thompson, J.C. Zhao, K.J. Hemker, *Intermetallics* ***18*** (2010), pp. 796-802.

[52] D.K. Das, V. Singh, S.V. Joshi, *Materials Science and Technology* ***19*** (2003), pp. 695-708.

[53] B.A. Pint, K.L. More, I.G. Wright, *Oxidation of Metals* ***59*** (2003), pp. 257-283.

[54] F. Pedraza, R. Podor, *Materials Characterization* ***113*** (2016), pp. 198-206.

[55] R. Streiff, D.H. Boone, *Journal of Materials Engineering* ***10*** (1988), pp. 15-26.

[56] H. Okamoto, *Journal of Phase Equilibria and Diffusion* ***29*** (2008), pp. 112-113.

[57] B. Hu, W. Zhang, Y. Peng, Y. Du, S. Liu, Y. Zhang, *Thermochimica Acta* ***561*** (2013), pp. 77-90.

[58] K. Mahdouk, J.-C.Gachon, *Journal of Phase Equilibria* ***21*** (2000), pp. 157-166.

[59] Y.Q. Wang, G. Sayre, *Surface and Coatings Technology* ***203*** (2009), pp. 1264-1272.

[60] V. Kolarik, M. Juez-Lorenzo, H. Fietzek, *Materials Science Forum* ***696*** (2011), pp. 290-295.

[61] R. Roussel, V. Kolarik, M. Juez Lorenzo, H. Fietzek, *Oxidation of Metals* ***81*** (2014), pp. 179-189.

[62] R. Roussel, *Investigación de recubrimientos multifuncionales en base de micropartículas esféricas de aluminio para aplicación a altas temperaturas,* PhD Thesis, Universidad Complutense de Madrid (2013).

Chapter V – Influence of the atmosphere (Ar, air) on the formation of thermal barrier coatings (TBC) from simple Al and Cr-Al double-layer slurry systems

I. General background on the oxidation of Al particles and the formation of hollow alumina spheres 159

II. Influence of the atmosphere (Ar, air) on the aluminizing of pure nickel from Al microparticles 163

II.1. Diffusion heat treatment (400°C-1h + 700°C-2h) 163

II.2. Complete heat treatment (400°C-1h + 700°C-2h + 1100°C-2h) 167

II.3. Complete heat treatment with the introduction of synthetic air upon annealing 173

II.4. Discussion 177

III. Influence of the atmosphere (Ar, air) for the Cr-Al double-layer system 181

III.1. Characterization of the top coat structure after heat treatment in Ar 181

III.2. Influence of the atmosphere (Ar, air) on the formation of the Cr-Al double-layer system on pure nickel 182

III.3. Reactivity between Al microparticles and oxide powders (NiO, Cr_2O_3 and Al_2O_3) 191

III.4. Discussion 196

IV. Summary and outlook 200

References 202

I. General background on the oxidation of Al particles and the formation of hollow alumina spheres

Recently, Pedraza et al. investigated the influence of the annealing conditions on the formation of hollow alumina microspheres from Al microparticles [1]. The composition of the atmosphere was found to play a significant role on the release of Al from the microparticles and their simultaneous oxidation as reported by other authors [2-5]. The release of Al from the particles was associated with concomitant mechanisms including the peripheral oxidation of the spheres and a volume variation due to the expansion of the Al core upon heating [1,6]. Depending on the atmosphere (inert or oxidizing), the thickness of the oxide shells and the amount of Al flowing out from the microspheres were different. These concomitant mechanisms were first proposed by Levitas et al. for nano-sized and micro-sized Al particles [7-10] and are presented on Fig. V-1. For micro-sized particles, the initial amorphous alumina shell grows until it reaches a critical thickness of approximately 4 to 5 nm [3,11,12]. The amorphous alumina shell therefore crystallizes into γ-Al_2O_3 usually at about 550°C before the melting of Al [2,3,13,14]. Since the density of γ-Al_2O_3 is greater than that of the amorphous layer [6,15], the newly formed γ-Al_2O_3 layer is no longer continuous on the aluminium surface, which induces cracks in the alumina shell (Fig. V-1). If the p_{O_2} is high enough, healing of the defective alumina shell occurs by oxidation of the exposed metallic Al. When the temperature is greater than that of the melting of Al, molten Al can diffuse through the cracks depending on the pressure build-up in the Al core and the mechanical strength of the alumina shell [6,7,10].

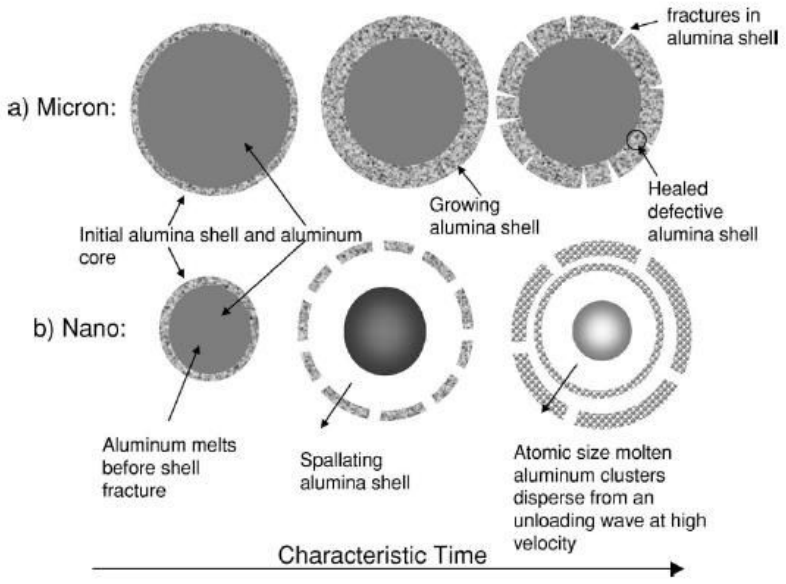

Fig. V-1. Mechanisms of oxidation and of Al diffusion for micro-sized and nano-sized particles proposed by Levitas et al. [7].

Trunov et al. [2,16] and Rufino and collab. [3] studied the oxidation behaviour of Al powders with different particles size in a dynamic dry air atmosphere. These authors identified up to four domains on the oxidation curves depending on the temperature range. Detailed explanations are given in Ref. [16] with the kinetics of aluminium oxidation and the calculation of activation energies for the different identified transformations. Fig. V-2 summarizes the different stages of oxidation of Al microparticles identified by thermal analysis (from Ref. [16]). Up to four stages of oxidation were considered from these studies [2,3,16]:

- **ambient-450°C (stage I):** weight loss due to desorption of water and organic compounds from the surface and to the dehydroxylation of the amorphous oxide layer, followed by a slow increase attributed to the growth of the amorphous oxide layer.
- **450°C-650°C (stage II):** stepwise oxidation in a narrow temperature range (crystallization of the amorphous alumina into γ-Al_2O_3). This transformation occurred when the amorphous layer reached a critical thickness of about 4 to 5 nm [3,11,12]. The newly formed γ-Al_2O_3 is no longer continuous on the aluminium surface exposing metallic Al to the atmosphere [6,15]. This induces an increase of the oxidation rate at the beginning of stage II while the γ-Al_2O_3 is healing and eventually covers the whole aluminium surface at the end of stage II.
- **650°C-950°C (stage III):** second acceleration of the oxidation rate attributed to the growth of the γ-Al_2O_3 layer accompanied by further crystallographic transformations. These transformations probably follow the γ-$Al_2O_3 \rightarrow \delta$-$Al_2O_3 \rightarrow \theta$-$Al_2O_3 \rightarrow \alpha$-$Al_2O_3$ sequence as reported in other studies [14,15,17,18] although the direct transformation γ-$Al_2O_3 \rightarrow \alpha$-$Al_2O_3$ has also been reported [2,15,19]. These transformations were not expected to significantly affect the oxidation rate of γ-Al_2O_3 according to Trunov et al. [16].
- **950°C-1500°C (stage IV):** progressive transformation of transition aluminas into the stable α-Al_2O_3 polymorph by the end of stage III. The phase transition γ-$Al_2O_3 \rightarrow \alpha$-$Al_2O_3$ induces a volume shrinkage of about 13.8% because of their different crystal structures [6,20]. This leads to the formation of pores and nano-cracks in the alumina shell [6]. When the oxide shell is completely converted into α-Al_2O_3, the oxidation rate rapidly decreases. This could be attributed to the slow grain boundary diffusion within the α-Al_2O_3 scale upon further oxidation [16].

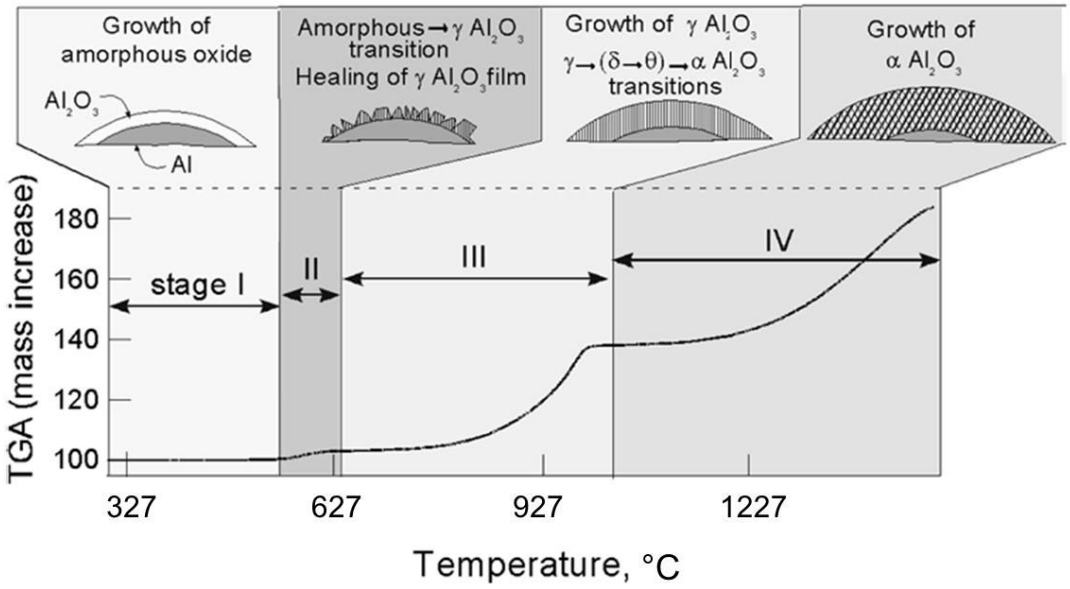

Fig. V-2. Mass variation of Al powder oxidizing in a thermal analyser with the identification of the different stages of oxidation. The respective changes in the growing alumina scale are presented schematically (from Ref. [16]).

It has to be noted that the temperature at which the events occur mainly depends on the size of the particles [1,3,16]. Thermal events are thus delayed to higher temperatures by increasing the particle size. Kolarik et al. investigated the oxidation of two types of micro-sized Al particles in air by *in situ* high-temperature X-ray diffraction [20]. The transformation of the amorphous alumina layer into γ-Al_2O_3 was detected from 425°C with 0.3-0.7 µm particles and from 550°C with 2-5 µm ones. Therefore, considering that the Al particles of the present study have a mean diameter of 8 µm (cf. Fig. II-2 in Chapter II), this transformation is expected to occur to at 550°C or even higher.

The mechanisms of formation of the environmentally friendly slurry coatings (from Al microparticles) have already been presented in inert atmosphere (Ar) [21,22] and air [23] on various nickel-based materials. However, none of such studies investigated the influence of the atmosphere on both the aluminizing of the substrate and the consolidation of the ceramic top coat composed of hollow alumina spheres. Therefore, the present study aimed at elucidating the influence of the atmosphere during the annealing treatment on these two features. Pure nickel was used as a model material before extrapolation to nickel-based superalloys. Note that in Ref. [23], the authors applied an intermediate electrodeposited nickel layer before slurry deposition. The intermediate layer was shown to increase the adherence of the ceramic top coat. If the authors described the mechanisms of formation of the complete thermal barrier system (aluminide coating + alumina top coat) in air, the benefit of the nickel intermediate layer was not fully explained.

Two different atmospheres were tested: Ar (inert) and synthetic air (oxidizing). Since the heating rate has a strong influence on the peripheral oxidation and the opening of the Al microparticles [1], this parameter was fixed at 5°C/min. Trunov et al. have shown that the slower the heating ramp, the thicker the aluminium oxide shell [2]. Two heat treatments were performed based on previous works done in the group of Pedraza et al. [24-26] for a better understanding of the mechanisms (Fig. V-3).

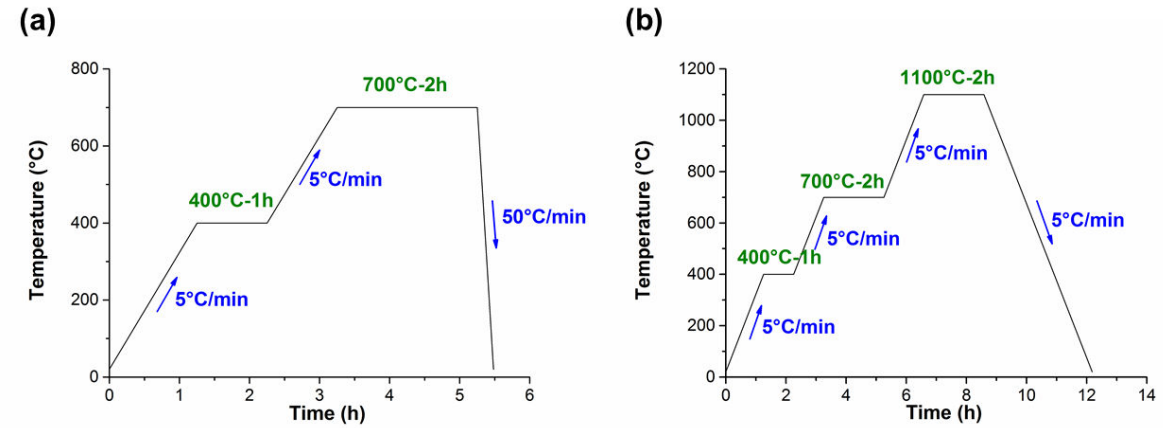

Fig. V-3. Details of the annealing treatments performed to investigate the influence of the atmosphere on the aluminizing of pure nickel with (a) the diffusion heat treatment and (b) the complete heat treatment.

II. Influence of the atmosphere (Ar, air) on the aluminizing of pure nickel from Al microparticles

II.1. Diffusion heat treatment (400°C-1h + 700°C-2h)

Pedraza et al. showed by using *in situ* E-SEM observations that the release of Al due to the shrinkage of the oxide shells developed on the microspheres was very fast [1]. For the different atmospheres investigated (He-4%H_2, O_2, air and H_2O), shrinkage of the oxide shells usually occurred in the 650-700°C range. It was also found that water vapour thickened the oxide shells of the alumina particles more than any other atmosphere. Galetz et al. confirmed that such oxide shells were very thin in inert atmosphere (Ar) allowing Al to react almost completely with the underlying substrate at 700°C [22]. In this case, the composition of the atmosphere is thus expected to play a significant role upon heating from 400°C to 700°C and the 2 hours dwell at 700°C (Fig. V-3a). One objective was to significantly increase the oxide shell thickness and the sintering of microparticles upon annealing to consolidate the ceramic top coat in a single heat treatment, without altering the microstructure of the diffusion layer.

The surface morphology of the top coat structure after the diffusion heat treatment in Ar and in synthetic air is given in Fig. V-4. With Ar atmosphere (Fig. V-4a), hollow spheres can be observed on the surface with a morphology comparable to the one presented by Pedraza et al. in 120 Pa He+4%H_2 [1]. The Al and O contents of the surface were very close according to the EDS area analyses of the surface (Fig. V-4c). A small fraction of nickel was also detected. For the sample heat treated in synthetic air (Fig. V-4b), the microparticles did not fully release the metallic Al as depicted with the EDS surface analyses (Fig. V-4c). From the SEM observations, it appeared that the larger microparticles burst preferentially whereas the smaller ones were still filled with metallic aluminium. It is known that the solid-liquid transformation of Al is accompanied with a volume expansion of approximately 12% that induces tensile stresses on the peripheral oxide shell [4]. Therefore, it is sound to believe that the smaller microparticles, hence containing less Al but a greater specific surface area, accommodate better the stresses while the Al core is in expansion [6,7,27]. This is in good agreement with data reported by Trunov et al. who estimated the formation of thicker oxide shells for smaller microspheres in dynamic dry air atmosphere [2]. The bright spots in the Al-containing microspheres were attributed to Ni enrichment (Fig. V-4b).

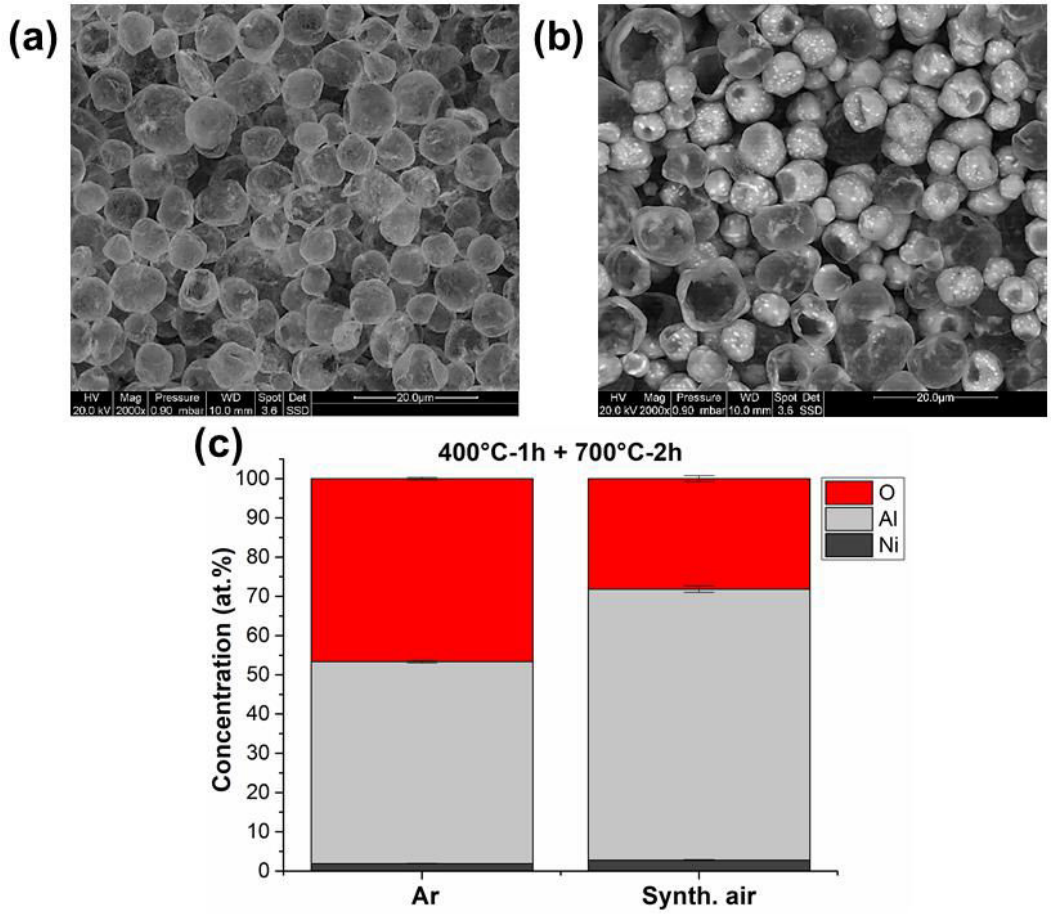

Fig. V-4. SEM surface morphology of the top coat structure after the diffusion heat treatment in (a) Ar and (b) synthetic air and (c) corresponding EDS surface analyses.

The cross-section micrographs and the corresponding XRD patterns of the surface for both systems are given in Fig. V-5. For the sample annealed in Ar, a continuous diffusion layer with a thickness of approximately 50-60µm was formed on the nickel substrate (Fig. V-5a). The top coat was composed of hollow spheres with thin oxide shells (barely visible with optical microscopy). The crystallographic structure of the Ni_2Al_3 phase was identified by XRD (Fig. V-5c). This phase resulted from the self-propagating high-temperature synthesis (SHS) occurring between Ni and Al [21,28]. Additional Ni_xAl_y phases were identified at the reaction front between the nickel substrate and the Ni_2Al_3 layer as shown by Pedraza et al. [21]. According to literature, the crystallization of the natural amorphous alumina layer into γ-Al_2O_3 takes place at around 550°C [2,3,13,14]. A special attention was therefore given on the XRD pattern of Fig. V-5c to identify the characteristic patterns of γ-Al_2O_3, by comparison with literature [2,20,29-31]. However, γ-Al_2O_3 and the other polymorphs of alumina were not detected by XRD and the top coat structure observed in Fig. V-4a seemed to be transparent to the X-rays. This might come from the limited thickness of the oxide shells developed on the microspheres. As a result, only the diffusion layer with the Ni_2Al_3 crystal structure was probed by the XRD [30]. Raman micro-spectrometry was carried out to characterize the hollow microspheres (results not shown), since the

sensitivity for this technique appears better than that of XRD to detect thin oxide scales [32,33] and shows a better ability to differentiate the alumina polymorphs [34,35]. The signature of the γ-Al_2O_3 phase could then be identified [34,35]. On several areas of the sample, the energy brought by the laser source was sufficient to transform the oxide shell into the stable α-Al_2O_3 polymorph. The mechanisms of formation are not yet completely understood but this observation could give an interesting way to promote the peripheral oxidation of Al microparticles and stabilize the stable α-Al_2O_3 polymorph. Note that several studies investigated the laser-induced transformation of γ-Al_2O_3 into α-Al_2O_3 for plasma sprayed coatings [31,36,37].

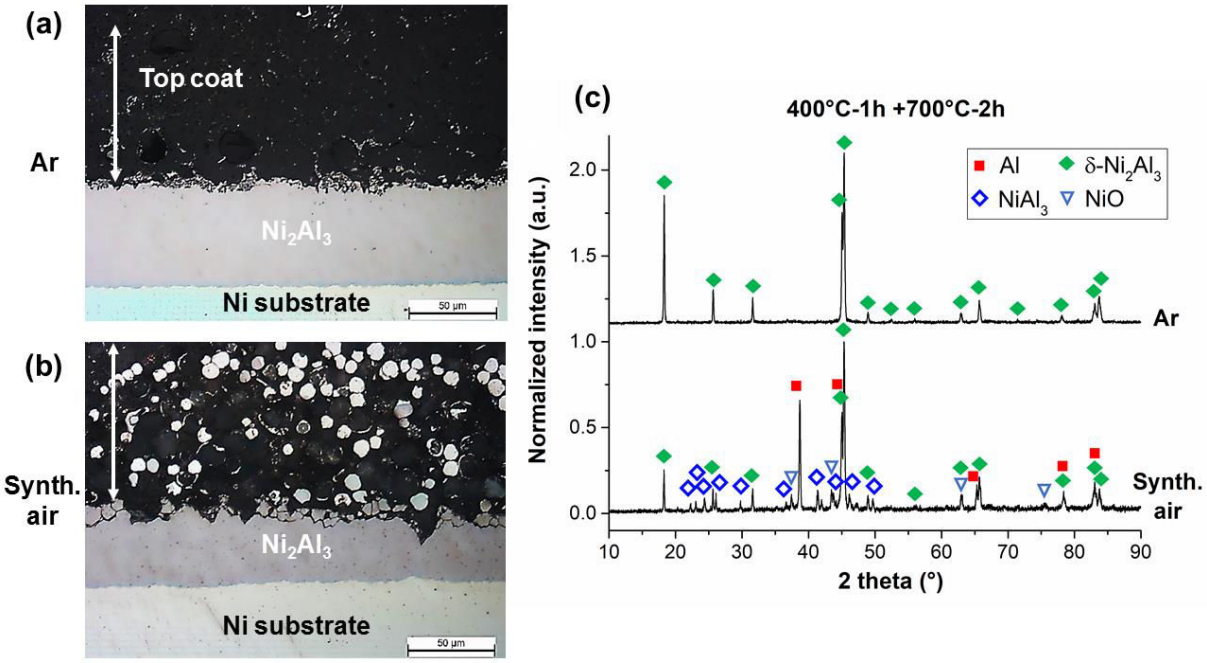

Fig. V-5. Cross-section micrographs of the full thermal barrier system elaborated on pure nickel after the diffusion heat treatment in (a) Ar and (b) synthetic air and (c) corresponding XRD patterns of the surface.

For the sample heat treated in synthetic air, additional crystal structures were identified on the XRD pattern in addition to Ni_2Al_3 (Fig. V-5c). As suggested by the SEM surface characterization (Fig. V-4b) and the cross-section micrograph (Fig. V-5b), metallic Al was still present in the top coat after the diffusion heat treatment (Fig. V-5c). This suggests that the oxide grown at the surface of the Al microparticles blocked the full release and/or reaction of Al with the gas [7,10]. As a result, metallic Al was still contained in the smaller microparticles in the top coat structure of Fig. V-5b. The $NiAl_3$ phase was also identified by XRD (Fig. V-5c). The composition of the atmosphere did not seem to significantly modify the mechanisms of formation of the diffusion layer previously reported by Galetz et al. [22]. The formation of the diffusion layer is governed by SHS reactions between Ni and Al occurring in both inert and oxidizing atmospheres [22]. The reaction is considered as a combustion

synthesis with air. Since a greater amount of metallic Al remained in the top coat after heat treatment in synthetic air, the diffusion layer was thinner than that of the sample annealed in Ar.

The thermogravimetric curves obtained for the diffusion heat treatment of Al slurry coated nickel in Ar and in synthetic air are given on Fig. V-6. Note that the organic binder used to elaborate the slurry coatings may also exert an influence on the oxidation rate of the microparticles. Nevertheless, the influence of the organic binder was not investigated in the present study. On the thermogravimetric curves presented in Fig. V-6, the events occurring below 150°C were mainly attributed to the release of water and to the homogenization of the temperature and of the atmosphere inside the reaction chamber. The strong weight loss recorded after 2 hours of annealing in both atmospheres was attributed to the decomposition of the organic binder [38]. During the dwell at 400°C, a stabilization of the mass was observed for the sample heat treated in synthetic air whereas a slow weight loss was identified for the one heat treated in Ar (stage I in Fig. V-2). This difference might be explained by a faster dehydroxylation of the amorphous oxide layer in synthetic air than in Ar because of the greater p_{O_2} in the reaction chamber.

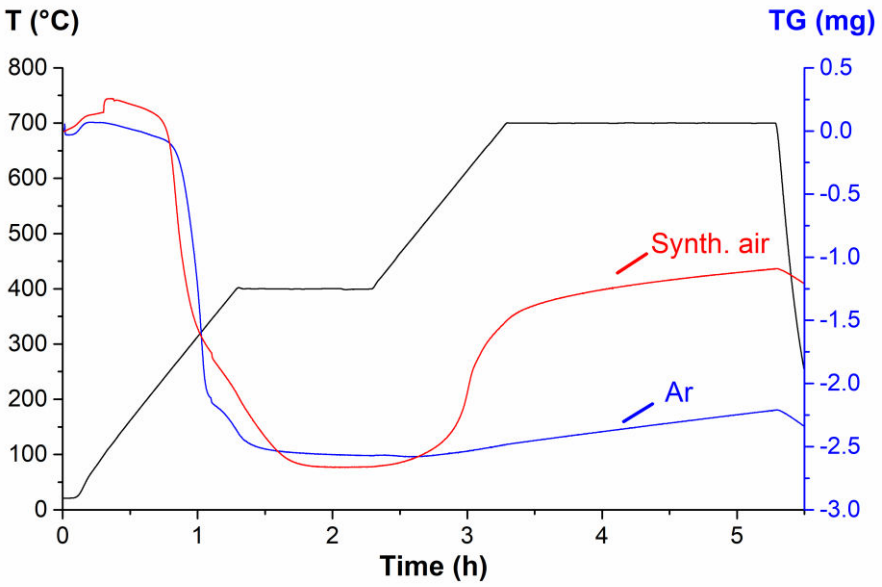

Fig. V-6. Thermogravimetric curves obtained for the diffusion heat treatment of pure nickel slurry coated with Al in Ar and synthetic air.

The mass variation for the two systems was completely different upon heating at 5°C/min between 400°C and 700°C (stage II in Fig. V-2). For the sample heat treated in synthetic air, a stepwise oxidation was observed and centred at approximately 615°C [3,16]. This could correspond to the fast crystallization of the amorphous alumina layer into γ-Al_2O_3 reported by Kolarik et al. [20]. Since the newly formed γ-Al_2O_3 layer was not continuous on the aluminium surface [2,16], healing of the film occurred by oxidation of exposed metallic Al. For the sample heat treated in Ar, only a small weight

gain was observed maybe indicating that healing of the γ-Al_2O_3 layer was significantly slower than in synthetic air and that the γ-Al_2O_3 film remained very thin. Upon annealing at 700°C for 2 hours, both systems presented similar slopes of the mass gain suggesting that the same oxide (i.e. γ-Al_2O_3) was growing (stage III in Fig. V-2). As a result, the oxide shells developed on the microspheres must be thicker (and more mechanically resistant) for the sample heat treated in synthetic air than the one heat treated in Ar. This would explain why the whole Al reacted with the nickel substrate in Ar whereas metallic Al was still present in the top coat structure after diffusion heat treatment in synthetic air (Fig. V-5).

II.2. Complete heat treatment (400°C-1h + 700°C-2h + 1100°C-2h)

The surface images of the top coat structure of the coatings after the complete heat treatment are given in Fig. V-7. For the sample heat treated in Ar (Fig. V-7a), the top coat structure was very close to the one obtained by Pedraza et al. after exposure to 1150°C in He-4%H_2 atmosphere [1]. Even though the microspheres were partially sintered after heat treatment in the inert gas, they were also deformed and broken. This could be related to the volume shrinkage occurring during the γ-Al_2O_3 → α-Al_2O_3 transition [1,6,20,27]. A Ni enrichment of the surface was observed by EDS after the final step at 1100°C (Fig. V-7c) in comparison with the results obtained after the diffusion heat treatment (Fig. V-4c). Since the whole metallic Al reacted with the nickel substrate after the two hours dwell at 700°C in Ar (Fig. V-5c), this Ni enrichment probably resulted from the outward diffusion of nickel during the two hours dwell at 1100°C. For the sample heat treated in synthetic air, the microspheres were less deformed and more sintered (Fig. V-7b) than the ones observed after heat treatment in Ar. Some microspheres were burst after annealing and resulted in oxide crusts similar to the ones observed by other authors [6,19]. The formation of these oxide crusts confirmed the important thickening of the alumina shells in synthetic air. Although the bright contrasted areas were found to be rich in Ni (about 10 at.% Ni), the overall Ni content of the surface was lower for the sample heat treated in synthetic air (Fig. V-7c). This difference might come from the thickness of the oxide shells formed after heat treatment. Indeed, the oxide shells formed in synthetic air were thicker than the ones obtained in Ar (Fig. V-8a and b) resulting in higher quantifications of Al and of O with respect Ni at the surface of the top coat in contact with the gas. This was also confirmed in the XRD patterns of Fig. V-8c, where the characteristic peaks of α-Al_2O_3 were better resolved in synthetic air than in Ar (Fig. V-8c).

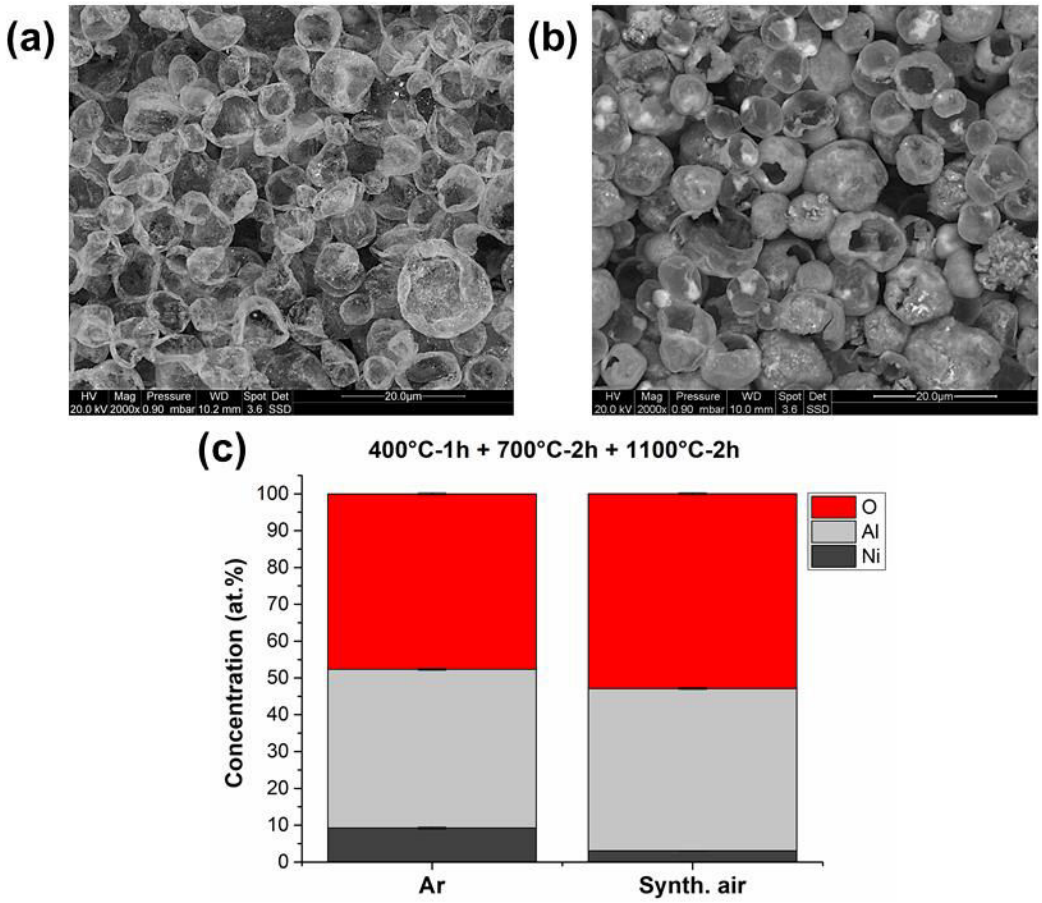

Fig. V-7. Surface morphology of the top coat structure after the complete heat treatment in (a) Ar and (b) synthetic air and (c) corresponding EDS surface analyses.

The microstructures of the diffusion layers formed after the complete heat treatment were similar in both atmospheres (Fig. V-8a and Fig. V-8b). The coatings were composed of two different layers: an external layer with the β-NiAl main composition and the γ'-Ni_3Al one at the grain boundaries and an inner layer with the γ'-Ni_3Al composition at the interface with the nickel substrate. Some β to γ' transformation was observed at the extreme surface of the coatings. This transformation was probably a consequence of Al outward diffusion to form the α-Al_2O_3 TGO scale at the extreme surface of the coating (confirmed by Raman-microspectrometry). For the same amount of slurry deposited on the surface, the overall thickness of the coating was larger after heat treatment in Ar (Fig. V-8a) than in synthetic air (Fig. V-8b). This suggests that the unreacted fraction of Al with the nickel substrate was greater in synthetic air than in Ar and therefore remained in the top coat structure to oxidize into alumina (Fig. V-8c).

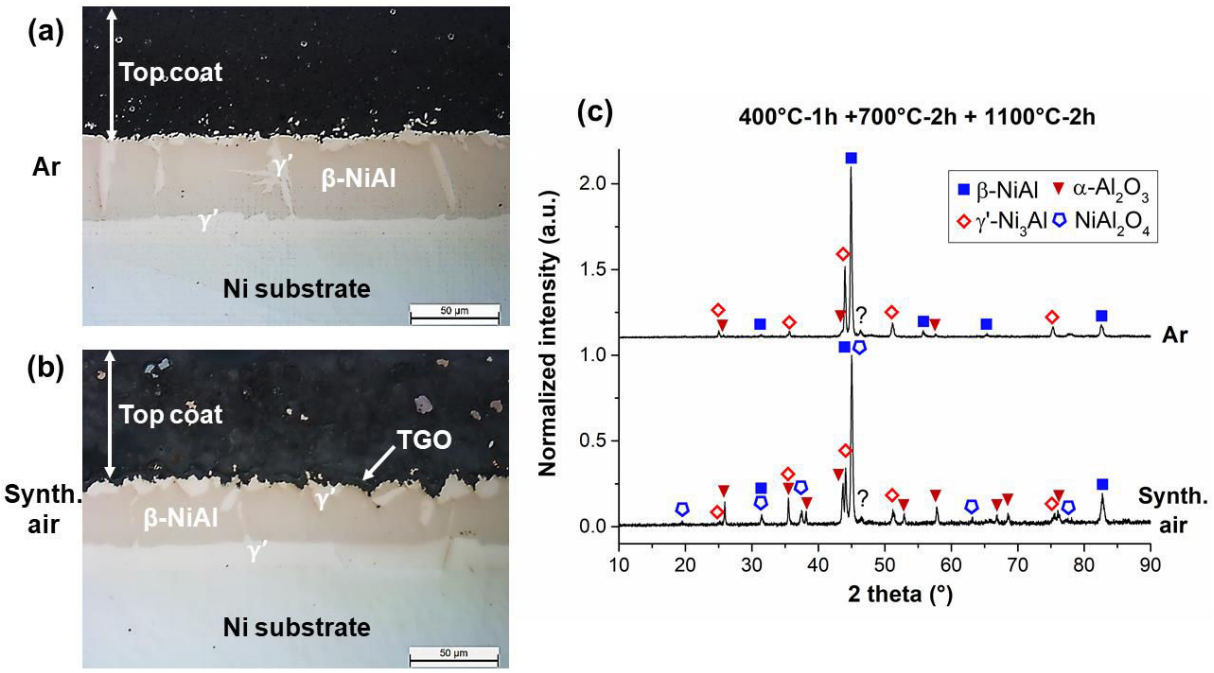

Fig. V-8. Cross-section micrographs of the full thermal barrier system elaborated on pure nickel after the complete heat treatment in (a) Ar and (b) synthetic air and (c) corresponding XRD patterns of the surface.

The mass variation of the samples during the heat treatment in TGA is given on Fig. V-9. From the beginning of the heat treatment to the end of the diffusion step (700°C-2h), the thermogravimetric curves were similar to the ones obtained in Fig. V-6. For the sample heat treated in Ar, the mass variation after the diffusion step was insignificant compared to the one heat treated in synthetic air (Fig. V-9). Such low mass gain suggests that the peripheral oxidation of the microspheres progressed slowly and that the TGO scale formed on the diffusion layer was very thin (Fig. V-8a). For the sample heat treated in synthetic air, an important mass gain was measured in the range 750-1100°C (stage III in Fig. V-2), which can be attributed to a further oxidation of the Al retained in the microspheres of the top coat [20] (Fig. V-5b and Fig. V-8b). This evolution is in good agreement with the high resolution gravimetry analyses of Al microparticles done by Rufino et al. [3] and with the results of Trunov et al. [2,16]. The increase of the oxidation rate was attributed to the growth of the γ-Al_2O_3 layer and further alumina crystallographic transformations from the γ phase (Fig. V-2). When the temperature reached 1100°C, the kinetics of oxidation decreased because of the exclusive growth of the stable α-Al_2O_3 in the top coat [20] and as a TGO scale [39]. The transformation of γ-Al_2O_3 in the top coat structure after complete heat treatment was confirmed by XRD (Fig. V-8c) and Raman micro-spectrometry (Fig. V-10).

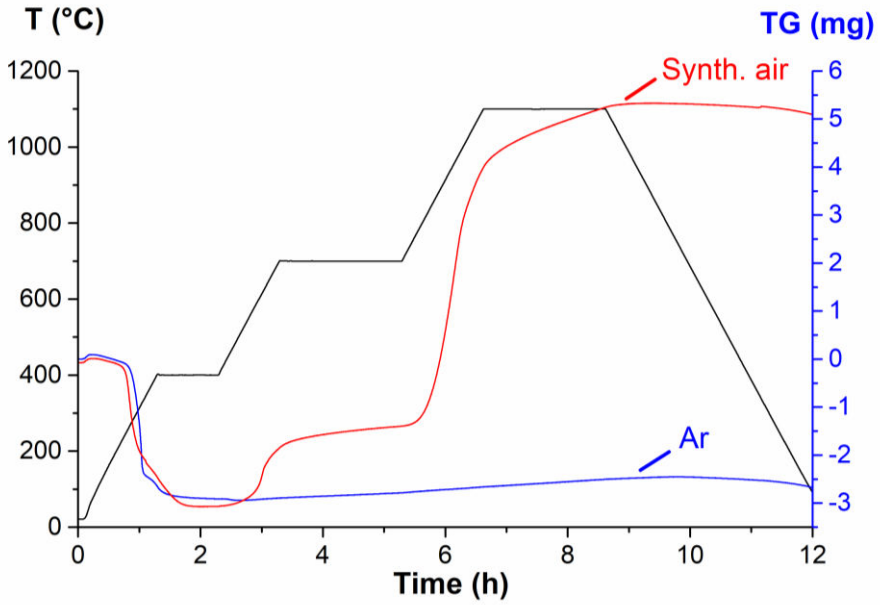

Fig. V-9. Thermogravimetric curves obtained for the complete heat treatment of pure nickel slurry coated with Al in Ar and in synthetic air.

As described in the experimental methods section (Chapter II), several Raman spot analyses were realized on the surface of the samples. After the complete heat treatment, the measurements were performed along the gas flow direction of the thermobalance (Fig. V-10). For the sample heat treated in synthetic air (Fig. V-10b), only α-Al_2O_3 was detected whereas both γ-Al_2O_3 and α-Al_2O_3 were detected for the sample heat treated in Ar (Fig. V-10a). The gas flow was found to exert an influence on the oxidation rate of the microspheres in the inert atmosphere. The presence of γ-Al_2O_3 after exposure to 1100°C for two hours was not relevant with the time-temperature diagram of alumina proposed by Garriga-Majo et al. [39] and the *in situ* XRD measurements of Kolarik et al. [20]. However, these studies were carried out in air. According to Pedraza et al. [1], performing the annealing treatment in inert atmosphere must considerably reduce the peripheral oxidation of the microspheres. The p_{O_2} inside the reaction chamber had therefore a critical effect on the oxidation rate of the microparticles and the transition of metastable alumina polymorphs into the stable α-Al_2O_3 phase. This would explain why the transformation of γ-Al_2O_3 into α-Al_2O_3 was not total after the complete heat treatment in Ar (Fig. V-10a). In this respect, the influence of the theoretical 5 vpm of H_2O (and of 2 vpm of O_2) contained in the Ar bottle on the potential delayed transformation of the metastable alumina into α-Al_2O_3 [40] has been disregarded since the content is too low to appreciate a marked effect in the conditions studied here. However, as introduced above, the laser source of the Raman was found to transform γ-Al_2O_3 into α-Al_2O_3 on some locations.

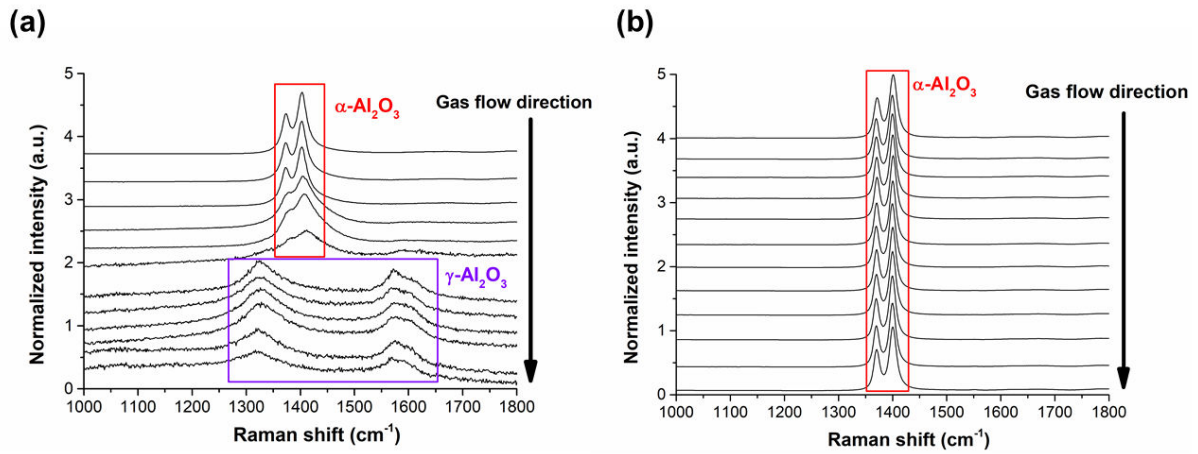

Fig. V-10. Raman surface analyses of pure nickel slurry coated with Al after complete heat treatment in (a) Ar and (b) synthetic air.

The SEM cross-section images of the full thermal barrier systems (diffusion zone + top coat structure) elaborated on pure nickel samples in Ar and in synthetic air are given on Fig. V-11. As observed with optical microscopy, the Al microparticles were completely empty after the diffusion step in Ar (only the alumina shell remained) whereas metallic Al was still present in synthetic air (dark spherical particles in the top coat structure). Brighter particles were also observed in the top coat structure after the diffusion step in synthetic air with a composition close to $NiAl_3$ according to the EDS spot analyses [23]. The bright spots in the microparticles were ascribed to Ni enrichment in the BSE mode of Fig. V-4b. This proved the formation of an interconnected network between the diffusion layer and the top coat upon aluminizing [22]. After the complete annealing in Ar, the oxide shells remained (visually) very thin with a weak sintering and the oxidation of the surface of the diffusion zone in contact with the top coat was insignificant. For the sample heat treated in synthetic air, the oxide shells of the microspheres were considerably thicker than the ones obtained in Ar. The microspheres also displayed a better sintering resulting in a more adherent and stronger top coat structure at the naked eye [23]. After the complete heat treatment in synthetic air, a thick α-Al_2O_3 TGO scale formed on the surface of the diffusion coating (confirmed with local Raman analyses). The compositions of the aluminized layers formed on the nickel substrate were similar in both atmospheres though.

The ceramic top coats were found to be more sintered after heat treatment in synthetic air than in Ar. However, in very local areas (e.g. corners of the samples), the coating did not completely cover the nickel substrate probably because the samples had not been chamfered (Fig. V-12a). This led to the formation of unprotective nickel oxide (NiO) and to some internal oxidation preferentially at the interface between the diffusion layer and the substrate (Fig. V-12b). Note that some reflections in the XRD patterns of Fig. V-5c and Fig. V-8c were attributed to the cubic structures of NiO and $NiAl_2O_4$. The optimization of the ceramic top coat by performing the annealing treatment in synthetic air therefore led to some degradation of the underlying diffusion layer. A switch between inert and

oxidizing atmospheres upon annealing was thus expected to be a good compromise to countercurrent these detrimental effects. The results are presented in the next paragraph.

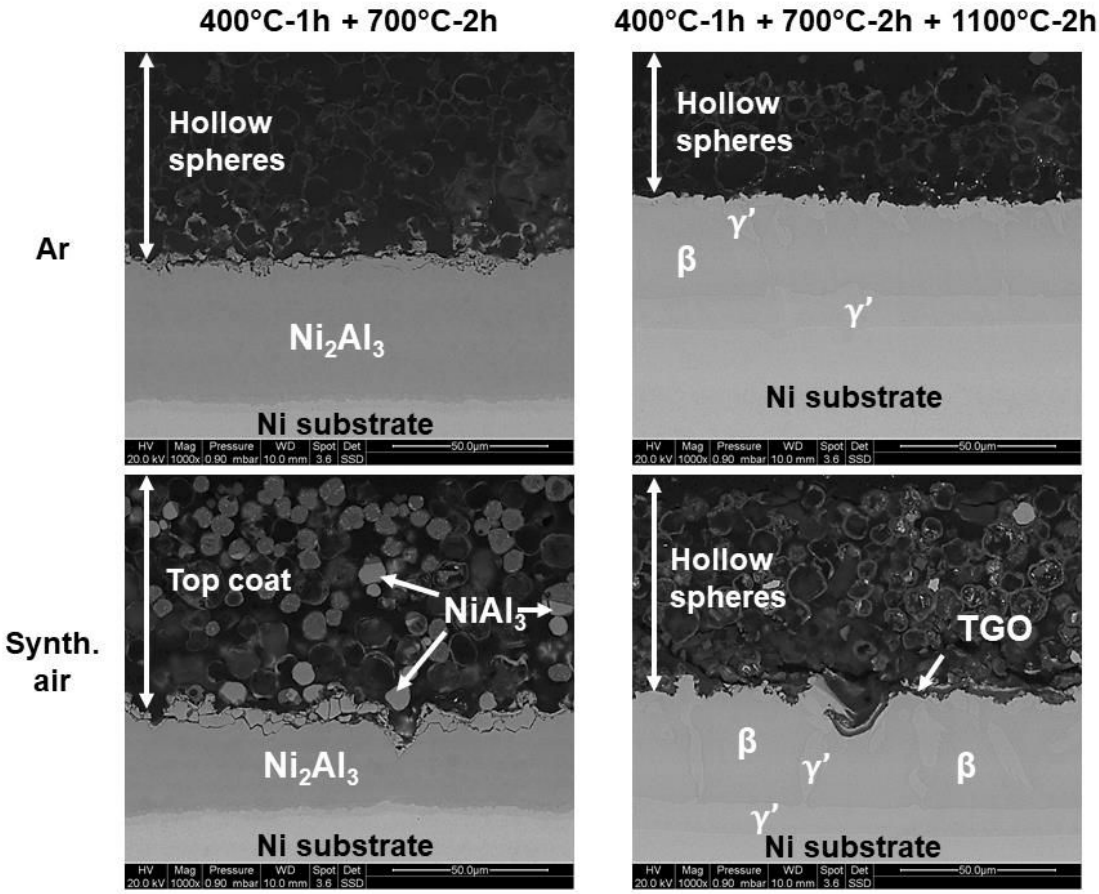

Fig. V-11. BSE cross-section images of the full thermal barrier systems elaborated on pure nickel substrate from Al microparticles. The thermal diffusivity of pure Ni with "PARTICOAT" (complete heat treatment in Ar) was measured to evaluate the thermal insulation behaviour of the alumina hollow spheres (cf. Annex 2).

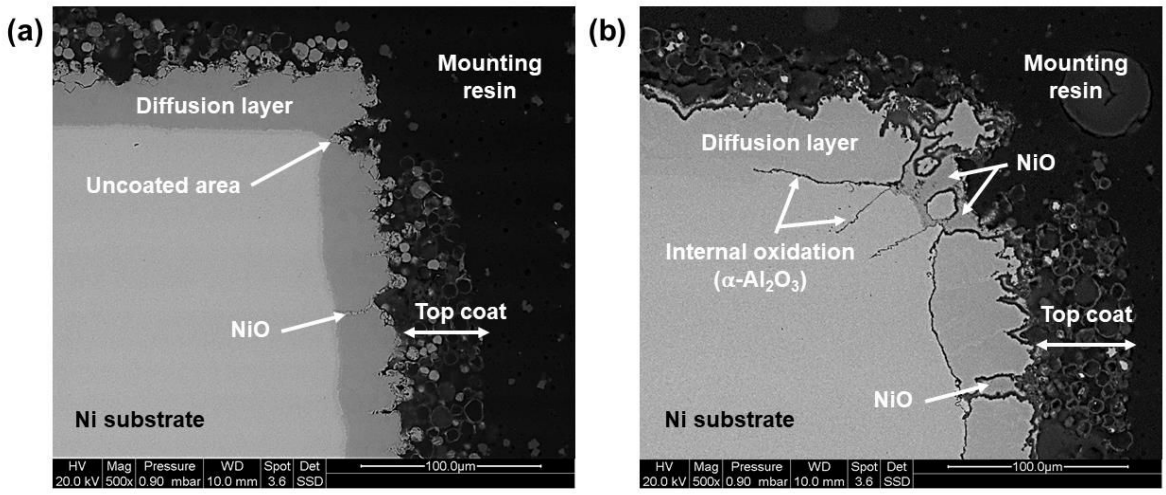

Fig. V-12. Details of the complete thermal barrier systems on sample corners after (a) the diffusion heat treatment and (b) the complete heat treatment in synthetic air.

II.3. Complete heat treatment with the introduction of synthetic air upon annealing

In paragraphs II.1 and II.2, it was shown that the composition of the atmosphere (Ar or synthetic air) had a critical effect on both the oxidation of the Al microparticles and their sintering in the top coat structure. The objective was here to propose a single heat treatment to elaborate a functional thermal barrier system (diffusion zone + top coat structure) by switching the composition of the atmosphere during the heat treatment. Two different heat treatments were performed (Fig. V-13) as follows:

- heating from ambient temperature to 400°C, one hour dwell at 400°C and then heating from 400°C to 700°C in flowing Ar (20 mL/min),
- stop of the flow of Ar and purge of the reaction chamber with a vacuum pump for 8 seconds after reaching 700°C ("Switch 1") **or** at the end of the two hours dwell at 700°C ("Switch 2"),
- introduction of synthetic air in the reaction chamber with a flow of 16 mL/min,
- second part of the heat treatment (1100°C) in synthetic air.

The complete rejuvenation of the atmosphere requires approximately 15 minutes and can be identified on both thermogravimetric curves by a step in Fig. V-13 (synthetic air is denser than Ar). As observed in Fig. V-6 and Fig. V-9, the binder was fully decomposed after one hour at 400°C. The interpretations of the thermal analyses were based on the work of Trunov et al. (Fig. V-2). For the "Switch 1" sample, a stepwise oxidation was observed as soon as synthetic air was introduced in the reaction chamber at the beginning of the plateau at 700°C. In contrast, the "Switch 2" sample presented a slow mass increase during the two hours of annealing at 700°C similar to the samples heat treated in Ar in paragraphs II.1 and II.2. These observations confirmed that the oxidation rate attributed to the crystallization of the amorphous alumina into γ-Al_2O_3 and its subsequent healing (stage II in Fig. V-2) was much faster in synthetic air than in Ar. The fast mass gain was attributed to the oxidation of exposed metallic Al. For the "Switch 2" sample, the introduction of synthetic air at the end of the two hours dwell at 700°C was accompanied with a rapid increase of the oxidation rate. However, the oxidation rate of "Switch 1" sample was greater in the range 700°C-1100°C (Stage III in Fig. V-2). This may indicate that the thickness of the γ-Al_2O_3 layer subjected to further crystallographic transformations was greater for the "Switch 1" sample than for the "Switch 2" one. The same evolution was observed by Trunov et al. by changing the initial size of the microparticles [2,16]: the smaller the microparticles, the faster the oxidation rate. When the temperature reached 1100°C, a stabilization of the mass was observed for both samples (stage IV in Fig. V-2). This suggested that most of the oxide shells had transformed into the stable α-Al_2O_3. It must be pointed out here that the formation of the TGO scale on the surface of the diffusion layer may also contribute to the mass variation of the samples. Even though several thermally activated processes overlapped during the annealing, the mechanisms of oxidation proposed by Trunov et al. seems to successfully describe the systems investigated in this study [16].

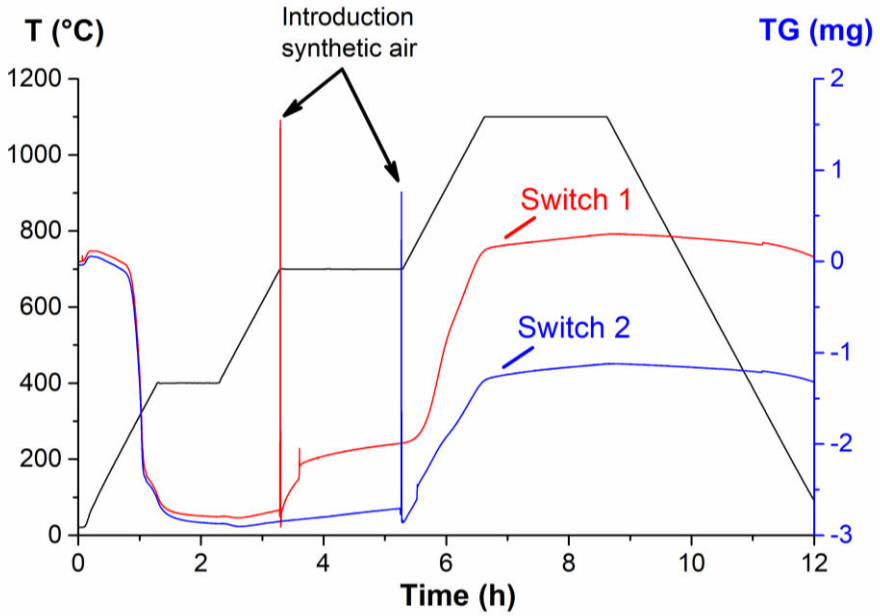

Fig. V-13. Thermogravimetric curves obtained for the complete heat treatment of pure nickel slurry coated with Al in Ar and in synthetic air. The sharp mass variation corresponds to the purge of the reaction chamber before introduction of synthetic air.

The surface morphology of the top coat structures obtained after annealing are given on Fig. V-14a and Fig. V-14b. The hollow alumina microspheres were easily identified on both samples [1,21]. The top coat structure of "Switch 2" sample (Fig. V-14b) was very close to the one obtained for the sample heat treated in Ar (Fig. V-7a). Shrinkage of the oxide shells occurred and suggested the occurrence of the γ-$Al_2O_3 \rightarrow \alpha$-$Al_2O_3$ transition [1,6,20,27]. Shrinkage of the oxide shells was also observed for the "Switch 1" sample (Fig. V-14a). However, the introduction of synthetic air at the beginning of the 2 hours dwell at 700°C seemed to result in the thickening of the oxide shells. These observations are in good agreement with data from Ref. [1] after exposure of the Al microspheres at 1150°C in inert or oxidizing atmospheres. This would explain the significantly higher mass gain observed for the "Switch 1" sample in comparison with the "Switch 2" one on the thermogravimetric curves (Fig. V-13). EDS window analyses were performed on several areas of the samples (results not shown). No significant difference was revealed by the EDS measurements except that some Ni-rich spots were observed for the "Switch 1" sample. This could indicate the outward diffusion of nickel upon annealing at 1100°C.

The cross-section micrographs of the full thermal barrier coatings elaborated on pure nickel after annealing are given in Fig. V-15. The microstructure of the diffusion layer was similar in both conditions. The light optical microscopy allowed to distinguish the different Ni_xAl_y phases formed on the surface through differences of contrast (Fig. V-15a and Fig. V-15b). The diffusion layer was composed of a thin intermediate γ'-Ni_3Al layer at the interface with the Ni substrate and the β-NiAl coating matrix. Some β to γ' transformation was observed at the grain boundaries and at the extreme surface of the coating. These observations were confirmed by EDS spot measurements and by XRD analyses (Fig. V-15c).

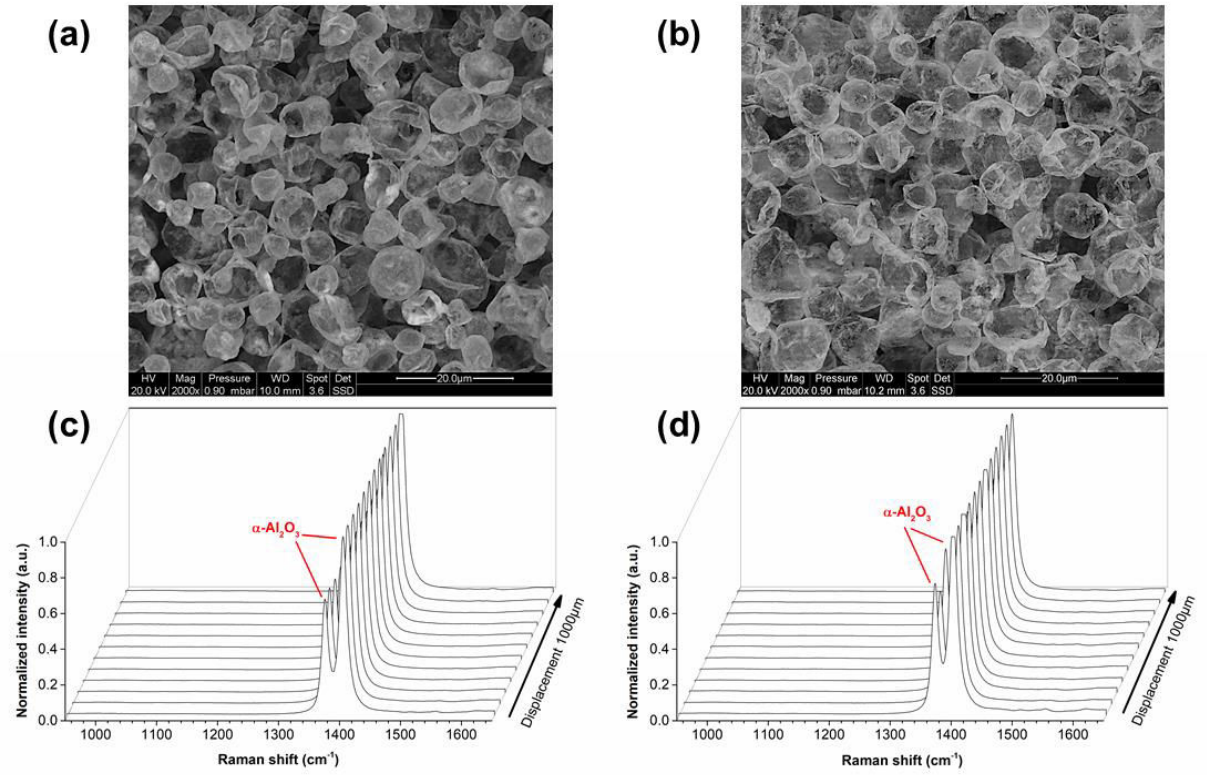

Fig. V-14. Surface morphology of the top coat structure after the complete heat treatment in Ar and synthetic air with (a) "Switch 1" and (b) "Switch 2" and (c), (d) corresponding Raman surface analyses.

The XRD patterns of the surface were very close for the two systems (Fig. V-15c). The crystal structure of the α-Al_2O_3 phase was identified whereas other alumina polymorphs were not detected after annealing. Raman micro-spectrometry gave the same results with the exclusive α-Al_2O_3 doublet detected over the whole length of the samples (Fig. V-14c and Fig. V-14d). This suggested the full conversion of the oxide shells into the stable α-Al_2O_3 phase after the two hours dwell at 1100°C, in good agreement with data reported by Velasco et al. [19] and Kolarik et al. [20]. For both systems, an exclusive α-Al_2O_3 TGO scale formed at the interface diffusion layer-ceramic top coat (Fig. V-16a and Fig. V-16b), confirmed with local Raman analyses. Some reflections of the XRD patterns were attributed to the $NiAl_2O_4$ spinel by comparison with JCPDS file number 00-010-0339. This indicated the presence of spinels in the top coat structures (Fig. V-16). The formation of spinels may come from the outward diffusion of nickel at such elevated temperatures (i.e. 1100°C) or from the initial Ni enrichment of the top coat during the high exothermal reactions occurring between the nickel substrate and metallic Al [23].

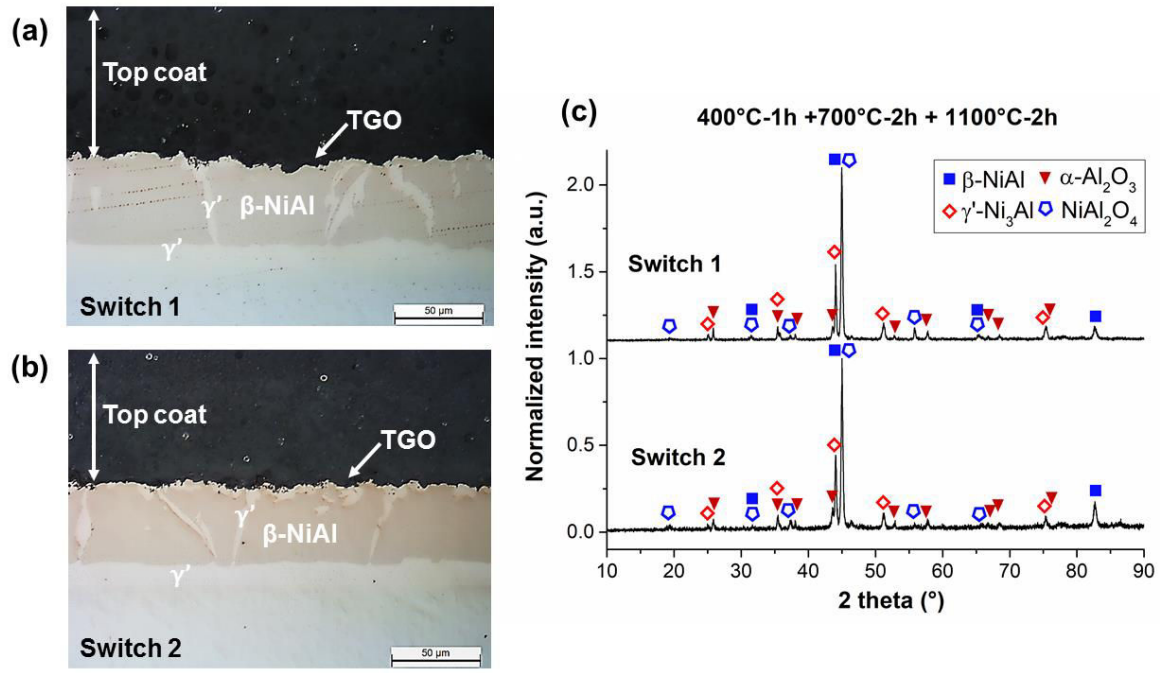

Fig. V-15. Cross-section micrographs of the full thermal barrier system elaborated on pure nickel after the complete heat treatment in Ar and synthetic air with (a) "Switch 1" and (b) "Switch 2" and (c) corresponding XRD patterns of the surface.

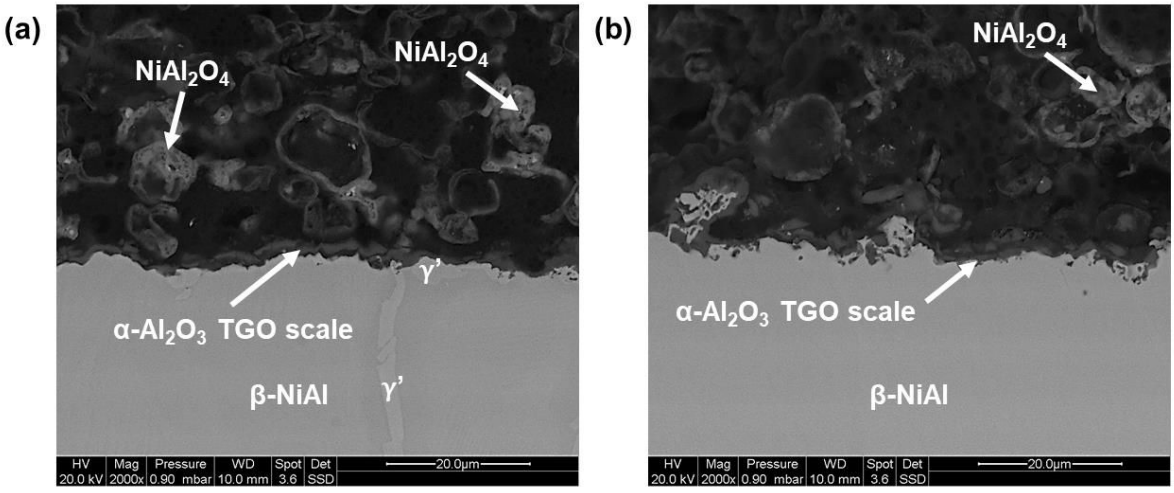

Fig. V-16. Details of the TGO scale and formation of $NiAl_2O_4$ spinels in the top coat structure for (a) the "Switch 1" and (b) the "Switch 2" samples.

II.4. Discussion

The thermogravimetric curves upon heating for the different investigated systems are presented in Fig. V-17. The oxidation stages proposed by Trunov et al. are also included in the graphs [16]. As discussed in paragraph II.1, the thermogravimetric curves between 400°C and 700°C were significantly different depending on the atmosphere (Fig. V-17a). The mass variation was very close for the two samples heat treated in synthetic air. The stepwise oxidation attributed to the crystallization of the amorphous alumina into γ-Al_2O_3 and subsequent healing of the γ-Al_2O_3 layer was centred at approximately 615°C. This value is in good agreement with that of other studies dealing with the oxidation of Al particles, considering the present heating ramp of 5°C/min [2,3,5,6]. For the four samples annealed in Ar, the mass still decreased up to approximately 500°C and this may indicate that the desorption of water and of the organic binder [38] was slower than in synthetic air. Then, a constant mass gain was observed for the samples heat treated in Ar. The slope was in this case considerably smaller than that of the samples heat treated in synthetic air (Fig. V-17a). This mass gain was associated with the growth of the γ-Al_2O_3 layer. Firmansyah et al. have shown with HR-TEM observations that the thickening of the oxide shell occurred even in flowing Ar before the melting point of Al [11]. The same authors observed that the aluminium core expanded under almost no constraint in flowing Ar because of the inhomogeneous crystallization of the amorphous alumina shell [11]. Consequently, molten Al very rapidly diffuses outwards from the microspheres to react with the underlying nickel substrate upon annealing in Ar [21] (Fig. V-5a). These observations therefore suggest that the thickness of the γ-Al_2O_3 layer covering the Al particles was presumably much greater after heat treatment in synthetic air than in Ar when melting of Al occurred (Fig. V-17a). In synthetic air, the alumina shells formed on the smaller microparticles were resistant enough to countercurrent the expansion of the molten aluminium core [6,27]. This should explain why metallic Al was still present in the top coat structure in Fig. V-5b even at temperatures higher than the Al melting.

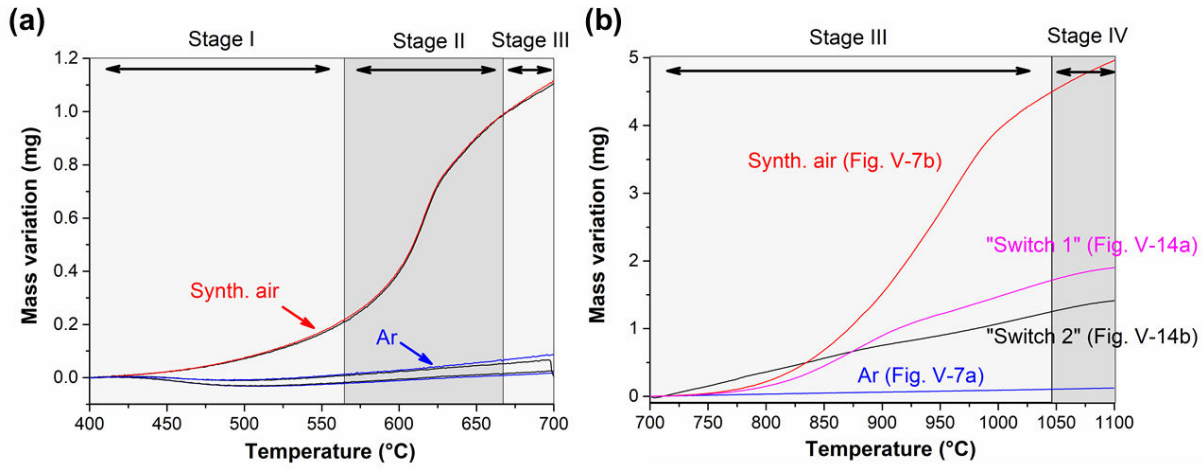

Fig. V-17. Comparison of the thermogravimetric curves upon heating (5°C/min) for the different systems (a) between 400°C and 700°C and (b) between 700°C and 1100°C.

The thermogravimetric curves obtained upon heating (5°C/min) between 700°C and 1100°C also differed significantly between the studied systems (Fig. V-17b). For the sample heat treated in synthetic air, the mass variation was in agreement with data from literature [2,5,6]. A second stepwise oxidation was observed corresponding to the growth of the γ-Al_2O_3 and its progressive transition into the stable α-Al_2O_3 polymorph. The slope change after reaching 1000°C was attributable to the predominant growth of α-Al_2O_3. The same observations were done for the "Switch 1" sample although the overall mass variation was less significant than that of the sample fully heat treated in synthetic air. This suggested that a fraction of the Al present in the top coat structure already reacted with the underlying substrate upon heating to 700°C in Ar. As a result, the diffusion layer was more homogeneous and the oxide shells were thinner (Fig. V-15a). For the "Switch 2" sample, there was barely no stepwise oxidation but a constant mass gain instead (Fig. V-17b). Since the introduction of synthetic air was done at the end of the two hours dwell time for this sample (Fig. V-13), the amount of Al flowing out from the spheres must have been the same than for the sample presented in Fig. V-5a. However, the overall mass gain was close to the "Switch 1" sample suggesting the growth of a γ-Al_2O_3 layer. It is important to mention here that for these three samples the conversion of the alumina shells into α-Al_2O_3 was complete. This was confirmed with both XRD and Raman analyses. The TGO scales developed in synthetic air (Fig. V-16) were expected to have little influence on the overall mass variation since the specific surface area of the top coat structure was much greater than the surface of the sample. Fig. V-18 allows to appreciate the difference in thickness of the oxide shells developed after the different annealing conditions.

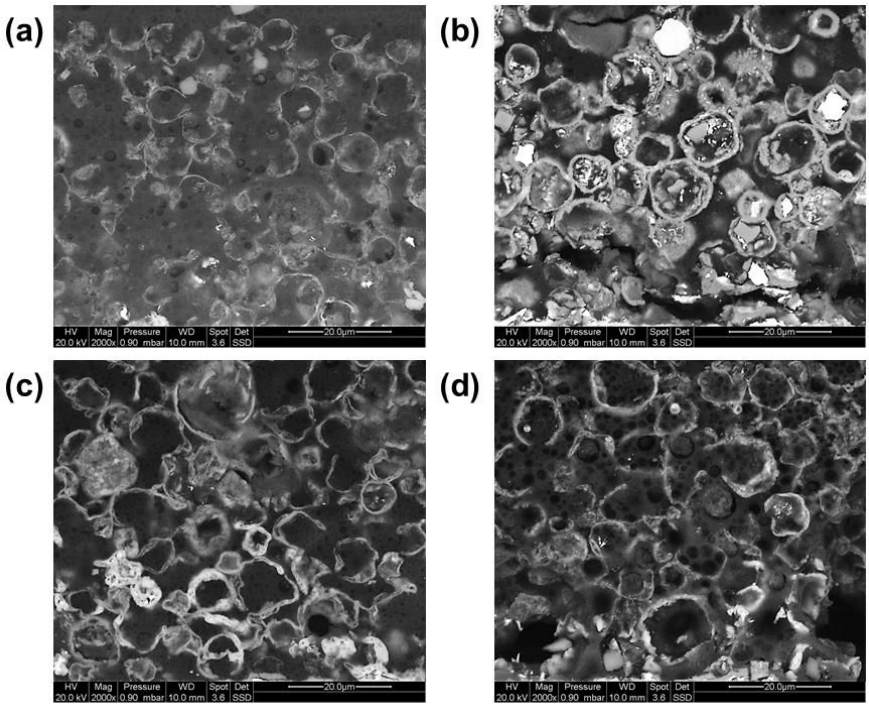

Fig. V-18. SEM cross-section images of the top coat structures after the complete heat treatment (a) in Ar, (b) in synthetic air, (c) for the "Switch 1" sample and (d) for the "Switch 2" sample.

- ***Influence of the atmosphere on the oxidation of Al microparticles and the release of Al:***

The atmosphere (inert or oxidizing) had a tremendous influence on both the peripheral oxidation of the particles and the release of Al from the metallic core. Based on the observations of the present work and from literature, the mechanisms of formation of the individual hollow alumina microspheres in Ar and in synthetic air are proposed in Fig. V-19. At room temperature, a native amorphous oxide layer covers the Al microparticle. The amorphous alumina layer grows until reaching a critical thickness of 4 to 5 nm to crystallize into γ-Al_2O_3 at about 550°C [3,11,12,16]. This transformation induces nano-cracks (fractures) in the alumina shell since γ-Al_2O_3 has a greater density than the initial amorphous layer [6,15]. The composition of the atmosphere (i.e. p_{O_2}) was then critical on the mechanisms of formation of hollow alumina microspheres. The mechanisms presented on Fig. V-19 are described separately for the sake of clarity.

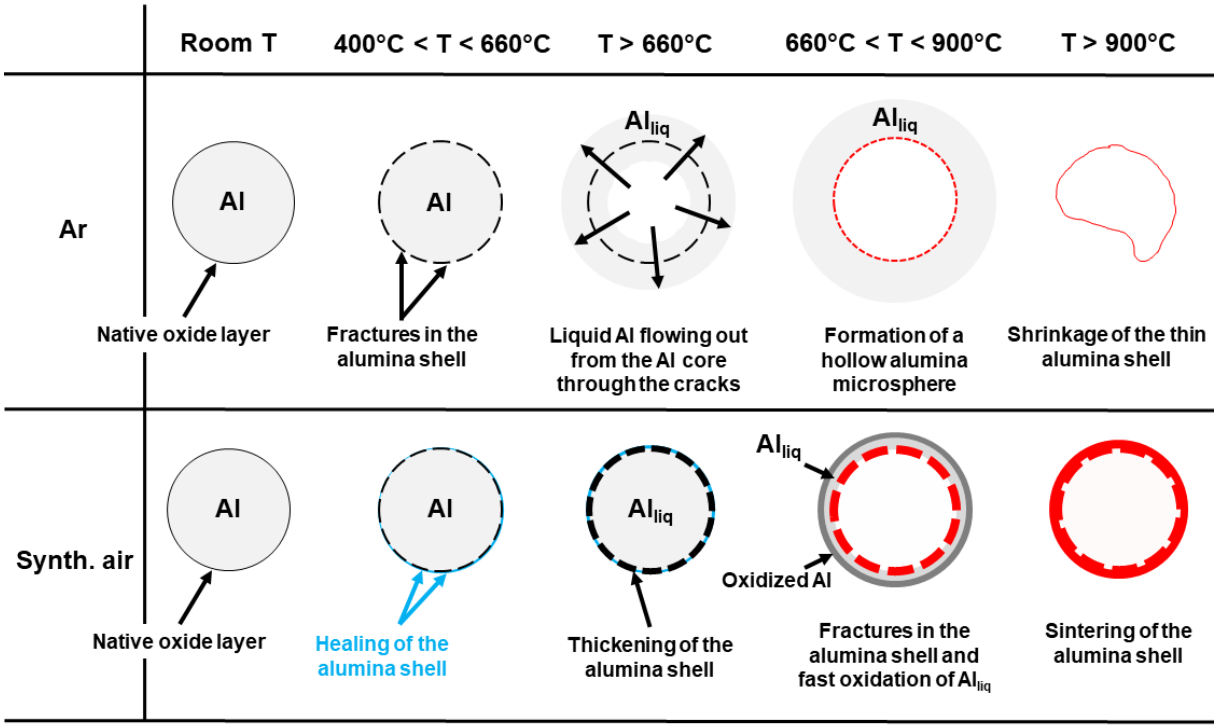

Fig. V-19. Mechanisms of formation of individual hollow alumina microspheres in Ar and in synthetic air proposed in this work.

- ***Mechanisms of formation in Ar:***

In Ar, the crystallization of the amorphous alumina layer is heterogeneous and the shell is not totally healed before the melting of Al [11]. Upon heating over the melting temperature of Al (about 660°C [41]), the molten Al core can expand under almost no constraint. As a result, liquid Al flows out through the nano-cracks and the microparticle progressively releases its Al content [1]. Simultaneously, the generated molten Al reacts with the underlying nickel substrate following the mechanisms described in Ref. [22] (i.e. dissolution of the metallic substrate and self-propagating high-temperature synthesis). In this work, Al microparticles were completely emptied after 2 hours dwell at 700°C forming a continuous Ni_2Al_3 layer with hollow alumina microspheres on top (Fig. V-11). At this stage, the alumina shells are very thin (Fig. V-11) with smooth surfaces (Fig. V-4a). Increasing the temperature up to 1100°C led to the progressive transformation of the γ-Al_2O_3 into α-Al_2O_3. Note that this transformation was incomplete at the sample surface after two hours dwell at 1100°C in Ar (Fig. V-10a). The γ-Al_2O_3 to α-Al_2O_3 transformation is accompanied with a volume shrinkage of about 13.8% because of a change of the crystallographic structure [6,20]. This volume shrinkage provokes the deformation of the thin alumina shell presenting a weak mechanical strength (Fig. V-19). This led to a broken hollow microspheres morphology observed on the surface (Fig. V-7a) and in cross-section (Fig. V-18a) after the complete heat treatment in Ar.

- ***Mechanisms of formation in synthetic air:***

Unlike Ar, the p_{O_2} of synthetic air atmosphere could heal the defective γ-Al_2O_3 layer by fast oxidation of the exposed metallic Al. This was confirmed by the stepwise oxidation occurring before the Al melting (stage II on Fig. V-17a). Upon further heating at a temperature greater than Al melting (i.e. 700°C), the mechanical strength of the healed alumina shell is high enough to countercurrent the expansion of the molten Al core [6,27]. This resulted in the thickening of the alumina shell probably by both outward diffusion of Al^{3+} cations and inward diffusion of O^{2-} anions through the alumina shell [11]. This could explain that metallic Al was still contained in the microparticles after two hours dwell at 700°C (Fig. V-5b). As observed in Ar, the γ-Al_2O_3 to α-Al_2O_3 transformation occurring upon heating between 700°C and 1100°C induces a volume shrinkage in the alumina shell of about 13.8%. Consequently, nano-cracks form in the alumina shell and molten Al can then flow out across these cracks [20,27]. Molten Al is then immediately oxidized because of the high p_{O_2} of synthetic air. This results in the thickening of the alumina shell and in an enhanced sintering of the individual alumina microspheres through the formation of a α-Al_2O_3 connecting network (Fig. V-7b and Fig. V-18b). The second acceleration of the oxidation rate upon heating between 700°C and 1100°C (stage III on Fig. V-17b) could therefore be attributed to the fast oxidation of molten Al in the top coat structure.

III. Influence of the atmosphere (Ar, air) for the Cr-Al double-layer system

III.1. Characterization of the top coat structure after heat treatment in Ar

For this study, the Cr-Al double-layer system has been developed on pure nickel after heat treatment in Ar with a ratio close to 50Cr-50Al in wt.% (cf. paragraph V.3. in Chapter V). Fig. V-20 presents the cross-section images of the top coat structure obtained after different annealing treatments in flowing Ar. As observed for the simple Al slurry coating elaborated in Ar (Fig. V-18a), the alumina oxide shells remained very thin with a relatively weak sintering. These results are in good agreement with data from Ref. [1] after annealing in He-4%H_2 inert atmosphere. Even though the Cr-Al double-layer system was highly beneficial to limit the SHS reactions between Ni and Al upon aluminizing, the Cr interlayer did not significantly change the top coat structure in flowing Ar.

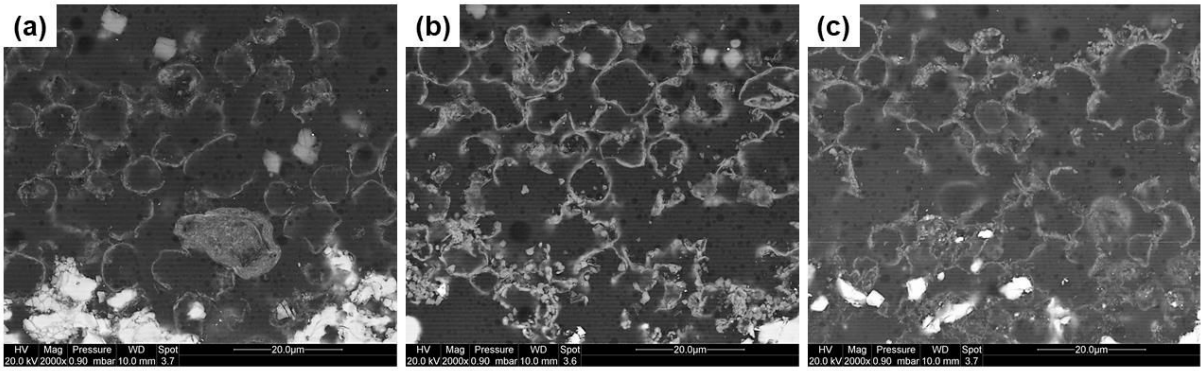

Fig. V-20. BSE cross-section images of the top coat structure after annealing for (a) 400°C-3h + 650°C-5h, (b) 400°C-3h + 650°C-5h + 1000°C-3h and (c) 400°C-3h + 1080°C-6h in flowing Ar.

A BSE surface image of the top coat structure after the "conventional low-activity" heat treatment is given on Fig. V-21a. The differences in contrast allowed to distinguish the hollow alumina microspheres (dark areas) from the intermetallic phases (bright areas). This suggested that a fraction of the top coat structure spalled off upon annealing. Fig. V-21b shows an isolated alumina hollow sphere at higher magnification.

The annealing treatments performed in Ar for the Cr-Al double-layer system led to the same conclusions than those from Al microparticles. By performing the annealing treatment in Ar, molten Al flows out from the microparticles through the nano-cracks of the thin alumina shell (Fig. V-19). This resulted in the fast consumption of metallic Al contained in the microspheres and the limited growth of the alumina shells. Molten Al subsequently reacted with the Cr interlayer and formed Al_xCr_y intermetallic phases in the slurry deposit (cf. paragraph V.3. in Chapter III). To increase the sintering between the alumina hollow spheres and consolidate the top coat structure, it is therefore necessary to introduce oxidizing species upon annealing (i.e. synthetic air).

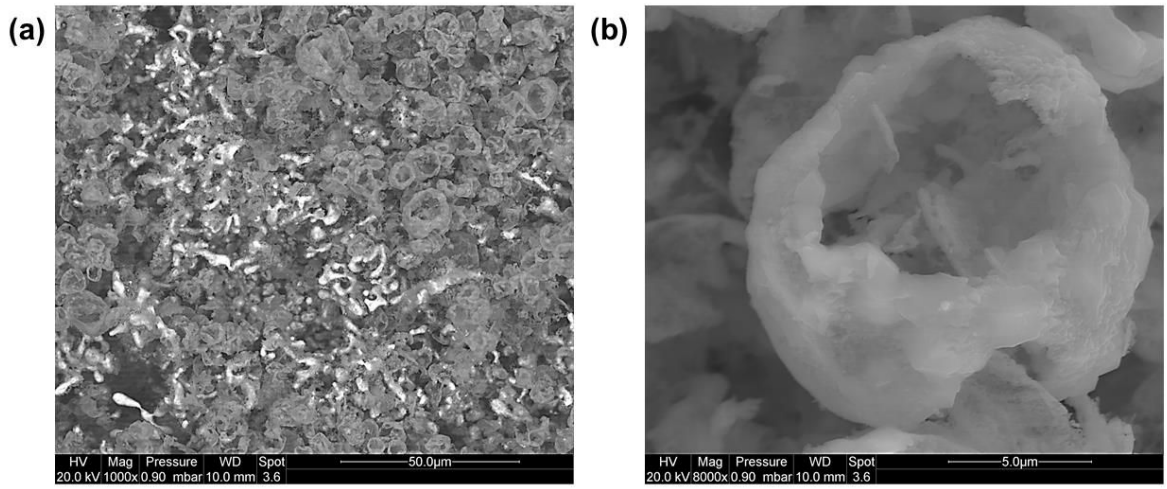

Fig. V-21. (a) BSE surface image of the top coat structure after annealing in flowing Ar (400°C-3h + 1080°C-6h) and (b) details of a broken hollow alumina microsphere.

III.2. Influence of the atmosphere (Ar, air) on the formation of the Cr-Al double-layer system on pure nickel

For a better comprehension of the mechanisms of formation, a selected heat treatment (400°C-3h + 1080°C-6h) was performed in different conditions by switching the atmosphere between Ar and synthetic air. A layer of approximately 10 mg.cm^{-2} of Cr and a second layer of approximately 10 mg.cm^{-2} of Al were deposited on the samples for an overall ratio close to 50Cr-50Al in wt.%. The samples were submitted to the same heat treatment and only differed by the stage at which synthetic air was introduced at the expense of Ar in the reaction chamber. The different tests carried out are summarized in Fig. V-22 and were numbered from "S1" to "S5" for the sake of clarity. Note that in the following paragraphs, sample "S6" refers to the one heat treated in flowing Ar. For sample "S3", synthetic air was introduced just after the exothermic reaction occurring between Al and Cr at approximately 640°C in Ar [42].

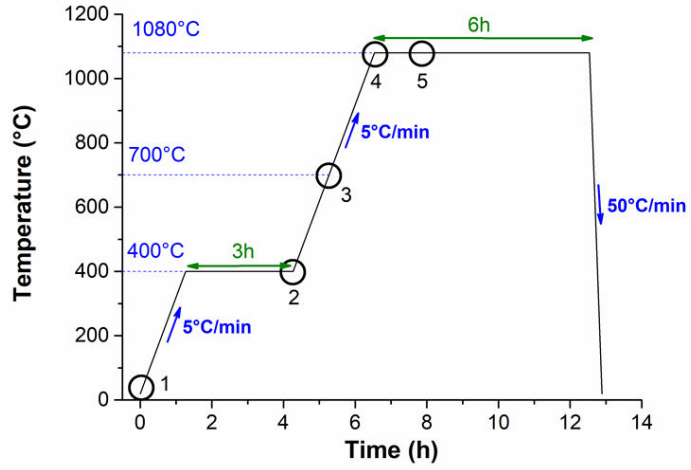

Sample test	Introduction of synthetic air
S1	Before heat treatment
S2	End of dwell at 400°C
S3	At 700°C upon heating
S4	At the end of the heating ramp
S5	After one hour dwell at 1080°C

Fig. V-22. Details of the heat treatments carried out to investigate the influence of the atmosphere (Ar, synthetic air) on the formation of the Cr-Al double-layer system on pure nickel.

- ***Thermogravimetric analyses:***

Fig. V-23a presents the thermogravimetric curves obtained during the different annealing treatments of the Cr-Al double-layer system elaborated on pure nickel. Note that the conditions of the annealing treatment greatly influenced the overall mass variation of the samples. The sharp mass variation observed at different stages of the annealing treatment for samples S2 to S5 corresponded to the purge of the reaction chamber before introduction of synthetic air. For a better comparison of the results, the thermogravimetric curves of Fig. V-23a were sectioned for the regions of interest.

For the three hours dwell at 400°C (Fig. V-23b), a similar mass loss was observed for all samples and was attributed to the removal of the organic binder [38]. The composition of the atmosphere seemed to exert no significant influence on the thermogravimetric curves up to 400°C. However, the heating curves presented in Fig. V-23c suggested that the samples S1 and S2 were affected by synthetic air from approximately 550°C. The mass gain observed from 550°C for these two samples was attributed to the growth of the amorphous alumina layer [2,3,16]. A stepwise oxidation was then observed and centred at approximately 615°C suggesting the crystallization of the amorphous alumina layer into γ-Al_2O_3 [2,3,16]. For samples S1 and S2, the oxidation rate considerably increased after reaching 750°C. The overall mass variation was much higher than the one recorded in Fig. V-17b for the sample slurry coated with Al microparticles and heat treated in synthetic air. This may indicate that a fraction of the Cr microparticles oxidized upon annealing which could increase the oxidation rate. For the samples heat treated in Ar, no significant mass change was observed upon heating from 400°C to 1080°C (Fig. V-23c) except for samples S3 and S4 since the introduction of synthetic air in the reaction chamber considerably increased the oxidation rate.

During the 6 hours dwell at 1080°C (Fig. V-23d), the mass gain was still insignificant for sample S6 heat treated in Ar. This was in good agreement with the thermogravimetric curve presented in Fig. V-9. Therefore, the p_{O_2} in the Ar flow seemed to be too low to significantly oxidize the Al microspheres and thicken the alumina oxide shells (Fig. V-19 and Fig. V-20c). For samples S1 to S4, the oxidation rate progressively decreased suggesting a parabolic growth rate. This was also observed for sample S5 with the introduction of synthetic air one hour after reaching 1080°C. The significant differences on the overall mass variation of the samples upon annealing suggested that the resulting coatings must be completely modified by the introduction of synthetic air at different stages of the annealing treatment.

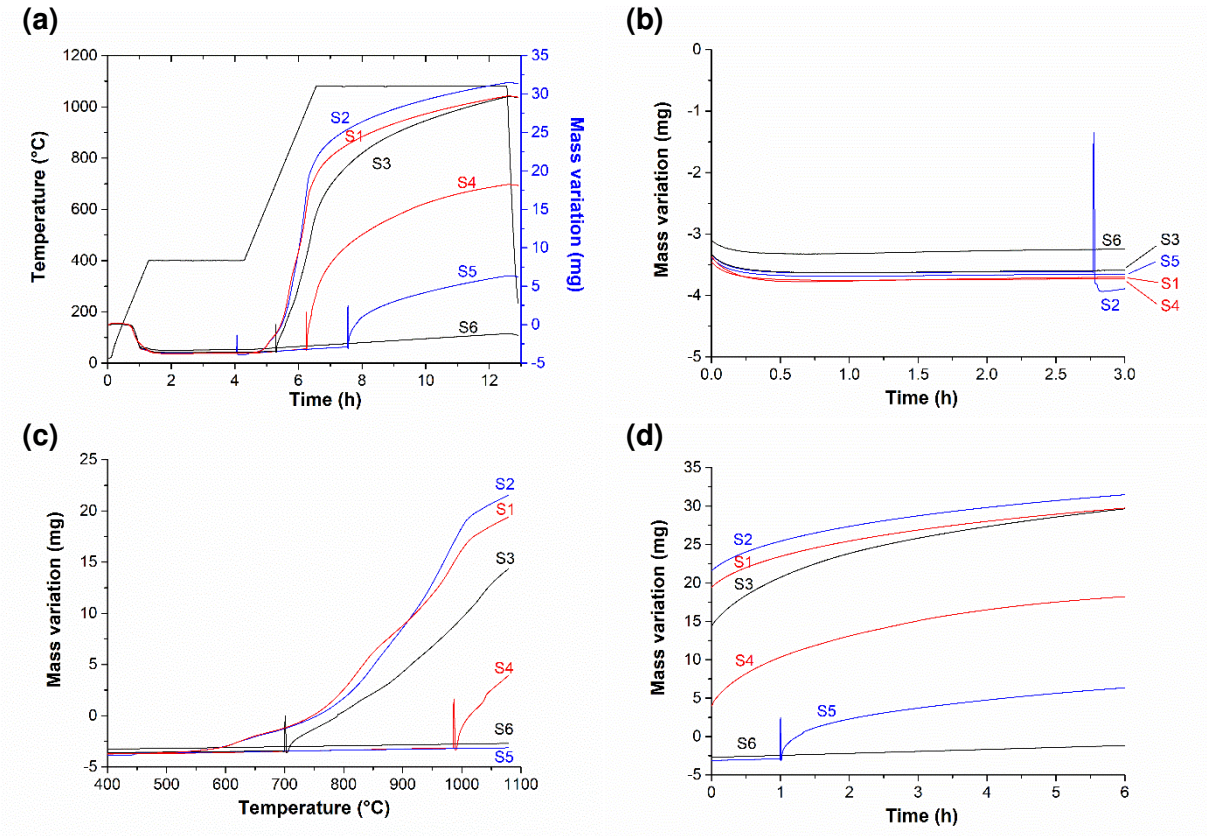

Fig. V-23. Thermogravimetric curves for the Cr-Al double-layer system elaborated on pure nickel in the different conditions (cf. Fig. V-22) for the (a) complete heat treatment, (b) isothermal section at 400°C, (c) heating ramp at 5°C/min between 400°C and 1080°C and (d) isothermal section at 1080°C.

- ***Surface characterization of the complete thermal barrier systems after annealing:***

The SEM characterization of the surfaces after the different annealing conditions is shown in Fig. V-24. As expected from the thermogravimetric curves, the morphology of the top coat structure significantly changed. For samples S1 and S2, a dense and adherent top coat structure was formed on the surface. The top coat structure was close to the one obtained by Montero et al. on IN738 Ni-based superalloy after exposure at 800°C for 100 hours [23]. The oxide shells were characteristic of the microstructure of α-Al_2O_3. The formation of α-Al_2O_3 was confirmed by XRD (Fig. V-25) and Raman surface analyses. For these two samples, the alumina microspheres were very well sintered whereas a spongy microstructure was also observed on the top coat surface. This microstructure probably resulted from the fast oxidation of Al when shrinkage of the oxide shell occurred upon annealing in synthetic air [6,20]. These observations are in good agreement with the mechanisms proposed on Fig. V-19 in synthetic air.

For samples S3 and S4, the top coat presented a white colour (see the macrographs) suggesting the formation of α-Al_2O_3. The SEM surface images attested that the thickness of the oxide shells progressively decreased from sample S1 to sample S5. The volume shrinkage induced by the γ-Al_2O_3 to α-Al_2O_3 transformation led to the deformation of the alumina shells. This volume shrinkage was more pronounced for thin alumina shells (samples S3 to S5) because of their lower mechanical strength. For sample S5, the top coat structure was no longer adherent but powdery-like. Some intermetallic phases were observed underneath the alumina hollow spheres presenting thin oxide shells.

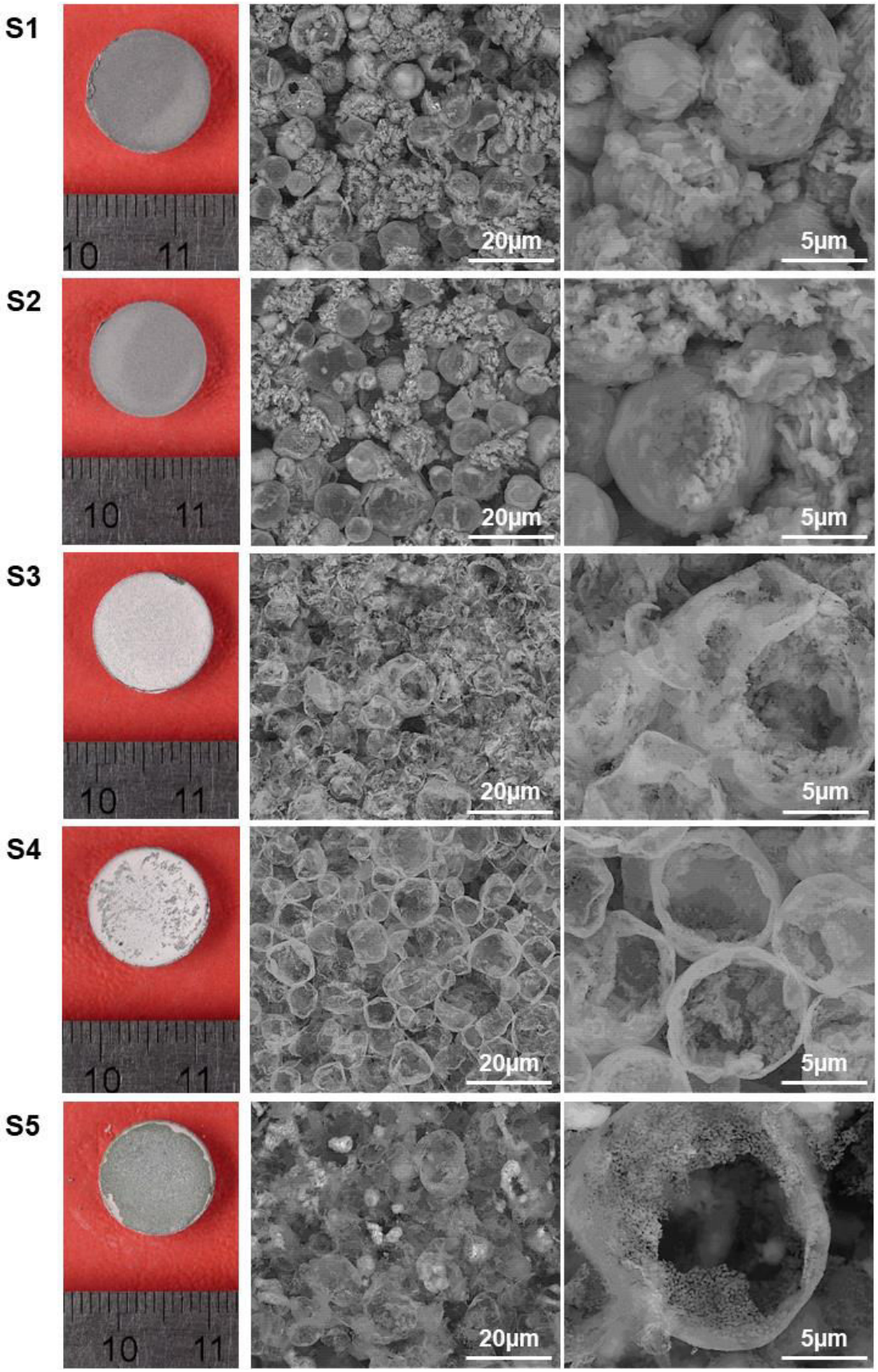

Fig. V-24. Macrographs and SEM surface images of the samples after the different annealing conditions (pure nickel + 50Cr-50Al double-layer system).

The XRD analyses are given in Fig. V-25. For samples S1 and S2, the XRD patterns were very similar and depicted the major contribution of the α-Al_2O_3 crystal structure. Some reflections of Cr_2O_3 were also identified. For samples S3 and S4, additional peaks were observed with the detection of Cr-rich phases formed in the slurry deposit. A cubic structure was identified, probably coming from a Cr solid solution, together with the two main peaks of the $AlCr_2$ tetragonal structure. Additional peaks were labelled with question marks and were presumably related to Al_xCr_y phases enclosed in the top coat structure after annealing. By correlation with SEM surface images, this suggested that the α-Al_2O_3 top coat was denser for samples S1 and S2. For the sample heat treated in Ar (S6), the detection of the Cr-rich phases (Cr solid solution and $AlCr_2$) was more significant than α-Al_2O_3.

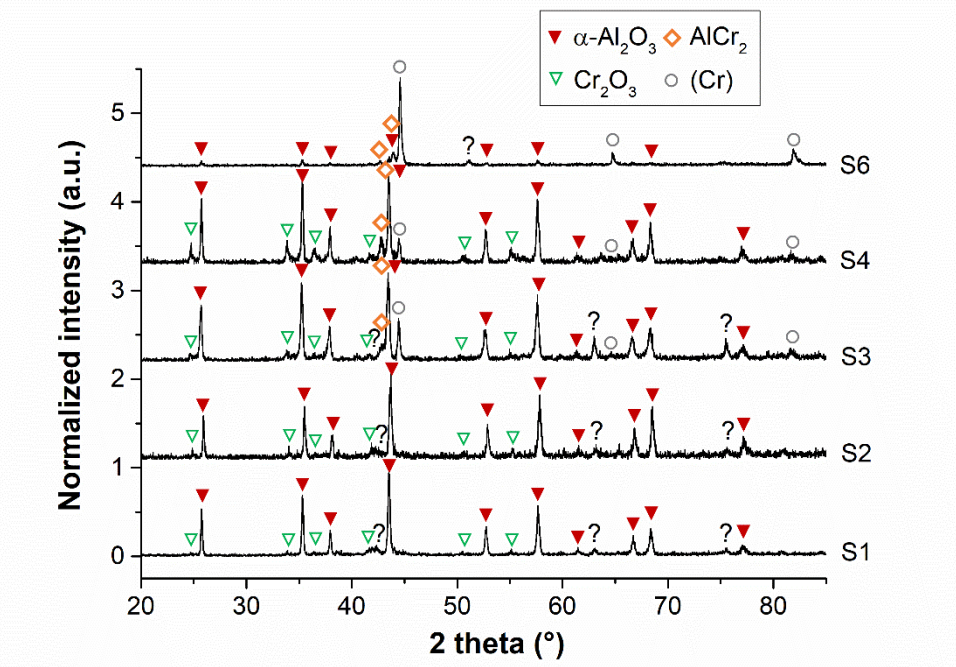

Fig. V-25. XRD patterns of the surface for the different samples after annealing (pure nickel + 50Cr-50Al double-layer system).

- ***Cross-section characterization of the complete thermal barrier systems after annealing:***

Fig. V-26 presents the cross-section micrographs of the coating systems obtained after the different annealing conditions on pure nickel substrate. As suggested by the thermogravimetric curves and the surface characterization of the samples, synthetic air had a critical effect on the coating microstructure. The resulting coating system was similar for samples S1 and S2 with an inner layer composed of oxides ("OL") and a top coat layer ("TC") composed of hollow alumina spheres. Some bright particles were observed in the top coat and were attributed to Al-Cr intermetallic phases. For these two samples, the top coat structure was greatly adherent to the underlying substrate and the alumina hollow spheres were well sintered. For sample S3, the coating microstructure was close to samples S1 and S2. However, the alumina microspheres were less sintered and there was a greater amount of Al-Cr

intermetallic phases in the top coat structure. These observations are in good agreement with the XRD surface analyses (Fig. V-25). It must be noted that for these three samples, the formation of Ni_xAl_y phases was completely hampered on the substrate surface.

The coating system obtained on sample S4 was completely different than the ones of samples S1 to S3. Some diffusion islands were randomly distributed on the substrate surface whereas the oxide layer was significantly thinner and discontinuous for sample S4. Since the heating ramp was performed in Ar for sample S4 (Fig. V-22), molten Al could be released from the Al microparticles (Fig. V-19). This promoted the formation of Al_xCr_y phases in the slurry deposit by reaction between molten Al and the Cr interlayer. The quantity of Al-Cr phases was therefore greater for sample S4 than that of samples S1 to S3, as observed in cross-section on Fig. V-26 and depicted by XRD surface analyses of Fig. V-25. The appearance of Ni_xAl_y diffusion islands suggested that interdiffusion between nickel from the substrate and Al from the top coat occurred upon heating. For sample S5, a discontinuous diffusion layer was formed on the surface whereas a great fraction of Cr-rich phases remained above the substrate. As suggested with the SEM surface characterization (Fig. V-24), the top coat structure

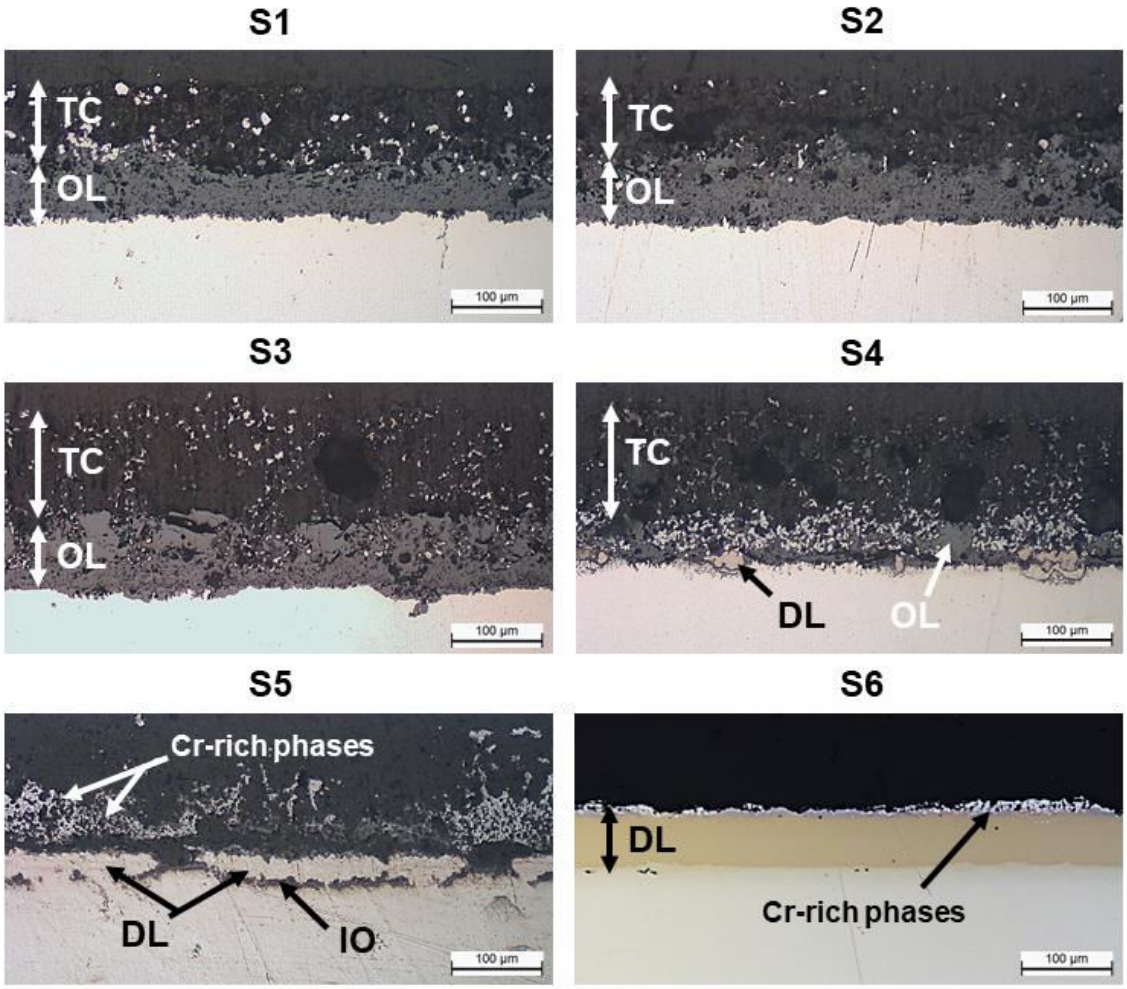

Fig. V-26. Cross-section micrographs of the 50Cr-50Al double-layer system elaborated on pure nickel after the different annealing conditions (TC: Top coat, OL: Oxide layer, DL: Diffusion layer and IO: internal oxidation).

composed of hollow alumina spheres was no longer adherent to the substrate after annealing. For the sample heat treated in Ar (sample S6), a homogeneous diffusion layer was formed with Cr-rich phases at the extreme surface. The top coat structure was not adherent and not resistant since the formed alumina oxide shells were very thin with barely any sintering (Fig. V-19 and Fig. V-20c).

SEM was carried out to further characterize the cross-section of sample S1 (Fig. V-27). The top coat structure was mainly composed of hollow alumina spheres with relatively thick oxide shells. These oxide shells were easily identified on the X-ray map of O (Fig. V-27c). As depicted on Fig. V-27b, Al remained in the top coat structure and did not incorporate into the substrate. Some particles were observed in the top coat structure with an intermediate contrast in BSE mode. These particles were rich in Al and in Cr according to the X-ray maps of Fig. V-27b and Fig. V-27d. The composition of these phases ranged from 82.7Al-14.2Cr-3.1Ni to 68.9Al-25.8Cr-5.3Ni suggesting the formation of different Al_xCr_y phases. The inner oxide layer was composed of several different oxides according to the BSE image and this result was highlighted with Ni (Fig. V-27a) and Cr (Fig. V-27d) distribution. Raman micro-spectrometry was carried out to identify the oxides formed after annealing by correlation with EDS spot measurements. Raman spot analyses were performed in cross-section every 10µm for a precise identification (Fig. V-28). Table V-1 summarizes the Raman shifts measured for the spot s07 to s11 for comparison with data from literature.

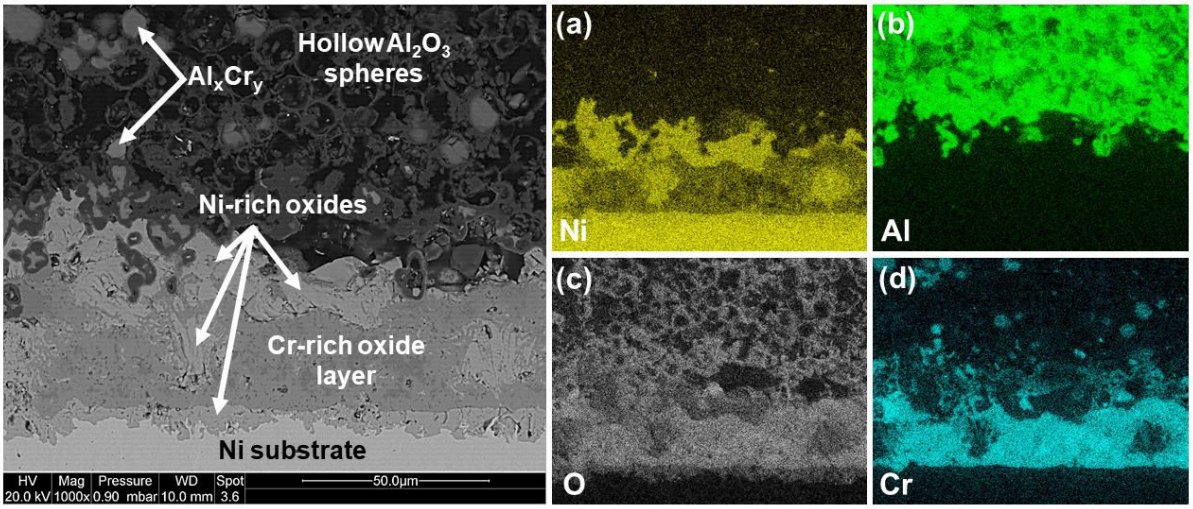

Fig. V-27. BSE cross-section image of the sample S1 (50Cr-50Al double-layer system) after annealing in synthetic air and corresponding X-ray maps of (a) Ni, (b), Al, (c), O and (d) Cr.

As suggested with the Al X-ray map (Fig. V-27b), the top coat structure was composed of α-Al_2O_3 with some Al_xCr_y intermetallic phases (spot s04 on Fig. V-28b). The Cr-rich oxide layer was mainly composed of the $NiCr_2O_4$ spinel type with some local reflections of Cr_2O_3 (Fig. V-28b). These observations confirmed that the Cr microparticles initially present on the substrate surface were completely oxidized after the annealing treatment. Oxidation of Cr microparticles acted as a diffusion barrier for Al, which remained in the top coat structure and oxidized into α-Al_2O_3. A Ni-rich oxide identified as NiO was also detected at the surface of the substrate (spot s11 on Fig. V-28b). Outward diffusion of nickel occurred upon annealing at 1080°C and converted Cr_2O_3 resulting from the oxidation of the Cr microparticles into a spinel type $NiCr_2O_4$. The outward diffusion of nickel was clearly demonstrated with the formation of NiO nodules above (spot s07) and through the Cr-rich oxide layer (Fig. V-27a).

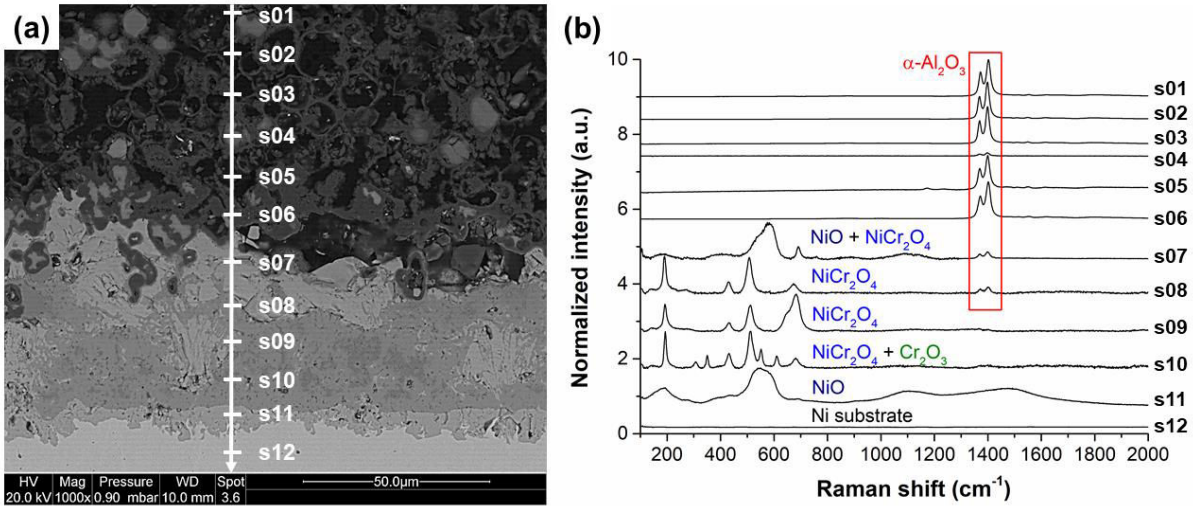

Fig. V-28. (a) BSE cross-section image of sample S1 and (b) corresponding Raman spot analyses after annealing in synthetic air.

Table V-1. Raman shifts (cm^{-1}) measured for the different spot analyses (Fig. V-26b).

This work					References				
s07	s08	s09	s10	s11	Cr_2O_3 [43,44]		$NiCr_2O_4$ [45,46]		NiO [47]
182	-	-	-	188	-	-	-	-	-
-	190	192	193	-	-	-	190	193	-
-	-	-	306	-	290	296	-	-	-
-	-	-	350	-	352	350	-	-	-
402	-	-	-	412	-	-	-	-	412-423
-	430	432	432	-	-	-	427	429	-
-	507	511	512	-	-	-	508	512	-
537	-	-	-	542	-	-	-	-	549-556
-	-	-	552	-	547	554	-	-	-
-	-	-	610	-	617	615	-	-	-
692	674	681	681	-	-	-	678	682	-
888	-	-	-	904	-	-	-	-	904-909
1092	-	-	-	1096	-	-	-	-	1081-1098
-	-	-	-	1475	-	-	-	-	1489-1503

III.3. Reactivity between Al microparticles and oxide powders (NiO, Cr_2O_3 and Al_2O_3)

Considering the aluminizing process of the Cr-Al double-layer system on pure nickel and in synthetic air, one could expect:

- the surface oxidation of pure nickel substrate into NiO,
- the peripheral oxidation of the Cr microparticles in the slurry deposit into Cr_2O_3,
- the peripheral oxidation of the Al microparticles and the oxidation of liquid Al in the slurry deposit into Al_2O_3.

- ***Overview of the aluminothermic reactions:***

For a better comprehension of the mechanisms of formation of the full thermal barrier systems in synthetic air, the reactivity between Al microparticles and these oxides (NiO, Cr_2O_3 and Al_2O_3) was studied by DSC. The aluminothermic reactions have been extensively studied in the last decades and are well known for their high exothermicity to produce aluminides [48,49] or intermetallic-ceramic composite materials [50-54]. Since Al has a very high affinity for oxygen, it is able to reduce the most of metal oxides such as NiO or Cr_2O_3 [48,49,55-57]. The aluminothermic reaction can be written as follows:

$$2Al + \frac{3}{y}Me_xO_y \rightarrow Al_2O_3 + \frac{3x}{y}Me \qquad \textbf{(Eq. V-1)}$$

Depending on the initial stoichiometry of reaction *(Eq. V-1)*, the reduction of the oxide can lead to the formation of corresponding metal or to an aluminide if an excess of Al is employed [48,49,53,58]. As a result, aluminides with different stoichiometries can be obtained by changing the ratio of the reactants, which also depend on the maximal temperature reached during the reaction. High energy ball milling was also found to decrease the ignition temperature and the activation energy of aluminothermic reductions [51,54,59].

- ***Characterization of the Al_2O_3, Cr_2O_3 and NiO powders:***

In this study, Al microparticles and powders of different oxides (Al_2O_3, Cr_2O_3 and NiO) were thoroughly manually mixed and submitted to a DSC experiment to study their reactivity. The Al_2O_3 and NiO microparticles were provided respectively, by Sigma Aldrich and Alfa Aesar whereas the Cr_2O_3 microparticles were obtained by oxidation of the fine Cr microparticles presented in Fig. II-3 of Chapter II. The XRD patterns and Raman analyses of the three oxide powders are given on Fig. V-29a and Fig. V-29b, respectively. The characteristic diffraction peaks of NiO (cubic), α-Cr_2O_3 (hexagonal) and α-Al_2O_3 (hexagonal) were detected (Fig. V-29a). Note that the cubic structure of α-Cr was also detected suggesting that only the periphery of the Cr microparticles was oxidized. Raman micro-spectrometry was carried out to get the reference signals of the different oxide powders (Fig. V-29b). The α-Al_2O_3 fluorescence doublet was clearly identified for the Al_2O_3 powder [34,60,61]. For the Cr_2O_3 powder, the five characteristic vibration modes of α-Cr_2O_3 were identified [32,33,43,44]. For the NiO powder, five broad Raman bands were obtained centred at approximately 204 cm^{-1}, 365 cm^{-1}, 545 cm^{-1}, 694 cm^{-1} and 1065 cm^{-1}. The Raman spectrum was close to the one obtained by Burmistrov et al. after annealing of nickel oxide nano-powders at 900°C for 1 hour in air [62].

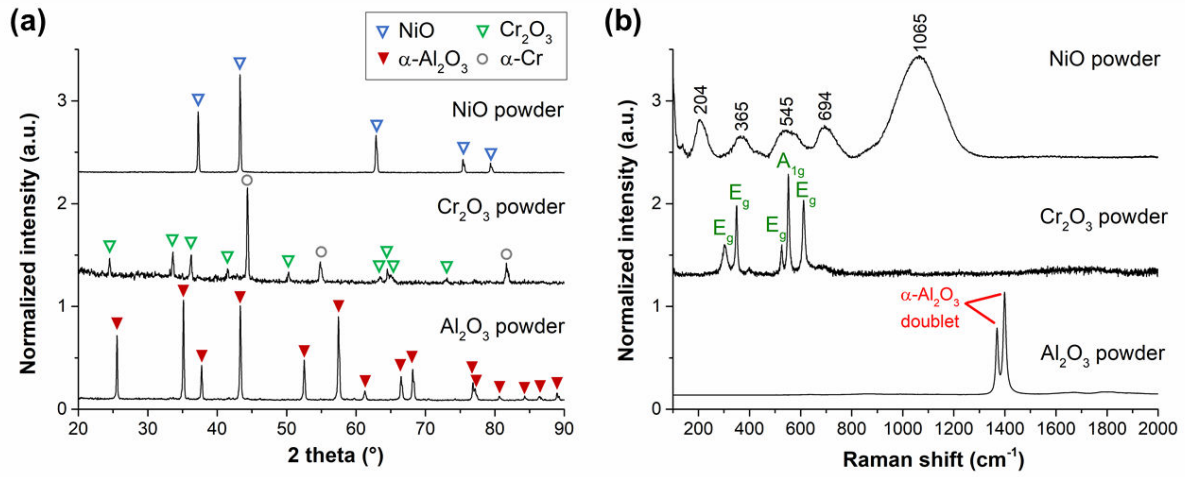

Fig. V-29. (a) XRD patterns and (b) Raman spectra of the different oxide powders.

The same procedure than that applied for the determination of the reactivity between Al and Cr microparticles (cf. paragraph I. in Chapter III) was followed here. The initial ratio of the Al and the oxide powders is given in Table V-2 and compared with the stoichiometric compositions of reaction *(Eq. V-1)*. For both Al-NiO and Al-Cr_2O_3 mixtures, Al was in excess compared to the stoichiometric compositions. The powder mixtures were heated to 1200°C at a heating rate of 5°C/min, left at 1200°C for 10 minutes and then cooled down to room temperature at 5°C/min. The DSC tests were performed in Ar to compare with data of Chapter III.

Table V-2. Composition of the different Al-oxide mixtures investigated by DSC and comparison with the stochiometric composition considering reaction (Eq. V-1).

Mixture	Actual composition		Stoichiometric composition	
	(at.%)	(wt.%)	(at.%)	(wt.%)
Al-NiO	54.3 Al-45.7 NiO	30 Al-70 NiO	40 Al-60 NiO	19.4 Al-80.6 NiO
Al-Cr_2O_3	74.4 Al-25.6 Cr_2O_3	34 Al-66 Cr_2O_3	66.7 Al-33.3 Cr_2O_3	26.2 Al-73.8 Cr_2O_3
Al-Al_2O_3	70.4 Al-29.6 Al_2O_3	38.6 Al-61.4 Al_2O_3	-	-

The heating branches of the DSC curves obtained for the different mixtures are presented on Fig. V-30. For the three mixtures, the endothermic signal of Al melting was observed at approximately 660°C. For the sake of clarity, the three systems will be investigated separately.

- ***Al + NiO system:***

For the Al + NiO mixture, an exothermic event occurred before the Al melting with a maximal heat flow value at about 620°C. This event had already been reported by Galetz et al. with DTA analyses of Al and Ni microparticles in air and was ascribed to the oxidation of the microparticles [22]. Since it was only observed for the Al + NiO system and not for the powders taken separately, it appeared that this exothermic event was associated with a solid-solid interaction between Al and NiO. This exothermic event occurring before the Al melting was also reported by other authors by mixing Al and NiO powders [52,53]. According to Zhu et al., the initial Al/NiO reaction at about 600°C led to the formation of Ni without any other phases [52]. Therefore, this event was attributed to the solid state reduction of NiO by Al following the reaction [48,52,56,57]:

$$2Al(l) + 3NiO(s) \rightarrow Al_2O_3(s) + 3Ni(s) \qquad \textbf{(Eq. V-2)}$$

After the melting of Al, a broad exothermic peak was observed. It initiated at approximately 750°C and ended at about 1020°C. This exothermic peak was associated with the liquid state reaction *(Eq. V-2)* [52,59,63]. Note that reaction *(Eq. V-2)* is highly exothermic with a ΔH value of -968 kJ/mol [59]. A second exothermic event was observed at about 1070°C and likely corresponded to the two-stage reduction of NiO [63]. This suggested the formation of Ni_xAl_y intermetallic phases because of the excess of Al in the initial powder mixture [48,52,58].

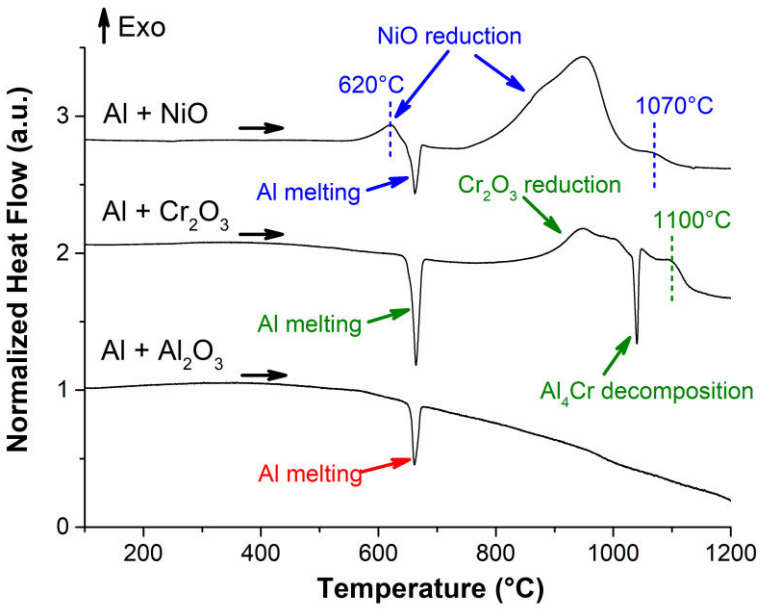

Fig. V-30. DSC curves (heating branches at 5°C/min) obtained for the mixtures of Al microparticles and oxide powders.

- ***Al + Cr_2O_3 system:***

Unlike the mixtures of Al and Cr microparticles [42], there was no exothermic reaction at about 640°C for the Al + Cr_2O_3 system (Fig. V-30). It therefore appeared that the peripheral oxidation of the Cr microparticles hampered the solid state reaction between Al and Cr_2O_3. When the temperature reached approximately 800°C, the heat flow progressively increased to reach a maximum value at about 950°C. This probably referred to the liquid state reduction of Cr_2O_3 by Al following the reaction:

$$2Al(l) + Cr_2O_3(s) \rightarrow Al_2O_3(s) + 2Cr(s) \qquad \textbf{(Eq. V-3)}$$

The reaction *(Eq. V-3)* is highly exothermic with a ΔH value of -541 kJ/mol [49]. A strong endothermic peak was observed at approximately 1035°C and convoluted with the broad exothermic peak on Fig. V-30. This endothermic reaction was attributed to the decomposition of Al_4Cr phase [42,64-66]. This confirmed that the excess of Al reacted with Cr to form Al_xCr_y phases upon heating. A second exothermic peak was recorded centred at about 1100°C suggesting a further transformation of the reacting products in the system.

- ***Al + Al_2O_3 system:***

For the Al + Al_2O_3 system, only the Al melting was observed on the DSC curve (Fig. V-30). No other thermal event than Al melting was identified on the DSC curve at higher temperatures. Since the experiment was performed in Ar with low p_{O_2} (not measured in this work), the oxidation of liquid Al was considerably limited by comparison with the heat treatments performed in synthetic air (Fig. V-19). Consequently, the sintering of liquid Al by oxidation with the alumina microparticles was prevented since the wettability of liquid Al and alumina is very low [67]. This would explain why the sintering of individual hollow alumina microspheres is more important in synthetic air than in Ar (Fig. V-18a and Fig. V-18b).

III.4. Discussion

- ***Reactivity between Al microparticles and the oxides:***

The DSC experiments highlighted that the potential oxidation of the nickel substrate and that of the Cr microparticles had a tremendous influence on their reactivity with Al microparticles upon annealing. In the vicinity of the Al melting, the oxide had a critical effect on its reactivity with Al (Fig. V-30). Whereas the NiO reduction was initiated at temperatures below 600°C, the Cr_2O_3 reduction was shifted to temperatures over 800°C with a heating rate of 5°C/min in flowing Ar. This would explain why the Cr interlayer in the Cr-Al double-layer system had a critical effect on the microstructure of the complete thermal barrier system in synthetic air (Fig. V-26). Note that the microstructure of the coatings was completely different between sample S2 and sample S4 (Fig. V-26). This suggested that the nature of the atmosphere (inert or oxidizing) had a tremendous influence upon heating between 400°C and 1080°C (Fig. V-22).

Since the heating ramp was performed in Ar for sample S4 (Fig. V-22), molten Al could be released from the Al microparticles (Fig. V-19). Simultaneously, the peripheral oxidation of Cr microparticles was limited, which fostered the synthesis of Al_xCr_y phases in the slurry deposit (cf. paragraph V.3. in Chapter III). When air was introduced into the reaction chamber (at about 1080°C), interdiffusion between nickel from the substrate and the Al-Cr phases just initiated resulting in the formation of isolated diffusion zones (Fig. V-26). An excess of Cr microparticles did not react with Al and oxidized on the surface between the Al_xCr_y phases and the nickel substrate (cf. Fig. in Chapter III-34). The nickel substrate also oxidized into NiO on the uncoated areas. Then Cr_2O_3 and NiO reacted together to result in $NiCr_2O_4$ spinels in the top coat [68]. This would explain the fast mass gain of sample S4 after introduction of synthetic air (Fig. V-23c).

- ***Influence of the Cr interlayer on the mechanisms of formation:***

Upon heating in synthetic air (sample S2), the peripheral oxidation of Al and Cr microparticles was considerably promoted as depicted by the sharp mass gain on thermogravimetric curves of Fig. V-23c. The peripheral oxide developed on Cr microparticles acted as a diffusion barrier for Al since the formation of Cr_2O_3 delayed the initiation of their exothermic reaction (Fig. V-30). Consequently, metallic Al remained in the top coat and did not react with the underlying nickel substrate. The presence of Al-Cr intermetallic phases surrounded by α-Al_2O_3 in the top coat structure of sample S2 (Fig. V-27) suggested that the reduction of Cr_2O_3 by molten Al occurred in the top coat. Molten Al was probably coming from the volume shrinkage of the alumina shells upon heating releasing liquid Al. This hypothesis is in good agreement with the XRD surface analyses of Fig. V-25. Therefore, the Cr interlayer promoted the oxidation of Al into α-Al_2O_3 in the top coat and the sintering of individual hollow alumina microspheres (Fig. V-24).

- ***Influence of the Cr-Al ratio on the mechanisms of formation of complete thermal barrier systems:***

In order to investigate the influence of the initial Cr-Al ratio on the microstructure of the complete thermal barrier coatings, pure nickel samples were slurry coated with a 25Cr-75Al double-layer system and annealed (Fig. V-22). Except for the sample heat treated in flowing Ar (S6 on Fig. V-31), the microstructure of the coatings was completely different than that of the 50Cr-50Al system (Fig. V-26). As expected, Ni_xAl_y diffusion islands were randomly distributed on the substrate surface of samples S1 and S2 whereas the rest of the surface was covered with a thick oxide layer. Some internal oxidation was observed in the substrate and at the interface substrate-diffusion layer. For sample S3, a continuous diffusion layer was formed and the oxidation of the substrate was confined to a few areas. The top coat was composed of a well sintered intermetallic-ceramic composite. For sample S4, a continuous diffusion layer had formed with a thickness of approximately 90µm. The microstructure obtained for sample S5 was similar to that of sample S6 suggesting that interdiffusion between the nickel substrate and the Al_xCr_y phases was nearly complete after one hour dwell at 1080°C.

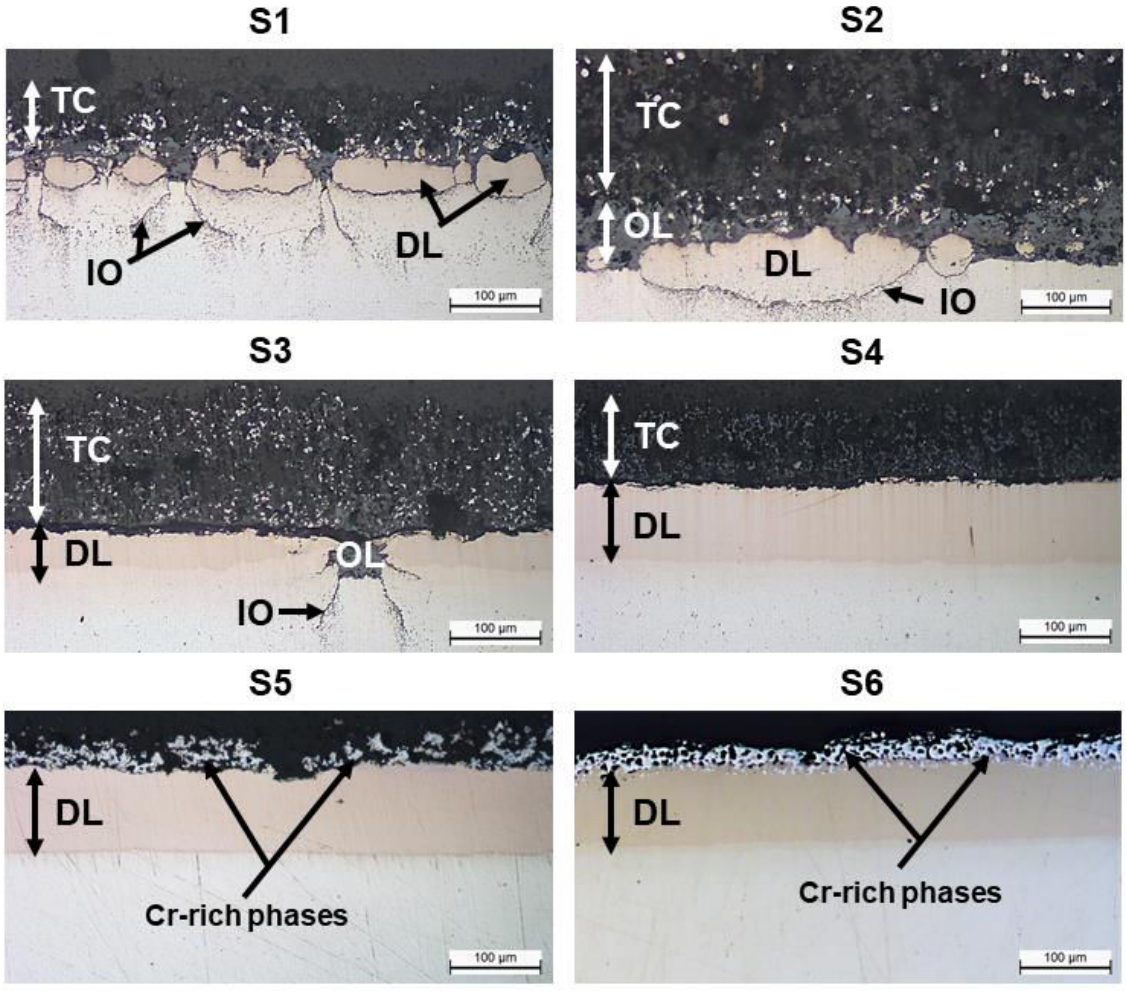

Fig. V-31. Cross-section micrographs of the 25Cr-75Al double-layer system elaborated on pure nickel after the different annealing conditions (TC: Top coat, OL: Oxide layer, DL: Diffusion layer and IO: internal oxidation).

These results therefore confirmed that the initial Cr-Al ratio has a critical effect on the microstructure of the coatings hence on their mechanisms of formation. Unlike the 50Cr-50Al double-layer system, Al was in excess in the 25Cr-75Al one. For samples S1 and S2, the excess of Al could diffuse towards the nickel substrate and react by combustion synthesis [22]. As a result, Ni_xAl_y diffusion layers formed on the substrate surface. The formation of α-Al_2O_3 at the interface substrate-diffusion layer may indicate that reduction of NiO occurred upon annealing by Al following the reaction *(Eq. V-2)*. Since Al was in excess in reaction *(Eq. V-2)*, formation of Ni_xAl_y intermetallic phases (i.e. NiAl) occurred [48,53,58]. The SEM characterization of sample S1 showed the random distribution of diffusion layers and oxide layers on the substrate surface. A BSE cross-section image and the corresponding X-ray maps of Ni, Al, O and Cr are given on Fig. V-32.

The evidence of alternating β-NiAl diffusion layers and oxide layers can be observed along the substrate surface on Fig. V-32. The β-NiAl diffusion layers were surrounded with α-Al_2O_3 whereas the oxide layers were composed of a Ni-rich oxide (NiO) and a Cr-rich one (Cr_2O_3), according to local Raman analyses. The top coat structure was composed of hollow alumina spheres with thick oxide shells and presenting a good sintering at the naked eye (Fig. V-32b and Fig. V-32c). Note that Al_xCr_y and Ni_xAl_y intermetallic phases were also observed in the top coat structure. Their random distribution suggested that highly exothermic reactions occurred upon annealing (i.e. aluminothermic reactions). The oxidation of Cr microparticles into Cr_2O_3 was considered to cause the heterogeneous growth of the diffusion layers on the surface. Thick Cr_2O_3 layers were thus formed between the β-NiAl diffusion layers (Fig. V-32d). Cr_2O_3 acted as diffusion barrier for Al which preferentially reacted with NiO. Since the reaction between Al and NiO and eventually Ni is highly exothermic, the heat released could subsequently melt the Al around the ignition zone. This resulted in the formation of random diffusion islands surrounded by α-Al_2O_3. When the whole metallic Al is consumed, oxidation of the nickel substrate into NiO occurs in the "uncoated" areas.

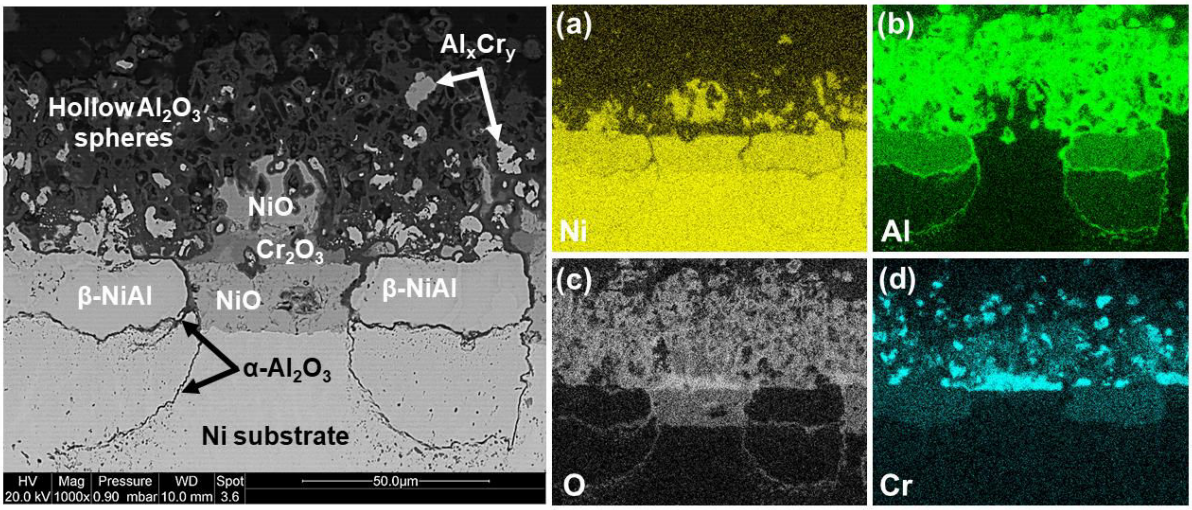

Fig. V-32.BSE cross-section image of the sample S1 (25Cr-75Al double-layer system) after annealing in synthetic air and corresponding X-ray maps of (a) Ni, (b), Al, (c), O and (d) Cr.

- ***Influence of Cr addition on the adherence of the top coat structure:***

The cross-section of sample S4 was also analyzed by SEM (Fig. V-33). The microstructure of the complete thermal barrier system was significantly different from the one observed on Fig. V-32. The diffusion layer was even on the surface with the β-NiAl composition. An intermediate γ'-Ni_3Al layer of approximately 5µm was identified between the β-NiAl layer and the nickel substrate (Fig. V-33a). Such diffusion layer microstructure confirmed that the release of Al from the microparticles was fast upon heating in Ar (Fig. V-19). This promoted the formation of Al_xCr_y phases in the deposit and the subsequent interdiffusion between nickel and Al to form the β-NiAl phase. When synthetic air was introduced into the reaction chamber, the growth of the diffusion layer was presumably completed which fostered the growth of an α-Al_2O_3 TGO scale on the surface (Fig. V-33b). Cr was completely solubilized in the β-NiAl phase with less than 2 at.%. Consequently, Cr was mainly distributed in the top coat structure (Fig. V-33a). The characteristic hollow alumina microspheres were no longer observed in the top coat structure of sample S4. The latter was composed of both α-Al_2O_3 and $(Al_{2-x},Cr_x)O_3$ ($0 \leq x \leq 2$) oxides [69].

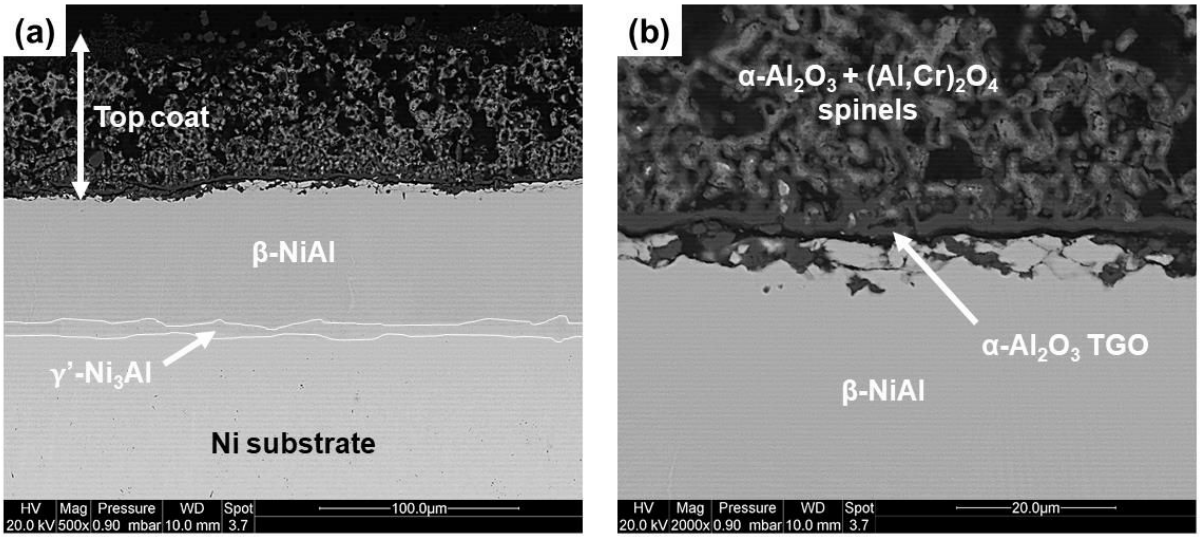

Fig. V-33. (a) BSE cross-section image of sample S4 (25Cr-75Al double-layer system) after annealing and (b) details of the TGO scale and the top coat structure formed.

IV. Summary and outlook

- ***Influence of the atmosphere on the oxidation of Al microparticles:***

The composition of the atmosphere (inert of oxidizing) had a critical effect on the peripheral oxidation of Al microparticles and the release of Al from the metallic core. Upon annealing in flowing Ar, a partial crystallization of the amorphous alumina layer occurred before the melting of Al. The defective γ-Al_2O_3 layer with nano-cracks was not healed upon Al melting and fostered the diffusion of molten Al through these nano-cracks. This resulted in the fast release of Al to react with the underlying substrate or with the Cr interlayer considering the Cr-Al double-layer system. Consequently, the hollow alumina microspheres formed in the top coat structure presented thin oxide shells with a low sintering. Upon annealing in synthetic air, healing of the defective γ-Al_2O_3 layer occurred before the Al melting. Molten Al was therefore kept inside the smaller microparticles whereas the larger microparticles burst probably because of greater stresses within the oxide shells. Upon further heating up to 1100°C, the γ-Al_2O_3 to α-Al_2O_3 transformation induced a volume shrinkage of the oxide shells with the formation of pores and nano-cracks. Molten Al then diffused through these nano-cracks and rapidly oxidized because of the high p_{O_2} in synthetic air. The hollow alumina microspheres therefore presented thicker oxide shells with a better sintering than for the ones heat treated in Ar.

- ***Influence of the atmosphere on the coating microstructures:***

The composition of the atmosphere did not seem to play any significant role on the formation of the diffusion layers from Al microparticles. The diffusion layers were formed by self-propagating high-temperature synthesis (SHS) by dissolution of nickel in molten Al and subsequent Ni_xAl_y intermetallic phases formation. The coating matrix was mainly composed of Ni_2Al_3 phase at 700°C and of β-NiAl phase at 1100°C. However, the microstructure of the top coat layer was significantly changed with the introduction of synthetic air into the reaction chamber. Synthetic air indeed promoted the thickening of the alumina shells and their sintering with extensive formation of α-Al_2O_3. This is expected to increase the mechanical strength of the top coat structure, in particular its erosion resistance.

- ***Influence of the Cr interlayer on the formation of complete thermal barrier systems:***

The influence of a Cr interlayer between the nickel substrate and the Al microparticles was also investigated for the formation of a complete thermal barrier coating. Upon annealing in Ar, the Cr interlayer did not affect the microstructure of the top coat layer since fast release of molten Al from the microspheres occurred upon heating. This resulted in the formation of Al_xCr_y phases in the slurry deposit and subsequent interdiffusion with nickel from the substrate to form continuous Ni_xAl_y diffusion layers. When annealing was performed in synthetic air, the mechanisms of formation of the coatings were completely different. The high p_{O_2} in synthetic air promoted the oxidation of the nickel substrate and of the Al and Cr microparticles thus modifying their reactivity. Peripheral oxidation of Cr microparticles appeared to suppress the exothermic reaction associated with the formation of Al_xCr_y phases at about 640°C. Consequently, the formation of Cr_2O_3 acted as a diffusion barrier and the Al was contained in the top coat structure. This resulted in the thickening of the hollow alumina spheres and their extensive sintering. After annealing, a thick oxide layer grew between the nickel substrate and the top coat structure with Cr_2O_3, $NiCr_2O_4$ and NiO oxides. This layer acted as a ceramic bond coat and ensured the adherence of the alumina top coat structure.

- ***Outlook***:

The present study opened a new way for the synthesis of intermetallic-ceramic composites based on aluminothermic reductions of NiO and of Cr_2O_3. The appearance of such reactions resulted in increased sintering of alumina top coat structures for thermal barrier coatings applications. The influence of the annealing conditions and of the architecture of the coatings was investigated for a better comprehension of the driving forces for the functionalization of thermal barrier systems. Since the optimization of the complete thermal barrier systems was not completed for functional applications, Chapter VI will be focused on the environmental resistance of the diffusion coatings (i.e. aluminide bond coats). The main objective of Chapter VI was to emphasize the functional applications of the diffusion coatings elaborated during this work by investigating their environmental resistance in different conditions.

References

[1] F. Pedraza, R. Podor, *Materials Characterization* ***113*** (2016), pp. 198-206.

[2] M.A. Trunov, M. Schoenitz, X. Zun, E.L. Dreizin, *Combustion and Flame* ***140*** (2005), pp. 310-318.

[3] B. Rufino, F. Boulc'h, M.V. Coulet, G. Lacroix, R. Denoyel, *Acta Materialia* ***55*** (2007), pp. 2815-2827.

[4] A. Rai, D. Lee, K. Park, M.R. Zachariah, *Journal of Physics and Chemistry B* ***108*** (2004), pp. 14793-14795.

[5] X. Zhu, M. Schoenitz, E.L. Dreizin, *Journal of Physics and Chemistry C* ***113*** (2009), pp. 6768-6773.

[6] S. Hasani, M. Panjepour, M. Shamanian, *Oxidation of Metals* ***78*** (2012), pp. 179-195.

[7] V.I. Levitas, B.W. Asay, S.F. Son, M. Pantoya, *Journal of Applied Physics* ***101*** (2007), pp. 083524-1-20.

[8] V.I. Levitas, B.W. Asay, S.F. Son, M.L. Pantoya, *Applied Physics Letters* ***89*** (2006), pp. 071909-1-3.

[9] V.I. Levitas, M.L. Pantoya, K.W. Watson, *Applied Physics Letters* ***92*** (2008), pp. 201917-1-3.

[10] V.I. Levitas, *Philosophical Transactions of the Royal Society A* ***371*** (2013), pp. 1-14.

[11] A.A. Firmansyah, K. Sullivan, K.S. Lee, Y.H. Kim, R. Zahaf, M.R. Zachariah, D. Lee, *Journal of Physical Chemistry C* ***116*** (2012), pp. 404-411.

[12] L.P.H. Jeurgens, W.G. Sloof, F.D. Tichelaar, E.J. Mittemeijer, *Thin Solid Films* ***418*** (2002), pp. 89-101.

[13] B. Rufino, M.V. Coulet, R. Bouchet, O. Isnard, R. Denoyel, *Acta Materialia* ***58*** (2010), pp. 4224-4232.

[14] K. Wefers, C. Misra, Oxides and hydroxides of aluminum. *ALCOA Technical Paper No.* ***19***, Rev. ALCOA Laboratories, Pittsburgh (1987).

[15] I. Levin, D. Brandon, *Journal of the American Ceramic Society* ***81*** (1998), pp. 1995-2012.

[16] M.A. Trunov, M. Schoenitz, E.L. Dreizin, *Combustion Theory and Modelling* ***10*** (2006), pp. 603-623.

[17] M. Bodaghi, A.R. Mirhabibi, H. Zolfonun, M. Tahriri, M. Karimi, *Phase Transitions* ***81*** (2008), pp. 571-580.

[18] C. Scott Nordahl, G.L. Messing, *Journal of the European Ceramic Society* ***22*** (2002), pp. 415-422.

[19] F. Velasco, S. Guzman, C. Moral, A. Bautista, *Oxidation of Metals* ***80*** (2013), pp. 403-422.

[20] V. Kolarik, M. Juez-Lorenzo, H. Fietzek, *Materials Science Forum* ***696*** (2011), pp. 290-295.

[21] F. Pedraza, M. Mollard, B. Rannou, J. Balmain, B. Bouchaud, G. Bonnet, *Materials Chemistry and Physics* ***134*** (2012), pp. 700-705.

[22] M.C. Galetz, X. Montero, M. Mollard, M. Gunthner, F. Pedraza, M. Schütze, *Intermetallics* ***44*** (2014), pp. 8-17.

[23] X. Montero, M.C. Galetz, M. Schütze, *Surface and Coatings Technology* ***206*** (2011), pp. 1586-1594.

[24] M. Mollard, *Elaboration de systèmes barrière thermique par barbotine. Comportement du nickel et de ses superalliages revêtus en oxydation cyclique à haute température*, PhD Thesis, Université de La Rochelle (2012).

[25] B. Rannou, *Slurry coatings from aluminium microparticles on Ni-based superalloys for high-temperature oxidation protection*, PhD Thesis, Université de La Rochelle (2012).

[26] M. Brossard, *Influence de l'eau (vapeur, liquide) et du régime d'oxydation sur la dégradation de revêtements alumino-formeurs sur superalliage à base nickel*, PhD Thesis, Université de La Rochelle (2014).

[27] S. Hasani, A.P. Soleymani, M. Panjepour, A. Ghaei, *Oxidation of Metals* ***82*** (2014), pp. 209-224.

[28] B. Bouchaud, B. Rannou, F. Pedraza, *Materials Chemistry and Physics* ***143*** (2013), pp. 416-424.

[29] R. Roussel, V. Kolarik, M. Juez Lorenzo, H. Fietzek, *Oxidation of Metals* ***81*** (2014), pp. 179-189.

[30] R. Roussel, *Investigación de recubrimientos multifuncionales en base de micropartículas esféricas de aluminio para aplicación a altas temperaturas,* PhD Thesis, Universidad Complutense de Madrid (2013).

[31] R. Moriya, M. Iguchi, S. Sasaki, J. Yan, *Procedia CIRP* ***42*** (2016), pp. 464-469.

[32] M. Kemdehoundja, J.F. Dinhut, J.L. Grosseau-Poussard, M. Jeannin, *Materials Science and Engineering A* ***435-436*** (2006), pp. 666-671.

[33] M. Kemdehoundja, J.L. Grosseau-Poussard, J.F. Dinhut, B. Panicaud, *Journal of Applied Physics* ***102*** (2007), pp. 093513-1-5.

[34] V.K. Tolpygo, D.R. Clarke, *Materials at High Temperatures* ***17*** (2000), pp. 59-70.

[35] E.A. Martínez, *Análisis de las capas de alumina formadas a eleveda temperatura sobre aleaciones MCrAlY y barreras térmicas (TBC),* PhD Thesis, Universidad Complutense de Madrid (2010).

[36] R. Krishnan, S. Dash, C. Babu Rao, R.V. Subba Rao, A.K. Tyagi, B. Raj, *Scripta Materialia* ***45*** (2001), pp. 693-700.

[37] R. Krishnan, S. Dash, R. Kesavamoorthy, C. Babu Rao, A.K. Tyagi, B. Raj, *Surface and Coatings Technology* ***200*** (2006), pp. 2791-2799.

[38] B. Rannou, F. Velasco, S. Guzman, V. Kolarik, F. Pedraza, *Materials Chemistry and Physics* ***134*** (2012), pp. 360-365.

[39] D.P. Garriga-Majo, B.A. Shollock, D.S. McPhail, R.J. Chater, J.F. Walker, *International Journal of Inorganic Materials* ***1*** (1999), pp. 325-336.

[40] S.R.J. Saunders, M. Monteiro, F. Rizzo, *Progress in Materials Science* ***53*** (2008), pp. 775-837.

[41] D.R. Lide, CRC Handbook of Chemistry and Physics, 1995. Boca Raton. Section 4:36.

[42] B. Grégoire, G. Bonnet, F. Pedraza, *Intermetallics* ***81*** (2017), pp. 80-89.

[43] J. Birnie, C. Craggs, D.J. Gardiner, P.R. Graves, *Corrosion Science* ***33*** (1992), pp. 1-12.

[44] J. Mougin, T. Le Bihan, G. Lucazeau, *Journal of Physics and Chemistry of Solids* ***62*** (2001), pp. 553-563.

[45] B.D. Hosterman, J.W. Farley, A.L. Johnson, *Journal of Physics and Chemistry of Solids* ***74*** (2013), pp. 985-990.

[46] I. Matulková, P. Holec, I. Němec, H. Kitazawa, T. Furubayashi, J. Vejpravová, *Journal of Molecular Structure* ***1090*** (2015), pp. 70-75.

[47] M. Marciuš, M. Ristić, M. Ivanda, S. Musić, *Journal of Alloys and Compounds* ***541*** (2012), pp. 238-243.

[48] D. Vrel, A. Hendaoui, P. Langlois, S. Dubois, V. Gauthier, B. Cochepin, *International Journal of Self-Propagating High-Temperature Synthesis* ***16*** (2007), pp. 62-69.

[49] C.L. Yeh, J.Z. Lin, *Intermetallics* ***33*** (2013), pp. 126-133.

[50] P. Matteazzi, G. Le Caër, *Journal of the American Ceramic Society* ***75*** (1992), pp. 2749-2755.

[51] D. Osso, O. Tillement, A. Mocellin, G. Le Caër, O. Babushkin, T. Lindbäck, *Journal of the European Ceramic Society* ***15*** (1995), pp. 1207-1212.

[52] H.X. Zhu, R. Abbaschian, *Materials Science and Engineering A* ***282*** (2000), pp. 1-7.

[53] D. Oleszak, *Journal of Materials Science* ***39*** (2004), pp. 5169-5174.

[54] L. Fazeli, M. Kalantar, *Journal of Alloys and Compounds* ***552*** (2013), pp. 511-517.

[55] L.L. Wang, Z.A. Munir, Y.M. Maximov, *Journal of Materials Science* ***28*** (1993), pp. 3693-3708.

[56] D. Vrel, P. Langlois, E.M. Heian, N. Karnatak, S. Dubois, M.F. Beaufort, *International Journal of Self-Propagating High-Temperature Synthesis* ***12*** (2003), pp. 261-270.

[57] W.W. Wu, A.V. Gubarevich, H. Wada, O. Odawara, *International Journal of Self-Propagating High-Temperature Synthesis* ***21*** (2012), pp. 146-150.

[58] T.M. Yue, H.O. Yang, T. Li, K.J. Huang, *Materials Transactions* ***50*** (2009), pp. 219-221.

[59] V. Udhayabanu, N. Singh, B.S. Murty, *Journal of Alloys and Compounds* ***497*** (2010), pp. 142-146.

[60] D. Renusch, M. Grimsditch, I. Koshelev, B.W. Veal, P.Y. Hou, *Oxidation of Metals* ***48*** (1997), pp. 471-495.

[61] B. Bouchaud, J. Balmain, D. Barrere, T. Delannoye, F. Pedraza, *Corrosion Science* ***68*** (2013), pp. 176-185.

[62] I. Burmistrov, D. Agarkov, I. Tartakovskii, V. Kharton, S. Bredikhin, *Electrochemical Society Transactions* ***68*** (2015), pp. 1265-1274.

[63] A.M. Padhan, M. Sathish, P. Saravanan, A. Perumal, *Journal of Physics D: Applied Physics* ***50*** (2017), pp. 1-10.

[64] B. Grushko, B. Przepiórzyński, E. Kowalska-Strzeciwilk, M. Surowiec, *Journal of Alloys and Compounds* ***420*** (2006), pp. 51-54.

[65] H. Wu, M. Zhang, B. Xu, G. Ling, *Journal of Alloys and Compounds* ***610*** (2014), pp. 492-497.

[66] B. Hu, W. Zhang, Y. Peng, Y. Du, S. Liu, Y. Zhang, *Thermochimica Acta* ***561*** (2013), pp. 77-90.

[67] S. Bao, K. Tang, A. Kvithyld, M. Tangstad, T.A. Engh, *Metallurgical and Materials Transactions B* ***42*** (2011), pp. 1358-1366.

[68] T.J. Nijdam, L.P.H. Jeurgens, W.G. Sloof, *Acta Materialia* ***53*** (2005), pp. 1643-1653.

[69] F. Bondioli, A.M. Ferrari, C. Leonelli, T. Manfredini, L. Linati, P. Mustarelli, *Journal of the American Ceramic Society* ***83*** (2000), pp. 2036-2040.

Chapter VI – Environmental resistance of diffusion coatings elaborated by slurry

I. State of the art 207

I.1. Simulation of Type-II hot corrosion conditions at laboratory scale 207

I.2. Oxidation resistance of simple and modified aluminide coatings 210

II. Oxidation resistance of uncoated and slurry coated nickel at 700°C 211

II.1. Characterization of the diffusion coatings elaborated on pure nickel 211

II.2. Influence of pSO_3 on the oxidation-sulfidation of pure nickel 213

a) Oxidation of pure nickel in synthetic air 213

b) Oxidation-sulfidation of pure nickel in synthetic air + 0.5% SO_2 215

c) Discussion 220

II.3. Influence of pSO_3 on the oxidation resistance of simple and Cr-modified slurry coatings 222

a) Oxidation in synthetic air 222

b) Oxidation in synthetic air + 0.5% SO_2 225

c) Discussion 229

III. Type-II hot corrosion resistance of uncoated and slurry coated nickel at 700°C 233

III.1. Hot corrosion of pure nickel at 700°C 233

III.2. Hot corrosion of simple and Cr-modified slurry aluminide coatings on pure nickel 238

III.3. Discussion 246

IV. Oxidation resistance of Cr-Al double-layer system developed on CM-247 LC 250

IV.1. Characterization of the low-activity high-temperature (LAHT) coating 250

IV.2. Cylic oxidation at 1000°C 251

IV.3. Isothermal oxidation at 1000°C 258

IV.4. Discussion 262

V. Summary and outlook 263

References 265

I. State of the art

As presented in Chapter I, different modes of degradation can be observed on materials exposed to high-temperature environments. Depending on the temperature regime and the activity of the aggressive substances, the corrosion rate can be significantly modified (cf. Fig. I-7 in Chapter I). In this Chapter, two different modes of degradation will be investigated. The Type-II hot corrosion generally occurring within the temperature range 650-800°C [1-3] and the high-temperature oxidation becoming predominant at temperatures higher than 1000°C [4]. The main objective of the present chapter was to give an overview of the potential applications of the diffusion coatings designed during this study based on their environmental resistance.

I.1. Simulation of Type-II hot corrosion conditions at laboratory scale

The Type-II hot corrosion conditions are schematically illustrated in Fig. VI-1. This mode of degradation is observed at temperatures lower than the melting point of Na_2SO_4, which is the most common salt deposit for aircraft gas turbines [4]. At such temperatures (i.e. 650-800°C), Na_2SO_4 can condensate on the metallic surfaces and form a solid and sticky deposit. The combustion gases produced for the power generation also play an important role on the hot corrosion process. A critical $\boldsymbol{p_{SO_3}}$ is indeed required to provoke the corrosion attack and initiate the Type-II hot corrosion process.

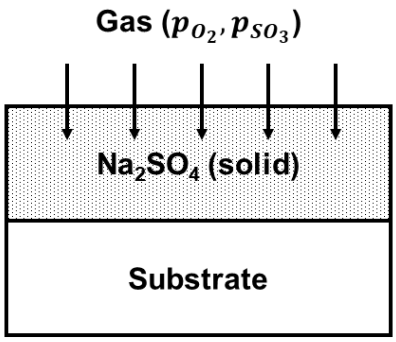

Fig. VI-1. Schematic illustration of the conditions to meet Type-II hot corrosion of metals and alloys (also called "under-deposit hot corrosion").

Therefore, when the p_{SO_3} is high enough in the gas composition (about 3×10^{-4} atm. [5]), the sulfation of NiO can occur following the reaction *(Eq. VI-1)*:

$$NiO(s) + SO_3(g) \rightarrow NiSO_4(s) \qquad \textbf{(Eq. VI-1)}$$

N.B.: in this work, the term "sulfation" refers to the formation of a metal sulfate phase from a metal oxide in presence of SO_3 whereas the term "sulfidation" refers to the formation of nickel sulfides from the pure metal.

The formation of $NiSO_4$ following reaction *(Eq. VI-1)* progressively saturates the salt deposit and leads to a liquid solution of Na_2SO_4-$NiSO_4$ (eutectic temperature of 671°C [6-8]). In dry air, the p_{SO_3} is not high enough to stabilize Na_2SO_4-$NiSO_4$ liquid solution and the hot corrosion attack is therefore suppressed. The stability of the different phases can generally be predicted by thermodynamics using stability diagrams where p_{O_2} and p_{SO_3} are used as coordinates (Fig. VI-2a).

At laboratory scale, it is therefore of utmost importance to control the p_{SO_3} within the gas composition to meet the Type-II hot corrosion conditions [9]. A SO_2-containing atmosphere is generally used to perform the hot corrosion tests. At 700°C (the test temperature), the oxidation of SO_2 into SO_3 following reaction *(Eq. VI-2)* is very slow. This implies the use of a catalyst to foster the oxidation of SO_2. The catalyst is generally placed in the reaction chamber upstream of the samples.

$$SO_2(g) + \frac{1}{2}O_2(g) \rightarrow SO_3(g) \qquad \textbf{(Eq. VI-2)}$$

In this work, the hot corrosion tests were performed with the experimental set up presented in Fig. II-9 of Chapter II (with the collaboration of Dr. Ing. Mathias C. Galetz and Dr. Xabier Montero from DECHEMA-Forschungsinstitut). The oxidation of SO_2 into SO_3 following reaction *(Eq. VI-2)* was fostered using iron zeolite catalysts placed upstream of the samples in the hot zone of the horizontal furnace. The calculated equilibrium p_{SO_3} from data in Ref. [4] was 7.5×10^{-3} atm at 700°C. According to the Na-Ni-O-S stability diagram (Fig. VI-2a), the available p_{SO_3} was therefore high enough to provoke the acidic reaction of NiO following reaction *(Eq. VI-1)*.

Considering now the Na-Al-O-S (Fig. VI-2b) and the Na-Cr-O-S (Fig. VI-2c) stability diagrams, both Al_2O_3 and Cr_2O_3 are stable in the SO_2-containing atmosphere. Therefore, the acidic reaction of Al_2O_3 *(Eq.* VI-3*)* and of Cr_2O_3 *(Eq. VI-4)* should not be observed in the experiments.

$$Al_2O_3(s) + 3SO_3\,(g) \rightarrow Al_2(SO_4)_3\,(s) \qquad \textbf{(Eq. VI-3)}$$

$$Cr_2O_3(s) + 3SO_3\,(g) \rightarrow Cr_2(SO_4)_3\,(s) \qquad \textbf{(Eq. VI-4)}$$

These thermodynamic considerations can be used to interpret the mechanisms of corrosion as a function of the p_{O_2} and p_{SO_3} variations. In this work, the samples were half-embedded in Na_2SO_4 to reproduce the Type-II hot corrosion conditions [10]. This method is generally more aggressive than real hot corrosion conditions but is interesting for the screening of different compositions. Using the half-embedding method, it is also possible to analyse different zones on the sample: the atmosphere side (no contact with Na_2SO_4), the salt side (embedded in Na_2SO_4) and the interface between the two areas.

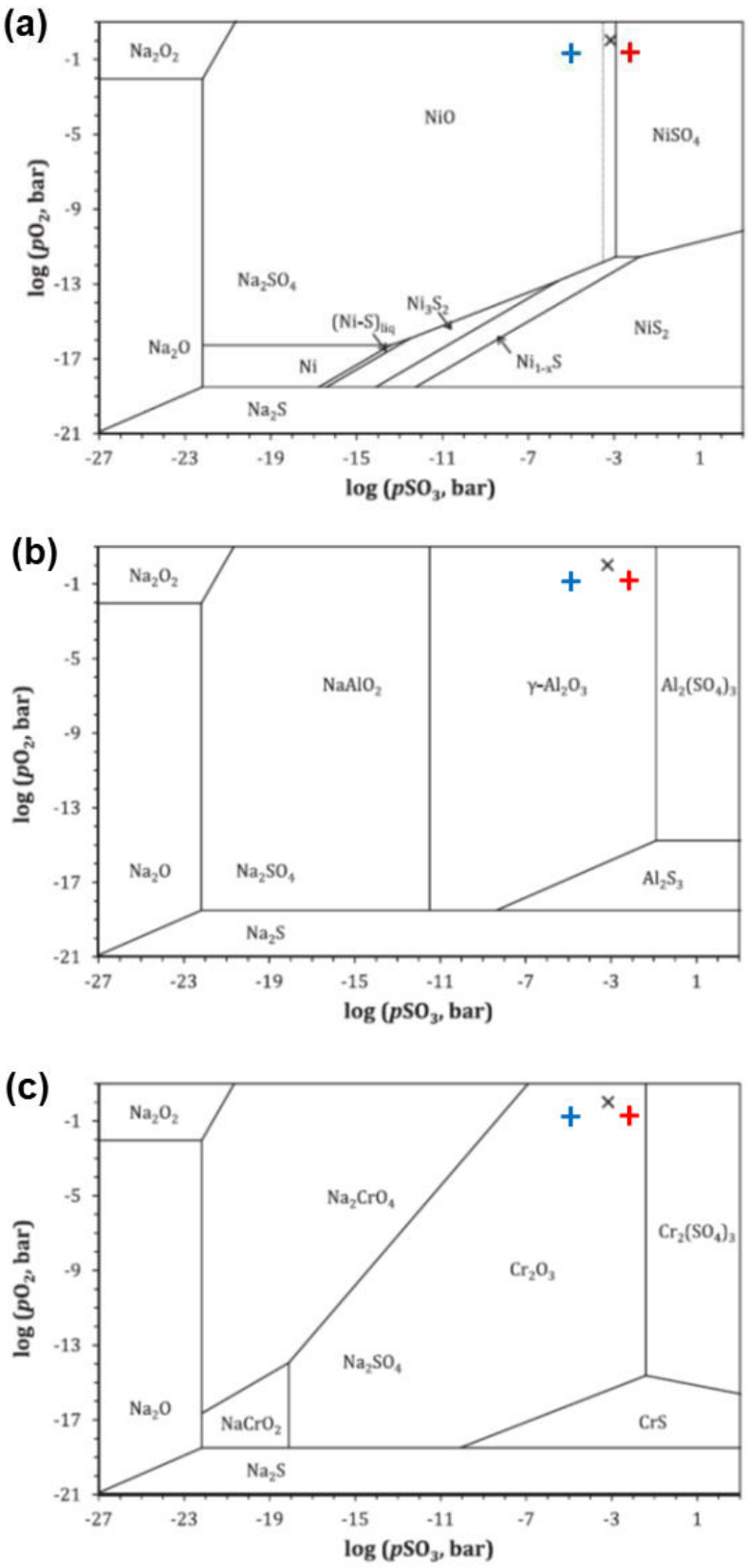

Fig. VI-2. Superimposed stability diagrams of (a) Na-Ni-O-S, (b) Na-Al-O-S and (c) Na-Cr-O-S systems at 700°C from Ref. [7]. The blue cross refers to synthetic air equilibrium and the red one to synthetic air + 0.5% SO_2 according to this work. The black one refers to the O_2 + 0.1% SO_2 equilibrium from Ref. [7].

I.2. Oxidation resistance of simple and modified aluminide coatings

The high-temperature oxidation of metals and alloys is another important concern in gas turbine engines. The oxidation or "dry corrosion" becomes predominant at temperatures beyond 1000°C (above the salt dew point). The oxidation phenomenon is usually more predictable than hot corrosion and is generally simulated at laboratory scale using muffle furnaces or cyclic oxidation rig tests in dry air. Even though both isothermal and cyclic conditions are used to simulate oxidation at laboratory scale [11], cyclic oxidation tests are closer to real conditions by inducing thermal stresses in the growing oxide scales [12].

The oxidation resistance of simple and modified aluminide coatings has been extensively studied in literature. The test temperature is generally selected regarding the application of the coating. If the oxidation resistance of bond coats for thermal barrier coatings is usually performed within the range 1150°C-1200°C [13-16], the oxidation tests for environmental bond coats are carried out within the range 1000°C-1100°C [17-22]. These temperatures are usually well recognized to simulate real conditions even at the atmospheric pressure since many metallurgical transformations observed on gas turbine components are thermally activated [21,23]. However, it is important to consider here that the temperature can vary locally on the surface of a component [24]. This can therefore lead to different modes of degradation on the same component [24,25]. If the simple aluminide coatings present a good oxidation resistance, they are generally very susceptible to both Type-I and Type-II hot corrosion [26-28]. The modification of simple aluminide coatings with Cr therefore appeared as a good alternative to confer both low temperature and high temperature resistance to the underlying material [26-31].

In this work, the oxidation resistance of Cr-modified coatings elaborated on a nickel-based superalloy (CM-247 LC) was investigated. The potential application of such coatings can be as low as 700°C to confer Type-II hot corrosion resistance and as high as 1100°C for the first stages of the low-pressure turbine (LPT). The oxidation temperature was fixed at 1000°C in this study since the oxidation of Cr-modified coatings was generally investigated at this temperature in literature [19,32]. The main objectives of this chapter were to study the surface stability of the coating and the microstructural evolutions that may happen at elevated temperatures. This could therefore inform on the maximal capability of the coating to confer high-temperature protection to the underlying material.

The Type-II hot corrosion resistance of the Cr-modified coating was investigated at 700°C on pure nickel for a better comprehension of the corrosion mechanisms. The use of superalloys with complex chemistry generally gives incomplete results in hot corrosion studies since each alloying element can adversely affect the corrosion mechanisms [33].

II. Oxidation resistance of uncoated and slurry coated nickel at 700°C

II.1. Characterization of the diffusion coatings elaborated on pure nickel

The SEM cross-section images of the simple aluminide and the Cr-modified aluminide coatings elaborated on pure nickel are respectively given in Fig. VI-3a and Fig. VI-3b. EPMA line scans were also performed across the coating thickness to identify the different phases formed on the nickel substrate after heat treatment in Ar. The mechanisms of formation for the high-Al activity slurry aluminizing in Ar atmosphere have already been described on pure nickel [34,35] and nickel-based superalloys [35]. The coating formation was found to be fast involving liquid phases and a strong exothermic reaction between the nickel-based substrate and the Al microparticles [36]. For the simple aluminide coating (Fig. VI-3a), the overall thickness of the diffusion zone was approximately 55µm with three different layers identified in the BSE mode of the SEM. An outer Al-rich β-NiAl layer, a thick Ni-rich β-NiAl layer and a γ'-Ni_3Al layer of about 5µm formed at the interface with the Ni substrate (Fig. VI-3c). The Cr-modified aluminide coating was thicker (approximately 70µm) and presented a Cr-rich layer at the extreme surface (Fig. VI-3d) resulting from the diffusion process (low solubility of Cr in β-NiAl phase [37,38]). Approximately 2 at.% of Cr was dissolved in the main β-NiAl phase.

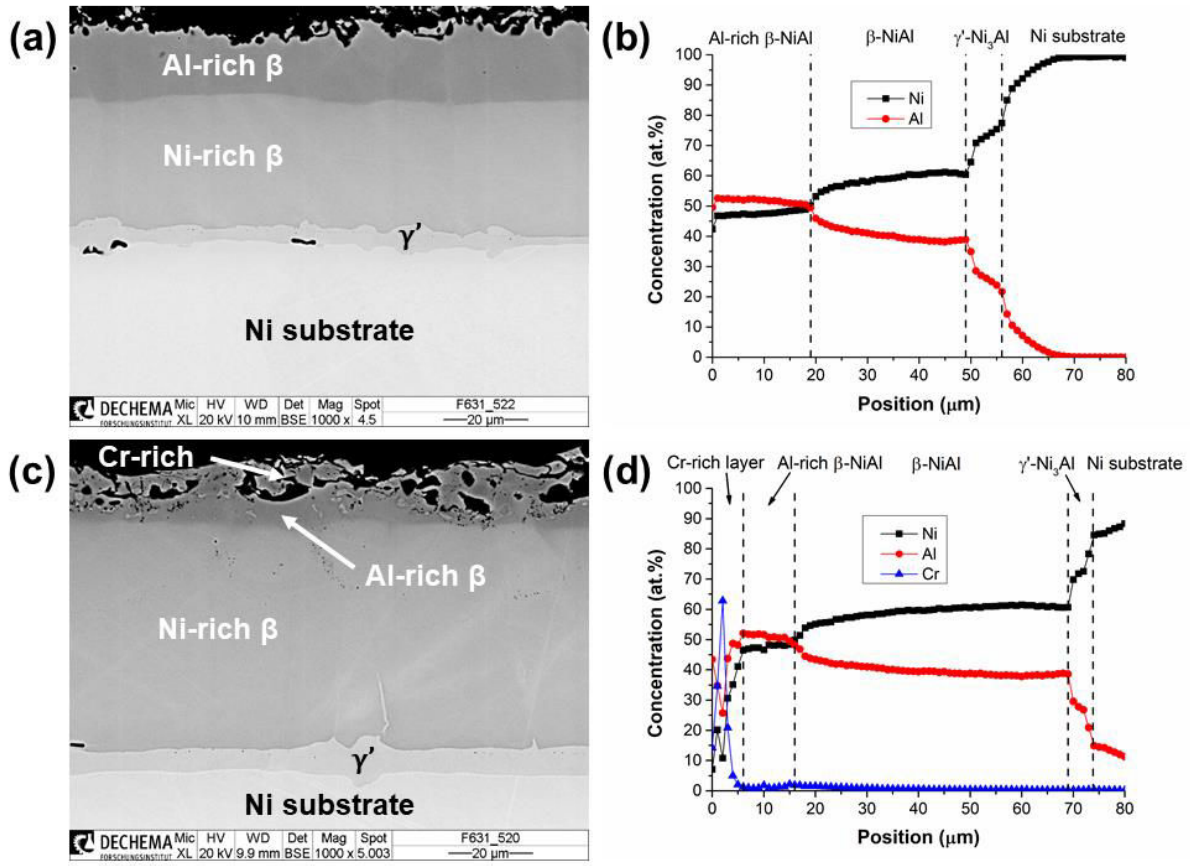

Fig. VI-3. BSE cross-section images and corresponding EPMA line scans of (a), (b) simple and (c), (d) Cr-modified slurry aluminide coatings elaborated on pure nickel.

The surface of the slurry coatings was also characterized before oxidation tests to obtain the initial state of the surface after the light grit blasting process (#220 mesh alumina). Both coatings presented a relatively rough surface after grit blasting which may increase the reactive surface area upon oxidation [13]. Several EDS window measurements were done on the coating surface to analyse the chemical composition. The mean concentration was 25O-46Al-29Ni (at.%) for the simple aluminide and 22O-23Al-23Cr-32Ni (at.%) for the Cr-modified one. The O concentration on the surface suggested that the coatings were slightly pre-oxidized after elaboration.

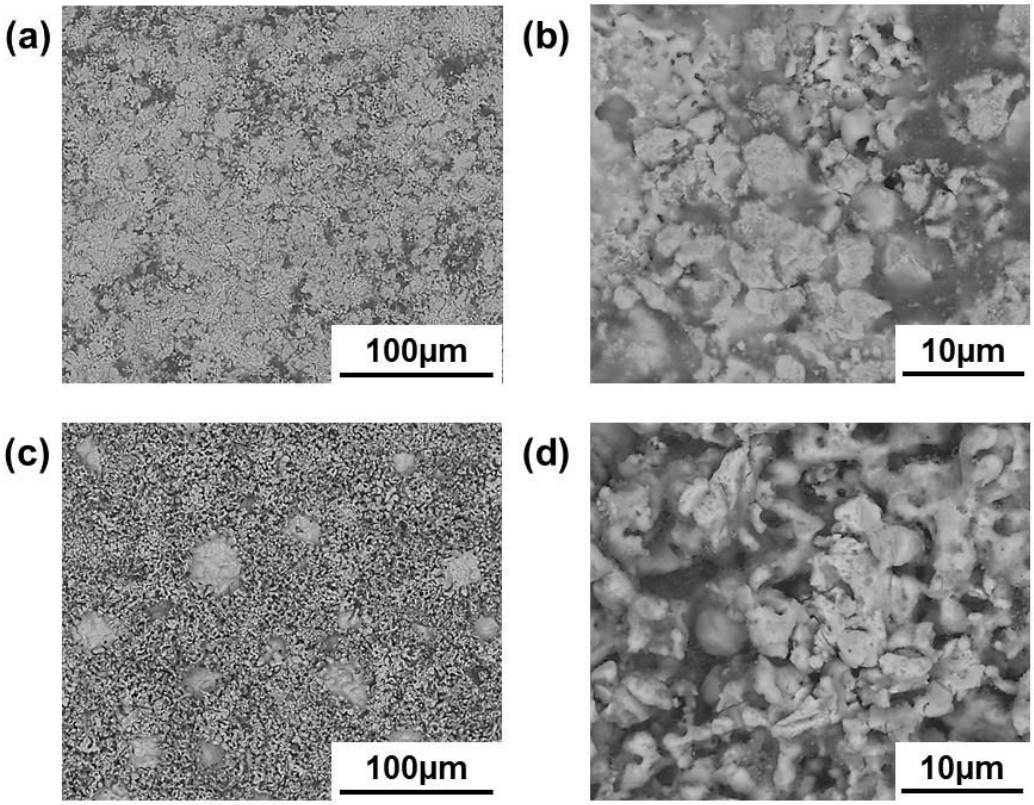

Fig. VI-4. SEM surface images of (a), (b) the simple and (c), (d) the Cr-modified aluminide coating elaborated on pure nickel after light grit blasting.

II.2. Influence of pSO_3 on the oxidation-sulfidation of pure nickel

a) Oxidation of pure nickel in synthetic air

For a better comprehension of the hot corrosion tests performed on pure nickel, its oxidation behaviour in synthetic air was first investigated. The oxidation of high purity nickel has been extensively studied in literature in both dry air [39] and pure oxygen [40,41]. NiO presents different morphologies depending on the temperature and the oxidation time and can be divided in three families: faceted grains, cellular and platelets [40]. At 700°C, NiO generally presents a cellular morphology with high porosity [8,39,40]. At temperatures lower than 800°C, NiO forms by predominant outward diffusion of Ni cations through the oxide scale [39].

In this work, high purity nickel (99.99%) was submitted to oxidation at 700°C in synthetic air under atmospheric pressure. The weight gain curves, recorded by TGA, are presented in Fig. VI-5. The parabolic rate constant k_p, calculated from the transformed curves, was in the same range of order that data from literature (Table VI-1).

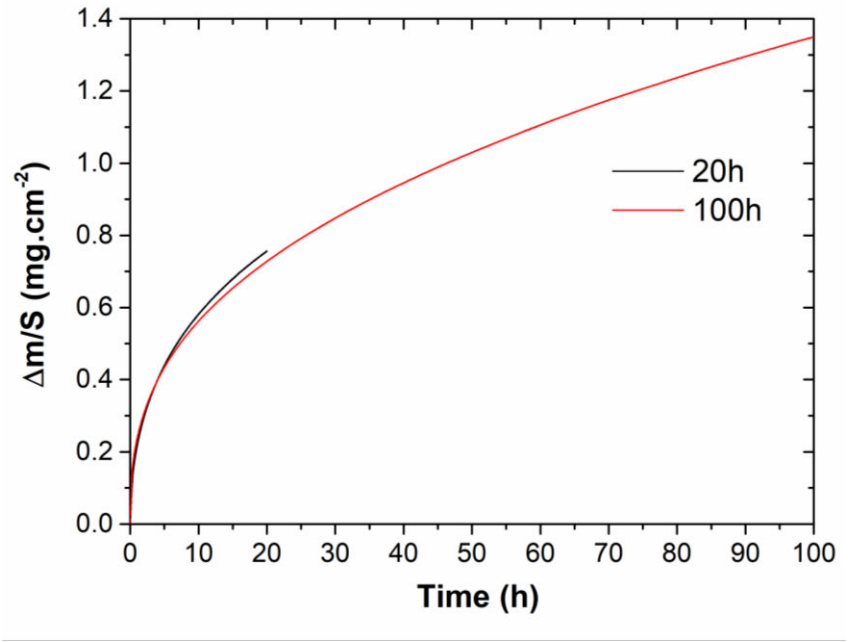

Fig. VI-5. Oxidation curves of pure nickel obtained by TGA in synthetic air at 700°C.

Table VI-1. Comparison of the parabolic rate constant k_p calculated in this work with data from literature.

	This work	Literature	
		[39]	[41]
k_p ($g^2.cm^{-4}.s^{-1}$)	4.3×10^{-12}	4.2×10^{-12}	8.9×10^{-12}

The surface morphology of the oxide scales developed on pure nickel after 20 and 100 hours exposure was imaged by SEM (Fig. VI-6a and Fig. VI-6b respectively). On both surfaces, the typical cellular morphology of NiO was observed with an extensive open porosity [39,40]. The samples were also observed in cross-section to measure the thickness of the oxide scales formed (Fig. VI-6c and Fig. VI-6d). The average oxide scale thickness measured after 20 hours and 100 hours of exposure was in agreement with data in Ref. [41]. This supported a growth rate based on short-circuit nickel diffusion [41]. Note that the NiO scales formed were very porous and that large vacancies formed at the interface with the nickel substrate.

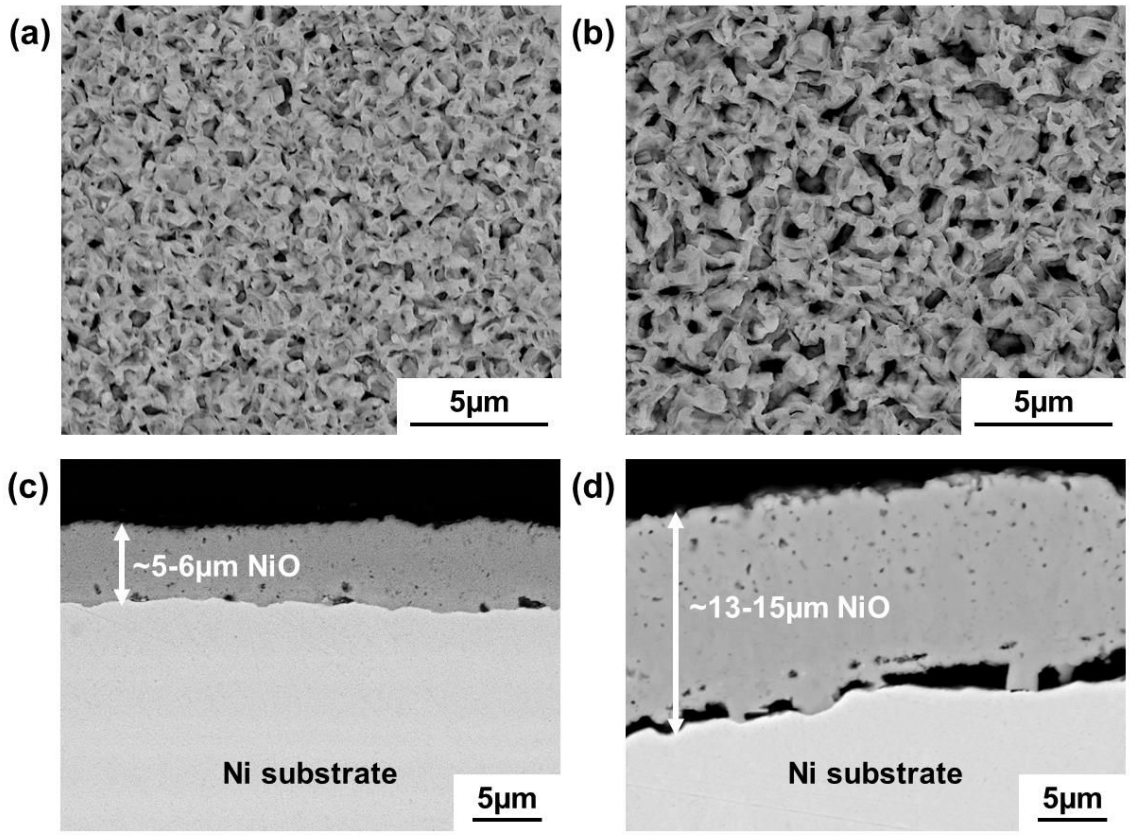

Fig. VI-6. SEM surface and cross-section images of pure nickel oxidized in synthetic air at 700°C for (a), (c) 20 hours and (b), (d) 100 hours.

The oxidized nickel samples were also characterized by XRD and Raman micro-spectrometry to get the reference signals of NiO grown at 700°C. On the XRD patterns (Fig. VI-7a), both FCC structure of γ-(Ni) and cubic structure of NiO were detected after 20 hours of exposure. After 100 hours, γ-(Ni) was no longer detected and only the cubic structure of NiO was identified on the XRD pattern. This could be attributed to the significant growth of the NiO scale that masked the γ-(Ni) structure of the nickel substrate from the X-rays. The characteristic vibration modes of NiO were observed on the Raman spectra after 20 hours and 100 hours of exposure [42].

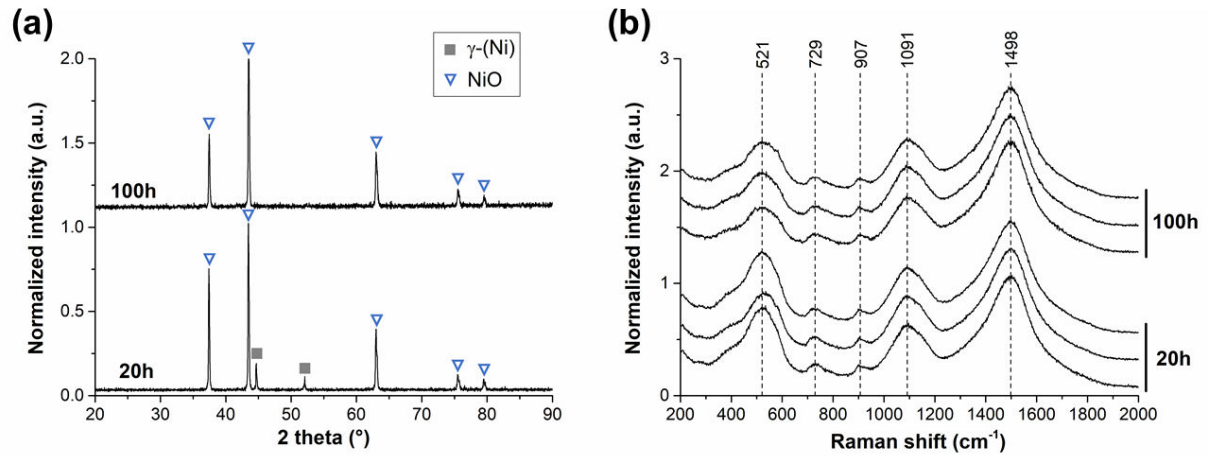

Fig. VI-7. (a) XRD patterns and (b) Raman surface analyses of pure nickel oxidized in synthetic air at 700°C.

b) Oxidation-sulfidation of pure nickel in synthetic air + 0.5% SO_2

The oxidation behaviour of pure nickel was then carried out in synthetic air with the addition of 0.5% SO_2 (i.e. 5000 ppm SO_2). Considering the Ni-O-S stability diagram at 700°C (Fig. VI-2a), the sulfation of NiO into $NiSO_4$ must occur in this atmosphere. The sulfation of NiO was therefore expected to increase the oxidation rate of the nickel substrate as reported by other authors in SO_2-containing atmosphere [6,8,43-45].

Pure nickel samples were thus oxidized for 20, 100 and 300 hours in synthetic air + 0.5% SO_2. The mass gain of the samples was compared with the oxidation curves obtained in synthetic air and plotted versus the square root of time (Fig. VI-8). The oxidation rate of pure nickel was more than two orders of magnitude higher with addition of 0.5% SO_2. The surface macrographs of the samples exposed to different conditions are given in Fig. VI-9. Whereas an even continuous oxide scale formed at the surface of the samples exposed to synthetic air (Fig. VI-9a), the scales were rough and uneven in the SO_2-containing atmosphere.

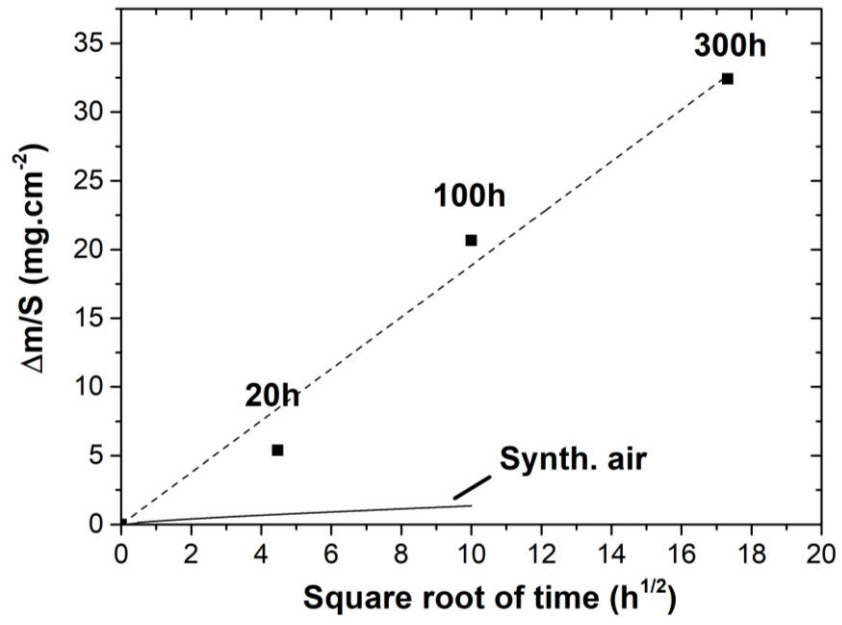

Fig. VI-8. Mass gain as a function of square root of time of high purity nickel in synthetic air and synthetic air + 0.5% SO_2 at 700°C.

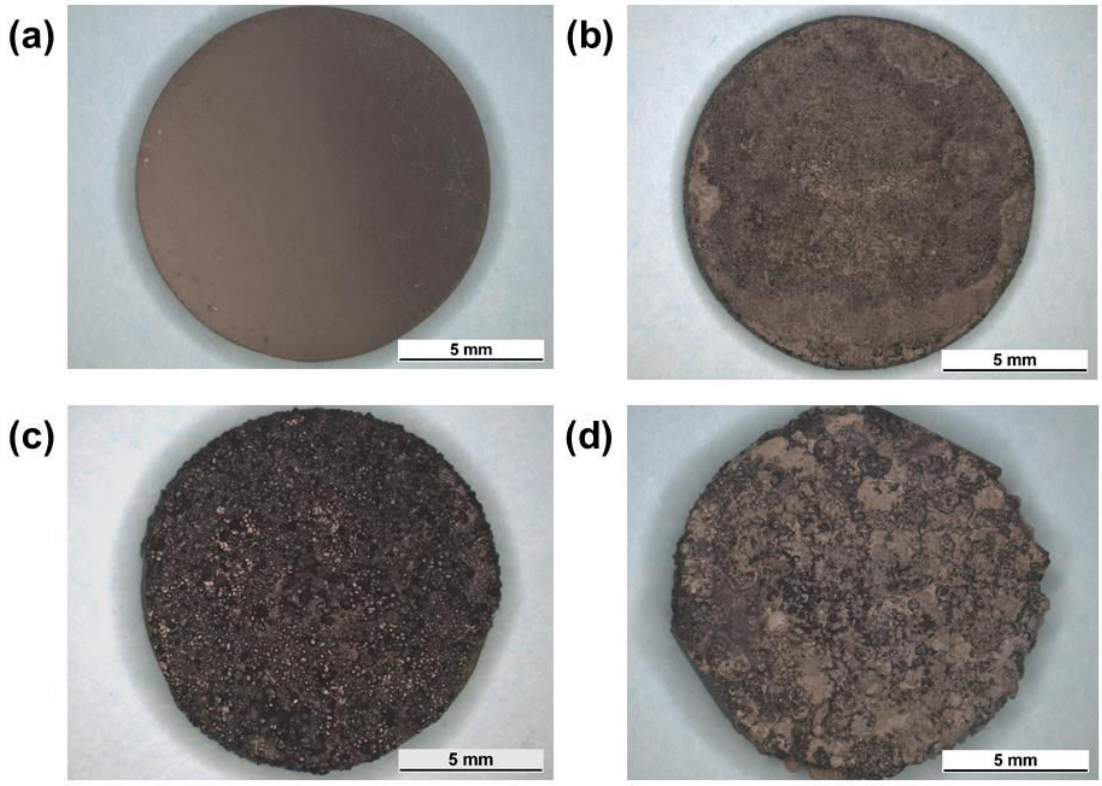

Fig. VI-9. Surface macrographs of pure nickel samples after exposure for (a) 100 hours in synthetic air and for respectively (b) 20 hours, (c) 100 hours and (d) 300 hours in synthetic air + 0.5% SO_2 at 700°C.

The samples were characterized in cross-section to measure the recession of the metal and observe the microstructure of the corrosion products (Fig. VI-10). As suggested with the surface macrographs and the oxidation curves, the corrosion scales formed on the surface were much thicker after exposure in the SO_2-containing atmosphere (50µm after 20 hours, cf. Fig. VI-10a) than in air (5µm after 20 hours, cf. Fig. VI-6c). A duplex microstructure was observed in the BSE cross-section images with a thick outer layer of porous NiO with dispersed nickel sulfides and a thin S-enriched zone at the interface between the metal substrate and the corrosion scale (Fig. VI-10b). Similar microstructures were observed for the reaction of pure nickel in SO_2-containing atmosphere [8,43,45]. After 300 hours of exposure (Fig. VI-10b), a lateral decohesion of the corrosion products from the nickel substrate occurred and was presumably coming from the cooling ramp. Since a large fraction of the nickel substrate was corroded during the reaction, metal loss measurements were performed across the full length of the sample to evaluate the corrosion attack (Fig. VI-10c). The results attested the progressive consumption of nickel in the SO_2-containing atmosphere. After 20 hours, more than 40% of the sample had undergone a metal loss of at least 50µm. After 300 hours, a metal loss greater than 250µm was observed for more than 60% of the sample.

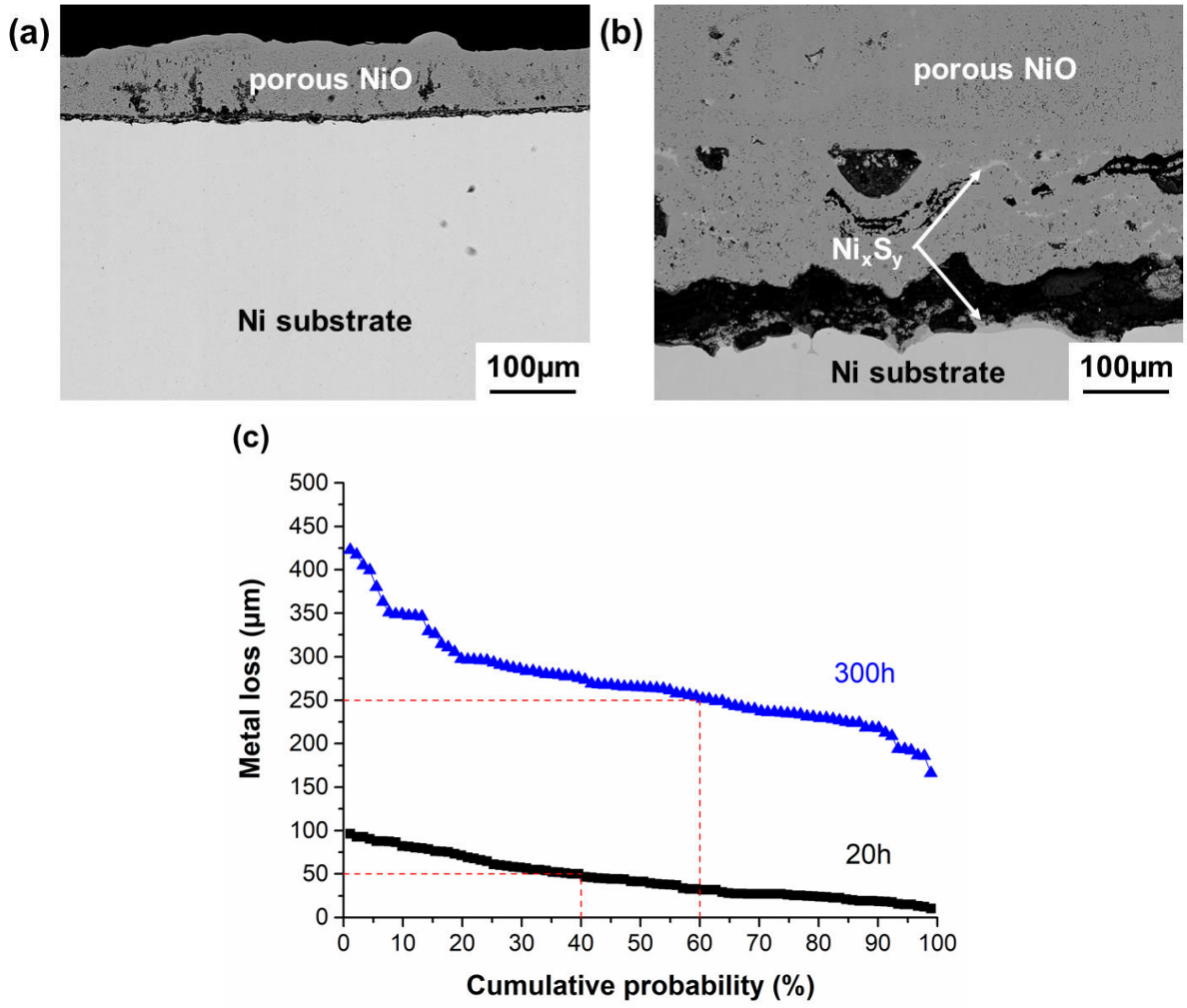

Fig. VI-10. BSE cross-section images of pure nickel exposed in synthetic air + 0.5% SO_2 at 700°C for (a) 20 hours and (b) 300 hours and (c) metal loss measurements.

EPMA analyses were conducted at higher magnification to get the elemental distribution at the interface between the nickel substrate and the corrosion products (Fig. VI-11b and Fig. VI-11c). The high S content at the interface between the substrate and the corrosion scale attested the formation of nickel sulfides (red continuous layer on the EPMA mapping of S, Fig. VI-11c). A fine precipitation of nickel sulfides was also observed within the porous NiO scale. The continuous nickel sulfide layer was observed at the surface of the substrate at higher magnification (Fig. VI-12a). Bright Ni precipitates were dispersed within the nickel sulfide layer and suggested that a Ni-S liquid solution was present at temperature (i.e. 700°C). The darker areas observed above the nickel sulfide layer were attributed to nickel oxide resulting probably to a higher p_{O_2} in this region at temperature [46]. These observations are in good agreement with the results obtained by Kofstad and co-workers [43-45].

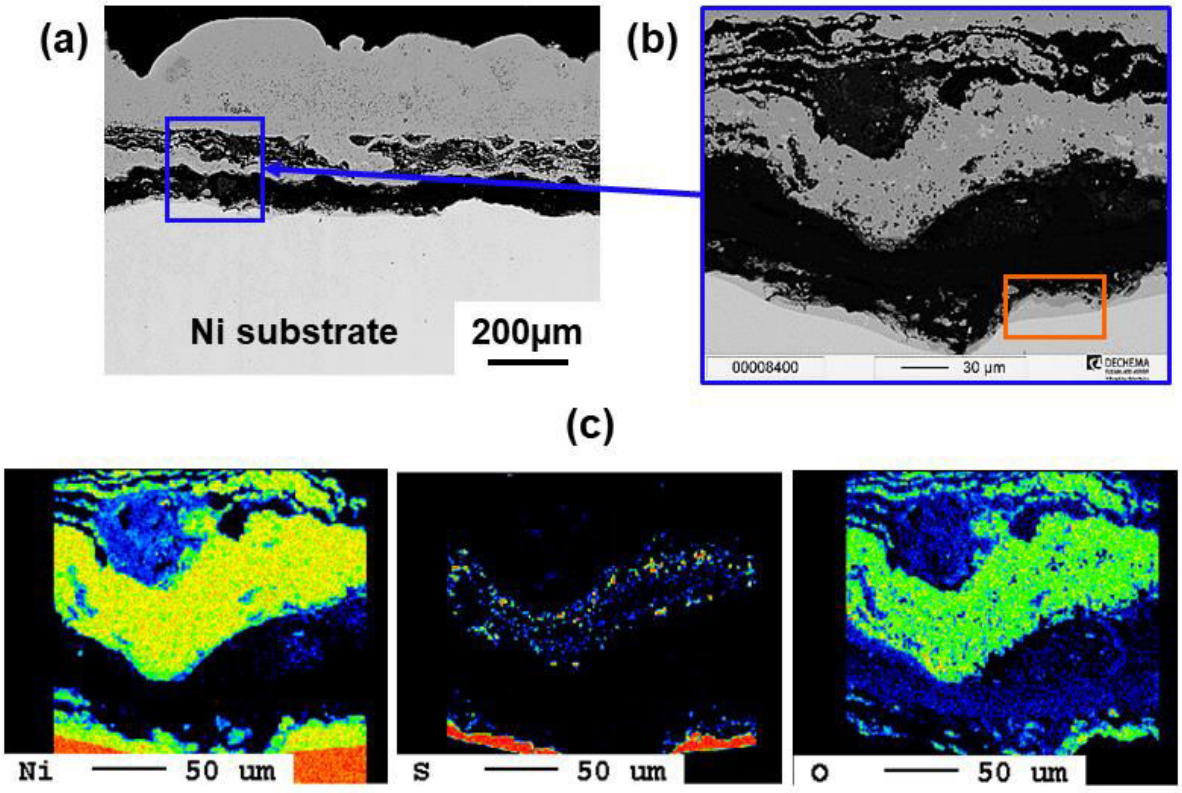

Fig. VI-11. (a), (b) BSE cross-section images of the corrosion scales formed on pure nickel after exposure to synthetic air + 0.5% SO_2 at 700°C for 300 hours and (c) corresponding EPMA mappings of Ni, S and O.

The EDS spot measurements done in cross-section are summarized in Table VI-2. The nickel sulfide layer was mainly composed of the Ni_3S_2 phase. The S concentration was very low in the nickel substrate with less than 1 at.% S at 10µm from the interface between the substrate and the sulfide layer (Table VI-2). The Raman local analyses performed in the cross-sections (Fig. VI-12b) confirmed the formation of NiO in the dark regions of Fig. VI-12a. The reference signal of Ni_3S_2 (highlighted in Fig. VI-12b) was obtained from these analyses with four peaks at approximately 190, 225, 306 and 352 cm^{-1}.

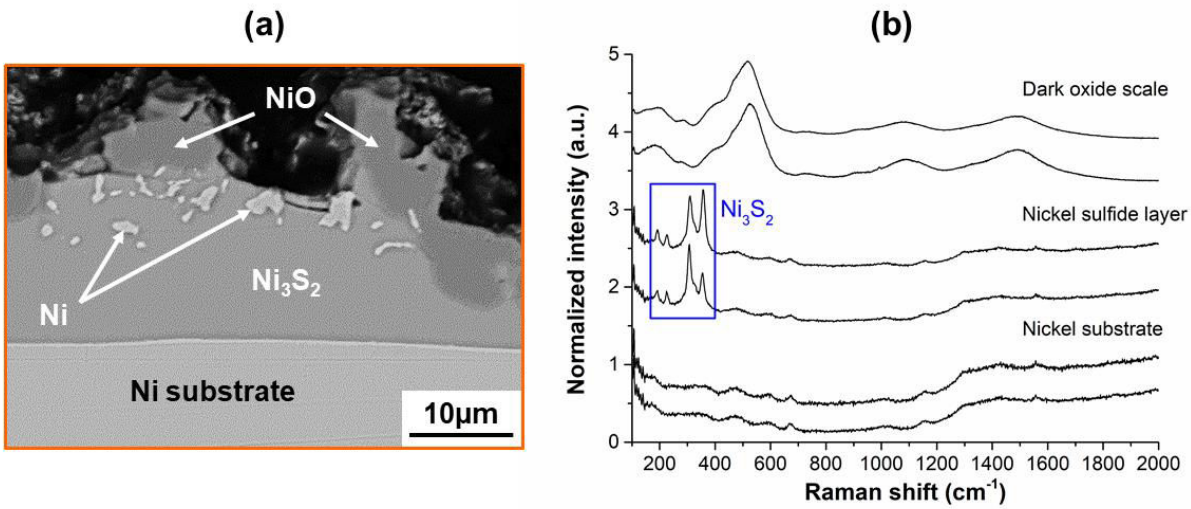

Fig. VI-12. (a) BSE cross-section image of the nickel sulfide layer formed on the substrate surface (cf. Fig. VI-11b) and (b) Raman spot analyses in the different areas.

Table VI-2. Summary of the EDS spot measurements done in cross-section (cf. Fig. VI-11c).

EDS spot location	O (at.%)	S (at.%)	Ni (at.%)	Possible phase
Dark oxide scale	48.0	0.3	51.7	NiO
Nickel sulfide layer	5.4	39.9	54.8	Ni_3S_2
Nickel substrate	5.0	0.6	94.4	γ-(Ni)

c) Discussion

The oxidation of high purity nickel in synthetic air at 700°C led to the formation of a porous NiO scale with a cellular morphology as reported in literature [8,39]. The growth of the NiO scale presumably occurred by major outward diffusion of Ni cations towards the gas atmosphere through the NiO grain boundaries [39]. When 0.5% SO_2 was introduced in synthetic air, the oxidation rate of pure nickel considerably increased (Fig. VI-8). The higher porosity and growth rate of NiO scales in presence of sulfur was unambiguously due to inward transport of SO_2-SO_3 through the scale [8,47]. The sulfation of NiO in synthetic air + 0.5% SO_2 following reaction *(Eq. VI-1)* was therefore promoted. These observations are in good agreement with the thermodynamic data from Gheno et al. (Fig. VI-2a) considering the stability domains of NiO and $NiSO_4$ with respect of the p_{SO_3}.

The sulfation of NiO fostered the formation of porous and unprotective oxide scales as observed on the surface macrographs (Fig. VI-9) and in cross-section (Fig. VI-10). The formation of NiSO4 was also attributed to increase the S activity on the corrosion scale [46]. The presence of Ni_3S_2 at the scale/substrate interface (Fig. VI-11c and Fig. VI-12a) and within the NiO scale (Fig. VI-11c) confirmed that NiO was permeable to sulfur-bearing molecules [8,47]. The formation of a mixed NiO + Ni_3S_2 scale has also been reported in high SO_2-containing environments [6]. In such microstructures, more than 90% of the scale consists of NiO in which the sulfides are present as a continuous network. The inward transport of SO_2-SO_3 also provided a sufficient S concentration (i.e. p_{S_2}) for sulfidation to occur at the scale/substrate interface as observed by Lillerud and Kofstad [6]. The sulfidation of nickel can be decomposed in two consecutive reactions following equations *(Eq. VI-5)* and *(Eq. VI-6)* [6]:

$$4\,\mathrm{Ni(s)} + \mathrm{NiSO_4(s)} \rightarrow 4\,\mathrm{NiO(s)} + \mathrm{[Ni\text{-}S](l)} \qquad \textbf{(Eq. VI-5)}$$

$$\mathrm{Ni(s)} + \mathrm{[Ni\text{-}S](l)} \rightarrow \mathrm{Ni_3S_2(s)} \qquad \textbf{(Eq. VI-6)}$$

The Ni-S solution was not detected in the corrosion scales but was included in the reaction sequence since it may form an intermediate reaction as proposed by Kofstad and co-workers [43-45]. The microstructures observed in Fig. VI-11a and Fig. VI-11b strongly supported the formation of a liquid solution at temperature (i.e. 700°C). According to the Ni-S phase diagram (Fig. VI-13), an eutectic is formed at 635°C and for a composition between 20 and 23 wt.% S [43,44]. The continuous supply of S-bearing molecules from the scale/gas interface towards the metal/scale interface probably sustained the formation of a Ni-S liquid solution at the reaction front. When the p_{O_2} was high enough (i.e. above the nickel sulfide layer), Ni-S protrusions oxidized into NiO (cf. Fig. VI-11b).

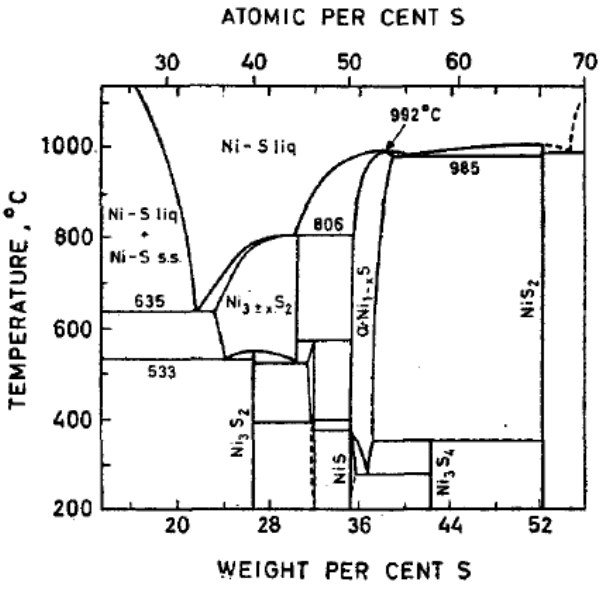

Fig. VI-13. Ni-S phase diagram [45].

The subsequent oxidation of Ni-S protrusions produced highly porous NiO scales and caused repeated cracking of the scales above the liquid Ni-S solution. This phenomenon was well illustrated by Kofstad and Akesson when submitting preoxidized nickel samples at high-temperatures in SO_2-containing atmospheres [44]. The appearance of nickel sulfides in the NiO scales is probably unoxidized remnants of the Ni-S protrusions. Since the diffusivity of nickel is faster in sulfides than in oxides by several orders of magnitude, the formation of sulfides on the substrate surface and through the corrosion products fostered the outward diffusion of nickel from the substrate into the scale. For long term exposure, this caused the decohesion of the corrosion products from the nickel substrate as observed in Fig. VI-11a and Fig. VI-11b.

When the samples containing Ni-S liquid solutions were cooled down, the liquid solution transformed to $Ni_{3\pm x}S_2$ below the eutectic temperature (i.e. 635°C) and disproportionated as Ni and Ni_3S_2 on cooling to room temperature (Fig. VI-13). As a result, only the products of disproportion were observed in the metallographic cross-sections of the samples (Fig. VI-12a) [45]. This also explains why nickel and NiO are not in contact in the microstructures (Fig. VI-12a).

II.3. Influence of pSO_3 on the oxidation resistance of simple and Cr-modified slurry coatings

a) Oxidation in synthetic air

The slurry coatings presented in paragraph II.1 were oxidized in synthetic air to follow the mass gain curves and compare with the results obtained with pure Ni substrate. The oxidation curves of the different systems are given in Fig. VI-14. The oxidation rate of pure Ni decreased with the application of slurry coatings and suggested a parabolic growth rate with both simple and Cr-modified aluminide coatings. The k_p values of the coatings were calculated from the transformed curves and are summarized in Table VI-3. By comparison with data from literature, the k_p value of the simple aluminide coating was close to the one of γ-Al_2O_3 at 700°C [48]. For the Cr-modified coating, the oxidation rate was approximately 30 times higher than that of the simple aluminide one. The k_p value for this coating was also higher than that of pure chromium at 700°C [49]. This could arise from the higher reactive surface area of the coating because of its relatively high roughness (Fig. VI-3b).

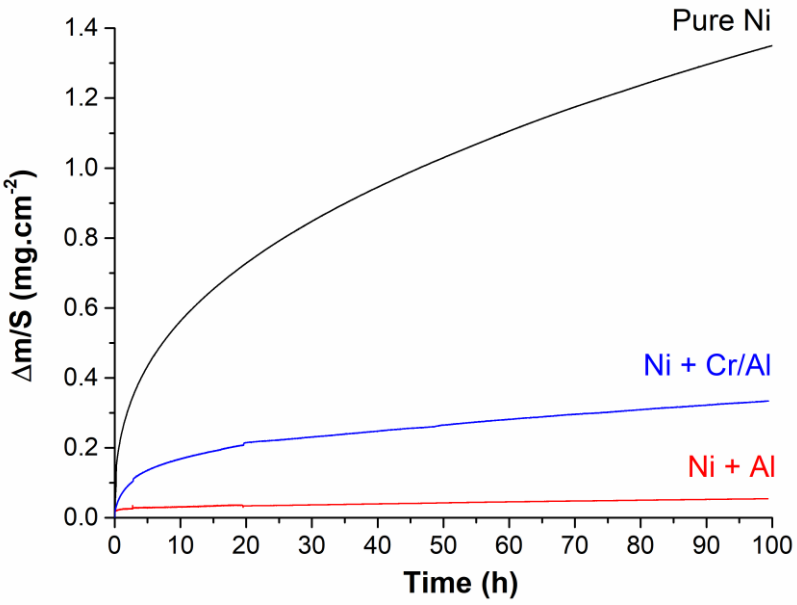

Fig. VI-14. Oxidation curves of uncoated and slurry coated nickel with a simple and a Cr-modified aluminide coating at 700°C in synthetic air.

Table VI-3. Comparison of the parabolic rate constant k_p calculated in this work with data from literature.

k_p values ($g^2.cm^{-4}.s^{-1}$)	This work	Literature	
Pure Ni	$4.3x10^{-12}$	$4.2x10^{-12}$ $8.9x10^{-12}$	[39] [41]
Ni + Al	$6.3x10^{-15}$	$3.0x10^{-15}$ (bulk Ni-50Al, at.%)	[48]
Ni + Cr/Al	$2.2x10^{-13}$	$6.4x10^{-14}$ (Pure Cr)	[49]

The surface of the slurry coatings was characterized with SEM after different oxidation times to observe the morphology of the oxide layers and perform chemical analyses. For the simple aluminide coating, the oxide layer was very thin and formed a dark film randomly distributed on the sample surface. The microstructure of the oxides was not clearly identified from the SEM surface images since the formed scales were very thin and thus blurred with the initial surface roughness. However, there was a clear O uptake with increasing time whereas the content of Ni decreased, which suggests the formation of an Al-rich oxide on the surface (Fig. VI-15).

For the Cr-modified coating, a rough surface was observed corresponding to the Cr-rich layer. The progressive oxidation of the Cr-rich phases was confirmed from the SEM images as well as from the EDS window analyses with the progressive O uptake with time on the coating surface. As observed for the simple aluminide coating, the Ni content of the surface decreased with time suggesting the formation of Al-rich and Cr-rich oxides on the coating surface. The higher reactive surface of the Cr-

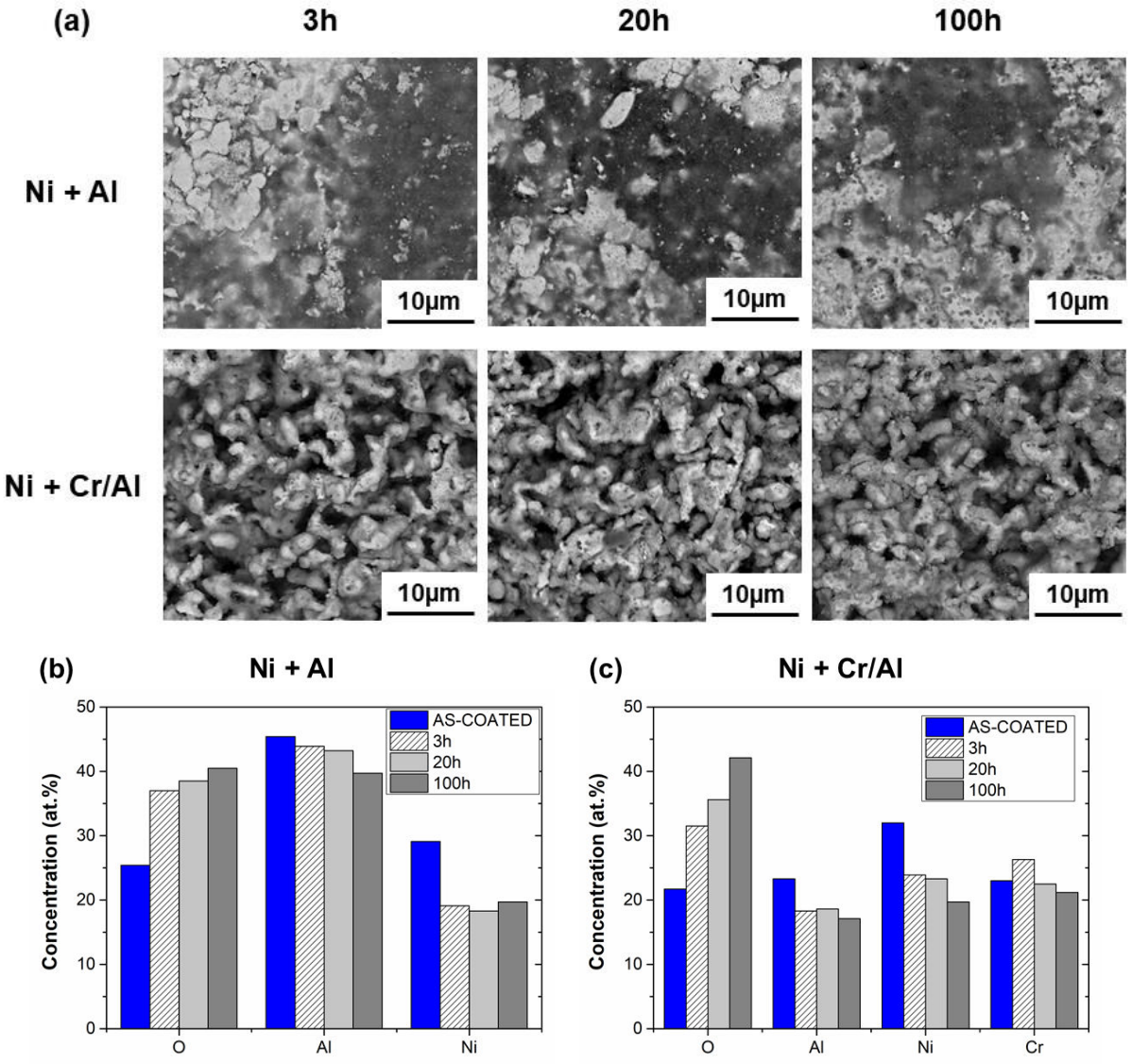

Fig. VI-15. (a) SEM surface images of the slurry coatings after exposure at 700°C in synthetic air and (b), (c) corresponding EDS window analyses of the coating surface.

modified coating was probably the cause for the higher mass gain of the sample upon oxidation since the O uptake was also greater (Fig. VI-14).

XRD and Raman analyses were conducted to identify the crystal structures and the oxide phases formed on the slurry coatings after oxidation at 700°C. The results are summarized in Table VI-4. For the simple aluminide coating, only the β-NiAl phase was detected by XRD using grazing incidence which suggested that the scales formed were very thin [7,50]. From Table VI-4, it can be concluded that the duration of transient oxidation stage was different for the two coating systems. The duration of transient oxidation stage was greater than 100 hours for the simple aluminide coating whereas α-Al_2O_3 was already formed on the Cr-modified coating after 3 hours exposure. These results are in good agreement with the ones obtained by Task et al. for Ni-36Al and Ni-36Al-5Cr alloys (in at.%) [51]. Cr (or Cr_2O_3) has indeed long be acknowledged to foster the nucleation and growth of α-Al_2O_3 [48,52-54].

Table VI-4. Summary of the XRD and Raman surface analyses of the slurry coatings elaborated on pure Ni after oxidation in synthetic air at 700°C.

Slurry coating	Oxidation time at 700°C	XRD patterns	Raman analyses
Simple	3h	-	γ-Al_2O_3
	20h	β-NiAl	γ-Al_2O_3, θ-Al_2O_3
	100h	β-NiAl	γ-Al_2O_3, θ-Al_2O_3, α-Al_2O_3
Cr-modified	3h	-	α-Al_2O_3, Cr_2O_3
	20h	β-NiAl, α-(Cr), Ni_3(Al,Cr), α-Al_2O_3, Cr_2O_3	α-Al_2O_3, Cr_2O_3
	100h	β-NiAl, α-(Cr), Ni_3(Al,Cr), α-Al_2O_3, Cr_2O_3	α-Al_2O_3, Cr_2O_3

As a result, the nature of the oxide scales developed on the surface of the coatings was expected to influence the oxidation and hot corrosion behaviour of the coatings in SO_2-containing atmosphere. Whereas α-Al_2O_3 was readily formed on the Cr-modified coating, the transformation of metastable aluminas (i.e. γ-Al_2O_3 and θ-Al_2O_3) into the stale α-Al_2O_3 could affect the mechanisms of degradation since this transformation is associated with a 13.8% volume reduction [55,56].

b) Oxidation in synthetic air + 0.5% SO_2

Pure Ni samples slurry coated with Al and Cr/Al were submitted to oxidation tests in synthetic air + 0.5% SO_2 atmosphere. The mass gain of the samples after 100 and 300 hours of exposure are given in Fig. VI-16 and compared with the values of pure Ni and the oxidation curves in synthetic air. Both coatings decreased the oxidation rate of the nickel substrate. The addition of 0.5% SO_2 in the gas composition seemed to have no influence on the oxidation behaviour of Ni + Cr/Al (Fig. VI-16). On the opposite, the mass gain of the simple aluminide coating was significantly higher with 0.5% SO_2 and reached approximately 10 mg.cm^{-2} after 300 hours exposure.

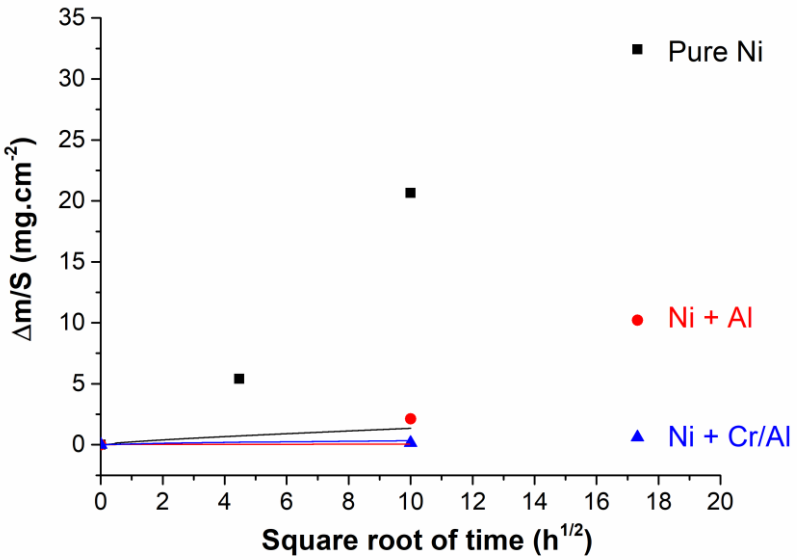

Fig. VI-16. Mass gain as a function of square root of time for the different systems in synthetic air + 0.5% SO_2 at 700°C. The oxidation curves in synthetic air are also given for comparison.

Uncoated and slurry coated Ni samples were imaged at low magnification in cross-section after 300 hours exposure to compare the degradation rate (Fig. VI-17). For uncoated Ni (Fig. VI-17a), the extensive oxidation-sulfidation of the substrate was observed with the formation of thick corrosion scales (cf. Fig. VI-11). The application of the slurry coatings considerably increased the oxidation-sulfidation resistance of the nickel substrate. For the simple aluminide coating (Fig. VI-17b), some protrusions [52] were observed randomly on the sample whereas the Cr-modified coating was not attacked after 300 hours exposure (Fig. VI-17c).

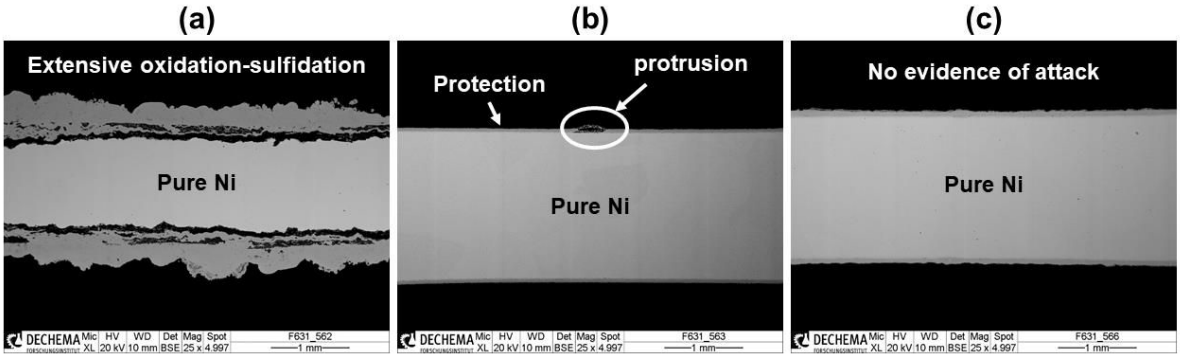

Fig. VI-17. Low magnification BSE cross-section images of (a) uncoated Ni, (b) Ni coated with simple aluminide coating and (c) Ni coated with Cr-modified coating after 300 hours exposure in synthetic air + 0.5% SO_2 at 700°C.

The surface of slurry coated Ni samples were characterized after 100 hours exposure. As observed in cross-section, the simple aluminide coating was prone to local attack in the form of round protrusions (Fig. VI-18a and Fig. VI-18b). Local EDS spot measurements and Raman analyses suggested that the protrusions were mainly composed of θ-Al_2O_3, α-Al_2O_3 and $NiAl_2O_4$ spinels. The Cr-modified coating was not attacked and underwent "normal" oxidation as observed in the SO_2-free atmosphere (Fig. VI-18c and Fig. VI-18d). The sample coated with the simple aluminide also presented edge effects showing preferential corrosion attack (Fig. VI-18a).

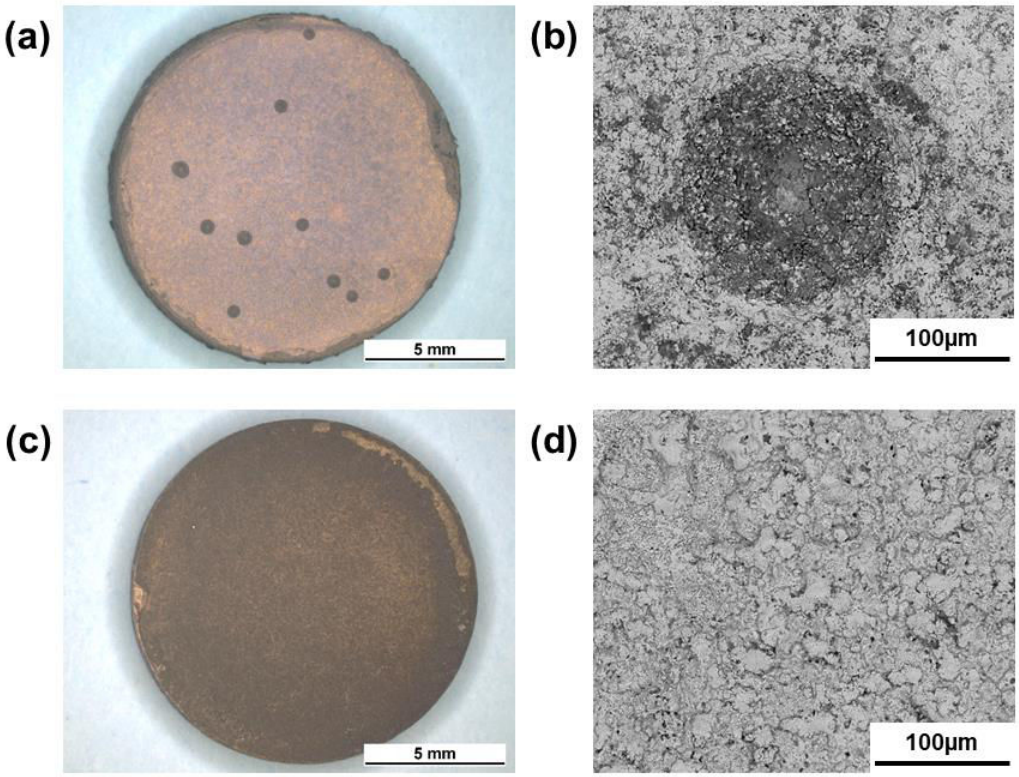

Fig. VI-18. Macrographs and BSE surface images of (a), (b) the simple aluminide and (c), (d) the Cr-modified coating after 100 hours exposure in synthetic air + 0.5% SO_2 at 700°C.

The cross-sections of the slurry coated samples were further characterized to evaluate the protective behaviour of the coatings in the SO_2-containing atmosphere. Light optical cross-section images of the coatings after 300 hours of exposure are given in Fig. VI-19a and Fig. VI-19b. The coating thicknesses were measured across the full length of the samples and compared with as-coated samples for probabilistic approach (Fig. VI-19c and Fig. VI-19d). In Fig. VI-19a, a large protrusion with internal oxidation of the coating layer was observed. Similar microstructures have already been reported by Brumm et al. for the oxidation of Ni-45Al (at.%) in 10^{-8} mbar O_2 at 700°C [52]. Such protrusion suggested that the coating was first prone to a local attack in a defective area leading to internal oxidation and then that lateral growth occurred by progressive depletion of Al in the coating. It should be mentioned here that the attack did not progress into the nickel substrate and that the internal oxidation stopped at the interface between the nickel substrate and the coating layer (Fig. VI-19a). It therefore seems that the attack was mainly sustained by both inward diffusion of O and outward diffusion of Al [52]. This would explain why the protrusion grew laterally after reaching the interface with the nickel substrate.

The Cr-modified coating was not affected by the presence of SO_2 in synthetic air and offered a complete protection to the underlying nickel substrate (Fig. VI-19b). For both coatings, some interdiffusion occurred with the nickel substrate and the thickness of the γ'-Ni_3Al intermediate layer increased with time by comparison with the as-coated samples (Fig. VI-3a and Fig. VI-3c). The cross-section of the slurry coated samples was further investigated by SEM and EPMA analyses to get higher magnification images and the elemental distribution for the regions of interest.

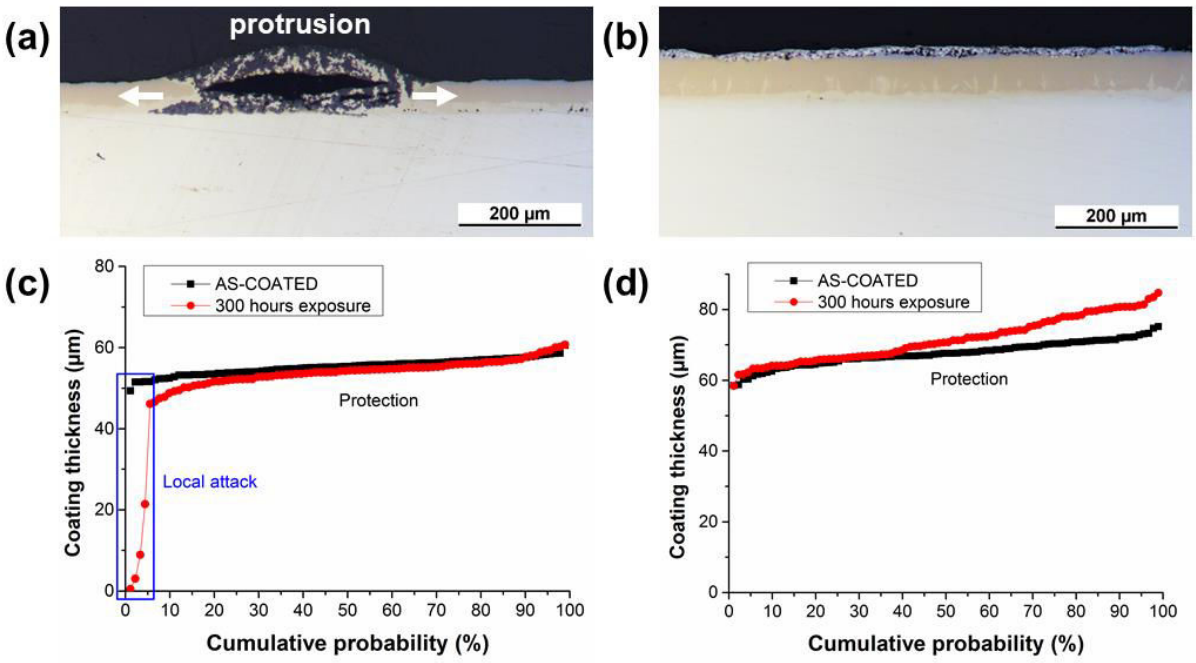

Fig. VI-19. Light optical cross-section micrographs and coating thickness measurements for (a), (c) the simple and (b), (d) the Cr-modified coating after 300 hours exposure at 700°C.

- ***SEM and EPMA analyses for the simple aluminide coating:***

For the sample slurry coated with Al, the analyses were carried out at the interface between a protrusion and unaffected coating (Fig. VI-20). The EPMA mapping confirmed the extensive internal oxidation of the coating in the form of finger-like Al_2O_3 precipitates [51,52]. $NiAl_2O_4$ spinels were also detected in cross-section by local Raman micro-spectrometry. The S enrichment of the coating was very limited and located mainly in the oxidized regions (see map of S, Fig. VI-20). Therefore, the role of S was mainly attributed to foster the formation of porous oxides and to prevent the formation of a protective Al_2O_3 scale on the intermetallic compounds [52]. One can see the progressive Al depletion of the coating because of the selective oxidation of Al to form Al_2O_3 precipitates. This led to the transformation of the β-NiAl phase into γ'-Ni_3Al and even γ-(Ni) highlighted by the EPMA map of Al in Fig. VI-20. The presence of both γ and γ' phases in the protrusion was probably the reason for the formation of $NiAl_2O_4$ spinels in the microstructure. Unlike the uncoated nickel sample (Fig. VI-11), no sulfidation was detected with the application of simple aluminide coating even in the protrusion regions. The internal oxidation did not progress into the nickel substrate, which confirmed that this attack was governed by diffusion of Al from the coating and diffusion of O from the atmosphere to form the Al_2O_3 precipitates.

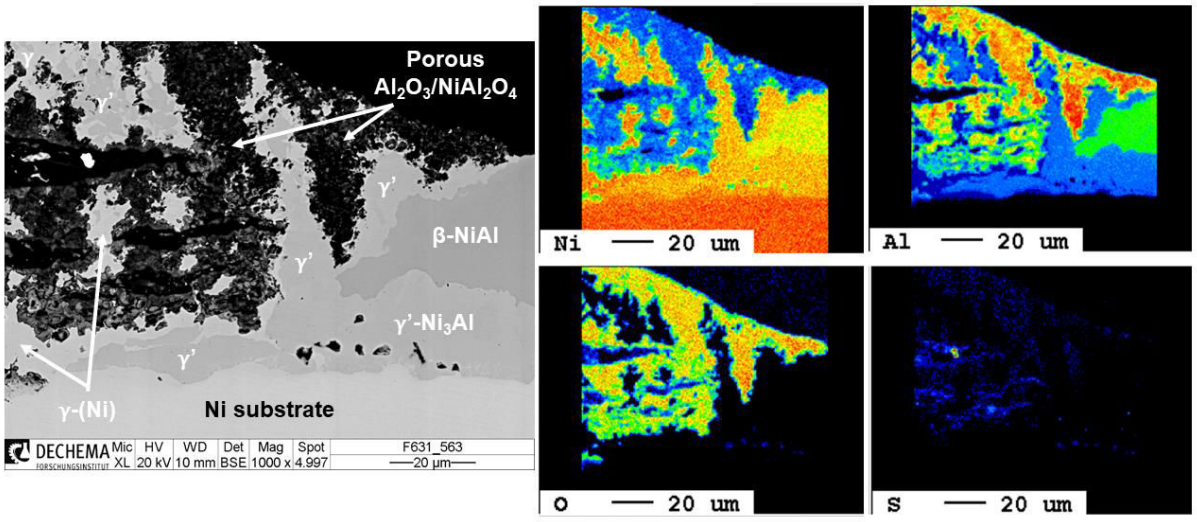

Fig. VI-20. BSE cross-section image and corresponding EPMA mapping of the aluminide coating after 300 hours exposure at 700°C in a protrusion region.

- ***SEM and EPMA analyses for the Cr-modified coating:***

The same analyses were conducted for the Cr-modified coating after 300 hours exposure in synthetic air + 0.5% SO_2 (Fig. VI-21). As suggested with the low magnification cross-section images, little transformation occurred in the coating. The Al-rich β-NiAl layer was still observed with Cr-rich phases at the extreme surface. Some fine α-(Cr) precipitates were also found in the outer region of the coating since Cr has a low solubility in the β-NiAl phase (about 2 at.% at 700°C [57]). There was no S enrichment in the coating and the upper part of the coating was slightly oxidized according to the EPMA map of O in Fig. VI-21. Some β to γ' transformation occurred to the grain boundaries of the diffusion coating and was attributed to the great concentration gradient between the coating and the nickel substrate causing Al inward diffusion upon annealing [58].

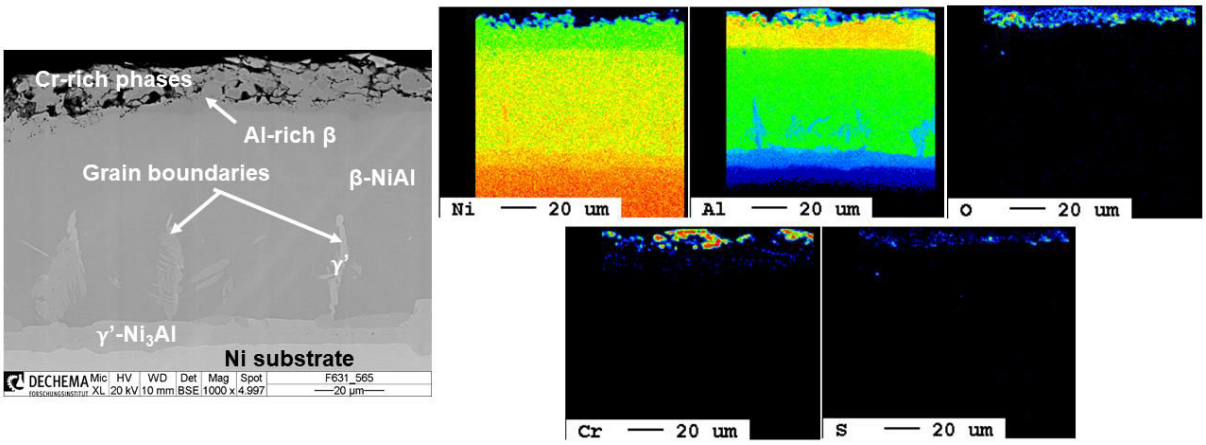

Fig. VI-21. BSE cross-section image and corresponding EPMA mapping of the Cr-modified coating after 300 hours exposure at 700°C in synthetic air + 0.5% SO_2.

c) Discussion

The application of slurry coatings was found to considerably increase the oxidation-sulfidation resistance of high purity nickel in synthetic air + 0.5% SO_2 at 700°C. This was attributed to the formation of a thin and adherent Al_2O_3 scale on the coating surface upon exposure. The oxidation tests of the coatings performed in synthetic air have shown that the duration of the transient oxidation stage was different for the two coatings (cf. Table VI-4). After 100 hours exposure, transition aluminas were still identified for the simple aluminide coating whereas α-Al_2O_3 was already formed for the Cr-modified coating after 3 hours exposure. These results are in good agreement with literature where Cr has long been acknowledged to limit the growth of metastable aluminas and to foster the nucleation of α-Al_2O_3 [48,52,53]. The presence of Cr was therefore expected to limit the inward diffusion of oxygen and internal oxidation as shown by Brumm et al. [52]. It has to be noted that Cr_2O_3 was also detected by XRD and Raman micro-spectrometry on the Cr-modified coating since Cr-rich phases were present on the surface (Fig. VI-3c). The formation of Cr_2O_3 may also have fostered the nucleation of α-Al_2O_3 since these two oxides have the same crystallographic structure [53,54,59].

- ***Mechanisms of formation of the protrusions on the simple aluminide coating:***

Even though the simple aluminide coating increased the oxidation resistance of the underlying nickel, some degradation occurred with time in the form of protrusions when exposed to the SO_2-containing atmosphere. It must be mentioned here that the morphology of the protrusions suggested that the coating was first attacked locally and then that internal oxidation of the coating took place by selective oxidation of Al into Al_2O_3 precipitates. The localized attacks observed on the surface (cf. Fig. VI-18a) were attributed to the inward transport of SO_2-SO_3 molecules through the defects of the Al_2O_3 scale [52]. Elemental maps of the surface of a protrusion highlighted the S enrichment in the middle of the protrusion (Fig. VI-22). The secondary electrons image of Fig. VI-22 confirmed the protrusion-like morphology. The protrusion was enriched in O and depleted in Ni by comparison with the unaffected coating confirming the preferential formation of Al_2O_3 in this region. It must be mentioned here that the formation of the protrusions was preceded by an incubation period. In this work, there was no attack of the simple aluminide coating after 20 hours exposure. After 100 hours exposure, some protrusions have already shown a diameter greater than 200µm suggesting that both initiation and propagation periods were very fast. The important O uptake to form these protrusions was probably responsible of the high mass gain of the simple aluminide coating in the SO_2-containing atmosphere (cf. Fig. VI-16).

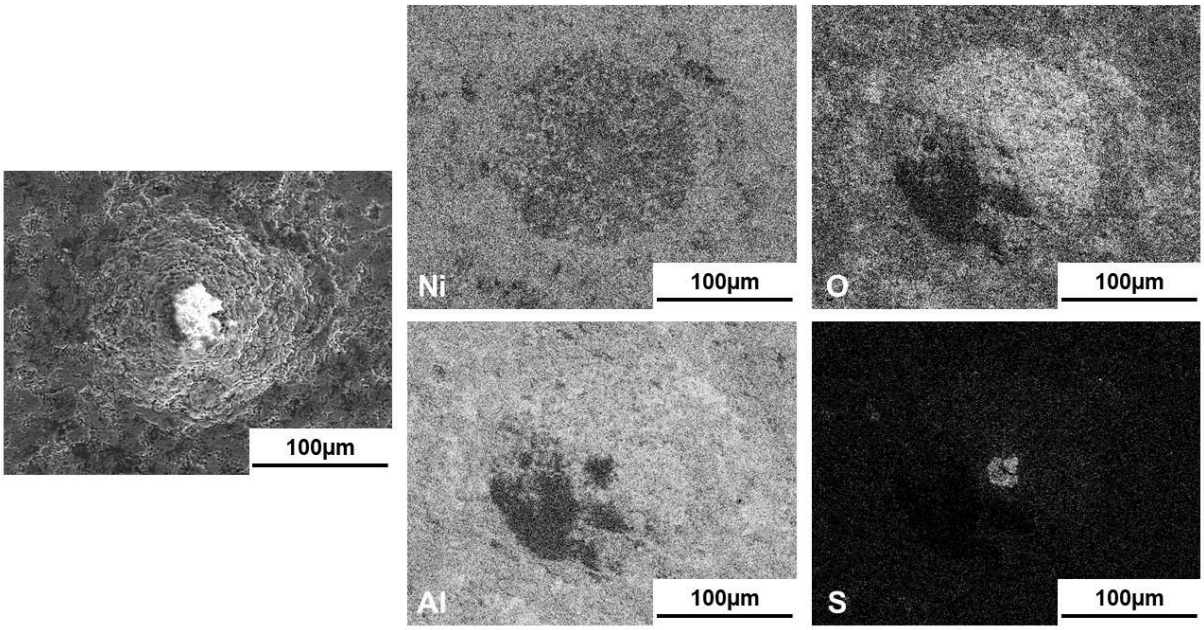

Fig. VI-22. Secondary electrons surface image of a protrusion formed on the simple aluminide coating after 100 hours exposure at 700°C in synthetic air + 0.5% SO_2 and corresponding X-ray maps.

Based on the work of Brumm et al. [52] and the present results, the mechanisms of formation of the protrusions on the simple aluminide coating were proposed in Fig. VI-23.

1. As-coated sample with an outer β-NiAl layer and a γ'-Ni_3Al intermediate layer (cf. Fig. VI-3a).

2. Penetration of SO_2-SO_3 molecules through the defects of the protective Al_2O_3 scale. The constant supply of SO_2-SO_3 molecules decreases the adherence of the oxide scales on the intermetallic phases. This causes Al depletion in the near-surface region of the coating.

3. Inward diffusion of O into the Al-depleted zone and formation of Al_2O_3 precipitates with finger-like morphology (internal oxidation). The selective oxidation of Al to form Al_2O_3 further depletes the coating in Al. This leads to the formation of a γ'-Ni_3Al layer at the interface between the protrusion and the β-NiAl phase. Therefore, a cyclic process initiates and causes repeated precipitation of porous Al_2O_3 within the nickel aluminide phases.

4. The cyclic process is governed by both inward diffusion of O and outward diffusion of Al from the coating. The selective oxidation of Al induces the progressive depletion of Al from the β-NiAl phase and the protrusion grows with an epitaxial morphology. S-bearing molecules play an active role in the process by decreasing the adherence of the oxide scales on the intermetallic phases.

5. When the internal oxidation reaches the nickel substrate, the cyclic process stops because the p_{O_2} is low enough to avoid oxidation of nickel. Thereafter, the protrusion grows laterally by selective oxidation of Al from the coating layer. This leads to the progressive depletion of the β-NiAl phase and to the growth of the protrusion.

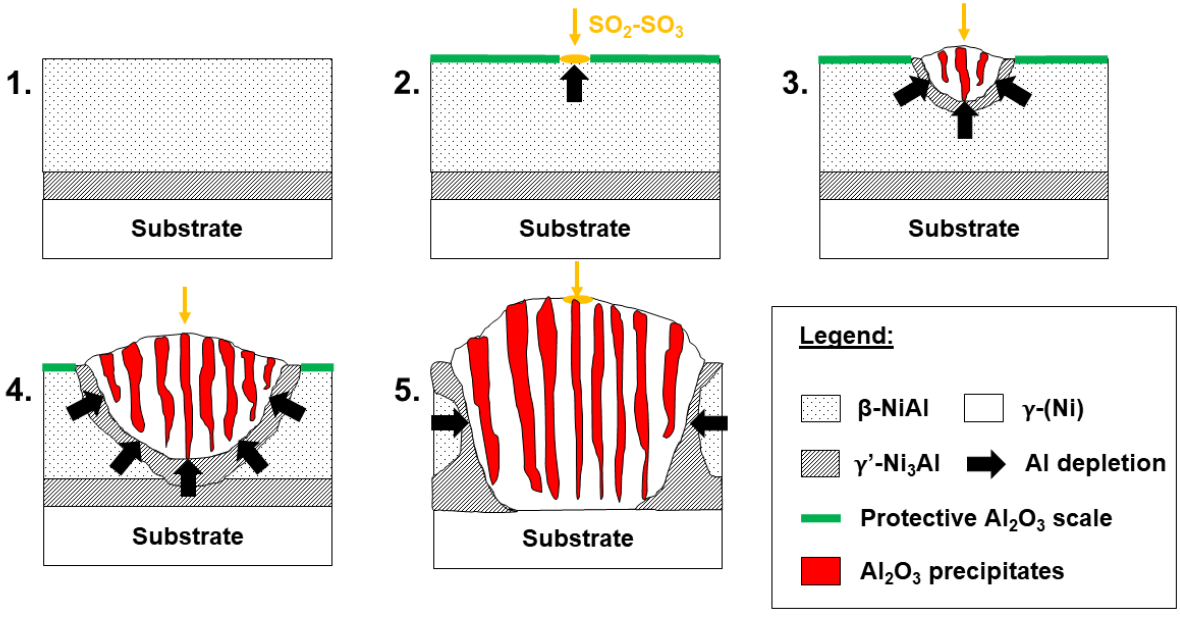

Fig. VI-23. Schematic representation of a protrusion formed by internal oxidation based on this work and Ref. [48].

A similar degradation mode was observed by Task et al. in Ref. [51] for the exposure of Ni-36Al alloy (at.%) in Type-II hot corrosion conditions (Na_2SO_4 deposit in a gas containing O_2 + 0.1% SO_2 at 700°C). Since Na_2SO_4 deposit was not used in this work, it can be concluded that the formation of such protrusion is due to the presence of SO_2-SO_3 rather than Type-II hot corrosion mechanisms. Therefore, in the work of Task et al., Na_2SO_4 acted as a catalyst to foster local breakage of the Al_2O_3 scale and internal oxidation of the nickel aluminide phase by selective oxidation of Al. This can be attributed to a higher p_{SO_3} and a lower p_{O_2} at the metal surface when a salt deposit is present as explained by F.S. Pettit in Ref. [4].

If the propagation stage was clearly identified in this work, the initiation stage was more difficult to understand as it was not directly observed in the microstructures. However, the S enrichment presented in Fig. VI-22 was observed for nearly all the protrusions and probably played an important role in the initial breakage of the Al_2O_3 scale. It must be considered here that no attack occurred within the first 20 hours of exposure and can be considered as the incubation period. On the other hand, only transition aluminas were detected on the coating surface after 20 hours exposure whereas α-Al_2O_3 was detected locally after 100 hours exposure. Therefore, the local S enrichments might be a consequence of the transformation of transient aluminas into the stable α-Al_2O_3 phase since this transformation is associated with a 13.8% volume reduction [55,56]. The local breakage of the Al_2O_3 scale due to the variation of the volume could possibly facilitate the adsorption of S-containing species at the coating surface. This could lead to the formation of less adherent Al_2O_3 scale and to the inward diffusion of O through the Al-depleted areas as proposed by Brumm et al. while oxidizing Ni-45Al (at.%) in low p_{O_2} atmospheres [52]. Thus, the cyclic degradation process could initiate and lead to the growth of the protrusion by selective oxidation of Al.

- ***Beneficial effect of Cr addition on the oxidation resistance in synthetic air + 0.5% SO_2:***

The presence of Cr in the aluminide coating was highly beneficial for the oxidation resistance in the SO_2-containing atmosphere. Unlike the simple aluminide coating, the Cr-modified one was not attacked even after 300 hours exposure. This enhanced oxidation resistance was attributed to the fast formation of the stable α-Al_2O_3 phase on the coating surface. Since Cr_2O_3 was also detected with both XRD and Raman surface analyses, it seems that the nucleation of α-Al_2O_3 was promoted because of the initial formation of Cr_2O_3 [48,53,54,59]. Therefore, even though the extreme surface of the coating was quite rough (cf. Fig. VI-21), the formation of a pure α-Al_2O_3 scale was ascribed to limit Al depletion in the near-surface region and to prevent internal oxidation [52]. As a result, the Al depletion in the coating mainly occurred by interdiffusion with the pure nickel substrate because of the great concentration gradient. This led to the β to γ' transformation at the grain boundaries of the coating layer (Fig. VI-21).

III. Type-II hot corrosion resistance of uncoated and slurry coated nickel at 700°C

In paragraph II, the influence of p_{SO_3} on the oxidation resistance of uncoated and slurry coated nickel was investigated at 700°C. The application of both the simple aluminide and Cr-modified coatings increased the resistance of nickel to oxidation-sulfidation. In this paragraph, the influence of Na_2SO_4 addition in the system was studied by half-embedding of the samples into Na_2SO_4 salt (cf. Chapter II). As a result, type-II hot corrosion conditions were fulfilled for these experiments.

III.1. Hot corrosion of pure nickel at 700°C

- ***Half-embedding of pure Ni in Na_2SO_4 and exposed in dry air:***

As presented in Fig. VI-1, a solid salt and a sufficient p_{SO_3} are required to meet the type-II hot corrosion conditions. The half-embedding method was first carried out in dry air to observe the behaviour of pure nickel in these conditions and to substantiate later the influence of p_{SO_3} on the corrosion attack. According to thermodynamic considerations, the type-II hot corrosion can only occur in the SO_2-containing atmosphere in this work since Na_2SO_4-$NiSO_4$ eutectic is not stable in dry air (Fig. VI-2). This should prevent the formation of $NiSO_4$-Na_2SO_4 eutectic phases responsible for the hot corrosion phenomenon.

The cross-section micrographs of high purity nickel samples half-embedded in Na_2SO_4 are given in Fig. VI-24. Representative micrographs of the atmosphere side and of the salt side are presented for comparison purposes. For the side exposed to dry air only, the oxidation of the nickel substrate occurred with the progressive growth of NiO (also observed in Fig. VI-6). Some rumpling of the scale was observed after cooling because of the high Pilling and Bedworth ratio of NiO (cf. paragraph IV.1 in Chapter I).

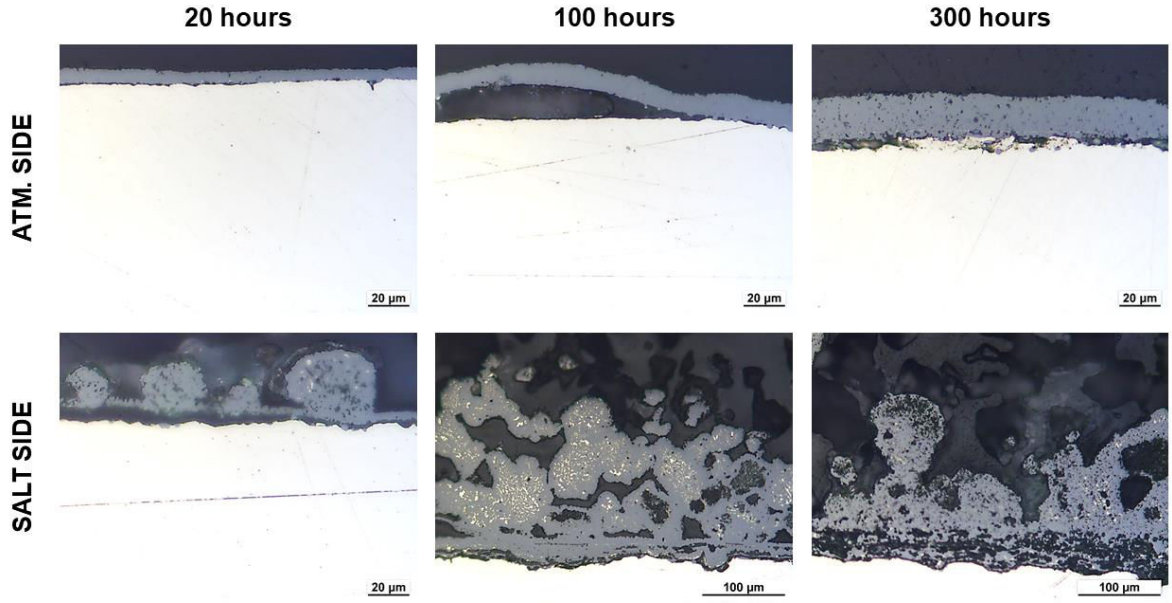

Fig. VI-24. Light optical cross-section micrographs of high purity nickel half-embedded in Na_2SO_4 and exposed in dry air at 700°C.

In the salt side, some nodules formed above a continuous NiO scale (Fig. VI-24). The formation of bright spots in the NiO nodules suggested the presence of nickel sulfides. EPMA analyses were conducted and confirmed the formation of nickel sulfides within the NiO nodules (Fig. VI-25). The local Raman analyses identified these phases as Ni_3S_2. There was little sulfidation of the nickel substrate probably because of the low p_{SO_3} at the scale-metal interface. The presence of mixed NiO-Ni_3S_2 nodules however suggested that the p_{SO_3} was high enough to stabilize sulfides. In the present system, additional S can only be obtained from dissociation of the sulfate, following equation *(Eq. VI-7)* [8]:

$$Na_2SO_4(s) \rightarrow Na_2O(s) + SO_3(g) \qquad \textbf{(Eq. VI-7)}$$

$$SO_3(g) \leftrightarrows \frac{1}{2}S_2(g) + \frac{3}{2}O_2(g) \qquad \textbf{(Eq. VI-8)}$$

The absence of a significant p_{SO_3} in the test conditions prevented the stabilization of Na_2SO_4-$NiSO_4$ solution and required reaction *(Eq. VI-7)* to proceed from the left to the right (i.e. the sulfate releases some SO_3) [8]. The characterization of the salt attested that it had remained solid after exposure and that the formation of Na_2SO_4-$NiSO_4$ eutectic phases was not observed. Therefore, the existence of Ni_3S_2 in the microstructures (cf. Fig. VI-25) was attributed to both low p_{SO_3} and low p_{O_2} because of the initial Na_2SO_4 deposit [8]. This could lead to local increase of the S activity (i.e. p_{S_2}) based on the SO_3 decomposition reaction *(Eq. VI-8)*. The tentative reaction paths for the exposure of pure nickel embedded in Na_2SO_4 and in dry air are given in Fig. VI-26. The p_{SO_3} was not sufficient in these conditions to provoke sulfidation of the nickel substrate.

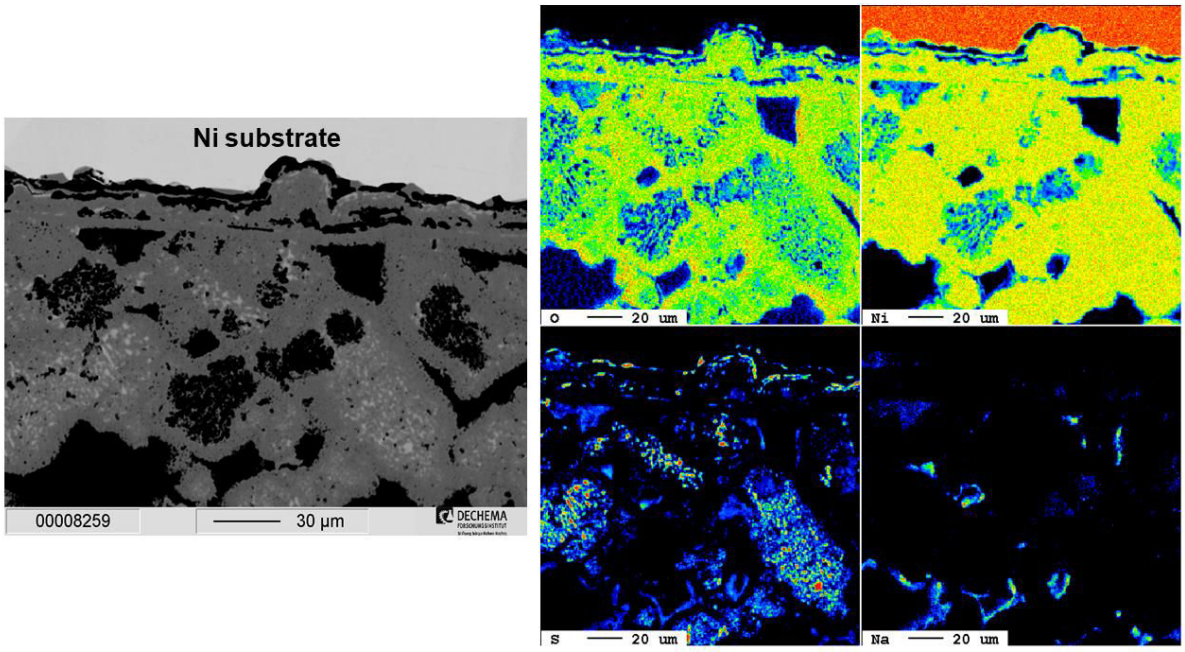

Fig. VI-25. BSE cross-section image and corresponding EPMA mapping of pure nickel embedded in Na_2SO_4 after 100 hours exposure at 700°C in dry air.

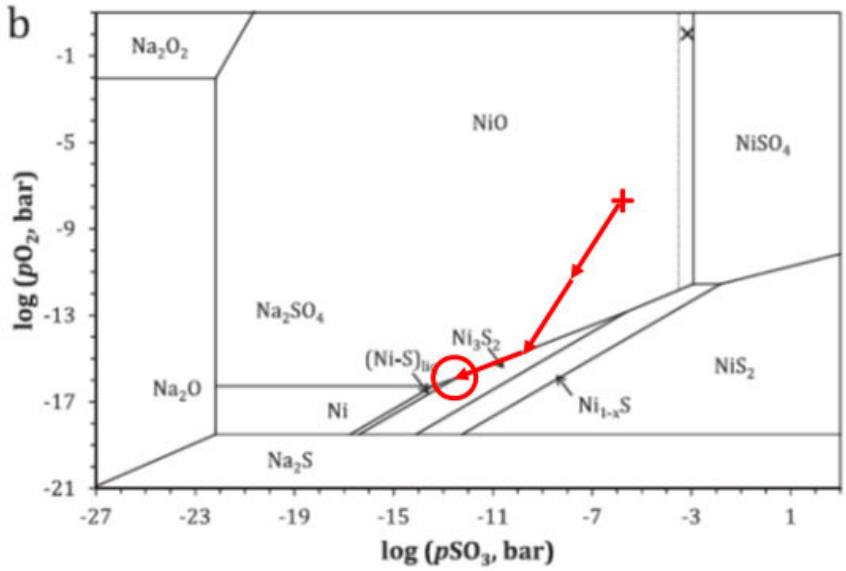

Fig. VI-26. Tentative reaction paths for the exposure of high purity nickel in Na_2SO_4 and in dry air at 700°C based on Ref. [8].

- ***<u>Half-embedding of pure Ni in Na_2SO_4 and exposed to synthetic air + 0.5% SO_2:</u>***

The half-embedding method was also carried out in synthetic air + 0.5% SO_2. This atmosphere was already found to foster the acidic reaction of NiO into $NiSO_4$ (cf. paragraph II.2). Therefore, the addition of Na_2SO_4 was expected to form Na_2SO_4-$NiSO_4$ eutectic phases as soon as the Na_2SO_4 salt became saturated with Ni. The cross-section micrographs at low magnification of pure nickel exposed to the type-II hot corrosion conditions are given on Fig. VI-27. One can see the progressive dissolution of the nickel substrate with time. The probabilistic plot measurements of the metal loss indicated that the corrosion attack was quite similar on both sides of the sample (Fig. VI-28).

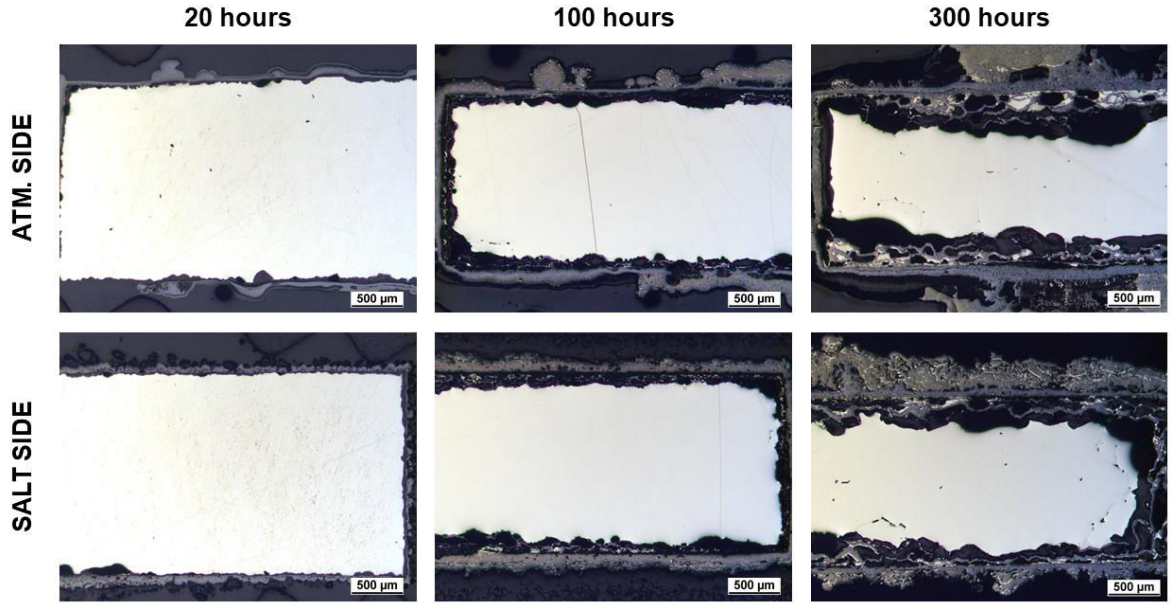

Fig. VI-27. Low magnification cross-section micrographs of half-embedded nickel samples in synthetic air + 0.5% SO_2 at 700°C.

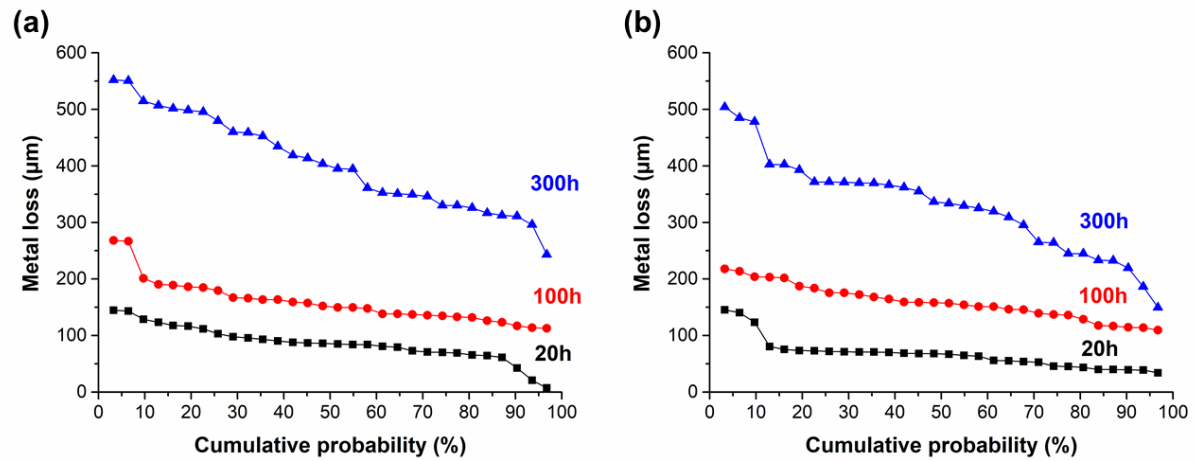

Fig. VI-28. Probabilistic plot measurements of the metal loss for pure nickel exposed to type-II hot corrosion conditions at 700°C in (a) the atmosphere side and (b) the salt side.

The corrosion attack was much more detrimental than the one observed for the samples half-embedded in Na_2SO_4 and exposed to dry air. The samples were further characterized by SEM for a better comprehension of the mechanisms (Fig. VI-29). On the salt side (Fig. VI-29a), a thick NiO + Ni_3S_2 mixed scale was formed above the nickel substrate. Extensive sulfidation of the substrate occurred at the metal/scale interface with the identification of Ni_3S_2. This indicated the presence of Ni-S liquid solution at temperature as observed in paragraph II.2. Na_2SO_4 particles were observed above the corrosion scale with limited Ni enrichment (less than 2 at.%). The local Raman analyses suggested that the initial structure of Na_2SO_4 (thenardite) evolved into the meta-thenardite one [6]. For the initially non-embedded side (Fig. VI-29b), the degradation rate was much more important than that of the sample exclusively exposed to the gas atmosphere after 20 hours (Fig. VI-11a). This confirmed the influence of Na_2SO_4 on the corrosion mechanisms on this side too.

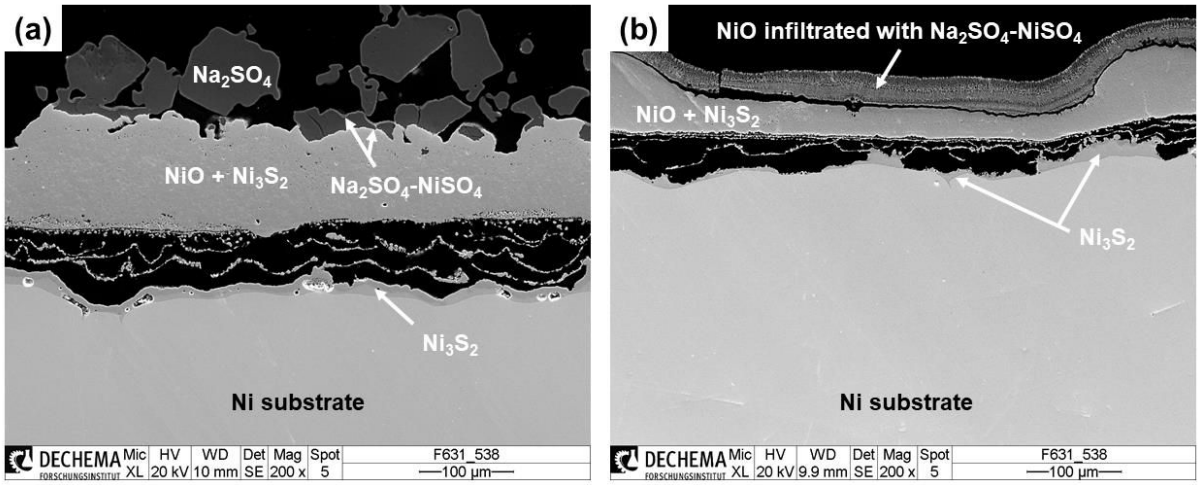

Fig. VI-29. Pure nickel samples after exposure for 20 hours at 700°C to synthetic air + 0.5% SO_2 in (a) the salt side and (b) the atmosphere side.

The extreme surface of the NiO + Ni_3S_2 mixed scale was covered with a NiO layer infiltrated with Na_2SO_4-$NiSO_4$ as observed by other authors [6,8]. This confirmed the formation of liquid phases at the test temperature (i.e. 700°C). This NiO infiltrated layer was observed all over the sample on the atmosphere side. Extensive sulfidation of the substrate was also observed in cross-section. These observations confirmed that the Type-II hot corrosion conditions were fulfilled with the present experimental set up [8].

The SEM cross-sections of pure nickel samples subjected to Type-II hot corrosion conditions (in the salt side) are shown on Fig. VI-30. At low magnification, a mixed NiO + Ni_3S_2 outer scale had grown above the Ni substrate. The microstructures suggested that Ni-S liquid solutions were present at temperature (i.e. 700°C) on the metal surface. As observed in paragraph II.2, the Ni-S liquid solution transformed into Ni_3S_2 on cooling to room temperature. Some Ni precipitates may be found in the nickel sulfide layer depending on the stoichiometry. A layered microstructure with alternatively NiO and Ni_3S_2 can be distinguished in BSE mode (confirmed with both EDS and Raman local analyses). NiO was also found to re-precipitate above the sulfide layer suggesting that a local variation of p_{O_2} and p_{SO_3} occurred in this region. After cooling, this resulted in large decohesion between the nickel substrate and the corrosion scale as observed by Kofstad and co-workers for the reaction of pure nickel in SO_2-containing atmospheres with and without sulfate deposit [6,44,45]. The microstructures obtained on Fig. VI-30 are also in good agreement with the observations of Gheno et al. [8].

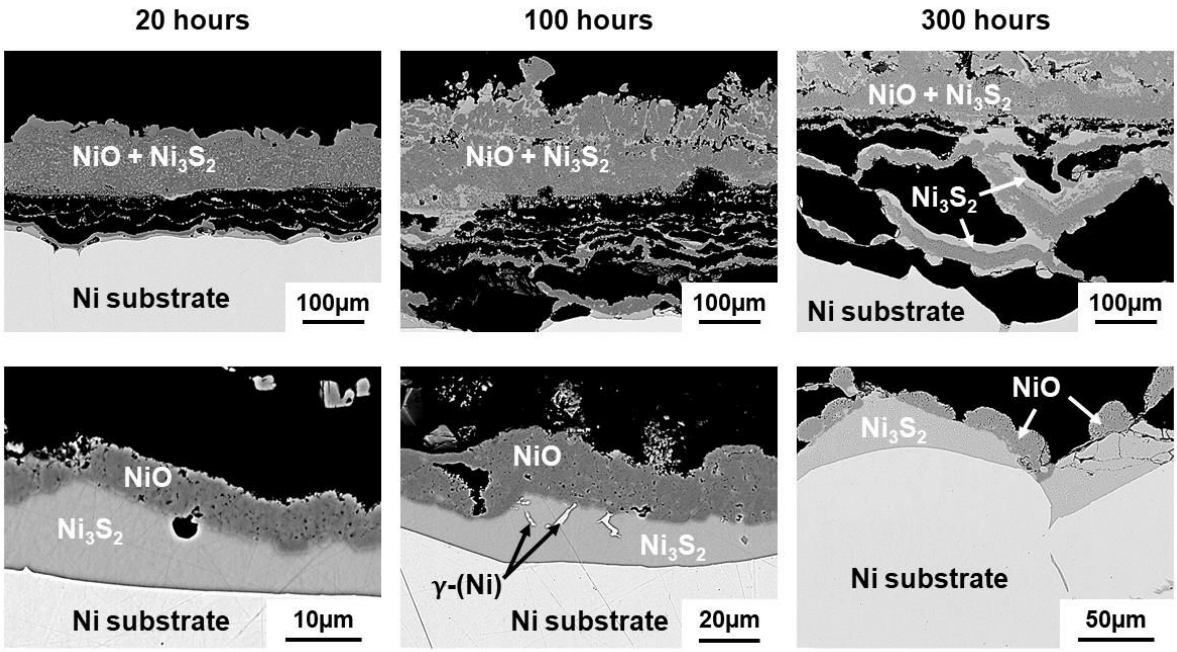

Fig. VI-30. BSE cross-section images of pure nickel samples exposed to Type-II hot corrosion conditions for 20, 100 and 300 hours. The sulfidation of the Ni substrate was observed at higher magnifications.

By comparison with the microstructures observed in paragraph II.2, more nickel sulfides were detected in the corrosion scale after exposure to Type-II hot corrosion conditions. It can therefore be concluded that in the test atmosphere, Na_2SO_4 accelerated the corrosion process probably by increasing the S activity (i.e. p_{S_2}) within the scale and at the metal/scale interface.

III.2. Hot corrosion of simple and Cr-modified slurry aluminide coatings on pure nickel

The half-embedding method was also conducted on slurry coated nickel to investigate the hot corrosion resistance of the simple and Cr-modified coatings. The oxidation tests presented in paragraph II.3 confirmed that the application of the slurry coatings considerably increased the oxidation-sulfidation resistance of the nickel substrate. This was attributed to the formation of protective oxide scales on coating surfaces such as Al_2O_3 and Cr_2O_3. Whereas the Cr-modified coating was not attacked after 300 hours exposure in synthetic air + 0.5% SO_2, the simple aluminide coating was prone to localized attack in the form of protrusions with internal oxidation. This was attributed to the rapid establishment of an α-Al_2O_3 scale on the Cr-modified coating that provided an effective barrier for SO_2-SO_3 molecules. These results will help to interpret the hot corrosion mechanisms with the addition of Na_2SO_4 in the system.

- ***Half-embedding of slurry coated Ni in Na_2SO_4 and exposed to dry air:***

The half-embedding method was first performed in dry air to later investigate the influence of p_{SO_3} on the corrosive attack. The top view of the samples half-embedded in Na_2SO_4 suggested that there was

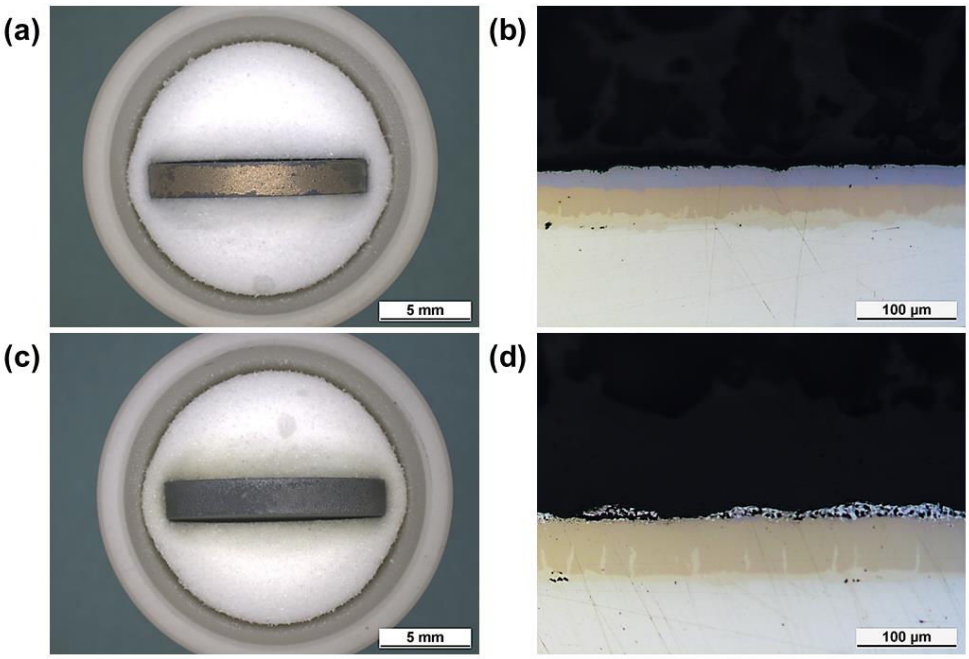

Fig. VI-31. Top view of the Ni samples half-embedded in Na_2SO_4 and cross-section micrographs in the salt side for (a), (b) the simple aluminide and (c), (d) the Cr-modified coating after 300 hours exposure at 700°C in dry air.

no interaction after 300 hours exposure (Fig. VI-31a and Fig. VI-31c). This was confirmed with the characterization of the slurry coated samples in cross-section (Fig. VI-31b and Fig. VI-31d).

The slurry coatings underwent "normal" oxidation after 300 hours exposure and presented little transformation in the microstructures. It was therefore concluded that the p_{SO_3} of dry air was too low to initiate corrosion in agreement with the thermodynamic considerations. This also indicates that Na_2SO_4 was stable at 700°C in dry air. After exposure, sintering of the salt occurred, highlighted by its decohesion with the alumina crucible (Fig. VI-31a and Fig. VI-31c). Na_2SO_4 was generally not adherent to the underlying coating after the half-embedding tests in dry air.

- ***Half-embedding of slurry coated Ni in Na_2SO_4 and exposed to synthetic air + 0.5% SO_2:***

When the half-embedded samples were exposed to synthetic air + 0.5% SO_2, the results were significantly different as can be seen in the crucibles (Fig. VI-32). For both coatings, there was no interaction with the salt after 20 hours suggesting that the incubation period was still ongoing. After 100 hours, the samples were highly corroded with the formation of nodules and needle-like products at the surface. The colour of the salt also changed into yellow in the corroded area. Such yellow colour was attributed to the formation of mixed Na-Ni sulfates by Lillerud and Kofstad [6].

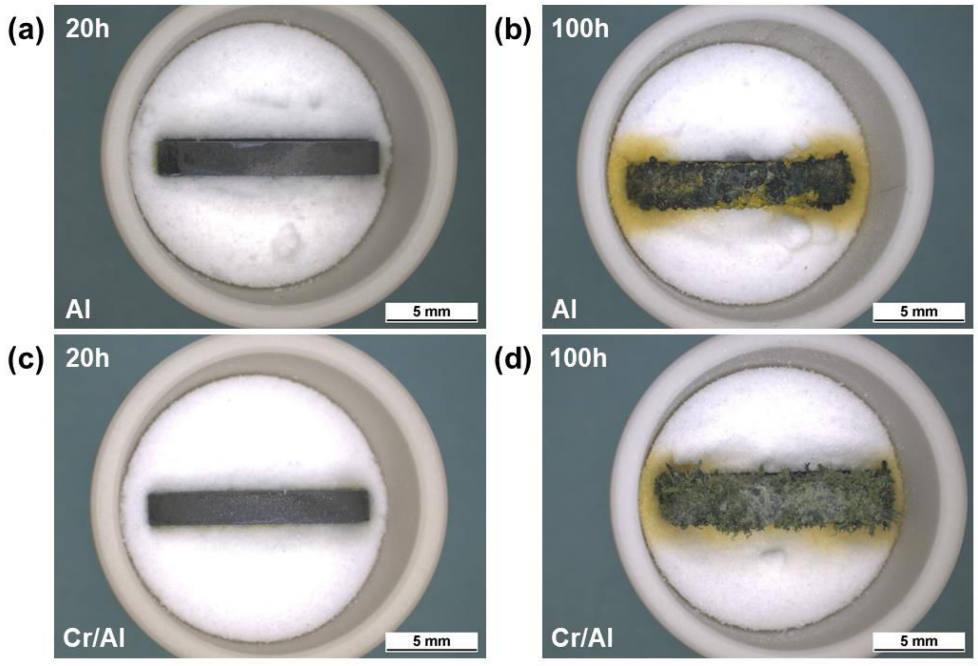

Fig. VI-32. Top view of the Ni samples half-embedded in Na_2SO_4 after exposure at 700°C in synthetic air + 0.5% SO_2 with (a), (b) the simple aluminide and (c), (d) the Cr-modified coating.

The low magnification cross-section images of the slurry coatings exposed for 20 hours and 100 hours to Type-II hot corrosion conditions are presented in Fig. VI-33. After 20 hours of exposure, both coatings were still at the incubation stage and the salt did not affect the oxidation behaviour of the underlying coating (Fig. VI-33a and Fig. VI-33c). For the simple aluminide coating, Al_2O_3 intrusions were randomly distributed as shown at higher magnification in Fig. VI-34 (γ-Al_2O_3 according to local Raman analyses). These intrusions were enriched in S according to EDS spot measurements. Similar observations were made by Gheno et al. for short term exposure of Ni-36Al (at.%) in Type-II conditions [7]. These authors highlighted that S accumulated at the interface between the intrusion and the intermetallic phase. The accumulation of S in these regions decreased the adherence of the growing Al_2O_3 scale and probably acted as preferential paths for internal oxidation to occur (cf. Fig. VI-23).

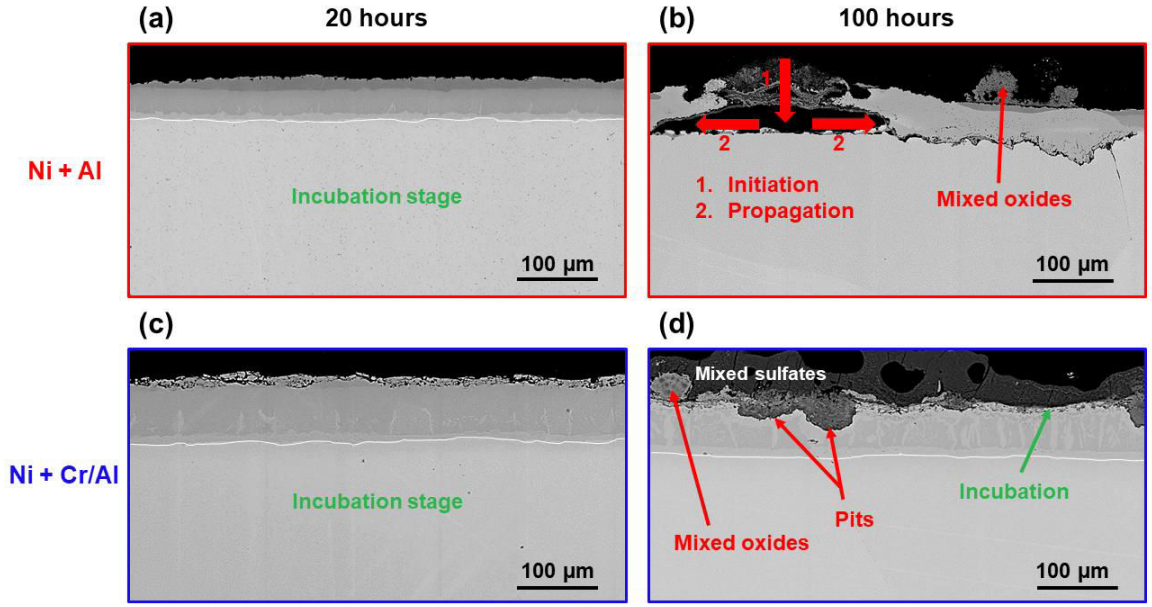

Fig. VI-33. BSE cross-section images of (a), (b) the simple aluminide and (c), (d) the Cr-modified coatings elaborated on pure Ni after exposure to Type-II hot corrosion conditions at 700°C.

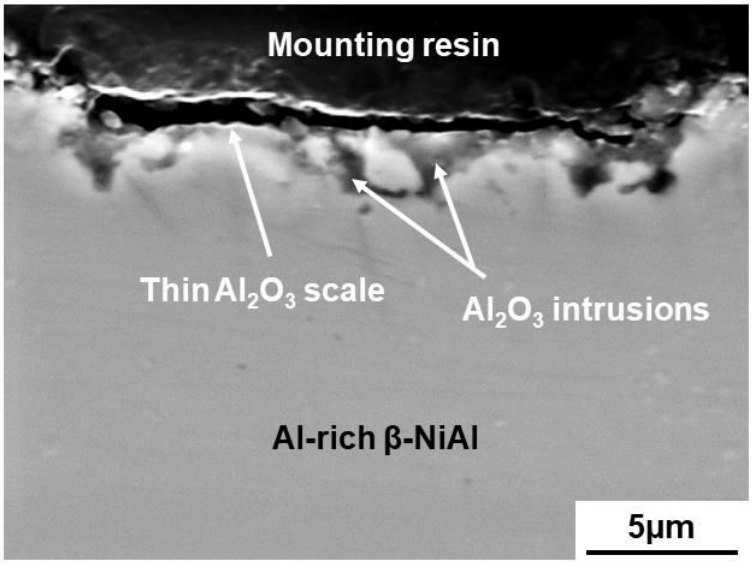

Fig. VI-34. SEM cross-section image of the simple aluminide coating exposed to Type-II hot corrosion conditions for 20 hours at 700°C showing thin Al_2O_3 scale and Al_2O_3 intrusions.

For the Cr-modified coating, the outer Cr-rich region (cf. Fig. VI-3c and Fig. VI-3d) was found to develop both α-Al_2O_3 and Cr_2O_3 after 20 hours exposure (Fig. VI-33c). A white line was added on the SEM images of Fig. VI-33 to highlight the interface between the coating and the substrate. After 100 hours exposure, both coatings exhibited corrosion attack (Fig. VI-33b and Fig. VI-33d) as suggested from the top view of the crucibles removed from the reaction chamber. Nevertheless, the propagation of the corrosion attack was significantly slower for the Cr-modified coating than for the simple aluminide coating. The Cr-modified coating was only prone to localized attacks in the form of pits whereas the rest of the sample was still under incubation (Fig. VI-33d). On the opposite, the simple aluminide coating suffered from extensive degradation and the microstructure of the coating was destroyed after 100 hours exposure (Fig. VI-33b). The morphology of the attack in Fig. VI-33b suggested that the coating was first prone to a localized attack and then that the attack progressed laterally at the interface between the coating and the nickel substrate. This is consistent with the observations made in paragraph II.3 (cf. Fig. VI-23) when the simple aluminide coating was exposed to the SO_2-containing atmosphere.

- ***SEM analyses for the simple aluminide coating in Type-II conditions:***

Further characterization of the samples was carried out by SEM to interpret the mechanisms of corrosion. In Fig. VI-35, a SEM cross-section image with associated elemental distribution of an affected area of the simple aluminide coating is presented. The coating microstructure was destroyed and only a γ'-Ni_3Al layer subsisted with barely no S enrichment (less than 1 at.%). It can therefore be concluded that the S enrichment at the coating-substrate interface (see map of S on Fig. VI-35) was coming from a pit region identified on Fig. VI-33. Sulfidation of both the coating layer and of the nickel substrate was observed and the appearance of a lateral decohesion suggested that liquid phases were present at temperature. The mean composition of the S-enriched area was 5O-12Al-22S-61Ni in at.%.

A thick Al-rich and O-rich scale was formed on the surface of the γ'-Ni_3Al layer. However, this scale was also enriched in Ni, Na and S according to the X-ray maps. Therefore, this scale was probably made of Al_2O_3 with infiltrated Na_2SO_4-$NiSO_4$ (liquid at 700°C). Above this layer, extensive dissolution of Ni and of Al occurred in the salt. This confirmed the appearance of liquid phases at 700°C provoking the progressive dissolution of the oxide scales formed on the surface as cationic species within the salt. By reaction with Na_2SO_4, this led to the formation of Ni and Al sulfates. These sulfates were formed within the salt deposit where the p_{SO_3} was high enough and were identified as large nodules on the surface (Fig. VI-32b). The microstructure therefore suggested that liquid phases formed above the coating layer as Na_2SO_4-$NiSO_4$ eutectics (T_e = 671°C [6-8]) and at the substrate-coating interface probably in the form of Ni-S liquid solution (eutectic temperature of 635°C, cf. Fig. VI-13).

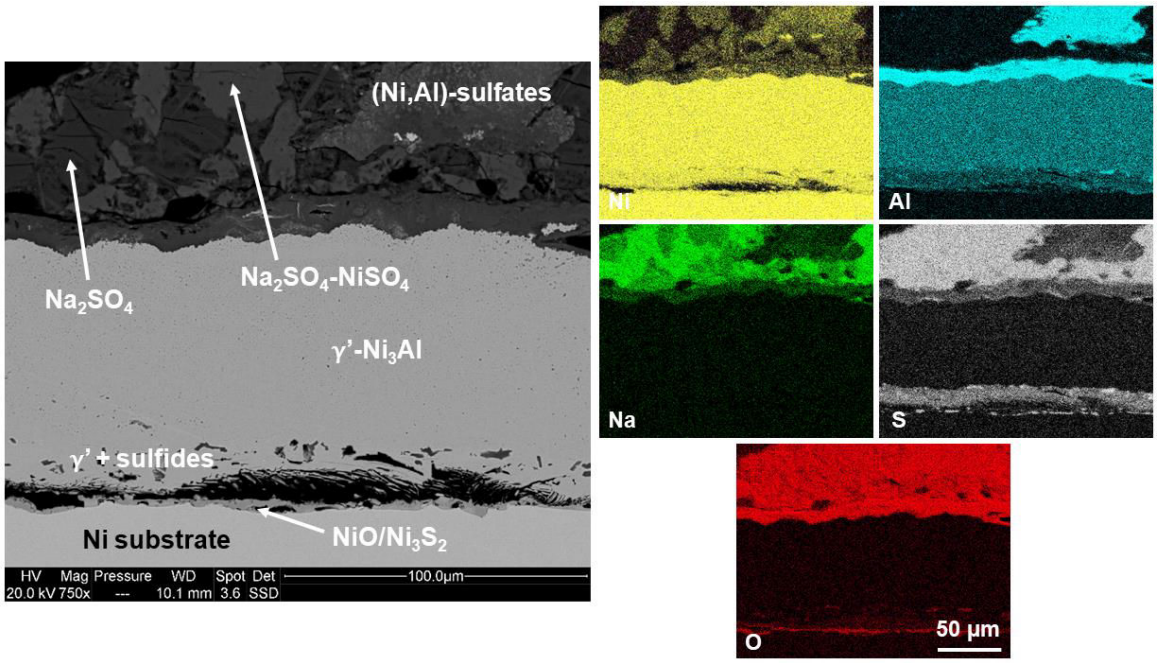

Fig. VI-35. BSE cross-section image and corresponding X-ray maps for nickel slurry coated with simple aluminide after 100 hours Type-II hot corrosion exposure at 700°C.

- ***SEM analyses for the Cr-modified coating in Type-II conditions:***

For the Cr-modified coating, further analyses were conducted in the regions with very little degradation and considered to be still at the incubation stage (Fig. VI-36). At lower magnification (Fig. VI-36a), one can see that a dark layer of mixed sulfates had formed above the coating layer (highlighted with the BSE mode of the SEM). The mixed sulfate layer was continuous and was enriched in Ni and Cr suggesting that some dissolution of Ni and Cr ions occurred in Na_2SO_4 upon exposure. It is important to mention here that Al was only detected at very low concentration in this layer (less than 0.1 at.%). β to γ' transformation occurred within the coating layer (Fig. VI-36a) but this did not affect the hot corrosion resistance of the coating as reported by Morbioli et al. for the hot corrosion of Cr-modified aluminide coatings [60]. At higher magnification, a duplex oxide scale was identified on the coating surface (Fig. VI-36b). Raman local analyses have shown that the inner layer was composed of Cr_2O_3 and the external layer of α-Al_2O_3. Cr_2O_3 was also detected in the outer region of the coating where it sealed the gaps between the intermetallic phases. There was no formation of sulfides in such areas and that was ascribed to the presence of both β and γ' phases in the outer region of the coating [60].

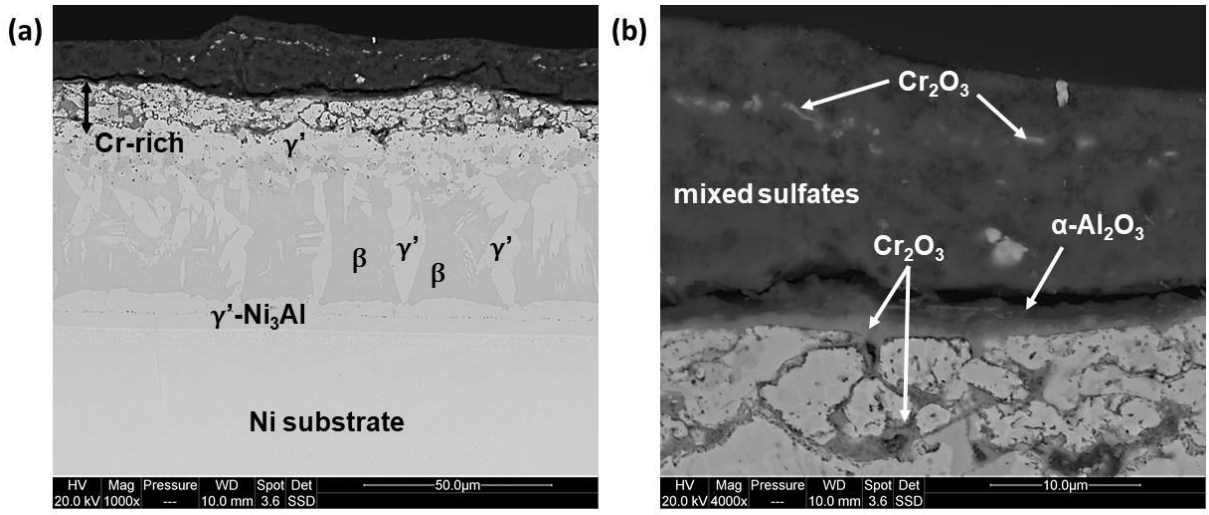

Fig. VI-36. BSE cross-section images of the Cr-modified coating elaborated on pure Ni after 100 hours exposure to Type-II conditions at 700°C. Images were taken in a region considered in incubation (cf. Fig. VI-33d).

Cr_2O_3 was also found to precipitate within the mixed sulfate layer (cf. Fig. VI-36b, confirmed with Raman local analyses). This indicates that Cr-containing ions were present in the salt chemistry and precipitated as Cr_2O_3 in a region where the solubility of the oxide is low [61,62]. According to Rapp and Otsuka [63], chromia solubilizes in fused Na_2SO_4 with chromate anions (CrO_4^{2-}) as the dominant solute at high oxygen activities whereas chromite anions (CrO_2^-) dominate at low oxygen activities. Chromite ($NaCrO_2$) is therefore the dominant basic solute under highly reducing conditions as expected near the oxide/salt interface [63].

The basic dissolution of Cr_2O_3 prevailing underneath the salt film at low p_{O_2} can be written following *(Eq. VI-9)*:

$$Cr_2O_3(s) + O^{2-} \rightarrow 2\ CrO_2^- \qquad \textbf{(Eq. VI-9)}$$

The chromite ions then oxidize in chromate ions in region with high oxygen activities following *(Eq. VI-10)*:

$$2\ CrO_2^- + \frac{3}{2} O_2 + O^{2-} \rightarrow 2\ CrO_4^{2-} \qquad \textbf{(Eq. VI-10)}$$

Acting as a strong acid solute, the presence of both chromite and chromate anions serve as a buffer for the salt chemistry mainly at the scale/salt interface [63]. The chromate anions were also expected to precipitate as Cr_2O_3, cf. *(Eq. VI-11)* in the reducing sites and thereby inhibit the corrosion attack by preventing the contact between the salt and the metal (i.e. prevent sulfidation) [61]. This would explain the sealing of the intermetallic coating with Cr_2O_3 which in turn fosters the nucleation and growth of a protective α-Al_2O_3 scale (Fig. VI-36b and Fig. VI-37).

$$2\ CrO_4^{2-} \rightarrow Cr_2O_3(s) + 2\ O^{2-} + \frac{3}{2} O_2 \qquad \textbf{(Eq. VI-11)}$$

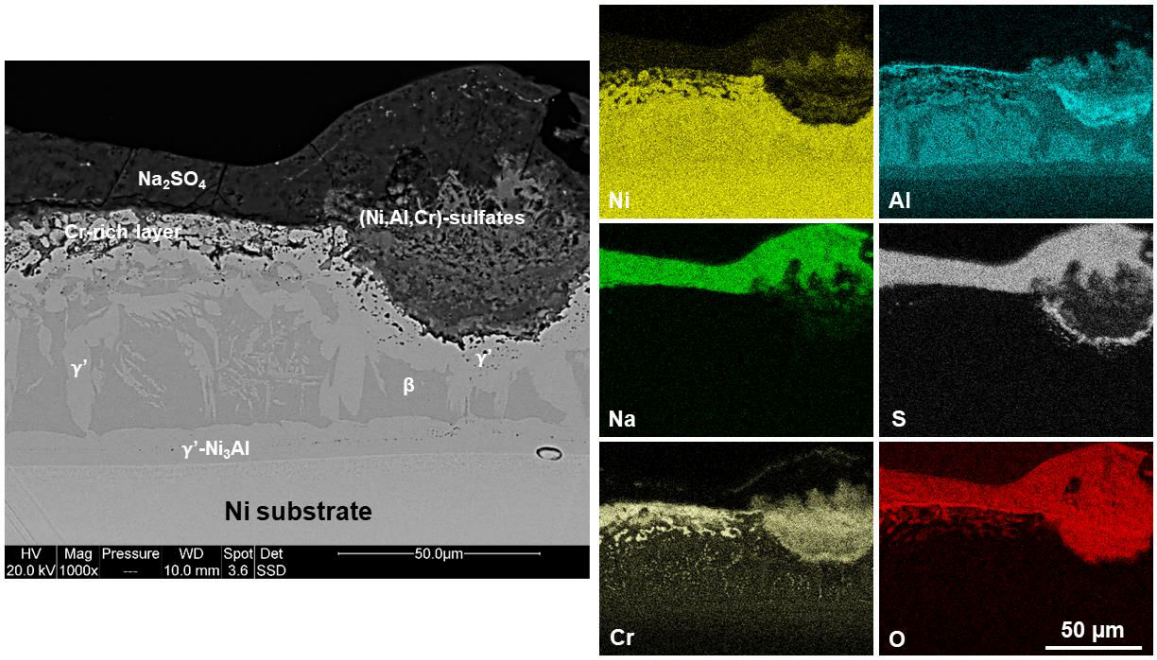

Fig. VI-37. BSE cross-section image and corresponding X-ray maps for nickel slurry coated with the Cr-modified coating after 100 hours Type-II hot corrosion exposure at 700°C.

By comparison with the results obtained for the simple aluminide coating, it therefore appeared that the presence of Cr-rich phases was found to passivate the surface of the coating through the formation of Cr_2O_3 and to prevent the initiation of the hot corrosion process.

After 100 hours exposure in Type-II conditions, some pits were observed on the Cr-modified coating (Fig. VI-33d). X-ray maps were done in a pitted region to interpret the corrosion mechanisms (Fig. VI-37). The formation of Cr sulfides was highlighted at the reaction front between the pit and the metallic coating and was probably due to the extensive Al depletion forming a continuous γ' layer underneath the oxide scale [60]. As a result, depletion of the protective element (i.e. Cr) occurred in the outer region of the coating. Any oxide scale that may form in these conditions were not protective and rapidly dissolve in the sulfate phase. The dissolution of the metallic elements in the pit region was highlighted with the X-ray maps (Fig. VI-37). The very low concentration of Na and the low concentration of S in the pit region suggest that it was mainly composed of oxides (i.e. dissolution/reprecipitation mechanisms). Similar microstructures were observed by Task et al. under Type-II hot corrosion conditions [64]. On the X-ray maps (Fig. VI-37), it appeared that Al was mostly concentrated near the reaction front whereas Ni was observed above the initial surface of the coating. This probably illustrates the existence of a p_{O_2}.gradient across the pit region with a low p_{O_2} at the scale/coating interface and a high p_{O_2} at the salt/pit interface. Consequently, the oxide with the higher affinity for oxygen (i.e. Al_2O_3) precipitates in the inner region of the pit.

The existence of a p_{O_2}.gradient across the pit region probably affects the gas composition such as the decomposition of SO_3 may be observed across the scale following *(Eq. VI-12)*:

$$SO_3(g) \leftrightarrows \frac{1}{2} S_2(g) + \frac{3}{2} O_2(g) \qquad \textbf{(Eq. VI-12)}$$

The increased S activity (i.e. p_{S_2}) at the scale/coating interface fosters the sulfidation of the metallic coating. Even though the sulfidation of the Cr-modified aluminide coating was observed after 100 hours exposure, the propagation was considerably lower than the corrosion attack of the simple aluminide coating (Fig. VI-33b). It is highly likely that the formation of Cr sulfides consumes the S at the reaction front thus preventing the formation of Ni_3S_2 at the metal/scale interface [65]. This considerably limited the formation of eutectic Ni-Ni_3S_2 solution and buffered the corrosion attack [65].

III.3. Discussion

Using the half-embedding method, it was possible to investigate three different zones on the samples: the atmosphere side (no contact with Na_2SO_4), the salt side (embedded in Na_2SO_4) and the interface between these two areas.

- ***Hot corrosion of pure Ni:***

The hot corrosion tests of pure Ni using this method confirmed that a sufficient p_{SO_3} is necessary to reproduce the Type-II conditions. When pure Ni half-embedded in Na_2SO_4 was exposed to dry air at 700°C, very little sulfidation of the substrate occurred even after 300 hours of exposure. In the atmosphere side (sample without contact with Na_2SO_4), a NiO scale was growing with a cellular morphology as observed for the oxidation of pure Ni in synthetic air (Fig. VI-6). In the salt side (sample embedded in Na_2SO_4), mixed NiO + Ni_3S_2 nodules have grown above the substrate surface. However, the microstructures suggested that there was no formation of liquid phases at temperature. The formation of nickel sulfides within the oxide was attributed to the decomposition of SO_3 at the low p_{O_2} prevailing within the thick oxide scale following *(Eq. VI-12)* [8]. In these conditions, the sulfides can form within the oxide scale or at the metal/scale interface where the p_{O_2} is minimum and the p_{S_2} is maximum [8,47].

When pure Ni half-embedded in Na_2SO_4 was exposed to synthetic air + 0.5% SO_2 at 700°C, the Type-II conditions were met. Fast corrosion attack of the Ni substrate occurred in both atmosphere and salt sides (Fig. VI-27 and Fig. VI-28). After 20 hours of exposure, NiO infiltrated with Na_2SO_4-$NiSO_4$ was observed all around the sample in the atmosphere side (Fig. VI-29b). Similar observations were reported by Gheno et al. in Ref. [8]. In their work, the Ni sample was coated with Na_2SO_4 only on one side. After 6.5h of reaction in O_2 + 0.1% SO_2, the initially non-coated side was also affected by the salt forming an external NiO scale infiltrated with Na_2SO_4-$NiSO_4$. This clearly indicates that the sulfate mixture was liquid at temperature (Na_2SO_4-$NiSO_4$ eutectic at 671°C [6,7]). The metal loss measurements confirmed that the presence of Na_2SO_4 in the system increased the corrosion rate in the atmosphere side by comparison of Fig. VI-10c and Fig. VI-28a. In this work, the Type-II conditions were therefore fulfilled for the whole sample using the half-embedding method (Fig. VI-27). Further characterization of the samples confirmed the extensive sulfidation of the pure nickel substrate (Fig. VI-30). The formation of intermixed NiO + Ni_3S_2 layers within the corrosion scale suggested that the sulfide layer was growing together with NiO at the sulfide/oxide interface [8]. In such microstructures, Ni_3S_2 was ascribed to form a continuous network [66]. Since Ni diffusivity is much higher within the sulfides than within the oxides, the reaction kinetics was governed by outward diffusion of Ni in the Ni_3S_2 network [8]. The reaction of pure Ni with synthetic air + 0.5% SO_2 was found to involve [Ni-S] liquid solution (cf. *(Eq. VI-5)* and *(Eq. VI-6)*). As a result, the sulfidation resulted in fast dissolution of Ni and enhanced outward diffusion from the substrate (Fig. VI-27).

From the hot corrosion tests of pure Ni, it can thus be concluded that Na_2SO_4 increased the S activity within the growing scales and at the metal/scale interface. Increasing the S activity led to higher p_{S_2} and thus to higher sulfidation rates. This was particularly evident by comparison of the scales after exposure in the SO_2-containing atmosphere only and the Type-II conditions (Fig. VI-38). The difference of brightness of NiO and Ni_3S_2 with optical light microscopy highlighted the greater amount of sulfide formation after exposure to Type-II conditions (Fig. VI-38c and Fig. VI-38d) than without Na_2SO_4 (Fig. VI-38a and Fig. VI-38b).

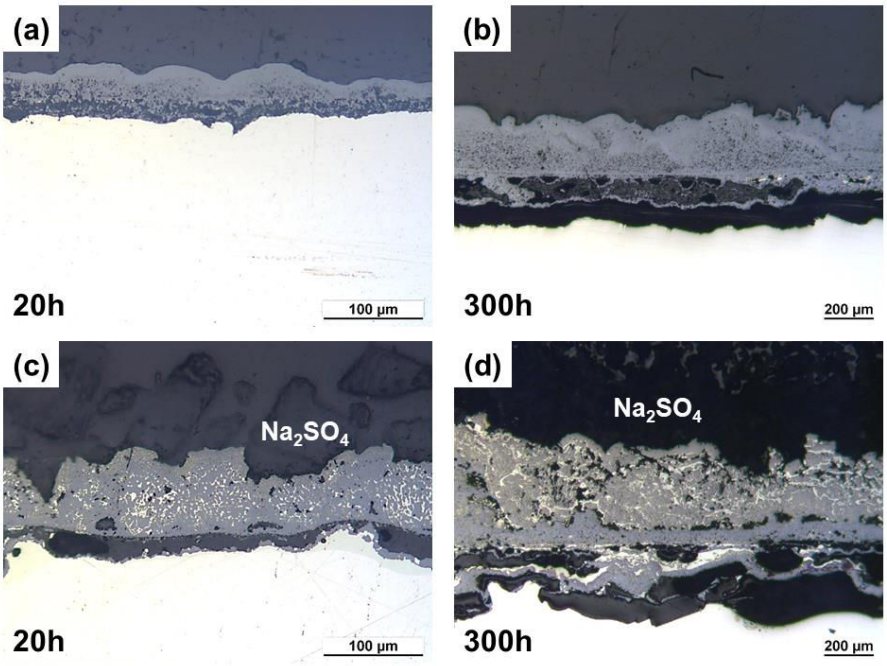

Fig. VI-38. Light optical micrographs of the corrosion scales formed on Ni substrate after exposure at 700°C to synthetic air + 0.5% SO_2 (a), (b) without Na_2SO_4 and (c), (d) with Na_2SO_4.

- ***Hot corrosion resistance of the slurry aluminide coatings elaborated on pure Ni:***

By applying slurry coatings on the pure Ni substrate, the corrosion attack was significantly decreased. The slurry coated samples half-embedded in Na_2SO_4 and exposed to dry air were not attacked and underwent "normal" oxidation. When the half-embedded samples were exposed to synthetic air + 0.5% SO_2, corrosion was observed after a first incubation period which lasted at least 20 hours in our test conditions (Fig. VI-32). The results obtained for the hot corrosion tests are summarized schematically in Fig. VI-39. In paragraph II.3, both application of the simple aluminide and the Cr-modified coatings was found to increase the oxidation-sulfidation resistance of pure Ni. Whereas the Cr-modified coating was not attacked after 300 hours exposure in synthetic air + 0.5% SO_2, the simple aluminide coating was prone to localized attack in the form of protrusions. This attack was preceded by an incubation period of at least 20 hours suggesting that the thin Al_2O_3 scale formed on the surface was initially protective. These protrusions were formed by selective oxidation of Al in S-enriched areas causing the precipitation of porous Al_2O_3 within the intermetallic phases. This progressively depleted

the β-NiAl layer from Al and led to the epitaxial growth of the protrusion (Fig. VI-23). The rapid formation of both Cr_2O_3 and α-Al_2O_3 for the Cr-modified coating was ascribed to its superior resistance.

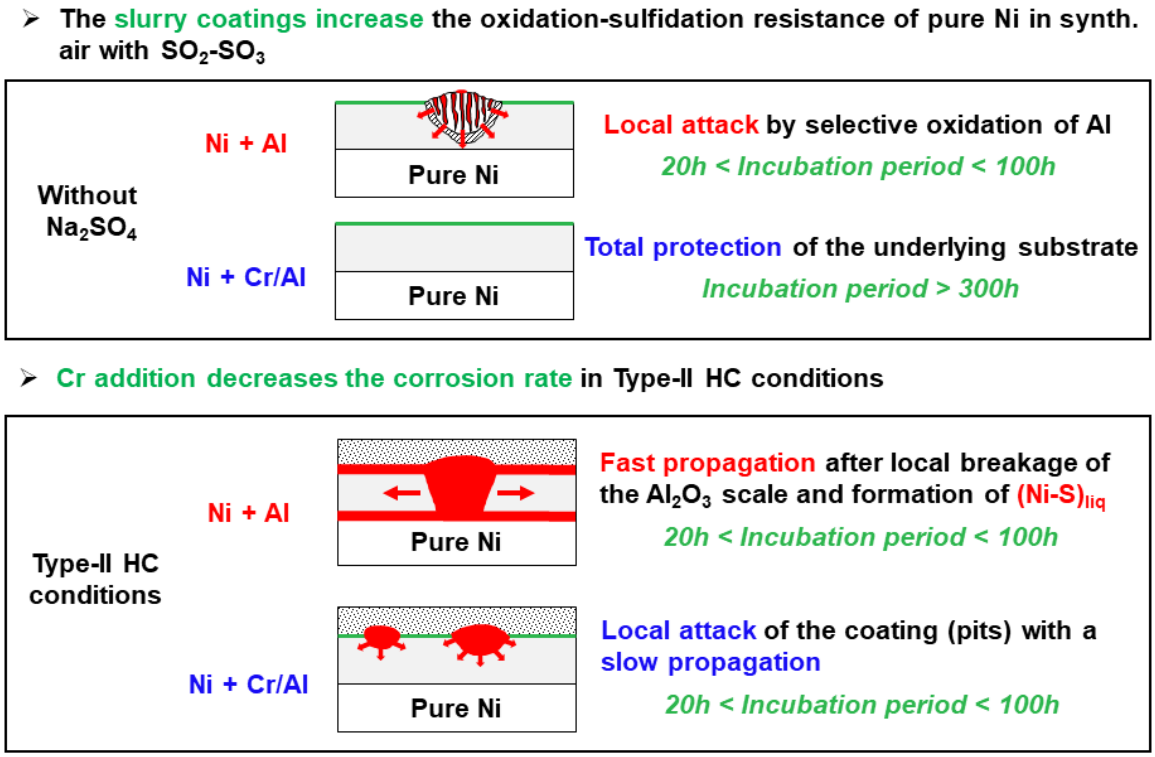

Fig. VI-39. Synthetic representation of the hot corrosion tests performed at 700°C on pure Ni slurry coated with the simple aluminide and the Cr-modified coating.

After the initial incubation period of more than 20 hours, the propagation of the corrosion attack was significantly lower for the Cr-modified coating than for the simple aluminide one (Fig. VI-39). For the simple aluminide coating, it is believed that the initiation of the corrosion attack was similar in both conditions (without Na_2SO_4 and Type-II conditions). The growth of a protrusion induces Al depletion and non-protective oxides (i.e. NiO or $NiAl_2O_4$) can start forming in this region [7]. The high p_{SO_3} of the atmosphere can therefore lead to the sulfation of NiO into $NiSO_4$. A progressive saturation of the salt with $NiSO_4$ occurs and liquid phases start to form when the eutectic composition is reached (40 mol.% $NiSO_4$) [6]. The liquid phase can then wet the surface of the coating and dissolve the formed oxides (Fig. VI-35). This causes the sulfate mixtures to be enriched in both Ni and Al (Fig. VI-35) and was associated with the yellow colour of the salt after exposure (Fig. VI-32b). This also increases the S activity (i.e. p_{S_2}) at the coating/substrate interface and fosters the formation of Ni-S liquid solution (eutectic at 635°C). This was particularly well illustrated in Fig. VI-33b, where the interface between the coating and the Ni substrate was no longer visible and lateral penetration of S occurred in this region. The appearance of liquid phases in the degradation mechanisms can explain the fast propagation of the attack.

It should be noted that the sulfidation of the Ni substrate was limited after 100 hours exposure. This could be explained by the different modes of transport of S during the corrosion attack [47]. For the sulfidation of pure Ni, the transport of S-bearing molecules (SO_2-SO_3) through the physical defects of NiO was found to control the attack [47]. In the present case, an intermetallic layer was still present on the substrate surface, which prevented the permeation of gas molecules before the attack. It could therefore be proposed that the S enrichment at the coating-substrate interface occurred by dissolution mechanisms [47]. The presence of liquid phases at temperature (i.e. 700°C) can explain the lateral decohesion observed in the microstructure after cooling since the phases must present different coefficients of thermal expansion (CTE).

For Ni samples coated with the Cr-modified coating, the corrosion attack was much slower than with the simple aluminide coating. After 100 hours exposure, some pits were randomly distributed on the sample surface (Fig. VI-33d) whereas some areas were still unaffected by the presence of Na_2SO_4 (Fig. VI-36). The superior corrosion resistance of the Cr-modified coating was ascribed to the rapid formation of Cr_2O_3 within the Cr-rich layer. It appeared also that Cr_2O_3 was precipitating in the layer of mixed sulfates (Fig. VI-36b). This may indicate the presence of chromate anions in the sulfate layer as proposed in reaction *(Eq. VI-9)* [61]. The precipitation of Cr_2O_3 was found to seal the reactive sites and thereby to isolate the salt mixture from the coating layer as proposed by Otsuka and Rapp for Type-I hot corrosion tests [61]. Cr_2O_3 also acted as nucleation sites for α-Al_2O_3 as suggested by the X-ray maps on Fig. VI-37 and local Raman analyses. This considerably increased the hot corrosion resistance of the Cr-modified coating with a fast healing of the oxide scales. The Ni solubility in the salt was considerably hampered thus preventing the formation of Na_2SO_4-$NiSO_4$ eutectic phases and Ni sulfidation (Fig. VI-37). The formation of Cr sulfides at the reaction front of the attacked regions was found to buffer the corrosion attack [65].

IV. Oxidation resistance of Cr-Al double-layer system developed on CM-247 LC

The oxidation resistance of Cr-Al double-layer coatings elaborated on CM-247 LC superalloy has been investigated under cyclic and isothermal conditions. The mechanisms of formation of the coatings were discussed in Chapter IV. The initial Cr/Al ratio of the slurry deposit was found to exert a critical influence on the resulting microstructure of the coatings. By adjusting the Cr/Al ratio and optimizing the thermal treatment, it was thus possible to obtain outward grown coatings with significant enrichment in Cr and inward grown coatings with a complete thermal barrier system. The oxidation resistance of these two systems was investigated in this work. However, only the results obtained for the low activity high temperature (LAHT) coating will be discussed here.

IV.1. Characterization of the low-activity high-temperature (LAHT) coating

The mechanisms of formation of the LAHT coating from the Cr-Al double-layer system have been presented in paragraph II.2 of Chapter IV. After deposition of the slurries by air brush (close to the 50Cr-50Al ratio in wt.%), the samples were heat treated in Ar following the conventional repair heat treatment (400°C-3h, 1080°C-6h). A secondary electrons cross-section image of the resulting coating is given on Fig. VI-40a. A light grit blasting of the surface using #220 alumina mesh was performed to remove the residues of the slurry after coating process (cf. paragraph II.2 in Chapter IV). As shown previously, the coating was composed of two main layers with an outer additive layer (A.L.) formed above the substrate surface based on β-NiAl and an inner interdiffusion zone (IDZ) enriched with precipitates containing refractory elements (Fig. VI-40b). The final OPS polishing allowed to reveal the precipitation of α-(Cr) phases within the β-NiAl additive layer.

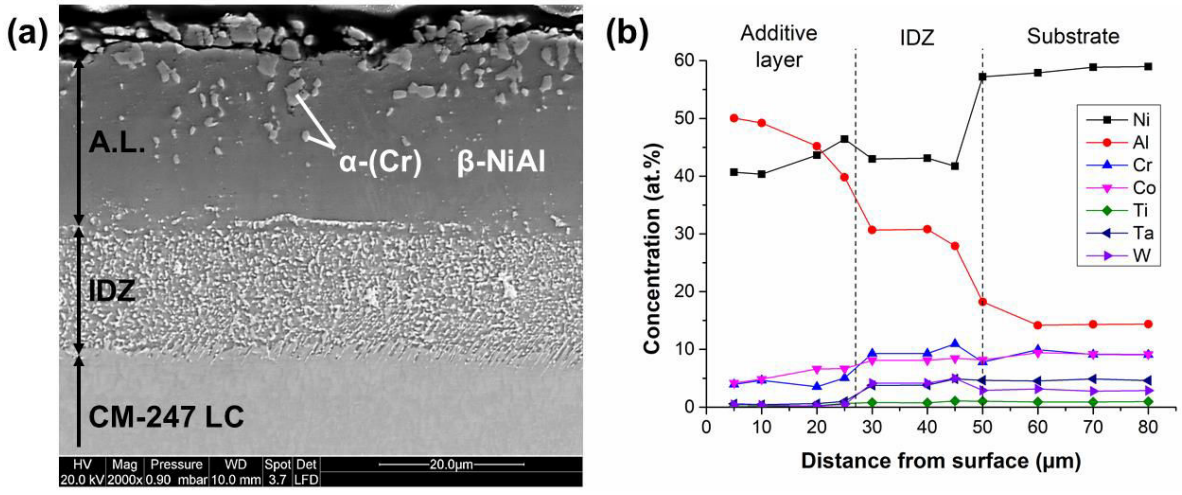

Fig. VI-40. (a) SEM cross-section image and (b) EDS concentration profile of the low-activity coating elaborated on CM-247 LC before oxidation tests.

IV.2. Cylic oxidation at 1000°C

The slurry coated samples were exposed to cyclic oxidation with 1h-cycles (45 minutes at 1000°C and 15 minutes under rapid air cooling). This oxidation test was expected to simulate industrial service conditions with the combination of both oxidation attack and thermally induced stresses [12]. Up to six slurry coated CM-247 LC samples (cf. Fig. VI-40a) were introduced in the Delta Thermique rig (cf. Chapter II) for the cyclic oxidation tests. Among these six samples, five were gently grit blasted after heat treatment to remove residual aluminizing materials whereas an additional sample was ground down to SiC #4000 paper grade. Tolpygo et al. have shown that grit blasting can adversely affect the oxidation behaviour of a Pt-modified aluminide coating during cyclic oxidation at 1150°C [13]. Grit blasting was attributed to contaminate the coating surface by various impurities (mainly alkali elements and Ti) that become incorporated within the α-Al_2O_3 scale upon oxidation. This accelerated the growth rate of α-Al_2O_3 and decreased the spallation resistance during cyclic oxidation [13]. Therefore, a polished sample was introduced for comparison with the grit blasted ones. An uncoated CM-247 LC sample was also introduced as a reference.

The mass gain curves of the different systems are presented in Fig. VI-41a. The uncoated CM-247 LC exhibited a fast weight gain during the first 20 hours of exposure up to approximately 1.0 mg.cm^{-2}. After this period, the weight change was quite stable and the overall weight gain remained around 1.0 mg.cm^{-2} after 1000 cycles. This oxidation kinetics is in good agreement with literature for the high-temperature oxidation of the CM-247 LC superalloy [12,67,68]. For the Cr/Al slurry coated CM-247 LC, the weight gain curves suggested a parabolic growth for both grit blasted and polished samples (Fig. VI-41a). A small deviation was observed between the oxidation curves of grit blasted and polished samples. The plot presenting the instantaneous k_p values as a function of the oxidation time however demonstrated that this difference was mainly associated with the initial transition period for the first 20 hours of exposure (Fig. VI-41b). After this transition period, steady-state oxidation took place with the stabilization of the k_p values for the Cr/Al slurry coating.

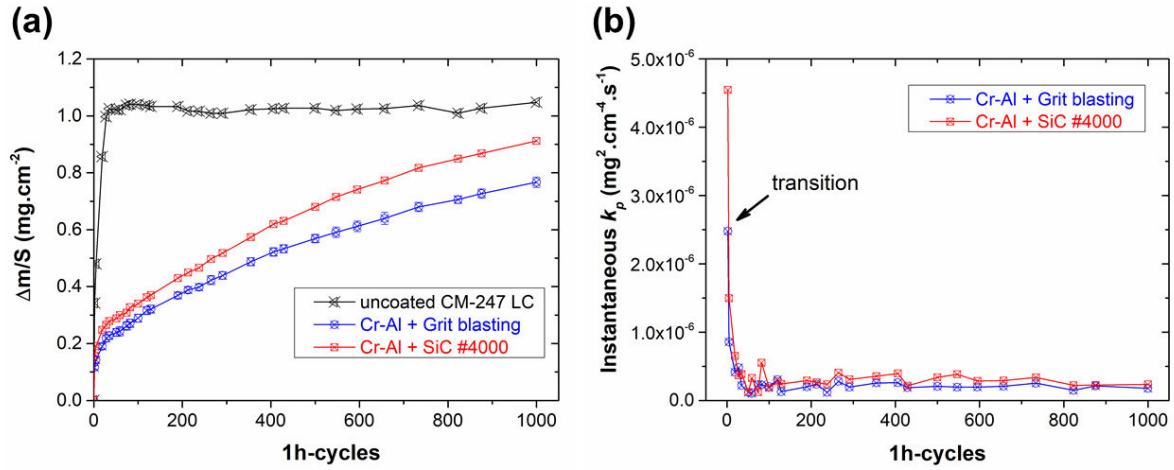

Fig. VI-41. (a) Weight change as a function of time and (b) instantaneous k_p for Cr/Al slurry coated CM-247 LC upon cyclic oxidation at 1000°C in air.

The mean k_p values for the grit blasted and the polished samples calculated after the transition period are given in Table VI-5 and compared with data from literature. The values of the Cr/Al slurry coating were in good agreement with the oxidation of Al_2O_3-former alloys at 1000°C (Table VI-5). Grit blasting of the coating surface was not found to significantly change the cyclic oxidation behaviour of the coating at 1000°C. Grit blasting was found to promote the formation of α-Al_2O_3 rather than metastable alumina polymorphs at the intermediate temperature range [13]. The rapid formation of α-Al_2O_3 on grit blasted samples could possibly decrease the initial oxidation rate of the coating by comparison with a polished sample. In this paragraph, only the grit blasted samples were characterized after oxidation tests since the surface preparation was not found to exert a significant influence on the oxidation kinetics.

Table VI-5. Comparison of the parabolic rate constant k_p calculated in this work with data from literature at 1000°C in dry air.

This work		**Literature**		
Conditions	**k_p ($g^2.cm^{-4}.s^{-1}$)**	**System**	**k_p ($g^2.cm^{-4}.s^{-1}$)**	**Ref.**
Grit blasting	$1.9x10^{-13}$	K417G + Y/Cr-modified aluminide coating	$4.7x10^{-13}$	[19]
SiC #4000	$3.0x10^{-13}$	DD32M + simple aluminide coating	$5.5x10^{-13}$	[20]
		NiAl-34Cr (at.%)	$2.0x10^{-13}$	[48]

The SEM was carried out to investigate the morphology of the oxide scales developed on the Cr/Al slurry coated CM-247 LC (Fig. VI-42). The SEM surface images suggested the great adherence of the oxide scales and very limited spallation or crack formation on the coating surface after cyclic oxidation. Lu et al. obtained similar oxide morphologies for the cyclic oxidation of Y/Cr-modified aluminide coatings [19]. At higher magnification (Fig. VI-42), a platelet-like morphology was identified and suggested the formation of α-Al_2O_3.

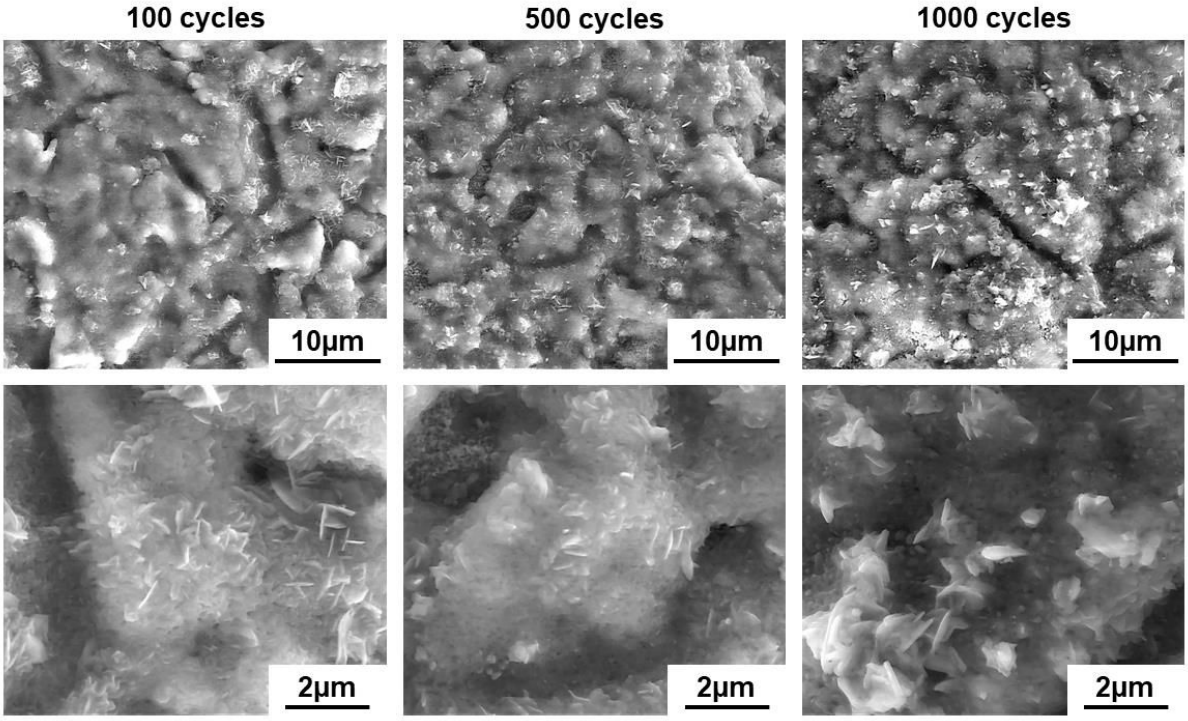

Fig. VI-42. SEM surface images of the oxide scales developed on the LAHT coating elaborated on CM-247 LC after cyclic oxidation at 1000°C in air.

Raman micro-spectrometry was carried out to characterize the oxide scales developed on the Cr/Al coating. Several measurements were performed on the sample surface to ensure reproducibility (Fig. VI-43). Raman surface analyses confirmed the formation of an exclusive α-Al_2O_3 scale even after 100 cycles at 1000°C (Fig. VI-43c).

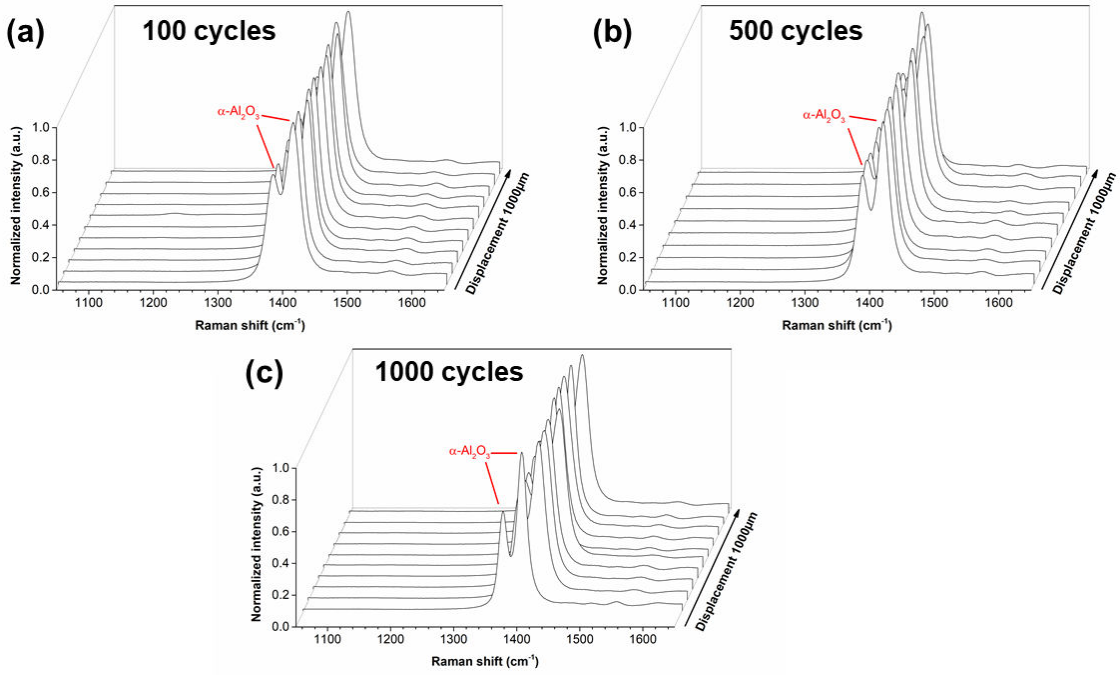

Fig. VI-43. Raman surface analyses of the Cr/Al coating after cyclic oxidation at 1000°C in air for (a) 100 cycles, (b) 500 cycles and (c) 1000 cycles.

EDS window analyses were also performed on the coating surface after cyclic oxidation and compared with the values obtained for an as-coated sample (Fig. VI-44). One can see the progressive O uptake of the coating upon cyclic oxidation corresponding to the formation of the oxide scale. The Al concentration was quite stable on the coating surface at about 35 at.% suggesting that the α-Al_2O_3 scale was adherent. The Ni+Co concentration drastically decreased upon oxidation and confirmed that these elements did not incorporate into the scale. The Cr concentration rapidly decreased after 100 cycles at 1000°C but subsisted at about 5 at.% for long term exposure. This could indicate that some Cr can incorporate within the oxide scale since α-Al_2O_3 and Cr_2O_3 form a continuous solid solution at 1000°C [48,69]. For the coated sample and after 100 cycles (Fig. VI-44), both concentrations of Ti and of refractory elements (W, Ta and Hf) were below the detection limit of the EDS. For longer exposure times, these elements (especially Ti, Ta and Hf) were detected at low concentrations at the surface. This suggests that these elements diffused from the coating layer towards the oxide scale and could eventually affect the adherence of the oxide scale [70-72].

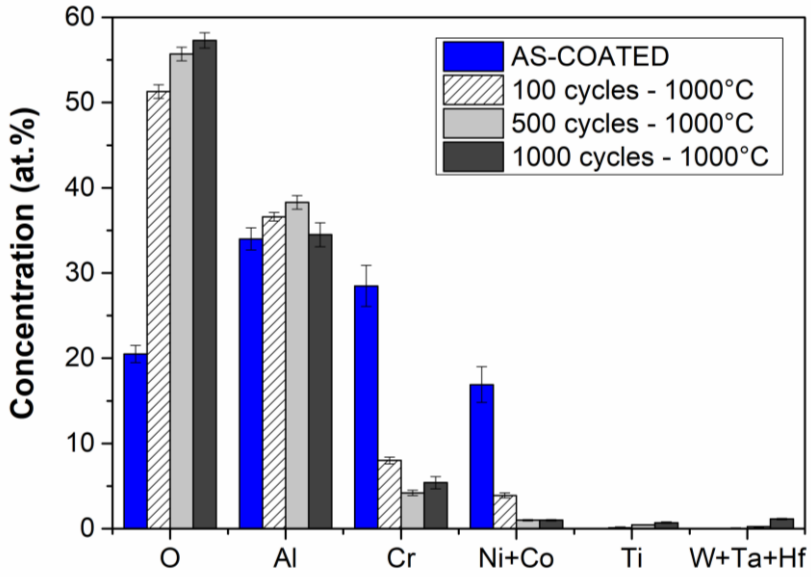

Fig. VI-44. Summary of the EDS window analyses performed on the surface of the samples after elaboration of the coating (AS-COATED) and cyclic oxidation at 1000°C in air.

XRD surface analyses were also conducted to investigate the crystallographic structures of the metallic / intermetallic structures and of the oxides. The results are summarized in Table VI-6. For the as-coated sample (Fig. VI-40a), the β-NiAl structure was identified with additional Cr-rich phases such as α-(Cr) and $AlCr_2$. Upon oxidation, both β-NiAl and α-(Cr) phases were still observed in the XRD patterns whereas γ'-Ni_3Al was also identified after 1000 cycles at 1000°C. After 100 cycles, only α-Al_2O_3 was detected as an oxide whereas both TiO_2 and HfO_2 were also observed for longer oxidation times. These observations are in good agreement with the EDS surface analyses indicating the progressive enrichment in Ti and in Hf of the surface (Fig. VI-44).

Table VI-6. Summary of the XRD analyses carried out on CM-247 LC slurry coated with the Cr-Al low activity coating after cyclic oxidation at 1000°C.

Conditions	Metallic / intermetallic structures	Oxides
AS-COATED	β-NiAl, α-(Cr), $AlCr_2$	-
100 cycles	β-NiAl, α-(Cr)	α-Al_2O_3
500 cycles	β-NiAl, α-(Cr)	α-Al_2O_3, TiO_2, HfO_2
1000 cycles	β-NiAl, α-(Cr), γ'-Ni_3Al	α-Al_2O_3, TiO_2, HfO_2

For a better identification of the oxide species, the samples were observed in cross-section after different exposure times. The BSE cross-section images of the oxide scales formed on the Cr/Al coating surface are presented in Fig. VI-45. After 100 cycles (Fig. VI-45a), a thin and pure α-Al_2O_3 scale has grown on the surface. For longer exposure (Fig. VI-45b and Fig. VI-45c), α-Al_2O_3 scale grew further and the microstructure of β-NiAl also evolved. Both Cr and Hf were found to segregate at the coating/oxide interface [73]. The Hf-rich phases were easily distinguishable in the microstructures in the form of bright spots (BSE mode). After 500 cycles and more, the oxide scale was no longer a pure α-Al_2O_3 scale and other elements incorporated within the scale. The EDS did not allow precise measurements but Ti, Cr, Ta and Hf were detected within the α-Al_2O_3 scale as suggested with the surface analyses (Fig. VI-44). Such enrichments were commonly observed for the oxidation of wrought CM-247 LC with the precipitation of Hf-rich and Ta-rich oxide particles within the external oxide scale [68]. The onset of β to γ' transformation was also highlighted in the microstructures after 1000 cycles at 1000°C. Complementary X-ray maps of the cross-sections were performed to get the elemental distribution upon cyclic oxidation (cf. Annex 3).

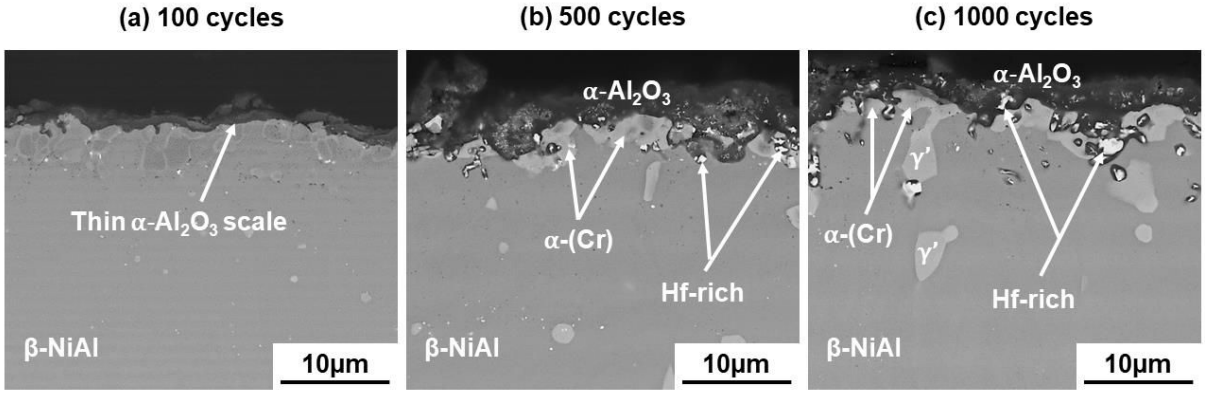

Fig. VI-45. BSE cross-section images at the extreme surface of the Cr/Al coating showing the growth of the α-Al_2O_3 scale and the enrichment of Cr and Hf at the oxide subscale.

The Cr/Al slurry coating elaborated on CM-247 LC exhibited superior high-temperature oxidation resistance through the formation of a dense and continuous α-Al_2O_3 scale at the surface. The microstructure of the coating was also investigated to evaluate its stability upon cyclic oxidation. A SEM cross-section image of the coating after 100 cycles is given in Fig. VI-46a. By comparison with the as-coated sample (cf. Fig. VI-40a), one can see that a fraction of the α-(Cr) phases were solubilized in the β-NiAl coating matrix. An additional zone appeared underneath the interdiffusion zone with the formation of oriented precipitates with needle-shaped morphology. This zone was identified as the secondary reaction zone (SRZ) and was formed because of Al inward diffusion into the superalloy lattice [22,74-77]. Local EDS measurements have shown that these precipitates were rich in W, Ta and Cr suggesting the formation of topologically-closed pack (TCP) phases [21,74,75,78]. In the additive layer, flattening of the Al and Ni concentrations occurred and the Al concentration decreased to about 36 at.% (Fig. VI-46b).

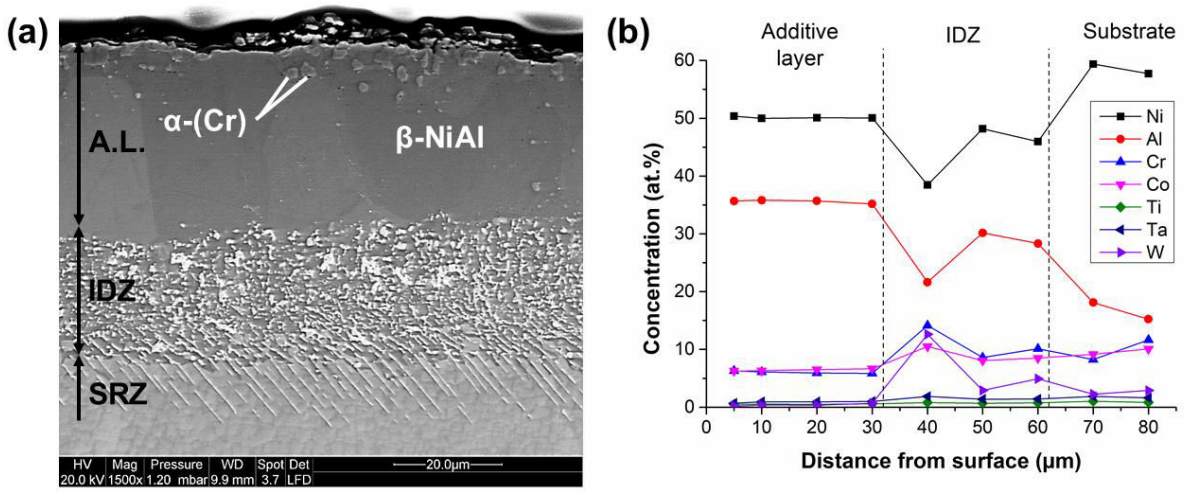

Fig. VI-46. (a) SEM cross-section image and (b) EDS concentration profile of the low-activity coating elaborated on CM-247 LC after 100 cycles at 1000°C in air.

To observe the microstructural evolutions in the coating layer and within the parent material, the samples were electrolytically etched with 10 vol.% $H_2C_2O_4$ (Fig. VI-47). One can observe on the cross-section images the progressive growth of the SRZ because of Al inward diffusion from the coating layer. The loss of the γ-γ' microstructure of the CM-247 LC superalloy underneath the coating layer was clearly observed at higher magnification [21]. The precipitation of TCP phases and the Al enrichment in this region first led to the rafting of the γ-γ' microstructure (after 500 cycles) [18,76]. The continuous Al supply eventually formed a continuous γ'-strip layer after 1000 cycles right underneath the coating.

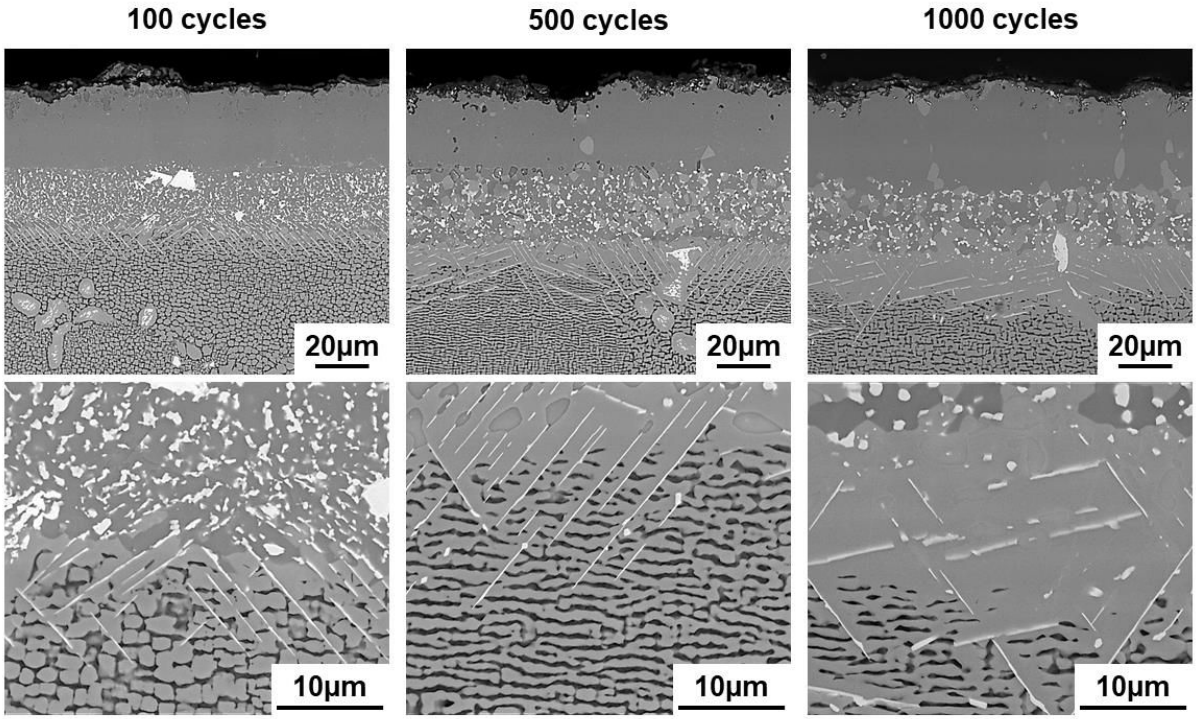

Fig. VI-47. Microstructural evolutions of the LAHT coating elaborated on CM-247 LC after cyclic oxidation at 1000°C in air (electrolytically etched with 10 vol.% $H_2C_2O_4$).

It therefore appeared that the Cr/Al coating exhibited a good surface stability by forming a dense and continuous α-Al_2O_3 scale on the surface. The scale was found to resist to the thermal stresses induced by cyclic oxidation and very little spallation of the scale occurred even after 1000 cycles at 1000°C. Cr and Hf were found to segregate at the interface coating/oxide without impairing the stability of the α-Al_2O_3 scale. Little transformation occurred in the additive layer and localized β to γ' transformation was observed after 1000 cycles. The main degradation mechanism was attributed to the growth of a SRZ underneath the coating layer because of Al inward diffusion. This SRZ was associated with the formation of needle-like precipitates depleting the strengthening elements of the superalloy. The growth of this SRZ led to the progressive loss of the γ-γ' microstructure of the CM-247 LC superalloy and formed rafted microstructures. These degradation mechanisms are commonly observed on aluminide coatings exposed to high-temperature oxidation [22,74-76].

IV.3. Isothermal oxidation at 1000°C

The isothermal oxidation behaviour of Cr/Al slurry coated CM-247 LC was also investigated in this work. The main objective was to compare the oxidation kinetics and the microstructural degradation of the coating with the samples exposed to cyclic oxidation. A first sample was subjected to isothermal oxidation in synthetic air for 100 hours to get the oxidation curve (Fig. VI-48). Four other samples were oxidized in dry air and were weighed after 500 and 1000 hours to plot the weight gain as a function of time in Fig. VI-48. The pseudo-oxidation curve suggested a parabolic growth rate. The parabolic rate constant was calculated from the modified curve between 500 and 1000 hours (steady-state oxidation) and was about 1.3×10^{-13} $g^2.cm^{-4}.s^{-1}$. This k_p value was in good agreement with the oxidation of Al_2O_3-former alloys at 1000°C and the results obtained under cyclic conditions (cf. Table VI-5).

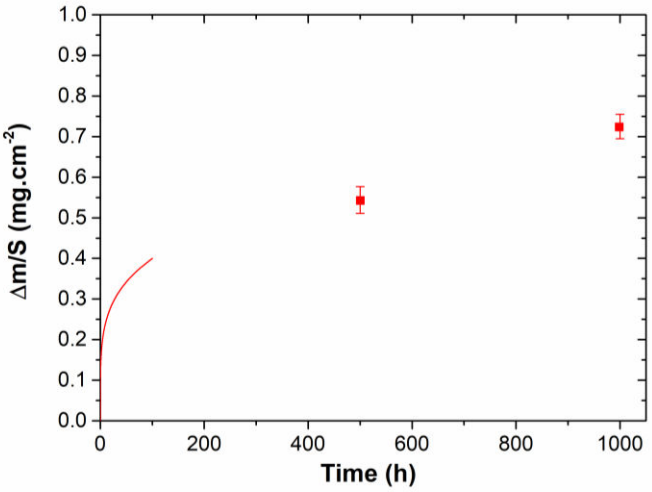

Fig. VI-48. Weight gain as a function of time for Cr/Al slurry coated CM-247 LC under isothermal conditions at 1000°C in air.

The oxide morphologies were observed with SEM (Fig. VI-49). Barely any spallation of the oxide scale occurred and the coating was covered with an Al-rich oxide. The progressive growth of needle-shaped oxides was observed at higher magnification by increasing the oxidation time. This microstructure is usually associated with θ-Al_2O_3 [48,79]. However, considering the temperature-time transformation diagram of β-NiAl alloy [80], α-Al_2O_3 should be formed on the coating surface after more than 100 hours. Raman micro-spectrometry was carried out and confirmed the exclusive formation of α-Al_2O_3 on the coating surface independently of the oxidation time (Fig. VI-50).

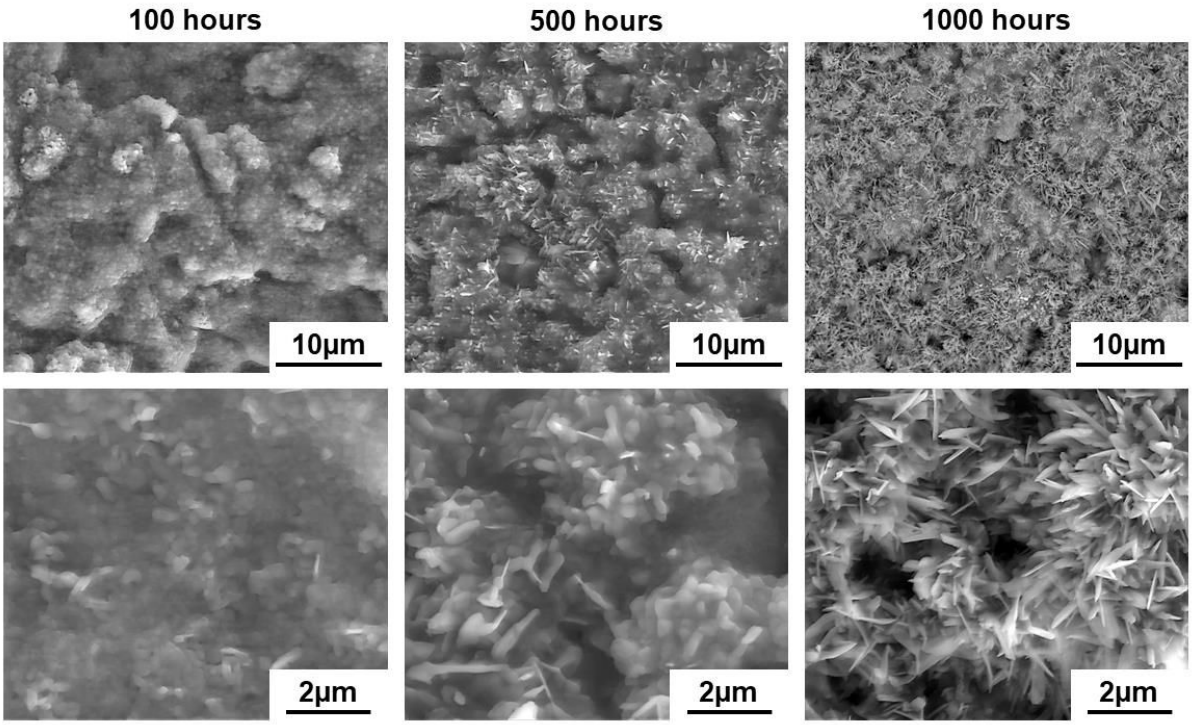

Fig. VI-49. SEM surface images of the oxide scales developed on the LAHT coating elaborated on CM-247LC after isothermal oxidation at 1000°C in air.

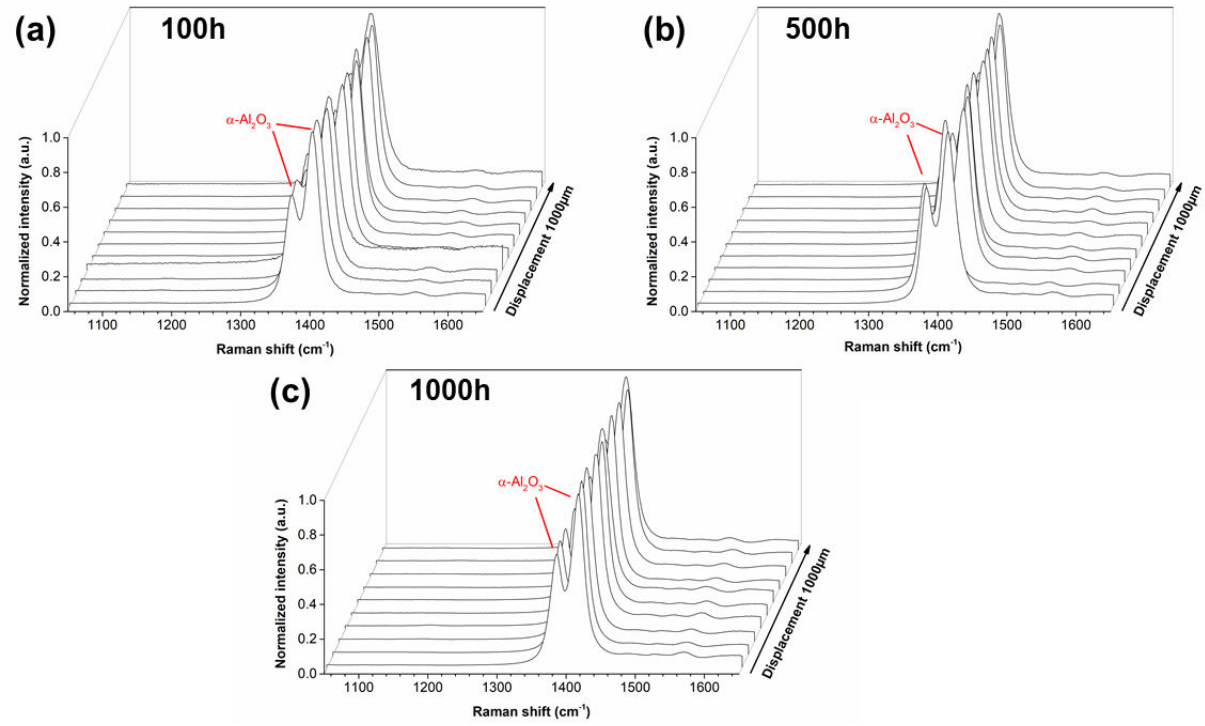

Fig. VI-50. Raman surface analyses of the Cr/Al coating after isothermal oxidation at 1000°C in air for (a) 100 hours, (b) 500 hours and (c) 1000 hours.

The oxide scales were also characterized in cross-section using SEM (Fig. VI-51). The scale morphologies and the microstructural evolutions in the outer region of the coating were very close to the ones observed upon cyclic oxidation (cf. Fig. VI-45). After 100 hours exposure, a pure α-Al_2O_3 scale had grown on the surface. Cr was found to segregate at the extreme surface of the coating in the form of α-(Cr) phases because of its limited solubility in the β-NiAl phase [37,38,81,82]. Significant Hf enrichment of the oxide subscale occurred and can be identified as bright spots in BSE mode (Fig. VI-51). After 1000 hours exposure, the α-Al_2O_3 scale was still adherent to the underlying coating and little β to γ' transformation was observed.

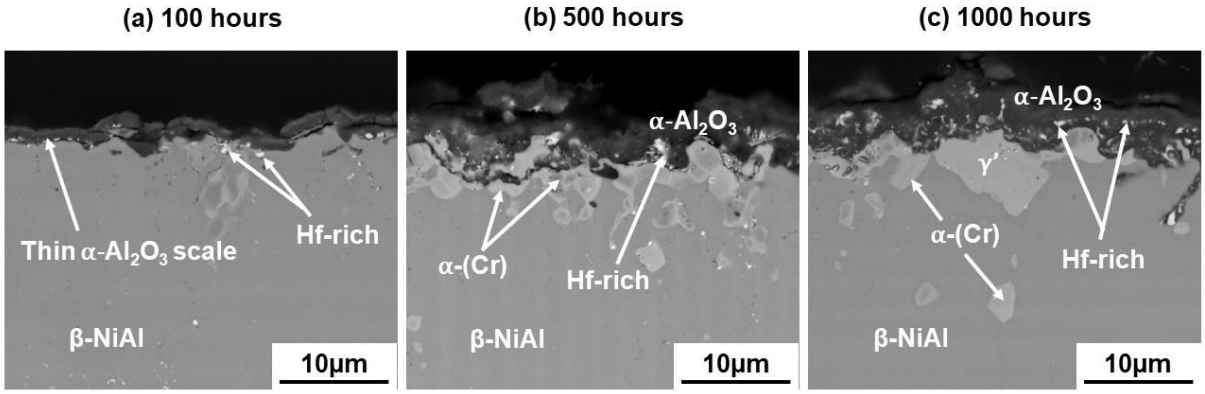

Fig. VI-51. BSE cross-section images at the extreme surface of the coating showing the growth of the α-Al_2O_3 scale and enrichment of Cr and Hf at the oxide subscale.

To highlight the results presented in Fig. VI-51, X-ray mapping was done at the extreme surface of the coating (Fig. VI-52). The X-ray maps confirmed the segregation of Cr in the outer region of the coating and the Hf and Ti enrichments within the α-Al_2O_3 scale.

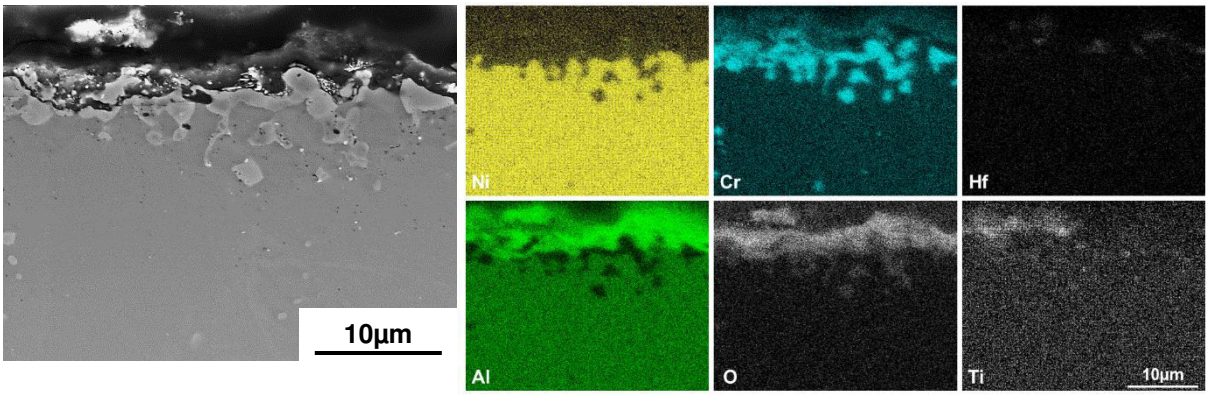

Fig. VI-52. Details of the extreme surface of the coating after 500 hours oxidation at 1000°C in air and corresponding X-ray maps.

The microstructural transformations of the slurry coatings and within the parent material were observed after electrolytic etching to highlight the γ-γ' microstructure of the substrate (Fig. VI-53). As observed with cyclic oxidation, the formation of a SRZ occurred upon isothermal oxidation with the precipitation of needle-shaped precipitates. The SRZ thickened with increasing oxidation time and reached approximately 50µm after 1000 hours at 1000°C. This degradation process was governed by inward diffusion of Al from the coating layer toward the substrate. This led to the onset of β to γ' transformation within the interdiffusion zone (highlighted with the difference in contrast of β-NiAl and γ'-Ni_3Al in BSE mode, cf. Fig. VI-53).

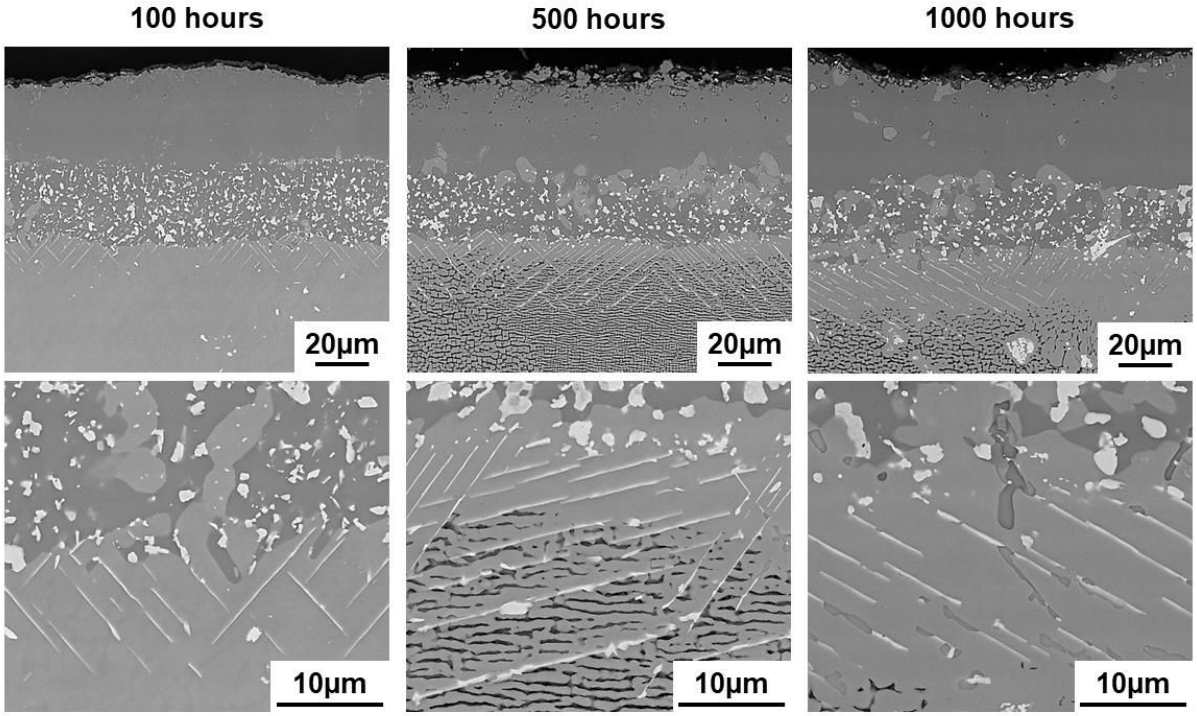

Fig. VI-53. Microstructural evolutions of the LAHT coating elaborated on CM-247 LC after isothermal oxidation at 1000°C in air (electrolytically etched with 10 vol.% $H_2C_2O_4$).

IV.4. Discussion

- ***High-temperature oxidation performance of the Cr-modified aluminide coating:***

The Cr-modified aluminide coating elaborated on CM-247 LC superalloy presented good thermal stability during cyclic and isothermal oxidation at 1000°C. The high-temperature oxidation resistance was conferred by the formation of a pure α-Al_2O_3 scale on the coating surface. This scale was found to exhibit good spallation resistance and a parabolic growth rate even in cyclic conditions. The light grit blasting process performed after coating elaboration to remove intermetallic phases resulting from the aluminizing treatment, was not found to influence the oxidation behaviour of the coating. The formation of the stable α-Al_2O_3 polymorph rapidly occurred. For longer exposure time (more than 500 hours), Ti, Hf and Ta were found to incorporate as TiO_2 and HfO_2 (and presumably Ta_2O_5) in the α-Al_2O_3 scale. Ti and Ta were usually ascribed to decrease the oxidation resistance of aluminide coatings at temperatures above 1100°C [70,72] whereas Hf increased the spallation resistance of α-Al_2O_3 scale [70,71]. However, they did not significantly affect the adherence of the α-Al_2O_3 scale for the oxidation time and the temperature investigated here.

- ***Microstructural evolutions upon oxidation:***

The characterization of the slurry coating has shown that Cr was present as α-(Cr) precipitates within the β-NiAl coating matrix (Fig. VI-40a). Upon oxidation, Cr was found to progressively segregate in the outer region of the coating since its solubility in the β-NiAl phase is low (Fig. VI-52, cf. Annex 3). The great Al concentration gradient between the coating layer and the substrate implies that Al from the coating progressively diffused inwardly. Consequently, a secondary reaction zone (SRZ) developed within the superalloy and was controlled by Al inward diffusion. The Al enrichment reduced the solubility of refractory elements and precipitation of needle-shaped TCP phases occurred in the sub-region of the coating layer (Fig. VI-47 and Fig. VI-53). This also progressively destroyed the cube-like γ-γ' microstructure of the superalloy and formed a rafted microstructure instead [18,76]. With time, a thick γ'-strip layer was observed at the interface between the substrate and the diffusion coating. The Al inward diffusion toward the substrate led to the onset of the β to γ' transformation in the interdiffusion zone (Fig. VI-47 and Fig. VI-53). In the additive layer, little β to γ' transformation occurred even after 1000 cycles or 1000h at 1000°C. This suggested that the main degradation mechanism of the Cr-modified coating resulted from inward diffusion of Al rather than spallation of the α-Al_2O_3 scale.

V. Summary and outlook

Hot corrosion and high-temperature oxidation resistance of slurry coated Ni-based materials have been investigated. For the hot corrosion tests, pure Ni was used as the substrate for a better comprehension of the corrosion mechanisms. In the SO_2-containing atmosphere (synthetic air + 0.5% SO_2), pure Ni suffered from extensive oxidation and sulfidation at 700°C. The high porosity of the scales formed on pure Ni fostered the molecular transport of S-bearing molecules (i.e. SO_2-SO_3) towards the substrate/scale interface. The increased S activity at the substrate surface led to its rapid sulfidation. When pure Ni was exposed to Na_2SO_4 and the SO_2-containing atmosphere at 700°C (Type-II hot corrosion conditions), the corrosion rate was even higher. This was attributed to an increase in S activity (i.e. p_{S_2}) in the scale and at the substrate/scale interface because of the formation of Na_2SO_4-$NiSO_4$ eutectic phases at the scale surface.

- ***Hot corrosion resistance of simple aluminide and Cr-modified coatings:***

The application of slurry coatings on pure Ni considerably increased its oxidation-sulfidation resistance. The Cr-modified coating offered a better protection than the simple aluminide coating in the SO_2-containing atmosphere at 700°C. The latter was prone to localized attacks in the form of protrusions with extensive internal oxidation. The mechanisms of formation and growth of the protrusions were described and were found to be controlled by both inward diffusion of O and outward diffusion of Al from the coating layer. The Cr-modified coating was not attacked after 300 hours exposure in the SO_2-containing atmosphere. The protection efficiency of the coatings was attributed to their ability to form and rejuvenate protective oxide scales on the surface. When exposed to Type-II hot corrosion conditions, the corrosion attack was preceded by an incubation period going from 20 hours to 100 hours for the two slurry coatings (simple aluminide and Cr-modified). After 100 hours exposure, both coatings have shown corrosion attack. However, the propagation rate of the attack was considerably lower for the Cr-modified coating than for the simple aluminide. This was attributed to the rapid oxidation of the Cr-modified coating and its ability to reform protective scales (i.e. Cr_2O_3 and α-Al_2O_3). On the other hand, the simple aluminide underwent fast degradation in Type-II conditions. The corrosion attack was found to initiate locally and then to propagate rapidly through the formation of liquid phases. This led to an important S enrichment at the interface between the substrate and the coating and an extensive metal dissolution (i.e. Ni and Al) within the sulfate deposit.

Based on the experimental results of this work, it appeared that the faster the establishment of protective oxide scales, the better the protection against the salt mixture. This therefore indicates that the pre-oxidation of the slurry coatings should increase their performances in hot corrosion conditions.

- ***Oxidation resistance of low-activity Cr-Al coatings elaborated on CM-247 LC:***

The oxidation of Cr-modified aluminide coatings elaborated on CM-247 LC was also investigated upon cyclic and isothermal conditions at 1000°C. The coating presented high surface stability forming a thin and adherent α-Al_2O_3 scale on the surface. The mass gain curves confirmed the parabolic growth of the oxide scale. The thermal stresses induced by cyclic conditions were not found to significantly influence the oxidation behaviour of the slurry coating. The α-Al_2O_3 scales were generally well adherent and little spallation was observed. The Cr was found to segregate in the outer region of the coating upon oxidation. This might have a beneficial effect against hot corrosion considering the conditions studied here and the literature. The main degradation mechanism observed for the Cr-modified coating was the formation of a secondary reaction zone (SRZ) in the sub-region of the diffusion coating. This zone was formed because of Al inward diffusion from the coating layer toward the superalloy substrate. The Al enrichment decreased the solubility of refractory elements forming then needle-shaped precipitates. This also destroyed the cube-like γ-γ' microstructure of CM-247 LC in this region. The SRZ thickened with increasing oxidation time. However, this did not impair the surface stability of the coating and little β to γ' transformation was noticed after long term exposure (1000 cycles and 1000 hours at 1000°C).

To conclude, the application of slurry coatings considerably increased the high-temperature corrosion and oxidation resistance of the underlying substrates. The modification of the slurry aluminide coating with Cr was highly beneficial for hot corrosion resistance in SO_2-containing atmosphere.

References

[1] J. Stringer, *Materials Science and Technology* ***3*** (1987), pp. 482-493.

[2] G.H. Meier, *Materials Science and Engineering A* ***120*** (1989), pp. 1-11.

[3] R. Rajendran, *Engineering Failure Analysis* ***26***, (2012) pp. 355-369.

[4] F.S. Pettit, *Oxidation of Metals* ***76*** (2011), pp. 1-21.

[5] A.K. Misra, D.P. Whittle, W.L. Worrell, *Journal of the Electrochemical Society* ***129*** (1982), pp. 1840-1845.

[6] K.P. Lillerud, P. Kofstad, *Oxidation of Metals* ***21*** (1984), pp. 233-270.

[7] T. Gheno, M. Zahiri Azar, A.H. Heuer, B. Gleeson, *Corrosion Science* ***101*** (2015), pp. 32-46.

[8] T. Gheno, B. Gleeson, *Oxidation of Metals* ***84*** (2015), pp. 567-584.

[9] J.E. García-Herrera, J.M. Alvarado-Orozco, J. Muñoz-Saldaña, L. Garcia-Fresnillo, G.H. Meier, *Oxidation of Metals* ***84*** (2015), pp. 233-240.

[10] ISO 17248:2015, Corrosion of Metals and Alloys – Test method for high temperature corrosion testing of metallic materials by embedding in salt, ash, or other solids (04.2015).

[11] M. Schütze, M. Malessa, *Reliable assessment of high temperature oxidation resistance by the development of a comprehensive code of practice for thermocycling oxidation testing (COTEST)*, EFC Publications Number 47, pp. 279-296, Woodhead Publishing in Materials (2008).

[12] M. Schütze, M. Malessa, *Influence of cycling parameter variation on thermal cycling oxidation testing of high temperature materials (COTEST)*, EFC Publications Number 47, pp. 334-362, Woodhead Publishing in Materials (2008).

[13] V.K. Tolpygo, D.R. Clarke, K.S. Murphy, *Metallurgical and Materials Transactions A* ***32*** (2001), pp. 1467-1478.

[14] C. Leyens, B.A. Pint, I.G. Wright, *Surface and Coatings Technology* ***133-134*** (2000), pp. 15-22.

[15] R.W. Jackson, D.M. Lipkin, T.M. Pollock, *Acta Materialia* ***80*** (2014), pp. 39-47.

[16] H.J. Kim, M.E. Walter, *Materials Science and Engineering A* ***360*** (2003), pp. 7-17.

[17] B. Rannou, B. Bouchaud, J. Balmain, G. Bonnet, F. Pedraza, *Oxidation of Metals* ***81*** (2014), pp. 139-149.

[18] J. Angenete, K. Stiller, E. Bakchinova, *Surface and Coatings Technology* ***176*** (2004), pp. 272-283.

[19] J. Lu, S. Zhu, F. Wang, *Oxidation of Metals* ***76*** (2011), pp. 67-82.

[20] C.T. Liu, J. Ma, X.F. Sun, P.C. Zhao, *Surface and Coatings Technology* ***204*** (2010), pp. 3641-3646.

[21] C.M.F. Rae, M.S. Hook, R.C. Reed, *Materials Science and Engineering A* ***396*** (2005), pp. 231-239.

[22] C. Oskay, M. Rudolphi, E.E. Affeldt, M. Schütze, M.C. Galetz, *Intermetallics* ***89*** (2017), pp. 22-31.

[23] L.R. Liu, T. Jin, N.R. Zhao, X.F. Sun, H.R. Guan, Z.Q. Hu, *Materials Science and Engineering A* ***361*** (2003), pp. 191-197.

[24] C.G. McCreath, *Corrosion Science* ***23*** (1983), pp. 1017-1023.

[25] M.R. Khajavi, M.H. Shariat, *Engineering Failure Analysis* ***11*** (2004), pp. 589-597.

[26] R.E. Malush, P. Deb, D.H. Boone, *Surface and Coatings Technology* ***36*** (1988), pp. 13-26.

[27] K. Godlewski, E. Godlewska, *Materials Science and Engineering* ***88*** (1987), pp. 103-109.

[28] M.N. Task, B. Gleeson, F.S. Pettit, G.H. Meier, *Surface and Coatings Technology* ***206*** (2011), pp. 1552-1557.

[29] R. Streiff, D.H. Boone, *Journal of Materials Engineering* ***10*** (1988), pp. 15-26.

[30] B. Gleeson, W.H. Cheung, W. Da Costa, D.J. Young, *Oxidation of Metals* ***38*** (1992), pp. 407-424.

[31] N. Eliaz, G. Shemesh, R.M. Latanision, *Engineering Failure Analysis* ***9***, (2002) pp. 31-43.

[32] R. Klumpes, C.H.M. Marée, E. Schramm, J.H.W. de Wit, *Materials and Corrosion* ***47*** (1996), pp. 619-624.

[33] I. Gurrappa, *Oxidation of Metals* ***51*** (1999), pp. 353-382.

[34] F. Pedraza, M. Mollard, B. Rannou, J. Balmain, B. Bouchaud, G. Bonnet, *Materials Chemistry and Physics* ***134*** (2012), pp. 700-705.

[35] B. Bouchaud, B. Rannou, F. Pedraza, *Materials Chemistry and Physics* ***143*** (2013), pp. 416-424.

[36] M.C. Galetz, X. Montero, M. Mollard, M. Günthner, F. Pedraza, M. Schütze, *Intermetallics* ***44*** (2014), pp. 8-17.

[37] H.L. Huang, Y.Z. Chen, D. Gan, *Materials Science and Engineering A* ***328*** (2002), pp. 238-244.

[38] W.H. Tian, C.S. Han, M. Nemoto, *Intermetallics* ***7*** (1999), pp. 59-67.

[39] S. Chevalier, F. Desserrey, J.P. Larpin, *Oxidation of Metals* ***64*** (2005), pp. 219-234.

[40] R. Peraldi, D. Monceau, B. Pieraggi, *Oxidation of Metals* ***58*** (2002), pp. 249-273.

[41] R. Peraldi, D. Monceau, B. Pieraggi, *Oxidation of Metals* ***58*** (2002), pp. 275-295.

[42] M. Marciuš, M. Ristić, M. Ivanda, S. Musić, *Journal of Alloys and Compounds* ***541*** (2012), pp. 238-243.

[43] P. Kofstad, G. Akesson, *Oxidation of Metals* ***12*** (1978), pp. 503-526.

[44] P. Kofstad, G. Akesson, *Oxidation of Metals* ***13*** (1979), pp. 57-76.

[45] M. Seiersten, P. Kofstad, *Corrosion Science* ***22*** (1982), pp. 487-506.

[46] K.P. Lillerud, B. Haflan, P. Kofstad, *Oxidation of Metals* ***21*** (1984), pp. 119-134.

[47] M.C. Pope, N. Birks, *Oxidation of Metals* ***12*** (1978), pp. 173-181.

[48] M.W. Brumm, H.J. Grabke, *Corrosion Science* ***33*** (1992), pp. 1677-1690.

[49] B. Pujilaksono, T. Jonsson, M. Halvarsson, I. Panas, J.E. Svensson, L.G. Johansson, *Oxidation of Metals* ***70*** (2008), pp. 163-188.

[50] Z. Zhang, L. Li, J.C. Yang, *Acta Materialia* ***59*** (2011), pp. 5905-5916.

[51] M.N. Task, B. Gleeson, F.S. Pettit, G.H. Meier, *Oxidation of Metals* ***80*** (2013), pp. 541-552.

[52] M.W. Brumm, H.J. Grabke, B. Wagemann, *Corrosion Science* ***36*** (1994), pp. 37-53.

[53] R. Prescott, M.J. Graham, *Oxidation of Metals* ***38*** (1992), pp. 233-254.

[54] Y. Huang, X. Peng, *Corrosion Science* ***112*** (2016), pp. 226-232.

[55] S. Hasani, M. Panjepour, M. Shamanian, *Oxidation of Metals* ***78*** (2012), pp. 179-195.

[56] V. Kolarik, M. Juez-Lorenzo, H. Fietzek, *Materials Science Forum* ***696*** (2011), pp. 290-295.

[57] Y. Wang, G. Cacciamani, *Journal of Alloys and Compounds* ***688*** (2016), pp. 422-435.

[58] A. Paul, A.A. Kodentsov, F.J.J. van Loo, *Journal of Alloys and Compounds* ***403*** (2005), pp. 147-153.

[59] C.S. Giggins, F.S. Pettit, *Journal of the Electrochemical Society* ***118*** (1971), pp. 1782-1790.

[60] R. Morbioli, P. Steinmetz, C. Duret, *Materials Science and Engineering* ***87*** (1987), pp. 337-344.

[61] N. Otsuka, R.A. Rapp, *Journal of the Electrochemical Society* ***137*** (1990), pp. 53-60.

[62] R.A. Rapp, *Corrosion Science* ***44*** (2002), pp. 209-221.

[63] R.A. Rapp, N. Otsuka, ECS Transactions 16 (2009), pp. 271-282.

[64] M.N. Task, B. Gleeson, F.S. Pettit, G.H. Meier, *Oxidation of Metals* ***80*** (2013), pp. 125-146.

[65] P.S. Sidky, M.G. Hocking, *Corrosion Science* ***27*** (1987), pp. 183-203.

[66] K.L. Luthra, W.L. Worrell, *Metallurgical Transactions A* ***9*** (1978), pp. 1055-1061.

[67] F.H. Yuan, Y.S. Yoo, C.Y. Jo, B.G. Choi, Z.Q. Hu, *Surface and Coatings Technology* ***183*** (2004), pp. 106-110.

[68] D.K. Das, V. Singh, S.V. Joshi, *Materials Science and Technology* ***19*** (2003), pp. 695-708.

[69] F. Bondioli, A.M. Ferrari, C. Leonelli, T. Manfredini, L. Linati, P. Mustarelli, *Journal of the American Ceramic Society* ***83*** (2000), pp. 2036-2040.

[70] B.A. Pint, K.L. More, I.G. Wright, *Oxidation of Metals* ***59*** (2003), pp. 257-283.

[71] C. Mennicke, M.Y. He, D.R. Clarke, J.S. Smith, *Acta Materialia* ***48*** (2000), pp. 2941-2949.

[72] B. Han, Y. Ma, H. Peng, L. Zheng, H. Guo, *Corrosion Science* ***102*** (2016), pp. 222-232.

[73] P.Y. You, T. Izumi, B. Gleeson, *Oxidation of Metals* ***72*** (2009), pp. 109-124.

[74] D.K. Das, K.S. Murphy, S. Ma, T.M. Pollock, *Metallurgical and Materials Transactions A* ***39*** (2008), pp. 1647-1657.

[75] D.K. Das, *Progress in Materials Science* ***58*** (2013), pp. 151-182.

[76] M. Reid, M.J. Pomeroy, J.S. Robinson, *Journal of Materials Processing Technology* ***153-154*** (2004), pp. 660-665.

[77] Y. Matsuoka, Y. Aoki, K. Matsumoto, A. Satou, T. Suzuki, K. Chikugo, K. Murakami, *The Minerals, Metals and Materials Society* (2004), pp. 637-642.

[78] K. Matuszewski, R. Rettig, H. Matysiak, Z. Peng, I. Povstugar, P. Choi, J. Müller, D. Raabe, E. Spiecker, K.J. Kurzydlowski, R.F. Singer, *Acta Materialia* ***95*** (2015), pp. 274-283.

[79] T.F. An, H.R. Guan, X.F. Sun, Z.Q. Hu, *Oxidation of Metals* ***54*** (2000), pp. 301-316.

[80] D.P. Garriga-Majo, B.A. Shollock, D.S. McPhail, R.J. Chater, J.F. Walker, *International Journal of Inorganic Materials* ***1*** (1999), pp. 325-336.

[81] W. Huang, Y.A. Chang, *Intermetallics* ***7*** (1999), pp. 863-874.

[82] B. Grushko, W. Kowalski, D. Pavlyuchkov, B. Przepiórzyński, M. Surowiec, *Journal of Alloys and Compounds* ***460*** (2008), pp. 299-304.

Conclusions and perspectives

The main objectives of the present study were first to control the aluminium activity during slurry aluminizing of nickel-based alloys by adding Cr microparticles in the slurry compositions, to get low-activity aluminide coatings, and then to study the effect of introduced Cr on the high-temperature oxidation and the hot corrosion resistance of the coating systems.

In a first step, it was necessary to control the exothermic reactions occurring between Al microparticles and nickel-based materials upon slurry aluminizing and to investigate the influence of the coating process parameters on the formation of metallic bond coats and of complete thermal barrier systems. In a second step, Cr was added in the slurry compositions and was found to be highly beneficial on several different aspects summarized below after.

The reactivity between Al and Cr microparticles was first determined by DSC using Al-Cr mixtures of different compositions. A highly exothermic reaction occurred by reaction of Al and Cr microparticles at a temperature below the melting point of Al (i.e. 660°C). This exothermic reaction was associated with the formation of Al_xCr_y intermetallic phases of different stoichiometry. The formation of these intermetallic compounds was found to be fast, involving liquid phases, and following self-propagating high-temperature synthesis (SHS) reactions. The following peritectic reactions sequence was proposed to account for the formation of intermetallic compounds: $L + Al_7Cr \rightarrow L + Al_{11}Cr_2 \rightarrow L + Al_4Cr$. The heat change of the system and the stoichiometry of the synthesized Al_xCr_y phases was dependent on the initial Al-Cr ratio and on the size of the microparticles involved in the reaction. After the initial exothermic reaction, solid state diffusion mechanisms of Al and of Cr were mainly involved. The reactivity between Al-Cr mixtures and pure nickel, as a model material, was also studied and demonstrated that the addition of Cr limited the exothermic reaction usually observed between pure Al microparticles and nickel-based materials.

From these results and based on literature, three compositions were then selected to investigate the role of Cr upon aluminizing of pure nickel substrate (67Al33Cr, 44Al56Cr and 20Al80Cr mixed slurries in wt.%). Upon aluminizing, Al preferentially reacted with Cr in the slurry rather than with the nickel substrate. This considerably limited the exothermic reactions between Al microparticles and the nickel substrate at low temperature (i.e. 650°C) by comparison with a Cr-free slurry composition. Consequently, the addition of Cr hampered the formation of Al-rich nickel aluminides at low

temperature. With further annealing at high temperature (i.e. 1000°C or 1080°C), interdiffusion between the nickel substrate and the Al_xCr_y phases synthesized in the slurry deposit was promoted. The predominant outward diffusion of nickel at high temperatures allowed to progressively dissolve the Al_xCr_y phases leading to the direct formation of the β-NiAl phase with undissolved Cr.

Thanks to the versatility of the slurry coating method, different coating architectures were then tested to optimize the coating properties. Two systems were thus investigated on pure nickel, the Al-Cr and the Cr-Al double-layer systems. The mechanisms of formation of the coatings were described based on the experimental observations and the DSC measurements. The Cr-Al double-layer system appeared as the most adequate functional design for the aluminizing of nickel-based materials.

The results obtained on pure nickel were then extrapolated to a Ni-Cr alloy (Ni-20Cr-1.5Si in wt.%) to CM-247 LC superalloy. The addition of Cr was found to allow the control of the exothermic reactions with the substrates upon aluminizing. As observed with pure nickel, the Cr-Al double-layer system appeared as the best coating design. It appeared that the initial Al-Cr ratio of the slurry deposit had a tremendous influence on the final coating microstructure. The threshold to achieve "low-activity" coating microstructures on CM-247 LC was between 56Cr-44Al and 67Al-33Cr compositions (in wt.%). Based on literature and on the experimental observations, the mechanisms of formation of the diffusion coatings could be explained. The results generally agree with the standard CVD aluminizing processes with two major coating microstructures: "low-activity" and "high-activity" coatings. The inert carbides present in the superalloy microstructure were used as natural markers to identify the initial surface of the substrate before aluminizing.

For the low-activity coatings (56Cr-44Al composition), the growth of the coating occurred by predominant outward diffusion of nickel at high temperature (i.e. 1080°C). The direct formation of the β-NiAl phase occurred and the coating presented a typical duplex microstructure with an outer additive layer formed above the initial surface of the substrate and an inner interdiffusion resulting from the nickel withdrawal. After annealing, undissolved Cr remained in the additive layer of the coating because of its limited solubility in the β-NiAl phase.

For the high-activity coatings (33Cr-67Al composition), the growth of the coating occurred by predominant inward diffusion of Al at low temperature and outward diffusion of nickel at high temperature. The initial inward diffusion of Al resulted in the precipitation of low solubility elements (i.e. Cr, Ta and W) in the outer region of the coating. The annealing temperature (1000°C or 1080°C) had a tremendous impact on the final microstructure of the coating and was ascribed to the enhanced

outward diffusion of nickel at 1080°C than the one at 1000°C. The high-activity coatings presented a fine distribution of Cr-rich phases and large substrate carbides in a β-NiAl matrix.

The different aluminizing treatments carried out on nickel-based materials in Chapters III and IV focused on the formation of the metallic bond coats. The different heat treatments were performed in Ar to prevent the oxidation of the microparticles. However, the ceramic top coats composed of hollow alumina spheres were generally very brittle after heat treatment in Ar. Therefore, the influence of the atmosphere (Ar, air) on the formation of complete thermal barrier systems was investigated (Chapter V).

The nature of the atmosphere (Ar, air) had a significant influence on the oxidation of Al microparticles and on the release of Al upon aluminizing. The thermogravimetric measurements were used to interpret the experimental observations. The introduction of air in the reaction chamber was found to significantly increase the growth of the oxide shells surrounding the Al microparticles. The thickening of the alumina shells in air considerably increased the sintering of the microspheres and their adherence to the underlying bond coat by comparison with the samples annealed in Ar. Consequently, the mechanical resistance of the ceramic top coat structure was greatly improved by performing the annealing treatment in air. On the opposite, the atmosphere had little influence on the aluminizing of the nickel substrate when only Al microparticles were used as donors. The metallic bond coats were then based on the β-NiAl phase after annealing at high temperature (i.e. 1100°C).

When a Cr interlayer was placed between the nickel substrate and the Al microparticles, the mechanisms of formation were significantly different in Ar and in air. The oxidation of the Cr microparticles into Cr_2O_3 was found to considerably decrease their reactivity with Al at temperatures lower than 900°C. The peripheral oxidation of Cr microparticles suppressed the exothermic reaction identified at about 640°C between Al and Cr microparticles. Consequently, the Cr interlayer acted as a barrier for diffusion for the Al, which was oxidized in the top coat structure. This resulted in the formation of a highly sintered ceramic top coat structure based on hollow alumina spheres. The introduction of air in the reaction chamber was also susceptible to initiate aluminothermic reactions.

Finally, the environmental resistance of the slurry coatings developed in this work was tested in hot corrosion and oxidation conditions. The use of pure nickel in the SO_2/SO_3-containing atmosphere confirmed that the p_{So_3} of the reaction chamber was sufficient to sustain Type-II hot corrosion conditions at 700°C. The application of slurry coatings (simple aluminide and Cr-modified coatings) was found to considerably increase the oxidation-sulfidation behaviour of pure nickel. After a total exposure of 300 hours in synthetic air + 0.5% SO_2, the Cr-modified coating was not attacked whereas the simple aluminide coating was prone to localized attacks in the form of protrusions. The growth of these protrusions was found to occur by inward diffusion of O and outward diffusion of Al forming porous Al_2O_3 precipitates within the nickel aluminide phases. In Type-II hot corrosion conditions (in presence of Na_2SO_4), the slurry coatings presented an incubation period greater than 20 hours. After initiation of the corrosion attack, the propagation rate was significantly lower for the Cr-modified coating than that of the simple aluminide coating. The beneficial effect of Cr on the Type-II hot corrosion resistance was attributed to the saturation of the salt mixture with chromate anions and the subsequent precipitation of Cr_2O_3 from the melt. The formation of Cr_2O_3 was found to seal the reactive sites of the coatings and isolating them from the salt mixture. Such observations had not been reported yet in Type-II hot corrosion conditions. This was also ascribed to foster the establishment of a dense and continuous α-Al_2O_3 scale on the surface.

The cyclic and isothermal oxidation behaviour of the low-activity coatings was tested on CM-247 LC at 1000°C. The coatings presented high surface stability forming a dense and continuous α-Al_2O_3 scale on the surface. The thermal stresses induced under cyclic conditions had little influence on the spallation resistance of the α-Al_2O_3 scale. For long term exposure, outward diffusion of Ti, Ta and Hf from the CM-247 LC substrate occurred and these elements became incorporated within the α-Al_2O_3 scale. However, these enrichments had little influence on the performances of the coating after exposure for 1000 hours and 1000 cycles at 1000°C. The Cr was found to segregate in the outer region of the coating and may have a beneficial effect under hot corrosion conditions. The main degradation mechanism observed for the low-activity coating was the formation and the growth of a secondary reaction zone (SRZ) in the sub-region of the diffusion coating. This SRZ resulting from the inward diffusion of Al decreased the solubility of refractory elements, which led to the formation of needle-shaped precipitates.

However, after this work, some questions have not yet been answered that can be considered as interesting perspectives of investigation in future works. A non-exhaustive list of these perspectives is given below after.

Concerning the reactivity of the metallic powders and the synthesis of the Al-Cr donors:

- *Thermodynamic calculations to determine the Al activity in the different slurry compositions and at different temperatures.*
- *Correlation of the thermodynamic calculations with experimental observations of slurry aluminizing.*

For the reactivity between Al-Cr donors and nickel-based materials:

- *Synthesis of bulk Al-Cr intermetallic compounds of different stoichiometry (e.g. Al_7Cr, Al_4Cr, Al_8Cr_5, $AlCr_2$) to investigate their reactivity with nickel-based materials.*
- *Investigate the reactivity of the Al-Cr mixed slurries with a nickel-based superalloy.*

For the aluminizing of nickel-based superalloys:

- *Extrapolate the results obtained on CM-247 LC superalloy to other nickel-based superalloys.*
- *Better control of the aluminizing process based on thermodynamic calculations.*
- *Aluminization tests on real turbine components (e.g. turbine blades).*

For the influence of the atmosphere on the formation of complete thermal barrier systems:

- *The determination of the partial pressure of oxygen in the reaction chamber upon coating formation should give valuable information on the mechanisms of oxidation and of sintering of the individual aluminium microspheres.*
- *Extrapolate the results obtained on nickel-based superalloys.*
- *To form intermetallic-oxides composite materials, it would be interesting to propose a coating design based on aluminothermic reactions (with NiO and Cr_2O_3 especially).*
- *Further determine the thermal insulation performances of the ceramic top coat structures using the laser flash method (LFA).*

For the environmental resistance of the slurry coatings:

- *Investigate the early-stage exposure of the slurry coatings under Type-II hot corrosion conditions for a precise identification of the initiation stage.*
- *Use XPS (X-ray Photoelectron Spectrometry) or other extreme surface techniques to precisely identify the oxide scales formed at low temperature (i.e. 700°C) and confirm Raman analyses.*
- *The influence of the Cr-rich phases (i.e. residues of the aluminizing process) on the hot corrosion resistance should be evaluated.*

- *The different coating microstructures obtained on CM-247 LC (Cr-modified aluminide coatings) give interesting perspectives for hot corrosion resistance. The distribution of the Cr-rich phases in the β-NiAl coating matrix is presumed to influence the hot corrosion resistance of the coating.*
- *Realize Type-II and Type-I hot corrosion tests of the Cr-modified aluminide coatings developed during this work on nickel-based superalloys.*
- *Increase the oxidation time upon cyclic conditions to reach the limit of the slurry coatings developed.*

For the erosion resistance and the repairability of the coatings:

- *The thermal barrier coatings elaborated in Ar presented low erosion resistance. Scratch tests and tests with erosive particles (e.g. grit blasting) could therefore be conducted to evaluate the erosion resistance of the complete thermal barrier systems elaborated in air. The increased sintering of the alumina hollow microspheres should be beneficial on this aspect.*
- *In the industrial repair processes, grit blasting is commonly employed to remove degraded thermal barrier coatings. It would therefore be valuable to investigate the potential repairability of the thermal barrier systems following industrial standard processes.*
- *The chemical stripping of the nickel aluminide coatings is also feasible for repair issues.*

Annexes

Annex I

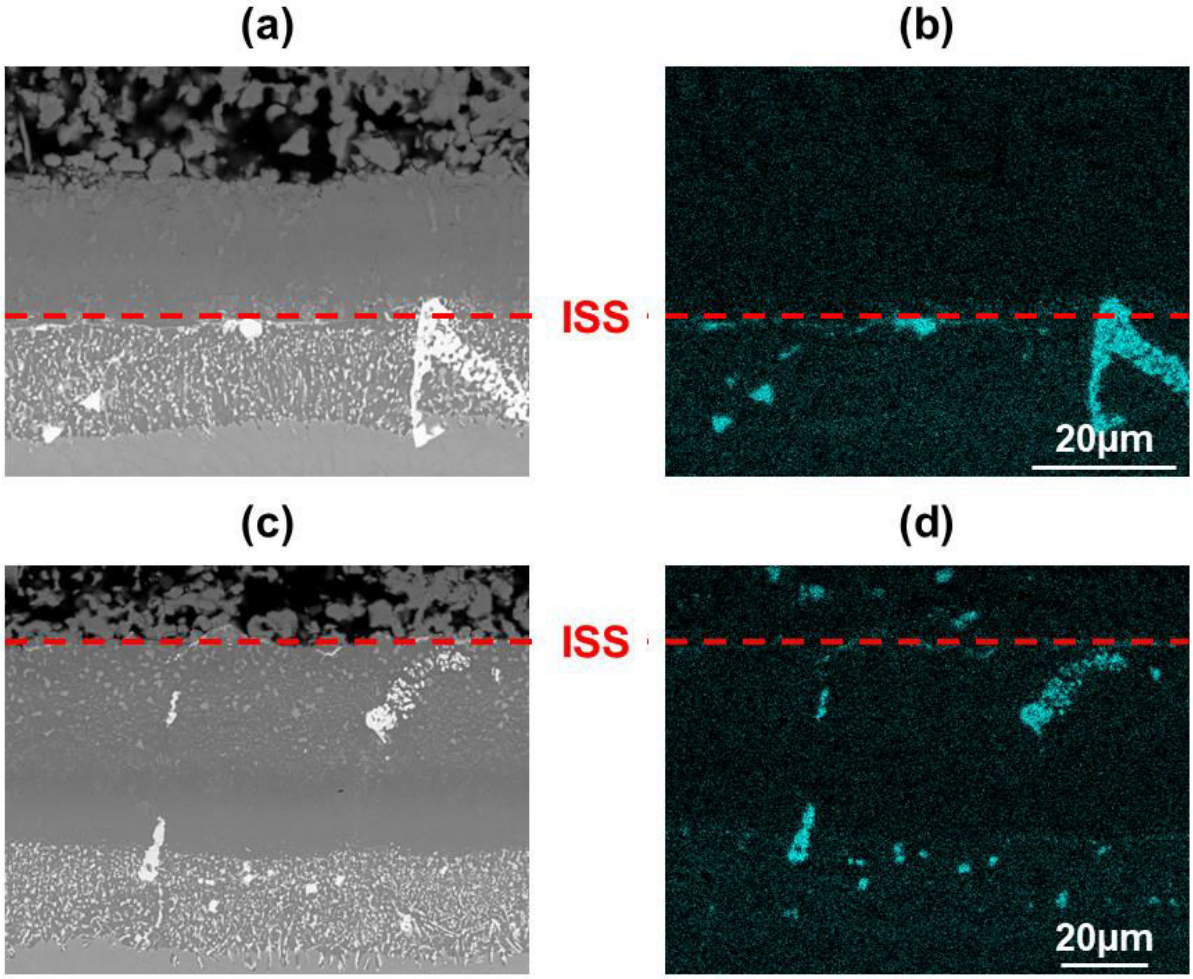

Fig. 1. BSE cross-section images and corresponding X-ray maps of Hf for (a), (b) an outwardly and (c), (d) an inwardly grown coating on CM-247 LC superalloy. The initial surface of the substrate (ISS) is highlighted with the position of the substrate carbides after the aluminizing process.

Annex 2

The laser flash analysis (LFA) was carried out to measure the thermal diffusivity of uncoated and coated samples to evaluate the thermal insulation behaviour of the slurry coatings (cf. paragraph IV.I. in Chapter II). The thermal diffusivity measurements for uncoated pure Ni and Ni slurry coated with "PARTICOAT" are given as examples in Fig. 2a (2 samples for each system). The thickness of the alumina foam (hollow alumina spheres, cf. Fig. I-13 in Chapter I) was approximately 45µm for the two slurry coated samples.

The thermal conductivity (Fig. 2b) was calculated following *(Eq. II-2)* (cf. Chapter II) from the specific heat capacity and the density of pure nickel (values taken from the literature). The thermal conductivity of the slurry coated samples was lower than pure Ni samples, which highlighted the beneficial role of the alumina foam on the thermal insulation. The data given in Fig. 2a and Fig. 2b was recalculated to estimate the thermal diffusivity (Fig. 2c) hence the thermal conductivity (Fig. 2d) of the alumina foam only. The values were in the same range of order than conventional YSZ (Yttria-Stabilized Zirconia) Air plasma spray coatings.

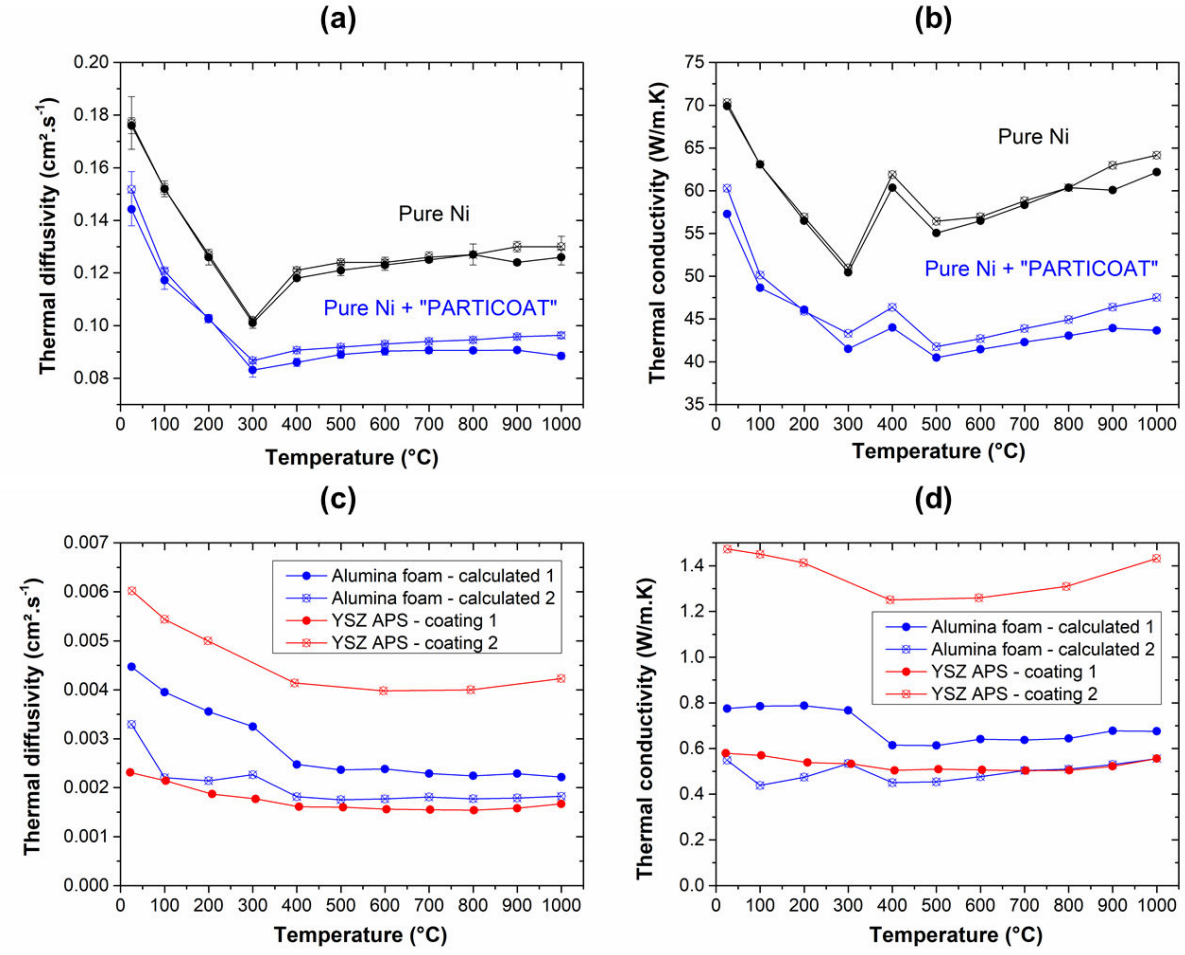

Fig. 2. (a) Thermal diffusivity measurements and (b) calculated thermal conductivity of pure Ni samples with no coating and with "PARTICOAT" and (c), (d) calculated values for the alumina foam (comparison with self-standing YSZ APS coatings).

Annex 3

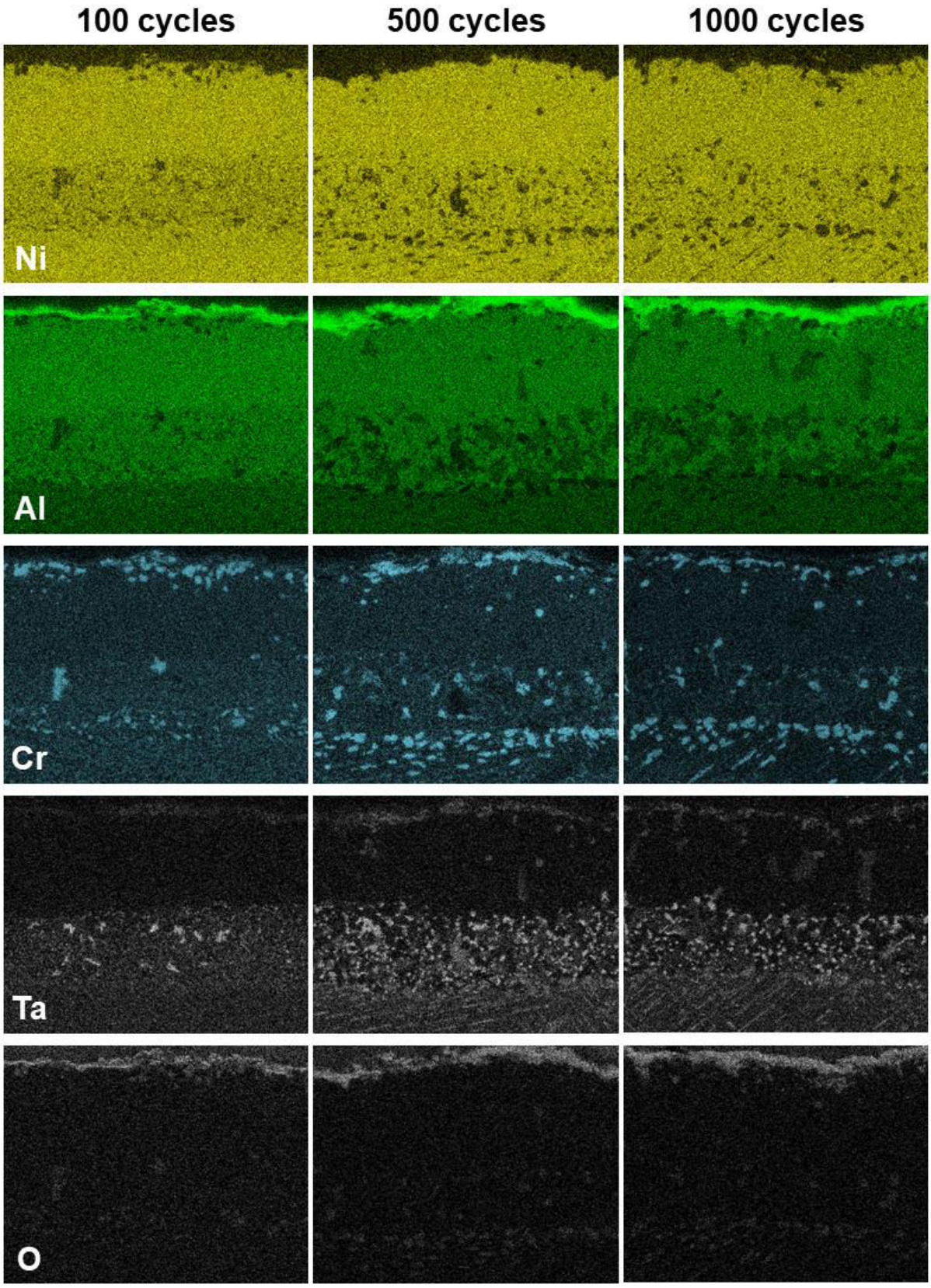

Fig. 3. X-ray maps of the Cr-Al coating elaborated on CM-247 LC superalloy after cyclic oxidation at 1000°C in air.

Fonctionnalisation des barrières thermiques aéronautiques élaborées par barbotines

La sélection des matériaux utilisés dans les moteurs aéronautiques est un enjeu majeur pour assurer la sécurité des passagers, optimiser les performances de l'avion et maîtriser les coûts. Dans les parties les plus chaudes des moteurs (i.e. chambre de combustion et turbine), les pièces sont généralement constituées de superalliages à base nickel en raison de leurs excellentes propriétés mécaniques à haute température. Vulnérables aux phénomènes de corrosion et d'oxydation à haute température, les superalliages doivent la plupart du temps être revêtus afin de prolonger leur durée de vie (ingénierie de surface). La composition chimique et l'architecture des revêtements sont alors adaptées en fonction du régime de température et des phénomènes de dégradation rencontrés (i.e. corrosion à chaud, oxydation et/ou érosion). En vue de répondre aux nouvelles réglementations environnementales, de nouvelles voies de synthèse et de fonctionnalisation sont à l'étude comme alternatives aux procédés industriels actuels.

Dans le cadre du projet Européen « PARTICOAT », le LaSIE a démontré la faisabilité d'élaborer des systèmes barrières thermiques complets (couche de diffusion + barrière thermique) en une seule étape à partir de barbotines (« *slurries* ») à base aqueuse contenant des microparticules d'Al. Dans cette étude, l'ajout de Cr comme dopant a été étudié. L'addition de Cr a permis d'abaisser l'activité de l'Al lors de l'étape d'aluminisation et de limiter les réactions exothermiques entre Al et substrat à base de nickel. L'optimisation des ratios entre Al et Cr a permis d'obtenir différentes microstructures de revêtement. Diverses architectures de dépôts ont également pu être testées grâce à la souplesse d'élaboration des revêtements par barbotines. L'influence de l'atmosphère (Ar, air) et celle des conditions de traitement thermique ont également été étudiées. Enfin, la durabilité des revêtements développés au cours de la thèse a été évaluée au cours d'essais de corrosion à chaud et d'oxydation.

Mots-clés: *Barbotines, aluminisation, protection haute température, corrosion à chaud, oxydation.*

Functionalization of aeronautical thermal barrier systems elaborated by slurry

The selection of materials is of utmost importance in gas turbine engines to ensure the security of the passengers, optimize the performances of the aircraft and be cost efficient. In the hottest region of the engines (i.e. combustion chamber and turbine), the components are usually made of nickel-based superalloys. These materials can resist to high mechanical loads at high temperature but are vulnerable to aggressive environments. Therefore, nickel-based superalloys are usually coated to increase their durability in the engine (surface engineering). The chemical composition and the coating architecture are carefully adjusted depending on the temperature regime and the mechanisms of degradation encountered (hot corrosion, oxidation and/or erosion). New synthesis routes and functionalization are currently developed as alternative solutions to industrial processes.

As a promising alternative approach, different studies were carried out in the LaSIE laboratory under the European project "PARTICOAT" and confirmed the possibility to elaborate complete thermal barrier systems (diffusion coating + thermal barrier coating) from Al-containing water-based slurries. In this work, the role of Cr as a doping agent was investigated. The addition of Cr decreased the thermodynamic activity of Al upon aluminizing and limited the exothermic reactions usually reported between Al and nickel-based materials. Different architectures of coatings were obtained thanks to the flexibility and the adaptability of the slurry coating process. The gas composition (Ar, air) and the heat treatment conditions were also investigated. Finally, the high temperature resistance of the slurry coatings developed during this work was evaluated under hot corrosion and oxidation conditions.

Keywords: *Slurry coatings, aluminizing, high-temperature protection, hot corrosion, oxidation.*

Laboratoire des Sciences de l'Ingénieur pour l'Environnement
LaSIE (UMR-CNRS 7356)
Bâtiment Marie Curie, Avenue Michel Crépeau
17042 La Rochelle Cedex 1